Investigating the Time-Resolved Spectroscopy of Singlet and Triplet State Dynamics in Conjugated Rylene and Quinoline Derivatives for Efficient Optoelectronic Systems

by

Angelar Kanini Muthike

A dissertation submitted in partial fulfillment
of the requirements for the degree of
Doctor of Philosophy
(Chemistry)
in the University of Michigan
2022

Doctoral Committee:

Professor Theodore G. Goodson III, Chair
Professor Ryan Castle Bailey
Professor David H. Kohn
Professor Charles McCrory

Angelar K. Muthike
amuthike@umich.edu
ORCID ID: 0000-0002-4850-0827

DEDICATION

This edition of my dissertation is dedicated to three women who built the strong foundation on which I stand today: my late mother, Ms. Petronillah Muthike Kisimbii (*Mami*) and my late grandmother, Mrs. Kathungi Kisimbii Munee (*Susu*). They were my first teachers who instilled in me the great life principles that I continue to live by, and rendered their unwavering support to their last days. May their sweet souls continue resting in heaven. Then there is Caroline Maithya, the little girl who dreamt of attending Precious Blood Girls School-Kilungu (my high school alma mater). Unfortunately, she died at the age of 4. To live her dream, her brother, Gerald Maithya, started the Precious Sisters (PS) Charity Fund, a program that paid my high school fees and has continued to support my academic journey to this day. PS has also supported hundreds of Kenyan girls from humble backgrounds through high school and college both in Kenya and abroad.

ACKNOWLEDGEMENTS

Completing this dissertation would not have been possible were it not for my Ph.D. advisor, Prof. Theodore Goodson III. When I joined the Chemistry Department at the University of Michigan, my research idea was to apply laser spectroscopy in just understanding biological systems. When I told Prof. Goodson about it, he was very supportive and helped me to not only explore but also expand this idea to make this dissertation a reality. With his help, I built collaborations that have enabled me to use time−resolved and nonlinear optical laser spectroscopy to understand charge and energy transfer for various optoelectronic applications. Charge transfer naturally happens during photosynthesis and therefore, laser spectroscopy of optoelectronics mimics this natural occurrence in biological systems (plants). Thank you Prof. Goodson for giving me the opportunity and support to explore the world of laser spectroscopy and scientifically contribute to the growing wealth of optoelectronic knowledge. The conclusions made in this dissertation will be useful in designing more efficient optoelectronic systems.

In Professor Goodson's group, I have met scholars in whom I have found a strong support system of both friends and scientific collaborators. Thanks to the current and past members of the GOODGroup for your support in settling in and navigating my Ph.D. journey. Special thank you to Dr. Bradley Keller, Dr. Prabhat Sahu, Dr. Benedetta Carlotti, Dr. Ifeanyi Madu, Dr. Ricardo Vazquez for their immense support in learning the fundamentals of laser spectroscopy research and their collaborative efforts. I would also like to acknowledge the very knowledgeable Dr. Oleg Varnavski for always answering my questions regarding instrumentation and core research.

To all the other scholars and collaborators th\at I have met and worked with, at the University of Michigan and beyond, you have all contributed to my growth as a scientist, and I thank you all. I would like to highlight the Zimmerman group at the University of Michigan, Yu's group at the University of Chicago, and Wilson's group at Michigan State University. You all made the work in this dissertation possible, I am grateful and I appreciate all your help. Thanks also to Steve Katnik, the laser spectroscopy expert who never hesitated to render his help when my laser broke down.

To the members of my dissertation committee: Prof. Charles McCrory, Prof. Ryan Castle Bailey, and Prof. David H. Kohn thank you for your immense support and for providing very valuable feedback throughout my journey as a Ph.D. student. Your suggestions were very instrumental in shaping and directing this dissertation.

To my undergraduate supervisor and mentor, Prof. Peter C. Chen, your guidance and mentorship throughout my undergraduate career was very influential in my decision to pursue a Ph.D. in Analytical Chemistry. It is through my experience in your research group that I developed an interest in research as a career. I am forever grateful. To all my other professors who believed in me and guided me in ways that I cannot list here, thank you. My time at Spelman College would not have been the same were it not for the support of Mary Nyacomba and Memo Acevedo, thank you for being the best host parents and taking me in as your child. May God bless both of you.

To my high school (Precious Blood Girls School-Kilungu) teachers and especially my STEM teachers Mr. Ndolo, Mr. Kinaka, Mr. Joseph Munyao, Mr. Christopher Muteti, Mr. Godfrey Muriugi, Mr. Muia, Mr. Ndalalu, and Mr. Eliakim Mureithi, thank you for making STEM so much fun and inspiring me to pursue a STEM-related field.

My education at Precious Blood would not have been possible were it not for the support of the Precious Sisters Charity Trust. Thank you, Wallace and Muthoni Garland, Ann Waweru, and all the PS mentors for running this charity trust that has helped so many girls go through high school. To **Norma and Martyn Boultwood**, thank you for not only sponsoring me through high school, but being more than mentors, you are my forever Auntie and Uncle and I love you two. I would never have met anyone from the PS community were it not for Gerald Maithya who started this Charity. Gerald, your idea to

give young African girls a chance to get an education is shaping generations and communities. Thank You, Gerald.

To my primary (Itithini Primary) school teachers especially Mr. Joseph Kilavi who was the head teacher during my time, your support throughout my primary school and putting everything aside to make sure I joined Precious Blood Kilungu High School is greatly appreciated. Thanks to all my other primary school teachers especially Mr. Joseph Munyao and Mr. Alexander Ngumbau for believing in me.

To my elder sister Agnes Mwende Muthike and my younger brother Brian Kalani Muthike, thank you for being my pillars of support from our childhood. My niece Angelar Muthike Mwende, who got the best name in the world, and my nephew Karl Kali Kalani, who I got the privilege to name, came at the right time and have brought along so much joy in my life. *Nawapenda sana, ninimwendete muno*.

TABLE OF CONTENTS

LIST OF FIGURES

LIST OF TABLES

ABSTRACT

The increasing global population has led to increased energy demand and consumption due to the rise in the value of electricity for lighting and powering entertainment, heating, medical and communication devices. This increase has also led to high demand for cheap next−generation devices with improved performance and a broad range of applications increasing the optoelectronics demand. While the conventional inorganic optoelectronics have shown great performances, their high cost of production, as well as low processability and flexibility, has shifted the attraction to organic optoelectronics which have shown high optical absorption, high mechanical flexibility and lightweight, high tunability and are cheap to fabricate. Since the demonstration of this first device, organic semiconductors have found their way into the consumer market with a myriad of applications like organic light-emitting diodes (OLEDs) for color display systems, organic photovoltaics (OPVs) for low lost and efficient organic solar cells, and organic light-emitting transistors (OLETs) which is a new class of optoelectronics that combine the switching capabilities of a transistor and the emissive properties of OLEDs.

Thus far, $\pi -$ conjugated systems with donor and acceptor moieties have shown the most semiconducting promise owing to the delocalization of $\pi -$ electrons that move along the conjugation chain. Bonding (π) and antibonding (π^*) molecular orbitals overlap at this conjugated backbone, creating a strong electron density which then supports moving charge carriers. The longer the conjugation chain, the stronger the overlap which determines the energy gap (E_g) between the highest occupied molecular orbital (HOMO) and the lowest unoccupied molecular orbital (LUMO). The energy gap, as well as the polymer structure, affect the processes of charge transfer (CT) and the energy transfer (ET) of the semiconducting material. Some of these processes that have been reported to influence the ultimate performance of the respective optoelectronics include singlet exciton fission (SEF), thermally activated delayed fluorescence, and diradical or biradical formation.

To design materials for highly efficient and stable optoelectronic devices, it is therefore very important to understand these processes and how they relate to the structure and function of materials. As a result, this thesis focuses on using both linear and nonlinear optical as well as time-resolved spectroscopy techniques to expand the understanding of CT and ET of key processes that define the photophysical properties of organic optoelectronic systems. In particular, the structure-function relationships that affect the charge and energy transfer dynamics of materials for efficient optoelectronics are elucidated.

In summary, it was found that for OPVs, the flexibility of the π–linker, its point of attachment in the PDI units, and its molecular dielectric environment are important in activating SEF which increases the device efficiency. For OLEDs, a new approach that can be used to experimentally calculate the rate of reverse intersystem crossing in TADF organic molecules was proposed. It was found that both large rates of intersystem crossing and high external quantum efficiency translate to low operating voltages of the investigated chromophores. It was also evident that molecules need a reverse intersystem rate greater than a millisecond to be able to undergo the TADF process. Finally, the first evidence of diradical formation which reduces the efficiency of OLETs is reported. Overall, this dissertation uses time-resolved spectroscopy to improve the current understanding of structure-function relationships that affect SEF, TADF, or diradical/biradical formation mechanisms in CT and ET processes for OPVS, OLEDS, and OLETs.

Chapter 1

Introduction, Background, and State of The Art of Organic Optoelectronic Systems

1.1 History of Organic Optoelectronics

Richard Soref defined optoelectronics as the integration of optics and electronics on the same substrate to obtain chips referred to as optoelectronic integrated circuits (OEICs) whose performance outdoes those of the individual optical and electrical circuits.[1] In short, optoelectronics are electronic devices that emit or detect light. Those that emit light use voltage and current to produce electromagnetic radiation (EMR) while those that detect light do the opposite, i.e., converting the electromagnetic energy into current and voltage (**Figure 1.1.1**).

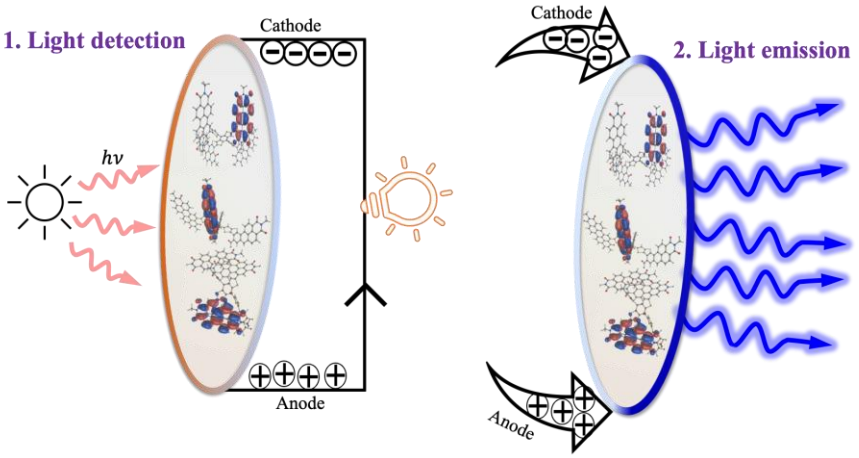

Figure 1.1.1: Illustration of light detecting and light emitting processes

Light emitting devices can be used for display systems and indicator lights while light-detecting devices have been used for light sensing in switches and communication in remote controls. In the earlier days, optoelectronics systems were made using inorganic semiconductors like silicon and gallium arsenide which, although they perform very well, huge mismatches existed in their application-based structure and properties.[2] Here,

controlling the inorganic thin film thickness and structure saw huge improvements in the optoelectronics based on multiple quantum wells (MQW) which affect the density of conduction and valence band states and the heterojunction energy band offsets.[3] These lead to low-threshold current laser diodes, low-noise avalanche photodetectors, and high bandwidth optical modulators.[3] However, these devices' large-scale production was very costly, and they faced low compatibility with flexible substrates. In addition, the processability of these inorganic compounds is difficult making it a challenge to use deposition and solution-based processes and hindering the extent of use.[4] One way around these drawbacks was to start using organic semiconducting materials which showed high optical absorption, high mechanical flexibility and lightweight, high tenability, and were cheap to fabricate, and use the same procedure to control the density of states as well as energy band offsets between differing materials. [3,5,6] It was possible to process these organic materials using different methods like spin-coating since they were processable, the thin-film deposition could be done at room temperature, their properties were tailorable, they were biocompatible and most importantly, their cost of production as well as a fabrication was significantly lower than that of organic semiconductors.[2] Halogen derivatives of polyacetylene which were among the first organic semiconductors were synthesized by Shirakwa *et al.* in 1977 following their initial success in the synthesis of highly flexible and good quality copper-colored films (**Figure 1.1.2**).[7]

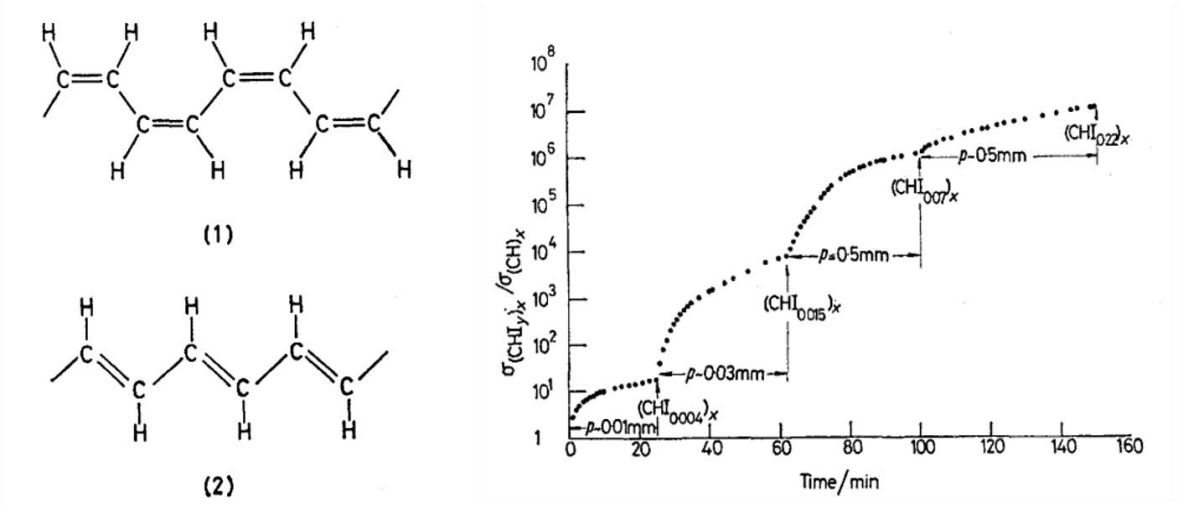

Figure 1.1.2: On the left is: (1) *cis*-isomer used to make flexible copper-colored films and (2) *trans*-isomer used to make silvery films. On the right is the increase in room

temperature conductivity of organic *trans*-polyacetylene $(CH)_x$ as a function of time at fixed iodine vapor pressures adapted from Shirakwa *et al.*).[7]

For more than 6 decades, scientists have focused on investigating the capabilities of organic electronics and sieved through the enormous practical application aspect to almost pure research in a domain right at the intersection of organic electronics and optical phenomena. [3,8] Despite concerns of device stability and hence performance in comparison the conventional silicon-based semiconductors, the growing understanding of organic materials and semiconductors has promoted the advancement of these optoelectronic systems over the years since Chin Tang and Steven VanSlyke of Kodak demonstrated the first light emitting diode (LED) in 1987s.[2,3,5,8,9] This novel electroluminescent device fabrication was based on the idea that most organic materials possess high fluorescence quantum yields in both the visible and the ultraviolet region making them ideal candidates for multicolor display applications.[9] Here, and in contrast to the previous attempts to make decent electroluminescent devices by using single layer semiconductors, this successful debut employed the use of a double layer of an organic thin film with distributed polar transportation roles as shown in **Figure 1.1.3**.

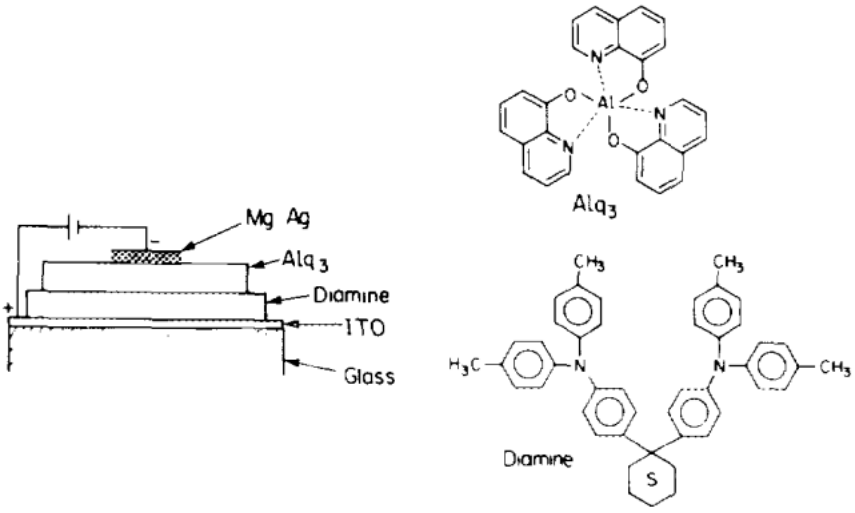

Figure 1.1.3: Device configuration and molecular structures of the indium-tin-oxide (ITO) coated glass device fabricated by Chin Tang and Steven VanSlyke.

An aromatic diamine was used as the first organic layer with around 750 Å while a luminescent film with 600 Å was used as the second layer. In this device, a low-work

function alloy was also employed as the cathode to enhance electron injection.[9] The electroluminescence diode of this device showed an external quantum efficiency (EQE) of 1%, a power conversion efficiency (PCE) of 0.46% at 5.5 V, and luminous efficiency of 1.5 lm/W which was analogous to the commercial LEDs at the time (**Figure 1.1.4**). However, the device's performance was not too low to get into the market, and more research needed to be done to tune the structural and electrical properties that would eventually result in better EQEs and PCEs. Ideally, organic photovoltaics need a PCE of around 20-25% to get into the market while display systems have achieved up to 80%.[10]

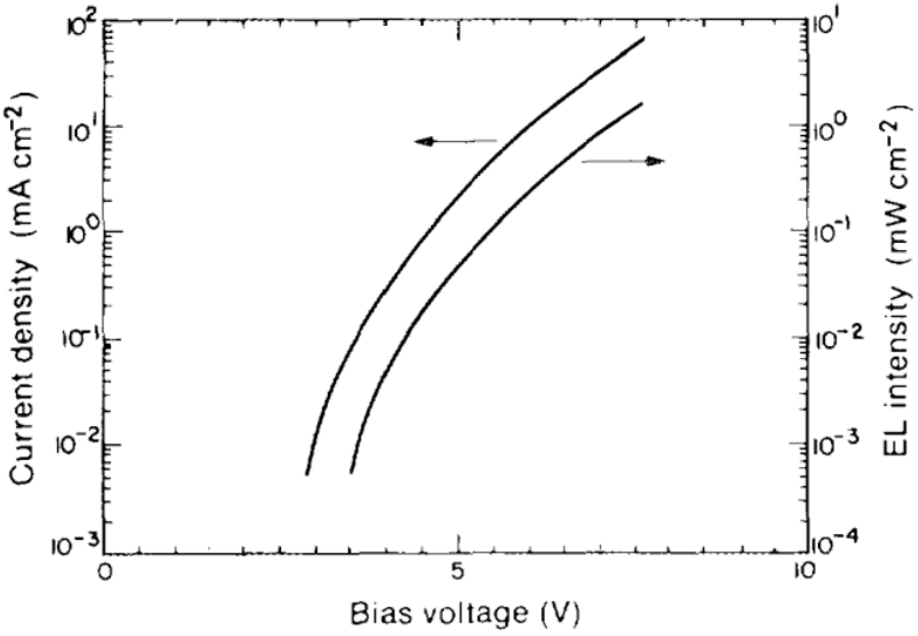

Figure 1.1.4: Brightness-current-voltage characteristics of the ITO/diamine.Alq3/Mg:Ag electroluminescent cell.

Since the demonstration of this first device, organic semiconductors have found their way into the consumer with a myriad of applications (**Figure 1.1.5**) like organic light emitting diodes (OLEDs) for color display systems, organic photovoltaics (OPVs) for low lost and efficient organic solar cells and organic light emitting transistors (OLETs) which is a new class of optoelectronics that combines the switching capabilities of a transistor and emissive properties of OLEDs.[8, 11] other applications include nonvolatile memory devices, photo- and vapor-sensing devices, biological and chemical sensors.[4]

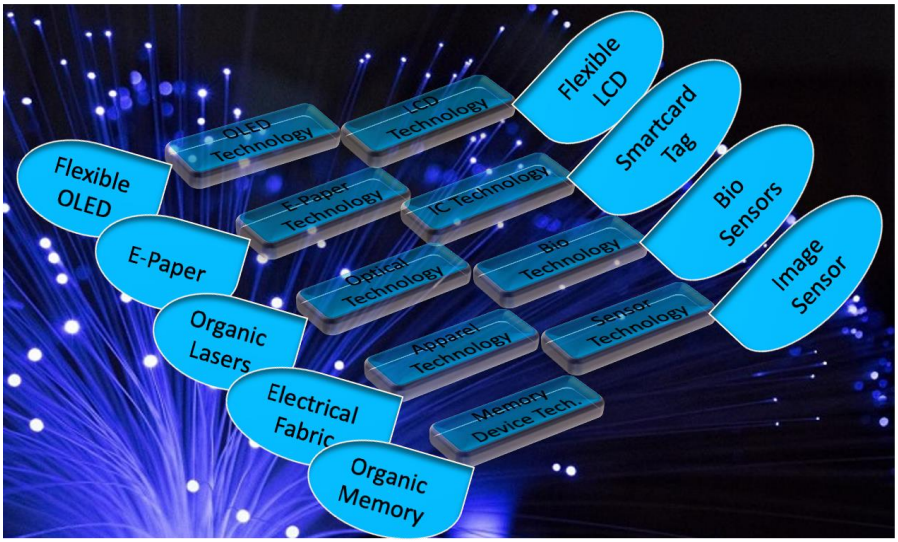

Figure 1.1.5: Myriad of technology that can benefit from organic semiconductors. The initials have been described at the beginning of this dissertation.

The increasing demand for next-generation electronics as shown in **Figure 1.1.5** with very high performance and multifaceted functions has been elevated by the emerging era of the Internet of Things.[12] As a result, a lot of multidisciplinary research has been dedicated to suit this demand. Mostly, researchers seem to study and understand the physical and chemical properties that could be used to develop low-cost, yet high performance optoelectronic devices. Yet, a lot of research is still needed to characterize these materials

1.2 Classifications of Investigated Optoelectronics

1.2.1 Organic Photovoltaics (OPVs)

The increasing global population growth has led to increased energy consumption and demand, which has not only skyrocketed the energy cost; but also led to excessive burning of fossil fuels. The main disadvantages attached to power plants that use coal oil and gas fuel include the usage of valuable and limited natural resources, digging up the earth or drilling wells to get the coal, oil, and gas, waste disposal problems for nuclear power plants, and a lot of pollution. The burning of coal, oil, and gas to generate energy is very harmful to the environment and has resulted in an overall climate change. The climate change is as a result of excessive carbon dioxide emissions that come from electricity

production, pollution that comes from extracting fossil fuels, and low water supply since a lot of water is used in these fossil fuel extraction and processing. Since the early 1970s, this demand has led to increased burning of fossil fuels which, to this day, has led to devastating global pollution. Early studies by researchers like Dasgupta, Heal, and Stiglitz show that exhaustible natural resources like fossil fuels can lead to a stunted economic growth and have pollution as a by-product adds even a more negative impact on the economic welfare.[13] The human-generated greenhouse gases have posed the biggest threat to ecology worldwide, and although there have been combined efforts to reduce the carbon emission footprints through less consumption and better technology, better numbers and technological advancements are still needed. For instance, it was reported that the carbon legacy of a single child can produce up to 20 times more greenhouse gas than a single person will save by driving a high-mileage car, recycling, using energy-efficient appliances and lightbulbs and so on. This report further added that every child born in the United States adds roughly 9,441 metric tons of carbon dioxide to the amount that an average parent contributes. This data point beats the logic of changing lifestyles in order to reduce carbon emissions.[14] This study was published in 2009 when the global population was roughly 6.8 billion. The current world population is ~8 billion, which gives a perspective of the rate of global pollution. Therefore, in addition to the detailed attention that people pay to home energy use, travel and other routine activities that affect carbon dioxide emissions, different policies have been put in place in order to reduce these carbon emissions. Most importantly, scientists started looking for alternative energy sources, renewable energy, which has been for long the least employed source of energy (**Figure 1.2.1.1**), to save the environment.

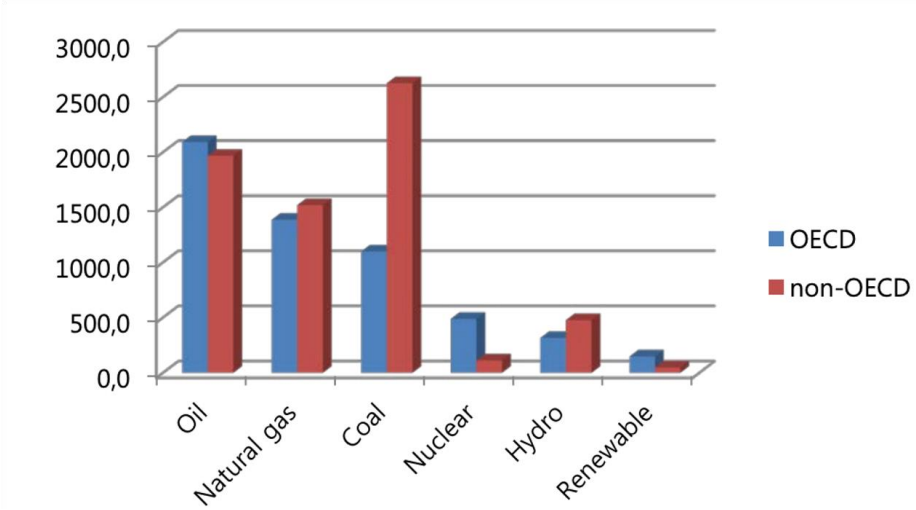

Figure 1.2.1.1: Primary energy consumption by source in 2011, worldwide highlighting differences between the Organization for Economic and Co-operation and Development (OECD) and non-OECD countries.

The major sources of renewable energy are hydro power, wind power, solar power and geothermal. Hydro power is the largest source of renewable energy source in the world and saw a remarkable increase in wattage production from 3400 terawatt-hour (TWh) in 1950 to 2994 TWh in 2005 which could cover a fifth of the required 15,000 TWh global energy consumption at that time.[15] In 2011, the hydropower increased to 1607 GW and today, it represents about 17% of total electricity production. The disadvantages attached to this magnificent source of renewable energy leading to difficulties in hydropower development include: high investment costs, hydrology dependence, inundation of land and wildlife habitat, loss or modification of fish habitat, fish entrainment or passage restriction, changes in water quality and even displacement of local populations. Wind power has continued to compete with hydro power and its installed capacity has shown an increase from 4.8 MW in 1995 to more than 239 GW in 2011. It has been reported that wind energy could generate as much electricity as a conventional power plant. However, there are crucial limitations to the successful use of wind energy. For instance, the cost of installing turbines as well as the operational expenditures can be very high. Geothermal energy is created through radioactive decay at temperatures up to 4,000 ℃ at the core of the earth and stored within the earth. While geothermal energy has the advantage of 24-hour availability and produced a total of 24 GW worldwide, considerations like the geothermal gradient and rock permeability affect the availability of this energy. Solar power is the

most promising source of clean, green and renewable energy. To put this into perspective, the amount of power that hits the earth every hour is more than the amount of power that the entire world's population consumes in a whole year. That is, the 173,000 terawatts of solar energy that strike the earth continuously is 10,000 times the world's total energy use. The amazing fact is, for as long as the sun lives which will be billions of years to come, this energy is completely renewable which is the biggest advantage. As a result, solar power can see great technological advancements if harnessed properly. With this potential, there is a skyrocketing research interest to make semi-conducting materials that could be used to efficiently convert sunlight to electricity.

The science behind the working principles of solar cells was demonstrated by Edmond Becquerel in 1839 who discovered the photovoltaic effect, a process that produces voltage or electric current when exposed to light or radiant energy. In 1883, Charles Fritts the first solar cell by coating selenium with a thin layer of gold. In 1888, Edward Weston received two patents where in both cases, he proposed to transform radiant energy harvested from the sun into electrical energy, or through electrical energy into mechanical energy.[16]

In the first demonstration of the photovoltaic effect (illustrated in **Figure 1.2.1.2**), Becquerel noticed that the voltage of the cell increased upon the exposure of its silver plates to sunlight. In a solar cell, there are two different types of semi-conductors, a p-type and an n-type that are joined together leading to the creation of a p-n junction. The p-type material is composed of atoms that have fewer electrons in their outer energy level while the n-type material is made by including atoms that have more electrons in their outer level than the p-types. As a result, the availability of excess electrons in the n-type layer and excess positively charged holes created by the lack of valence electrons leads to a movement across the p-n junction. This movement of electrons from the n-type layer into the holes on the p-type layer creates a region around the junction called the depletion zone in which the electrons fill up the holes. When all the holes are filled up with electrons in the depletion zone, the p-type side of the depletion zone now contains negatively charged ions and the n-type side of the depletion zone contains positively charged ions. The interaction between these oppositely charged ions leads to an internal electric field that

hinders electrons in the n-type layer from filling holes in the p-type layer and therefore creating a constant flow of electricity.

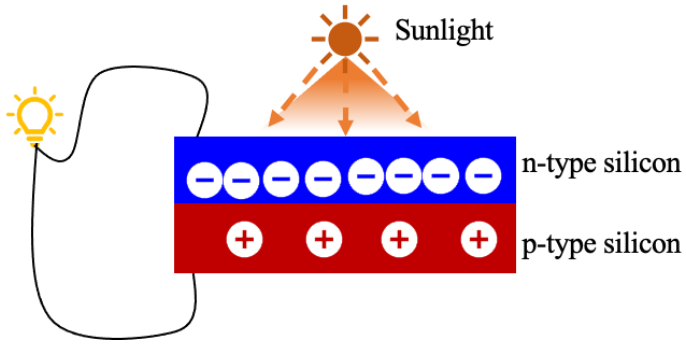

Figure 1.2.1.2: The photovoltaic effect

Traditionally, the p−type was made by adding atoms that had one less electron in their outer energy levels like boron and gallium while the n−type was made from atoms like phosphorous. When the light of the suitable wavelength hits the solar cell, energy from the light photons are transferred to the atom on the silicon semiconducting material leading to the ejection of electrons to a higher energy state called the conduction band. This leads to the creation of holes in the valence band as a result of the ejected electron. The movement of the electron as a result of added energy creates two charge carriers, an electron-hole pair. The resultant electric field will move the electrons to the n-type layer and holes to the p-type layer and with a metallic wire, the electrons can cross the depletion zone and go through the external wire which completes the circuit by connecting to the back of the n-type layer, creating a flow of electricity.

Since the reinvigoration of semiconductor photo-electrochemistry in the 1940s, a lot of research has been dedicated to improving the current literature and expanding the breadth of knowledge and applications in this field. With the first breakthrough of the solar p-n junction solar cells at Bell Labs in 1954 using silicon, silicon has continued to dominate the photovoltaic industry for more than 65 years now. Although silicon-based photovoltaics went through a challenge in supply due to a limited supply line for processor quality silicon for the production industry, the massive expansion of silicon modules in the early 2000s in Europe attracted more investors in the field. This expansion has increased the wattage of

photovoltaics to 0.5 TW and reduces the prices for modules and photovoltaic electricity by almost 80% (**Figure 1.2.1.3**).[17,18]

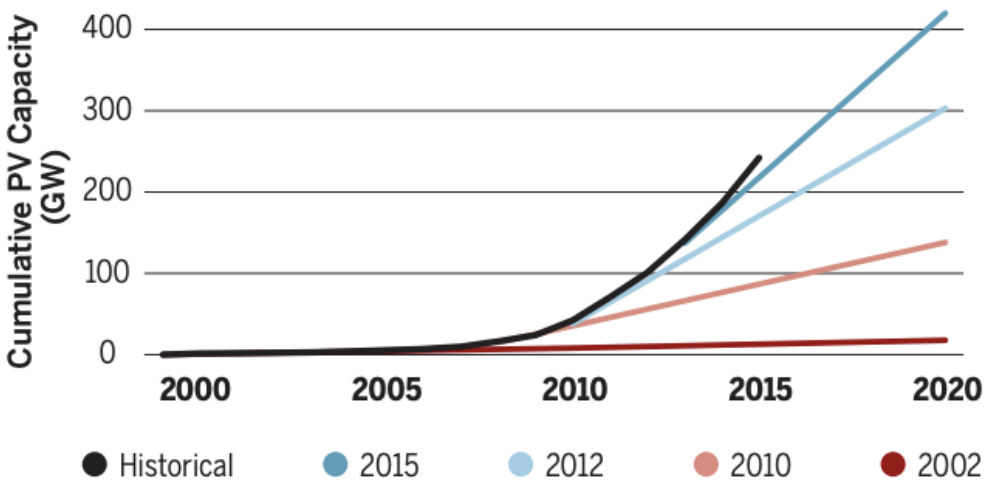

Figure 1.2.1.3: Projected (labeled by year of IEA publication) versus actual (labeled as historical).

However, the disadvantages attached silicon like its over-the-room processing and production cost of silicon, scientists started looking at alternative semiconducting materials. Some materials that have been successfully used include: Cadmium Telluride (CdTe), copper indium gallium selenide (CIGS) whose films were made through the vacuum or electrochemical modes of deposition. The absorption limits led to more focus on organic dyes which have a very strong optical absorption. For a long time, the performance of these organic photovoltaics remained very low based on their power conversion efficiencies (PCE).

PCE is the measure that is used to check the performance of solar cells and it is determined by the maximum power output over the device as a ratio of power output to power input. Usually, this conversion efficiency, η, is derived from relating the open-circuit voltage (V_{OC}), the short-circuit current (J_{SC}), and the fill factor (FF) in the equation below and illustrated by **Figure 1.2.1.4**.[19]

$$\eta = \frac{FF \times J_{SC} \times V_{OC}}{P_{in}} \times 100\% \qquad \text{(Eqn 1.2.1.1)}$$

where P_{in} is the measure of power output per unit volume (power density) of the incident light.

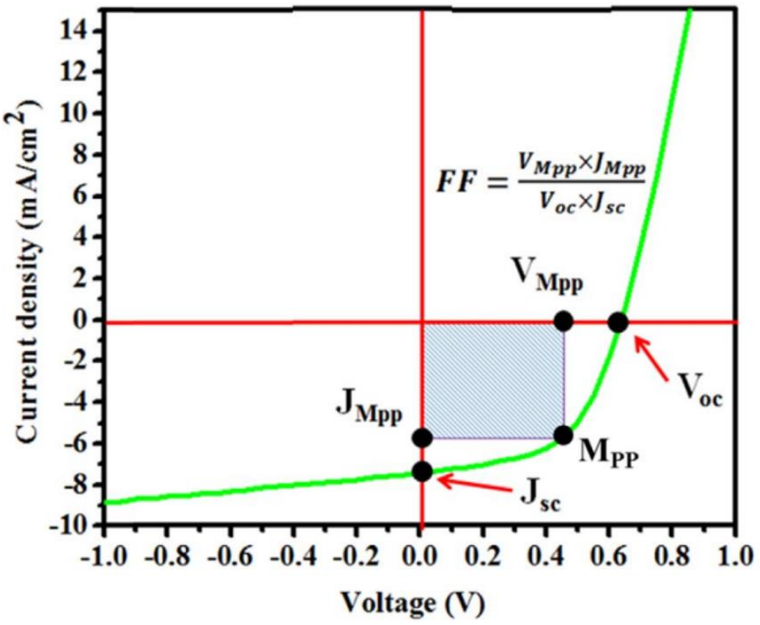

Figure 1.2.1.4: Typical current density-voltage (J-V) curves of an OSC.

As a result, a holistic strategy that can simultaneously improve theopen-circuitt voltage, short circuit current and field factor has been sought to improve the PCE. However, morphological and structural constraints has led to performance tradeoffs. The ideal OPV device simultaneously maximizes light absorption, enhances exciton splitting, and facilitates the carrier extraction. Conventional OPVs were made using a single layer that is sandwiched between two dissimilar electrodes. As such, the built-in potential is derived from either the different work functions of the electrodes or from a Schottky-type potential barrier at one of the matter/organic compounds. In both of these cases, the photovoltaic properties strongly depend on the nature of the electrodes. Another disadvantage of these single-layer OPVs is their poor FF which is usually attributed to their large series of resistance from the insulating nature of the organic layer or the field-dependent generation of charges. Therefore, for these single layer cells, PCEs remained less than 1%.

One way to increase the efficiency of these OPVs was through absorbing more light through making a nonhomogeneous absorbent layer. While a lot of organic materials were

investigated, it was not until 1986 that photovoltaic devices with a power conversion efficiency of 1% from a two-layer organic photovoltaic cell.[20] In a two-layer OPV, the interface especially that responsible for the generation of charges, between the two thin organic layers determines the photovoltaic properties of the solar cell. Since the charge generation efficiency is barely dependent on the bias field, this double layer cell achieves a higher FF compared to a single layer cell.[20] The V_{OC} magnitude in this two-layer cell shows a stronger dependence on the nature of the organic-organic interface than on that of the electrode-organic interface. As a result, the two-layer cells attained a PCE of 1% which was a great improvement.

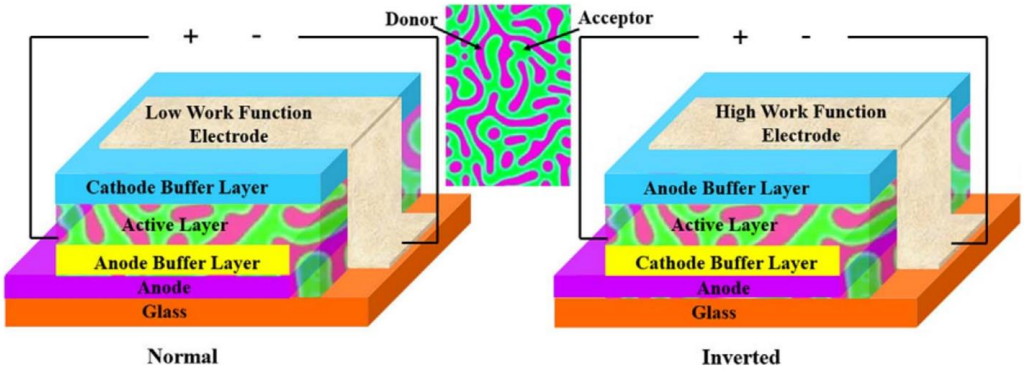

Figure 1.2.1.5: Device architecture of the normal and inverted BHJ OPV.

A major improvement in the two-layer solar cells came with reports of bulk heterojunctions (BHJ) which consists of a multilayer and the absorbent layer consists of a blend of donor and acceptor materials (**Figure 1.2.1.6**). The donor material was usually a conjugated polymer while the acceptor material was composed of fullerene derivatives. While this step saw an increase in PCEs to 10% and a lifetime of several thousand hours under favorable conditions, the stability of solar cells is still an issue. Rafique *et al*. suggested several ways to improve the stability of these BHJ like encapsulation, interfacial engineering, optimization of hole and electron transport layer, morphology control in the photoactive layer, use of inverted geometry and alternative electrodes.[19] Some of the fullerene derivatives used for OSC development included $PC_{61}BM$, $PC_{71}BM$ and $ICBA$.[21–23] Despite the fact that terrific PCEs of up to 18% has been achieved using these fullerene-based solar cells, their fabrication cost remains very high.[21,24,25]

Non-fullerene acceptors (NFAs) have therefore gained a lot of interest due to their facile synthesis, easily tunable optoelectronic properties, strong absorption which can reach the near infrared (NIR) and low fabrication cost.[24,26] The Brookhaven National Lab in collaboration with the U.S. Department of Energy reported a highly efficient NFA using Poly[[4,8-bis[5-(2-ethylhexyl)-4-fluoro-2-thienyl]benzo[1,2-*b*:4,5-*b*′]dithiophene-2,6-diyl]-2,5-thiophenediyl[5,7-bis(2-ethylhexyl)-4,8-dioxo-4*H*,8*H*-benzo[1,2-*c*:4,5-*c*′]dithiophene-1,3-diyl]-2,5-thiophenediyl] (PM6) and dithieno[200 ,300:40 ,50]thieno[20 ,30 :4,5]pyrrolo[3,2-e:20 ,30 -g] [2,1,3]benzothiadiazole (BTP) derivative (BTP-BO-4Cl) as donor and acceptor, respectively, and processed using a halogen-free (using benzyl viologen, BV, instead of halogenated additives solvent reaching an efficiency of 17.33%.[27] The BTP core had a great impact on the molecular aggregation and blend morphology which affected the device performance.

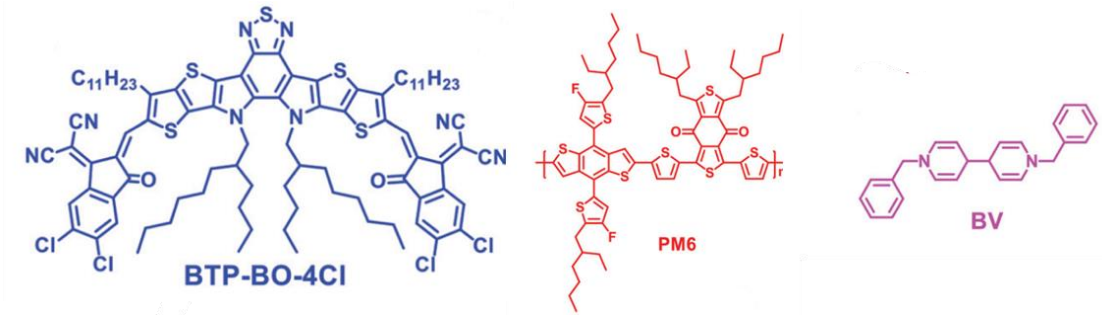

Figure 1.2.1.6: Chemical structure of PM6, BTP-BO-4Cl and BV used for the efficient NFAs to achieve a PCE of 17.3%.

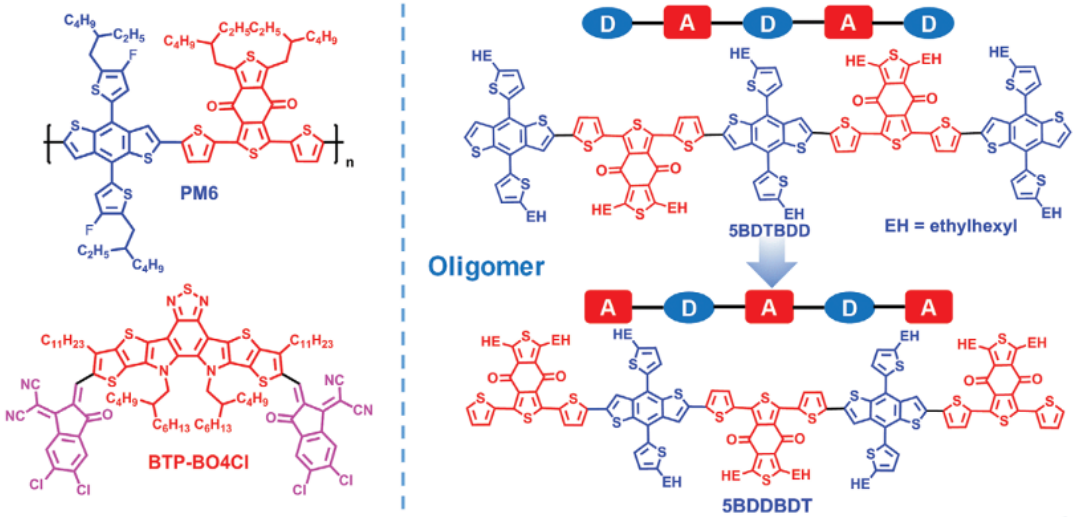

Figure 1.2.1.7: Chemical structure of PM6 and 5BDDBDT used for the efficient NFAs to achieve a PCE of 17.54%.

As a follow-up study, Xia et al. recently reported a new record of NFA PCEs standing at 17.54% where they used synthesized two novel structurally similar oligomers (**Figure 1.2.1.7**) (named 5BDTBDD and 5BDDBDT) with D-A-D-A-D and A-D-A-D-A for the high-performance ternary OSCs with low energy loss.[28] This state-of-the-art shows the potential that lies in these low-cost NFAs and with more research, their power conversion efficiency can beat that of silicon-based OPVs (~25%) and meet the market requirements of 20-25%.[26,29] With this milestone, there are still critical aspects of the NFA and OPVs that need to be fully comprehended to ensure the production of more efficient devices. Understanding the structure-function relationships that affect the charge and energy transfer dynamics will be useful in designing better organic photovoltaics.

1.2.2 Organic Light Emitting Diodes (OLEDs)

Organic light emitting diodes (OLEDs) is a new cutting-edge display technology that has seen the production of next-generation display monitors and lighting, an advancement from light emitting diodes (LEDs) and liquid crystal displays (LCDs). LCDs are non-emissive materials that were invented in the 1960s and have continued to grow, dominating the current display market which ranges from smartphone screens, to computer monitors and televisions, to data projectors.[30–32] The reasons for LCD market domination are high brightness, long lifetime, low cost and high-resolution density.[33] However, the slow response time, low contrast ratio and narrow color gamut has led to the poor image quality of LCDs. However, the emissive property of OLEDs leads to the true black state, a fast response time and an ultra-thin profile, wider color gamut properties desired for second generation flexible display systems.

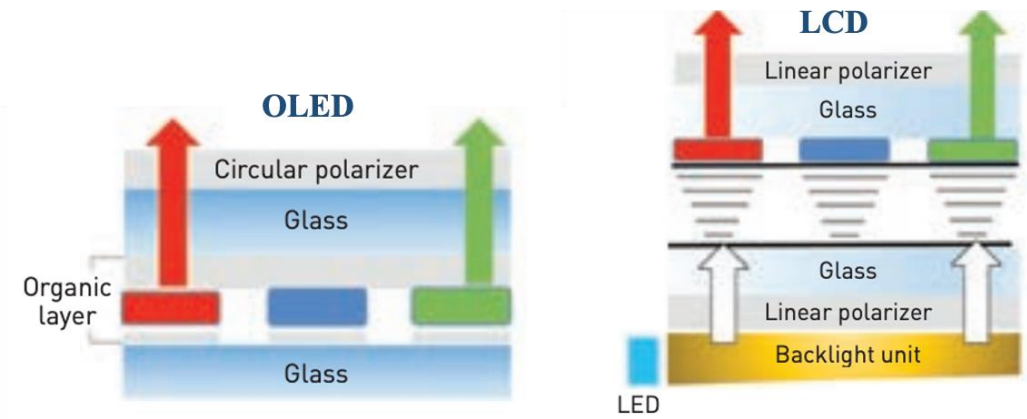

Figure 1.2.2.1: Device comparison of an OLED vs LCD adapted from Luo et al.[34]

OLEDs were first proposed by Chin Tang and Steven VanSlyke of Kodak 1987s (**Figure 1.2.2.2**).[9] Since then, they have been improved significantly with multiple layers to enhance their performance. The different layers include the electron−injection layer (EIL), the electron−transporting layer (HTL), the emitting layer (EML), the hole−transporting layer and the hole−injection layer (HIL). The role and location of each of these layers are summarized in **Table 1.2.2.1** below.

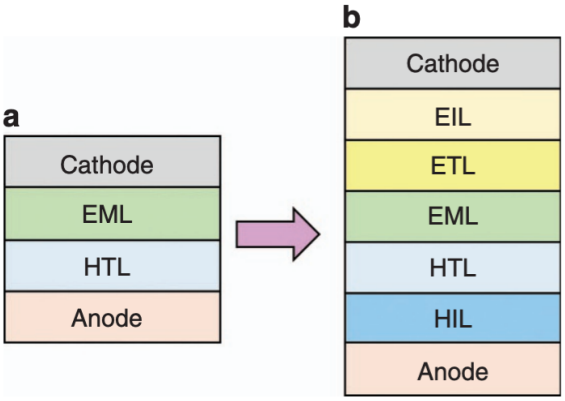

Figure 1.2.2.2: Schematic diagram of an OLED. (a) Basic structure proposed by Tang and VanSlyke in 1987. (b) Multi-layer structure employed in current OLED products highlighting the OLEDs principles of operation. EIL, electron-injection layer; ETL, electron-transporting layer; EML, emitting layer; HTL, hole-transporting layer; HIL, hole-injection layer. Image adapted from Chen *et al.* [33]

Table 1.2.2.1: Different layers of organic light emitting diodes and their roles.

Layer	**Location in Device**	**Role**
EIL	Between the cathode and ETL	Facilitate electron injection from the conductor towards the organic layer

ETL	Between the EIL and emissive layer	Bring electrons to the emissive layer for recombination
EML	Between the ETL and HTL	Used for light emission after recombination, and consists of materials with high quantum efficiency and high carrier mobility
HTL	Between EML and HIL	Bring holes to the emissive layer for recombination
HIL	Between the HTL and anode	Facilitate hole injection from the conductor towards the organic layer

The core of these systems is the emissive layer where the charge carrier recombination occurs leading to light emission. Classifications of OLEDs are based on the emitters used in the device, and there are 4 main classes of these emitters: fluorescence (FOLEDs), triplet−triplet fluorescence (TTFOLEDs), phosphorescence (PHOLEDs), and thermally activated delayed fluorescence (TADF OLEDs) as shown in **Figure 1.2.2.3**.

Upon photoexcitation, only 25% of the excited excitons which are at a higher energy formed are singlets, and the rest of them are triplets (75%) whose energy is lower than that of the triplets. For normal fluorescent materials, the transition between two electronic states with the same spin multiplicity is allowed while that between two electronic states with different spin multiplicities like intersystem crossing with spin changes, is not allowed. As a result, radiative decay through fluorescence is allowed while phosphorescence is forbidden. For fluorescent OLEDs, the theoretical internal quantum efficiency (IQE) limit therefore becomes only 25% with a short lifetime of only a few nanoseconds.

To circumvent this disadvantage, heavy metals like iridium and platinum have been introduced to the emitter. These metals enhance the spin−orbit coupling between the exciton and the orbital angular momentum resulting to a radiative transition from the triplet (T_1) to the ground state (S_0) through radiative phosphorescence whose lifetime is in μs. This spin-orbit coupling also promotes intersystem crossing between S_1 and T_1, populating the T_1 and making the maximum attainable IQE 100%. This makes the phosphorescent OLEDs more promising and efficient than their fluorescent counterparts. Under high current, it is possible that the produced triplets can interact with other triplets leading to triplet−triplet annihilation which leads to efficiency roll−off.[35] This interaction is also supported by the long lifetime of these triplets. The problem is that it is difficult to make stable phosphorescent emitters that emit in the blue which is important for portable

electronics with improved battery life. In addition, the metals employed in enhancing the spin-orbit coupling are rare and expensive.

A promising solution to the PhOLED problem is through the use of metal-free and emitting materials that exhibit a phenomenon called thermally activated delayed fluorescence (TADF) which will be discussed in detail later in this chapter. It is a process where a molecule in a non-emitting state incorporates surrounding thermal energy to change states, and only then, does it undergo light emission. While this process was reported almost a century ago by Perrin *et al.*, it is not until 2012 when Adachi created an efficient OLED display system using the TADF mechanism.[36] Here, he reported an organic electroluminescent molecule with a minimal energy gap between its singlet and triplet excited state, ΔE_{ST}, $(0.5 - 1.0\, eV)$ which could go through efficient spin-up conversion from the non-radiative triplet states to the radiative singlet states, harnessing both triplet and singlet excitons and leading to an IQE of 90%. Without heavy atoms in the organic emitting material, it is possible to achieve an IQE of 100% which reduces the material cast and can be used to make flexible OLEDs.

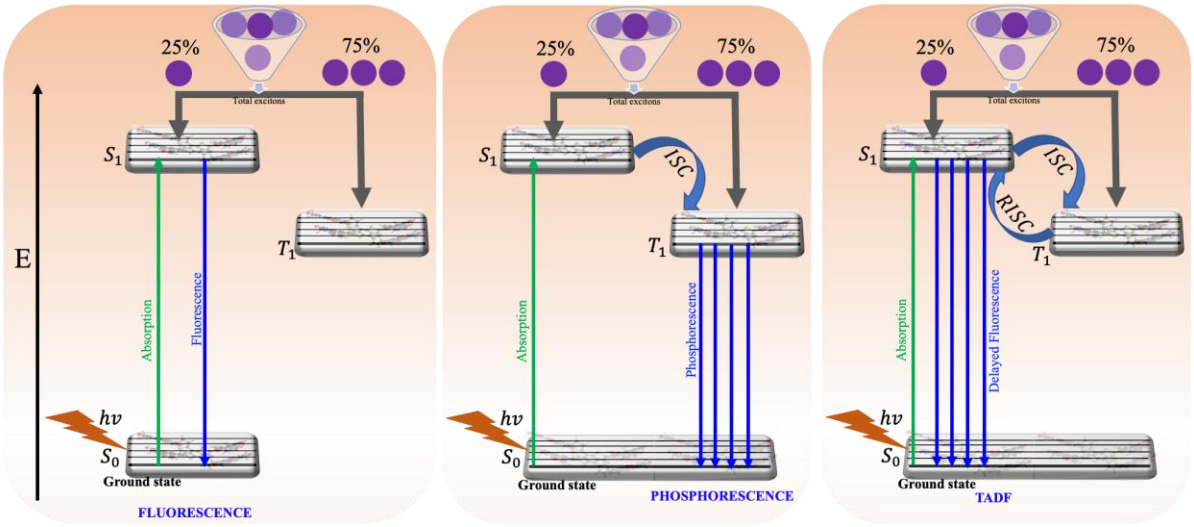

Figure 1.2.2.3: Emission mechanisms of OLEDs

The most promising OLEDs have been described to have a small spatial overlap between the highest occupied molecular orbital (HOMO) and the lowest unoccupied molecular orbital (LUMO), a reduced energy gap between the lowest singlet and triplet, efficient reverse intersystem crossing rate which outdoes the rate of phosphorescence, high

fluorescence quantum yield, increased optical output coupling/extraction efficiency, presence of emitting dipoles in the emissive layer.

To ensure that there is a balance between all the contributing factors, the overall performance of OLEDs is presented using the external quantum efficiency (EQE). EQE is the number of charge carriers that are collected to the number of photons that enter incidentally. This measure of performance can be calculated based on Equation 1.2.2.1 below.

$$EQE = \gamma \times \eta_{S/T} \times \eta_{PL} \times \eta_{out} \qquad \text{(Equation. 1.2.2.1)}$$

where:

γ is the electron-hole balance,

$\eta_{S/T}$ is the triplet-singlet factor,

η_{PL} is the photoluminescence quantum yield and

η_{out} is the outcoupling efficiency.[37]

1.2.3 Organic Light Emitting Transistors (OLETs)

Organic light emitting transistors (OLET) are an emerging class of optoelectronic device that merges the switching abilities and amplification mechanisms of organic field effect transistors (OFETs) and the emissive properties of an organic light emitting diode (OLED) which was first demonstrated in 2003.[38] Transistors which were originally designed by John Bardeen and Walter Brattain in 1948, are basically devices that transfer resistance, allowing them to amplify signals and make them an important component of modern-day electronics and were initially made of doped silicon as a semiconductor.[39] A doped silicon (using elements like arsenic, phosphorous, or antimony) will have extra electrons making it an n-type or p-type if impurities like boron, gallium or aluminum are used. A field effect transistor (FET) is a three terminal active semiconducting device, where the output current is controlled by an electric field that is generated by the input voltage. It is made of 3 main parts: the source (the terminal through which charge carriers in the form of current enters), the gate (which is formed by the diffusion of an n-type semiconductor with a p-type semiconductor creating a heavily doped p-n junction that controls the flow of current, that is produced by charges, from the source to the drain), and the drain (the terminal through which majority of the charge carriers exit the FET) as shown

in **Figure 1.2.3.1**. The moment a positive voltage is applied to the gate, an electric field is created that allows the flow of electrons from the device source to its drain. This generated field effect allows a current to flow and switch the transistor on (**Figure 1.2.3.1**). When a transistor functions as an amplifier, it takes in a bigger current at the source and produces a bigger current at the drain which can be used in hearing aids and microphones. In simpler words, a small current can be switched into a bigger current by a transistor.

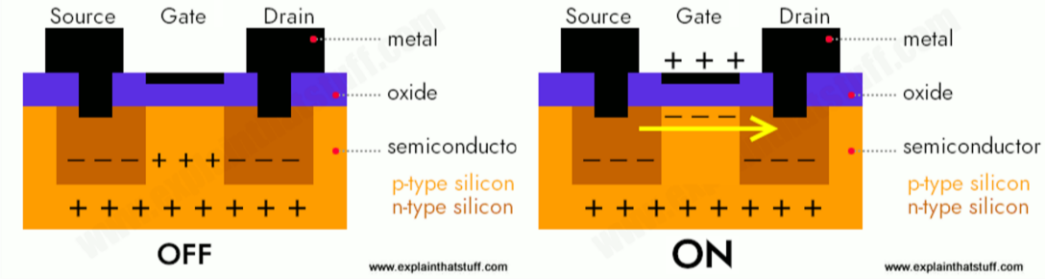

Figure 1.2.3.1: Metal oxide (silicon) semiconductor transistor (MOSFET).

Because of the high cost of silicon and metal oxides, low-cost organic materials have been used to make organic field effect transistors (OFETs). The operation of OFETs is just the same as that of FETs. Usually and in the linear mode, as the gate voltage increases, the drain current increases as shown below.

$$I_{D_{lin}} = \frac{W}{L}\mu C_i(V_G - V_T)V_D \qquad \text{(Equation. 1.2.3.1)}$$

where:

W is the channel width,

L is the channel length,

μ is the mobility,

C is the capacitance of the dielectric,

V_G is the gate voltage,

V_T is the threshold voltage and

V_D is the drain voltage.

However, when the transistor is in the active or saturation region, the drain current is given by Eqn 1.2.3.2:

$$I_{D_{sat}} = \frac{W}{2L}\mu C_{gd}(V_G - V_T)^2 \qquad \text{(Equation. 1.2.3.2)}$$

where:

W is the channel width,

L is the channel length,

μ is the mobility,

C is the capacitance of the dielectric,

V_G is the gate voltage, and

V_T is the threshold voltage.

Here, the drain current does not depend on the source voltage once the voltage is above the threshold.

The combination of these two abilities (switching and transistor from OFET and luminescence from OLED) results in a multifunctional device with either unipolar or ambipolar nature. A unipolar OLET uses either electrons or holes as majority carriers while the ambipolar OLET uses both electrons and holes as majority carriers. As such, these devices can be used for multiple applications like 1) applied physics which is an intersection of material science and engineering as it explores the charge transport, charge injection and optical characteristics of device architectures simultaneously, 2) integrated circuitry and high speed signal processing which involves both electrical and optical signals, 3) electrically pumped lasing because of their high current densities coupled to low optical loses at the electrodes, and 4) display circuitry due to their intrinsic combination of transistor and OLED which could be used to simplify the circuitry required for display applications.[11,37]

Research to understand this new field has been limited with less than 25 papers published annually and only about 270 papers published since 2003 (**Figure 1.2.3.2**).[37] This study by Qin *et al*. suggested that the reason for the limited studies as i) limited availability of ideal active materials for OLETs and ii) incompatibility of the conventional device fabrication technology with the OLET structure fabrication requirements.

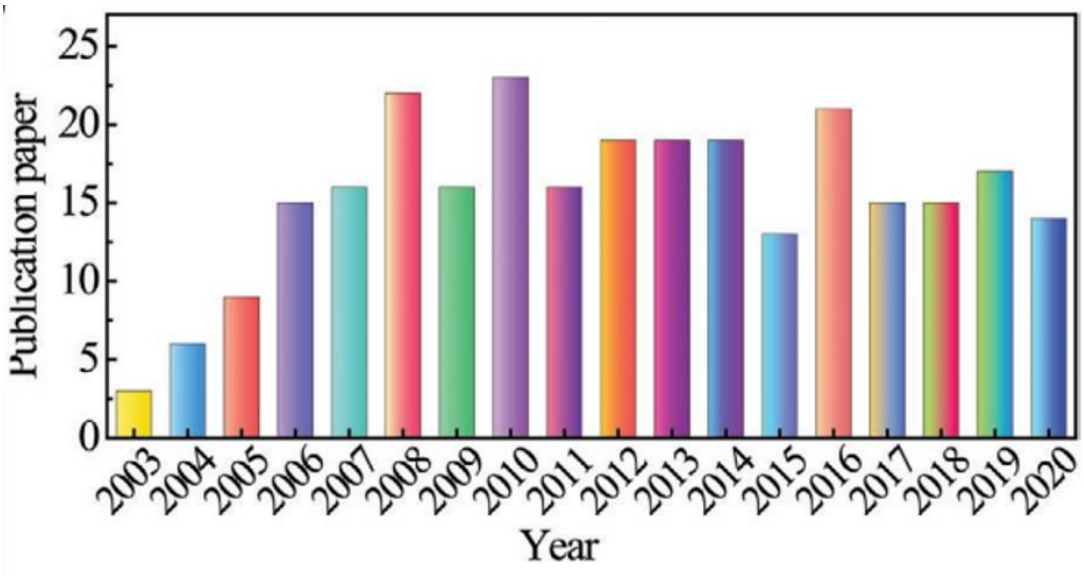

Figure 1.2.3.2: Summary of the number of articles related to the OFETs published between 2003 and 2020.

OLETs working mechanism is as follows:

i) Both holes and electrons are injected from the drain and source electrodes separately and transported to the active layer.

ii) In the ambipolar region, holes and electrons recombine to form excitons

iii) These high energy excitons decay to the ground state by emitting photons

iv) The emitted light is eventually detected as the final output.

Some of the most crucial parameters for a good OLET include: high carrier charge mobility, good gate modulation capacity, high on/off current ($I_{on}/_{off}$) ratio, low threshold voltage and small subthreshold slope, balanced carrier transportation, efficient recombination, low optical energy loss and efficient light outcoupling.[37,40] Simply, characterizing a good OLET takes into account the components of this dual functionality device such that ideally, a good OLET is made of a good transistor and a good OLED. For instance, to ensure great switching capabilities, one must look into the device mobility, the threshold voltage, the contact resistance and the ON/OFF ratio. On the other hand, the optical characteristics of an OLED like a good external quantum efficiency (EQE) and brightness are considered (**Eqn. 1.2.2.1**).

While it is expected that devices will have a good EQE and brightness, this is not the case for OLEDs. This challenge arises from the fact that high charge carrier mobility

and strong emission are mutually exclusive. [11,37] With immense efforts from recent studies, scientists have been able to come up with some organic semiconductors with both high charge mobility and high fluorescence quantum yield as shown in **Figure 1.2.3.3.**

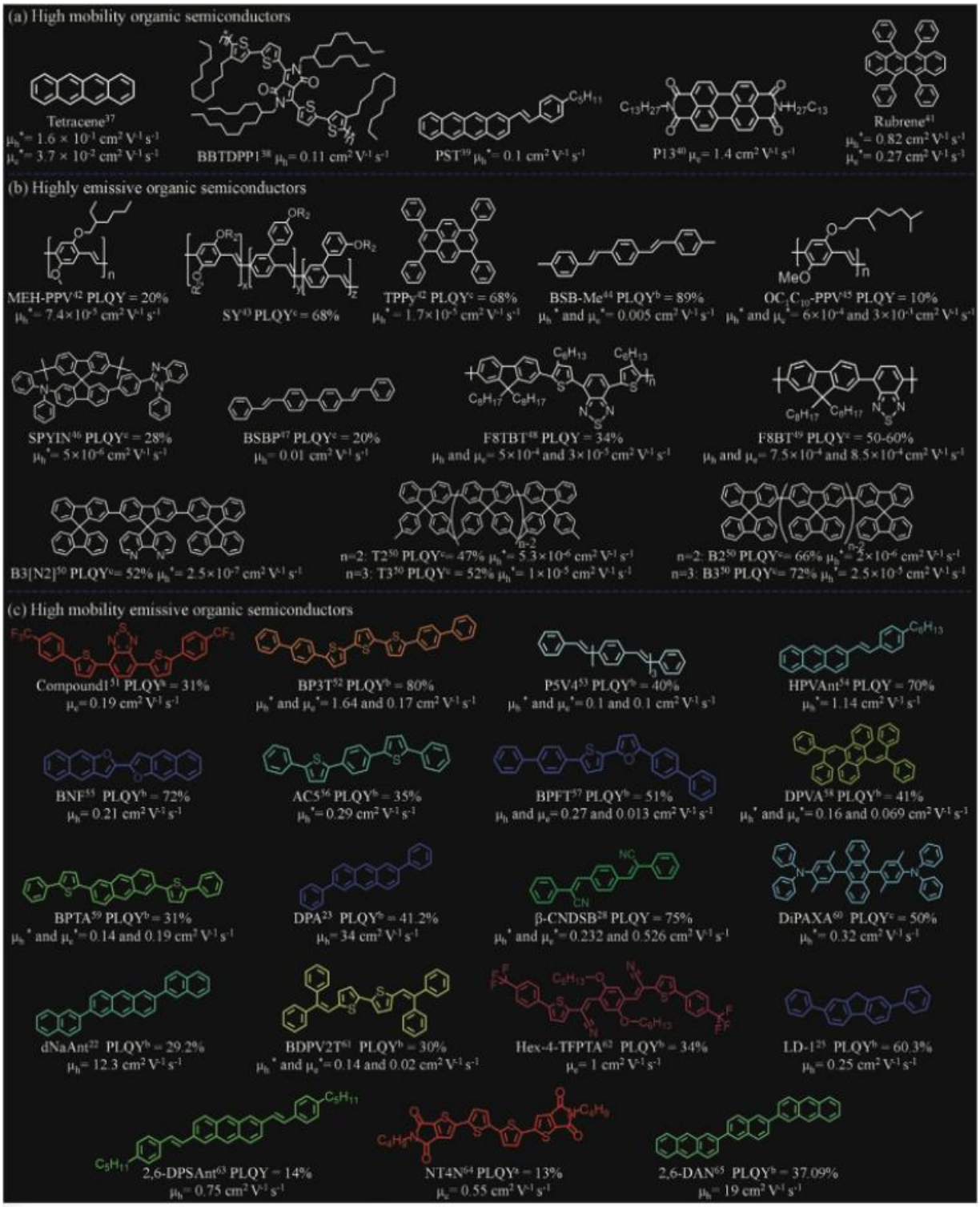

Figure 1.2.3.3: Chemical structures of structures that have been reported so far compiled by Qui et al.[37]

Tetracene which was used for the first OLET showed great mobility but low brightness of only 45 Cd/m^2 compared to the current emitting OLED brightness of 1000 Cd/m^2.[38,41] While single-component OLETs have been successfully developed, only an EQE of 1.61% has been obtained.[42] Due to the difficulties in attaining large mobilities in a single OLET materials, multilayer devices where different functions are delegated to different materials have been developed and shown EQEs of up to 9.01%.[43] For the multi-layered devices, however, the device fabrication process becomes extremely complicated as more layers are added since it becomes very difficult to control the mutually exclusive device properties of the OSC active materials while keeping their optoelectronic performance optimal.[44] For instance, high mobility materials show efficient intermolecular charge transport owing to their optimal $\pi - \pi$ stacking and electronic coupling; the efficient $\pi - \pi$ stacking may lead to the formation of excited state dimers or other charge transfer states which quench fluorescence and reduces the performance of OLETs.[45]

To date, some of the things that need to be done to improve the efficiency of OLETs include: improving charge transport properties as well as the PLQY while ensuring a balanced transport of holes and electrons with increased exciton utilization, selecting the right charge injection, charge transportation and light emitting layers for the multi-layer OLETs, maintaining a good gate field capacity, incorporating the characteristic of charge transport and light emission and exploring other applications. Most importantly, understanding the mechanisms of charge and energy transfer in materials for OLET applications which is an area that is not yet understood will be a huge step towards making highly efficient OFET devices.

1.3 Working Principles of Organic Optoelectronic

As mentioned previously, optoelectronic devices are divided into two: those that emit light by using voltage and current to produce electromagnetic radiation (EMR) while those that detect light do the opposite, i.e., converting the electromagnetic energy into current and voltage. Organic optoelectronic devices are made of organic semiconductors are their absorbing or emissive layer for light detecting (OPVs) or light-emitting

(OLEDs/OLETs) functions, respectively. These organic semiconductors are donor-acceptor (D-A) materials sandwiched between the other device layers and electrodes. To understand the working principles of these materials, one needs to understand the electronic properties of these materials which can be illustrated using the Jablonski diagram (**Figure 1.3.1**).

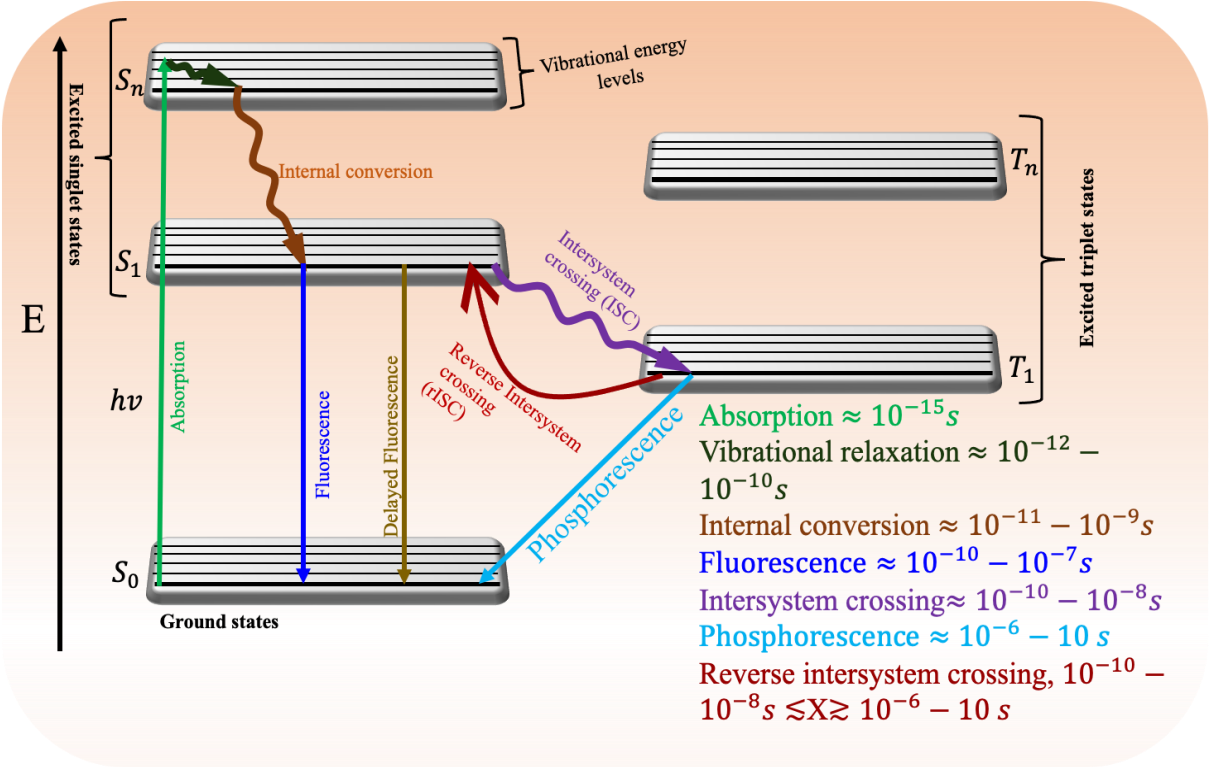

Figure 1.3.1: The Jablonski Diagram highlighting excited state events.

Organic light absorbing and emitting materials should possess good absorption and emissive properties, respectively. For conjugated donor-acceptor compounds which we will explore, the semiconducting properties stem from the delocalization of $\pi-$ electrons that move along the conjugation chain. Bonding (π) and antibonding (π^*) molecular orbitals overlap at this conjugated backbone, creating a strong electron density which then supports moving charge carriers. The longer the conjugation chain, the stronger the overlap which determines the energy gap (E_g) between the highest occupied molecular orbital (HOMO) and the lowest unoccupied molecular orbital (LUMO) which usually ranges between $1-4$ eV.[46] This E_g can be optimized or tuned by modifying the chemical structure which tunes

the optical excitations. This is important because the electronic properties of these organic semiconductors are described in terms of their molecular orbitals.

As shown in **Figure 1.3.1**, upon photoabsorption, an electron is promoted from the ground state, S_0, to an excited state, S_n, generating a tightly bound electron-hole pair called an exciton. This process occurs within 10^{-15}s. There are several states and energies that the exciton can go through before relaxing back to the ground state.

1) vibrational relaxation – this is a non-radiative transition where the molecule in an excited state is not in equilibrium loses excess vibrational energy to its vibrational modes within the same molecule or to surrounding molecules until the lowest vibrational level is reached. This is the fastest transition and happens within a timescale of $10^{-12} - 10^{-10}$ s.

2) Internal conversion – this is a non-radiative transition between two electronic states of the same spin multiplicity. Here, a molecule in a higher-lying singlet electronic state undergoes internal conversion to a lower-lying singlet state and is immediately followed by vibrational relaxation. The rate of this transition depends on the energy gap between the two states, and it happens within a timescale of $10^{-11} - 10^{-9}$ s.

3) Fluorescence – this is a radiative transition between two electronic states of the same multiplicity. The emission of photons from $S_1 - S_0$ occurs within a timescale of $10^{-10} - 10^{-7}$ s

4) Intersystem crossing – this is a non-radiative transition between two isoenergetic vibrational transitions that belong to electronic states of different spin multiplicity. This transition occurs within a timescale of $10^{-10} - 10^{-6}$ s

5) Phosphorescence – this is a radiative transition between two electronic states of the same multiplicity and occurs within a timescale of $10^{-6} - 10$ s

6) Delayed fluorescence – this is a radiative transition that occurs when a molecule in the triplet state transition to the singlet state followed by a radiative transition to the singlet ground state.

1.3.1 Charge Transfer (CT) Process

For OPVs which are the light detecting devices, a 4-step fundamental process happens which, all together, explains the working principles of these devices. First, light

is absorbed, and excitons are generated. Light from the sun is absorbed by the donor part of the high extinction coefficient D-A material. When photons with high energy are incident on the donor portion of the semiconducting material, electrons are excited from the highest occupied molecular orbital (HOMO) to the lowest unoccupied molecular orbital (LUMO). This leads to the formation of a tightly bound and localized electron-hole pair, which is also known as a localized exciton in a singlet exciton state. Here, the electron and hole have opposite spins. The binding energy usually ranges between 0.1 – 1.4 eV.[47,48] This binding energy tends to be larger than the one in inorganic materials since the electron and hole wavefunctions are localized and the dielectric constants are low ($\varepsilon \sim 3-4$) which enhances the Coulomb attraction between the electron and hole. The low dielectric constants are associated with the reduced intermolecular coupling which leads to localized molecular excitation and prevents band-to-band transitions. These excitons then move to the D-A interface where there is enough chemical potential to drive the exciton dissociation.

To ensure that this first step is done efficiently, materials with a high extinction coefficient are essential in the photoactive layer in order to absorb maximum sunlight. Low absorption may lead to low photocurrent generation. In addition, a low thickness (~100 nm) of the photoactive layer is recommended due to low charge-carrier mobilities in D-A materials which limits absorption to only 60% of the incident light at the absorption maximum.[48] In addition, light absorption can be maximized by reducing the band gap of the donor polymers which can ensure absorption of the maximum number of photons.[49] For instance, a band gap of 1.1 eV can cover 77% of the photon flux which outdoes the reported capabilities of inorganic materials whereas a band gap of 1.9% only covers 30% of the same photon flux.[19]

Second, the exciton diffuses, and the charges dissociate. With the high binding energy of around 0.4 eV of the photogenerated electron-hole pair, it is difficult for the surrounding thermal energy to dissociate this exciton into independent electrons and holes which serve as charge carriers. As a result, the acceptor is needed to facilitate the generation of free carriers. Therefore, the bound excitons migrate to the D-A interface where there is enough chemical potential to drive the exciton dissociation. The energy offset in the LUMO between the donor and acceptor, as well as the electron affinities of

the donor and acceptor help create a driving force for a rapid transfer of an electron from the donor to the acceptor. Due to efficient acceptor materials, the coulombic attraction is broken, and excitons dissociate into an electron and hole which serve as free energy carriers. This step occurs at the interface of the donor and the acceptor resulting in the transient formation of a *charge-transfer state* whereby the electron and hole exist on different molecules. This is a very important step since it governs the transfer of the photoexcitation energy towards the D-A interfaces where charge carriers are formed.

To ensure that this step proceeds efficiently, some factors need to be put into consideration. First, the distance traveled by the exciton before recombination, which is also called the diffusion length, L_D, is very critical. Most excitons from organic donor materials are very short-lived (<1 ns) and therefore require a diffusion length, L_D,shorter than their optical pass length which is between 100 – 200 nm to obtain a quantitative charge generation.[50] Usually, L_D is limited to a few nanometers, usually less than 20 nm.[19,50] For a bi-layer cell, the efficiency is limited to the number of photons that can be absorbed within the effective L_D range of the polymer/acceptor interface. Most of the time, scientists blend polymers with soluble electron acceptors to avoid the problem of additional L_D which would limit photocurrent generation in bulk heterojunction. Improving the exciton diffusion enables the use of bigger polymers leading to enhanced absorption of highly efficient solar cells. One direct way to determine the L_D is by probing the photogenerated exciton population by observing the change in photoluminescence with varying polymer layer thickness.[48] However, this method is inaccurate since intermixed evaporated molecules obscure the intrinsic exciton diffusion process. A new method was developed to accurately calculate the exciton quenching yield, as a function of the polymer thickness, L (Eqn 1.3.1.1).

$$Q = \frac{(a^2L^2{}_D + aL_D \tanh(L/L_D))\exp(-aL) - a^2L^2{}_D(cosh(L/L_D))^{-1}}{(1-a^2L^2{}_D)(1-\exp(-aL))} \qquad \text{(Eqn 1.3.1.1)}$$

where:

a is the absorption coefficient,

L_D is the exciton diffusion length, and

L is the polymer thickness.

The dissociation efficiency depends on the distance between the charge carriers as well as the strength of the applied field in cases where the exciton's Coulombic potential is modified by an electric field.[48,51] it has also been proposed that excitons can directly dissociate into free charge carriers owing to the excess photon energy after exciton dissociation is used to separate the bound pair and the D-A interface. Additionally, the D-A interface is also important in that the orientation of the electric dipole favors separation perpendicular to the interface which aligns with the field, and large mobility plays a crucial role as well.

Third, the charges are then transported towards the respective electrodes in the free charge carriers transport step. This step only happens if the free charge carriers do not recombine in the previous step or are trapped in a disordered organic material on their way to the electrodes. The existence of an internal electric field which is formed as a result of electrodes' Fermi Level difference, leads to the hopping of free charge carriers from one localized state to another, enabling the charge transport. [19] This transport can also be driven by carrier diffusion.[19,47] The current that gets to the electrodes without an applied field is called the short-circuit current, J_{SC}, and the maximum potential generated by the device is called open-circuit voltage, V_{OC}.46 The quality of the device is directly related to these two parameters, as well as the Fill Factor which is the ratio between the maximum power generated and the product of J_{SC} and V_{OC}. These are the performance characteristics that will be used to calculate the power conversion efficiency (PCE) of these OPV devices.

In ideal cases where there is no recombination or exciton trapping happening, photocurrent can be directly measured where the internal field, E, is given by **Eqn 1.3.1.2.**

$$E = (V_{OC} - V)/L \qquad \text{(Eqn 1.3.1.2)}$$

where:

V is the applied voltage,

V_{OC} is the open-circuit voltage and

L is the thickness of the active layer

The photocurrent generated by holes, J_{ph}, can also be calculated by **Eqn 1.3.1.3**

$$J_{ph} = ep\mu E \qquad \text{(Eqn 1.3.1.3)}$$

where:

μ is the hole mobility,

p is the density of the photogenerated holes, which is given by their lifetime and generation rate (G), $p = \tau G$, at the steady state, while at long lifetimes, it is equal to the transit time, $\tau_T = L^2/\mu V$,

e is the electric charge and

E is the internal electric field.

Thus, the hole photocurrent through the external circuit is given by **Eqn 1.3.1.4** which is obtained by substituting parameters in **Eqn 1.3.1.2.** and **Eqn 1.3.1.3.**

$$J_{ph} = eGL \qquad \text{(Eqn 1.3.1.3)}$$

where all the parameters have been described above.

With diffusion factored in, the photocurrent is given by **Eqn 1.3.1.4**:

$$J_{ph} = eGL\left[\frac{\exp(^{eV}/_{kT})+1}{\exp(^{eV}/_{kT})-1} - \frac{2kT}{eV}\right] \qquad \text{(Eqn 1.3.1.4)}$$

where:

eGL is the saturated photocurrent,

k is the Boltzmann constant and

T is the temperature.

In reality, not all excitons dissociate to form free charge carriers. When this happens, in ideal cases, the generation rate is given by G_{MAX}. However, for most organic semiconductors, only a fraction of this G_{MAX} dissociates into free charge carriers. This fraction is dependent on the applied field as well as the temperature. As a result, G can be described as shown in **Eqn 1.3.1.5**:

$$G(T,E) = G_{MAX}\,P(T,E) \qquad \text{(Eqn 1.3.1.5)}$$

where:

$P(T,E)$ is the probability of charge separation at the D-A interface.

Another important factor to note is that the exciton can also decay into the ground state with a rate constant of k_F or form free carriers with an electric-field-dependent constant $k_D(E)$ where these separate carriers can re-bind at a rate of k_R. This explains why very long-lived charge transfer states are precursors for free charge carriers. With these possibilities in mind, Braun came up with a new model to determine $P(T,E)$ at a given electric field E and temperature T (**Eqn 1.3.1.6**).

$$P(T,E) = \frac{k_D(E)}{k_D(E)+K_F} \qquad \text{(Eqn 1.3.1.6).}$$

Finally, the photogenerated charge carriers that do not recombine are collected at the electrodes. For maximum charge extraction, any possible barrier at the photoactive layer should be reduced such that the work function of the anode matches the with the HOMO of the donor material and that of the cathode matches the LUMO of the acceptor material, aligning the Fermi level at the negative and positive electrodes, respectively.[19] the electrode work function in this is pinned close to the LUMO/HOMO level meaning that the V_{OC} will be governed by the energetics of the acceptor LUMO and the donor HOMO. Any mismatch could lead to a reduced performance of the solar cell. In this case, the Fermi levels of the anode and cathode contacts are within the insulator bandgap which is sufficiently away from the HOMO and LUMO levels, respectively. It, therefore, follows that the work function of the anode is highly relevant for the V_{OC}.[48] This concludes the mechanism of charge transfer in OPVs and is illustrated in **Figure 1.3.1.1**.

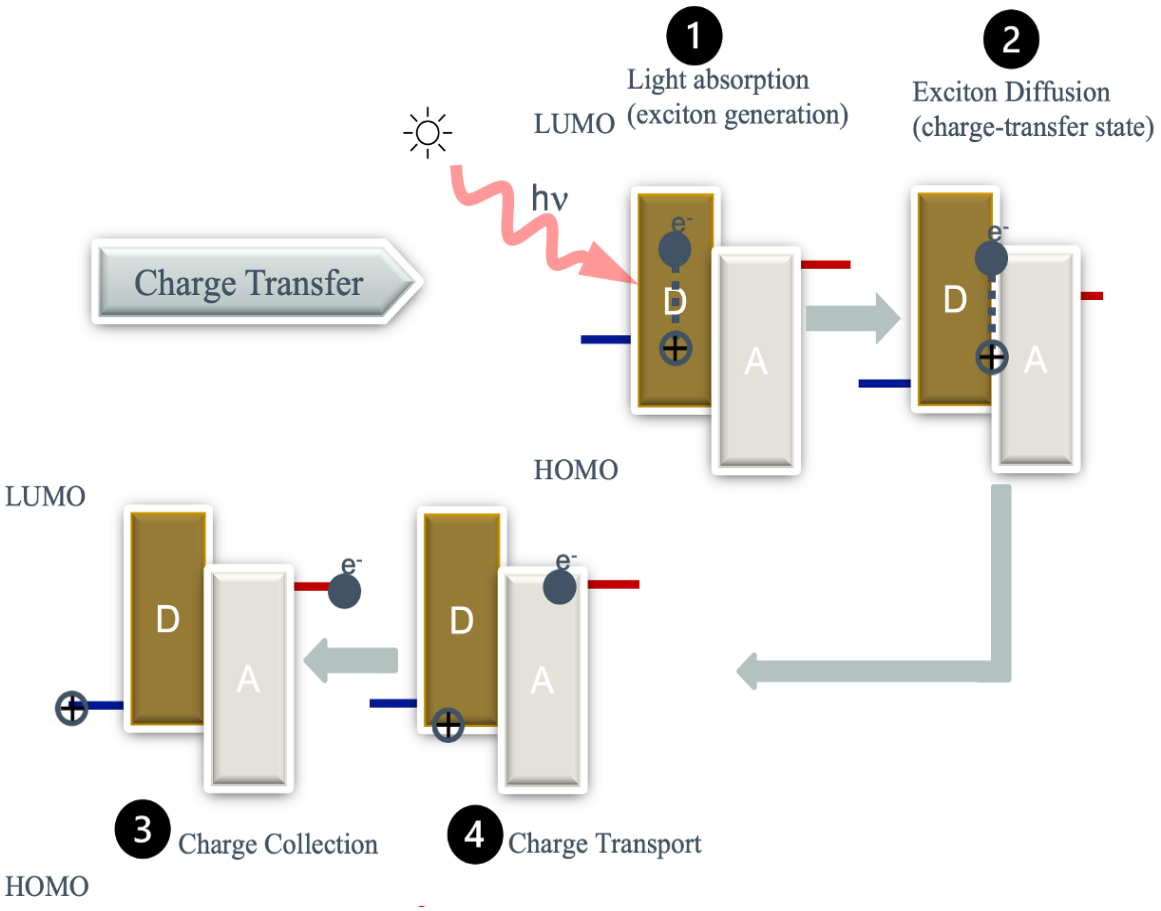

Figure 1.3.1.1: Working principles of organic photovoltaics illustrating charge transfer.

To determine the power conversion efficiency (PCE) as shown in **Eqn 1.2.1.1**, there are three major parameters that should be taken into consideration:

a) Short-Circuit Current (J_{SC}) – Maximum photocurrent density generated at zero applied potential or the number of charge carriers getting to the electrodes without any applied field/potential. There is no power produced at this point.

b) Open-Circuit voltage (V_{OC}) – Maximum voltage that can be extracted for an external circuit when the current is zero.

c) Fill Factor (FF) – The ratio of the maximum output power to the product of the J_{SC} and V_{OC}.

1.3.2 Energy Transfer (ET) Process

For the light emitting device, the process of light emission occurs in the opposite direction as the process of light absorption that's described in the charge transfer section

above. This process has been discussed by Brédas *et al*. in their 2004 review and I will summarize it below.[52] First, electrons (negative charges) and holes (positive charges) are injected from the Fermi level of the high and low work function, respectively, into the LUMO and HOMO electronic levels of the semiconducting material at their respective electrodes. Then, these separate charge carriers migrate to the donor-acceptor material where they meet each other at the D-A interface. Here, they bind to form excitons. These excitons then recombine radiatively generating light through electroluminescence (**Figure 3.2.1**).

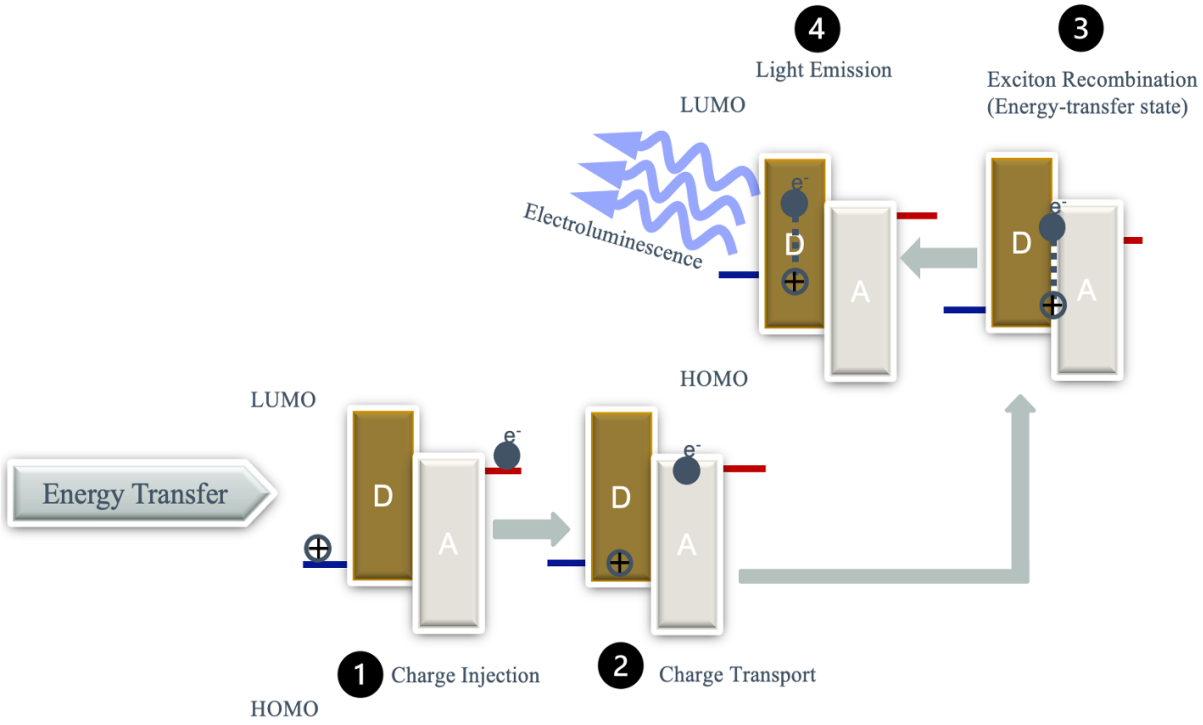

Figure 1.3.2.1: Working principles of light emitting illustrating energy transfer.

The number of photons emitted per a couple of charges injected is called the internal quantum efficiency (IQE or η_{int}). To obtain a high IQE, the work function of the metal electrodes should also match the HOMO and LUMO energies to generate the right potential barriers for the electrons and holes. A high mobility of charges is also needed in order to form excitons farther from the electrodes that usually act as quenching points.[46] Additional

charge regulating layers have also been proposed which may enhance the exciton formation and recombination leading to more efficient emissive systems.

The formation of excitons in emissive systems results in 25% singlet with antiparallel spins and 75% triplet excitons with parallel spins. As a result, emissive devices can take advantage of both triplets and singlets and have a theoretical $IQE = 1$ in contrast to light absorbing materials that only utilize singlets (25%). For an emissive system that does not show phosphorescence, the display maximum IQE will be 0.25 counting only singlets since the triplet states recombine non-radiatively.

1.4 Mechanisms of Singlet− and Triplet−State Energy and Charge Transfer

1.4.1 Singlet Exciton Fission (SEF)

SEF is a spin-allowed mechanism that has been extensively studied and it happens when an excited singlet exciton splits to form two spin-correlated triplet excitons via a double-triplet state (**Figure 1.4.1.2**).[53] Since the theoretical calculation of the Shockley-Queisser (SQ) efficiency limit (~33%) for single-junction solar cells in 1991[54], a lot of research has focused on different ways of circumventing this limit.[55–61] One of the most interesting photoinduced processes to study are those with the capabilities to go through multi exciton generation (MEG) in the form of singlet fission (SF). Literature reports that SF in organic photovoltaic devices (OPVs) reduces the thermal relaxation losses due to the SQ limit and therefore has the capability to boost their efficiency from 33 to 47%; this potential increase has led to increased curiosity and research in singlet exciton fission (SEF) materials (**Figure 1.4.1.1**).[57,62]

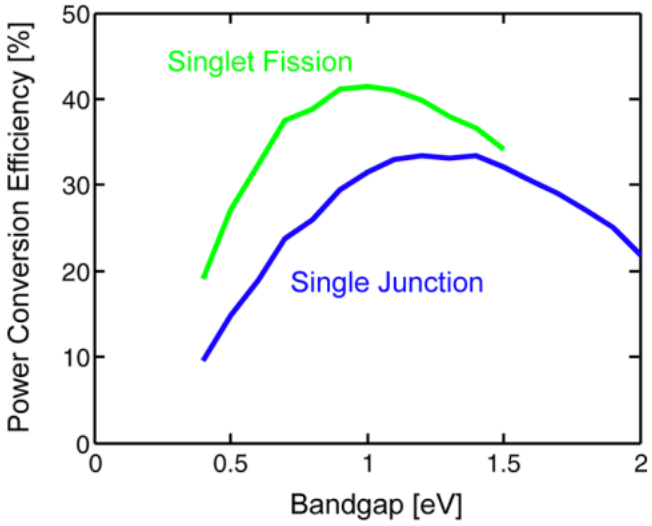

Figure 1.4.1.1: Theoretical maximum power conversion efficiency as a function of bandgap ($S_1 \rightarrow S_0$ for single-junction; $T_1 \rightarrow S_0$ for singlet fission) for single-junction (blue) and singlet fission (green) solar cells.

This mechanism was initially used to explain the observation of delayed fluorescence in crystalline acenes.[53,63,64] For singlet fission to occur, electronic and structural conditions have to be fulfilled: a) adiabatic energy conditions $E(T_2) > E(S_1)$ and $E(S_1) > 2[E(T_1)]$, b) molecular packing that optimizes intermolecular electronic coupling for SF while minimizing competitive singlet deactivation pathways and c) efficient separation of triplet excited state into free charges.[17] There are two different mechanisms through which SEF proceeds. One is the direct coupling of a singlet exciton involving two adjacent chromophores $^1(S_1S_0)$ produces a multiexciton correlated triplet pair $^1(T_1T_1)$ with an overall singlet spin and the $^1(T_1T_1)$ then decouples through a special spin dephasing separation process to generate two independent triplet excitons ($T_1 + T_1$).[65] SF Second, SEF can be mediated indirectly through intermediate states like through a charge transfer (CT) state where the conversion of $^1(S_1S_0)$ to $^1(T_1T_1)$ is facilitated by coupling to higher-lying charge transfer (CT) state or excimer states.[66–71] Charge transfer states have been shown to enhance intramolecular singlet exciton fission (iSEF) while excimer states have been a subject of discussion as to whether they enhance or inhibit or enhance iSEF. [72–75]

Recent studies report that the SEF mechanisms can either be inter or intramolecular. In intermolecular exciton SF (ISEF), the optically excited singlet state on one molecule couples with neighboring molecules to form an intermolecular triplet pair can be improved by tuning the interchromophore interactions. This process highly depends on chromophore packing motifs. It is

challenging to come up with highly ordered molecular structures to fulfill the packing requirement, and reproducibility is often an issue.[76] However, polymers and other small molecules can show SEF as an intrinsic property through intramolecular singlet fission (iSEF) where the double triple pair state is located on the same molecule. The iSF mechanism, which shows high processability in solution, high tunability in both molecular and electronic structures, and ability to create tailored interfaces, is not well understood.[76–78]

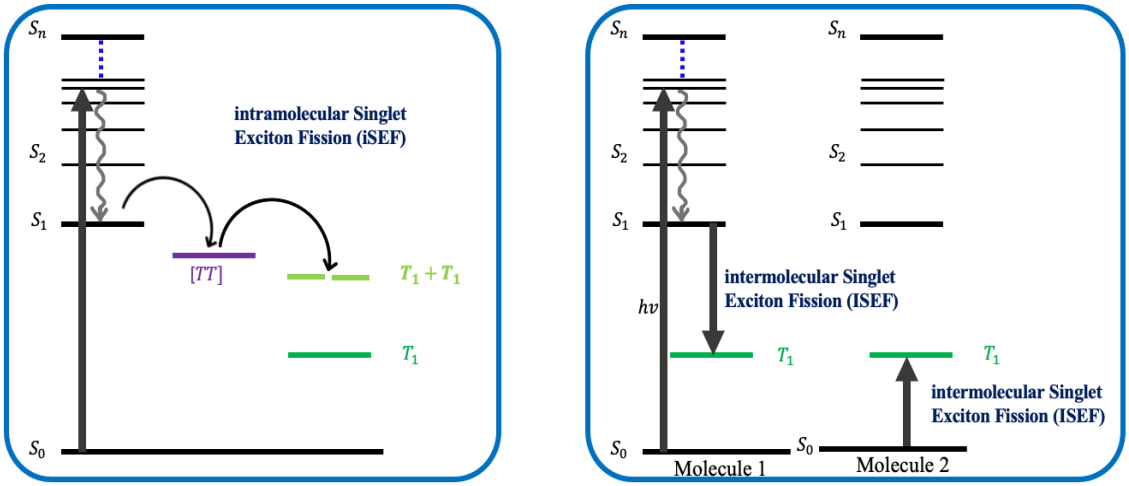

Figure 1.4.1.2: Intramolecular and Intramolecular Singlet Exciton Fission.

Most of the research surrounding the idea of singlet fission in organic photovoltaics (OPVs) has been carried out on dimeric systems of acenes. These molecules have shown structural tunability, which allows control of the molecular orientation and geometry.[65,72,77,79–92] In these studies, the rate and yield of SEF are reported to be affected by the coupling between the molecular units, and the degree of contortion in the structure.[93,94] Although the previously mentioned acene molecules have shown great SF yields, their limitations like photo-instability have made researchers venture into new materials with SF potential.[79,95,96] Perylene Diimides (PDIs) are a class of chromophores whose packing is easily controllable, possesses high thermal/photo-stability, have high extinction coefficients in the visible region, and holds desirable triplet energies for semiconductor sensitization.[79,95,97]

Furthermore, other studies have shown that in addition to the nature of the chromophore, the π-linker plays a crucial role in contributing to the occurrence of iSEF. It has been reported that structural flexibility of the covalent linker is necessary to activate iSEF.[80] However, these studies do not isolate the effect of the attachment position of the linker to the chromophore units.

Additional studies point out that excimer formation affects singlet fission process.[98,99] These low-lying excimer states inhibit the formation of the correlated triplets. [98] However, other studies have shown that the correlated triplet pair state in SEF can be preceded by excimer formation. In this case, excimer states act as precursors to triplet formation.[75] Excimer states and their relationship to singlet fission have been a subject of discussion with some literature reporting excimer mediated singlet fission [100,101] while others report that excimer formation hinders the SEF process. [102,103] The complication in understanding excimer states and their role in SEF is as a result of the indistinguishable nature of the $^1(S_1S_0)$ and $^1(T_1T_1)$ states and their interactions. For instance, an excimer or excimer-like state has been identified as a singlet-triplet hybrid state, as the $^1(T_1T_1)$ state or as a state with significant CT character.[99] For most chromophores, the potential excited states are singlets $^1(S_1S_0)$, charge transfer state CT, double triplets $^1(T_1T_1)$, and triplets $^3(T_1)$. One report showed that excimers form when the electronic coupling between the CT state and the singlet excited state of two identical chromophores is strong.[103] This results in the stabilization of the resulting CT $+^1(S_1S_0)$ mixture state – an excimer. The individual CT state or $^1(S_1S_0)$ can themselves individually act to inhibit the production of double triplets from the singlet state via a highly stabilized CT (lower CT state) process or radiative decay, respectively.

In other studies, singlet fission has been reported as a solvent-dependent process for molecules like terylenediimide (TDI) dimers.[104] In these TDI dimers, SF was observed in low dielectric constant solvents while symmetry breaking charge separation was observed in high dielectric constant solvents. In this case, it follows that the higher dielectric constant solvent stabilizes the CT state and lowers its energy allowing it to act as a trap state. On the other hand, minimal or lack of the CT state stabilization in low dielectric environments enables the CT state to act as a virtual state in a superexchange interaction that promotes SEF.[89] On the contrary, other reports show symmetry breaking as a crucial step to activating singlet fission. [89,105] In fact, coherent singlet fission has been reported to proceed through an initial superposition of $^1(S_1S_0)$ and $^1(T_1T_1)$ which eventually dephases into the dark state. Coherent SF occurs through symmetry-breaking vibrational modes, which allow the (S_1S_0) and $^1(T_1T_1)$ to mix.

With the $^1(T_1T_1)$ being a critical state for singlet fission to occur, a lot of studies have been dedicated to elucidate this state and its excited state character. Reported information about this triplet correlated state has been ambiguous owing to the difficulties in the direct observation of the $^1(T_1T_1)$. There has been a lot of debate and a lot is needed to understand the mechanism of

the double triplet state formation, which affects the mechanism of charge transfer in SEF materials for OPV applications.

1.4.2 Thermally Activated Delayed Fluorescence (TADF)

The electronic states of light emitting materials can be changed by tuning the molecular structure. For these emitting materials, emission occurs through energy transfer. When voltage is applied across the organic semiconducting layer, the injected electrons and holes strongly bind forming an exciton that can either have a total spin of $S = 0$ which is a singlet, or a total spin of $S = 1$ which is a triplet exciton. Therefore, in these systems, 25% of the excitons formed are singlets while 75% of these are triplets. For emitting materials, what matters most is the luminescence which is a radiative deactivation of excitons from the excited state to the ground state which occurs through fluorescence (from the singlet excited state) or phosphorescence (triplet excited state). Important to note, the transition between two electronic states with the same spin multiplicity is allowed while that between two electronic states with different spin multiplicities like intersystem crossing with spin changes, is not allowed. It, therefore, follows that fluorescence, which is a short lifetime process, is allowed while phosphorescence, which has a lifetime ranging from microseconds to milliseconds is forbidden. At this condition, the maximum internal quantum efficiency (IQE) obtainable for these display systems is 25%.

One way to get around this problem and increase the IQE was to use heavy metals which increased the spin-orbit coupling between the exciton and the orbital angular momentum resulting in a radiative transition from the triplet (T_1) to the ground state (S_0). This spin-orbit coupling also promotes intersystem crossing between S_1 and T_1, populating the T_1 and making the maximum attainable IQE 100%. One disadvantage of the materials that showed these capabilities was that it was challenging to get stable deep blue phosphorescent emitters. This is a challenge to this day.

A very promising solution to this is through thermally activated delayed fluorescence (TADF). This is a phenomenon where a molecule in a non-emitting state incorporates surrounding thermal energy to change states, and only then, does it undergo light emission. While this process was reported almost a century ago by Perrin *et al.*, it is not until 2012 that Adachi created an efficient OLED display system using the TADF

mechanism.[36] Here, he reported an organic electroluminescent molecule with a minimal energy gap between its singlet and triplet excited state, ΔE_{ST}, $(0.5 - 1.0\, eV)$ which could go through efficient spin-up conversion from the non-radiative triplet states to the radiative singlet states, harnessing both triplet and singlet excitons and leading to an IQE of 90%.

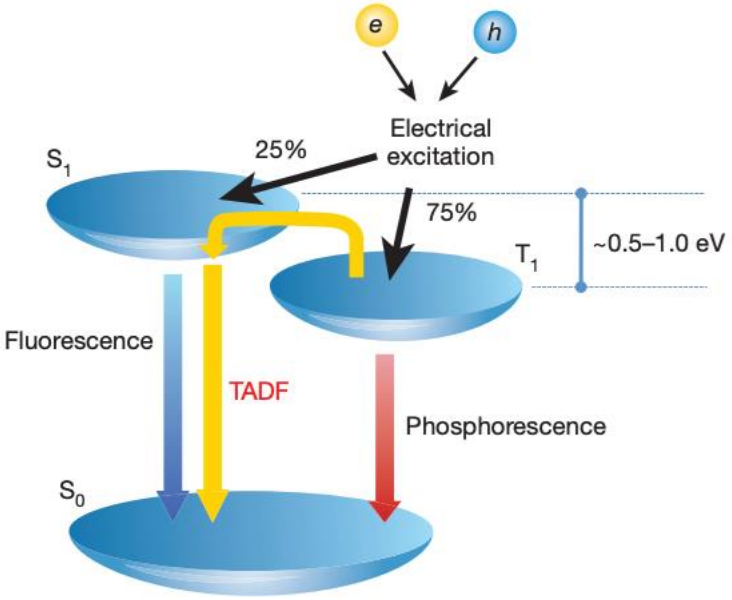

Figure 1.4.2.1: Energy level diagram of a conventional organic molecule illustrating TADF

Adachi suggests that careful molecular design can lead to even a smaller ΔE_{ST} which makes the reverse intersystem crossing from $T_1 \rightarrow S_1$ easier, enhancing TADF. He highlighted characteristics of a good TADF material to have: 1) a small ΔE_{ST} of $\lesssim 100\, meV$, 2) reasonable radiative decay of $> 10^6 s^{-1}$ which will help in overcoming non-radiative decay and 3) a balance in the HOMO/LUMO overlap. In this report, he synthesized emitting molecules where carbazolyl was the donor and dicyanobenzene was the acceptor based molecules shown in **Figure 1.4.2.2**. These materials had a small ΔE_{ST} due to the huge steric hindrance that leads to a distortion of the carbazolyl unit from the dicyanobenzene plane. As such, the HOMOs are localized on the donor while the LUMOs are localized on the acceptor moiety. It is also important to note that carbazole is known for the emission of various colors while dicyanobenzene is known for its high photoluminescence and breaking chemical bonds in the excited state to change the electronic properties.

Figure 1.4.2.2: Molecular Structures of investigated CDCBs where Me is methyl and Ph is phenyl.

Adachi proposes an experimental method to calculate the rate of reverse intersystem crossing, k_{RISC}, by using the rate constants and the quantum yields of the prompt and delayed fluorescence components (**Equation 1.4.2.1**).

$$k_{RISC} = \frac{k_p k_d \phi_d}{k_{ISC} \phi_p} \qquad \textbf{Equation 1.4.2.1}$$

where:

k_p and k_d are the rate constants for the prompt and delayed fluorescence component, respectively,

k_{ISC} is the rate of intersystem crossing from $S_1 \rightarrow T_1$ and

ϕ_p and ϕ_d are the photoluminescence quantum yields of the prompt and delayed components, respectively.

Most scientists report the performance of emissive devices in terms of external quantum efficiencies (η_{ext} *or* EQE). Pereira *et al.* describe a method to measure this performance using an integrating sphere that collects all the light from a source placed inside it and the configuration must allow integration over 4ϖ steradian of solid angle.[106] Here, the calibration lamp (with a known (certified) power spectrum output, $P_{cal}\ (\lambda)$ in W/nm) is positioned with the same experimental setup (sample position) used for the devices (which will have a power spectrum output, $P_{dev}(\lambda)$ in W/nm). By applying a constant current, the intensity of the lamp, $I_{cal}\ (\lambda)$ is measured and the Reference spectra, $R(\lambda)$ calculated from **Equation 1.4.2.2**.

$$R(\lambda) = \frac{P_{cal}(\lambda)}{I_{cal}(\lambda)}$$ (**Equation 1.4.2.2**)

Since the shape of the calibration lamp affects the measurements, an auxiliary spectrum is measured. The spectra with only a calibration lamp and only a device holder is measured and the ratio between the two intensities gives the auxiliary area, $A(\lambda)$, given in **Equation 1.4.2.3**.

$$A(\lambda) = \frac{I_{aux,cal}(\lambda)}{I_{aux,dev}(\lambda)}$$ (**Equation 1.4.2.3**)

The power spectrum, $P_{device}(\lambda)$ device of the device is given by the product of the response of the system to the auxiliary correction and the current of the device as shown in **Equation 1.4.2.4** which can enable one to calculate the power efficiency by integrating the power spectrum over wavelength divided by the electrical power (**Equation 1.3.2.5**).

$$P_{device}(\lambda) = A(\lambda).R(\lambda).I_{device}(\lambda)$$ (**Equation 1.4.2.4**)

$$\eta_P = \frac{\int_\lambda P_{device}(\lambda)d\lambda}{VI}$$ (**Equaiton 1.4.2.5**)

The power at each wavelength is converted to the number of photons emitted per second. This is then integrated over wavelength and the ratio by the number of electrons flowing into the device per second as shown in **Equation 1.4.2.6** and **Equation 1.4.2.7**.

$$\eta_B = \int_\lambda \frac{P(\lambda)C}{\hbar\lambda}\, d\lambda$$ (**Equation** 1.4.2.6)

$$\eta_{ext} = \frac{\eta_B e}{I}$$ (**Equation** 1.4.2.6)

Alternatively, the EQE can be calculated based on **Eqn. 1.2.3.3**. described already described, by relating the electron-hole balance, the triplet-singlet factor, the photoluminescence quantum yield and the outcoupling efficiency.

Adachi *et al*. reported the performance of the TADF devices in EQE as a function of current density as shown in **Figure 1.4.2.3.**

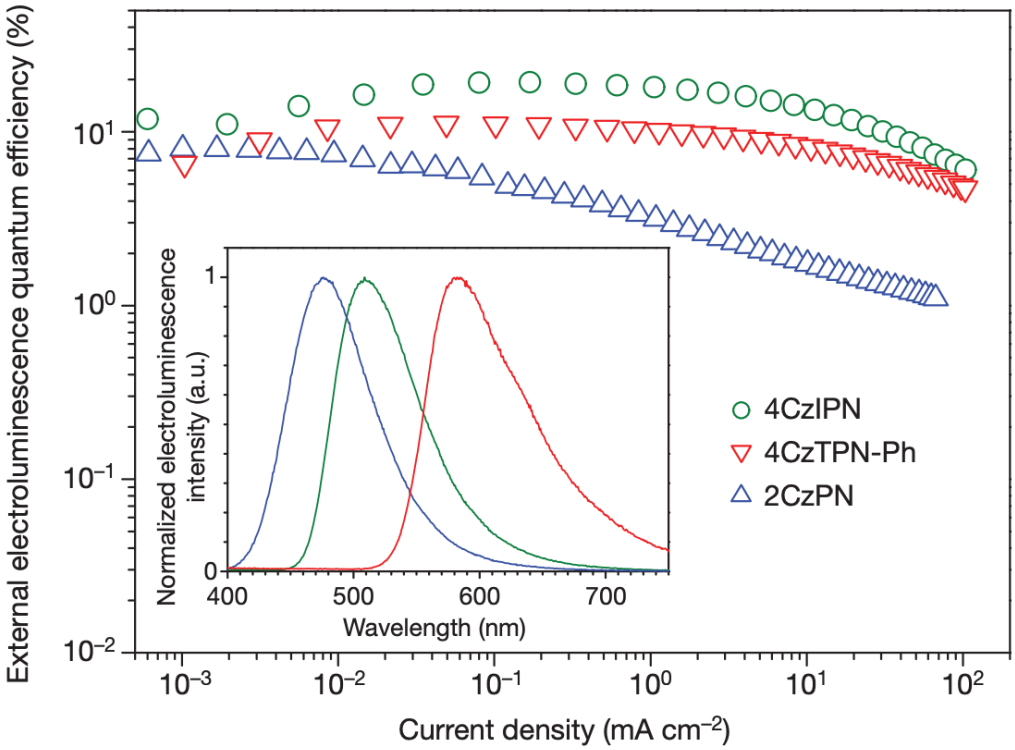

Figure 1.4.2.3: External electroluminescence quantum efficiency as a function of current density for the investigated emitting materials. Inset is the electroluminescence spectra of the same emitting materials at a current density of $10 mA\ cm^{-2}$.

Since this first demonstration, multiple studies have been carried out to design more materials with TADF character since they are highly promising luminescence materials for organic light emitting diodes. One method that has been used to enhance this design is constructing twisted molecular conformations with electron donors and acceptors in order to separate the HOMO and LUMO ensuring a small separation between their lowest excited singlet state and their lowest triplet excited state and achieving a high rate of reverse intersystem crossing, spiral donors structures with intrinsically bulky and rigid molecular structure.[107–114] These designs have successfully balanced the dilemma between high photoluminescence quantum yield and a small singlet-triplet energy gap leading to high EQE values of above 35%.[107–109]

According to a review compiled by Yang *et al*. not only do we require a small ΔE_{ST} for efficient TADF materials, a large radiative decay constant, k_r, of S_1 excitons is very important to obtain a high electroluminescence efficiency. Mostly, a large k_r is accompanied by a large ΔE_{ST} which makes it challenging to design materials that show both

large k_r and small ΔE_{ST}.[115] On the brighter side, studies have shown that interactions between acceptors and donors from either intramolecular or intermolecular can lead to a small ΔE_{ST} by reducing the HOMO-LUMO overlap. Two ways can be used to increase k_r. 1) Increasing the overlap density distribution between the electronic wavefunction of the ground state in which the S_1 state can promote $S_1 \rightarrow S_0$ radiative decay process which improves the photoluminescence quantum yield, 2) ensuring a large delocalization of molecular orbitals with well separated HOMO and LUMO suppresses a decrease in the radiative decay rate k_f for fluorescence while lowering ΔE_{ST}. New methods have been devised to ensure a good HOMO-LUMO separation that leads to a small ΔE_{ST}: physical separation of the donor and acceptor units, X-shaped molecular structures, dual acceptor/donor units and multiple resonance effect. [115]

For purely organic D-A systems, design principles have been summarized as: 1) D–A molecular structure with a twist between the donor and acceptor moieties, caused by bulky substituents or a spiro-junction, to achieve a small ΔE_{ST}., 2) densely combining donors and acceptors as well as strengthening the rigidity of the molecular structure to enhance radiative luminescence efficiency, 3) the π-conjugation length, 4) the redox potential of the donor and acceptor moieties along with the interruption of the conjugation between them.[115,116]

While a great number of TADF materials have been synthesized and reported as summarized by Yang *et al*, the commercial application of TADF OLEDs has not been possible due to their short device lifetimes. As a result, more studies are still required to not only design long-lived TADF materials, but also come up with alternative ways to accurately calculate the rate of reverse intersystem crossing.

1.4.3 Organic Open-Shell Systems and their effect of Effect on Energy and Charge Transfer

Organic open-shell systems have one or more unpaired electrons in their electronic structure which enables the systems to participate in covalent bonding processes in order to satisfy valency. Since these unpaired electrons occupy the highest molecular orbitals, they make these systems very reactive which explains their intrinsic property as thermodynamically and kinetically unstable. Some of these processes include dimers doubling, hydrogen abstraction, recombination,

or disproportion.[117] However, researchers have been able to make stable radicals by protecting the reactive side of the radical to eliminate contact with the external active species which improves the thermodynamic and chemical stability. The first stable radical was triphenylmethyl which was reported in 1900 and its reactive site was protected using large phenyl rings.[118] It was noted that chlorinating the three phenyl rings with sp^2 hybridization provided polychlorinated triphenylmethyl radicals (PTM), where the bulky chlorine atoms provide more steric protection effect and further enhance the thermal and chemical. It has been reported that these PTM radicals are stable nearly indefinitely to oxygen in solution, decomposing only in the presence of light. Another way to stabilize radicals is through the enhancement of the π −conjugation delocalization to modulate their electronic structure. This method works to achieve controlled and perturbed resonance of planar π −conjugated systems which tend to form multiple resonance structures with a spin density that is delocalized along the planar π −conjugation backbone.[119] The versatilities of the chemistry of organic open shell radicals enable the tuning of their spin-spin interactions making it easier to control their chemical and physical properties for various applications. Open-shell materials have a broad range of applications ranging from spintronics like quantum computers, conducting materials, researchable batteries, thermoelectric devices, optoelectronics and biological technologies.[120–124]

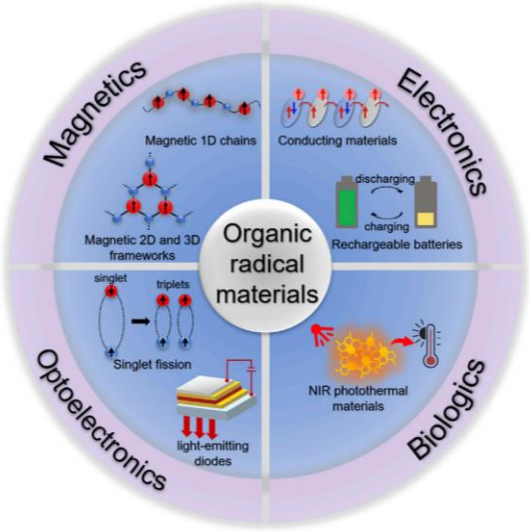

Figure 1.4.3.1: Organic open-shell radical applications (adapted from Chen *et al*. report[119])

Organic radicals can be placed in different classes as shown in **Table 1.4.3.1** below. To make an efficient organic open-shell system, one has to find a balance between the molecular geometric conformations and the electronic structures, properties that cannot be mutually inclusive

in a device. In most cases, these diradicals will fall in the last category which bases the classification on the number of unpaired electrons. The presence of multiple spins in the open shell polyradicals renders them highly reactive making them difficult to design, synthesize and purify. Thus, a lot of focus has been on materials with one or two unpaired electrons. While monoradicals are quite straightforward, it gets a little bit complicated when it comes to the presence of two unpaired electrons. To this day, most literature reports use both diradicals and biradicals interchangeably, which disregards their thermodynamics as well as coupling between the two unpaired electrons.

Table 1.4.3.1: Classification of organic open-shell radicals

Classification	Groups	Definition
Valence	Neutral	Electrically neutral with incomplete valencies
	Doped (radical ions)	Electrically charged by gaining or losing ≥ 1 electrons
Lifetimes	Persistent	Short-lived (hours or days) under an inert environment
	Stable	Can be readily purified as an isolated compound with high thermal and electrochemical stability
Number of unpaired electrons	Monoradical	Contain one unpaired electron in a single molecule with one magnetic moment and a spin quantum number of $S = \frac{1}{2}$ hence a spin multiplicity of doublet $(2S + 1)$
	Diradical/Biradical	Contain two unpaired electrons and can be differentiated by the electron exchange interaction, J, between the unpaired electrons which will be discussed later.
	Polyradical	Contain more than two unpaired electrons and are characterized by their high spin which leads to multiple reactive sites.

A diradical can be described as a molecule with two unpaired electrons where the electron interaction energy, J, so large it increases the coupling between the two unpaired electrons such that these two electrons act as one.[125] The dipole-dipole interaction for diradicals is so large that it can produce two spin states, singlet, and triplet. Diradicals can therefore be further divided into two based on the number of spin multiplicities (which is used to describe their ground-state electronic configurations without the excitation of photons) available after applying an external magnetic field: 1) singlet diradical where $S = 0$ and the spin multiplicity $= 1$, and 2) triplet diradicals where $S = 1$ and the spin multiplicity $= 3$. In ideal cases, the two non-bonding molecular orbitals are energetically degenerate. For nearly degenerate molecular orbitals, the term used is diradicaloid, diradical-like or molecule with a diradical character. On the other hand, a biradical is a molecule where the two unpaired electrons have a separation distance long enough such that there is negligible interaction between the two spins. Ideally, these two separated electrons are energetically degenerate and act independently. Biradicaloids are molecules where

there is the existence of some interaction, and the electrons are almost independent and with similar energy.

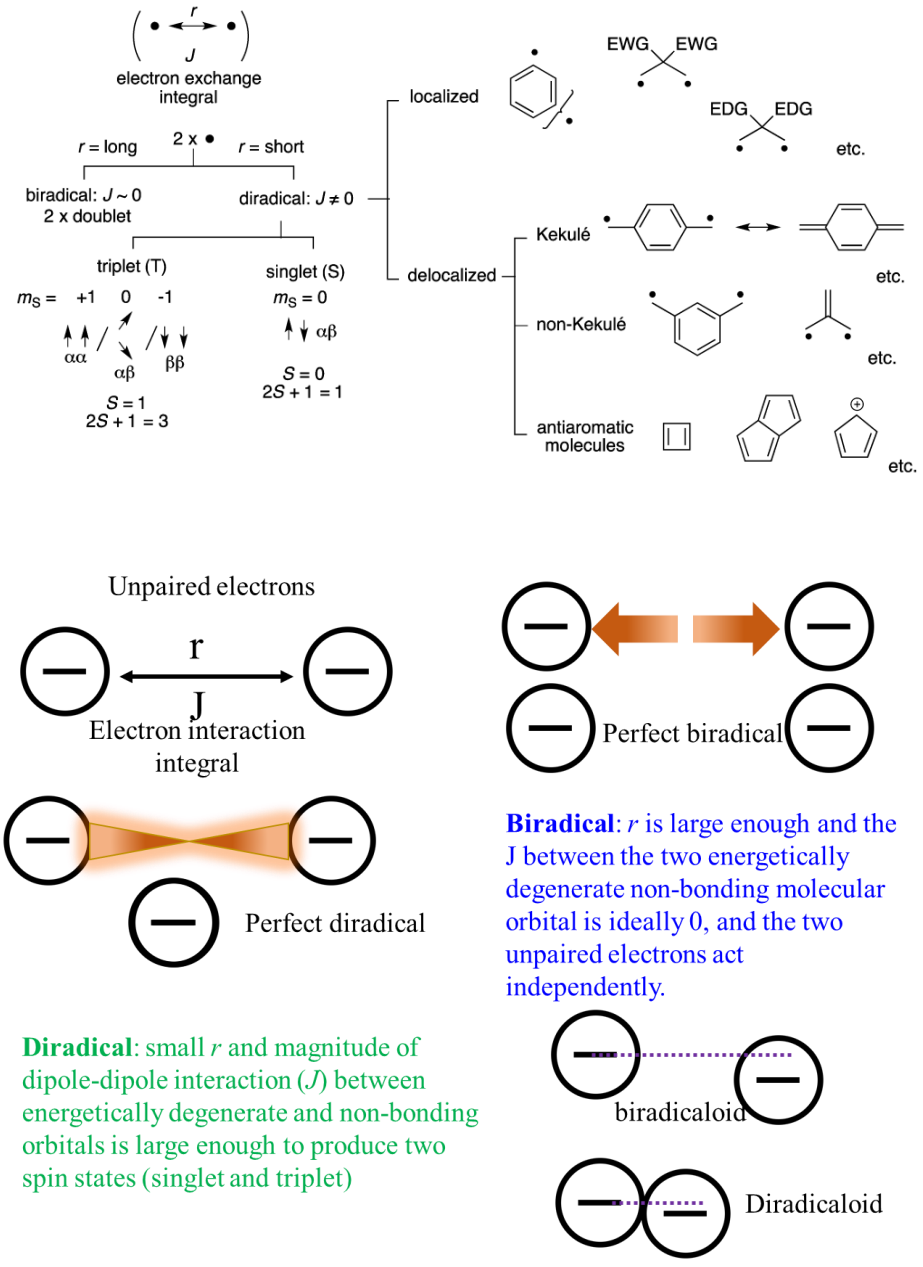

Figure 1.4.3.2: Diradical vs biradical and diradicaloid vs diradicaloid (adapted from Abe's report[125])

For two electrons in nonbonding molecular orbitals, there are 6 electronic configurations: $T_{1,2}, T_{1,2}', S_{1,2}, S_{1,2}', S_{1,1}, S_{2,2}$. When filling two degenerate orbitals in the absence of an external

magnetic field, the triplet electronic configuration is more stable than the singlet configuration based on Hunds' Rule. Here, $T_{1,2} = T_{1,2}{}' > S_{1,2} = S_{1,2}{}' \gg S_{1,1}, S_{2,2}$ and therefore, the triplet should be the ground state spin multiplicity for diradicals or biradicals. In both biradicals and diradicals, the singlet−triplet energy gap, ΔE_{ST}, can be calculated from the electron exchange interaction, J, as shown in **Equation 1.4.3.1**.

$$\Delta E_{ST} = E_S - E_T = 2J \qquad \textbf{(Equation 1.4.3.1)}$$

Where:

E_S is the singlet energy and E_T is the triplet energy.

Here, a negative J value indicates a singlet ground state while a positive J value indicates a triplet ground state.

To quantify the diradical character, a lot of indices have been proposed. For instance, Bachler *et al*. proposed the index below for $\langle \hat{S}^2 \rangle$ of a broken symmetry spin correlated wave function (Eqn 1.4.3.2).[126,127]

$$\eta_{rad} = 1 - \sqrt{1 - \langle \hat{S}^2 \rangle_{BS'}} \qquad \textbf{(Equation 1.4.3.2)}$$

where:

$\langle \hat{S}^2 \rangle_{BS'}$ is the unrestricted Hertree−Fock (UHF) broken symmetry wave function.

Another study calculates the extent of diradical character, y, from the occupation numbers as shown in equation Eqn 1.4.3.3.[126]

$$y = \frac{(1-T)^2}{(1+T)^2} \quad \text{where } T = \frac{n_{HOMO} - n_{LUMO}}{2} \qquad \textbf{(Equation 1.4.3.3)}$$

where:

n_{HOMO} is the occupation number of the bonding spin-unrestricted natural orbitals, and

n_{LUMO} is the occupation number of the nonbonding spin-unrestricted natural orbitals

Kamada *et al*. used a 2-site system to present an analytical form of the diradical character as:

$$y = {1 - 4|t|}\Big/{(U^2 + 16t^2)^{1/2}} \qquad \textbf{(Equation 1.4.3.4)}$$

where:

U is the difference between on-site and intersite Coulomb integrals, and

t is a transfer integral using the localized natural orbital basis.

From this formula, a derivation was done which could be used to experimentally calculate the diradical character.[128]

$$y = 1 - \sqrt{1 - \left(\frac{{}^1E_{1_u} - {}^3E_{1_u}}{{}^1E_{2_g} - {}^1E_{1_g}}\right)^2}$$

$$y = 1 - \sqrt{1 - \left(\frac{E_{S_{1u}S_{1g}} - E_{T_{1u}S_{1g}}}{E_{S_{2g},S_{1g}}}\right)^2} \qquad \textbf{(Equation 1.4.3.5)}$$

where:

${}^1E_{1_g}$ is the energy of the neutral lowest−energy singlet state of g symmetry $|S_{1g}\rangle$
${}^1E_{1_u}$ is the energy of the ionic singlet state with u symmetry $|S_{1u}\rangle$
${}^1E_{2_g}$ is the energy of another singlet state of g symmetry but essentially ionic $|S_{2g}\rangle$
${}^1E_{2_g}$ is the energy of the neutral triplet state $|T_{1u}\rangle$
$E_{S_{1u}S_{1g}}$ is the given by the lowest energy peak of the one photon absorption spectra,
$E_{T_{1u}S_{1g}}$ is the obtained from phosphorescence peak measurements and
$E_{S_{2g},S_{1g}}$ corresponds to the lowest energy peak of the two-photon absorption spectra.

Biradicaloids have been reported to possess low-lying triplet energy levels making them promising structures for singlet exciton fission (SEF) described in **section 1.4.1**. Varnavski *et al*. reported the thermodynamics of biradicaloids as shown in **Figure 1.4.3.3**.[78] Femtosecond and nanosecond transient absorption measurements ultrafast formation of the reported triplet-like species (biradicaloids) with a lifetime is $57\ \mu s$. the absorption spectra of these compounds show absorption that is extended further to the red, a biradicaloid character that fulfills the SEF energetic requirement where $[2E(T_1) < E(S_1)]$. As a result, biradicaloids have proven to be great candidates for organic photovoltaic applications.

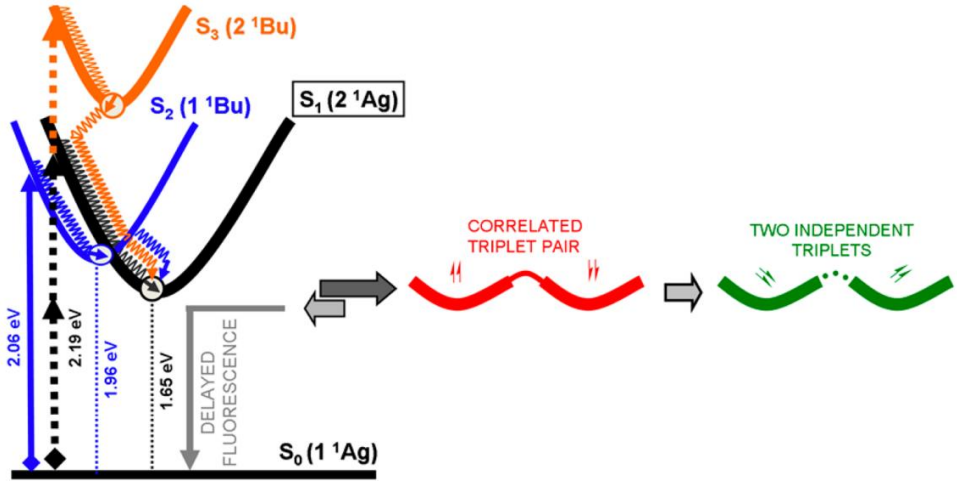

Figure 1.4.3.3: Low-lying electronic states of biradicaloids reported by Varnavski *et al.*[78]

In another report by Lukman *et al.*, the thermodynamics of diradicaloids are highlighted with applications to SEF.[129] The large activation energy reported would lead to the suppression of triplet−pair separation. It was found that the radiative and non-radiative decay of the $[TT]$, assuming total suppression of the separation to form $[T + T]$, was dependent on the diradical character. Therefore, the formation of diradicals had a negative effect on SEF materials given that it prevented the progression of the second step of singlet fission where the double triplet state dephases to form two independent triplets.

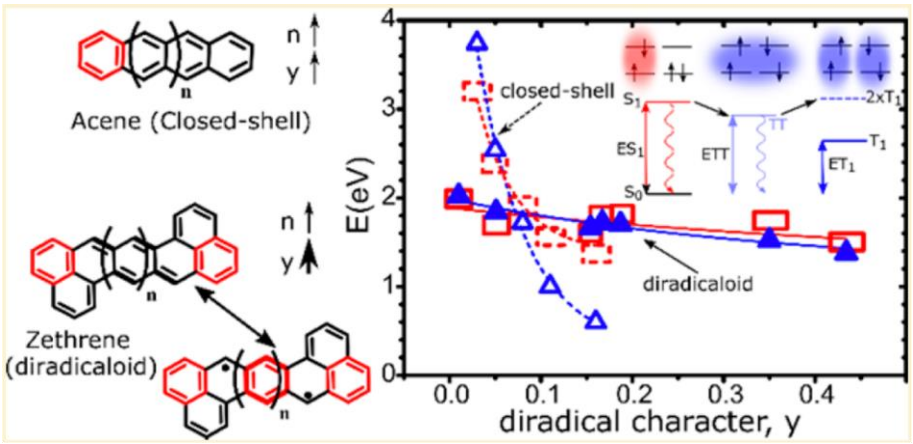

Figure 1.4.3.4: Electronic states of diradicaloids and their effect on SEF as highlighted by Lukman *et al.*[129]

Due to their unique characteristics of low-lying triplet states and the feasible conversion between singlets (S_0) and triplets (T_1) that do not follow the spin prohibition due to the existence

of the generated or nearly generated nonbonding orbitals containing radicals. These diradical characters can offer intermolecular spin-spin interactions which lead to σ −aggregation and formation of σ −polymerization which affects intermolecular stacking and charge transport.[130]

As shown in **Figure 1.4.3.5**, A) shows the quinoidal and aromatic resonance structure of the studied thiophene based structures and B) shows the diradical character, y_0, n −doped electrical conductivity, ambient stability and supramolecular aggregation change with extended π −conjugation.

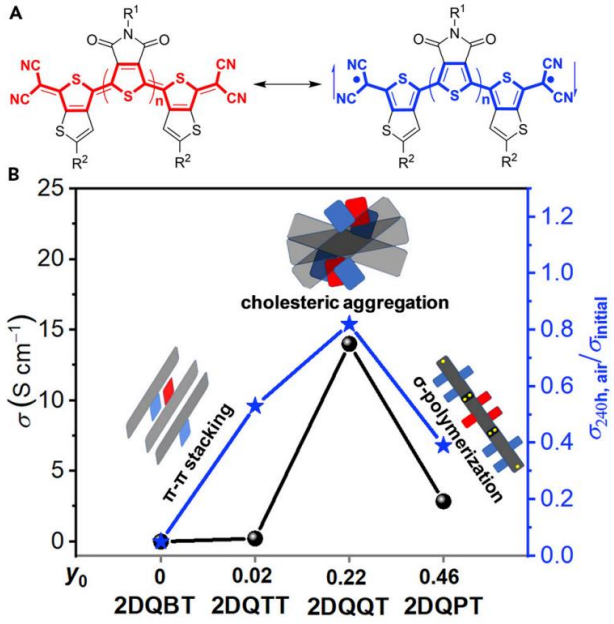

Figure 1.4.3.5: Molecular structures and n −doped property adapted from Yuan.[130]

Another field that has attracted a lot of interest in diradicals is the organic field effect transistors (OFETs). This is because of the amazing characteristics like narrow bandgaps, intimate intermolecular interactions, and redox amphoterism which increase the overall efficiency of OFETs.[131] Although diradicaloid materials have been used as semiconductors for OFET materials with attractive hole mobilities of $1.4\ cm^2V^{-1}s^{-1}$ and ambipolar transport with balanced electron and hole mobilities in the order of $10^{-3}\ cm^2V^{-1}s^{-1}$, their stability is still a huge problem. This problem has been solved by using organic light emitting transistors, which combines the switching capabilities of OFETs and emissive properties of organic light emitting diodes (OLEDs). While diradical characters have been reported to improve the emissive properties of OLEDs,[132] there is no report on the diradical character and its effect on the performance of OFETs.

1.5 Bigger Picture and Dissertation Outline

The increasing global population has increased the energy demand and consumption due to the rise in the value of electricity for lighting and powering entertainment, heating, medical, and communication devices. Previous research shows that solar energy is the most promising source of renewable and sustainable energy and if harnessed properly, it can see excellent technological advances. However, a lot of research is still needed to increase the efficiencies of optical electronic technological devices in order to get them into the market at affordable costs. Therefore, this thesis focuses on using both time resolved and nonlinear optical spectroscopic techniques to probe the dynamics of charge and energy transfer processes which are important to the mechanisms of intramolecular singlet exciton fission and thermally activated delayed fluorescence for organic optoelectronic systems.

In chapter one, the history of optoelectronics is given where the advantages of these organic optoelectronics have been highlighted compared to their conventional counterparts. The different applications which have driven these technologies have been discussed, which has led to the increasing research in a bid to design better optoelectronics for technological advancement.

In chapter two, the experimental methods and techniques that were used to contribute to this science are discussed. With donor-acceptor molecules being the most prominent materials for optoelectronic systems, a lot of research has been done to improve the electron donating and electron accepting capabilities of these materials, with an aim of improving their overall performance while keeping their fabrication cost low. Understanding the two principles, charge transfer and energy transfer, under which these systems operate calls for both linear and nonlinear optical techniques that can probe the dynamics of these processes at different timescales. Therefore, various time resolved and nonlinear optical spectroscopic techniques were used to understand the charge and energy transfer mechanisms that are important in the characterization of these optoelectronics.

In chapter three, the first study where an investigation of the optical properties of thiophene additions to s-Indacene donors with diketopyrrolopyrrole, isoindigo and thienothiophene acceptors was done is discussed. While different studies have reported the importance of the electron donating or withdrawing capability of monomers in a D-A polymer system in improving the PCE

of organic photovoltaic (OPV) devices, the influence of acceptor strength on the photophysical properties of OPVs is still unclear. In this collaboration, different linear and nonlinear optics, as well as time resolved spectroscopic techniques to probe the photophysics of polymers where differently conjugated donors were incorporated with acceptors of varied strengths. It was found that enhanced charge-transfer characteristics for the polymers with extended donor conjugation and stronger acceptor and note that the size of the donor and acceptor (steric hindrance) played a significant role in the photophysical properties of the polymers. These investigations pointed out that not only the donor conjugation and the acceptor strength, but also the size of the donor and acceptor should be considered while designing suitable D−A systems for organic photovoltaic applications. This work was accepted and published by the *Journal of Physical Chemistry, C* (JPC C)

In chapter four, a second study that looks at the effect of altering the π-bridge flexibility in perylene diimide (PDI) trimers activates intramolecular singlet exciton fission and how it affects the efficiency of the resulting organic solar cells is discussed. Donor–Acceptor configuration, which induces an intramolecular charge transfer character, is a molecular design strategy for intramolecular singlet exciton fission (iSEF), a process reported to enhance the theoretical efficiency limit of photovoltaic (PV) devices. Although some studies report the nature of the chromophore and the D-A π–linker to play a crucial role in contributing to the occurrence of iSEF in organic perylene diimide (PDI) chromophores, the iSEF process is still not well understood. In this study, we use nonlinear optical, and time resolved spectroscopic techniques to investigate two analogous perylene diimide (PDI) trimers, whose structures show rotatable single bond π−bridge connection (twisted) vs. rigid/fused π−bridge connection (planar). A fast (~300 ps) and efficient (170% triplet yield) iSEF was observed in the twisted β trimer compound, which leads to the conclusion that the linker flexibility in these multichromophoric PDI systems strongly affects the triplet yield and triplet formation rate. This work was accepted and published by the *Chemical Science* division of the Royal Society of Chemistry.

In chapter five, the role of the core attachment positioning in triggering intramolecular singlet exciton fission in perylene diimide (PDI) tetramers is investigated. Our previous studies suggested that a flexible π–bridge linker is crucial in activating intramolecular singlet exciton fission (iSEF) in multichromophoric systems. In this study, we use time resolved and nonlinear optical techniques to report the photophysical properties of three analogous perylene diimide (PDI) dendritic

tetramers showing flexible/twisted π–bridged structures with $\alpha-$ and $\beta-$substitutions, and a rigid/planar structure with a $\beta-$fused ring (βC) connection to benzodithiophene–thiophene (BDT-Th) core. We find that while the $\alpha-$single–bond connection interrupts the coupling among the PDI units leading to a fast and efficient iSEF (with a triplet quantum yield of 124%), the β connection leads to strong π–π co–facial interactions between the adjacent PDI units in its structure, forming excimer states which trap the singlet excitons inhibiting iSEF. We propose that the formation of the double triplet (^{1}[TT]) state is through a superposition of singlet states known as $[S_1S_0]_{[TT]}$CT which has been suggested previously for pentacene derivatives. This work was accepted and published by the *Journal of Physical Chemistry, B* (JPC B)

In chapter six, a new direct approach for determining the reverse intersystem crossing rate in organic thermally activated delayed fluorescent (TADT) emitters is presented. Thermally activated delayed fluorescence (TADF) is a mechanism that has recently proven to improve the efficiency of optoelectronic devices is by harvesting the 75% triplet excitons (through reverse intersystem crossing) that usually go to waste upon a molecule's photoexcitation. The conventional emission lifetime-based methods used to estimate the rate of reverse intersystem crossing do not factor in the known oxygen quenching effect on triplet species. To improve this area, we used carbazole or acridine derivatives as donors and triazine or benzonitrile derivatives as acceptor moieties to develop a new approach that can be used to calculate the rate of reverse intersystem crossing in TADF organic molecules. We found that a large rate of intersystem crossing and high external quantum efficiency translates to low operating voltages of the investigated chromophores; and that these molecules need a reverse intersystem rate greater than a millisecond to be able to undergo the TADF process. This work was accepted and published by the *Journal of American Chemical Society (*JACS).

In chapter seven, a novel study that highlights the first-ever reported case of long-lived diradical formation in thiophene-based polymer aggregates for organic light emitting transistors (OLETs) is presented. Although traditional materials for organic light-emitting diodes (OLEDs) or organic field-effect transistors (OFETs) have shown modest performance in Organic Light Emitting Transistors (OLET) devices, design strategies towards high-performance OLET materials and the crucial structure–performance relationship remain unclear. Here, we use time resolved and nonlinear optical techniques to study the effect of furan on the charge and energy transfer properties of cross-conjugated weak acceptor-weak donor polymers showing

intramolecular H-aggregation that leads to their exceptional OLET properties in terms of high external quantum efficiencies. Here, we investigate the excited state energy transfer dynamics of two foldable polymer aggregates with two different acceptor monomers: thienopyridothienoquinoline incorporated with a thiophene (TPTQ) and thienopyridothienoquinoline incorporated with a furan molecule (TPTQF), both coupled to a carbazole donor monomer moiety. With the current steady state and nonlinear optical measurements, it was found find furan-based acceptor leads to enhanced energy transfer character as shown by the blue shifted absorption and emission, decreased Stokes Shift, increased molar extinction coefficient, increased photoluminescence quantum yield and enhanced transition dipole moments for TPTQF_C, the molecule that showed enhanced external quantum efficiencies. We find that thiophene-acceptor based foldamers show a diradical character with reduced dipole moments which lowers the charge separation in the resonance structures, reducing the charge transfer and the external quantum efficiency of the TPTQ_C molecule (0.005%). However, no observed diradical character in the furan-based foldamers which exhibits superior device performance with 3.5%. These results will be a step towards producing materials that can be used for high-performance devices. The manuscript of this work is under preparation and will be submitted to the *Journal of American Chemical Society* for consideration.

In chapter 8, a summary of the work is given as well as suggestions for future direction. This could further enhance the current understanding and therefore improve the design of organic optoelectronics

References

(1) Soref, R. A. Silicon-Based Optoelectronics. *Proceedings of the IEEE* **1993**, *81* (12), 1687–1706. https://doi.org/10.1109/5.248958.

(2) Chen, Z.; Obaid, S. N.; Lu, L. Recent Advances in Organic Optoelectronic Devices for Biomedical Applications. *Optical Materials Express* **2019**, *9* (9), 3843. https://doi.org/10.1364/ome.9.003843.

(3) Forrest, S. R. *Ultrathin Organic Films Grown by Organic Molecular Beam Deposition and Related Techniques*; 1997.

(4) Saragi, T. P. I.; Spehr, T.; Siebert, A.; Fuhrmann-Lieker, T.; Salbeck, J. Spiro Compounds for Organic Optoelectronics. *Chemical Reviews*. April 2007, pp 1011–1065. https://doi.org/10.1021/cr0501341.

(5) Nawar, A. M.; Abd-Elsalam, M.; El-Mahalawy, A. M.; El-Nahass, M. M. Analyzed Electrical Performance and Induced Interface Passivation of Fabricated Al/NTCDA/p-Si MIS–Schottky Heterojunction. *Applied Physics A: Materials Science and Processing* **2020**, *126* (2). https://doi.org/10.1007/s00339-020-3289-y.

(6) Jacob, M. v. Organic Semiconductors: Past, Present and Future. *Electronics (Switzerland)*. MDPI AG September 30, 2014, pp 594–597. https://doi.org/10.3390/electronics3040594.

(7) Hideki Shirakawa, B.; Louis, E. J.; Macdiarmid, A. G.; W A N K Chiang, C. H.; HEEGERt, A. J. *Synthesis of Electrically Conducting Organic Polymers : Halogen Derivatives of Polyacetylene, (CH)*; 1977.

(8) Forrest, S. R.; Thompson, M. E. Introduction: Organic Electronics and Optoelectronics. *Chemical Reviews*. April 2007, pp 923–925. https://doi.org/10.1021/cr0501590.

(9) Tang, C. W.; Vanslyke, S. A. Organic Electroluminescent Diodes. *Applied Physics Letters* **1987**, *51* (12), 913–915. https://doi.org/10.1063/1.98799.

(10) Zissis, G.; Bertoldi, P.; Serrenho, T.; European Commission. Joint Research Centre. *Update on the Status of LED-Lighting World Market since 2018.*; Luxembourg, 2021.

(11) Chaudhry, M. U.; Muhieddine, K.; Wawrzinek, R.; Sobus, J.; Tandy, K.; Lo, S. C.; Namdas, E. B. Organic Light-Emitting Transistors: Advances and Perspectives. *Advanced Functional Materials*. Wiley-VCH Verlag May 1, 2020. https://doi.org/10.1002/adfm.201905282.

(12) Ko, J.; Berger, R.; Lee, H.; Yoon, H.; Cho, J.; Char, K. Electronic Effects of Nano-Confinement in Functional Organic and Inorganic Materials for Optoelectronics. *Chemical Society Reviews*. Royal Society of Chemistry March 7, 2021, pp 3585–3628. https://doi.org/10.1039/d0cs01501f.

(13) Withagen, C. *Withagen, C. Pollution and Exhaustibility of Fossil Fuels. Resour. Energy Econ.*; 1994.

(14) Murtaugh, P. A.; Schlax, M. G. Reproduction and the Carbon Legacies of Individuals. *Global Environmental Change* **2009**, *19* (1), 14–20. https://doi.org/10.1016/j.gloenvcha.2008.10.007

(15) Abolhosseini, S.; Heshmati, A.; Altmann, J. *A Review of Renewable Energy Supply and Energy Efficiency Technologies*; 2014.

(16) Elizabeth Chu and D. Lawrence Tarazano. A Brief History of Solar Panels. *U.S. Patent and Trademark Office*. 2018.

(17) Haegel, N. M.; Margolis, R.; Buonassisi, T.; Feldman, D.; Froitzheim, A.; Garabedian, R.; Green, M.; Glunz, S.; Henning, H. M.; Holder, B.; Kaizuka, I.; Kroposki, B.; Matsubara, K.; Niki, S.; Sakurai, K.; Schindler, R. A.; Tumas, W.; Weber, E. R.; Wilson, G.; Woodhouse, M.; Kurtz, S. Terawatt-Scale Photovoltaics: Trajectories and Challenges. *Science*. American Association for the Advancement of Science April 14, 2017, pp 141–143. https://doi.org/10.1126/science.aal1288.

(18) Inganäs, O. Organic Photovoltaics over Three Decades. *Advanced Materials*. Wiley-VCH Verlag August 29, 2018. https://doi.org/10.1002/adma.201800388.

(19) Rafique, S.; Abdullah, S. M.; Sulaiman, K.; Iwamoto, M. Fundamentals of Bulk Heterojunction Organic Solar Cells: An Overview of Stability/Degradation Issues and Strategies for Improvement. *Renewable and Sustainable Energy Reviews*. Elsevier Ltd March 1, 2018, pp 43–53. https://doi.org/10.1016/j.rser.2017.12.008.

(20) Tang, C. W. Two-Layer Organic Photovoltaic Cell. *Applied Physics Letters* **1986**, *48* (2), 183–185. https://doi.org/10.1063/1.96937.

(21) Zhang, M.; Zhu, L.; Zhou, G.; Hao, T.; Qiu, C.; Zhao, Z.; Hu, Q.; Larson, B. W.; Zhu, H.; Ma, Z.; Tang, Z.; Feng, W.; Zhang, Y.; Russell, T. P.; Liu, F. Single-Layered Organic Photovoltaics with Double Cascading Charge Transport Pathways: 18% Efficiencies. *Nature Communications* **2021**, *12* (1). https://doi.org/10.1038/s41467-020-20580-8.

(22) He, Y.; Chen, H. Y.; Hou, J.; Li, Y. Indene - C60 Bisadduct: A New Acceptor for High-Performance Polymer Solar Cells. *Journal of the American Chemical Society* **2010**, *132* (4), 1377–1382. https://doi.org/10.1021/ja908602j.

(23) Zhao, G. J.; He, Y. J.; Li, Y. 6.5% Efficiency of Polymer Solar Cells Based on Poly(3-Hexylthiophene) and Indene-C60 Bisadduct by Device Optimization. *Advanced Materials* **2010**, *22* (39), 4355–4358. https://doi.org/10.1002/adma.201001339.

(24) Guo, Q.; Guo, Q.; Geng, Y.; Tang, A.; Zhang, M.; Du, M.; Sun, X.; Zhou, E. Recent Advances in PM6:Y6-Based Organic Solar Cells. *Materials Chemistry Frontiers*. Royal Society of Chemistry April 21, 2021, pp 3257–3280. https://doi.org/10.1039/d1qm00060h.

(25) Ma, L.; Zhang, S.; Wang, J.; Xu, Y.; Hou, J. Recent Advances in Non-Fullerene Organic Solar Cells: From Lab to Fab. *Chemical Communications* **2020**, *56* (92), 14337–14352. https://doi.org/10.1039/d0cc05528j.

(26) Li, S.; Li, C. Z.; Shi, M.; Chen, H. New Phase for Organic Solar Cell Research: Emergence of Y-Series Electron Acceptors and Their Perspectives. *ACS Energy Letters*. American Chemical Society May 8, 2020, pp 1554–1567. https://doi.org/10.1021/acsenergylett.0c00537.

(27) Xu, X.; Yu, L.; Yan, H.; Li, R.; Peng, Q. Highly Efficient Non-Fullerene Organic Solar Cells Enabled by a Delayed Processing Method Using a Non-Halogenated Solvent. *Energy and Environmental Science* **2020**, *13* (11), 4381–4388. https://doi.org/10.1039/d0ee02034f.

(28) Xia, H.; Zhang, Y.; Deng, W.; Liu, K.; Xia, X.; Su, C.; Jeng, U.; Zhang, M.; Huang, J.; Huang, J.; Yan, C.; Wong, W.; Lu, X.; Zhu, W.; Li, G. Novel Oligomer Enables Green Solvent Processed 17.5% Ternary Organic Solar Cells: Synergistic Energy Loss Reduction and Morphology Fine-Tuning. *Advanced Materials* **2022**, 2107659. https://doi.org/10.1002/adma.202107659.

(29) Green, M. A.; Dunlop, E. D.; Hohl-Ebinger, J.; Yoshita, M.; Kopidakis, N.; Hao, X. Solar Cell Efficiency Tables (Version 59). *Progress in Photovoltaics: Research and Applications* **2022**, *30* (1), 3–12. https://doi.org/10.1002/pip.3506.

(30) Heilmeier, G. H.; Zanoni, L. A.; Barton, L. A. Dynamic Scattering: A New Electrooptic Effect in Certain Classes of Nematic Liquid Crystals. *Proceedings of the IEEE* **1968**, *56* (7), 1162–1171. https://doi.org/10.1109/PROC.1968.6513.

(31) Heilmeier, G. H.; Zanoni, L. A.; Barton, L. A. Further Studies of the Dynamic Scattering Mode in Nematic Liquid Crystals. *IEEE Transactions on Electron Devices* **1970**, *ED-17* (1), 22–26. https://doi.org/10.1109/T-ED.1970.16918.

(32) Heilmeier, G. H.; Zanoni, L. A.; Barton, L. A. Dynamic Scattering in Nematic Liquid Crystals. *Applied Physics Letters* **1968**, *13* (1), 46–47. https://doi.org/10.1063/1.1652453.

(33) Chen, H. W.; Lee, J. H.; Lin, B. Y.; Chen, S.; Wu, S. T. Liquid Crystal Display and Organic Light-Emitting Diode Display: Present Status and Future Perspectives. *Light: Science and Applications*. Springer Nature March 1, 2018, p 17168. https://doi.org/10.1038/lsa.2017.168.

(34) Luo, Z. *OLED versus LCD: Who Wins? Advanced Fast-Response LC Displays and Devices View Project*; 2016.

(35) Song, D.; Zhao, S.; Luo, Y.; Aziz, H. Causes of Efficiency Roll-off in Phosphorescent Organic Light Emitting Devices: Triplet-Triplet Annihilation versus Triplet-Polaron Quenching. *Applied Physics Letters* **2010**, *97* (24). https://doi.org/10.1063/1.3527085.

(36) Uoyama, H.; Goushi, K.; Shizu, K.; Nomura, H.; Adachi, C. Highly Efficient Organic Light-Emitting Diodes from Delayed Fluorescence. *Nature* **2012**, *492* (7428), 234–238. https://doi.org/10.1038/nature11687.

(37) Qin, Z.; Gao, H.; Dong, H.; Hu, W. Organic Light-Emitting Transistors Entering a New Development Stage. *Advanced Materials*. John Wiley and Sons Inc August 1, 2021. https://doi.org/10.1002/adma.202007149.

(38) Hepp, A.; Heil, H.; Weise, W.; Ahles, M.; Schmechel, R.; von Seggern, H. Light-Emitting Field-Effect Transistor Based on a Tetracene Thin Film. *Physical Review Letters* **2003**, *91* (15). https://doi.org/10.1103/PhysRevLett.91.157406.

(39) Bardeen John; Summit; Brattain Walter H; N.J. Morristown. THREE-ELECTRODE CIRCUIT ELEMENT UTILIZING SEMCONDUCTIVE MATERIAELS . 33466, June 17, 1948.

(40) Cho, S. Y.; Kim, S. Y.; Jeon, S.; Choi, R.; Lee, J. H. A Strategy to Boost External Quantum Efficiency of Organic Light-Emitting Transistors. *Applied Physics Letters* **2019**, *115* (4). https://doi.org/10.1063/1.5094925.

(41) Bail, R.; Kang, J. W.; Kang, Y. J.; Chin, B. D. Binary Solvent Effects on Thermally Crosslinked Small Molecular Thin Films for Solution Processed Organic Light-Emitting

Diodes. *Electronic Materials Letters* **2021**, *17* (1), 74–86. https://doi.org/10.1007/s13391-020-00258-5.

(42) Qin, Z.; Gao, H.; Liu, J.; Zhou, K.; Li, J.; Dang, Y.; Huang, L.; Deng, H.; Zhang, X.; Dong, H.; Hu, W. High-Efficiency Single-Component Organic Light-Emitting Transistors. *Advanced Materials* **2019**, *31* (37). https://doi.org/10.1002/adma.201903175.

(43) Chen, H.; Xing, X.; Miao, J.; Zhao, C.; Zhu, M.; Bai, J. W.; He, Y.; Meng, H. Highly Efficient Flexible Organic Light Emitting Transistor Based on High-k Polymer Gate Dielectric. *Advanced Optical Materials* **2020**, *8* (6). https://doi.org/10.1002/adom.201901651.

(44) Soldano, C. Engineering Dielectric Materials for High-Performance Organic Light Emitting Transistors (Olets). *Materials* **2021**, *14* (13). https://doi.org/10.3390/ma14133756.

(45) Yuan, D.; Sharapov, V.; Liu, X.; Yu, L. Design of High-Performance Organic Light-Emitting Transistors. *ACS Omega*. American Chemical Society January 14, 2020, pp 68–74. https://doi.org/10.1021/acsomega.9b03630.

(46) *Applied Photochemistry Light Meets Molecules*; Bergamini, G., Silvi, S., Eds.; 2016; Vol. 92.

(47) Mayer, A. C.; Scully, S. R.; Hardin, B. E.; Rowell, M. W.; Mcgehee, M. D. *Polymer-Based Solar Cells*; 2007.

(48) Blom, P. W. M.; Mihailetchi, V. D.; Koster, L. J. A.; Markov, D. E. Device Physics of Polymer:Fullerene Bulk Heterojunction Solar Cells. *Advanced Materials* **2007**, *19* (12), 1551–1566. https://doi.org/10.1002/adma.200601093.

(49) Brabec, C. J.; Winder, C.; Sariciftci, N. S.; Hummelen, J. C.; Dhanabalan, A.; van Hal, P. A.; Janssen, R. A. J. *A Low-Bandgap Semiconducting Polymer for Photovoltaic Devices and Infrared Emitting Diodes***.

(50) Scharber, M. C.; Sariciftci, N. S. Efficiency of Bulk-Heterojunction Organic Solar Cells. *Progress in Polymer Science*. December 2013, pp 1929–1940. https://doi.org/10.1016/j.progpolymsci.2013.05.001.

(51) Kersting, R.; Lemmer, U.; Deussen, M.; Bakker, H. J.; Mahrt, R. I.; Kurz, H.; Arkhipov, V. I.; Bassler, H.; GObel-, E. O. *Ultrafast Field-Induced Dissociation of Excitons in Conjugated Polymers*; 1994; Vol. 73.

(52) Brédas, J. L.; Beljonne, D.; Coropceanu, V.; Cornil, J. Charge-Transfer and Energy-Transfer Processes in π-Conjugated Oligomers and Polymers: A Molecular Picture. *Chemical Reviews* **2004**, *104* (11), 4971–5003. https://doi.org/10.1021/cr040084k.

(53) Smith, M. B.; Michl, J. Singlet Fission. *Chemical Reviews* **2010**, *110* (11), 6891–6936. https://doi.org/10.1021/cr1002613.

(54) Shockley, W.; Queisser, H. J. Detailed Balance Limit of Efficiency of P-n Junction Solar Cells. *Journal of Applied Physics* **1961**, *32* (3), 510–519. https://doi.org/10.1063/1.1736034.

(55) Wfirfel, P. *Limiting Efficiency for Solar Cells with Defects from a Three-Level Model*; 1993; Vol. 29.

(56) Keevers, M. J.; Green, M. A. Efficiency Improvements of Silicon Solar Cells by the Impurity Photovoltaic Effect. *Journal of Applied Physics* **1994**, *75* (8), 4022–4031. https://doi.org/10.1063/1.356025.

(57) Markvart', T.; Landsberg2, P. T. *Everyman's Guide to Third Generation Efficiencies*; 2003.

(58) Pnjwels, H.; Vos, A. de. *DETERMINATION OF THE MAXIMUM EFFICIENCY SOLAR CELL STRUCTURE*; 1980.

(59) de Vos, A. *Detailed Balance Limit of the Efficiency of Tandem Solar Cells*; 1980; Vol. 13.

(60) Bremner, S. P.; Levy, M. Y.; Honsberg, C. B. Analysis of Tandem Solar Cell Efficiencies under AM1.5G Spectrum Using a Rapid Flux Calculation Method. *Progress in Photovoltaics: Research and Applications* **2008**, *16* (3), 225–233. https://doi.org/10.1002/pip.799.

(61) Luque, A.; Martí, A. *Increasing the Efficiency of Ideal Solar Cells by Photon Induced Transitions at Intermediate Levels*; 1997.

(62) Hanna, M. C.; Nozik, A. J. Solar Conversion Efficiency of Photovoltaic and Photoelectrolysis Cells with Carrier Multiplication Absorbers. *Journal of Applied Physics* **2006**, *100* (7). https://doi.org/10.1063/1.2356795.

(63) Singh, S.; Jones, W. J.; Siebrand, W.; Stoicheff, B. P.; Schneider, W. G. Laser Generation of Excitons and Fluorescence in Anthracene Crystals. *The Journal of Chemical Physics* **1965**, *42* (1), 330–342. https://doi.org/10.1063/1.1695695.

(64) Bimolecular Radiationless Transitions in Crystalline Tetracene. **1968**.

(65) Mandal, A.; Chen, M.; Foszcz, E. D.; Schultz, J. D.; Kearns, N. M.; Young, R. M.; Zanni, M. T.; Wasielewski, M. R. Two-Dimensional Electronic Spectroscopy Reveals Excitation Energy-Dependent State Mixing during Singlet Fission in a Terrylenediimide Dimer. *Journal of the American Chemical Society* **2018**, *140* (51), 17907–17914. https://doi.org/10.1021/jacs.8b08627.

(66) Berkelbach, T. C.; Hybertsen, M. S.; Reichman, D. R. Microscopic Theory of Singlet Exciton Fission. I. General Formulation. *Journal of Chemical Physics* **2013**, *138* (11). https://doi.org/10.1063/1.4794425.

(67) Berkelbach, T. C.; Hybertsen, M. S.; Reichman, D. R. Microscopic Theory of Singlet Exciton Fission. II. Application to Pentacene Dimers and the Role of Superexchange. *Journal of Chemical Physics* **2013**, *138* (11). https://doi.org/10.1063/1.4794427.

(68) Monahan, N.; Zhu, X. Y. Charge Transfer-Mediated Singlet Fission. *Annual Review of Physical Chemistry* **2015**, *66*, 601–618. https://doi.org/10.1146/annurev-physchem-040214-121235.

(69) Chan, W. L.; Berkelbach, T. C.; Provorse, M. R.; Monahan, N. R.; Tritsch, J. R.; Hybertsen, M. S.; Reichman, D. R.; Gao, J.; Zhu, X. Y. The Quantum Coherent Mechanism for Singlet Fission: Experiment and Theory. *Accounts of Chemical Research*. June 18, 2013, pp 1321–1329. https://doi.org/10.1021/ar300286s.

(70) Zimmerman, P. M.; Bell, F.; Casanova, D.; Head-Gordon, M. Mechanism for Singlet Fission in Pentacene and Tetracene: From Single Exciton to Two Triplets. *Journal of the American Chemical Society* **2011**, *133* (49), 19944–19952. https://doi.org/10.1021/ja208431r.

(71) Greyson, E. C.; Stepp, B. R.; Chen, X.; Schwerin, A. F.; Paci, I.; Smith, M. B.; Akdag, A.; Johnson, J. C.; Nozik, A. J.; Michl, J.; Ratner, M. A. Singlet Exciton Fission for Solar Cell Applications: Energy Aspects of Interchromophore Coupling. *Journal of Physical Chemistry B* **2010**, *114* (45), 14223–14232. https://doi.org/10.1021/jp909002d.

(72) Miller, C. E.; Wasielewski, M. R.; Schatz, G. C. Modeling Singlet Fission in Rylene and Diketopyrrolopyrrole Derivatives: The Role of the Charge Transfer State in Superexchange and Excimer Formation. *Journal of Physical Chemistry C* **2017**, *121* (19), 10345–10350. https://doi.org/10.1021/acs.jpcc.7b02697.

(73) Feng, X.; Krylov, A. I. On Couplings and Excimers: Lessons from Studies of Singlet Fission in Covalently Linked Tetracene Dimers. *Physical Chemistry Chemical Physics* **2016**, *18* (11), 7751–7761. https://doi.org/10.1039/c6cp00177g.

(74) Ye, T.; Singh, R.; Butt, H. J.; Floudas, G.; Keivanidis, P. E. Effect of Local and Global Structural Order on the Performance of Perylene Diimide Excimeric Solar Cells. *ACS Applied Materials and Interfaces* **2013**, *5* (22), 11844–11857. https://doi.org/10.1021/am4035416.

(75) Katoh, R.; Sinha, S.; Murata, S.; Tachiya, M. *Origin of the Stabilization Energy of Perylene Excimer as Studied by Fluorescence and Near-IR Transient Absorption Spectroscopy*; 2001; Vol. 145.

(76) Fuemmeler, E. G.; Sanders, S. N.; Pun, A. B.; Kumarasamy, E.; Zeng, T.; Miyata, K.; Steigerwald, M. L.; Zhu, X. Y.; Sfeir, M. Y.; Campos, L. M.; Ananth, N. A Direct Mechanism of Ultrafast Intramolecular Singlet Fission in Pentacene Dimers. *ACS Central Science* **2016**, *2* (5), 316–324. https://doi.org/10.1021/acscentsci.6b00063.

(77) Low, J. Z.; Sanders, S. N.; Campos, L. M. Correlating Structure and Function in Organic Electronics: From Single Molecule Transport to Singlet Fission. *Chemistry of Materials*. American Chemical Society August 25, 2015, pp 5453–5463. https://doi.org/10.1021/cm502366x.

(78) Varnavski, O.; Abeyasinghe, N.; Aragó, J.; Serrano-Pérez, J. J.; Ortí, E.; López Navarrete, J. T.; Takimiya, K.; Casanova, D.; Casado, J.; Goodson, T. High Yield Ultrafast Intramolecular Singlet Exciton Fission in a Quinoidal Bithiophene. *Journal of Physical Chemistry Letters* **2015**, *6* (8), 1375–1384. https://doi.org/10.1021/acs.jpclett.5b00198.

(79) Hong, Y.; Kim, J.; Kim, W.; Kaufmann, C.; Kim, H.; Würthner, F.; Kim, D. Efficient Multiexciton State Generation in Charge-Transfer-Coupled Perylene Bisimide Dimers via Structural Control. *Journal of the American Chemical Society* **2020**, *142* (17), 7845–7857. https://doi.org/10.1021/jacs.0c00870.

(80) Korovina, N. v.; Das, S.; Nett, Z.; Feng, X.; Joy, J.; Haiges, R.; Krylov, A. I.; Bradforth, S. E.; Thompson, M. E. Singlet Fission in a Covalently Linked Cofacial Alkynyltetracene Dimer. *Journal of the American Chemical Society* **2016**, *138* (2), 617–627. https://doi.org/10.1021/jacs.5b10550.

(81) Huang, H.; Wu, Q. *Achieving Long-Lived Triplet States in Intramolecular SF Films through Molecular Engineering*; 2019.

(82) Weiss, L. R.; Bayliss, S. L.; Kraffert, F.; Thorley, K. J.; Anthony, J. E.; Bittl, R.; Friend, R. H.; Rao, A.; Greenham, N. C.; Behrends, J. Strongly Exchange-Coupled Triplet Pairs in an Organic Semiconductor. *Nature Physics* **2017**, *13* (2), 176–181. https://doi.org/10.1038/nphys3908.

(83) Papadopoulos, I.; Zirzlmeier, J.; Hetzer, C.; Bae, Y. J.; Krzyaniak, M. D.; Wasielewski, M. R.; Clark, T.; Tykwinski, R. R.; Guldi, D. M. Varying the Interpentacene Electronic Coupling to Tune Singlet Fission. *Journal of the American Chemical Society* **2019**, *141* (15), 6191–6203. https://doi.org/10.1021/jacs.8b09510.

(84) Miyata, K.; Kurashige, Y.; Watanabe, K.; Sugimoto, T.; Takahashi, S.; Tanaka, S.; Takeya, J.; Yanai, T.; Matsumoto, Y. Coherent Singlet Fission Activated by Symmetry Breaking. *Nature Chemistry* **2017**, *9* (10), 983–989. https://doi.org/10.1038/nchem.2784.

(85) Basel, B. S.; Zirzlmeier, J.; Hetzer, C.; Phelan, B. T.; Krzyaniak, M. D.; Reddy, S. R.; Coto, P. B.; Horwitz, N. E.; Young, R. M.; White, F. J.; Hampel, F.; Clark, T.; Thoss, M.; Tykwinski, R. R.; Wasielewski, M. R.; Guldi, D. M. Unified Model for Singlet Fission within a Non-Conjugated Covalent Pentacene Dimer. *Nature Communications* **2017**, *8*. https://doi.org/10.1038/ncomms15171.

(86) Basel, B. S.; Zirzlmeier, J.; Hetzer, C.; Reddy, S. R.; Phelan, B. T.; Krzyaniak, M. D.; Volland, M. K.; Coto, P. B.; Young, R. M.; Clark, T.; Thoss, M.; Tykwinski, R. R.; Wasielewski, M. R.; Guldi, D. M. Evidence for Charge-Transfer Mediation in the Primary Events of Singlet Fission in a Weakly Coupled Pentacene Dimer. *Chem* **2018**, *4* (5), 1092–1111. https://doi.org/10.1016/j.chempr.2018.04.006.

(87) Stern, H. L.; Cheminal, A.; Yost, S. R.; Broch, K.; Bayliss, S. L.; Chen, K.; Tabachnyk, M.; Thorley, K.; Greenham, N.; Hodgkiss, J. M.; Anthony, J.; Head-Gordon, M.; Musser, A. J.; Rao, A.; Friend, R. H. Vibronically Coherent Ultrafast Triplet-Pair Formation and Subsequent Thermally Activated Dissociation Control Efficient Endothermic Singlet Fission. *Nature Chemistry* **2017**, *9* (12), 1205–1212. https://doi.org/10.1038/nchem.2856.

(88) Greyson, E. C.; Vura-Weis, J.; Michl, J.; Ratner, M. A. Maximizing Singlet Fission in Organic Dimers: Theoretical Investigation of Triplet Yield in the Regime of Localized Excitation and Fast Coherent Electron Transfer. *Journal of Physical Chemistry B* **2010**, *114* (45), 14168–14177. https://doi.org/10.1021/jp907392q.

(89) Alvertis, A. M.; Lukman, S.; Hele, T. J. H.; Fuemmeler, E. G.; Feng, J.; Wu, J.; Greenham, N. C.; Chin, A. W.; Musser, A. J. Switching between Coherent and Incoherent Singlet Fission via Solvent-Induced Symmetry Breaking. *Journal of the American Chemical Society* **2019**, *141* (44), 17558–17570. https://doi.org/10.1021/jacs.9b05561.

(90) Sanders, S. N.; Kumarasamy, E.; Pun, A. B.; Appavoo, K.; Steigerwald, M. L.; Campos, L. M.; Sfeir, M. Y. Exciton Correlations in Intramolecular Singlet Fission. *Journal of the American Chemical Society* **2016**, *138* (23), 7289–7297. https://doi.org/10.1021/jacs.6b00657.

(91) Korovina, N. v.; Joy, J.; Feng, X.; Feltenberger, C.; Krylov, A. I.; Bradforth, S. E.; Thompson, M. E. Linker-Dependent Singlet Fission in Tetracene Dimers. *Journal of the American Chemical Society* **2018**, *140* (32), 10179–10190. https://doi.org/10.1021/jacs.8b04401.

(92) Krishnapriya, K. C.; Musser, A. J.; Patil, S. Molecular Design Strategies for Efficient Intramolecular Singlet Exciton Fission. *ACS Energy Letters* **2019**, *4* (1), 192–202. https://doi.org/10.1021/acsenergylett.8b01833.

(93) Rickhaus, M.; Mayor, M.; Juríček, M. Strain-Induced Helical Chirality in Polyaromatic Systems. *Chemical Society Reviews*. Royal Society of Chemistry March 21, 2016, pp 1542–1556. https://doi.org/10.1039/c5cs00620a.

(94) Maliakal, A.; Raghavachari, K.; Katz, H.; Chandross, E.; Siegrist, T. Photochemical Stability of Pentacene and a Substituted Pentacene in Solution and in Thin Films. *Chemistry of Materials* **2004**, *16* (24), 4980–4986. https://doi.org/10.1021/cm049060k.

(95) Chen, W.; Zhang, Q. Recent Progress in Non-Fullerene Small Molecule Acceptors in Organic Solar Cells (OSCs). *Journal of Materials Chemistry C*. Royal Society of Chemistry 2017, pp 1275–1302. https://doi.org/10.1039/c6tc05066b.

(96) Hartnett, P. E.; Timalsina, A.; Matte, H. S. S. R.; Zhou, N.; Guo, X.; Zhao, W.; Facchetti, A.; Chang, R. P. H.; Hersam, M. C.; Wasielewski, M. R.; Marks, T. J. Slip-Stacked Perylenediimides as an Alternative Strategy for High Efficiency Nonfullerene Acceptors in Organic Photovoltaics. *Journal of the American Chemical Society* **2014**, *136* (46), 16345–16356. https://doi.org/10.1021/ja508814z.

(97) Margulies, E. A.; Miller, C. E.; Wu, Y.; Ma, L.; Schatz, G. C.; Young, R. M.; Wasielewski, M. R. Enabling Singlet Fission by Controlling Intramolecular Charge Transfer in π-Stacked Covalent Terrylenediimide Dimers. *Nature Chemistry* **2016**, *8* (12), 1120–1125. https://doi.org/10.1038/nchem.2589.

(98) Feng, X.; Luzanov, A. v.; Krylov, A. I. Fission of Entangled Spins: An Electronic Structure Perspective. *Journal of Physical Chemistry Letters* **2013**, *4* (22), 3845–3852. https://doi.org/10.1021/jz402122m.

(99) Kolomeisky, A. B.; Feng, X.; Krylov, A. I. A Simple Kinetic Model for Singlet Fission: A Role of Electronic and Entropic Contributions to Macroscopic Rates. *Journal of Physical Chemistry C* **2014**, *118* (10), 5188–5195. https://doi.org/10.1021/jp4128176.

(100) Liu, H.; Nichols, V. M.; Shen, L.; Jahansouz, S.; Chen, Y.; Hanson, K. M.; Bardeen, C. J.; Li, X. Synthesis and Photophysical Properties of a "Face-to-Face" Stacked Tetracene Dimer. *Physical Chemistry Chemical Physics* **2015**, *17* (9), 6523–6531. https://doi.org/10.1039/c4cp05444j.

(101) Brown, K. E.; Salamant, W. A.; Shoer, L. E.; Young, R. M.; Wasielewski, M. R. Direct Observation of Ultrafast Excimer Formation in Covalent Perylenediimide Dimers Using Near-Infrared Transient Absorption Spectroscopy. *Journal of Physical Chemistry Letters* **2014**, *5* (15), 2588–2593. https://doi.org/10.1021/jz5011797.

(102) Young, R. M.; Wasielewski, M. R. Mixed Electronic States in Molecular Dimers: Connecting Singlet Fission, Excimer Formation, and Symmetry-Breaking Charge Transfer. *Accounts of Chemical Research* **2020**, *53* (9), 1957–1968. https://doi.org/10.1021/acs.accounts.0c00397.

(103) Chen, M.; Bae, Y. J.; Mauck, C. M.; Mandal, A.; Young, R. M.; Wasielewski, M. R. Singlet Fission in Covalent Terrylenediimide Dimers: Probing the Nature of the Multiexciton State Using Femtosecond Mid-Infrared Spectroscopy. *Journal of the American Chemical Society* **2018**, *140* (29), 9184–9192. https://doi.org/10.1021/jacs.8b04830.

(104) Lukman, S.; Musser, A. J.; Chen, K.; Athanasopoulos, S.; Yong, C. K.; Zeng, Z.; Ye, Q.; Chi, C.; Hodgkiss, J. M.; Wu, J.; Friend, R. H.; Greenham, N. C. Tuneable Singlet Exciton Fission and Triplet-Triplet Annihilation in an Orthogonal Pentacene Dimer. *Advanced Functional Materials* **2015**, *25* (34), 5452–5461. https://doi.org/10.1002/adfm.201501537.

(105) Tayebjee, M. J. Y.; Sanders, S. N.; Kumarasamy, E.; Campos, L. M.; Sfeir, M. Y.; McCamey, D. R. Quintet Multiexciton Dynamics in Singlet Fission. *Nature Physics* **2017**, *13* (2), 182–188. https://doi.org/10.1038/nphys3909.

(106) De, D.; Pereira, S.; Data, P.; Monkman, A. P. *Methods of Analysis of Organic Light Emitting Diodes †*; Vol. 2.

(107) Wei, J.; Zhang, C.; Zhang, D.; Zhang, Y.; Liu, Z.; Li, Z.; Yu, G.; Duan, L. Indolo[3,2,1-Jk]Carbazole Embedded Multiple-Resonance Fluorophors for Narrowband Deep-Blue Electroluminescence with EQE≈34.7 % and CIEy≈0.085. *Angewandte Chemie - International Edition* **2021**, *60* (22), 12269–12273. https://doi.org/10.1002/anie.202017328.

(108) Li, W.; Li, M.; Li, W.; Xu, Z.; Gan, L.; Liu, K.; Zheng, N.; Ning, C.; Chen, D.; Wu, Y. C.; Su, S. J. Spiral Donor Design Strategy for Blue Thermally Activated Delayed Fluorescence Emitters. *ACS Applied Materials and Interfaces* **2021**, *13* (4), 5302–5311. https://doi.org/10.1021/acsami.0c19302.

(109) Lin, T. A.; Chatterjee, T.; Tsai, W. L.; Lee, W. K.; Wu, M. J.; Jiao, M.; Pan, K. C.; Yi, C. L.; Chung, C. L.; Wong, K. T.; Wu, C. C. Sky-Blue Organic Light Emitting Diode with 37% External Quantum Efficiency Using Thermally Activated Delayed Fluorescence from Spiroacridine-Triazine Hybrid. *Advanced Materials* **2016**, *28* (32), 6976–6983. https://doi.org/10.1002/adma.201601675.

(110) Peng, C. C.; Yang, S. Y.; Li, H. C.; Xie, G. H.; Cui, L. S.; Zou, S. N.; Poriel, C.; Jiang, Z. Q.; Liao, L. S. Highly Efficient Thermally Activated Delayed Fluorescence via an Unconjugated Donor–Acceptor System Realizing EQE of Over 30%. *Advanced Materials* **2020**, *32* (48). https://doi.org/10.1002/adma.202003885.

(111) Kothavale, S.; Chung, W. J.; Lee, J. Y. High Efficiency and Long Lifetime Orange-Red Thermally Activated Delayed Fluorescent Organic Light Emitting Diodes by Donor and Acceptor Engineering. *Journal of Materials Chemistry C* **2021**, *9* (2), 528–536. https://doi.org/10.1039/d0tc04465b.

(112) Tang, X.; Cui, L. S.; Li, H. C.; Gillett, A. J.; Auras, F.; Qu, Y. K.; Zhong, C.; Jones, S. T. E.; Jiang, Z. Q.; Friend, R. H.; Liao, L. S. Highly Efficient Luminescence from Space-Confined Charge-Transfer Emitters. *Nature Materials* **2020**, *19* (12), 1332–1338. https://doi.org/10.1038/s41563-020-0710-z.

(113) dos Santos, P. L.; Ward, J. S.; Congrave, D. G.; Batsanov, A. S.; Eng, J.; Stacey, J. E.; Penfold, T. J.; Monkman, A. P.; Bryce, M. R. Triazatruxene: A Rigid Central Donor Unit for a D–A3 Thermally Activated Delayed Fluorescence Material Exhibiting Sub-Microsecond Reverse

Intersystem Crossing and Unity Quantum Yield via Multiple Singlet–Triplet State Pairs. *Advanced Science* **2018**, *5* (6). https://doi.org/10.1002/advs.201700989.

(114) Zhang, Y.; Zhang, D.; Wei, J.; Hong, X.; Lu, Y.; Hu, D.; Li, G.; Liu, Z.; Chen, Y.; Duan, L. Achieving Pure Green Electroluminescence with CIEy of 0.69 and EQE of 28.2% from an Aza-Fused Multi-Resonance Emitter. *Angewandte Chemie - International Edition* **2020**, *59* (40), 17499–17503. https://doi.org/10.1002/anie.202008264.

(115) Yang, Z.; Mao, Z.; Xie, Z.; Zhang, Y.; Liu, S.; Zhao, J.; Xu, J.; Chi, Z.; Aldred, M. P. Recent Advances in Organic Thermally Activated Delayed Fluorescence Materials. *Chemical Society Reviews*. Royal Society of Chemistry February 7, 2017, pp 915–1016. https://doi.org/10.1039/c6cs00368k.

(116) Tao, Y.; Yuan, K.; Chen, T.; Xu, P.; Li, H.; Chen, R.; Zheng, C.; Zhang, L.; Huang, W. Thermally Activated Delayed Fluorescence Materials towards the Breakthrough of Organoelectronics. *Advanced Materials*. Wiley-VCH Verlag December 23, 2014, pp 7931–7958. https://doi.org/10.1002/adma.201402532.

(117) Ratera, I.; Veciana, J. Playing with Organic Radicals as Building Blocks for Functional Molecular Materials. *Chemical Society Reviews* **2012**, *41* (1), 303–349. https://doi.org/10.1039/c1cs15165g.

(118) Gomberg, G. AN INSTANCE OF TRIVALENT CARBON- TRIPHENYLMETHYL. *J. Am. Chem. Soc.* **1900**, *22* (11), 757–771.

(119) Chen, Z. X.; Li, Y.; Huang, F. Persistent and Stable Organic Radicals: Design, Synthesis, and Applications. *Chem*. Elsevier Inc. February 11, 2021, pp 288–332. https://doi.org/10.1016/j.chempr.2020.09.024.

(120) Yuan, D.; Guo, Y.; Zeng, Y.; Fan, Q.; Wang, J.; Yi, Y.; Zhu, X. Air-Stable N-Type Thermoelectric Materials Enabled by Organic Diradicaloids. *Angewandte Chemie* **2019**, *131* (15), 5012–5016. https://doi.org/10.1002/ange.201814544.

(121) Minami, T.; Nakano, M. Diradical Character View of Singlet Fission. *Journal of Physical Chemistry Letters* **2012**, *3* (2), 145–150. https://doi.org/10.1021/jz2015346.

(122) Peng, Q.; Obolda, A.; Zhang, M.; Li, F. Organic Light-Emitting Diodes Using a Neutral π Radical as Emitter: The Emission from a Doublet. *Angewandte Chemie* **2015**, *127* (24), 7197–7201. https://doi.org/10.1002/ange.201500242.

(123) Sanvito, S. Part of the Molecule-Based Magnets Themed Issue. *Chemical Society Reviews* **2011**, *40* (6), 3336–3355. https://doi.org/10.1039/c1cs15047b.

(124) Janoschka, T.; Hager, M. D.; Schubert, U. S. Powering up the Future: Radical Polymers for Battery Applications. *Advanced Materials* **2012**, *24* (48), 6397–6409. https://doi.org/10.1002/adma.201203119.

(125) Abe, M. Diradicals. *Chemical Reviews*. September 11, 2013, pp 7011–7088. https://doi.org/10.1021/cr400056a.

(126) Ramos-Cordoba, E.; Salvador, P. Diradical Character from the Local Spin Analysis. *Physical Chemistry Chemical Physics* **2014**, *16* (20), 9565–9571. https://doi.org/10.1039/c4cp00939h.

(127) Bachler, V.; Olbrich, G.; Neese, F.; Wieghardt, K. Theoretical Evidence for the Singlet Diradical Character of Square Planar Nickel Complexes Containing Two O-Semiquinonato Type Ligands. *Inorganic Chemistry* **2002**, *41* (16), 4179–4193. https://doi.org/10.1021/ic0113101.

(128) Kamada, K.; Ohta, K.; Shimizu, A.; Kubo, T.; Kishi, R.; Takahashi, H.; Botek, E.; Champagne, B.; Nakano, M. Singlet Diradical Character from Experiment. *Journal of Physical Chemistry Letters* **2010**, *1* (6), 937–940. https://doi.org/10.1021/jz100155s.

(129) Lukman, S.; Richter, J. M.; Yang, L.; Hu, P.; Wu, J.; Greenham, N. C.; Musser, A. J. Efficient Singlet Fission and Triplet-Pair Emission in a Family of Zethrene Diradicaloids. *Journal of the American Chemical Society* **2017**, *139* (50), 18376–18385. https://doi.org/10.1021/jacs.7b10762.

(130) Yuan, D. Stable N-Doped Conductors Enabled by Organic Diradicals. *Chem* **2019**, *5* (4), 744–745. https://doi.org/10.1016/j.chempr.2019.03.018.

(131) Zong, C.; Zhu, X.; Xu, Z.; Zhang, L.; Xu, J.; Guo, J.; Xiang, Q.; Zeng, Z.; Hu, W.; Wu, J.; Li, R.; Sun, Z. Isomeric Dibenzoheptazethrenes for Air-Stable Organic Field-Effect Transistors. *Angewandte Chemie - International Edition* **2021**, *60* (29), 16230–16236. https://doi.org/10.1002/anie.202105872.

(132) Hattori, Y.; Michail, E.; Schmiedel, A.; Moos, M.; Holzapfel, M.; Krummenacher, I.; Braunschweig, H.; Müller, U.; Pflaum, J.; Lambert, C. Luminescent Mono-, Di-, and Triradicals: Bridging Polychlorinated Triarylmethyl Radicals by Triarylamines and Triarylboranes. *Chemistry - A European Journal* **2019**, *25* (68), 15463–15471. https://doi.org/10.1002/chem.201903007.

Chapter 2

Experimental Methods and Techniques

2.1 Overview

To understand materials' singlet and triplet state dynamics, time-resolved and nonlinear optical spectroscopy techniques are required. This is because these techniques can probe the excited state dynamics that can characterize these materials' energy and charge transfer dynamics. Here, excited-state processes like intramolecular singlet exciton fission (iSEF), excimer formation, thermally activated delayed fluorescence (TADF), and diradical states are investigated. Therefore, it is critical to understand the techniques and methods used to perform the measurements that ultimately help understand these optoelectronic systems' thermodynamic and kinetic properties. Since the studies reported in this dissertation were all carried out in the solution phase, the experimental methods described will be calibrated and configured for solution−state measurements.

The absorption and emission measurements are done in all samples and used to determine the reference standards that can be used for all other measurements. In the case of fluorescence measurements like fluorescence quantum yield, ultrafast fluorescence up−conversion and time−correlated single−photon counting, reference standards that closely match the fluorescence of the sample are picked. On the other hand, excitation wavelengths are for all measurements are picked based on the samples' absorption maxima. For all the measurements, photo−degradation was checked by measuring the absorption spectrum of the sample before and after conducting the experiments. In cases where the samples' photo-stability is a concern, fresh samples are prepared and used for each experiment. In cases where triplet species needed to be checked, the measurements were conducted in oxygen-rich (unpurged/air) and oxygen−free (purged) environments. To achieve oxygen−free environment, the solutions were purged by bubbling nitrogen for ~10 min. The fluorescence and excited−state lifetime of the investigated systems are determined by fitting the decay or growth curves of the experimentally obtained data to the best exponential function using the fitting function in Origin.

2.2 Steady-State Absorption and Emission Spectroscopy

When light hits a material, the material interacts with this light and absorbs its radiation in terms of energy photons as a function of frequency (ν) or wavelength (λ), to create an absorption spectrum. The y −axis of the absorption spectrum is the intensity of absorption and the x −axis is either ν or λ. For optoelectronic systems that are geared towards detecting light from the sun, the focus is on materials that can absorb well within the strongest solar photon flux which lies between the ultraviolet (UV) and the near−infrared (nIR) range of the electromagnetic spectrum. The strongest spectra irradiation from the sun lies in the visible (Vis) wavelengths. Once the material molecule absorbs the light photons in terms of a quantum of energy that corresponds to or is higher than the transition energy between two molecular orbitals, electrons are excited from the ground state to the excited state leaving a positively charged electron hole. Due to electrostatic Coulombic forces, the negatively charged electron is tightly bound to the positively charged hole. This pair tightly bound electron−hole pair is also known as an exciton and is described as an electronically excited state. While the excited electron occupies the lowest unoccupied molecular orbital (LUMO), the hole occupies the highest occupied molecular orbital (HOMO). At the excited state, the molecule can go through vibrational relaxation back to the lowest singlet state (S_1). While the excited molecule can lose excess energy in form of heat as it collides with neighboring molecules, it will emit the rest of its energy through the release of electromagnetic radiation. As a result, the emitted radiation will be of low energy (longer wavelength) than the absorbed energy as shown in **Figure 2.2.1.** This low energy emission from a relaxed singlet state and which happens at a longer wavelength, is known as fluorescence, and substances that exhibit this phenomenon are called fluorescent materials, and it happens very fast, as shown in **Figure 1.3.1** in the introduction. When these ground−state molecules absorb high−energy photons, this energy can change the spin−multiplicity from the singlet state to a slower and low energy emitting triplet state, which is quantum−mechanically spin forbidden. This transition happens through intersystem crossing from the singlet state to the triplet state. Then, the molecules are emitted back to the ground state. This emission continues even when the absorption of radiation has been cut off and is long−lived and happens at even lower energies or longer wavelengths, as shown in **Figure 2.2.1**.

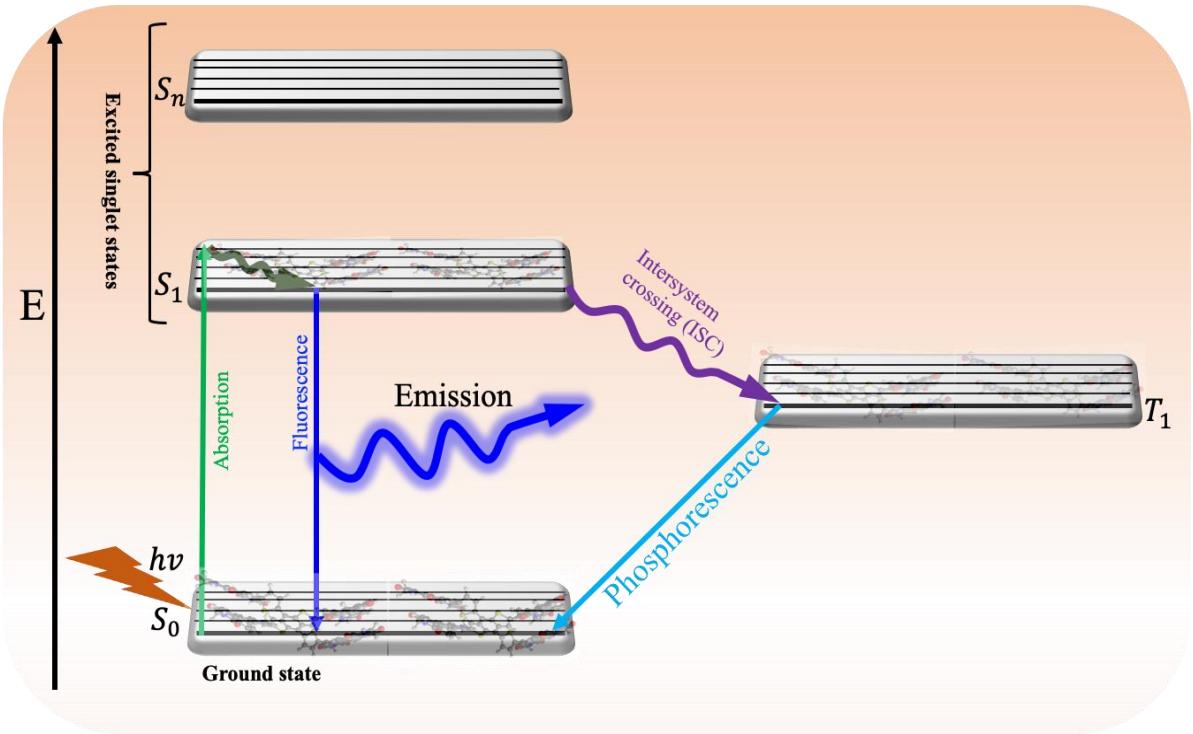

Figure 2.2.1: Jablonski diagram illustrating absorption and emission

Absorption and emission are crucial processes that need to be measured to start thinking about exploring the excited state dynamics of semiconducting materials. For most optoelectronic systems, their absorption tends to lie around the region of maximum solar photon flux, which, although is most intense in the visible region, extends to the UV and the nIR as shown in **Figure 2.2.2**.[1] As a result, a UV−Vis spectrometer whose wavelength ranges between 190 nm and 1100 nm is used to measure the absorption.

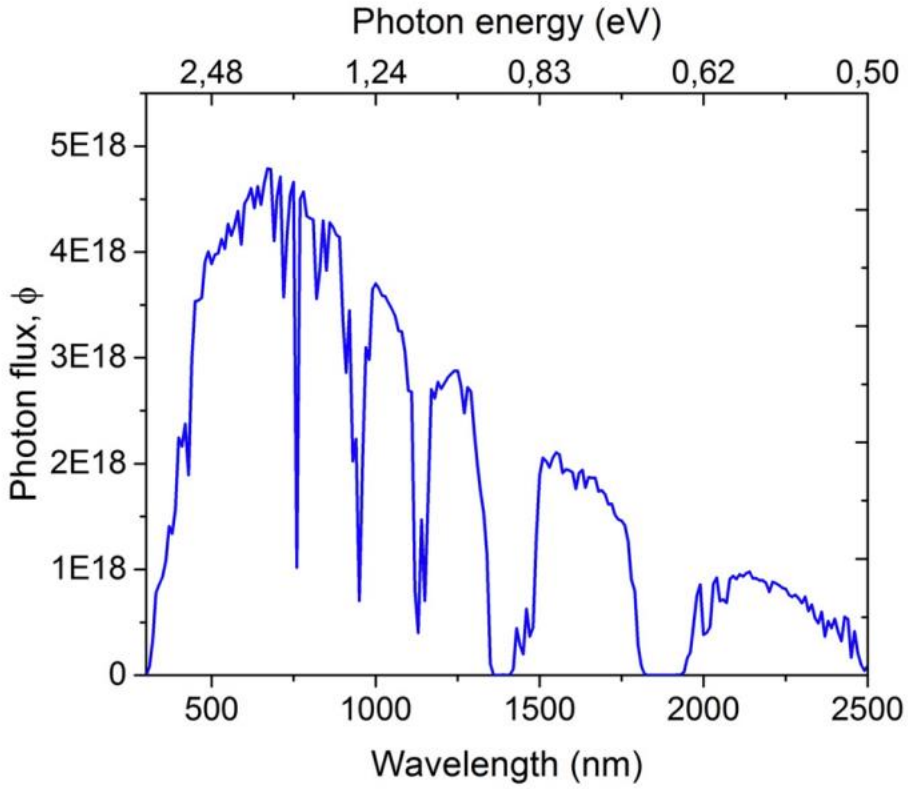

Figure 2.2.2: Variation of photon flux of Sun's spectrum with wavelength and photon energy (adapted from reference 1).

A material's absorption is better explained by Lambert$t$ −Beer's Law. The light that passes through a material entirely loses its energy through absorption, scattering, and reflection.[2] Since the spectrophotometer cannot differentiate between absorption, scattering, and reflection, a background measurement is measured to account for these additional interactions. The absorbance of a material can be related to its transmission, concentration, and beam path. It can be used to determine the extinction coefficient of the material at a specific wavelength (**Equation 2.2.1**).

$$A = -\log T = \log \frac{I_0}{I} = \varepsilon . C . l \qquad \textbf{Equation 2.2.1}$$

where:

A is the absorbance

T is transmittance

I_0 is the intensity of the measuring beam before passing through the sample;

I is the intensity of the measuring beam after passing through the sample;

ε is the molar absorption coefficient or molar absorptivity or molar extinction coefficient given in $l.mol^{-1}.cm^{-1}$;

C is the concentration given in $mol.l^{-1}$;

l is the pathlength of the measuring beam in the sample in cm

ε is a critical parameter in this process as it indicates the capability of a molecule to absorb light photons at a given wavelength. From Equation 2.2.1, the absorbance of a solute is directly proportional to its concentration. This equation can be used to calculate the concentration of an unknown compound. Absorption spectra in this work are plotted as *A vs.* wavelength or *ε vs.* wavelength. For all the absorption measurements reported here, Agilent 8453 UV-Vis absorption spectrophotometer was used, and the schematic is shown in **Figure 2.2.3** below.[3]

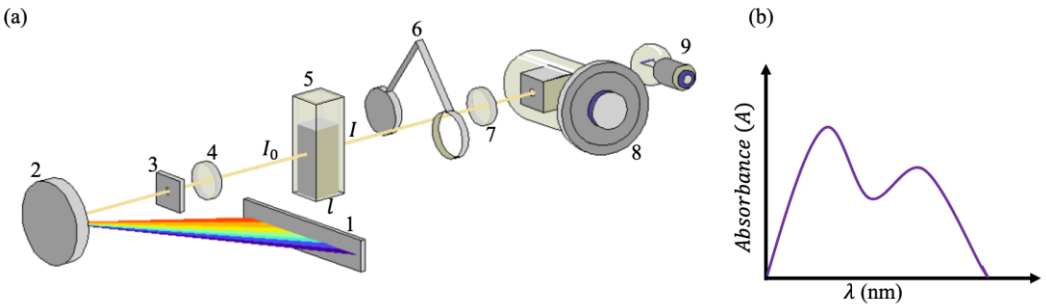

Figure 2.2.3: **a**) Agilent 8453 spectrophotometer highlighting showing the: 1) photodiode array, 2) monochromator grating, 3) slit, 4) source lens, 5) sample holder, 6) shutter, 7) source lens, 8) Deuterium lamp, 9) Tungsten lamp and I_0, I and l are described in **Equation 2.2.1** above and **b**) an example of obtained absorption spectra.

The emission of materials is obtained using a Horiba Scientific Fluorimeter (**Figure 2.2.4**).[4] The excitation wavelength is picked from the absorption spectra, usually the maximum peak. Since a material emits at a longer wavelength than its absorption, a longer wavelength is selected as the emission wavelength, usually 10 nm longer than the excitation wavelength. The fluorimeter used uses a xenon arc lamp as the excitation light source, producing light between 190 nm to 2000 nm. The detector is a photomultiplier tube that can detect a wavelength range of 190 nm to 900 nm.

This instrument also has an optional liquid nitrogen cooled detector that can cover the wavelength range from 800 nm to 1600 nm.[4]

A shorter excitation wavelength than the absorption maximum is picked for materials whose emission spectrum overlaps with their absorption spectra. The emission wavelength is adjusted accordingly until the entire emission spectrum is captured. Every emissive material has a characteristic excitation and emission wavelength pair to show maximum fluorescence. The emission spectrum can be affected by temperature, pressure, viscosity, polarity, pH, hydrogen bonding, or ionic potential, leading to a decrease or increase in fluorescence intensity a blue or red shift in fluorescence emission.[5] Mostly, decrease or increase in fluorescence leads to a red or blue shift in emission, respectively, and vice versa.

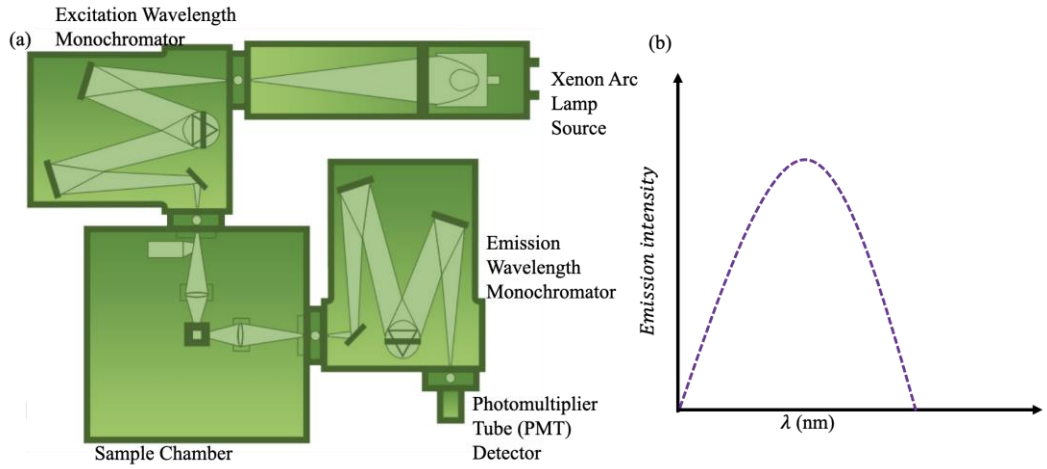

Figure 2.2.4: a) Horiba Scientific Fluorimeter adapted from the Horiba Scientific_PTI Quantamaster Series Manual [4] and b) an example of an emission spectrum.

Per the Beer−Lambert Law, the fluorescence intensity of an emissive material is directly proportional to its concentration and can be shown by **Equation 2.2.2** below.[5]

$$I_F(C, \lambda_{ex}, \lambda_{em}) = KCd\Phi(\lambda_{ex})\varepsilon(\lambda_{ex})I_{ex}(\lambda_{ex})E_M(\lambda_{em}) \qquad \textbf{Equation 2.2.2}$$

Where:

I_F is fluorescence intensity;

C is concentration;

λ_{ex} is the excitation wavelength;

λ_{em} is the emission wavelength;

Φ is the quantum yield;

ε is the molar absorption coefficient and

I_{ex} is the intensity of the excitation light source;

E_M is the characteristic emission profile of a fluorescing compound.

The fluorescence quantum yield, Φ, is an important parameter that is used to quantify the quantum efficiency of fluorophores. Φ is described as the ratio of absorbed photons to that of emitted photons at a given wavelength. Upon absorption, energy can be dissipated through different radiative or non-radiative pathways, which all together contribute to the ultimate quantum efficiency of the material.[6] This is shown by **Equation 2.2.3** below.

$$\Phi = \frac{k_f}{k_f + k_{isc} + k_{ec} + k_{ic} + k_{pd} + k_d} \qquad \textbf{Equation 2.2.3}$$

where:

Φ is the quantum yield;

k_f is the rate of fluorescence;

k_{isc} is the rate of intersystem crossing;

k_{ec} the rate of external conversion;

k_{ic} the rate of internal constant;

k_{pd} the rate of pre-dissociation; and

k_d the rate of dissociation.

The Williams comparative method employs heavily studied and previously reported emissive chromophores with similar steady−state properties. These well−known chromophores act as standards, and some of them include coumarin and rhodamine derivatives.[7,8] In this dissertation report, Φ was calculated using **Equation 2.2.4** below.

$$\Phi_s = \Phi_{std} \frac{Grad_s {\eta_s}^2}{Grad_{std} {\eta_{std}}^2} \qquad \textbf{Equation 2.2.4}$$

where:

Φ_s is the sample quantum yield in question;

Φ_{std} is the known quantum yield of the standard;

$Grad_s$ is the slope obtained from plotting the fluorescence area versus the optical density of the sample's absorption;

$Grad_{std}$is the slope obtained from plotting the fluorescence area versus the optical density of the standard's absorption;

η_s is the refractive index of the solvent used for the sample;

η_{std} is the refractive index of the solvent used for the standard;

Absorption and emission spectroscopy can be used to show the existence of charge transfer (CT)in a donor(D)−acceptor(A) molecule, determine the molecular HOMO−LUMO bandgap of a molecule, determining the extent of the ground state coupling between the individual acceptor moieties in a D−A compound, the planarity of a compound based on the compounds Stokes Shift as well as the emissive properties of a material through calculating its fluorescence quantum yield.[9]

2.3 Two-Photon Absorption Spectroscopy

Two−photon absorption (TPA) spectroscopy is a nonlinear process that involves the simultaneous absorption of two photons of equal or different frequencies to excite a molecule from the ground state to an excited electronic state as shown **Figure 2.3.1**.

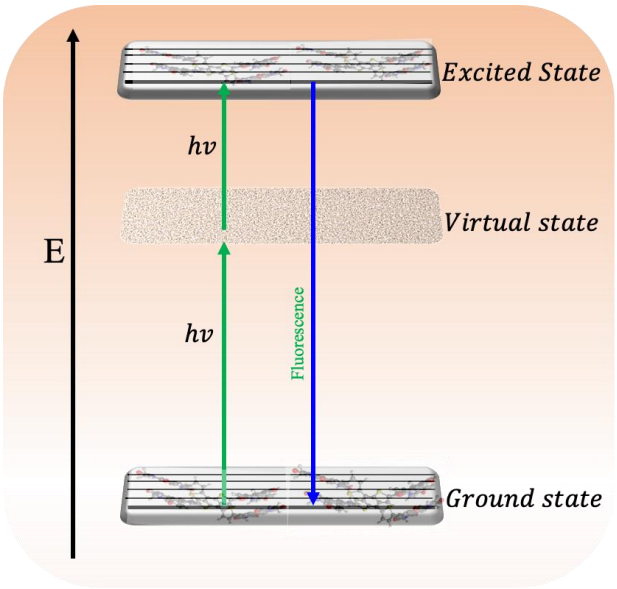

Figure 2.3.1: Two−photon absorption (TPA) process

Quantum two-photon processes which include two−photon emission (TPE) and two−photon absorption (TPA) spectroscopy, were predicted by Maria Goeppert-Mayer in 1930 in the early days of electrodynamics.[10,11] The TPA phenomena was observed experimentally in 1961 and has attracted a lot of interest due to its potential applications in three−dimensional data storage, two-photon fluorescence imaging, charge transfer optoelectronics, and microfabrication. TPE was observed in accelerator beam−foil spectroscopy while TPA was observed in nonlinear optics. [11] The capability of a material TPA is characterized by its two−photon absorption cross−section (σ). One mostly known method to determine the σ is the two−photon Excited Fluorescence (TPEF) owing to the fact the two−photons induce an electric field that has a non−linear response to the polarization density of the absorbing material. In this set-up, a mode-locked Ti:Sapphire laser with a wavelength that is tunable from 700 to 900 nm. The output is 110 fs pulse with a repetition rate of 80 MHz. This pulse pumps the OPAL optical parametric oscillator (OPO) lithium borate (LBO) crystal leading to a 1.3 and 1.5 μm output with an output power of 200 mW. This beam is then propagated through a set of mirrors to a neutral density filter which controls the power of the excitation beam. Additionally, optical glass is used to split the excitation beam where a small percentage is reflected into a high−speed silicon photodiode. The photodiode which monitors the excitation beam power is connected to a multimeter. The sample fluorescence photons are collected at a right angle to the excitation beam and detected by a photomultiplier tube (PMT). The perpendicular setting is meant to avoid the excitation beam.

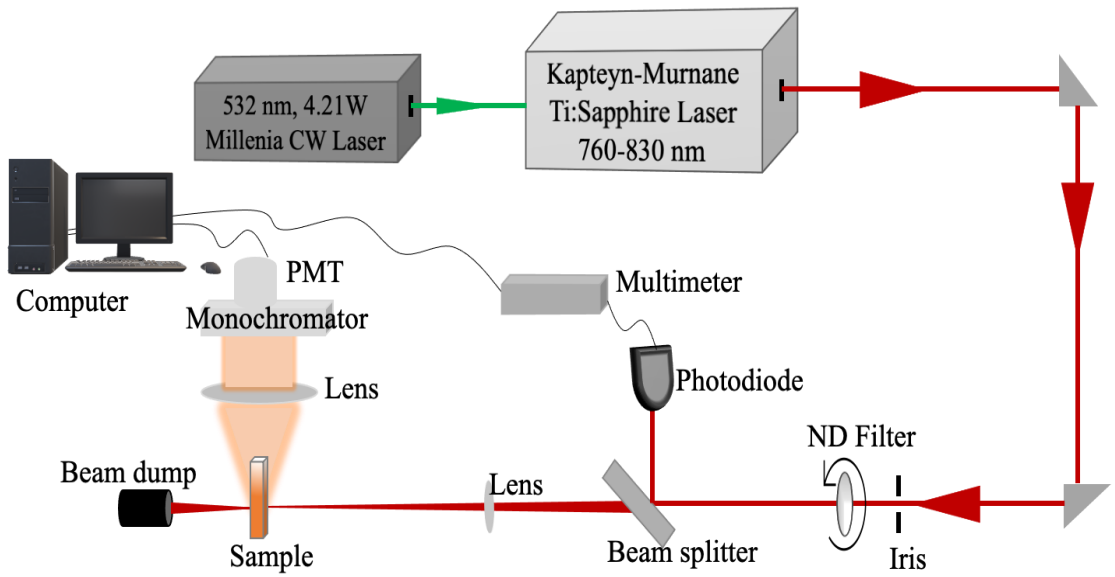

Figure 2.3.2: Schematic of the Two−Photon Absorption (TPA) spectroscopy experimental setup.

The fluorescence photons, $F(t)$, collected per second (voltage) is given by **Equation 2.3.1** below:

$$F(t) = \frac{1}{2}\phi\sigma[c]\eta\frac{g_p}{\pi v\lambda\tau}f\langle P(t)\rangle^2 \qquad \textbf{Equation 2.3.1}$$

where:

ϕ is the fluorescence quantum yield of the material;

σ is the two−photon absorption cross−section of the sample;

$[c]$ is the concentration;

η is the refractive index of the solvent;

g_p is the shape factor of the pulsed laser, which is 0.66 for a Gaussian shape;

v is the frequency of the laser;

λ is the excitation wavelength;

τ is the pulsed duration;

f is the collection efficiency and

$P(t)$ is the input power intensity;

Equation 2.3.1 can be expressed in its linear regression form ($y = mc + b$) by taking its logarithm as shown in **Equation 2.3.2** below. Here, the parameters associated with the laser can be treated as a constant, b. As a result, a quadratic response with a slope of two is expected in a graph of the fluorescence intensity as a function of the power of the incident excitation for both the sample and the standard. If the logarithm of the input power for both the sample and the standard is assumed to be zero, the equation can be further simplified as shown in **Equation 2.3.2-2.3.5** to give the two−photon absorption cross−section (σ).

$$Log\left(F(t)\right) = 2log\langle P(t)\rangle + log\left(\frac{1}{2}\phi\sigma[c]\eta\frac{g_p}{\pi v\lambda\tau}f\right) \qquad \textbf{Equation 2.3.2}$$

$$Log\left(F(t)_{Sample}\right) - b_{sample} = Log\left(F(t)_{standard}\right) - b_{standard} \qquad \textbf{Equation 2.3.3}$$

$$Log\left(F(t)_{Sample}\right) - Log\left(F(t)_{standard}\right) = b_{sample} - b_{standard} \qquad \textbf{Equation 2.3.4}$$

$$\sigma_{sample} = \frac{10^{\left(b_{sample} - b_{standard}\right)} . \sigma_{standard} \phi_{standard} [c]_{standard} \eta_{standard}}{\phi_{sample} [c]_{sample} \eta_{sample}}$$ **Equation 2.3.5**

2.4 Ultrafast Fluorescence Up-Conversion Spectroscopy

The ultrafast fluorescence up-conversion (FUC) is a technique used to investigate the energy transfer processes with lifetimes ranging from hundreds of femtoseconds to hundreds of picoseconds. It is used to measure the emissive lifetimes within this lifetime range. In the FUC set−up shown in **Figure 2.4.1**, a Spectra−Physics Millenia laser with neodymium−doped yttrium vanadate (Nd:YVO4) nonlinear crystal as its gain medium produces produce 4.21 W of CW power at 532 nm through frequency doubling. This laser is powered using a continuous laser diode. The 532 nm beam is the input for the second laser, the Spectra−Physics Tsunami which, through mode−locking, its Ti−Sapphire nonlinear crystal can generate 80 fs pulses at wavelengths between 780 and 820 nm at a repetition rate of 82 MHz and a power range between 680−720 mW. It is worth noting that throughout this dissertation, 800 nm was used as the excitation wavelength.

This 800 nm beam is propagated through various optics and focused onto a second harmonic generation crystal made of β–barium borate (BBO) to upconvert part of the 800 nm fundamental beam to a 400 nm beam. A dichroic mirror is used to separate the 400 nm output from the 800 nm fundamental. The residual 800 nm fundamental beam from the dichroic mirror is directed into an optical delay line whose step size is 6.25 fs while the 400 nm beam is reflected towards the 1 mm circular cuvette sample holder that rotates to minimize the potential photo-degradation of the sample. In addition, a Berek compensator is used to control the polarization of the beam so that the beam that excites the sample is polarized on the same plane (parallel). An achromat is used to collect the sample fluorescence. This fluorescence is then directed into a β −barium borate (BBO) nonlinear crystal where sum−frequency generation (SFG) happens to generate a wavelength range of 300−400 nm. At this BBO, the fluorescence is recombined and overlapped in space and time, with the fundamental beam gate pulse with a step size of 6.25 fs to produce maximum fluorescence up-conversion.[12]

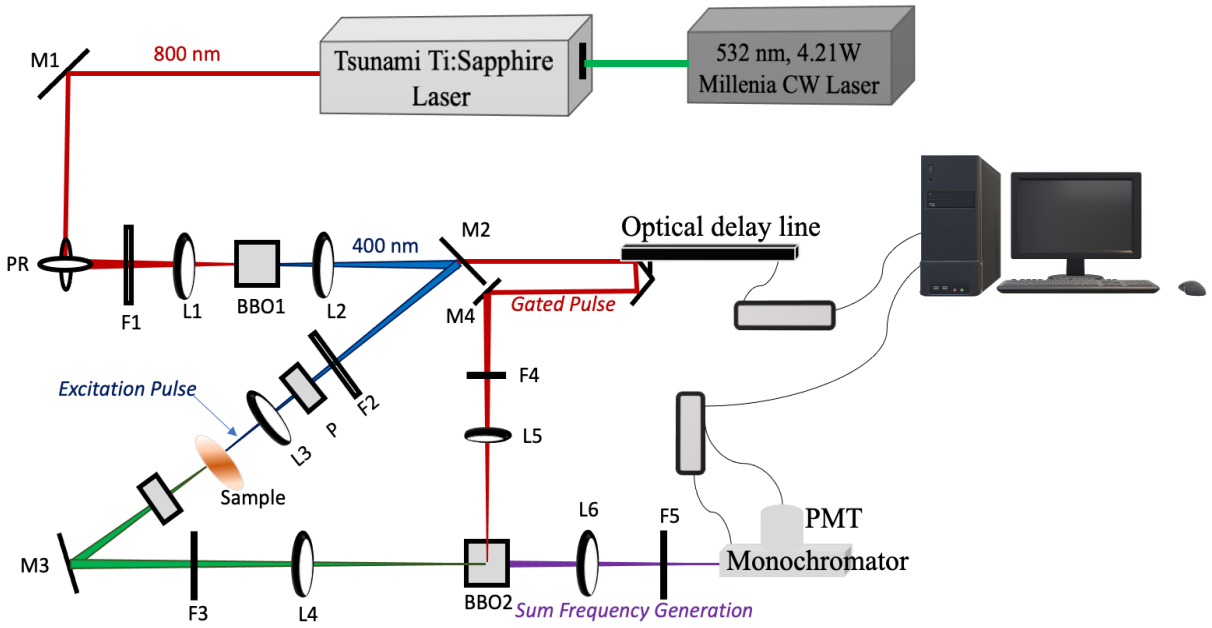

Figure 2.4.1: Schematic of the Ultrafast Fluorescence Up-Conversion Spectroscopy experimental setup

The resultant SFG beam is propagated and focused into a monochromator which selects the desired wavelength from the up−converted beam and a photomultiplier tube, PMT (Hamamatsu R152P) is used as a detector.

2.5 Time-Correlated Single Photon Counting Spectroscopy

Time-Correlated Single Photon Counting (TCSPC) spectroscopy is used to characterize the time−resolved emission of materials whose decay lifetime is too long to be captured by the fluorescence up-conversion method described in section 2.4 above, usually ranging from the nanosecond to the microsecond timescale.

As shown in **Figure 2.5.1**, the TCSPC setup consists of a 4W, 532 nm spectra physics Millenia CW Nd: YVO4 laser which pumps a Kapteyn Murnane (KM) Laboratories Ti-sapphire femtosecond laser. The KM tunable output ranges from 780 to 830 nm. However, the KM output was set to 800 nm with a pulse duration of 30 fs and a repetition rate of 90 MHz for all the TCSPC experimental work carried out in this dissertation. The fundamental 800 nm from the KM is doubled through a β −barium borate (BBO) nonlinear crystal to produce a 400 nm pulsed beam. Unlike in the fluorescence up−conversion spectroscopy experiment, the 800 nm fundamental from

the BBO crystal is not used. The beam was focused on the sample cuvette (1.0 cm path length) using a lens with a focal length of 11.5 cm.

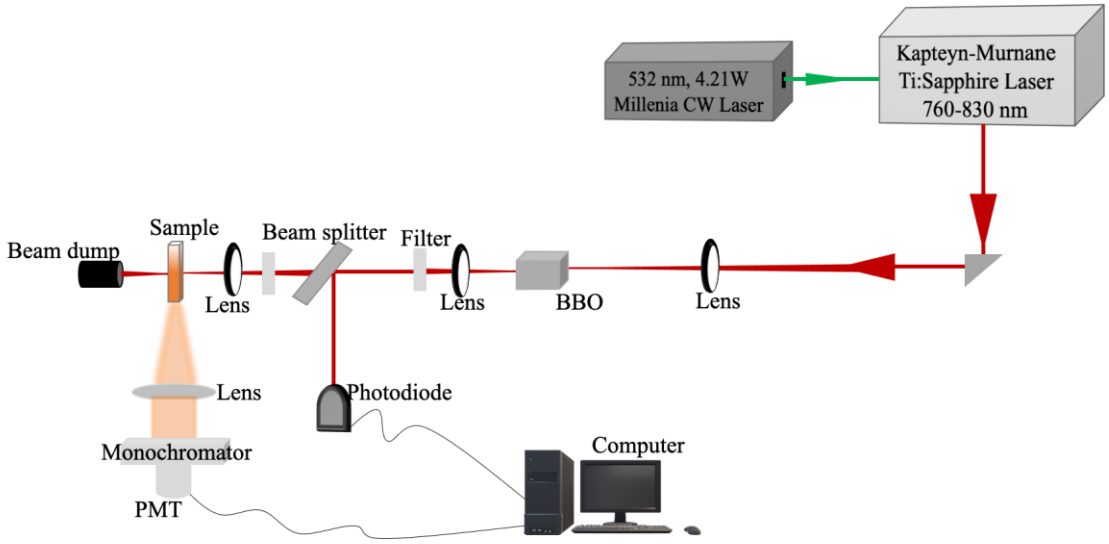

Figure 2.5.1: Schematic of the Time-Correlated Single Photon Counting (TCSPC) spectroscopy experimental set−up.

To avoid electrical interference, the time−resolved emission of the investigated systems is collected perpendicular to the excitation source. A monochromator is placed in front of the photomultiplier (PMT) to filter any potential external photon that can be converted into a signal. The PMT detects the signal and sends it to the computer through a TimeHarp200 interface card. The computer displays the created histogram using specialized software called PicoQuant. The decay lifetimes were determined by fitting log plots of the obtained spectra to a linear fit. This histogram is created by detecting and resolving the arrival time of single photons with respect to a triggering signal, which is usually the excitation source. In order to ensure that the observed decay is legitimate, the instrument response function (IRF) is measured using Rayleigh Scattering and its expected full width at half max (FWHM) is 330 ps.

2.6 Femtosecond Transient Absorption Spectroscopy

The femtosecond Transient Absorption Spectroscopy (fsTAS) is a pump-probe technique used to probe short-lived excited state dynamics of systems. This system can capture events that happen as fast as 150 fs. A Spectra Physics Spitfire amplified laser system was used for the fsTAS measurements in this dissertation. The amplified system is composed of many systems, however, the main parts include the 800 nm light source, the optical parametric amplifier (OPA) and the

spectrometer as shown in the figure below. A 4.2 W and 532 nm Nd:YVO4 CW laser is used to pump the Tsumani Ti:sapphire laser to produce fast (100 fs) 3nJ of 800 nm with a high repetition rate of 80 MHz that act as the seed pulses. These seed pulses are amplified in the spitfire which is pumped by the 527 nm, 7W Empower from Spectra Physics to produce 130 fs pulses with the high energy of 1mJ and a low repetition rate of about 1kHz. After a series of stretching and compressing in the Spitfire, an 130 fs and 800 nm pulse with an average power of 1 W is produced, and a beam diameter of 7 mm. this 800 nm is split into two using a beam splitter to generate the pump (85%) and the probe beam (15%).

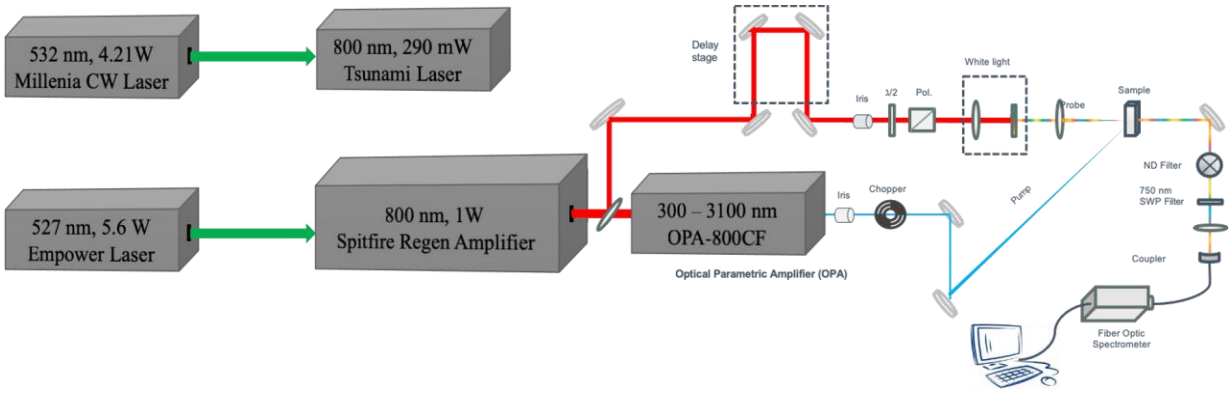

Figure 2.6.1: Schematic of the femtosecond Transient Absorption Spectroscopy (fsTAS) experimental set−up.

The 85% pump is directed into the optical parametric amplifier (OPA) where various configurations can be used to produce pump beam wavelengths ranging from 300 nm to 10µm. The 800 nm is passed through a type II β −barium borate (BBO) crystal to produce a signal (1100 nm – 1600 nm) and idler (1600 nm – 3100 nm) beam through optical parametric generation (OPG). Additional configurations are possible enabling the production of a longer range of wavelengths. These configurations include second and fourth harmonic generation (SHG and FHG) of the signal and idler to generate wavelength ranges of 580 nm – 1200 nm and 300 nm – 600 nm, respectively; sum frequency mixing (SFM) of the signal and idler with the 800 nm residual pump to generate 480 nm – 600 nm and difference frequency mixing (DFM) of the signal and idler with the 800 nm fundamental to produce 480 nm – 600 nm.

The other 15% of the 800 nm fundamental probe beam is propagated into the transient box and focused into a sapphire plate to produce a white light continuum. This white light, which acts

as the probe, is overlapped with the pump (the excitation beam) at the sample cuvette. The resultant light is focused into a fiber-coupled UV-Vis spectrometer with a spectral range of 350 nm to 850 nm. This system records the change in absorption as a function of time and wavelength. The Helios software by Ultrafast Systems Inc was used for the transient data acquisition, while the data analysis was completed using Surface Explorer Pro and Glotaran software.

2.7 Nanosecond Transient Absorption Spectroscopy

The nanosecond Transient Absorption Spectroscopy (nsTAS) is a pump-probe technique used to probe the emissive and non-emissive excited state dynamics of systems and the details of the system have been described in its manual.[13] The nsTAS is composed of 3 main parts, the laser head, the optical parametric oscillator (OPO) and the transient spectrometer. The laser head is a Lab Series 170 neodymium-doped yttrium aluminum garnet (Nd:YAG) Quanta-Ray (Spectra Physics) laser. This Quanta-Ray laser is used to a pump β −Barium Borate (BBO) crystals in an Optical Parametric Oscillator (OPO) which can be used to generate a broad range of pump wavelengths. The Edinburg transient spectrometer is the part of the system composed of the probe lamp, the sample chamber, the monochromator, and the detection unit. This is where the transient measurements happen.

The Nd:YAG laser has a pump chamber assembly with two xenon flash lamps that pump Nd:YAG rods which generate a 1064 nm beam. To obtain short pulses, a Q-switch which is composed of a polarizer, a quarter-wave plate, and a Pockels cell is located at the end of the pump chamber and is used to generate 10 ns pulses and increase the peak power. In its normal mode, the Q-switch delay circuit fires a fixed delay which triggers the Marx bank, a circuit that generates high-voltage pulses from a DC voltage source. This high voltage pulse triggers a Pockels cell, an electro-optical crystal that controls light propagation through it by controlling the phase delay of the crystal by applying a variable voltage, generating the short laser pulses ($< 10\ ns$)with a high peak power (tens of megawatts). When there is no voltage applied to the Pockels cell, the light entering the Q-switch is polarized horizontally by the polarizer and the quarter-wave plate converts the polarization to circular polarization. The circularly polarized reflects off the high reflector and the quarter-wave plate converts the circularly polarized light to vertically polarized light. The polarizer only allows horizontally polarized light to be transmitted, thus the vertically polarized light is reflected out of the resonator, resulting in high cavity loss. When the high voltage pulse

triggers the Pockels cell, the polarization of the Pockels cell changes, canceling the polarization retardation of the quarter-wave plate, allowing horizontally polarization light to exit the Q-switch, resulting in the high peak power pulses.

The high peak power pulse of the 1064 nm fundamental beam from the Nd:YAG is used to pump the harmonic generator composed of potassium dideuterium phosphate (KD*P) crystals. Through the second harmonic generation (SHG) of the 1064 nm fundamental beam, a 450 mJ of 532 nm beam is produced. This 532 nm beam is then mixed with the 1064 nm fundamental through sum-frequency mixing (SFM) to produce a 240 mJ of 355 nm, the desired wavelength that is used to pump the OPO as shown in **Figure 2.7.1** below.

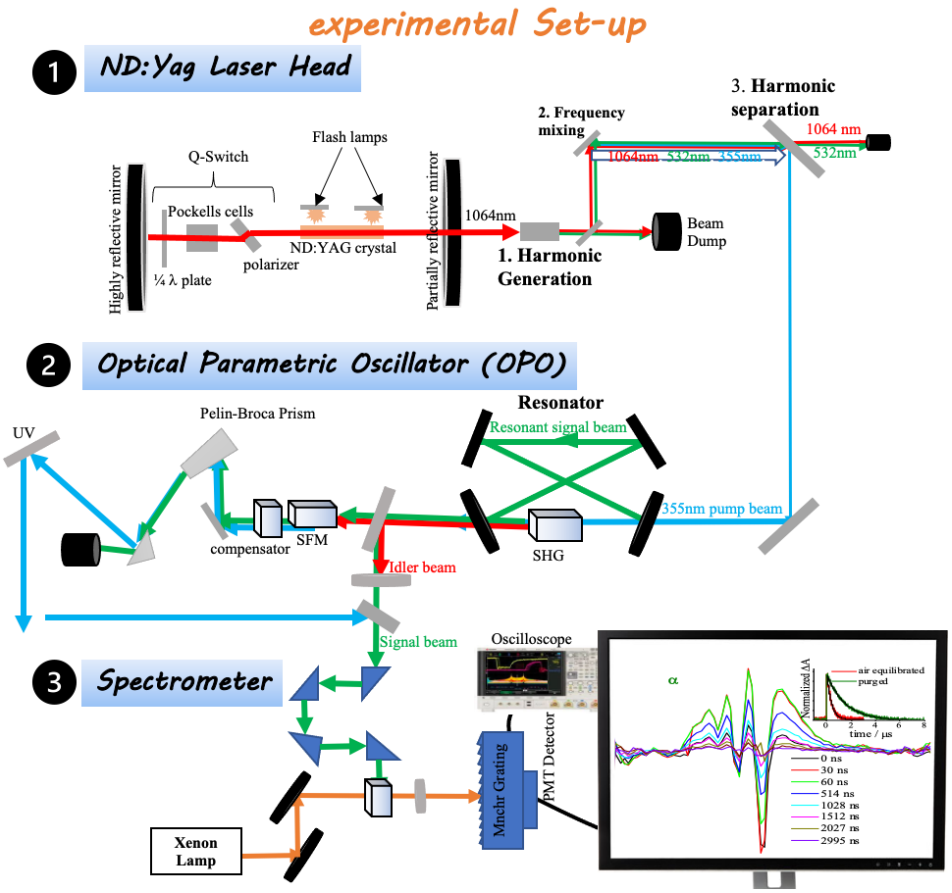

Figure 2.7.1: Schematic of the nanosecond Transient Absorption Spectroscopy (nsTAS) experimental set−up.

The Optical Parametric Oscillator (OPO) is composed of the visible which is in the VersaScan portion of the OPO and the ultraviolet which is in the UVScan portion of the OPO which is described in the respective manuals[14,15]. For the visible light production in OPO to

happen, the 355 nm pump photon passes through a nonlinear BBO crystal, splitting into two lower-energy photons that add up to the energy of the pump photon. Due to the birefringent properties of the BBO crystal, its rotation leads to changes in its index of refraction and results in unique frequency output of the two low energy photons, resulting in a signal photon and an idler photon. The signal beam ranges between 410 nm – 709.4 nm while the idler beam ranges between 709.5 nm – 2630 nm. The UV beam can be produced by mixing the signal portion of the visible and the 1064 nm fundamental through Sum Frequency Mixing to produce a wavelength range of 257 nm – 409.5 nm.

To obtain these wavelengths, both modes of the OPO need to be calibrated. It is very straightforward to calibrate the versaScan and obtain the wavelengths in the visible range as described in the manual.[14] The angle of the BBO crystal is tuned via an electric motor via a computer using Spectra Physics supplied software to obtain the desired signal or idler wavelength output. The electric motor position is accomplished by the following procedure:

1. Access the calibration by opening the ScanMaster SHG GWU program on the desktop. Click on "Config" then open the calibration wizard. The base calibration window opens with a drop-down menu where the calibration mode will be picked. Select any of the previously saved calibrations and then click "OK".
2. A window for crystal configuration appears and for the visible calibration, pick the UV-L crystal on Stage 1 and then click "OK".
3. A calibration wizard to calibrate the electric motor position opens. Construct a 5-point calibration table by picking 5 wavelengths between 410 nm and 709 nm.
4. For the 1st position, select a wavelength in the middle of the calibration range, like 550 nm. Then click "Go To" in order to move the motor to a wavelength of 550 nm. Monitor the wavelength by measuring it's the reflection of its output beam using a fiber optic and check its power using a power meter. Maximize the power by clicking the "move in" and "move out" buttons, the speed of motor position search is controlled by the sliding bar under the moving in and moving out buttons. When the maximum power is obtained, the exact output wavelength is recorded from the OceanView software. This is inputted in the wavelength window for the first position. This position is saved by clicking on the Get position from adjust button.

5. For the 2nd position, pick a wavelength at the start of the calibration range and click “Go To” in order to move the motor to that wavelength. Follow step 4 to obtain the maximum power in this position.
6. Repeat this process for the 3rd, 4th and 5th wavelength positions and then click “next”. Use the same procedure to calibrate the SHG crystal and prism positions.
7. Save the calibration and click “Finish”.

However, it gets a little bit complicated to obtain the UV wavelengths. In this dissertation, the potential of the OPO was pushed to its limits and its uvScan was successfully calibrated as described below. This made it possible to study systems that absorb light in the UV region.

There are two ways to calibrate the uvScan of the OPO: 1) Second Harmonic Generation (SHG) of the OPO signal wave, covering the wavelength range 257 – 354 nm with the crystal UV-L and 2) Sun Frequency Mixing (SFM) of the OPO signal wave with 1064 nm of the pump laser, covering 297 – 410 nm with the crystal UV-L.

The software ScanMaster, configured for a flexiScan offers 2 different shortcuts (start buttons on the desktop of the computer) to launch the software ScanMaster:

a) ScanMaster SHG: If you launch the software with this shortcut, then the UV light is generated inside the uvScan by doing SHG of the OPO signal wavelength.
b) ScanMaster SFM: If you launch the software with this shortcut, then the UV light is generated inside the uvScan by doing SFM of 1064 nm with the OPO signal wavelength.

In order to generate tunable UV in the uvScan, you HAVE TO take out the “OPO direct out” prism which directs the OPO signal out of the VersaScan. ***Laser safety:*** Always switch off the pump laser light, when you open the cover plates of flexiScan and versaScan or uvScan. Fasten the screws of the cover plates of versaScan and uvScan only softly.

1. **To calibrate the uvScan for the SHG option**, ensure that the 1064 nm fundamental is blocked, the OPO direct out prism is taken out of the VersaScan. Then start the software ScanMaster, navigate to the calibration dialogue and select the previously done calibration of the OPO and click “OK”.

2. Then select the installed UV crystal option(s) and click “OK”. In our case, click the UV-L crystal.
3. Click 2 times on “Next” to enter the calibration dialogue for the Pellin- Broca-Prism. Calibrate the Pellin-Broca-Prism with the visible signal wave of the OPO, i.e. at 600 nm since this is a 355 nm pumped OPO. Enter the wavelength 600 nm at the 1st position and click on “Go to”. This step forces the OPO to tune to this wavelength. Do not use a wavelength above 650 nm for a 355 nm pumped OPO. Ensure that the micrometer screw of the OPO is completely turned out. Now use the buttons “Moving in” and “Moving out” to turn the prism rotation stage until the visible OPO radiation exits through the uvScan exit slit without clipping as near to the exit slit blade. Then click on the button “left to red”. For the Pellin-Broca-Prism it is sufficient to do a 1−point calibration and select “left to red”.
4. Click on “Back” to enter the calibration dialogue window for the “SHG” crystals. Note down 5 wavelengths within the UV crystal option wavelengths range. All 5 wavelength shall be distributed about equally distant over the whole wavelength range of the active UV crystal option.
5. Type in a wavelength that is in the middle of the wavelength range of the present selected UV crystal option (i.e. 300 nm for UV-L) at the “1st position”. Click on “Go to” to force the OPO and the prism to go to the corresponding wavelength to be able to generate the corresponding UV wavelength in the uvScan.
6. Now search for the uvScan crystal angle that generates the UV radiation. Click on “Moving in” and “Moving out” and hold down the mouse button until the UV radiation is observed on the paper screen as a bluish glowing. The motor stops when the mouse bottom is released.
7. Once the UV radiation is found, measure the output power using a power meter. Optimize the output by setting the “Interval” to 1000 counts and counting the single steps that are executed by clicking on “+” and “-“ to find the maximum output power. Now not only the OPO and prism, but as well the SHG crystal is turning to the new wavelength using the information from the already done 1st calibration position.
8. Click on “2nd position” and type in a new UV wavelength and follow processes 5-7 above. Then click on “Go to”. If the UV crystal turns in the wrong direction, click on “left to red”

if “right to red” is highlighted and vice versa (click on “right to red” if “left to red” was chosen) and click again on “Go to”. Optimize the UV output power for this new wavelength. Start with slow motor speed and “Moving in” or “Moving out” or set the “Interval” to 4000 and use “+” or “-“. For the final fine-tuning set the “Interval” to 1000 and use “+” or “-“.

9. Continue until all the 5 chosen wavelengths are done. After the calibration of the UV crystals is finished click on “Next” and then on “Finish”. Choose a new name for this calibration and click “OK”.
10. Save all calibrations that are present in the list under the display field “Calibration” on the hard disk by clicking on “File” > “Save calibration set”.

For the UV production using SFM, ensure that the 1064 nm fundamental is entering the uvScan by removing the 1064 nm beam dump that is located behind the versaScan OPO. ***DANGER, LASER SAFETY:*** When the 1064 nm beam dump is removed, the invisible intense 1064 nm radiation can possibly be emitted through the beam exit aperture of the flexiScan. Before switching on the pump laser always launch the software ScanMaster first and command the whole flexiScan OPO system to a UV wavelength (< 405 nm). If wavelength above 410 nm shall be generated, always mount the 1064 nm beam dump in its place. Switch off the pump laser light, when mounting or removing the beam dump. A similar procedure is used for this calibration just like the SHG mode calibration.

1. Ensure that the OPO versaScan-ULD is calibrated to have a working signal wavelength. Start the ScanMaster software, navigate to the calibration dialogue and select the previously done calibration of the OPO and click “OK”. The versaScan-ULD is calibrated by looking at the (signal) wavelength. Thus to calibrate the versaScan-ULD you need to measure the wavelength of the visible signal light. All subsequent calibrations rely on the correct calibration of the versaScan-ULD wavelength.
2. When the versaScan-ULD is calibrated, then you proceed to the calibration of the PBP prism. Thus, skip the SFM1064 calibration (by clicking on “next” 2x). If you get the error message “invalid calibration” when trying to skip the SFM1064 calibration window, just enter a valid 1 position fake calibration: Click on 1st position, enter 350 nm, click on “get position from adjust”. Now you have the same data written in all 5

positions and a valid wavelength. This 1-point calibration is always valid and you can enter the PBP calibration table. For the calibration of the PBP, a calibration at 1 position is sufficient and typically works better than a multi-point calibration there.

3. **You have to set the parameter "left to red" for the 1 position calibration of the PBP**. Do it like the following: Click on 1st position. Enter a visible wavelength (for example 600 nm). Click on "Go to wavelength" and wait until the wavelength is reached (now the OPO generates 600 nm). Use "Move In" or "Move Out" until the visible OPO light passes trough the ceramic beam exit slit of the uvScan. Preferably as near as possible to the ceramic edge, which is near to the beam dump. You need to hold down the mouse button on "Move In" or "Move Out", that the motor continues to move. Click on "left to red". Now the PBP calibration is done and this takes care that the commanded wavelength will be directed through the uvScan output slit.
4. **Click on "Back" and calibrate the SFM 1064 by measuring the UV output energy**. Do it like the following: Click on 1st position. Enter preferably a wavelength in the middle of the wavelength range you want to calibrate (the full SFM 1064 wavelength range is 300 nm – 405 nm, thus 350 nm is a good start point). Click on "Go to wavelength" and wait until the wavelength is reached. (Now the PBP prism is set to direct 350 nm through the beam exit slit and the OPO is set to generate the wavelength that mixes with the 1064 nm to the demanded UV wavelength (350 nm in our example: 521.5 nm + 1064.14 nm and 350 nm)). Place a white business card in the beam path near the beam exit slit. Reduce the motor speed to about 1/3 on the speed bar and use "Move In" or "Move Out" to search for a motor position that generates UV light, which is visible on the business card as a blueish glowing. Once you see UV on the business card, check that the UV is done by mixing with 1064 nm: Block the 1064 nm light to enter the uvScan. (A good position to block the 1064 nm is on its beam pass where it passes by the back side of the versaScan OPO.) When you block the 1064 nm light then the UV has to vanish. If the UV is still generated, then you have found the motor position where the UV crystal generates SHG of the OPO, which is a different wavelength (in our example: SHG of 521.5 nm is 260.75 nm). In this case go on searching for the correct motor position that generates SFM with 1064 nm. Once you see the correct UV on the business card, take out the business card and place a power

meter in the UV beam. Then use clicks on the "+" and "-" buttons to move the motor and search for the maximum UV output energy (measured with a power meter). It is recommended to set the step size 1000 [counts] for the "+" and "-" button. Now the calibration of the 1st position is completed.

5. Go on to the next position (-s, until the calibration table is completed): Click on the position below. (If you do not click on the next position in the row first, any movement of the motors would change the data of the previous position – an error that happens often and lead to "Invalid calibration"). Enter a different wavelength. (There are 4 more positions to calibrate. Recommended wavelengths are: 300 nm, 325 nm, 375 nm, 400 nm (when 350 nm is the 1st position). The order of these wavelengths is not important. Only the wavelength in the middle of the range shall be the 1st wavelength. Click on "Go to wavelength" and wait until the wavelength is reached. Optimize the UV output for each wavelength as described above (with the business card first and "Move In" and "Move Out" with slow speed and then with the power meter and "+" and "-" buttons).
6. The calibration is now completed, and you can save it as described in the previous SHG mode procedure.

Even if the system is calibrated, one more step is recommended. In order to achieve the maximum UV output you might need to execute the software function "Fine adjust" on the UV crystal (Motor = "SHG" or "SFM") after the system warms up on a daily base. Refer to pages 32 – 33 in the software manual ScanMaster. Just command 1 UV wavelength and optimize the UV output by clicking on "Moving IN" or "Moving OUT" (holding down the mouse button that the motor continues to move). Do not forget to click on "Commit" before you click on "OK" to exit the "Fine Adjust" dialogue.

The pump beam is then propagated using various optics to the sample chamber where it excites the sample. The delayed probe beam hits the sample perpendicular to the pump and probes the excited state dynamics of the systems. The generated light is then directed into a monochromator and detected using a PMT (Hamamatsu R928) with a spectral range from 185 to 870 nm. The Edinburgh supplied software converts the electrical signal into a change of optical density.[16] This technique is used to record the change in absorption as a function of wavelength and time.

While the nsTAS is used to look at the spectral properties and the lifetimes of long lived transient species, this set-up was used to carry out experiments that were used to accurately determine the triplet extinction coefficients as well as the triplet quantum yields of compounds by using the *triplet energy transfer sensitization* and the *relative actinometry experiments*, respectively.

The triplet energy transfer sensitization experiment, as its name suggests, is an experiment where a molecule with a known triplet energy, triplet extinction coefficient and triplet quantum yield as a triplet energy donor (to transfer triplet energy to a compound with lower triplet energy) or triplet energy acceptor (to receive triplet energy from a compound with a higher triplet energy) as shown in **Figure 2.7.2.** As a result, this method can be used to estimate the relative triplet state energies of compounds based on whether the compound with the unknown triplet energy accepts or donates triplet energy (E_T) from the standard with a known triplet energy. For example, if tetraphenyl porphyrin whose $E_T = 1.43\ eV$ is used as a reference compound, it can transfer triplet energy to compounds whose $E_T < 1.43\ eV$ and receive triplet energy from a compound whose $E_T > 1.43\ eV$.

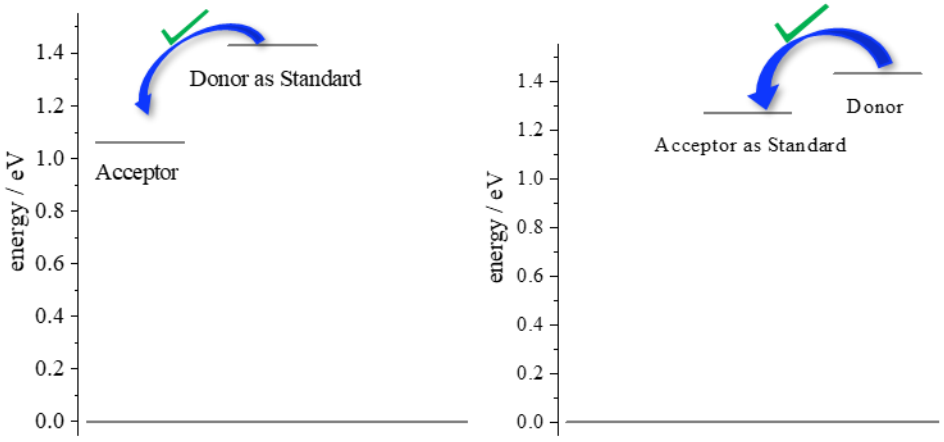

Figure 2.7.2: Energy level diagram of a triplet energy transfer sensitizer where in one case, the known standard/reference acts as the triplet energy transfer donor and in the other case, the standard/reference acts as the triplet energy transfer acceptor.

Below is a step-by-step process on how to carry out the triplet energy transfer experiment using the nsTAS set-up.

1. Pick a standard with a known triplet energy, the transient absorption spectroscopy triplet species wavelength, ground state absorption energy, the singlet energy

wavelength, triplet extinction coefficient and triplet quantum yield. Ensure that the ground state absorption of this standard does not overlap with the ground state absorption of the compound (sample) with an unknown triplet extinction coefficient and triplet quantum yield, you do not want to excite both the sample and the reference as this introduces an error that needs to be accounted for during the calculations, hence complicating the process. This reference will act as the triplet energy donor (sensitizer) or acceptor.

2. Measure the ground state absorption of both the standard and the sample.
3. Exciting at the compound's absorption max, obtain the nanosecond transient absorption spectrum of both the sample and the standard, and determine the triplet species wavelength. These triplet species are excited state absorptions (ESAs) whose kinetic lifetimes are highly enhanced upon oxygen purging as shown in the example below

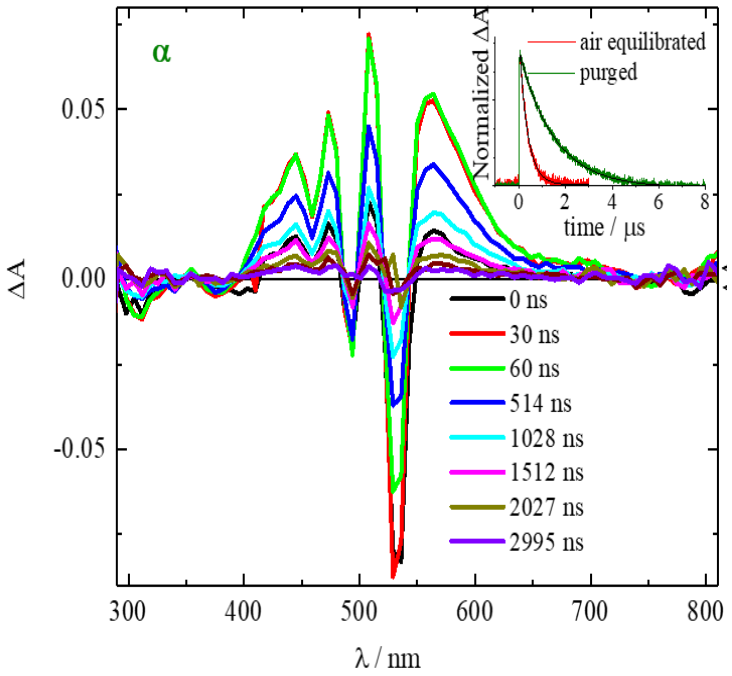

Figure 2.7.3: nsTAS spectrum of a perylene diimie (PDI) tetramer where the π −linker is connected to the individual PDI units at their α position. Here, the excited state absorption (ESA) is peaked at 510 nm. Inset shows the ambient and oxygen purged kinetics of the 510 nm species indicating that these are triplets.

4. Prepare a solution of the reference (in this case the donor) only where the optical density (OD) is approximately ~1 at the absorption.

5. Measure the triplet kinetic lifetime of this reference at the triplet wavelength determined in step 3 to obtain the maximum change in absorption ($\Delta A_{max,D}$), donor triplet lifetime (τ_D) and respective triplet rate (k_D) rate
6. Measure the triplet kinetic lifetime of the same reference at the triplet wavelength of the sample (acceptor) as determined in step 3 to obtain ΔA_{max}. In ideal cases, you should not see an ESA peak at this wavelength but a negative peak is mostly observed.
7. Check the ground state absorption of the solution to check photodegradation. If the sample's absorption spectrum is the same and its absorption at the maximum peak is still ~1, proceed to step 8. If the sample's absorption spectrum and/or the absorption intensity changed, prepare a new solution with an absorption max of ~1 before proceeding to step 8.
8. Add a pinch of the solid sample into the reference solution and measure the absorption of the mixture at the absorption max of the reference. The OD should remain the same (~1) since the sample should not absorb at the same wavelength as the reference.
9. Obtain the nsTAS spectra of the mixture of the reference and the sample. You should notice a decrease in the intensity of the reference's triplet ESA (change in optical density $-\Delta OD$) and a new peak should form an increase in the ΔOD of the sample's triplet ESA.
10. Measure the triplet kinetic lifetime of the mixture of the reference and the sample at the reference's triplet wavelength determined in step 3. Here, you should observe a decrease in the kinetic ΔOD. Obtain the different lifetime denoted as $\tau_D{}'$ and the respective rate denoted as $k_D{}'$.
11. Measure the triplet kinetic lifetime of the mixture of the reference and the sample at the sample's (acceptor's) triplet wavelength determined in step 4 and you should see a *rise* in the kinetics with increased ΔOD, also known as the $\Delta A_{max,A}$. This *rise* signifies the transfer of triplet energy from the reference triplets to the sample triplets. Here you should obtain two lifetimes where one is a formation as a result of triplet energy transfer from the donor with the lifetime and rate denoted as $\tau_D{}'$ and $k_D{}'$, respectively, and the other one is a decay with the decay time and rate from the acceptor triplet denoted as τ_A and k_A, respectively. In ideal cases, the $\tau_D{}'$ and $k_D{}'$obtained here should match those obtained in step 10.

12. From the above measurements, use the equation below to calculate the triplet extinction coefficient of the sample (acceptor) using **Equation 2.7.1** below.

$$\varepsilon_A = \varepsilon_D \times \frac{\Delta A_{max,A}}{\Delta A_{max,D}} \times \frac{1}{f_D \times p_{ET} \times w} \qquad \textbf{Equation 2.7.1}$$

where:

ε_A = triplet-triplet extinction coefficient of the acceptor (UNKNOWN)

ε_D = triplet-triplet extinction coefficient of the donor/sensitizer (KNOWN)

$\Delta A_{max,A}$ = maximum absorbance change of the Acceptor in the "Donor + Acceptor" mixture

$\Delta A_{max,D}$ = maximum absorbance change of the Donor/sensitizer **alone**

f_D = fraction of light absorbed by the Donor/sensitizer in the "Donor + Acceptor" mixture w.r.t. the Donor alone

k'_D = rise rate constant of the Acceptor in the "Sensitizer + Acceptor" mixture (should be similar to the quenched Sensitizer decay rate constant)

k_D = decay rate constant of the Donor ONLY

k_A = decay rate constant of the Acceptor in the "Donor + Acceptor" mixture

and:

$f_D = \frac{A_D}{A_{D+A}} \times \left(\frac{1-10^{-A_{D+A}}}{1-10^{-A_D}}\right)$ is the fraction of light absorbed by the donor

$p_{ET} = \frac{k'_D - k_D}{k'_D}$ is the energy transfer probability

$w = exp\left[-\frac{\ln\left(\frac{k'_D}{k_A}\right)}{\frac{k'_D}{k_A}-1}\right]$ is a factor accounting for the quenched donor and acceptor lifetimes

The obtained triplet extinction coefficient of the sample is then used in a separate experiment known as relative actinometry to determine the triplet extinction coefficient of the sample (donor) as shown below.

13. Make solutions of the sample and the reference with the same ground state absorption at the same excitation wavelength.
14. Measure the triplet kinetics to obtain the sample's and reference's respective ΔA.

15. Use Equations 2.7.2 and 2.7.3 below to calculate the triplet quantum yield of the sample (acceptor).

$$\frac{[\phi_T \varepsilon_T]_{sample}}{[\phi_T \varepsilon_T]_{ref.}} = \frac{[\Delta A]_{sample}}{[\Delta A]_{ref.}} \qquad \textbf{Equation 2.7.2}$$

$$[\phi_T \varepsilon_T]_{sample} = [\phi_T \varepsilon_T]_{ref.} \times \frac{[\Delta A]_{sample}}{[\Delta A]_{ref.}} \qquad \textbf{Equation 2.7.3}$$

Where:

$\varepsilon_{T\ sample\ (\beta)}$ = triplet-triplet extinction coefficient of the sample (computed using ***energy transfer means.***)

$\phi_{T\ sample\ (\beta)}$ = triplet quantum yield of the sample

$[\Delta A]_{sample\ (\beta)}$ = change in absorption of the sample (whose OD is similar to that of the reference at $\lambda_{excitation}$)

$[\Delta A]_{ref}$ = change in absorption of the reference compound. (whose OD is similar to that of the sample at $\lambda_{excitation}$)

The above description is in ideal cases of a donor (sensitizer whose triplet energy is higher than that of the sample. However, there are two occasions where changes need to be done in the procedure above.

1) In cases where the triplet energy of the reference is lower than that of the sample. In this case, the triplet energy transfer goes from the sample to the reference. In this case, the sample will be treated as the energy transfer donor while the reference will be treated as the triplet energy transfer acceptor. The procedure to calculate the triple extinction coefficient will be the same, except that the wavelengths need to be changed accordingly, and the initial absorption recorded is that of the sample ONLY, before adding a solid of the reference into the sample solution. In this case, where the sample is the donor, a small change is done in the equation to calculate the triplet extinction coefficient of the donor (sample) as shown in **Equation 2.7.4** below.

$$\varepsilon_D = \varepsilon_A \times \frac{\Delta A_{max,D}}{\Delta A_{max,A}} \times f_D \times p_{ET} \times w$$

Where although everything else remains the same, the calculation of these parameters changes as follows:

$f_D = \frac{A_D}{A_{D+A}} \times \left(\frac{1-10^{-A_{D+A}}}{1-10^{-A_D}}\right)$ is the fraction of light absorbed by the donor

$p_{ET} = \frac{k'_D - k_D}{k'_D}$ is the energy transfer probability

$w = exp\left[-\frac{\ln\left(\frac{k_D'}{k_A}\right)}{\frac{k_D'}{k_A}-1}\right]$ is a factor accounting for the quenched donor and acceptor lifetimes

2) In cases where there is some overlap between the absorption of the sample and that of the reference, the $\tau_D{}'$ and $k_D{}'$ obtained in step 10 differ from those obtained in step 11. In this case, the rise time obtained in step 11 is used to obtain $k_D{}'$ since at this wavelength, only the acceptor absorbs and not the reference. In addition, make sure to account for the absorption overlap by subtracting the ΔA of the sample (acceptor) only from the ΔA of both the sample and the reference at the sample's triplet wavelength to obtain an accurate *rise*.

Therefore, to accurately and successfully determine the ε_T of a sample experimentally, the above procedure should be followed. In the donor (reference) + acceptor (sample) mixture, a decrease in the triplet lifetime (i.e. higher decay rate) is observed at the donor (reference) λ_T in comparison to its lifetime with only the donor (reference) in solution. Also, at the acceptor (sample) λ_T, a triplet concentration rise has to be observed. These observations thus confirm triplet energy transfer from a donor (reference) to the sample (acceptor). Using the decay rate of the donor (reference) only (k_D) and the sample (acceptor) (k_A) alongside the rate of energy transfer (k_{ET}), the ΔA_A and ΔA_D, the ε_T of the donor (reference) or acceptor (sample) can be evaluated knowing the ε_T of the other.

References

(1) Krishnan Kothandaraman, R. Development of Four-Terminal Devices Utilising Thin-Lm Solar Cells, 2018.

(2) Mäntele, W.; Deniz, E. UV–VIS Absorption Spectroscopy: Lambert-Beer Reloaded. *Spectrochimica Acta - Part A: Molecular and Biomolecular Spectroscopy*. Elsevier B.V. February 15, 2017, pp 965–968. https://doi.org/10.1016/j.saa.2016.09.037.

(3) Agilent Technologies. *Agilent 8453 UV-Visible Spectroscopy System Operator's Manual Agilent 8453 UV-Visible Spectroscopy System Operator's Manual Notices*.

(4) Horiba Scientific. *Modular Research Fluorometers for Lifetime and Steady State Measurements*.

(5) Kumar, K.; Tarai, M.; Mishra, A. K. Unconventional Steady-State Fluorescence Spectroscopy as an Analytical Technique for Analyses of Complex-Multifluorophoric Mixtures. *TrAC - Trends in Analytical Chemistry*. Elsevier B.V. December 1, 2017, pp 216–243. https://doi.org/10.1016/j.trac.2017.09.004.

(6) Vázquez, R. Characterizing the Excited State Dynamics of Organic Materials for Efficient Energy Conversion: From Current to Photons and Vice-Versa, 2019.

(7) M Ismail, L. F.; Antonious, M. S.; Mohamed, H. A.; Abdel-hay Ahmed, H. *Fluorescence Properties of Some Coumarin Dyes and Their Analytical Implication*; 1992; Vol. 104.

(8) Kubin, R. F.; Fletcher, A. N. *FLUORESCENCE QUANTUM YIELDS OF SOME RHODAMINE DYES*; 1982; Vol. 27.

(9) Muthike, A. K.; Carlotti, B.; Madu, I. K.; Jiang, H.; Kim, H.; Wu, Q.; Yu, L.; Zimmerman, P. M.; Goodson, T. The Role of the Core Attachment Positioning in Triggering Intramolecular Singlet Exciton Fission in Perylene Diimide Tetramers. *Journal of Physical Chemistry B* **2021**, *125* (19), 5114–5131. https://doi.org/10.1021/acs.jpcb.1c02534.

(10) Guarin, C. A.; Mendoza-Luna, L. G.; Haro-Poniatowski, E.; Hernández-Pozos, J. L. Two-Photon Absorption Spectrum and Characterization of the Upper Electronic States of the Dye IR780. *Spectrochimica Acta - Part A: Molecular and Biomolecular Spectroscopy* **2021**, *249*. https://doi.org/10.1016/j.saa.2020.119291.

(11) Hansen, S. B.; More, R.; Bailey, J.; Pain, J.-C.; Nagayama, T. Two-Photon Absorption in Plasmas; APS Division of Plasma Physics Meeting, 2020.

(12) Zhao, L.; Lustres, J. L. P.; Farztdinov, V.; Ernsting, N. P. Femtosecond Fluorescence Spectroscopy by Upconversion with Tilted Gate Pulses. *Physical Chemistry Chemical Physics* **2005**, *7* (8), 1716–1725. https://doi.org/10.1039/b500108k.

(13) Spectra Physics. *Quanta-Ray Lab-Series Pulsed Nd:YAG Lasers User Manual*; Mountain View, 2003.

(14) GWU-Lasertechnik. *GWU VersaScan Beta-Barium Borate Optical Parametric Oscillator User Manual*; 2012.

(15) GWU-Lasertechnik. *GWU UvScan User Manual*; 2013.

(16) Edinburg Instruments Ltd. *Nsta-Lp980-User-Manual*; Livingston, 2016.

Chapter 3

Investigating The Optical Properties of Thiophene Additions to s-Indacene Donors with Diketopyrrolopyrrole, Idoindigo and Thienothiophene Acceptors

3.1 Original Publication Information and Author Contribution

Portions of this chapter were taken from a paper that was published in the *Journal of Physical Chemistry C* entitled:

"Investigating the Optical Properties of Thiophene Additions to s-Indacene Donors with Diketopyrrolopyrrole, Isoindigo, and Thienothiophene Acceptors" Bradley Keller, Zhengxu Cai, Angelar K. Muthike, Prabhat Kumar Sahu, Hyungjun Kim, Audrey Eshun, Paul M. Zimmerman, Deqing Zhang, Theodore Goodson III. *J. Phys Chem. C*, **2018**, 122 (48), 27713-27733.

In this work, my contribution was on the nanosecond transient absorption section where I obtained the experimental data of all the six investigated chromophores and analyzed this data. Although most of the paper was written by the first author, I wrote the discussion and conclusion sections of the paper and revised the paper since the first author had graduated. Here, I concluded that in addition to the extended donor conjugation and acceptor strength, the bulkiness of the system which leads to steric hindrance affects the charge transfer of these conjugated systems.

3.2 Abstract

New donor-acceptor light harvesting polymers with either a 4,4,9,9-tetrakis(4-hexylphenyl)-4,9-dihydro-s-indaceno[1,2-b:5,6-b']dithiophene (**IDT**) or a 4,4,9,9-tetrakis(4-hexylphenyl)-4,9-dihydro-s-indaceno[1,2-b:5,6-b']dithienothiophene (**IDTT**) donor subunit and either a 2-(nonadecan-9-yl)-5-(2-octyldodecyl)-3,6-di(thiophen-2-yl)-2,5-dihydropyrrolo[3,4-c]pyrrole-1,4-dione (**DPP**), (E)-1,1'-bis(2-octyldodecyl)-[3,3'-biindolinylidene]-2,2'-dione (**II**), or 3-ethyl-1-(thieno[3,4-b]thiophen-2-yl)heptan-1-one (**TT**) acceptor were synthesized. In this study, the effects of donor conjugation length and donor-acceptor combination on the optical properties were investigated using steady state, up-conversion, quantum chemical simulations and ultrafast

and transient spectroscopic techniques. At high energies, it was observed that polymers with extended donor conjugation had significantly enhanced absorption while those with stronger acceptors showed higher extinction coefficients at lower energies. Fluorescence up-conversion experiments revealed that the donor conjugation length increased the fluorescence lifetimes for the extended conjugated polymers. Two-Photon Absorption (TPA) experiments and quantum chemical simulations showed that polymers with stronger acceptors exhibited enhanced charge transfer characteristics. Transient Absorption (TA) investigations revealed new optical species for the extended donor polymers. This study has shown the considerable effect that donor conjugation has on the optical properties of donor-acceptor light harvesting conjugated polymers. The results from this work can be used in the design and synthesis of new donor-acceptor polymers for organic photovoltaics.

3.3 Introduction

The rapid growth in the global population has led to increased energy consumption which has resulted in a high rate of burning fossil fuels hence climate change.[1-3] This has led to interest in cleaner, renewable, and greener sources of energy, such as solar energy harvesting.[1] These solar energy harvesting systems have seen an average annual growth in global photovoltaic capacity of 40%.[2] The most prominent solar harvesting systems are solar cells which consist of electron rich and electron poor active material that absorb sunlight, converting photonic energy into electron; and hole charge carriers that are responsible for electricity generation.[3] Traditionally, solar cell absorbing active materials have used inorganic semiconductors for light harvesting, however, these materials are brittle, inflexible, have low optical absorption coefficients in the visible region of the electromagnetic spectrum, require high temperature and pressures for manufacturing, or contain toxic elements.[4–7] These downsides have limited the number of applications that the inorganic materials can be used in and contributed to the overall cost of using these technologies and created a huge interest in organic light harvesting materials.

Organic solar energy harvesting materials have high optical absorption coefficients, flexible, lightweight, easily tunable band gaps, and are readily solution processable.[8–11] In organic solar cells, an absorbing organic layer is sandwiched between two conducting electrodes, typically a conducting glass on the top and a metallic electrode on the bottom. Light is absorbed by the absorbing organic layer forming a tightly bound exciton, an electron-hole pair. Another organic

layer is used to overcome the binding energy of the exciton to dissociate the electron from the hole, forming free charge carriers that then flow to the electrodes, with the electrons flowing to the cathode and the holes flowing to the anode. The most promising organic solar harvesting devices have incorporated low band gap organic donor-acceptor (D-A) with conjugated donors that serve as the photon absorbing material and hole transporting material, and an organic acceptor material that has high electron affinity to ease charge separation and electron transport.[15]

Donor-acceptor polymers have a relatively simple motif but finding suitable donor and acceptor monomers that lead to high power conversion efficiencies (PCE) is not easy. Electron-rich donors with strong acceptors are imperative in promoting charge transfer along the polymer backbone. The HOMO of the donor significantly influences the HOMO of the polymer, and the polymer HOMO and acceptor material LUMO offset determine the open circuit voltage.[12] Strong donors have lower onset oxidation potentials and contribute to lower band gaps.[13] But too strong of a donor results in poor charge carrier extraction due to poor energy level mismatch in the device. Attempts have been made to enhance the donating ability of the donor monomer to increase the power efficiency of donor-acceptor devices. One method has focused on increasing the donor conjugation, but too large of a conjugated donor system results in out of plane twisting of the donor with respect to the acceptor resulting in poorer power efficiencies.[14] Donating groups have also been added to the donor monomer to increase the donating ability, but oftentimes the donating groups can also increase steric hindrance between the donor and the acceptor decreasing the conjugation length along the polymer backbone.[15–17]

Much research has focused on synthesizing new donor materials and acceptor materials, device architectures, morphologies, optical properties of devices, electrical properties of devices, but limited attention has been on the dynamic fundamental optical properties of the D-A conjugated polymers light absorbing materials.[18–22] In fact, there is still much debate on the mechanisms that lead to the optoelectronic properties of these materials.[23–25] Numerous studies have investigated the optoelectronic properties of bulk heterojunction donor-acceptor systems, but a deeper understanding of the dynamic optical properties of D-A conjugated polymers that are used as the donating materials in organic solar cells will go a long way in unraveling the mysteries responsible for high power conversion efficiency organic solar cells.[26–28]

There have been a few promising donor monomers that have been incorporated in light harvesting D-A polymers that have resulted in high power conversion efficiencies like

Benzodithiophene (BDT), carbazole and indacenodithiophene (**IDT**) .[33- 40] Our studies focus on the **IDT** aromatic fused-ring system which provides a rigid structure that promotes planarity for extended conjugation, and restricts twisting and out of plane rotation due to steric hindrance.[29] The **IDT** structure provides great tunability with modification of the bridging atom, the introduction of electronic influencing groups, and the introduction of side groups. **IDT** polymers have shown high hole mobilities and resulted in PCE of more than 12%.[41, 42]

As important as the donor monomer is to the D-A polymer, the acceptor monomer is equally important and much research has been devoted to designing electron-withdrawing acceptors. The electron-withdrawing strength of the acceptor has a significant influence on the electronic and optical properties of the donor-acceptor polymer. From electrochemical studies and computations, it is known that the LUMO of the acceptor closely matches the LUMO of the donor-acceptor polymer.[30,31] By introducing electron-withdrawing groups to the acceptor monomer, the band gap of the donor-acceptor polymer can be easily tuned.[32] Acceptor strength has also had profound effects on the optical properties of light-harvesting D-A polymers. D-A Polymers with strong acceptors have seen an enhancement of light absorbing capabilities in the high solar flux regions of the visible spectrum,[33] greater charge transfer, and quenched fluorescence; leading to high PCE D-A polymers such as PTB7.[47] One promising acceptor monomer is diketopyrrolopyrrole (**DPP**), a strong electron withdrawing acceptor that has demonstrated high electron and hole mobilities.[34,35] The introduction of thiophene subunits on both ends of **DPP** connects the **DPP** to the donor monomer as well as creates a Donor-Acceptor-Donor motif between the electron deficient **DPP** and electron rich thiophenes.[36] D-A polymers that have incorporated **DPP** have seen high PCEs of up to 10%.[37] Another promising acceptor monomer is isoindigo (**II**) which consists of two oxindole rings centro-symmetrically conjugated to each other at their 3-carbons by a central double bond that binds two electron-withdrawing carbonyls and two electron-rich benzene rings in trans conformation. It has good electron-withdrawing properties, two amides that are readily functionalized, the phenyl rings have sites for conjugation elongation, high hole mobilities, planar backbone, and strong inter-chain interactions due to the rigidity of the **II** core.[38,39] Isoindigo also has the advantage of large scale availability from natural sources which leads to a greener overall synthetic pathway.[40] Polymers that have incorporated **II** as acceptor units have seen efficiencies of up to 8%.[41] Another mostly studied and commonly incorporated acceptor monomer is thienothiophene (**TT**).[42,43] Thienothiophene is composed of two thiophene

rings fused to each other. The fused ring promotes planarity and enhances conjugation along the monomer backbone. Thienothiophene has four isomers: thieno[2,3-b]thiophene, thieno[3,4-c] thiophene, thieno[3,2-b]thiophene, and thieno[3,4-b]thiophene; with thieno[3,4-b]thiophene proving to be the most successfully incorporated isomer as an acceptor in donor-acceptor polymers because it introduces an anisotropic charge distribution that is good for charge transport.[44,45] The doubly unsaturated cyclopentadiene does not show aromaticity, but aromaticity is achieved by substituting the central carbon atom with a heteroatom having a lone pair that contributes to the π resonancy.[56] One of the best aspects of the thienothiophene is its ease of functionalization. The conjugation length can be extended or electron-withdrawing groups can be attached to the monomer to impart optical and electronic changes to the structure.[46,47] D-A polymers that have incorporated thienothiophene acceptors have achieved high power conversion efficiencies (7.4%) , in fact, the seminal work of Liang et al demonstrated the great potential these acceptors can have on the optoelectronic properties of D-A polymers.[48] However, some D-A polymers with strong acceptors and great charge transfer characteristics, quenched fluorescence, and good absorption properties have also produced low power conversion efficiencies due to local exciton trapping preventing efficient transfer along the polymer backbone.[49] Thus more investigation is needed in order to get a better understanding of the influence of acceptors on the fundamental optoelectronic properties of light harvesting donor-acceptor polymers.

In this study, six donor-acceptor polymers were synthesized. A detailed synthetic procedure is provided in the supporting information (**Figure 3.8.1.1**). Each polymer had a 4,4,9,9-tetrakis(4-hexylphenyl)-4,9-dihydro-s-indaceno[1,2-b:5,6-b']dithiophene (**IDT**) or a 4,4,9,9-tetrakis(4-hexylphenyl)-4,9-dihydro-s-indaceno[1,2-b:5,6-b']dithienothiophene (**IDTT**) donor with either a 2-(nonadecan-9-yl)-5-(2-octyldodecyl)-3,6-di(thiophen-2-yl)-2,5-dihydropyrrolo[3,4-c]pyrrole-1,4-dione (**DPP**), (E)-1,1'-bis(2-octyldodecyl)-[3,3'-biindolinylidene]-2,2'-dione (**II**), or 3-ethyl-1-(thieno[3,4-b]thiophen-2-yl)heptan-1-one (**TT**) acceptor. These make up the polymers with longer conjugated donors, P1 (**IDTT-DPP**), P2 (**IDTT-II**), P3 (**IDTT-TT**) and their shorter conjugated donor analogues, P4 (**IDT-DPP**), P5 (**IDT-II**) and P6 (**IDT-TT**). Spectroscopic techniques like steady state spectroscopy, ultrafast two photon excitation fluorescence (TPEF), ultrafast up-conversion, and transient (femtosecond and nanosecond) and quantum chemical simulations were used to investigate the optical and nonlinear properties, two photon absorption (TPA) properties, fluorescence lifetimes, excited state dynamics

and effect of polymerization and donor conjugation length of these polymers on their optical properties.

3.4 Experimental Methods

3.4.1 Steady State UV-Vis and Emission Measurements

The investigated polymers were dissolved in chloroform for all steady state experiments. Concentrations of 3.0 X 10^{-6} M were used for all steady state experiments and concentrations of 3.0 X 10^{-6} M or lower were used for quantum yield experiments. Steady state absorption spectra were measured using an Agilent 8432 UV-visible absorption spectrophotometer. Steady state emission spectrum measurements were carried out using a Fluoromax-2 spectrophotometer. Styryl 9m (ϕ = 0.07) in chloroform was used as the fluorimetric standard for the calculation of the fluorescence quantum yield for P1, P2, P4 and P5 using the well-known comparative method.[50,51] Zinc phthalocyanine (ϕ = 0.30) in pyridine was used as the fluorimetric standard for quantum yield determination of P3 and P6.[52] The quantum yields were measured at 430 nm excitation.

3.4.2. Two-Photon Absorption (TPA) Experiments

The two-photon-absorption (TPA) cross sections were measured using the two-photon excited fluorescence (TPEF) method.[53] The setup employs a mode-locked Spectra-Physics femtosecond Mai Tai laser, which is tunable from 700 to 900 nm, to generate 110-fs pulses. For the experiments in this study, the Spectra-Physics Mai Tai laser generated a 775 nm with 110-fs pulse width to pump a Spectra-Physics femtosecond synchronously pumped optical parametric oscillator (Opal), which produced 1250 nm(for P3 and P6 excitation) or 1300 nm(for P1, P2, P4, and P5 excitation) with 150-fs excitation pulses. The beam was directed into a solution in a sample cell (quartz cuvette, 1 cm path length), and the resultant fluorescence was collected in a direction perpendicular to the incident beam. A lens was used to direct the collected fluorescence into a monochromator. The output from the monochromator was directed into a photomultiplier tube (PMT), and the photons were converted into counts by a photon counting unit. The photomultiplier tube was connected to the computer through a photon counting unit (Hamamatsu) for signal recording. Zn 2,9,16,23-tetra-tert-butyl-29H,31H-phthalocyanine and Styryl 9m have known TPA cross-sections and were used as standards for comparative method determination of TPA cross-sections.[54]

3.4.3. Fluorescence Up-conversion Experiments

The time-resolved fluorescence experiments were performed using a fluorescence setup that had previously been described.[55] A femtosecond Mode-locked Ti-sapphire pulsed laser (Spectra Physics Tsunami) was used to generate 80 fs pulses at 800 nm wavelength with a repetition rate of 82 MHz. The Tsunami was pumped by a 532 nm continuous wave Millennia (Spectra Physics) laser. An excitation pulse of 400 nm was generated by a second harmonic BBO crystal, and the residual 800 nm beam was used as an optical gate by a computer-controlled motorized optical delay line. The polarization of the excitation beam was controlled by a berek compensator. The fluorescence signal of the sample was up-converted by a BBO crystal by using the residual 800 nm beam, which is delayed by the optical delay line with a gate step size of 6.25 fs. This allows the fluorescence decay dynamics to be measured temporally. A monochromator is used to select the wavelength of the up-converted signal which is detected by a photomultiplier tube (R152P, Hamamatsu). The instrument response function (IRF) has been determined from the Raman signal of water to have a width of 110 fs.

3.4.4. Femtosecond Transient Absorption Experiments

The femtosecond transient absorption experiment setup has been described previously.[56] The femtosecond transient absorption investigations were carried out using ultrafast pump-probe techniques with detection in the visible region. The laser system produces 1-mJ, 100-fs pulses at 800 nm with a repetition rate of 1 kHz that were obtained from an Nd:YLF (Spectra Physics Empower)-pumped Ti:Sapphire regenerative amplifier (Spectra Physics Spitfire) with the input from a continuous wave Nd:YVO4 (Spectra Physics Millennia)-pumped Ti:Sapphire oscillator (Spectra Physics Tsunami). The output of laser beam was split to generate pump and probe beam pulses with a beam splitter (85% and 15%, respectively). The pump beam was generated by an optical parametric amplifier (Spectra Physics OPA-800). The 400 nm pump beam was produced from the second harmonic of the idler beam using a BBO. The white light continuum probe beam was generated from the amplified beam by a Helios system (Ultrafast Systems Inc). The probe beam was generated by a 2 mm sapphire plate generating a white light continuum from 450 nm to 750 nm. The time delay between the pump and probe was controlled with a computer-controlled motion controller. The white light and the pump beam were overlapped in a 2 mm quartz cuvette containing the sample with a magnetic stirrer. The typical energy probe beam is < 0.1 μJ, while

the pump beam energy is ~1 – 2 μJ per pulse. Magic angle polarization is kept consistent between the pump and probe using a polarizer. The change in absorbance as a function of time for the signal was collected by a CCD detector (Ocean Optics). Data acquisition was controlled by software from Ultrafast Systems Inc.

3.4.5. Nanosecond Transient Absorption Experiments

The nanosecond transient absorption system is made up of two major components: the excitation laser and the LP980-K spectrometer. The excitation laser is used to pump the optical parametric oscillator (OPO) to produce the required excitation wavelength between 250nm and 2600nm. On the other hand, the spectrometer contains the probe source, the sample compartment and the monochromator. The probe source, a 150W, ozone free xenon lamp continuously produces a 6ms pulse within a wavelength range of 190nm to 2600nm and creates the background for the time dependent absorption measurements. The excitation laser, which hits the sample perpendicular to the probe light and after the lamp trigger stabilizes, creates the transient species which reduces triplet-triplet annihilation and photodegradation. The light from the sample is then directed into the monochromator and detected by a photomultiplier tube (PMT - Hamamatsu R928 – with a detection range of 185nm to 870 nm). The PMT converts the transmission response of the sample into electric signals that are measured by a TDS3052B Model oscilloscope. These electrical signals are converted from volts into optical density by use of the software supplied by Edinburgh.

3.4.6. Quantum Chemical Calculations

Quantum chemical simulations were conducted to analyze the experimental absorption spectra, and two-photon absorption spectra. The photophysical properties of polymers should not be described based on a single repeat unit due to the significant coupling between repeating units.[69,70] Therefore, the minimum geometry that can include the coupling, a dimer, was chosen as models for the photophysical properties of the polymers. The methyl groups replace all solubilizing groups in the dimer model, since these structural alternations only weakly affect the low-lying electronic transitions occurring within the π backbone. The ground state geometries of each dimer were optimized with density functional theory (DFT), using the ωB97X-D functional and 6-31G* basis sets.[71,72]

Based on the optimized geometries, time-dependent DFT (TD-DFT) single point energy calculations were performed with a system-dependent, non-empirically tuned ωB97X-D which is known to significantly improve the charge delocalization problems in conventional DFT functionals. [73] The tuned ω value was chosen to minimize the square sum of the difference between HOMO energy and ionization potential (IP), and LUMO energy and electron affinity (EA), $(\epsilon_{HOMO}+IP)^2+(\epsilon_{LUMO}+EA)^2$ of the monomer model. The range-split parameter ω is heavily affected by the environment, and the inclusion of solvent dielectric field induced a reduction in ω value.[74] This process yielded the optimal ω value to be 0.006, 0.008, 0.008, 0.006, 0.008, 0.010, for P1 to P6, where chloroform (dielectric constant is 4.31) was used as the dielectric through a polarizable continuum model.[75,76] This quantum chemical approach has proven its capability to predict the absorption energy of various chromophores highly accurately.[70,77,78] Character of excitations were analyzed with natural transition orbitals (NTOs). [79, 80] All TD-DFT simulations were carried out using Q-Chem 5.0. [81]

The TPA cross section is calculated as follows: $\sigma(\omega) = \frac{8\pi^2\alpha^2\omega^2}{\Gamma}(a_0^4 t_0)\delta(\omega)$, where α is the fine structure constant, ω is the frequency of the applied field (here, we consider the degenerate TPA where ω is half of the absorption energy), Γ is the full width at half maximum of the Lorentzian lineshape broadening, which is set to 0.1 eV, and δ(ω) is the TPA transition probability.[82] For TPA calculations, we employed BH&HLYP functional which contains 50 % HF exchange, and only monomer model was considered due to the limit of computational resource. All TPA related simulations were conducted using GAMESS. [83,84]

3.5. Results

3.5.1. Synthesis of the D-A Polymers

The D-A polymers used in this experiment were successfully synthesized. All of the chemicals were purchased from Aldrich or Alfa. All reagents purchased commercially were used without further purification except for toluene and tetrahydrofuran (THF), which were dried over sodium/benzophenone. ^{1}H NMR spectra shown in the supporting information (**Figure 3.8.1.2-3.8.1.7**) were recorded on a Bruker DRX-400 spectrometer, with tetramethylsilane as an internal reference. Detailed synthetic procedure can be found in the supporting information.

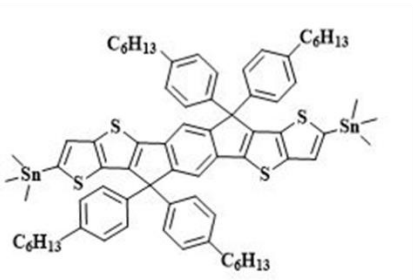

1

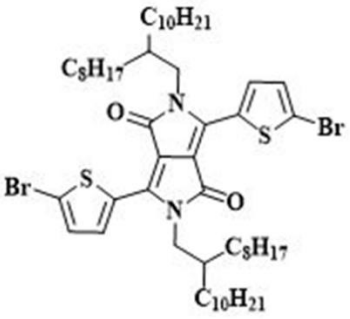

3

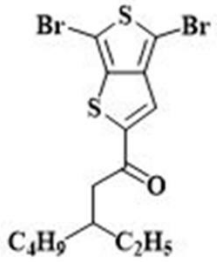

5

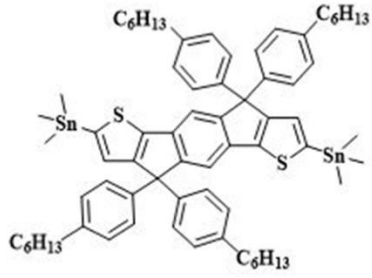

2

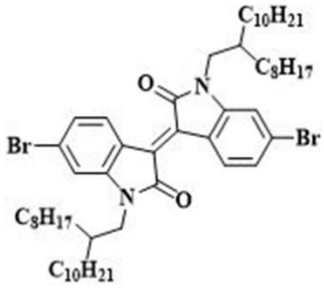

4

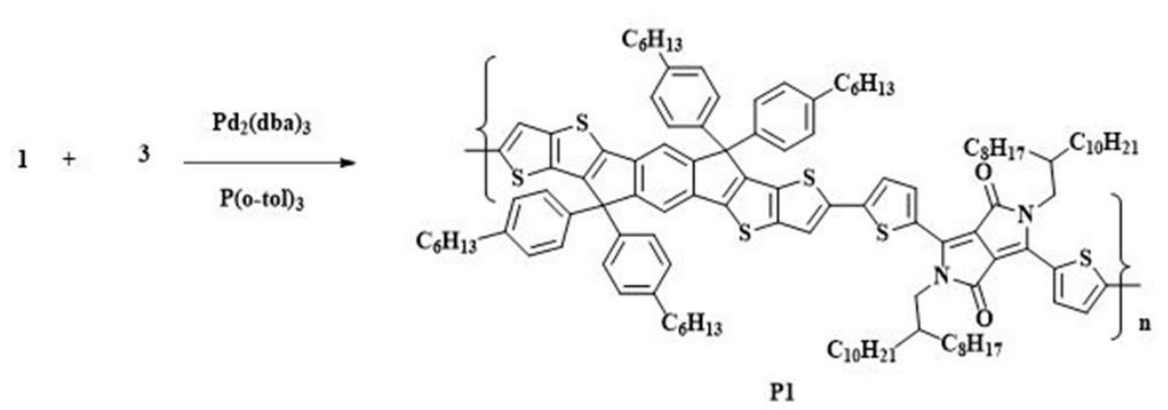
1 + 3
Pd2(dba)3
P(o-tol)3
C6H13
C8H17
C10H21
S
O
N
n

P1

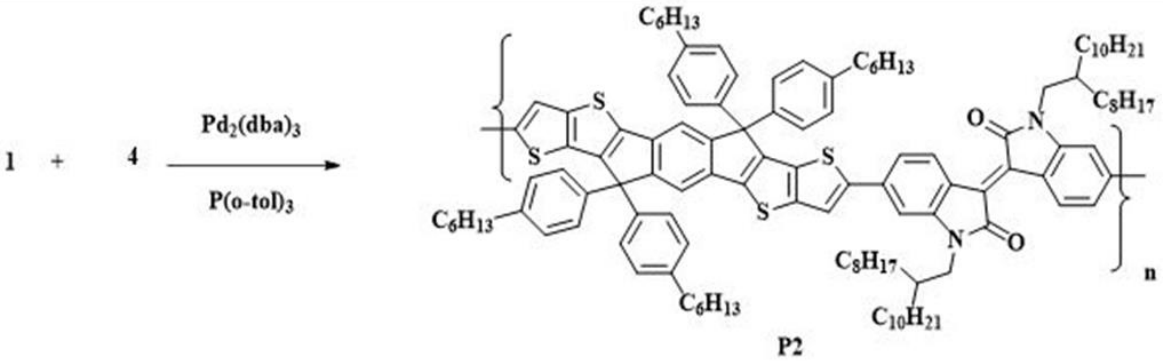
1 + 4
Pd2(dba)3
P(o-tol)3
C6H13
C8H17
C10H21
S
O
N
n

P2

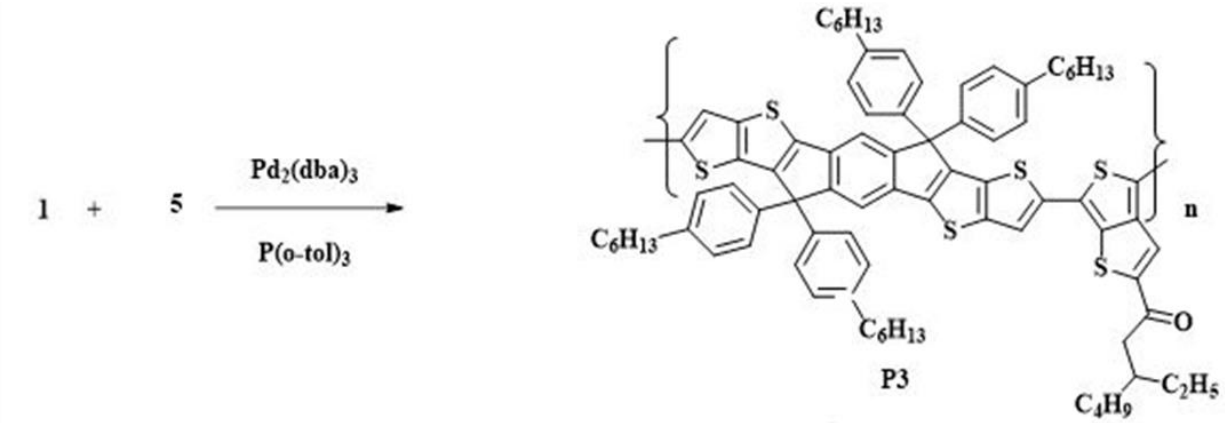
1 + 5
Pd2(dba)3
P(o-tol)3
C6H13
C2H5
C4H9
S
O
n

P3

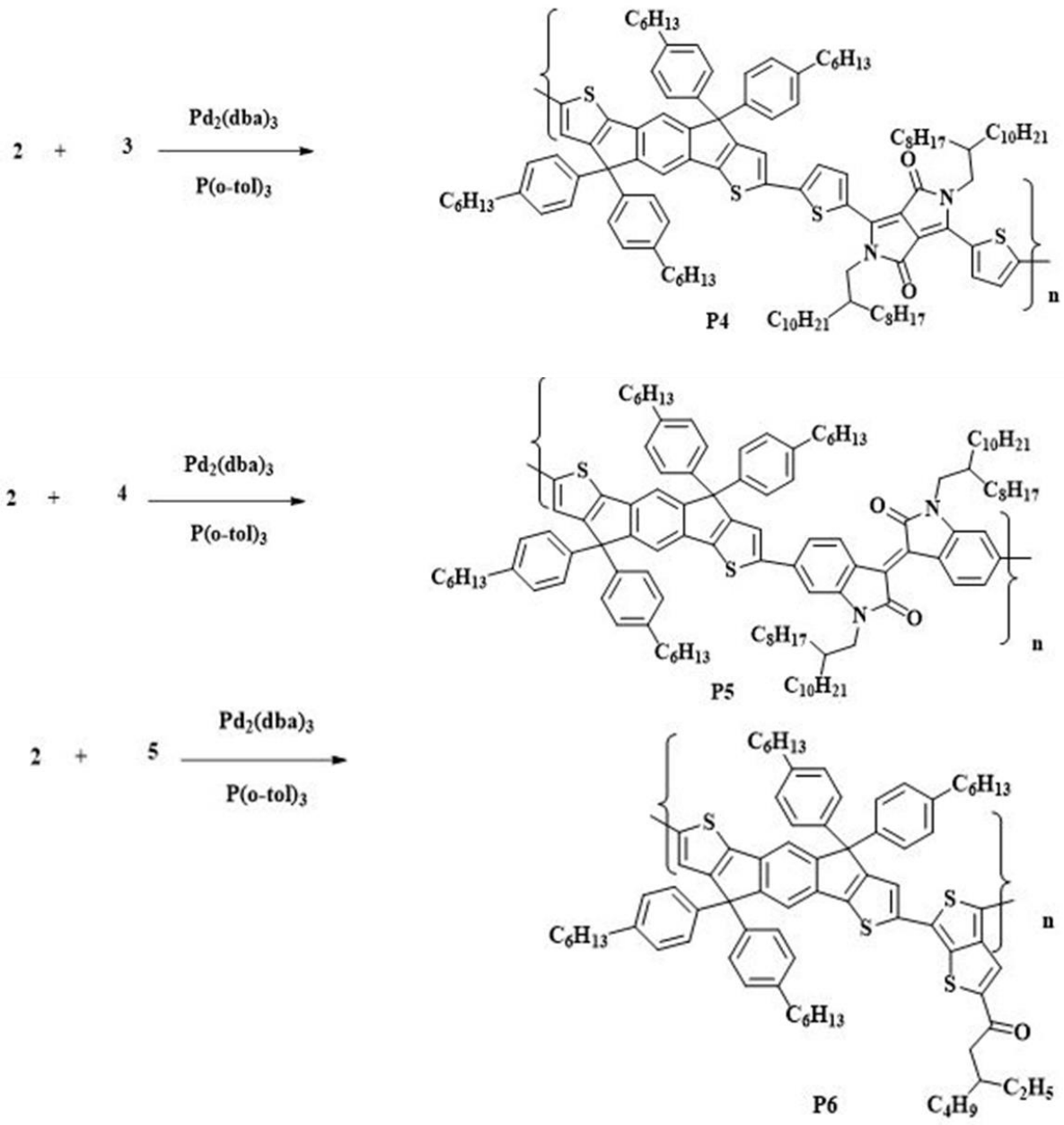

Figure 3.5.1.1. The synthetic route of D-A polymers and their molecular structures.

3.5.2. Molecular Structures and Molecular Properties

The molecular properties of the investigated properties can be seen in **Table 3.5.1.1** and the molecular structures can be seen in **Figure 3.5.1.1**. All of the polymers had a polydispersity (PDI) near 2 except for P3, which had a slightly higher PDI of 2.61. The average number molecular weight (Mn) for all the polymers was between 20 kDa and 40 kDa. The weight average molecular weight (Mw) was between 40 kDa to 90 kDa. The number of repeat units varied from

13 repeat units (RPU) to 24 RPU. The number of repeat units was fairly close between polymers with the same acceptor type, except for P2 and P5, where P2 has two times the number of repeat units in P5. The two polymers are still comparable because the persistence length of conjugated light harvesting polymers are much smaller than the length of the polymer, and optical properties can be normalized to the number of repeat units.

Table 3.5.1.1. Molecular Properties of the investigated polymers

Polymer	Mn (Da)	Mw (Da)	PDI	RPU
P1	25900	48200	1.86	14
P2	42500	88400	2.08	23
P3	22600	59100	2.61	17
P4	34100	62800	1.84	19
P5	22600	42800	1.90	13
P6	28300	55500	1.96	24

3.5.3. Steady State Absorption Measurements

The steady state absorption spectra of the investigated polymers were performed in chloroform solutions with concentrations of 3.0 X 10^{-6} M. The normalized steady state absorption spectra for the polymers can be seen in **Figure 3.5.3.1.** All of the investigated polymers have broad absorption in the visible spectral region with distinct absorption peaks in the 400-500 nm region and absorption maxima in the 600-800 nm region. Poly(4,9-Dihydro-s-indaceno[1,2-b:5,6-b']dithiophene) polymers generally absorb in the 500 nm region, poly(bithienyl diketopyrrolopyrrole) polymers have a weak absorption peak near 450 nm and broad maxima near 700-800 nm, poly(Isoindigo) polymers have weak absorption at 450 nm and broad maxima near 700 nm, and polymers with thienothiophene acceptors have an absorption maxima near 650 nm, which makes each subunit ideal for incorporation in a donor-acceptor polymer. [35,41,42,57–59] The strong absorption in the 400-500 nm region of the 4,9-Dihydro-s-indaceno[1,2-b:5,6-b']dithiophene donor subunit, and the overlap of the weak absorption of the Isoindigo, thienothiophene, and the bithienyl diketopyrrolopyrrole acceptor subunits in the 400-500 nm

region with strong absorption in the 600-800 nm region makes a stronger absorbing polymer and potentially introduces unique optical properties for the investigated polymers. The steady state absorption properties of the investigated polymers can be seen in **Table 3.5.3.1**.

The polymers with the bithienyl diketopyrrolopyrrole and isoindigo acceptor moieties showed distinct absorption peaks, whereas the polymers with the thienothiophene acceptor moiety had an overlap of the lower energy and higher energy absorption peaks, regardless of donor subunit conjugation length. For both polymer series P1-P3 and P4-P6, a bathochromic shift of the lower energy absorption peak is seen with increasing strength of the acceptor, which is typically seen for polymers with stronger acceptors.[49] With about 20-30 nm bathochromic shift of the low energy absorption of the polymers with the BTDPP acceptor compared to the polymers with **II** acceptor, and 70-100 nm bathochromic shift of the low energy absorption of polymers with BTDPP acceptor compared to the polymers with the **TT** acceptor. The higher energy absorption peak is less affected by the acceptor strength, with red shifts of 30-40 nm for the peak absorption for the more conjugated donor polymers with stronger acceptors and up to ~60 nm bathochromic shift for the less conjugated donor polymers with stronger acceptors. This suggests that the acceptor strength has more influence on the lower energy absorption than the higher energy absorption.

The donor conjugation length had a small effect on the peak absorption wavelength for the low energy transition with ~10 nm blue shift of the low energy absorption peak maxima. Interestingly, for P3 and P6, there was a drastic change in the low energy absorption peak maxima of a ~30 nm blue shift for the longer conjugated donor polymer.

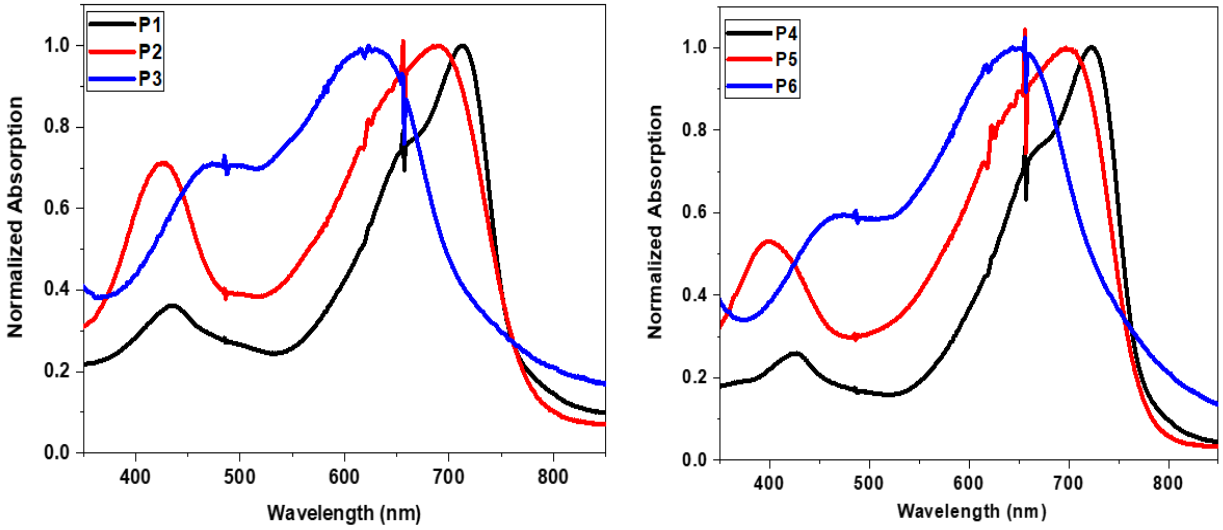

Figure 3.5.3.1. Normalized steady state absorption spectra of more conjugated donor polymer series P1-P3 (left) and less conjugated polymer series P4-P6 (right).

Table 3.5.3.1. Steady state absorption properties (Molar absorptivities: $\varepsilon \times 10^4$ L mol^{-1} cm^{-1})

Polymer	High Energy Absorption(nm)	ε	Low Energy Absorption (nm)	ε
P1	437	2.35	715	7.01
P2	424	4.85	693	5.46
P3	471	1.65	622	1.83
P4	423	1.81	726	8.47
P5	405	2.45	697	4.36
P6	462	1.45	656	3.14

3.5.4. Steady State Fluorescence Measurements

The normalized steady state fluorescence spectra for all of polymers can be seen in **Figure 3.5.4.1.** In order to establish that we are not selectively exciting a specific emission maximum, the polymers were excited using 430 nm and >600 nm excitation to target the donor monomer and acceptor monomer of the polymer, respectively. The emission maxima are independent of the excitation wavelength, which is congruent with Kasha's rule.[88] All of the polymers exhibit steady state fluorescence maxima in the near-infrared region of the electromagnetic spectra, ~700 nm – 800 nm, with minor peaks near 500 nm for P2 and P5, and a minor peak near 550nm for P6. The fluorescence spectra are narrower than the absorption spectra for the investigated polymers. This is attributed to different absorption units that occur in polymers due to bending or twisting that cause different conjugation absorbing segments of the polymer. Whereas the emission is attributed to longer conjugated segments, with excitons migrating from the higher energy shorter segments to the lower energy longer conjugated segments that serve as the major emitters.[60]

Since the polymers followed Kasha's rule, 430 nm excitation was used for the Quantum Yield (QY) determination. This wavelength is useful for exploring the direct excitation of the higher energy transition as well as investigating the lower energy major emission maxima, thus the contribution of the lower energy emission can be analyzed, if present, to the overall emission behavior. The steady state fluorescence properties are summarized in **Table 3.5.4.1**. There were significant differences between the polymer donor analogues in terms of their QYs.

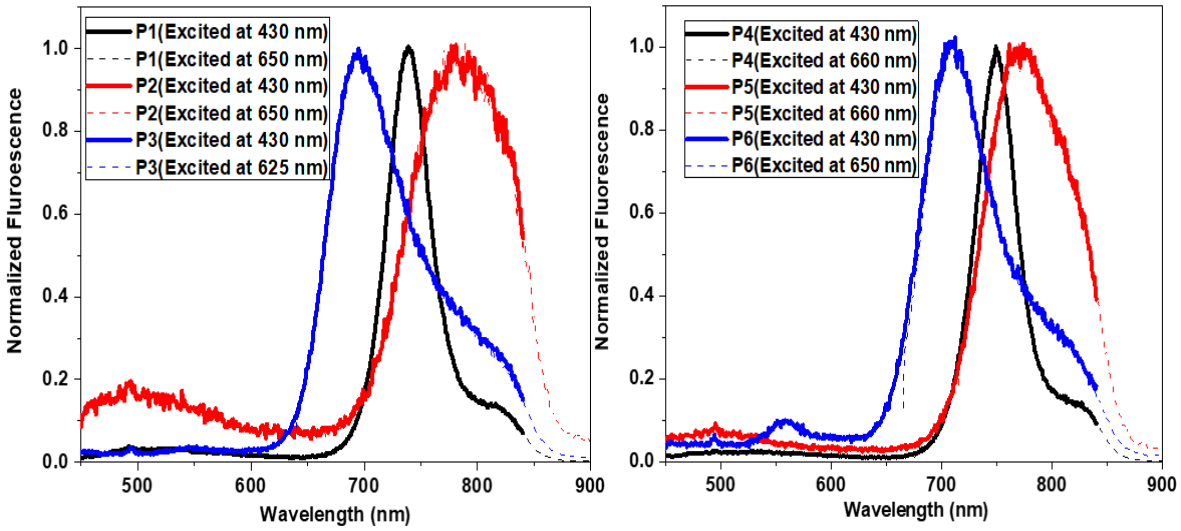

Figure 3.5.4.1. Normalized steady state fluorescence of P1-P3 (Left) and P4-P6 (Right) at 430 nm excitation for donor excitation (solid line) and >600 nm excitation for acceptor excitation (dashed line).

Table 3.5.4.1. Steady state fluorescence properties

Polymer	Max. Fluorescence (nm)	QY	Stokes Shift (nm)
P1	738	0.45	23
P2	780	0.13	88
P3	695	0.18	75
P4	749	0.27	24
P5	772	0.08	76
P6	709	0.07	52

3.5.5. Quantum Chemical Simulations

The optimized ground state dimer model structures are graphically illustrated in **Figure 3.5.5.1**. With these structures, the electrochemical and optical properties are theoretically estimated. Bandgap of the polymer is strongly correlated to the efficiency of solar cell. The quantum chemical simulations estimated bandgap determined as the difference between HOMO and LUMO energy levels, and the results are provided in **Table 3.5.5.1**. The dimer representation significantly improves the overestimated bandgap calculated based on the monomer models and the relative bandgap trend obtained from optical measurements was correctly reproduced. (see SI for the bandgap evaluated with the monomer models)

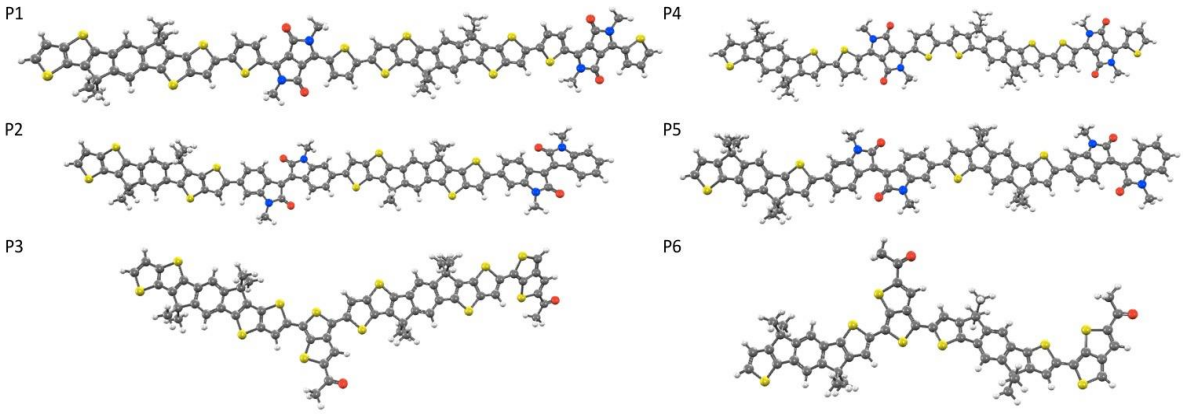

Figure 3.5.5.1. Optimized ground state dimer model structures of P1-P6. Color scheme: carbon atom, gray; hydrogen atom, white; oxygen atom, red; nitrogen atom, blue; sulfur atom, yellow.

Table 3.5.5.1. Bandgap of polymers P1-P6 using ωB97X-D functional with the dimer model in eV and cyclic voltammetric studies

Polymer	Monomer	Dimer	Elec (CV)	Opt
P1	2.13	1.90	1.90	1.64
P2	2.02	1.84	2.01	1.62
P3	2.61	2.13	2.16	1.74
P4	2.20	1.90	2.01	1.61
P5	2.10	1.90	1.99	1.61
P6	2.74	2.20	2.03	1.71

TD-DFT simulation gave the first absorption energies of 1.90, 1.84, 2.13, 1.90, 1.90, and 2.20 eV, which is quite accurate prediction for the experimental absorption energies of 1.73, 1.79, 1.99, 1.71, 1.78, and 1.89 eV for the P1-P6 polymers, respectively. **Figure 3.5.5.2** shows the hole–electron Natural Transition Orbitals (NTOs) for the vertical excitation into first singlet state for the polymer P1-P6 with the ground state dimer structures. It is found that one dominant hole–electron NTO pair (>94 %) can represent the vertical excitation for all cases. The hole orbitals are delocalized over the first repeating unit and the donor part of the second repeating unit, which implying the significant coupling between the repeating units and the necessity of dimer models at least to describe exciton's behavior in the polymer. The electron orbitals tend to localize on the acceptor moiety of the first repeating unit and the small portion resides on the donor part of the second repeating unit. The difference in the hole and electron orbitals indicates the significant charge transfer with non-legligible amount of π-π^* transition in all six polymers.

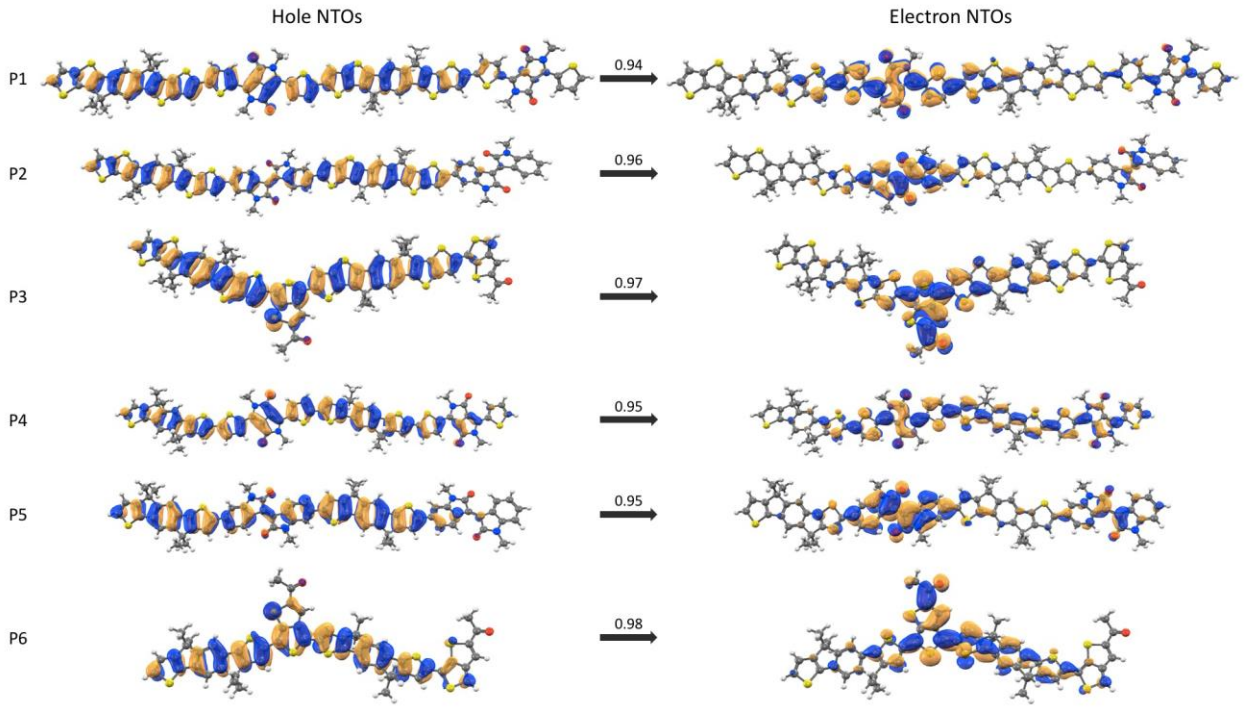

Figure 3.5.5.2. Natural transition orbitals of P1-P6 for the vertical excitation into the first singlet state at the ground-state geometries. The contribution of each transition is given above the arrow (Isovalue = 0.05).

The HOMO, LUMO, HOMO-1 and LUMO+1 geometries for the monomers were calculated and can be seen in **Figure 3.8.2.1.** We have observed a more symmetric distribution of electron density for the HOMO, LUMO, HOMO-1 and LUMO+1 for P3 and P6 which differs from the anti-symmetrical electron density distribution seen for other investigated polymers. This suggests a less pronounced charge transfer in P3 and P6.

The electronic structure of the trimers in the ground and excited state of P1 and P4, P2 and P5, and P3 and P6 are provided in **Figure 3.8.2.2-3.8.2.7** in the SI. We have observed a more localized distribution of electron density in the excited state of the polymers with more conjugated donor moiety. However, the effect of donor conjugation in P2 is insignificant on the electronic structures like what was seen for P1 and P4. This may be due to bulky **II** acceptor having similar interaction with both donor types due to the steric hindrance introduced by **II** acceptor that is not seen with the less bulky **DPP** acceptor.

3.5.6. Two-Photon Absorption Studies

The TPA cross sections were determined by using the TPEF method as discussed in the experimental section. An excitation wavelength of 1300 nm was used for P1, P2, P4, P5, and styryl 9m; and emission was collected at 740 nm. The excitation wavelength was chosen for these polymers because they exhibit one photon absorption maxima near 650 nm, and emission was collected at 740 nm after performing wavescans and identifying the emission maxima, which can be blue or red shifted from the one photon emission maxima. An excitation wavelength of 1250 nm was used for P3, P6, and Zn-tetra-tert-pc; and the emission was collected at 695 nm. The excitation wavelength was chosen for these polymers because they exhibit one photon absorption maxima near 625 nm, and emission was collected at 695 nm.

The two-photon excited fluorescence as a function of power for the TPA standards and investigated polymers can be seen in **Figure 3.5.6.1**. The two-photon cross-sections calculated using the comparative method can be seen in **Table 3.5.6.1**. P1, P2, P4, and P5 had higher two photon cross sections as well as the highest two-photon cross-section per repeat unit compared to P3 and P6. P3, which has a weaker dithiophene acceptor, had the lowest TPA cross-section and TPA per repeat unit. The TPA cross-section could not be determined for P6 due to a likely smaller TPA cross-section and smaller QY of P6. Calculations showed that P6 would have the lowest TPA cross-section, and if P6 follows the same trend seen for P1, P2, and P3; it is likely that the P6 would have an even lower TPA cross-section than P3.

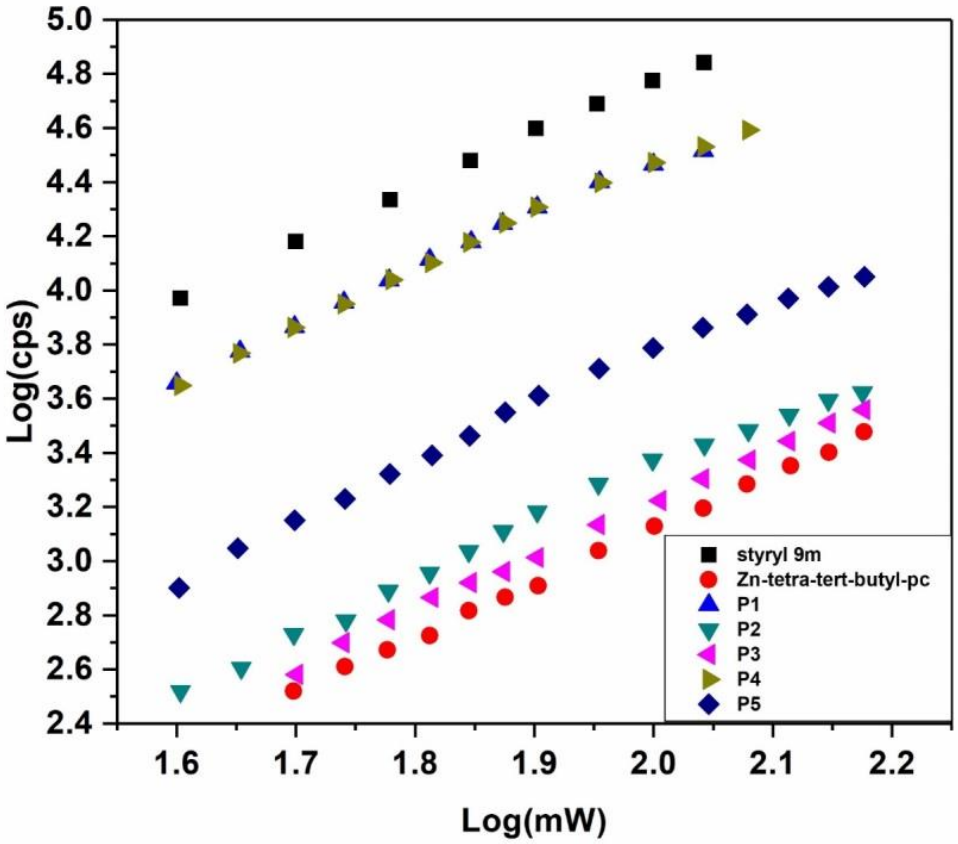

Figure 3.5.6.1. Logarithmic plot of the quadratic dependence (counts per second vs power) for standards styryl 9m, zn-tetra-tert-butyl-pc, and the investigated polymers. 1300 nm excitation was used for P1, P2, P4, P5, and styryl 9m. 1250 nm excitation was used for P3 and P6 (not shown), and zn-tetra-tert-butyl-pc. All have a slope ~2 and R^2>0.99.

Table 3.5.6.1. TPA cross-section of the investigated polymers

Sample	TPA cross-section (GM)	BH&HLYP TPA cross-section	TPA/RPU
P1	1000.4	52.9	71.46
P2	192.92	14.9	8.39
P3	0.17	1.0	0.01
P4	1247.03	42.3	65.63
P5	642.25	11.4	49.40
P6	-	0.2	-

3.5.7. Time Resolved Fluorescence Measurements

Fluorescence decay dynamics of the investigated polymers were performed in chloroform solutions at the same concentrations that were used for the steady state experiments. The samples were excited at 400 nm and the fluorescence decay dynamics were investigated at 680 nm. The decay dynamics were investigated at 680 nm in order to investigate the polymer's emission maxima as well as to avoid the upconverting of the 800 nm gate signal which interferes with collection at longer sample emission wavelengths due to the upconverting crystal angle. The donor fluorescence decay dynamics were also investigated between 500 nm – 550 nm, but the emission was too weak for the upconverting and collection process. Thus, our study focused on the major emission decay dynamics. Unfortunately, the decay dynamics for P2 and P5 were not able to be investigated because their emission maxima were too far into the near-infrared where the gate upconversion signal made it impossible to investigate. To rule out emissive irregularities due to degradation of the sample, steady state absorptions were taken before and after the upconversion experiment. No change in intensity or spectral changes were seen between the steady state absorptions before and after the upconversion experiment, thus no degradation was observed. The decay dynamics can be seen in **Figure 3.5.7.1**. The fluorescence decay dynamics were fitted using biexponential functions, the decay times can be seen in **Table 3.5.7.1**. The investigated polymers had a short initial decay (<3ps) and a longer second decay component. P1 and P4 had the longest long-lived decay components compared to polymers with weaker acceptors, 745 ps and 37 ps, respectively. P3 and P6, which had the weakest acceptors of the investigated polymers, had the shortest long-lived decay components within their respective donor series, 129 ps and 19 ps, respectively.

Table 3.5.7.1. Fluorescence decay dynamics

Polymer	**τ_1 (ps)**	**τ_2 (ps)**
P1	0.79	745
P3	1.27	129
P4	0.64	37
P6	2.04	19

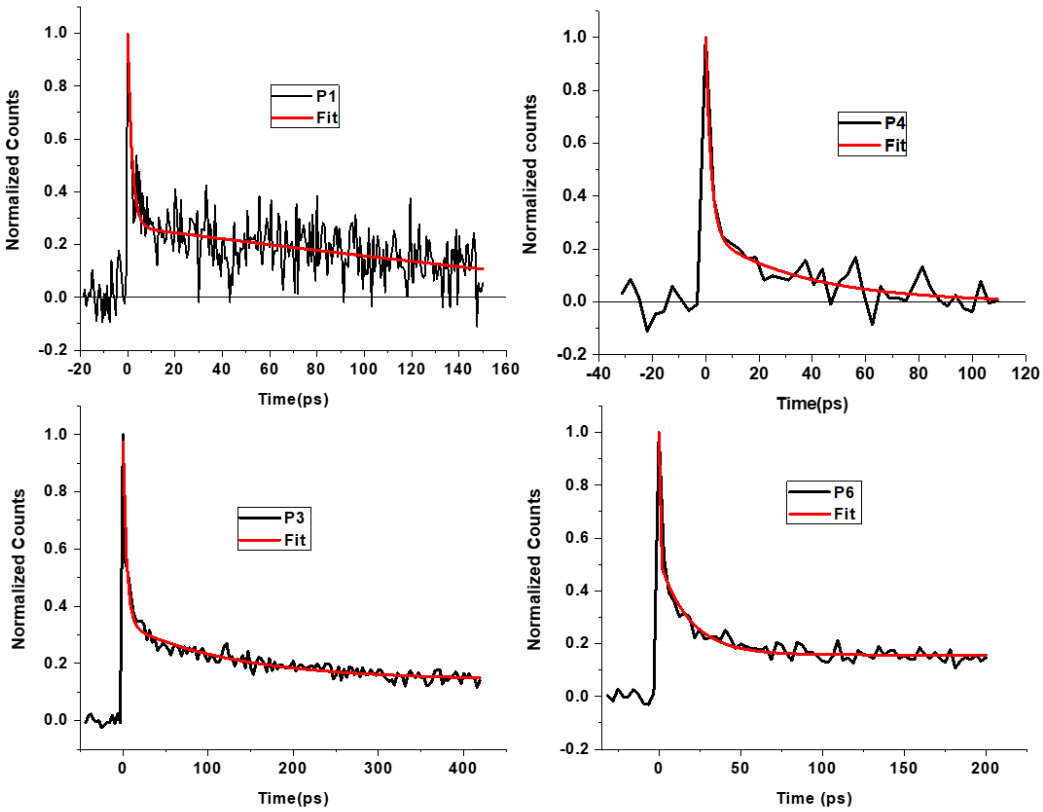

Figure 3.5.7.1. Fluorescence upconversion of P1 (top left), P4 (top right), P3 (bottom left), and P6 (bottom right) at 400 nm excitation and 680 nm emission.

3.5.8. Ultrafast Transient Absorption Measurements

Ultrafast transient absorption experiments were performed in chloroform solutions at the same concentrations that were used for the steady state experiments. Experiments were carried out by exciting the polymer samples with 400 nm femtosecond pulses and probing the excited state with a white light continuum at different delays, giving insight into the ultrafast excited-state dynamics of the investigated polymers. The transient absorption spectra for P1 and P4 can be seen in **Figure 3.5.8.1** and the fitted lifetimes can be seen in **Table 3.5.8.1.** The transient absorption spectra for P1 and P4 are quite similar, with a ground state bleach (GSB) near 650 nm and a stimulated emission (SE) near 730 nm with overlap between the two bands. This matches well with the steady state absorption and steady state fluorescence for both polymers. The GSB at ~650 nm for both polymers exhibited a biexponential decay and the SE at ~730nm for both polymers exhibited a biexponential decay. The initial decay component of the GSB for both polymers was ~20 ps and is attributed to a hot relaxation to the S_1 state. This was followed by a ~500 ps

relaxation from S_1 state to the charge transfer state. This is followed by a <100 ps relaxation from a hot charge transfer state, CT_1, to a relaxed charge transfer state, CT_0 via SE. This was followed by a relaxation of the charge transfer state to the ground state via SE. The energy level diagrams for the overall photophysical processes for P1 and P4 can be seen in **Figure 3.5.8.2**.

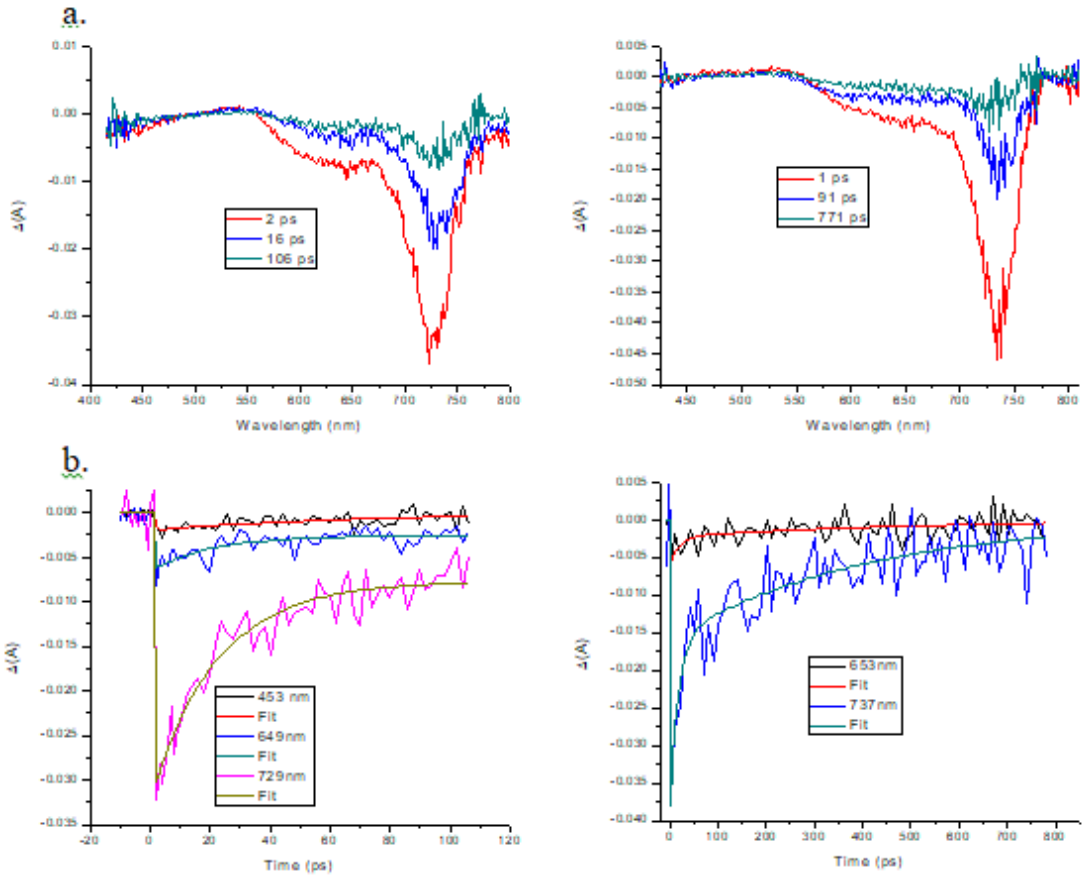

Figure 3.5.8.1. Transient absorption spectra and kinetic fits of P1 (a.) and P4 (b.).

Table 3.5.8.1. Transient absorption kinetic fits at selected wavelengths for P1 and P4

P1	Wavelength (nm)	τ_1 (ps)	τ_2 (ps)	P4	Wavelength (nm)	τ_1 (ps)	τ_2 (ps)
	453	69	-		453	-	-
	649	20	658		653	19	488
	729	22	435		737	65	1028

Polymer	Wavelength (nm)	τ_1 (ps)	τ_2 (ps)
P1	**453**	**69**	**-**
	649	**20**	**658**
	729	**22**	**435**
P4	**453**	**-**	**-**
	653	**19**	**488**
	737	**65**	**1028**

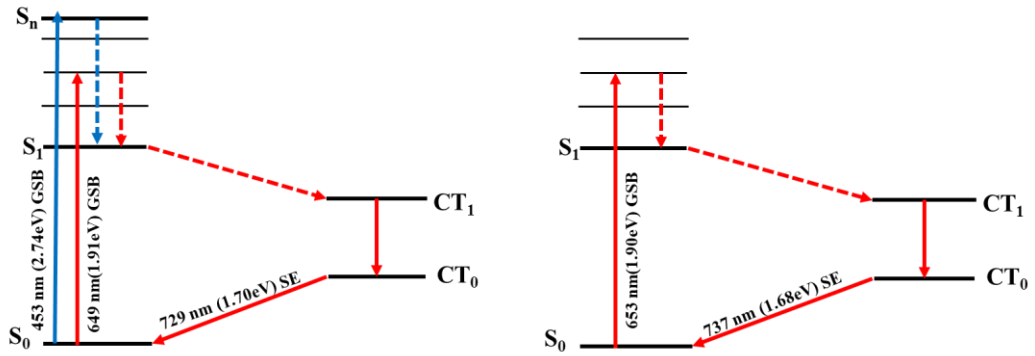

Figure 3.5.8.2. Energy level diagrams of transient absorption processes for P1 (left) and P4 (right).

The transient absorption spectra for P2 and P5 can be seen in **Figure 3.5.8.3** and the fitted lifetimes can be seen in **Table 3.5.8.2**. P2 and P5 had a ground state bleach (GSB) near 435 nm and 620 nm and a stimulated emission (SE) near 700 nm with overlap between the later GSB and SE emission peaks. This matches well with the steady state absorption and steady state fluorescence for both polymers. Both polymers also had an ESA at 779 nm that overlaps with the fluorescence seen in the steady state emission spectra. P2 also had an ESA near 500 nm that was not seen for P5. The high energy GSB lifetimes for both polymers were fitted to exponential to monoexponential decays of 531 ps and 644 nm, respectively. Both low energy GSB lifetimes exhibited monoexponential decays of approximately 200 ps. The SE for both polymers had a decay time of 200 ps, with a monoexponential decay for P2 and a biexponential decay for P5. The biexponential decay of P5 has a short component of 41 ps that can be attributed to a hot relaxation in the excited state. The energy level diagrams for the overall photophysical processes for P2 and P5 can be seen in **Figure 3.5.8.4**.

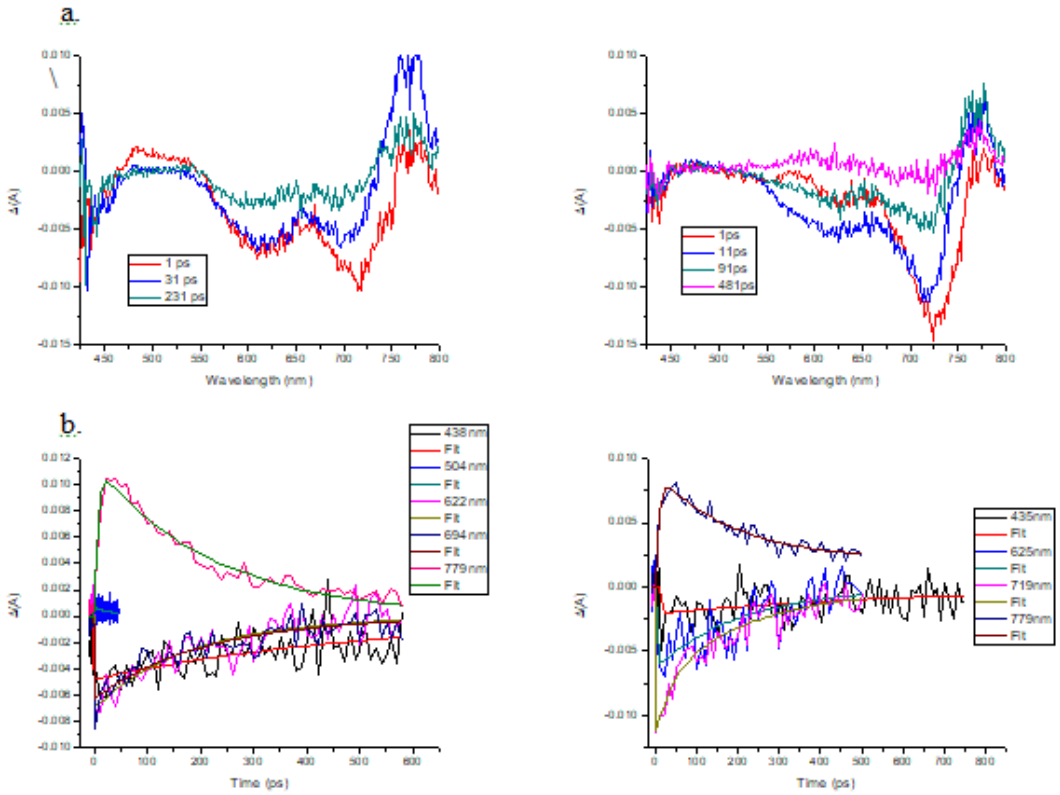

Figure 3.5.8.3. Transient absorption spectra and kinetic fits of P2 (a.) and P5 (b.).

Table 3.5.8.2. Transient absorption kinetic fits at selected wavelengths for P2 and P5

P2	Wavelength (nm)	τ_1 (ps)	τ_2 (ps)	P5	Wavelength (nm)	τ_1 (ps)	τ_2 (ps)
	438	531	-		435	644	-
	504	45	-		504	-	-
	622	184	-		625	212	-
	694	210	-		719	41	243
	779	6	222		779	6	193

Polymer	Wavelength (nm)	τ_1 (ps)	τ_2 (ps)
P1	453	69	-
	649	20	658
	729	22	435
P4	453	-	-
	653	19	488
	737	65	1028

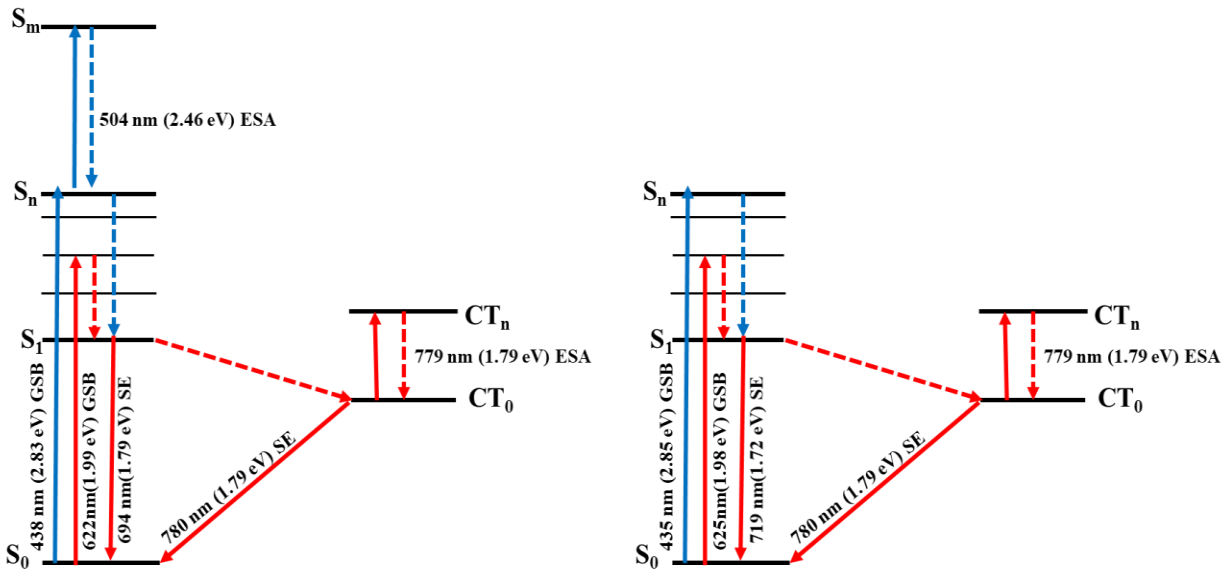

Figure 3.5.8.4. Energy level diagrams of transient absorption processes for P2 (left) and P5 (right).

The transient absorption spectra for P3 and P6 can be seen in **Figure 3.5.8.5** and the fitted lifetimes can be seen **Table 3.5.8.2**. The transient absorption spectra for P3 and P6 are quite similar, with a ground state bleach (GSB) near 460 nm and a GSB near 600 nm with overlap between the two bands, which matches the steady state absorption. There is a weak tail at ~700 nm for P6 that may be stimulated emission, which would match well with the steady state fluorescence, but it is not well resolved due to the strength of the GSB, which is also the case for P3 where the SE, if present, is masked by the strong GSB. The GSB at ~460 nm and ~600 nm for both polymers exhibited a biexponential decay and the SE at ~700 nm for P6 exhibited a biexponential decay. For both GSBs and for both Polymers, the first decay component is ~150 ps and is attributed to the relaxation of the hot excited state to the first excited state, followed by a long decay to the charge transfer state that is longer than the experimental window of this experimental set up. The energy level diagrams for the overall photophysical processes for P3 and P6 can be seen in **Figure 3.5.8.6**. This is followed by a decay of the hot charge transfer state to a relaxed charge transfer state, which then relaxes to the ground state.

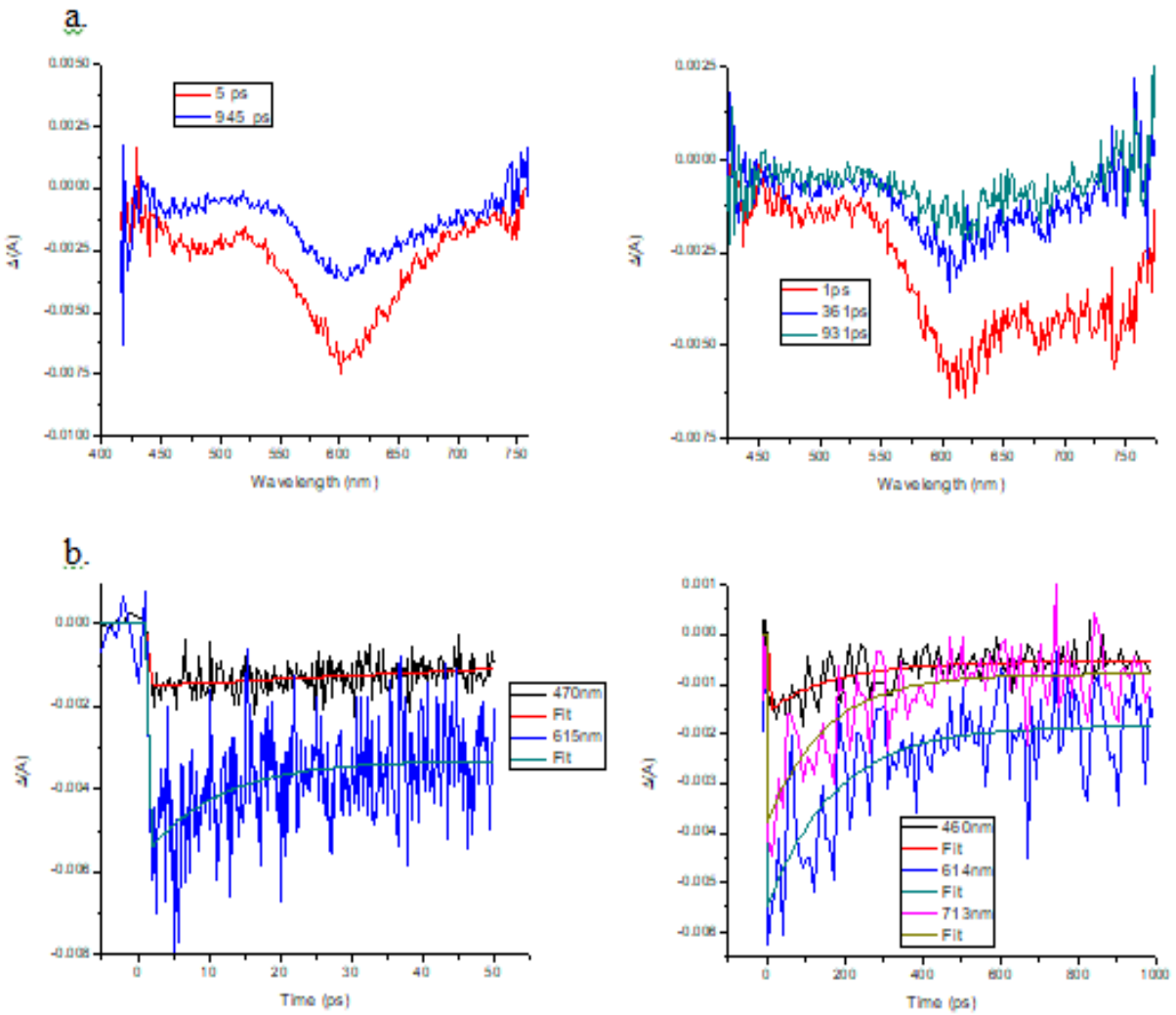

Figure 3.5.8.5. Transient absorption spectra and kinetic fits of P3 (a.) and P6 (b.).

Table 3.5.8.3. Transient absorption kinetic fits at selected wavelengths for P3 and P6

P3	Wavelength (nm)	τ_1 (ps)	τ_2 (ps)	P6	Wavelength (nm)	τ_1 (ps)	τ_2 (ps)
	470	151	inf		460	173	inf
	615	159	inf		614	172	inf
	693	-	-		713	150	inf

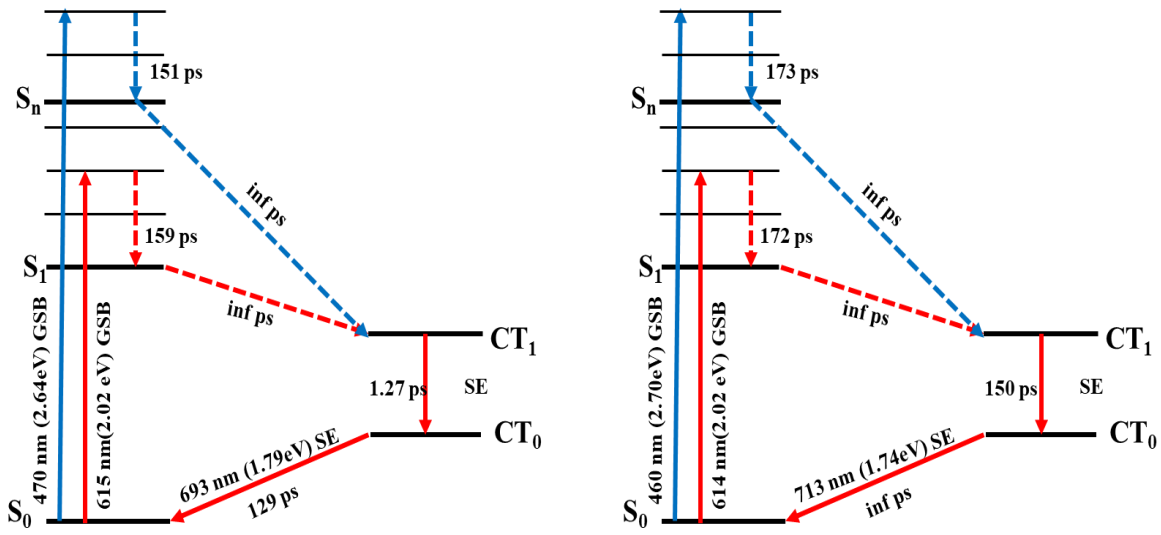

Figure 3.5.8.6. Energy level diagrams of transient absorption processes for P3 (left) and P6 (right).

3.5.9. Nanosecond Transient Absorption Measurements

As mentioned earlier, the main objective of this study was to investigate the optical properties of the polymers. Nanosecond transient experiments were carried out to investigate the contribution of the long-lived excited species to the overall photophysical properties of the polymers. A recent study on PDPP-TNT (poly{3,6-dithiophene-2-yl-2,5-di(2-octyldodecyl)-pyrrolo[3,4-c]pyrrole1,4-dione-alt-naphthalene}) has reported that the bleaching signal are associated with the charge carrier and a small population of the charge carriers is long-lived and decay in hundreds of nanoseconds.[90] In another report, Jones et al. have shown that increasing conjugation of thiophene (T_n) oligomers up to a certain length (from T_4 to T_6) increases the excited triplet state lifetime and decreases as the length increases further. [91] In this report, we have conducted nanosecond transient experiments in chloroform and maintained an approximate concentration of 3.0×10^{-5}M of the polymers. For this investigation P2 was excited at 415 nm while the rest of the polymers (P1, P3, P4, P5, and P6) were excited at 425 nm.

With an excitation wavelength of 425nm, both P1 and P4, showed two ground state bleaching (GSB) regimes around 440nm and 650nm as shown in **Figure 3.5.9.1** which matches with their steady state absorption spectra. In P1, the GSB at high energy had a longer recovery time (~1.6 times) compared to the GSB at low energy while for P4, the GSB recovery time for both high and low energy are comparable (**Table 3.5.9.1**).

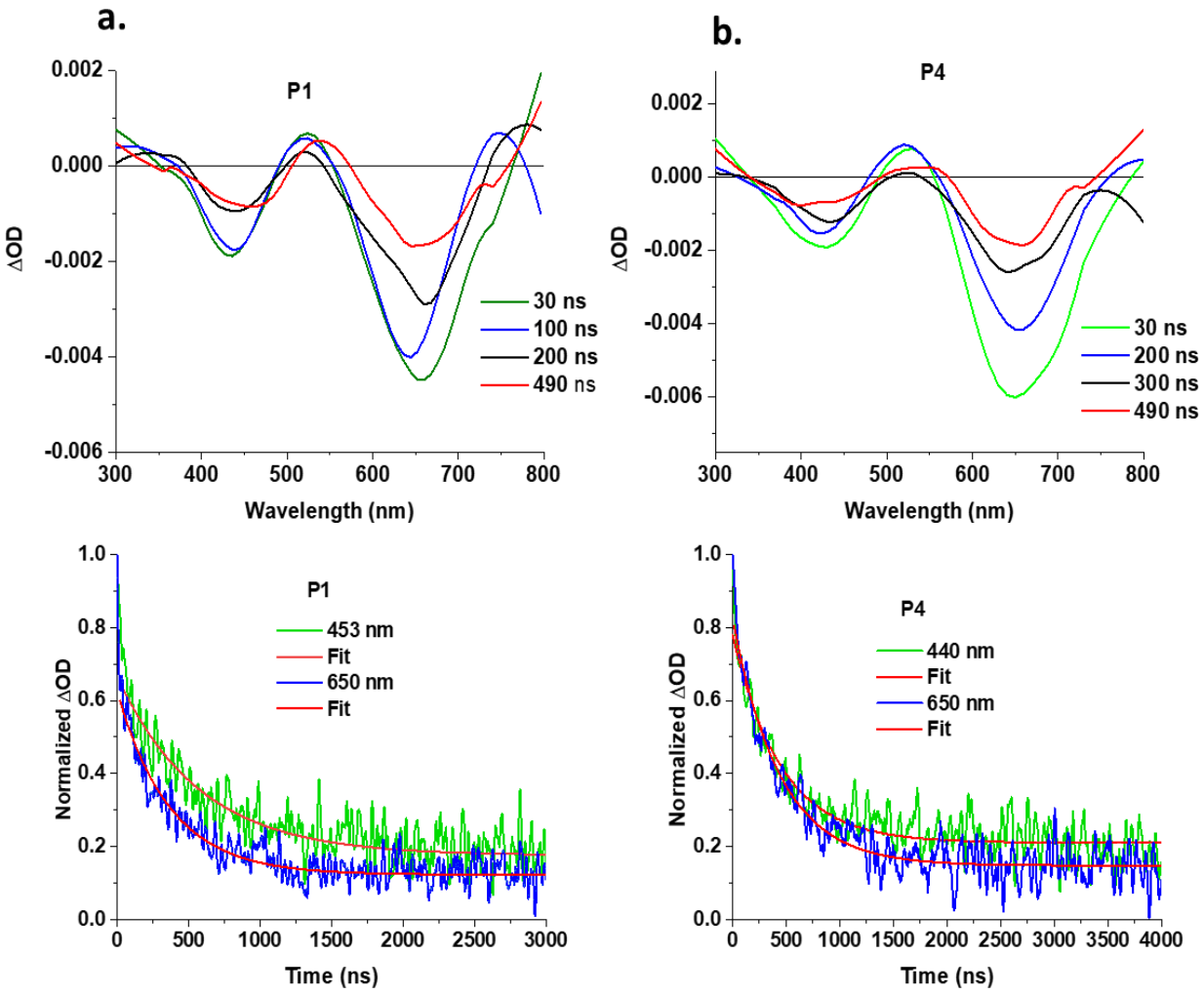

Figure 3.5.9.1. Nanosecond Transient absorption spectra and kinetic fits of P1 (a.) and P4 (b.).

Table 3.5.9.1: Nanosecond transient lifetimes for both P1 and P4 at selected wavelengths

Polymer	Wavelength (nm)	τ (ns)
P1	453	574
	650	368
P4	440	452
	650	440

As seen in **Figure 3.5.9.2**, P2 and P5 exhibited only one GSB regime at around 440nm with P2 recovery time being two times faster than that of P5 (**Table 3.5.9.2**). We have also observed stimulated emission at around 550 nm for both P2 and P5 which vanishes within a delay of 50 ns after excitation (inset **Figure 3.5.9.2**).

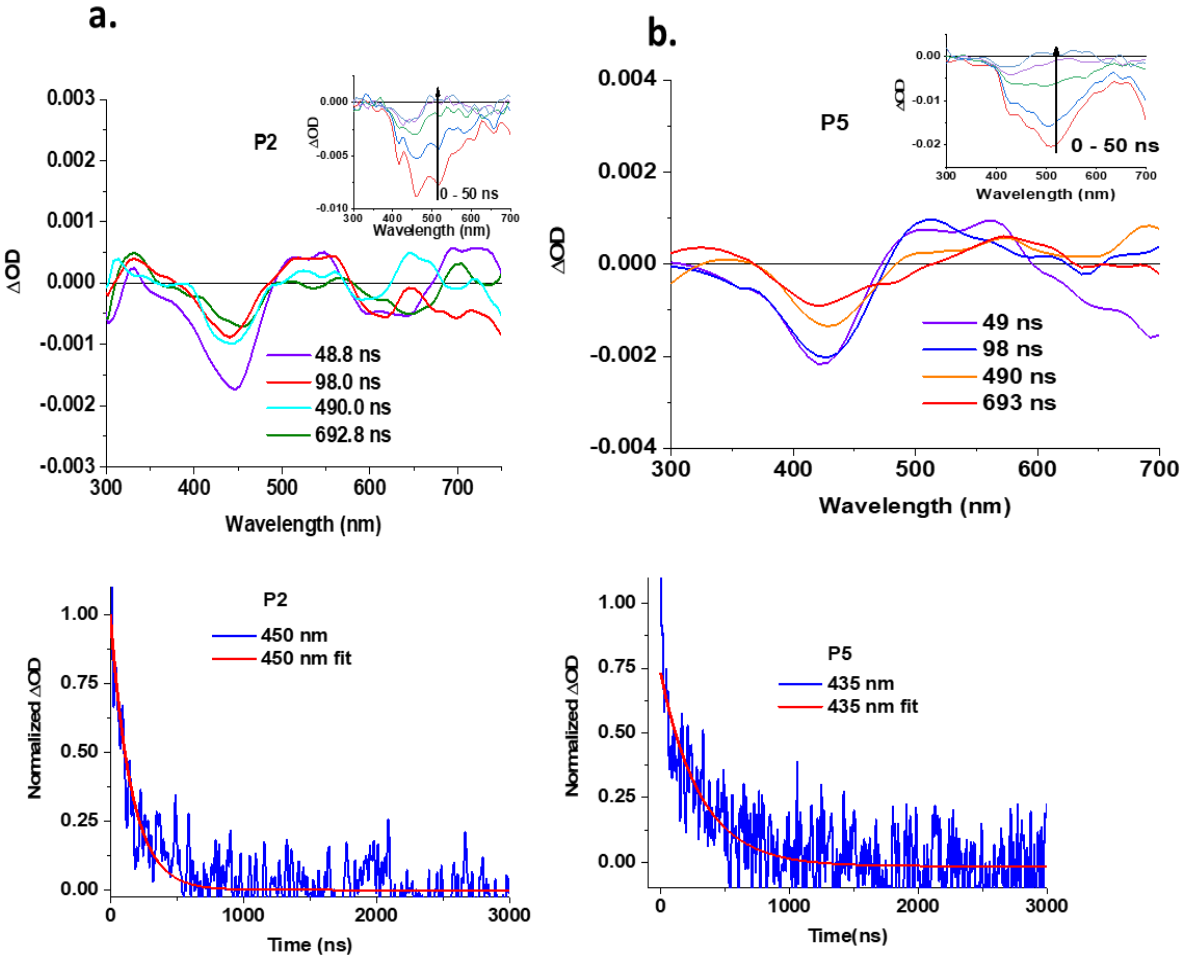

Figure 3.5.9.2. Nanosecond Transient absorption spectra and kinetic fits of P2 (a.) and P5 (b.).

Table 3.5.9.2: Nanosecond transient lifetimes for both P2 and P5 at selected wavelengths

Polymer	Wavelength (nm)	τ (ns)
P2	**453**	**158**
P5	**440**	**309**

Both P3 and P6 contain the weakest acceptor among the investigated polymers. Both P3 and P6 show similar GSB recovery times at both higher and lower energies (**Figure 3.5.9.3**). However, in both cases, the GSB recovery time at higher energies is observed to be 1.4 times slower than that in lower energies (**Table 3.5.9.3**). When P3 was excited at 600 nm, an ESA around 740 nm was seen alongside the two GSB regimes (**Figure 3.5.9.4**) with a lifetime of 199 ns.

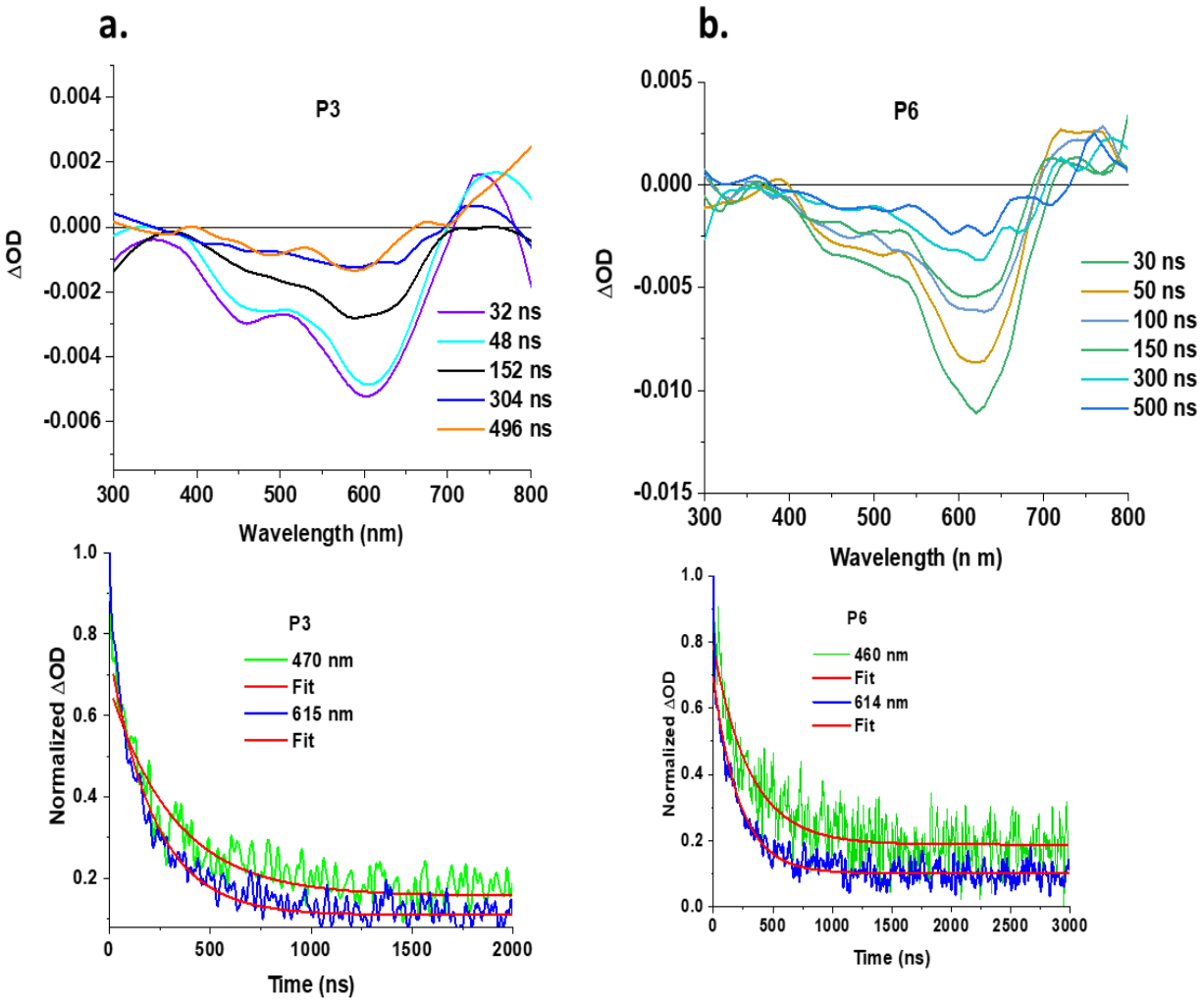

Figure 3.5.9.3. Nanosecond Transient absorption spectra and kinetic fits of P3 (a.) and P6 (b.).

Table 3.5.9.3: Nanosecond transient lifetimes for both P3 and P6 at selected wavelengths

Polymer	Wavelength (nm)	τ (ns)
P3	470	320
	615	222
P6	460	306
	614	218

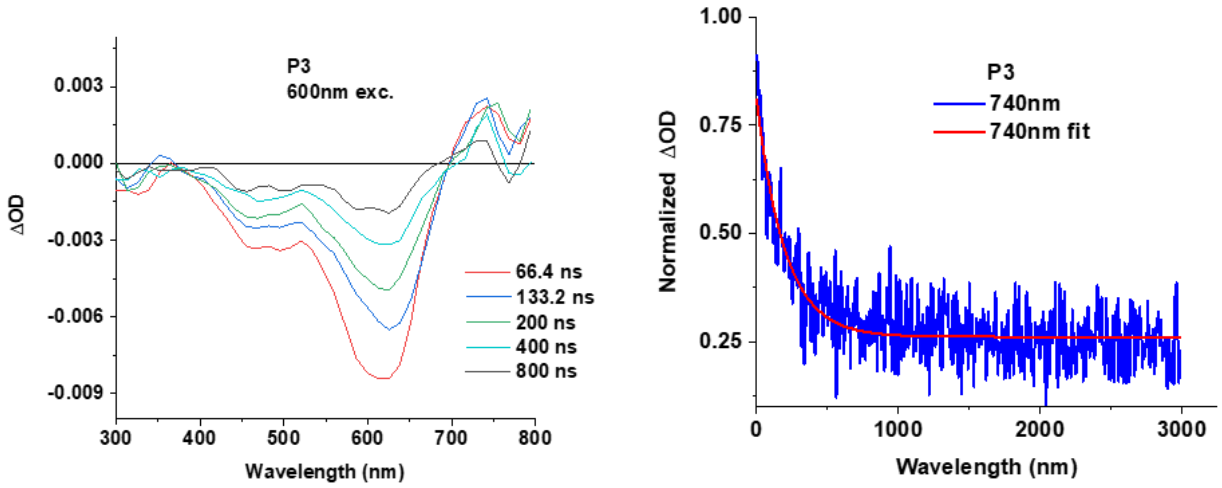

Figure 3.5.9.4. Nanosecond Transient absorption spectra (a.) and kinetic fits of P3 (b.).

As discussed in the quantum-mechanical calculations section, the investigated polymers are expected to have a high charge carrier mobility due to localization of charge density in the excited state. It has been observed that enhanced conjugation length enhances charge carrier transport properties [92,93] hence the dynamical change in the excited state absorption spectrum (ESA) would give a better insight to the charge transfer dynamics of the investigated polymers. However, in our femtosecond and nanosecond transient studies, we did not observe ESA for all the polymers except for P2 and P5 in the femtosecond transient absorption studies. In recent studies, polymers containing the indacenodithiophene (**IDT**) moiety have been observed to contain an excited state absorption at near infrared region. [94, 95] In their picosecond-microsecond studies on polymers containing silaindacenodithiophene (**IDT**) donor, Utzat et. al. observed an excited state absorption in the near infrared region (900nm-1300nm).[94] In a similar femtosecond study, Holliday at al also observed an excited state absorption between 900nm and 1350nm. [95] In line with these studies, the absence of ESA in our femtosecond and nanosecond transient studies can be due to the detection range in our setups (i.e. 185nm to 870 nm for nanosecond detection and 400nm to 800 ns for femtosecond detection). However, in fs-TA of P2 and P5 polymers, an ESA in the visible range (around 779nm) can be assigned to the weaker D-A interaction because the steric hindrance arising from the bulkiness of the isoindigo acceptor.

3.6. Discussion

All the investigated polymers showed a broad absorption with maxima in the 600-800 nm region (**Figure 3.5.3.1**) which makes them ideal candidates for light harvesting for photovoltaics to match the high photon flux region of the sun. The polymers with longer conjugated donors (P1, P2 and P3) had higher molar absorptivities for the higher energy transitions, whereas the lower energy molar absorptivity was relatively unaffected by the donor conjugation length. The higher molar absorptivities for the high energy transition for the more conjugated donor polymers could be due to the more conjugated system enhancing delocalization or may be due to the additional rigidity promoting planarity along the polymer backbone.[61,62] This suggests that the donor may have a higher contribution than the acceptor to the high energy absorption transition. The polymers with the stronger acceptors had higher molar absorptivities for the low energy transition and no effect on the high energy transitions, which suggests that the acceptor contributes more to the low energy transition.[63] In addition, a red shift of the absorption spectra in polymers with increased donor conjugation and acceptor strength has been observed. The above discussion indicates that a higher donor conjugation and increased acceptor strength narrows the HOMO-LUMO bandgap. Interestingly, there is an observed blue shift in low energy absorption of P3 compared to P6 which may be due to steric hindrance introduced by the additional thiophene units of the donor of P3 that is alleviated in the smaller donor of P6. This pronounced effect is not seen in the other series of polymers because the acceptor monomers in those polymers are more bulky than the **TT** acceptors of P3 and P6. These bulkier acceptors which result in structures that relieve the steric hindrance in polymers P1, P2, P4 and P5 with both the high and the less conjugated donors. The emission maxima can be attributed to the relaxation of the lower energy transition of the polymer. The minor peaks near 500 nm and 550 nm can be attributed to the relaxation of high energy states from hot excitons that recombine during relaxation before the energy can migrate to the lower energy transition to be emitted. P1 and P4 only had one emission peak near 740 nm, lacking the 500 nm emission seen in the other series of polymers. This suggests that these donor-acceptor motifs, regardless of the donor conjugation length, can suppress other fluorescence pathways that are seen in the other investigated polymers. The 500 nm emission is more pronounced in P2 than in P5, which suggests that the longer conjugation donor of P2 promotes other radiative pathways. The 550 nm emission for P6 is attributed to the promotion of the higher energy transition state. The emission maxima for polymers with comparative donors were relatively unaffected by the increase in donor conjugation length, with the largest shifts amounting to only ~10 nm suggesting that the

donor conjugation length does not have significant influence on the lower energy fluorescence transition. The polymers with stronger acceptors had emissions that were more red shifted, which is typical for donor-acceptor polymers due to the narrowing of the bandgap which is often dominated by the acceptor strength.[33,49] The Stokes shifts for comparative donor analogues were also relatively unaffected by the increase in donor conjugation length, although P3 did have larger Stokes shifts compared to P6 which is due to the better planarity of the polymer backbone of P3 attributed to its longer conjugated donor system.

Recent investigations have shown that the conjugated length of polymers play a role in the optical properties of these polymers. Yamaguchi et al found that longer conjugated systems and longer conjugated donor-acceptor systems of the same type had an increase in both QY and emission maximum.[64] Whereas, Kurowska et al found in small molecule donor-acceptor systems, that the QY decreased and the emission maximum increased with an increase in donor ratio.[65] Surprisingly, there has not been much investigation of conjugation length of the donor in donor-acceptor polymers with tailored donor and acceptor subunits. The polymers in this study with longer donor conjugation lengths had higher QYs than their corresponding shorter donor polymer analogues. This suggests that the two additional fused thiophenes promotes radiation relaxation pathways compared to their less conjugated donor polymers. The emission maxima for the polymers increased with increasing acceptor strength due to the narrowing of the optical bandgap, which is typically seen with polymers with strong acceptors.[66] Interestingly, quenching of the fluorescence was not seen with increasing acceptor strength for the investigated polymers, which is also typically seen with polymers with strong acceptors.[67] This suggests that the acceptors are strong enough to promote exciton formation, but too strong where the exciton is trapped and then quenched. In order to have efficient solar harvesting polymers, the exciton must be able to survive long enough to eventually get to the donor polymer and acceptor interface for the exciton dissociation.

Although electronic structures calculations can give great insight into the charge transfer within the polymer backbone, two-photon absorption spectroscopy can be used to quantify the charge transfer characteristics of the donor-acceptor polymers.[68] The polymers with diketopyrrolopyrrole and isoindigo acceptors (P1, P2, P4, and P5) had the highest TPA cross sections as well as the highest TPA cross-section per repeat unit compared to P3 and P6 with the weaker **TT** acceptors. This observation is consistent with the trend seen in the calculated TPA

cross-sections shown in **Table 3.5.6.1**, and with other reports for strong acceptor donor-acceptor organic conjugated molecules.[69] The effect of donor conjugation on the TPA cross-section was not so obvious. Calculations have indicated that the extended conjugated donor polymers should have a higher TPA cross-section than their corresponding analogs. P1 and P4 had similarly high TPA cross sections and presumably P3 has a higher cross-section than P6, according to calculations. But this trend is not seen for P2 and P5. The discrepancy is most likely due to two factors. The emission maxima for P2 and P5 are much further in the NIR, which means the emission collection for the TPEF is collected at the tail of the emission which affects the accuracy of the TPA determination. The efficiency of the PMT also decreases as detection wavelength shifts towards the red, which makes collection difficult. Thus, the effects of donor conjugation on the TPA cross section are not clear.

In the time resolved fluorescence measurements, all the investigated polymers had a short initial decay and a long second decay. The observed short initial decay was relatively unaffected by the donor conjugation length and acceptor strength. This short decay component has been attributed to relaxation of the hot excited singlet state and conformational relaxation, and the longer decay component has been attributed to the relaxation of the charge transfer state.[49,70–73] The polymers with the longer donor conjugation all had significantly longer long-lived decay components compared to their corresponding analog, about an order of magnitude larger. This is consistent with what others have reported, where the fluorescence rate increases for longer conjugated systems of the same type.[74] The longer decay can be explained by the charge separation that occurs in the excited state and has been seen for other conjugated donor-acceptor systems.[75] In the excited state, the charge transfer states localize on specific segments, and therefore the probability of recombining for emission is lower for states that are more separated, which occurs when the longer conjugated donor is taken into account resulting in longer fluorescence decay lifetimes. The importance of the acceptor strength cannot be understated. Too strong of an acceptor can result in electron trapping and exciton trapping.[49,76–78] Too weak of an acceptor, the exciton lifetime will be too short for the exciton dissociation by an organic accepting material.[79,80] The polymers with stronger acceptors within the same donor series showed longer exciton life-times than their weaker acceptor counterparts. The **DPP** acceptor is strong enough to sufficiently promote the charge transfer along the polymer, while not being too strong where the charge is not able to migrate along the polymer backbone before recombining. The **TT** acceptor is also able to

promote the charge transfer, but not to the extent that is seen with the **DPP** acceptor. This is consistent with the results of the two-photon absorption spectroscopy and electronic structure calculations, with larger charge transfer seen with the polymers with the stronger acceptors.

From the femtosecond transient measurements, the ground state recovery time near 650 nm for both polymers was observed to be ~500 ps, suggesting that extended conjugation of the donor of P1 had a marginal effect on the ground state recovery. The fast emission process has been attributed to structural relaxation of the polymers, before a slow decay of the charge transfer state back to the ground state.[81] The SE lifetime of P4 was more than two times longer than the SE of P1, suggesting a greater influence of the donor on the SE dynamics. Interestingly, P1 had a fast GSB with a monoexponential decay at 453 nm of 69 ps, whereas no such process exists for P4, suggesting that the GSB is a result of the extension of the conjugation donor unit changes the relaxation process for the polymer. For P2 and P5, the high energy GSB lifetimes were 3 times longer than the lower energy GSB, suggesting two different recovery mechanisms. Interestingly, both polymers had a biexponential ESA at 779 nm of 6ps and ~200 ps, which is the same wavelength that these polymers had fluorescence in the steady state. The lack of SE at this wavelength, and strong ESA indicates that excited state absorption cross-section must be larger than the emission cross section at the same wavelength. The changes in the transient absorption spectra of P2 and P5 compared to the other investigated polymers demonstrate the effect that the conjugation of the donor has on the optical properties of these polymers, but also how donor and acceptor interaction can produce major changes to the optical properties. Both P3 and P6 showed similar time constants of the GSB at ~460 nm and ~600 nm suggesting that the extended conjugation of the donor of P3 does not have an effect on the relaxation dynamics. This is a striking finding compared to the stronger acceptor polymers where the polymers with extended donor conjugation had other relaxation pathways compared to their less conjugated counterparts. This may be due to the weaker acceptor strength of P3 and P6 as well as the less bulky acceptor compared to polymers with the stronger acceptors. The more bulky acceptor polymers are more constrained due to steric hindrance, whereas the smaller **TT** acceptors are not impinged by the extended conjugation of the larger donors.

In the nanosecond transient measurements, the GSB recovery time for P1 at higher energy region is observed to be 1.3 times slower than P4 (**Table 3.5.9.1).** As has been mentioned earlier, the energy absorption peaks are significantly affected by donor conjugation. Hence, a longer GSB

recovery time for P1 compared to P4 can be attributed to the high donor conjugation of P1 and hence higher charge transfer. The GSB recovery time for P2 is observed to be two times faster than that of P5 (**Table 3.5.9.2**). As shown in the computational studies, the stronger donor of P2 has less effect on the electronic structures (as seen in P1 and P4) which may be due to bulky isoindigo acceptor. The isoindigo acceptor is expected to have similar interactions with the donor moieties in both P2 and P5. However, the steric hindrance is expected to be more pronounced in P2 which has a long conjugated bulky donor. On the other hand, D-A interaction is expected to be more facilitated in P5 with a smaller donor and the same **II** acceptor. This can lead to longer GSB recovery lifetime of P5 compared to P2. It has been discussed under the steady state studies that the acceptor has a stronger influence on the longer wavelength region of the absorption spectra. Therefore, the steric hindrance due to the bulkiness of the **II** acceptor in both P2 and P5 can be the reason behind the absence of GSB at longer wavelengths. In both cases, the GSB recovery time at higher energies is observed to be 1.4 times slower than that in lower energies (**Table 3.5.9.3**). This can be attributed to the strong donor contribution on the high energy ground state bleaching. It also indicates that the D-A interactions are similar in both P3 and P6 and hence follow similar charge transfer dynamics. The GSB lifetimes for both P3 and P6 are observed to be faster than P1 and P4 (**Table 3.5.9.3**). The presence of weaker **TT** acceptor in P3 and P6 leads to weaker donor-acceptor interactions as compared to P1 and P4. P2 and P5, with a stronger acceptor, are expected to have higher GSB lifetimes compared to P3 and P6. Interestingly, the GSB lifetimes for P3 and P6 are slower compared to P2. This observation can be due to steric hindrance arising from the bulky donor and acceptor in P2 leading to weaker donor-acceptor interactions. However, P5 with a less bulky donor compared to P2, experiences a less steric hindrance. Hence, the GSB lifetimes of P5 are observed to be comparable to that of P3 and P6.

The ultrafast and nanosecond transient absorption spectra for P1 and P4 can be seen in **Figure 3.6.1.** No additional excited states are seen from the ultrafast to the longer nanosecond regimes. This suggests that the larger donor system for this donor-acceptor motif does not contribute to other excited species at longer timescales in the visible region, although there may be charge separated states or evidence of polaron changes at wavelengths longer than 870 nm, which were not observed due to the limitation of the detector. In the nanosecond spectra, there is an additional GSB around 450nm which is not observed in the femtosecond transient experiment. Our computational studies have shown more localization of the electron density in excited state of

highly conjugated polymers and predicted higher charge transfer properties. This may lead to longer charge transfer dynamics. Hence, we observed a very slow GSB recovery time (in the ns timescale) around 450nm (**Table 3.5.9.1**) which could not be probed by fs transient experiment.

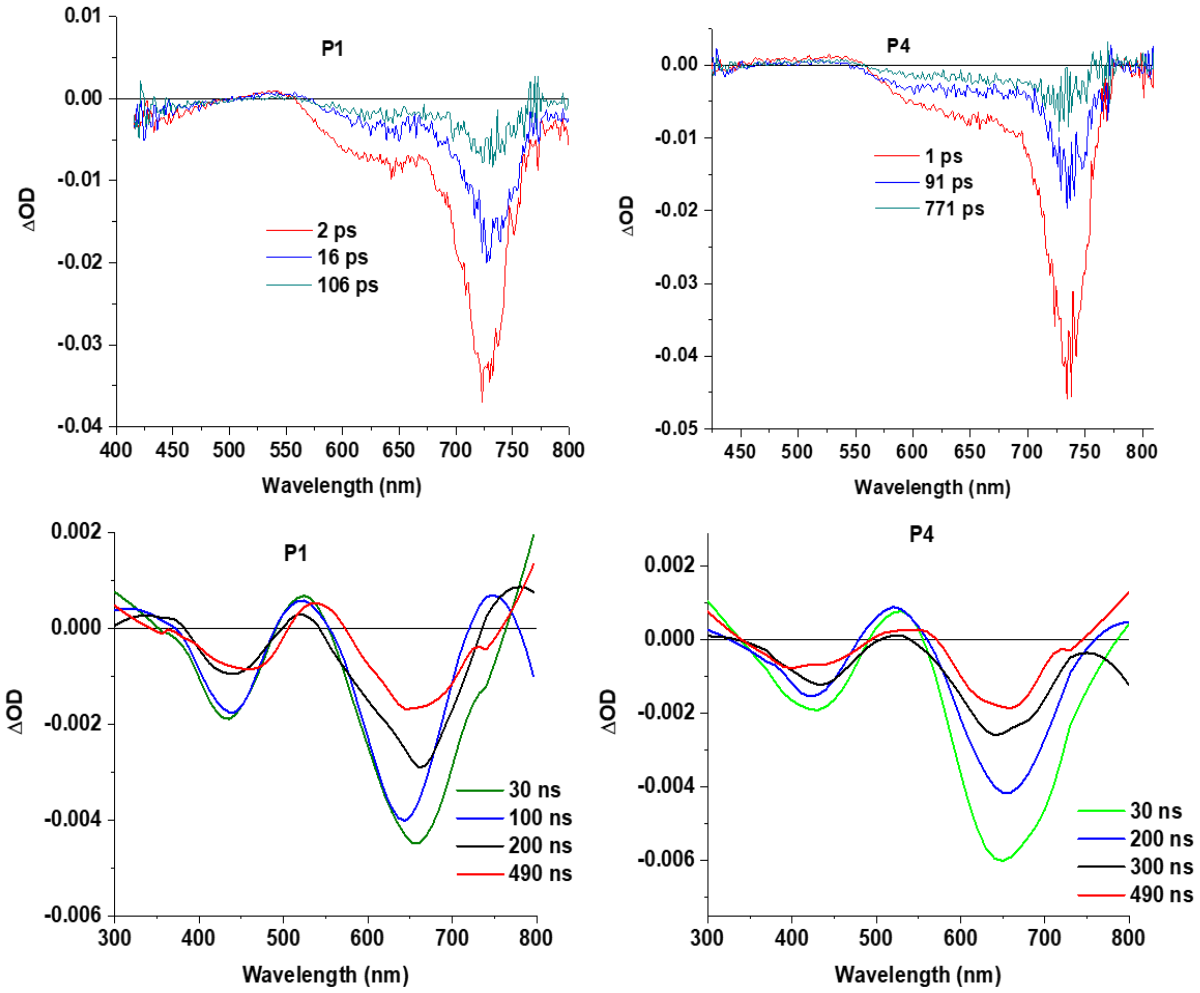

Figure 3.6.1. Ultrafast transient absorption spectra (top) for P1 (left) and P4 (right). Nanosecond transient absorption spectra (bottom) for P1 (left) and P4 (right).

The ultrafast and nanosecond transient absorption spectra for P2 and P5 can be seen in **Figure 3.6.2**. There are significant differences between P2 and P5 in the ultrafast regime and nanosecond regime. For P2, in the ultrafast there is a bleach at 430 nm, an ESA at ~500 nm, and a bleach and SE from 600 nm to 750 nm. Whereas in the longer nanosecond regime, a bleach at 430 nm and an SE around 550nm has been observed but no ESA. This suggests that after the initial singlet state is formed, a short-lived triplet state is formed at higher energies which is not observed in the longer ns regime. The absence of ESA in higher energy for P5 compared to P2

may be due to the shorter donor conjugation in P5. In the femtosecond regime, the observed ESA around 775nm for both polymers (P2 and P5) which is not seen in the nanosecond regime suggests a short-lived triplet state at lower energies.

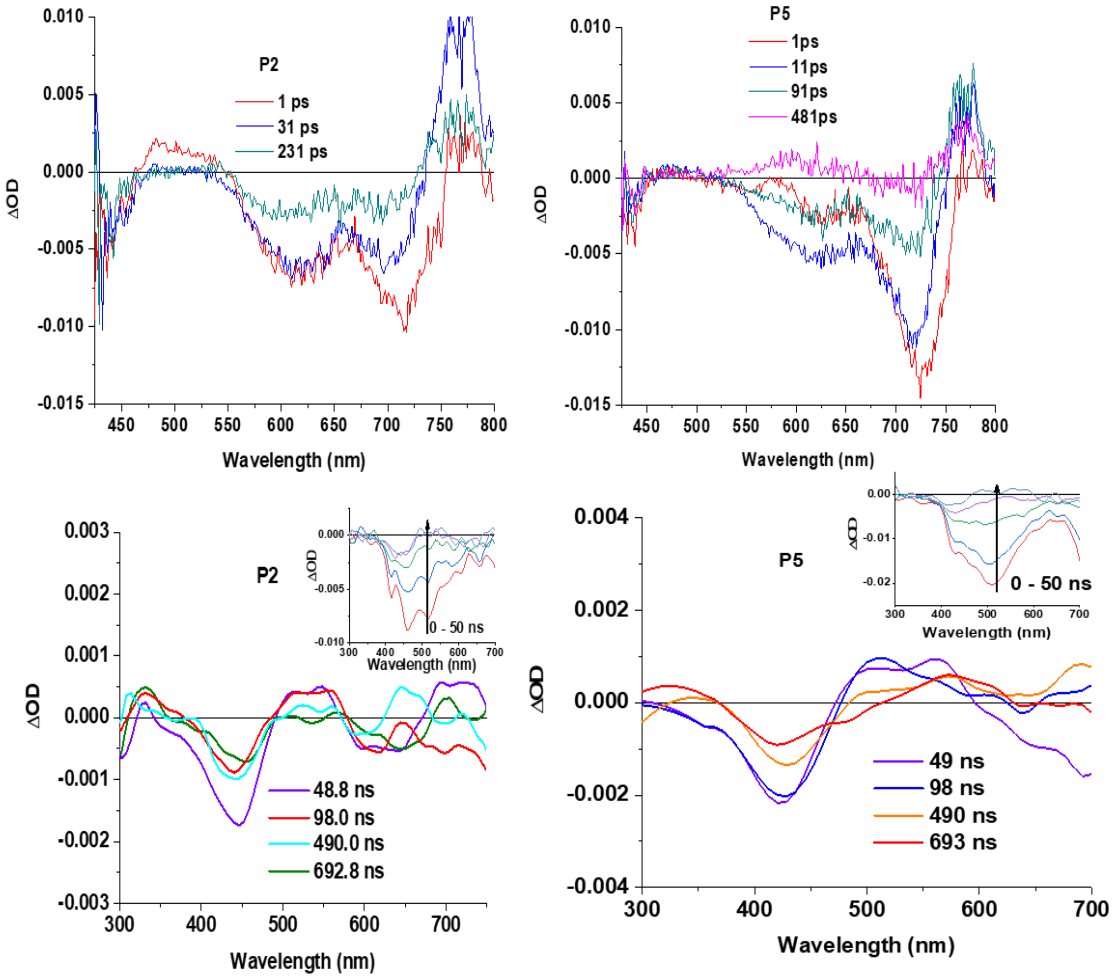

Figure 3.6.2. Ultrafast transient absorption spectra (top) for P2 (left) and P5 (right). Nanosecond transient absorption spectra (bottom) for P2 (left) and P5 (right).

The ultrafast and nanosecond transient absorption spectra for P3 and P6 can be seen in **Figure 3.6.3**. There are no significant differences between P3 and P6 in the nanosecond regime. In both the ultrafast and the nanosecond regime, there is a bleach in the 430 nm region and 630 nm region for both polymers. However, an ESA at 740 nm with a lifetime of 199 ns was observed for P3 when excited at 600 nm (**Figure 3.6.1**). The same has not been observed for P6. This indicates that P3 with larger conjugated donor contributes to long-lived triplet state which is not seen for P6.

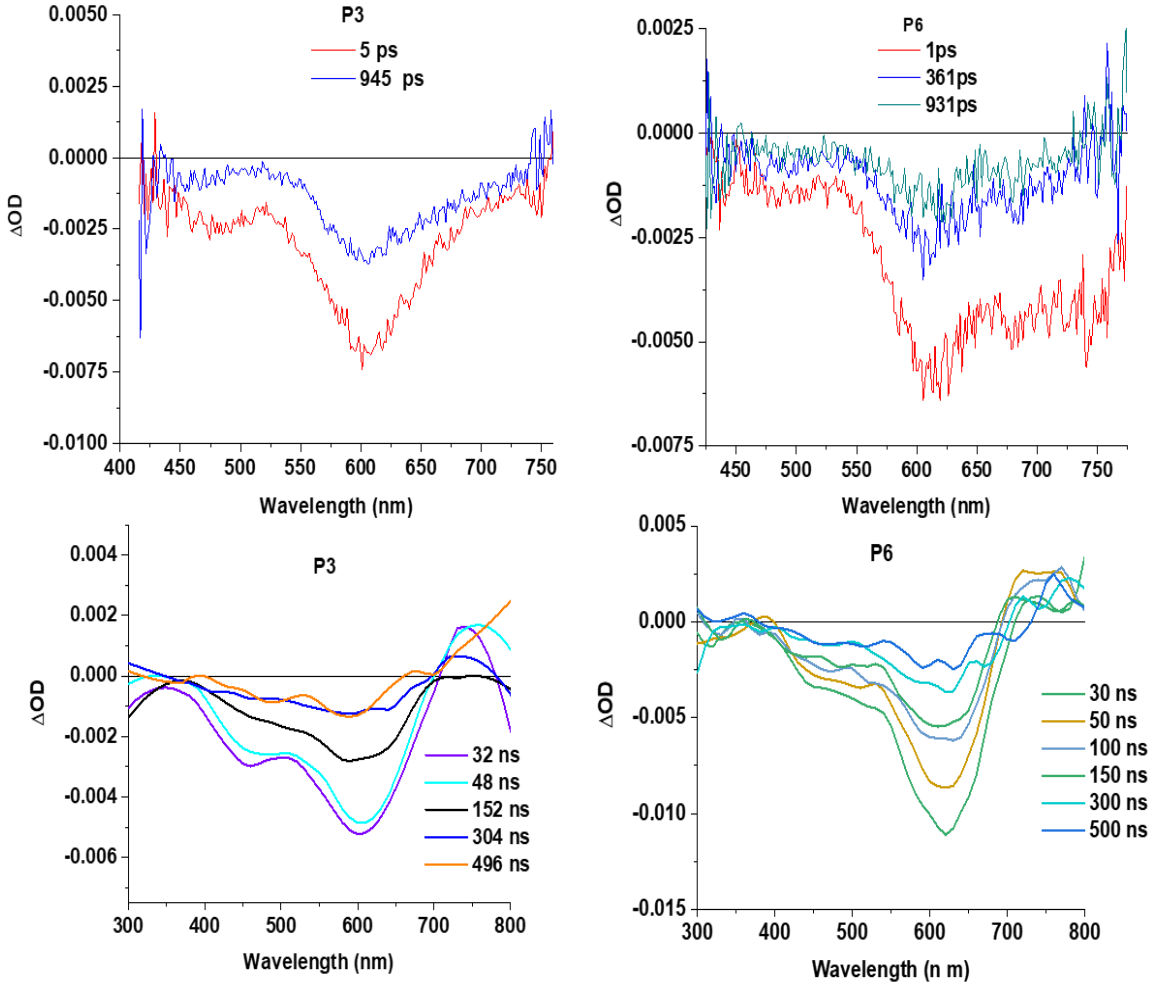

Figure 3.6.3. Ultrafast transient absorption spectra (top) for P3 (left) and P6 (right). Nanosecond transient absorption spectra (bottom) for P3 (left) and P6 (right).

These results show that increased donor conjugation and enhanced acceptor strength lead to high molar extinction coefficients, high TPA cross sections, high fluorescence lifetime and longer GSB recovery time. Previous studies have reported higher PCEs in polymers having **DPP** [51] followed by **II** [55] and **TT** [36] acceptors. Polymers with **IDT** donor have also shown high PCE [41,42] In line with these reports, the results of our present investigations indicate enhanced charge transfer characteristics of the polymers with extended donor conjugation and stronger acceptor. Hence, these polymers can be used in manufacturing better photovoltaic devices. However, along with extended conjugation and acceptor strength, size of the donor and acceptor (steric hindrance) is also observed to play a significant role on the photophysical properties of the polymers. This

study points out that size of the donor and acceptor should also be taken into account while designing suitable D-A systems for photovoltaic applications.

3.7. Conclusion

In this study, six polymers consisting of **DPP**, **II** or **TT** acceptors with an s-indacene donor fused with a thiophene or a thienothiophene on either end were synthesized. The presence of thiophenes increases the donor conjugation of these polymers. The optical properties of these six polymers were investigated using different spectroscopic techniques as well as computational methods. The steady state experimental results showed that increased donor conjugation leads to increased extinction coefficient at higher energies while enhanced acceptor strength resulted in increased extinction coefficient at lower energies for the investigated polymers. In addition, increased donor conjugation and enhanced acceptor strength of these polymers resulted in a significant red shift in the absorption spectra indicating reduced HOMO-LUMO bandgap in the polymers. The fluorescence up-conversion results showed longer excitonic lifetimes for the polymers with extended conjugated donor systems. Computational studies on these polymers show that polymers with extended donor conjugation and higher acceptor strength have more localized electron density in the excited state indicating enhanced charge transfer characteristics. In addition, the TPA experiments showed enhanced charge transfer characteristics for the polymers (P1 and P4) with strong acceptors. Femtosecond and nanosecond transient studies revealed significant differences in excited state dynamics in polymers with different donor conjugation lengths. This work clearly demonstrates the effect of donor conjugation, acceptor strength as well as the relative sizes of the donor and acceptor on the charge transfer properties of donor-acceptor light-harvesting conjugated polymers. The outcomes of the present investigations will help in the design and development of efficient donor-acceptor polymers for organic photovoltaics.

References

(1) Gibson, L.; Wilman, E. N.; Laurance, F. How Green Is ‘ Green ’ Energy ? *Trends in Ecology & Evolution* **2017**, *32* (12), 922–935. https://doi.org/10.1016/j.tree.2017.09.007.

(2) Ragoussi, M.-E.; Torres, T. New Generation Solar Cells Concepts, Trends. *Chem. Commun.* **2015**, *51*, 3957–3972. https://doi.org/10.1039/C4CC09888A.

(3) Miles, R. W.; Hynes, K. M.; Forbes, I. Photovoltaic Solar Cells : An Overview of State-of-the-Art Cell Development and Environmental Issues. *Progress in Crystal Growth and Characterization of Materials* **2005**, *51*, 1–42. https://doi.org/10.1016/j.pcrysgrow.2005.10.002.

(4) Paggi, M.; Berardone, I.; Infuso, A.; Corrado, M. Fatigue Degradation and Electric Recovery in Silicon Solar Cells Embedded in Photovoltaic Modules. *Scientific Reports* **2014**, *4*, 1–7. https://doi.org/10.1038/srep04506.

(5) Shi, G.; Kioupakis, E. Electronic and Optical Properties of Nanoporous Silicon for Solar-Cell Applications. *ACS Photonics* **2015**, *2* (2), 208–215. https://doi.org/10.1021/ph5002999.

(6) Deligiannis, D.; Vasudevan, R.; Smets, A. H. M.; van Swaaij, R. A. C. M. M.; Zeman, M. Surface Passivation of C-Si for Silicon Heterojunction Solar Cells Using High-Pressure Hydrogen Diluted Plasmas. *AIP Advances* **2015**, *5* (9), 1–8. https://doi.org/10.1063/1.4931821.

(7) Babayigit, A.; Ethirajan, A.; Muller, M.; Conings, B. Toxicity of Organometal Halide Perovskite Solar Cells. *Nature Materials* **2016**, *15* (3), 247–251. https://doi.org/10.1038/nmat4572.

(8) Günes, S.; Neugebauer, H.; Sariciftci, N. S. Conjugated Polymer-Based Organic Solar Cells. *Chemical Reviews* **2007**, *107* (4), 1324–1338. https://doi.org/10.1021/cr050149z.

(9) Vezie, M. S.; Few, S.; Meager, I.; Pieridou, G.; Dörling, B.; Ashraf, R. S.; Goñi, A. R.; Bronstein, H.; Mcculloch, I.; Hayes, S. C.; Campoy-quiles, M.; Nelson, J. Exploring the Origin of High Optical Absorption in Conjugated Polymers. *Nature Materials* **2016**, *15*, 746–753. https://doi.org/10.1038/NMAT4645.

(10) Seo, J. H.; Um, H. D.; Shukla, A.; Hwang, I.; Park, J.; Kang, Y. C.; Kim, C. S.; Song, M.; Seo, K. Low-Temperature Solution-Processed Flexible Organic Solar Cells with PFN/AgNWs Cathode. *Nano Energy* **2015**, *16*, 122–129. https://doi.org/10.1016/j.nanoen.2015.06.013.

(11) Zhong, H.; Li, Z.; Buchaca-Domingo, E.; Rossbauer, S.; Watkins, S. E.; Stingelin, N.; Anthopoulos, T. D.; Heeney, M. Low Band Gap Dithienogermolodithiophene Copolymers with Tunable Acceptors and Side-Chains for Organic Solar Cells. *Journal of Materials Chemistry A* **2013**, *1* (47), 14973–14981. https://doi.org/10.1039/c3ta13778c.

(12) Cravino, A. Origin of the Open Circuit Voltage of Donor-Acceptor Solar Cells: Do Polaronic Energy Levels Play a Role? *Applied Physics Letters* **2007**, *91* (24), 1–4. https://doi.org/10.1063/1.2817930.

(13) Chen, S.; Zhang, D.; Wang, M.; Kong, L.; Zhao, J. Donor–Acceptor Type Polymers Containing the 2,3-Bis(2-Pyridyl)-5,8-Dibromoquinoxaline Acceptor and Different Thiophene Donors:

Electrochemical, Spectroelectrochemistry and Electrochromic Properties. *New J. Chem.* **2016**, *40* (3), 2178–2188. https://doi.org/10.1039/C5NJ02651B.

(14) Osaka, I.; Abe, T.; Shimawaki, M.; Koganezawa, T.; Takimiya, K. Naphthodithiophene-Based Donor-Acceptor Polymers: Versatile Semiconductors for OFETs and OPVs. *ACS Macro Letters* **2012**, *1* (4), 437–440. https://doi.org/10.1021/mz300065t.

(15) Beaujuge, P. M.; Subbiah, J.; Choudhury, K. R.; Ellinger, S.; McCarley, T. D.; So, F.; Reynolds, J. R. Green Dioxythiophene-Benzothiadiazole Donor-Acceptor Copolymers for Photovoltaic Device Applications. *Chemistry of Materials* **2010**, *22* (6), 2093–2106. https://doi.org/10.1021/cm903495b.

(16) Gokce, G.; Karabay, B.; Cihaner, A.; Icli Ozkut, M. [1,2,5]Thiadiazolo[3,4-g]Quinoxaline Acceptor-Based Donor–Acceptor–Donor-Type Polymers: Effect of Strength and Size of Donors on the Band Gap. *Journal of Polymer Science, Part A: Polymer Chemistry* **2017**, *55* (20), 3483–3493. https://doi.org/10.1002/pola.28730.

(17) Zhao, D.; Li, L.; Lo, W.; Zhang, N.; Goodson, T.; Yu, L. Two Photon Absorption Study of Low-Bandgap, Fully Conjugated Perylene Diimide-Thienoacene-Perylene Diimide Ladder-Type Molecules. *Chemistry of Materials* **2017**, *29*, 6726–6732. https://doi.org/10.1021/acs.chemmater.7b01512.

(18) Chochos, C. L.; Kalogirou, A. S.; Ye, T.; Tatsi, E.; Katsouras, A.; Zissimou, G. A.; Gregoriou, V. G.; Avgeropoulos, A.; Koutentis, P. A. 4H-1,2,6-Thiadiazine-Containing Donor-Acceptor Conjugated Polymers: Synthesis, Optoelectronic Characterization and Use in Organic Solar Cells. *J. Mater. Chem. C* **2017**, 1–10. https://doi.org/10.1039/C7TC03889E.

(19) Nagarjuna, P.; Bagui, A.; Garg, A.; Gupta, V.; Singh, S. P. One-Step Synthesis of New Electron Acceptor for High Efficiency Solution Processable Organic Solar Cells. *The Journal of Physical Chemistry C* **2017**, *121*, 26615–26621. https://doi.org/10.1021/acs.jpcc.7b08167.

(20) Adam, G.; Munkhbat, B.; Denk, P.; Ulbricht, C.; Hrelescu, C.; Scharber, M. C. Different Device Architectures for Bulk-Heterojunction Solar Cells. *Frontiers in Materials* **2016**, *3*, 1–10. https://doi.org/10.3389/fmats.2016.00039.

(21) Ltaief, A.; Davenas, J.; Bouazizi, A.; Chaâbane, R. Ben; Alcouffe, P.; Ouada, H. Ben. Film Morphology Effects on the Electrical and Optical Properties of Bulk Heterojunction Organic Solar Cells Based on MEH-PPV/C60 Composite. *Materials Science and Engineering C* **2005**, *25* (1), 67–75. https://doi.org/10.1016/j.msec.2004.09.003.

(22) Erb, T.; Zhokhavets, U.; Gobsch, G.; Raleva, S.; Stühn, B.; Schilinsky, P.; Waldauf, C.; Brabec, C. J. Correlation between Structural and Optical Properties of Composite Polymer/Fullerene Films for Organic Solar Cells. *Advanced Functional Materials* **2005**, *15* (7), 1193–1196. https://doi.org/10.1002/adfm.200400521.

(23) Trukhanov, V. A.; Bruevich, V. V.; Paraschuk, D. Y. Fill Factor in Organic Solar Cells Can Exceed the Shockley-Queisser Limit. *Scientific Reports* **2015**, *5*, 1–10. https://doi.org/10.1038/srep11478.

(24) Street, R. A. Carrier Mobility, Structural Order, and Solar Cell Efficiency of Organic Heterojunction Devices. *Applied Physics Letters* **2008**, *93* (13), 1–3. https://doi.org/10.1063/1.2996029.

(25) Kupijai, A. J.; Behringer, K. M.; Schaeble, F. G.; Galfe, N. E.; Corazza, M.; Gevorgyan, S. A.; Krebs, F. C.; Stutzmann, M.; Brandt, M. S. Bipolar Polaron Pair Recombination in Polymer/Fullerene Solar Cells. *Physical Review B - Condensed Matter and Materials Physics* **2015**, *92* (24), 1–8. https://doi.org/10.1103/PhysRevB.92.245203.

(26) Street, R. A. Electronic Structure and Properties of Organic Bulk-Heterojunction Interfaces. *Advanced Materials* **2016**, *28* (20), 3814–3830. https://doi.org/10.1002/adma.201503162.

(27) Larson, B. W.; Reid, O. G.; Coffey, D. C.; Avdoshenko, S. M.; Popov, A. A.; Boltalina, O. V.; Strauss, S. H.; Kopidakis, N.; Rumbles, G. Inter-Fullerene Electronic Coupling Controls the Efficiency of Photoinduced Charge Generation in Organic Bulk Heterojunctions. *Advanced Energy Materials* **2016**, *6* (24), 1–11. https://doi.org/10.1002/aenm.201601427.

(28) Serbenta, A.; Kozlov, O. V.; Portale, G.; Van Loosdrecht, P. H. M.; Pshenichnikov, M. S. Bulk Heterojunction Morphology of Polymer:Fullerene Blends Revealed by Ultrafast Spectroscopy. *Scientific Reports* **2016**, *6*, 1–11. https://doi.org/10.1038/srep36236.

(29) Li, Y.; Gu, M.; Pan, Z.; Zhang, B.; Yang, X. Indacenodithiophene : A Promising Building Block for High Performance Polymer Solar Cells. *Journal of Materials Chemistry A: Materials for energy and sustainability* **2017**, *5*, 10798–10814. https://doi.org/10.1039/C7TA02562A.

(30) Kose, M. E. Evaluation of Acceptor Strength in Thiophene Coupled Donor − Acceptor Chromophores for Optimal Design of Organic Photovoltaic Materials. *Journal of Physical Chemistry A* **2012**, *116*, 11503–12509. https://doi.org/10.1021/jp309950f.

(31) Creamer, A.; Casey, A.; Marsh, A. V.; Shahid, M.; Gao, M.; Heeney, M. Systematic Tuning of 2,1,3-Benzothiadiazole Acceptor Strength by Monofunctionalization with Alkylamine, Thioalkyl, or Alkoxy Groups in Carbazole Donor-Acceptor Polymers. *Macromolecules* **2017**, *50* (7), 2736–2746. https://doi.org/10.1021/acs.macromol.7b00235.

(32) Kim, B. G.; Ma, X.; Chen, C.; Ie, Y.; Coir, E. W.; Hashemi, H.; Aso, Y.; Green, P. F.; Kieffer, J.; Kim, J. Energy Level Modulation of HOMO, LUMO, and Band-Gap in Conjugated Polymers for Organic Photovoltaic Applications. *Advanced Functional Materials* **2013**, *23* (4), 439–445. https://doi.org/10.1002/adfm.201201385.

(33) Adegoke, O. O.; Jung, I. H.; Orr, M.; Yu, L.; Goodson III, T. G. Investigations of the Effect of the Acceptor Strength on the Optical and Electronic Properties in Conjugated Polymers for Solar Applications. *Journal of the American Chemical Society* **2015**, 150407115828001. https://doi.org/10.1021/ja513002h.

(34) Falzon, M.-F.; Zoombelt, A. P.; Wienk, M. M.; Janssen, R. A. J. R. a J. Diketopyrrolopyrrole-Based Acceptor Polymers for Photovoltaic Application. *Physical chemistry chemical physics : PCCP* **2011**, *13* (19), 8931–8939. https://doi.org/10.1039/c1cp20313d.

(35) Turbiez, M.; Leeuw, D. M. De; Janssen, A. J. Poly (Diketopyrrolopyrrole - Terthiophene) for Ambipolar Logic and Photovoltaics. *J am chem Soc Communications* **2009**, *131*, 16616–16617. https://doi.org/10.1002/adma.200901819.

(36) Mori, H.; Suetsugu, M.; Nishinaga, S.; Chang, N.; Nonobe, H.; Okuda, Y.; Nishihara, Y. Synthesis, Characterization, and Solar Cell and Transistor Applications of Phenanthro[1,2-*b*:8,7- *b ′*]Dithiophene-Diketopyrrolopyrrole Semiconducting Polymers. *Journal of Polymer Science Part A: Polymer Chemistry* **2015**, *53* (5), 709–718. https://doi.org/10.1002/pola.27500.

(37) Li, W.; Hendriks, K. H.; Wienk, M. M.; Janssen, R. A. J. Diketopyrrolopyrrole Polymers for Organic Solar Cells. *Accounts of Chemical Research* **2016**, *49*, 78–85. https://doi.org/10.1021/acs.accounts.5b00334.

(38) Grand, C.; Baek, S.; Lai, T. H.; Deb, N.; Zajaczkowski, W.; Stalder, R.; Müllen, K.; Pisula, W.; Bucknall, D. G.; So, F.; Reynolds, J. R. Structure-Property Relationships Directing Transport and Charge Separation in Isoindigo Polymers. *Macromolecules* **2016**, *49* (11), 4008–4022. https://doi.org/10.1021/acs.macromol.6b00540.

(39) Estrada, L. A.; Stalder, R.; Abboud, K. A.; Risko, C.; Brédas, J. L.; Reynolds, J. R. Understanding the Electronic Structure of Isoindigo in Conjugated Systems: A Combined Theoretical and Experimental Approach. *Macromolecules* **2013**, *46* (22), 8832–8844. https://doi.org/10.1021/ma4013829.

(40) Duan, C.; Huang, F.; Cao, Y. Recent Development of Push–Pull Conjugated Polymers for Bulk-Heterojunction Photovoltaics: Rational Design and Fine Tailoring of Molecular Structures. *Journal of Materials Chemistry* **2012**, *22* (21), 10416–10434. https://doi.org/10.1039/c2jm30470h.

(41) Stalder, R.; Mei, J.; Graham, K. R.; Estrada, L. A.; Reynolds, J. R. Isoindigo , a Versatile Electron-Deficient Unit For High-Performance Organic Electronics. *Chemistry of Materials* **2014**, *26*, 664–678. https://doi.org/10.1021/cm402219v.

(42) Homyak, P. D.; Tinkham, J.; Lahti, P. M.; Coughlin, E. B. Thieno [3 , 4 - b] Thiophene Acceptors with Alkyl , Aryl , Perfluoroalkyl , and Perfluorophenyl Pendants for Donor − Acceptor Low Bandgap Polymers. *Macromolecules* **2013**, *46*, 8873–8881.

(43) Cinar, M. E.; Ozturk, T. Thienothiophenes , Dithienothiophenes , and Thienoacenes : Syntheses , Oligomers , Polymers , and Properties. *Chemical Reviews* **2015**, *115*, 3096–3140. https://doi.org/10.1021/cr500271a.

(44) Deka, B. C.; Purkayastha, S. K.; Sharma, H.; Bhattacharyya, P. K. Ground and Excited States of Neutral and Cationic Thieno[3,2-b]Thiophene: A DFT Study. *Computational and Theoretical Chemistry* **2016**, *1091*, 41–48. https://doi.org/10.1016/j.comptc.2016.07.004.

(45) Singh, R.; Pagona, G.; Gregoriou, V. G.; Tagmatarchis, N.; Toliopoulos, D.; Han, Y.; Fei, Z.; Katsouras, A.; Avgeropoulos, A.; Anthopoulos, T. D.; Heeney, M.; Keivanidis, P. E.; Chochos, C. L. The Impact of Thienothiophene Isomeric Structures on the Optoelectronic Properties and Photovoltaic Performance in Quinoxaline Based Donor–Acceptor Copolymers. *Polym. Chem.* **2015**, *6* (16), 3098–3109. https://doi.org/10.1039/C5PY00075K.

(46) Výprachtický, D.; Demirtas, I.; Dzhabarov, V.; Pokorná, V.; Ertas, E.; Ozturk, T.; Cimrová, V. New Copolymers with Thieno[3,2-b]Thiophene or Dithieno[3,2-b:2′,3′-d]Thiophene Units Possessing Electron-Withdrawing 4-Cyanophenyl Groups: Synthesis and Photophysical, Electrochemical, and Electroluminescent Properties. *Journal of Polymer Science, Part A: Polymer Chemistry* **2017**, *55* (16), 2629–2638. https://doi.org/10.1002/pola.28657.

(47) Niimi, K.; Shinamura, S.; Osaka, I.; Miyazaki, E.; Takimiya, K. Dianthra[2,3- b:2′,3′- f]Thieno[3,2- b]Thiophene (DATT): Synthesis, Characterization, and FET Characteristics of New π-Extended Heteroarene with Eight Fused Aromatic Rings. *Journal of the American Chemical Society* **2011**, *133* (22), 8732–8739. https://doi.org/10.1021/ja202377m.

(48) Liang, Y.; Xu, Z.; Xia, J.; Tsai, S. T.; Wu, Y.; Li, G.; Ray, C.; Yu, L. For the Bright Future-Bulk Heterojunction Polymer Solar Cells with Power Conversion Efficiency of 7.4%. *Advanced Materials* **2010**, *22*, 135–138. https://doi.org/10.1002/adma.200903528.

(49) Keller, B.; McLean, A.; Kim, B.-G.; Chung, K.; Kim, J.; Goodson, T. Ultrafast Spectroscopic Study of Donor–Acceptor Benzodithiophene Light Harvesting Organic Conjugated Polymers. *The Journal of Physical Chemistry C* **2016**, acs.jpcc.6b01727. https://doi.org/10.1021/acs.jpcc.6b01727.

(50) Berezin, M. Y.; Zhan, C.; Lee, H.; Joo, C.; Akers, W. J.; Yazdanfar, S.; Achilefu, S. Two-Photon Optical Properties of near-Infrared Dyes at 1.55 Mm Excitation. *Journal of Physical Chemistry B* **2011**, *115* (39), 11530–11535. https://doi.org/10.1021/jp207618e.

(51) Williams, A. T. R.; Winfield, S. A.; Miller, J. N. Relative Fluorescence Quantum Yields Using a Computer-Controlled Luminescence Spectrometer. *Analyst* **1983**, *108*, 1067–1071. https://doi.org/10.1039/an9830801067.

(52) Seybold, P. G.; Gouterman, M. Porphyrins. *Journal of Molecular Spectroscopy* **1969**, *31*, 1–13. https://doi.org/10.1016/0022-2852(69)90335-X.

(53) McLean, A. M.; Socher, E.; Varnavski, O.; Clark, T. B.; Imperiali, B.; Goodson, T. Two-Photon Fluorescence Spectroscopy and Imaging of 4-Dimethylaminonaphthalimide Peptide and Protein Conjugates. *The journal of physical chemistry. B* **2013**, *117* (50), 15935–15942. https://doi.org/10.1021/jp407321g.

(54) Makarov, N. S.; Drobizhev, M.; Rebane, A. Two-Photon Absorption Standards in the 550-1600 Nm Excitation Wavelength Range. *Optics Express* **2008**, *16* (6), 4029–4047.

(55) Adegoke, O. O.; Ince, M.; Mishra, A.; Green, A.; Varnavski, O.; Martínez-Díaz, M. V.; Bäuerle, P.; Torres, T.; Goodson, T. Synthesis and Ultrafast Time Resolved Spectroscopy of Peripherally Functionalized Zinc Phthalocyanine Bearing Oligothienylene-Ethynylene Subunits. *Journal of Physical Chemistry C* **2013**, *117*, 20912–20918. https://doi.org/10.1021/jp404406b.

(56) Flynn, D. C.; Ramakrishna, G.; Yang, H.; Northrop, B. H.; Stang, P. J.; Iii, T. G. Ultrafast Optical Excitation in Supramolecular Metallacycles with Charge Transfer Properties. *Journal of american chemical society* **2010**, No. 14, 1348–1358.

(57) Shin, N.; Yun, H.; Yoon, Y.; Son, H. J.; Ju, S.; Kwon, S.; Kim, B.; Kim, Y. Highly Stable Polymer Solar Cells Based on Poly (Dithienobenzodithiophene- Co -Thienothiophene). *Macromolecules* **2015**, *48*, 3890–3899. https://doi.org/10.1021/acs.macromol.5b00514.

(58) Teng, W.; Ye, Q.; Ting, T.; Jin, S.; Xu, J. 4,9-Dihydro-s-Indaceno[1,2-b:5,6-b']Dithiophene-Embedded Electrochromic Conjugated Polymers with High Coloration Efficiency and Fast Coloration Time. *Solar Energy Materials and Solar Cells* **2015**, *136*, 92–99. https://doi.org/10.1016/j.solmat.2015.01.007.

(59) Schneider, J. A.; Dadvand, A.; Wen, W.; Perepichka, D. F. Tuning the Electronic Properties of Poly(Thienothiophene Vinylene)s via Alkylsulfanyl and Alkylsulfonyl Substituents. **2013**. https://doi.org/10.1021/ma402018n.

(60) Lim, T.; Hsiang, J.; White, J. D.; Hsu, J. H.; Fan, Y. L.; Lin, K. F.; Fann, W. S. Single Short-Chain Conjugated Polymer Studied with Optical Spectroscopy : A Donor-Accepter System. *Physical Review B* **2007**, *75*, 1–9. https://doi.org/10.1103/PhysRevB.75.165204.

(61) Gettinger, C. L.; Heeger, A. J.; Drake, J. M.; Pine, D. J. THE EFFECT OF INTRINSIC RIGIDITY ON THE OPTICAL PROPERTIES OF PPV. *Mol. Cryst. Liq. Cyst.* **1994**, *256*, 507–512.

(62) Nijegorodov, D. The Influence of Planarity and Rigidity on the Absorption and Fluorescence Parameters and Intersystem Crossing Rate Constant in Aromatic Molecules. *J. Phys. Chem. B* **1994**, *98*, 5639–5643. https://doi.org/10.1021/j100073a011.

(63) Salzner, U. Effect of Donor − Acceptor Substitution on Optoelectronic Properties of Conducting Organic Polymers. *Journal of Chemical Theory and Computation* **2014**, *10*, 4921–4937. https://doi.org/10.1021/ct500816c.

(64) Yamaguchi, Y.; Matsubara, Y.; Ochi, T.; Wakamiya, T.; Yoshida, Z. How the π Conjugation Length Affects the Fluorescence Emission Efficiency. *J am chem Soc Communications* **2008**, *130*, 13867–13869.

(65) Zheleznova, Y.; Andryukhova, K. V; Fisyuk, A. S. Effect of Donor to Acceptor Ratio on Electrochemical and Spectroscopic Properties of Oligoalkylthiophene 1,3,4-Oxadiazole Derivatives. *Physical Chemistry Chemical Physics* **2017**, *19*, 30261–30276. https://doi.org/10.1039/C7CP05155G.

(66) Mi, S.; Wu, J.; Liu, J.; Zheng, J.; Xu, C. Donor – p -Bridge – Acceptor Fluorescent Polymers Based on Thiophene and Triphenylamine Derivatives as Solution Processable Electrochromic Materials. *ORGANIC ELECTRONICS* **2015**, *23*, 116–123. https://doi.org/10.1016/j.orgel.2015.04.014.

(67) Khetubol, A.; Van Snick, S.; Clark, M. L.; Fron, E.; Couti??o-Gonz??lez, E.; Cloet, A.; Kennes, K.; Firdaus, Y.; Vlasselaer, M.; Leen, V.; Dehaen, W.; Van Der Auweraer, M. Improved Spectral Coverage and Fluorescence Quenching in Donor-Acceptor Systems Involving Indolo[3-2-b]Carbazole and Boron-Dipyrromethene or Diketopyrrolopyrrole. *Photochemistry and Photobiology* **2015**, *91* (3), 637–653. https://doi.org/10.1111/php.12437.

(68) Huang, X.; Shi, Q.; Chen, W.; Zhu, C.; Zhou, W.; Zhao, Z. Low-Bandgap Conjugated Donor - Acceptor Copolymers Based on Porphyrin with Strong Two-Photon Absorption. **2010**, 9620–9626. https://doi.org/10.1021/ma102275h.

(69) Boujtita, M.; Zales, R.; Vivas, M. G.; Silva, D. L.; Bartkowiak, W.; Canuto, S.; Boni, L. De; Mendonca, C. R. Molecular Structure – Optical Property Relationships for a Series of Non-Centrosymmetric Two-Photon Absorbing Push-Pull Triarylamine Molecules. *Scientific Reports* **2014**, *4*, 1–11. https://doi.org/10.1038/srep04447.

(70) Scarongella, M.; Laktionov, A.; Rothlisberger, U.; Banerji, N. Charge Transfer Relaxation in Donor-Acceptor Type Conjugated Materials. *J. Mater. Chem. C* **2013**, *1* (12), 2308–2319. https://doi.org/10.1039/C3TC00829K.

(71) Banerji, N.; Angulo, G.; Barabanov, I.; Vauthey, E. Intramolecular Charge-Transfer Dynamics in Covalently Linked Perylene - Dimethylaniline and Cyanoperylene - Dimethylaniline. *J. Phys. Chem. A* **2008**, *112*, 9665–9674. https://doi.org/10.1021/jp803621z.

(72) Pigliucci, A.; Duvanel, G.; Daku, L. M. L.; Vauthey, E. Investigation of the Influence of Solute−Solvent Interactions on the Vibrational Energy Relaxation Dynamics of Large Molecules in Liquids. *The Journal of Physical Chemistry A* **2007**, *111* (28), 6135–6145. https://doi.org/10.1021/jp069010y.

(73) Hu, Z.; Willard, A. P.; Ono, R. J.; Bielawski, C. W.; Rossky, P. J.; Bout, D. A. Vanden. An Insight into Non-Emissive Excited States in Conjugated Polymers. *Nature Communications* **2015**, *6*, 1–9. https://doi.org/10.1038/ncomms9246.

(74) Bixon, M.; Jortner, J.; Heitele, H. Energy Gap Law for Nonradiative and Radiative Charge Transfer in Isolated and in Solvated. *J. Mater. Chem.* **1994**, *98*, 7289–7299. https://doi.org/10.1021/j100081a010.

(75) Jiang, J.; Alsam, A.; Wang, S.; Aly, S. M.; Pan, Z.; Mohammed, O. F.; Schanze, K. S. Effect of Conjugation Length on Photoinduced Charge Transfer in π - Conjugated Oligomer-Acceptor Dyads. *J. Mater. Chem. A* **2017**, *121*, 4891–4901. https://doi.org/10.1021/acs.jpca.7b03547.

(76) Mikhnenko, O. V; Kuik, M.; Lin, J.; Kaap, N. Van Der; Nguyen, T.; Blom, P. W. M. Trap-Limited Exciton Diffusion in Organic Semiconductors. *Advanced Materials* **2014**, *26*, 1912–1917. https://doi.org/10.1002/adma.201304162.

(77) Collado-fregoso, E.; Bou, P.; Fei, Z.; Gann, E.; Ashraf, S.; Li, Z.; Mcneill, C. R.; Durrant, J. R.; Heeney, M. Increased Exciton Dipole Moment Translates into Charge-Transfer Excitons in Thiophene-Fluorinated Low-Bandgap Polymers for Organic Photovoltaic Applications. *Chemistry of Materials* **2015**, *27*, 7934–7944. https://doi.org/10.1021/acs.chemmater.5b02948.

(78) Revoju, S.; Biswas, S.; Eliasson, B.; Sharma, G. D. Effect of Acceptor Strength on Optical, Electrochemical and Photovoltaic Properties of Phenothiazine-Based Small Molecule for Bulk Heterojunction Organic Solar Cells. *Dyes and Pigments* **2018**, *149*, 830–842. https://doi.org/10.1016/j.dyepig.2017.11.048.

(79) Lim, S. H.; Zhou, Y.; Su, H.; Ong, S. A Stable Solution-Processed Polymer Semiconductor with Record High-Mobility for Printed Transistors. *Scientific Reports* **2012**, *2*, 1–9. https://doi.org/10.1038/srep00754.

(80) Carsten, B.; Szarko, J. M.; Son, H. J.; Wang, W.; Lu, L.; He, F.; Rolczynski, B. S.; Lou, S. J.; Chen, L. X.; Yu, L. Examining the Effect of the Dipole Moment on Charge Separation in Donor À Acceptor Polymers for Organic Photovoltaic Applications. **2011**, 20468–20475. https://doi.org/10.1021/ja208642b.

(81) Matsuzaki, H.; Furube, A.; Katoh, R.; Singh, S. P.; Sonar, P. Excited-State Dynamics in Diketopyrrolopyrrole-Based Copolymer for Organic Photovoltaics Investigated by Transient Optical Spectroscopy Excited-State Dynamics in Diketopyrrolopyrrole-Based Copolymer for Organic Photovoltaics Investigated by Transient Opti. *Japanese Journal of Applied Physics* **2014**, *53*, 1–5.

3.8 Supporting Information

Figure 3.8.1.1: Structure of the starting compounds used for polymer 1-6 synthesis.

Figure 3.8.1.2-3.8.1.7: NMR spectra of polymers P1-P6.

Figure 3.8.2.1. Electronic geometries for donor-acceptor monomers.

Figure 3.8.2.2: Electronic structure for the ground state (left) and excited state (right) that contribute to the low energy S_0 to S_1 transition for P1 (a.) and P4 (b.). The red arrows represent the qualitative magnitudes of the electron density change.

Figure 3.8.2.3: Electronic structure for the ground state (left) and excited state (right) that contribute to the high energy transition for P1 (a.) and P4 (b.). The red arrows represent the qualitative magnitudes of the electron density change.

Figure 3.8.2.4: Electronic structure for the ground state (left) and excited state (right) that contribute to the low energy S_0 to S_1 transition for P2 (a.) and P5 (b.). The red arrows represent the qualitative magnitudes of the electron density change.

Figure 3.8.2.5: Electronic structure for the ground state (left) and excited state (right) that contribute to the high energy S_0 to S_{22} transition for P2 (a.) and P5 (b.). The red arrows represent the qualitative magnitudes of the electron density change.

Figure 3.8.2.6: Electronic structure for the ground state (left) and excited state (right) that contribute to the low energy S_0 to S_1 transition for P3 (a.) and P6 (b.). The red arrows represent the qualitative magnitudes of the electron density change.

Figure 3.8.2.7: Electronic structure for the ground state (left) and excited state (right) that contribute to the high energy S_0 to S_9 transition for P3 (a.) and P6 (b.). The red arrows represent the qualitative magnitudes of the electron density change.

Figure 3.8.2.8: Cyclic voltammograms of P1 to P6.

3.8.1 The synthetic Procedure of D-A polymers

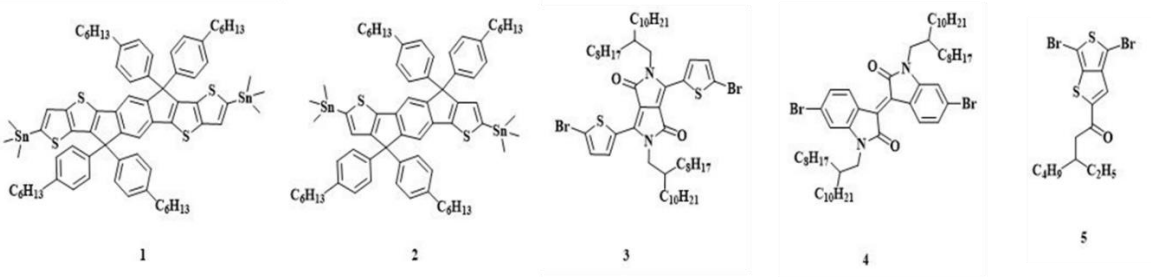

Figure 3.8.1.1. Compound 1 and 2 was synthesized according to the previous report.[1,2]

Synthesis of P1. Compound 1 (130 mg, 0.10 mmol) and compound 3 (71 mg, 0.10 mmol) were taken in a Schlenk tube under nitrogen atmosphere with 10 mL of anhydrous toluene. Tris(dibenzylideneacetone)dipalladium (0) ($Pd_2(dba)_3$) (0.88 mg) and tri(o-tolyl)phosphine (P(o-tol)$_3$) (2.4 mg) were added in one portion. The tube was charged with nitrogen through a freeze−pump−thaw cycle for three times. The mixture was stirred for 24 h at 90 °C under nitrogen. After cooling to room temperature, the highly viscous black gel-like solution was poured into methanol and the resulting precipitate was filtered. The polymer was purified by Soxhlet extraction using methanol, acetone, hexane and chloroform sequentially. The residue was collected and dried under vacuum to afford polymer (172 mg, 95%). ^{1}H NMR (400 MHz, $CDCl_3$, δ): 8.91 (s, 2H), 7.51 (s, 4H), 7.19 (d, 8H), 7.11 (d, 8H), 4.04 (m, 4H), 2.57 (s, 8H), 1.96 (m, 2H), 1.59 (s, 8H), 1.31-1.20 (m, 92H), 0.86-0.83 (m, 24H) GPC: Mn = 25.9 kDa, Mw = 48.2 kDa, PDI = 1.86. Anal. Calcd for $C_{122}H_{160}N_2O_2S_6$: C, 77. 98; H, 8.58; N, 1.49, S, 10.24. Found: C, 78.25; H, 8.56; N, 1.56; S, 10.25.

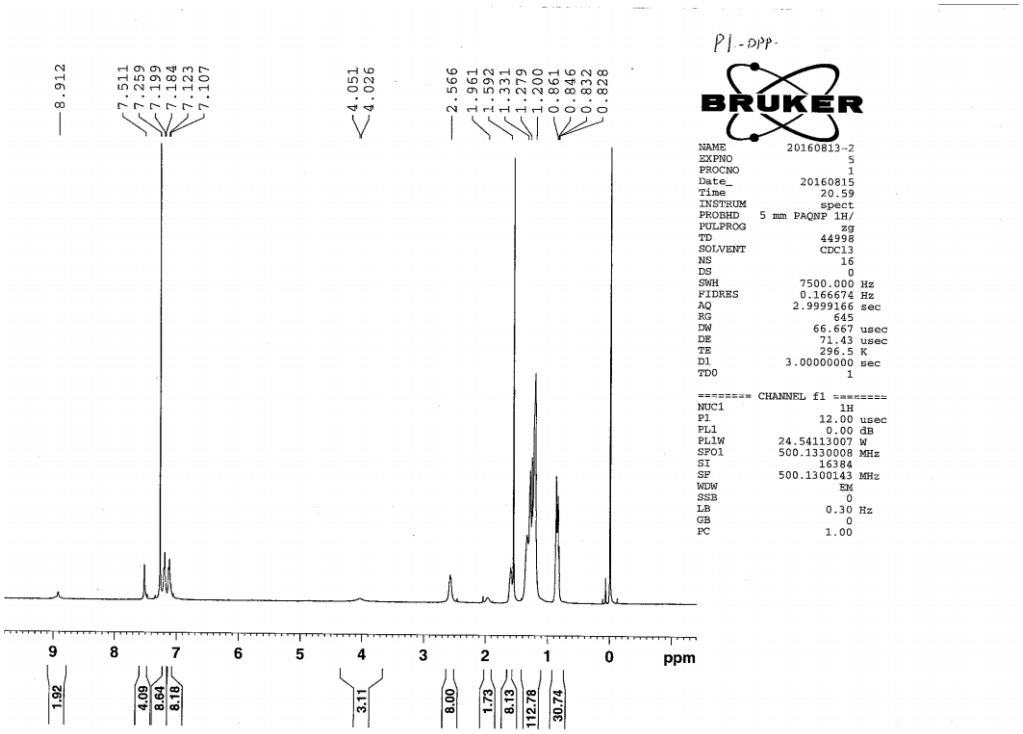

Figure 3.8.1.2.

Synthesis of P2. This was prepared following the general procedure given for the preparation of **P1**. From 1 (130 mg, 0.10 mmol) and 4 (93 mg, 0.10 mmol), there was obtained **P2** (164 mg, 92.7 % yield). ^{1}H NMR (400 MHz, $CDCl_3$, δ): 9.13 (s, 2H), 7.62 (s, 2H), 7.52 (d, 2H), 7.22 (d, 8H), 7.11 (d, 8H), 6.94 (s, 2H), 3.70 (d, 2H), 2.57 (s, 8H), 1.94 (s, 2H), 1.59 (s, 8H), 1.34-1.22 (m, 94H), 0.86-0.84 (m, 24H) GPC: Mn = 42.5 kDa, Mw = 88.4 kDa, PDI = 2.08. Anal. Calcd for $C_{124}H_{162}N_2O_2S_2$: C, 80.90; H, 8.87; N, 1.52, S, 6.97. Found: C, 80.73; H, 8.82; N, 1.54; S, 7.09.

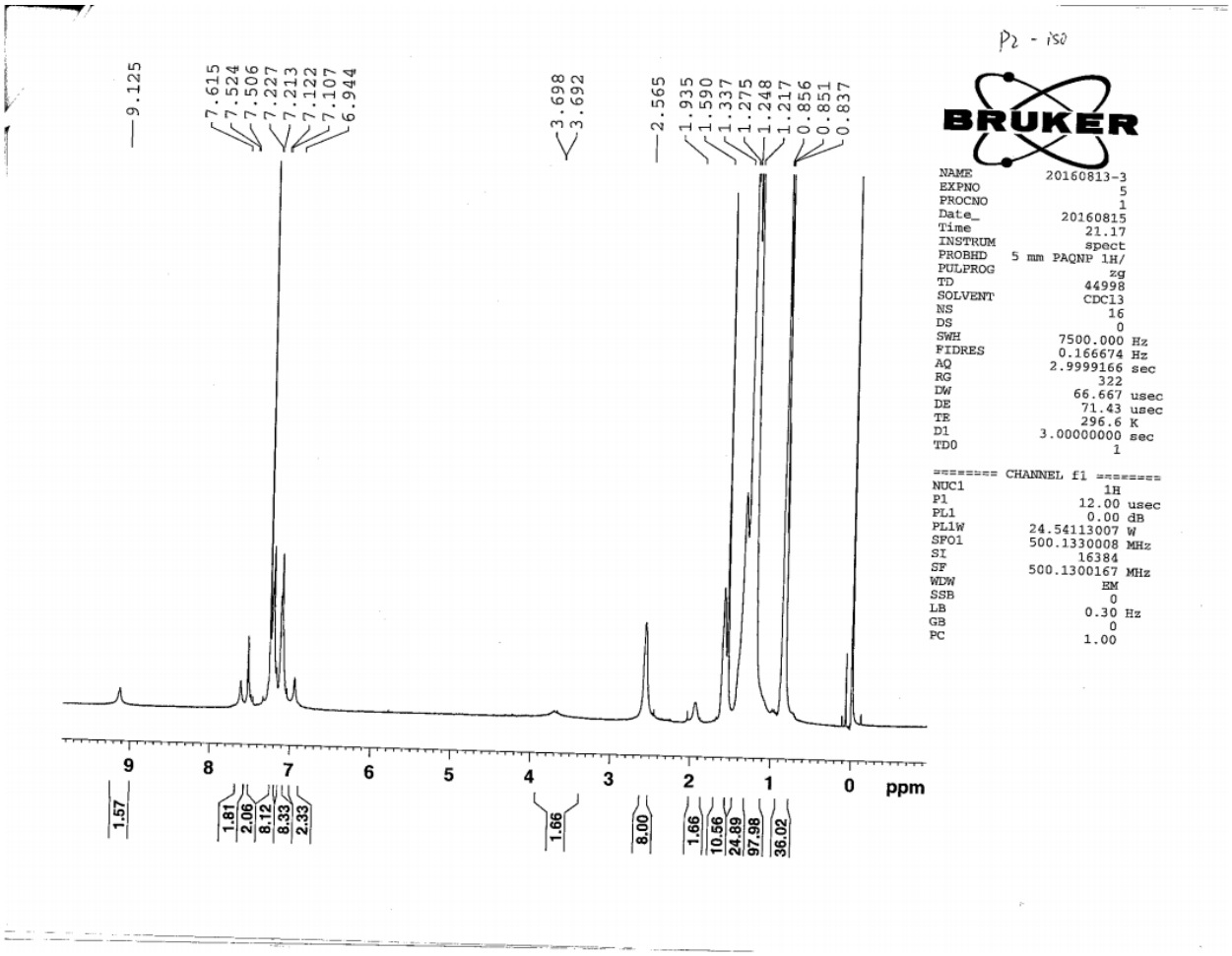

Figure 3.8.1.3.

Synthesis of P3. This was prepared following the general procedure given for the preparation of **P1**. From 1 (133 mg, 0.10 mmol) and 5 (41.1 mg, 0.10 mmol), there was obtained **P3** (118 mg, 92.9 % yield). ^{1}H NMR (400 MHz, $CDCl_3$, δ): 7.57 -7.52 (m, 3H), 7.23 (m, 8H), 7.16 (m, 8H), 3.25 (s, 2H), 2.60 (s, 8H), 1.91 (s, 1H), 1.88 (s, 10H), 1.36-1.11 (m, 30H), 1.00 (s, 4 H), 0.89 (m, 18H). GPC: Mn = 22.6 kDa, Mw = 59.1 kDa, PDI = 2.61. Anal. Calcd for $C_{83}H_{92}OS_6$: C, 76.80; H, 7.14; S, 14.82. Found: C, 74.85; H, 6.95; S, 14.20.

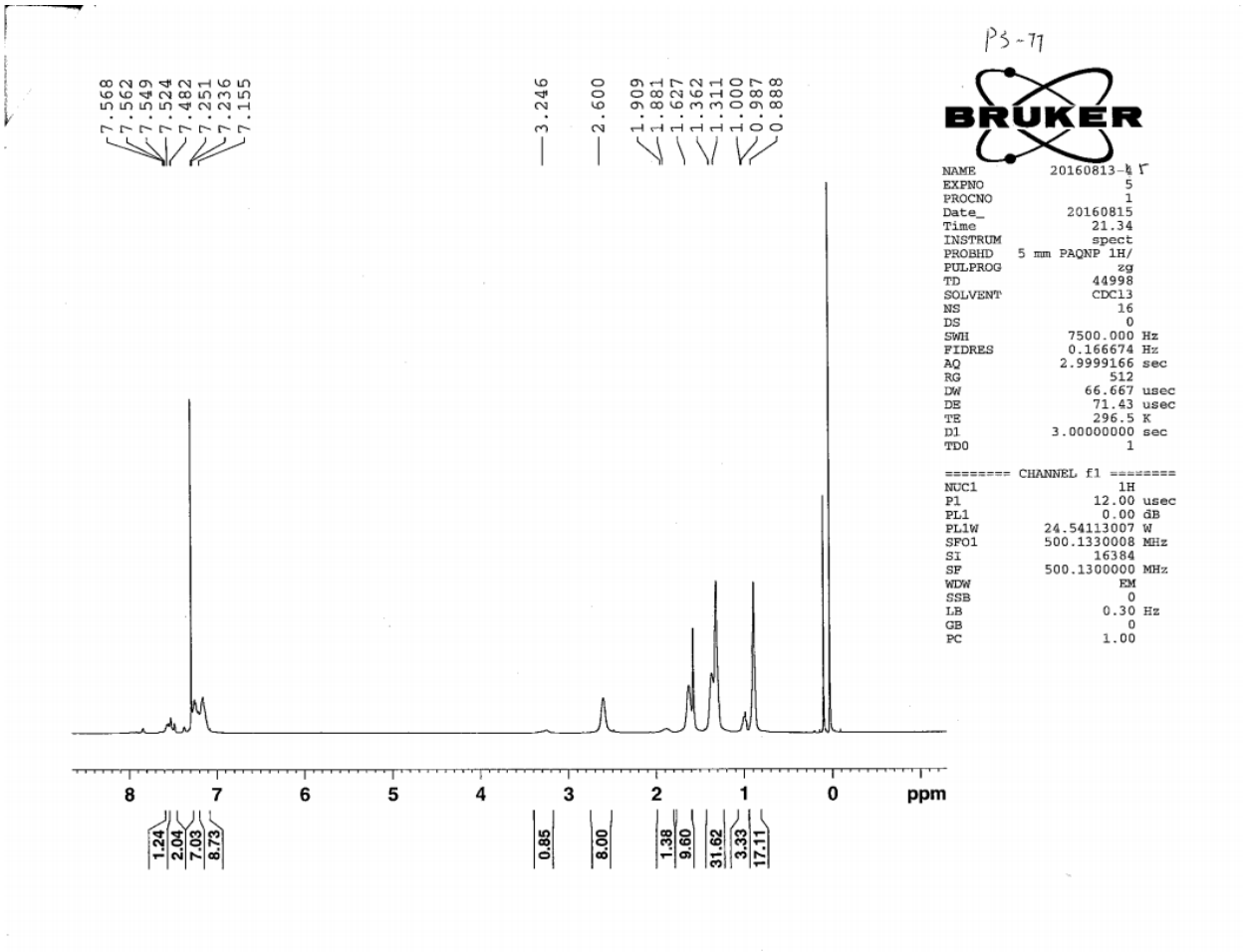

Figure 3.8.1.4.

Synthesis of P4. This was prepared following the general procedure given for the preparation of **P1**. From 3 (200 mg, 0.16 mmol) and 3 (162 mg, 0.16 mmol), there was obtained **P4** (262 mg, 90.8 % yield). ^{1}H NMR (400 MHz, $CDCl_3$, δ): 8.86 (s, 2H), 7.41 (s, 2H), 7.17 (m, 10H), 7.09 (m, 8H), 3.01 (s, 4H), 2.57 (s, 8H), 1.94 (s, 2H), 1.59 (m, 8H), 1.23-1.81 (m, 92H), 0.87-0.81 (m, 24H). GPC: Mn = 34.1 kDa, Mw = 62.8 kDa, PDI = 1.84. Anal. Calcd for $C_{118}H_{160}N_2O_2S_4$: C, 80.22; H, 8.13; N, 1.59; S, 7.26. Found: C, 80.25; H, 8.13; N, 1.66; S, 7.27.

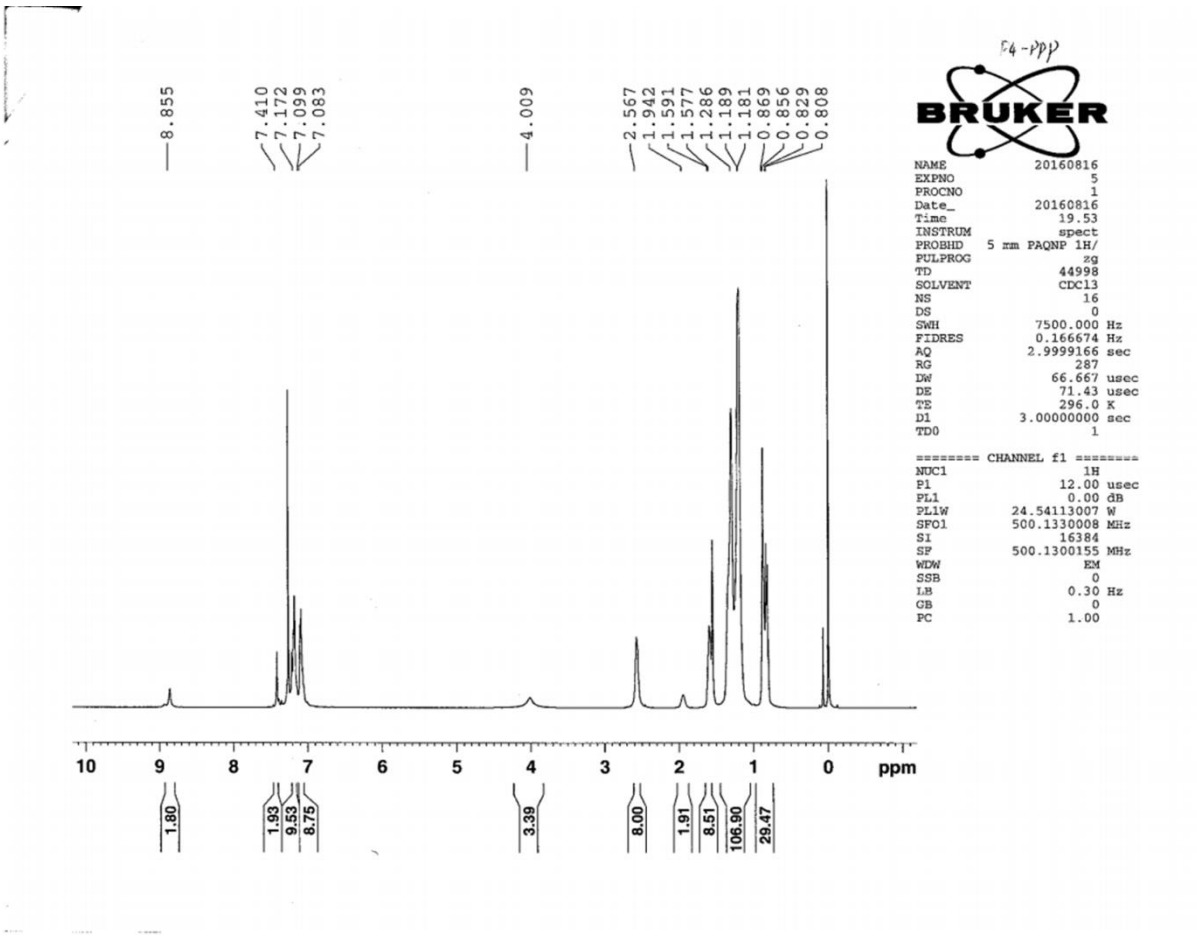

Figure 3.8.1.5.

Synthesis of P5. This was prepared following the general procedure given for the preparation of **P1**. From 2 (200 mg, 0.16 mmol) and 4 (68 mg, 0.16 mmol), there was obtained **P5** (261 mg, 94.3 % yield). ^{1}H NMR (400 MHz, $CDCl_3$, δ): 9.12 (s, 2H), 7.45 (s, 2H), 7.33 (s, 2H), 7.22 (d, 8H), 7.09 (m, 8H), 6.93 (s, 2H), 3.69 (s, 2H), 2.57 (s, 8H), 1.92 (s, 2H), 1.59 (m, 8H), 1.34-1.20 (m, 94H), 0.87-0.82 (m, 24H). GPC: Mn = 22.6 kDa, Mw = 46.8 kDa, PDI = 1.90. Anal. Calcd for $C_{120}H_{162}N_2O_2S_2$: C, 83.37; H, 9.45; N, 1.62; S, 3.71. Found: C, 83.27; H, 9.34; N, 1.61; S, 3.79.

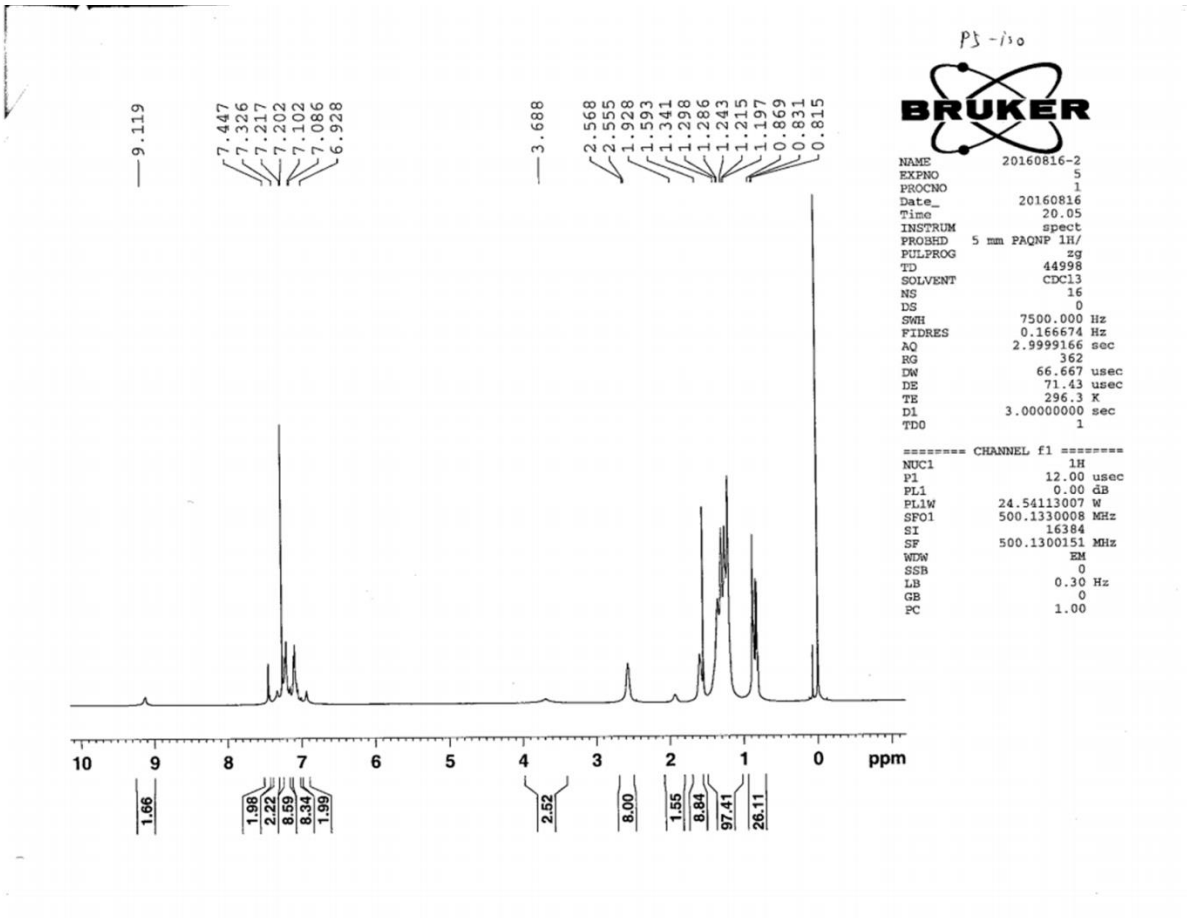

Figure 3.8.1.6.

Synthesis of P6. This was prepared following the general procedure given for the preparation of **P1**. From 2 (200 mg, 0.16 mmol) and 5 (157 mg, 0.16 mmol), there was obtained **P6** (173 mg, 91.2 % yield). ^{1}H NMR (400 MHz, $CDCl_3$, δ): 8.02 (m, 1H), 7.49 (m, 2H), 7.20 (m, 8H), 7.11 (m, 8H), 3.26 (s, 2H), 2.60 (s, 8H), 1.81 (s, 1H), 1.62 (m, 10H), 1.32 (m, 30H), 1.0-0.9 (m, 22H). GPC: Mn = 28.3 kDa, Mw = 55.5 kDa, PDI = 1.96. Anal. Calcd for $C_{79}H_{92}N_2OS_4$: C, 80.01; H, 7.82; S, 10.82. Found: C, 80.01; H, 7.64; S, 10.60.

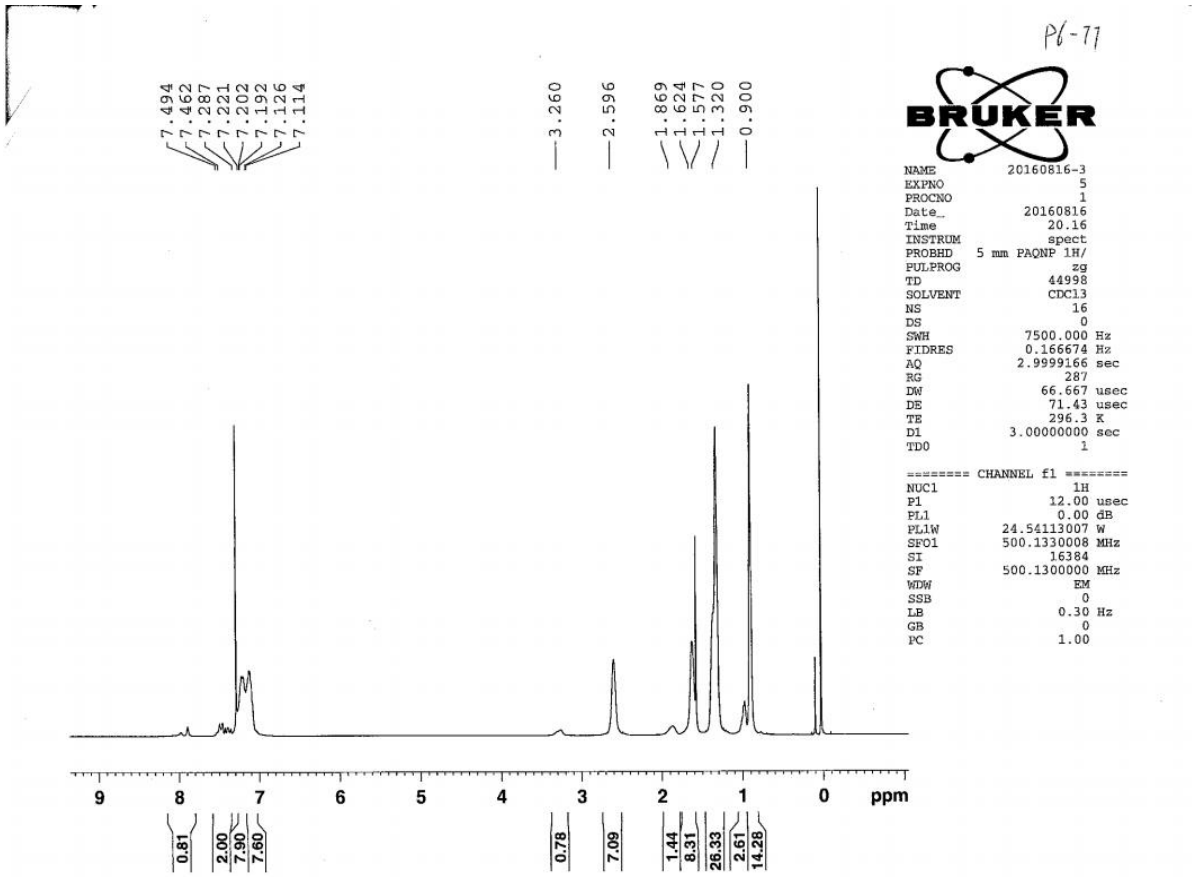

Figure 3.8.1.7.

3.8.2 Quantum Chemical Calculations

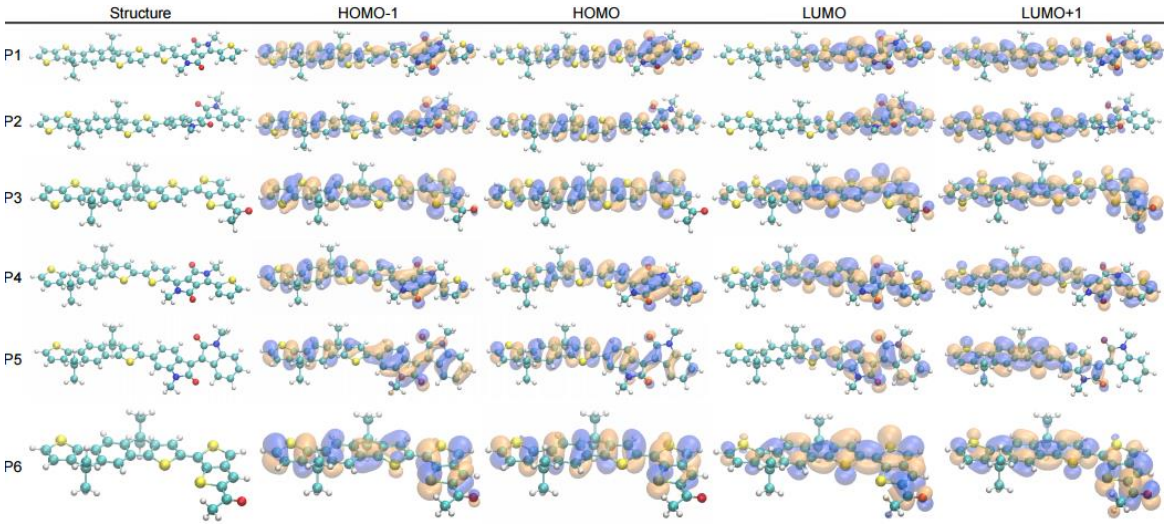

Figure 3.8.2.1.

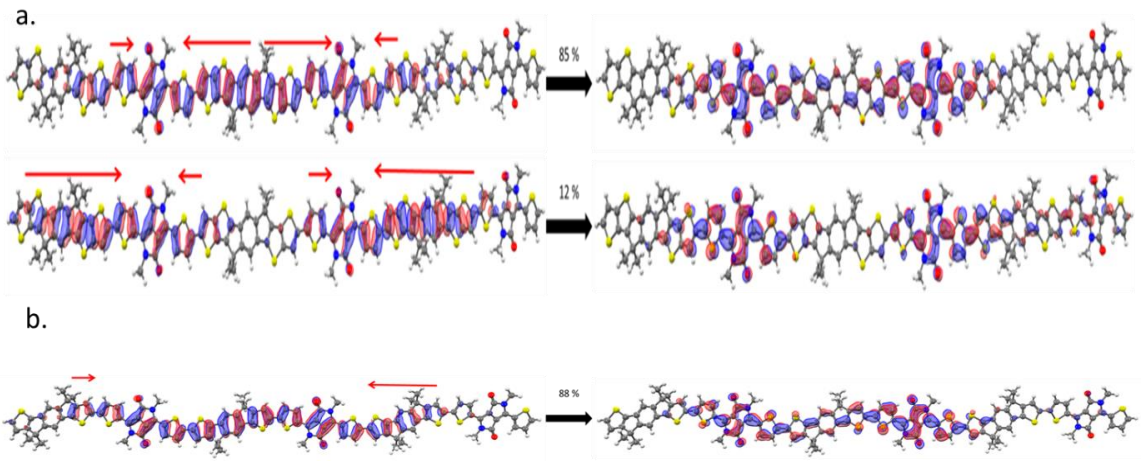

Figure 3.8.2.2.

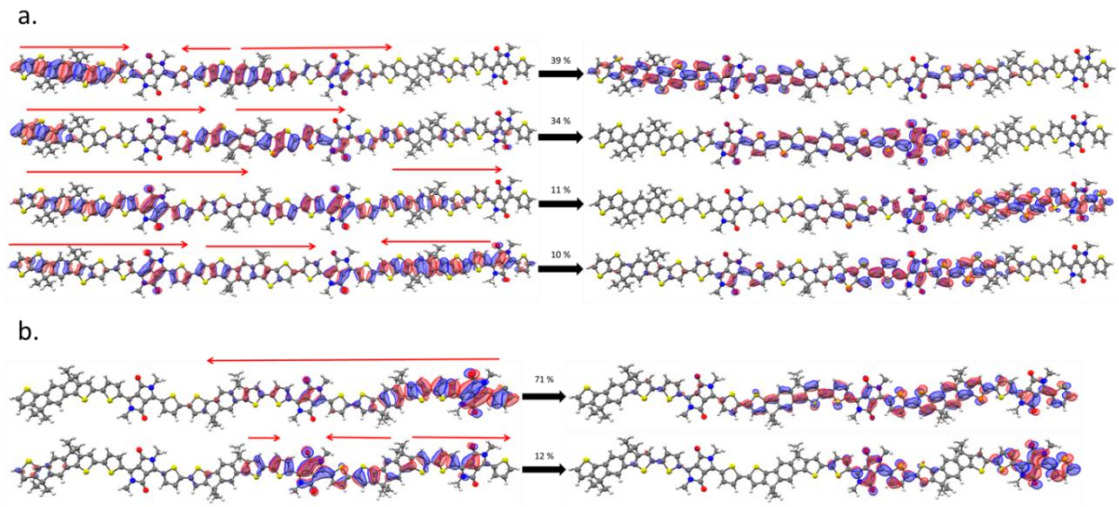

Figure 3.8.2.3.

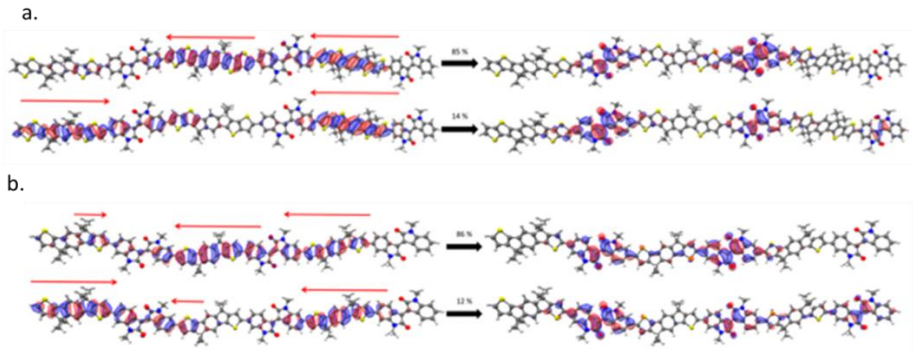

Figure 3.8.2.4.

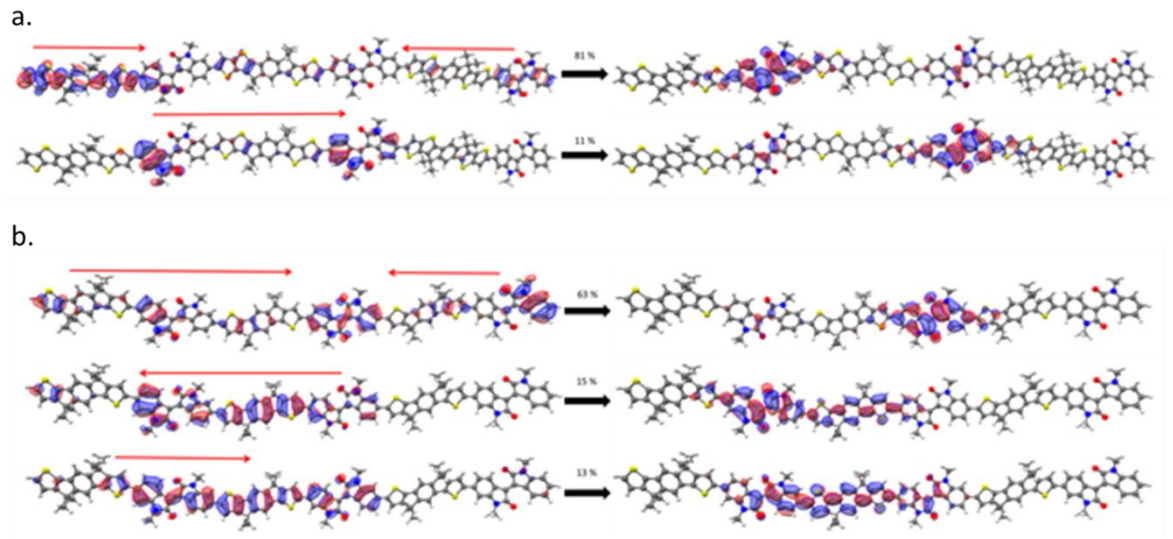

Figure 3.8.2.5.

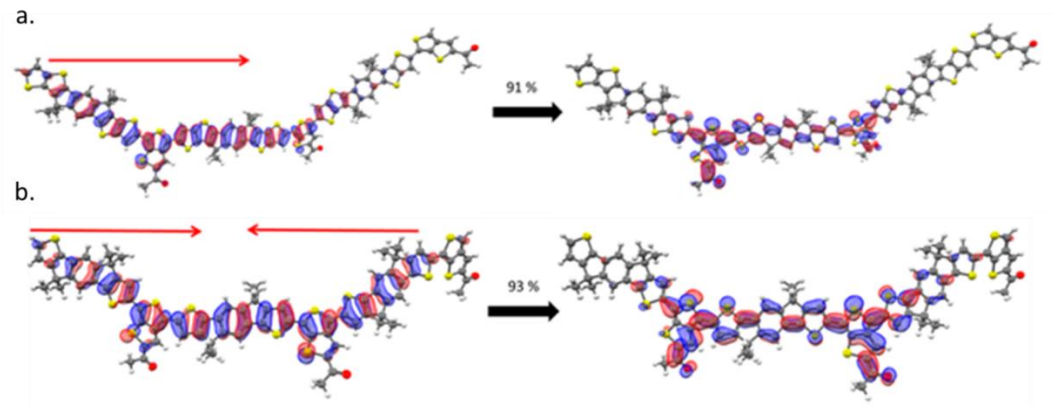

Figure 3.8.2.6.

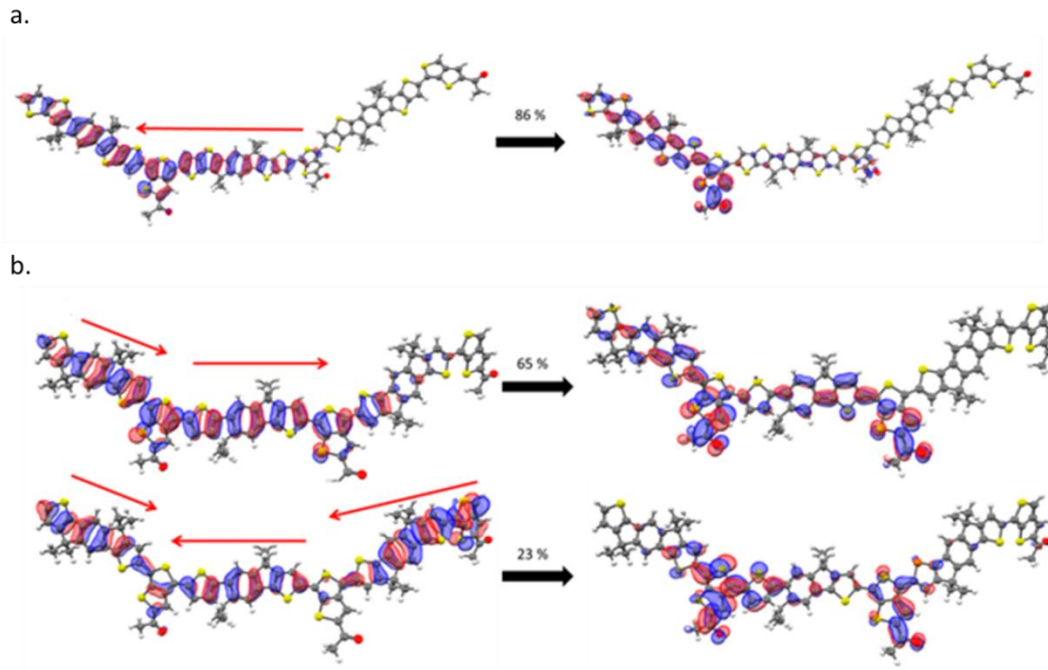

Figure 3.8.2.7.

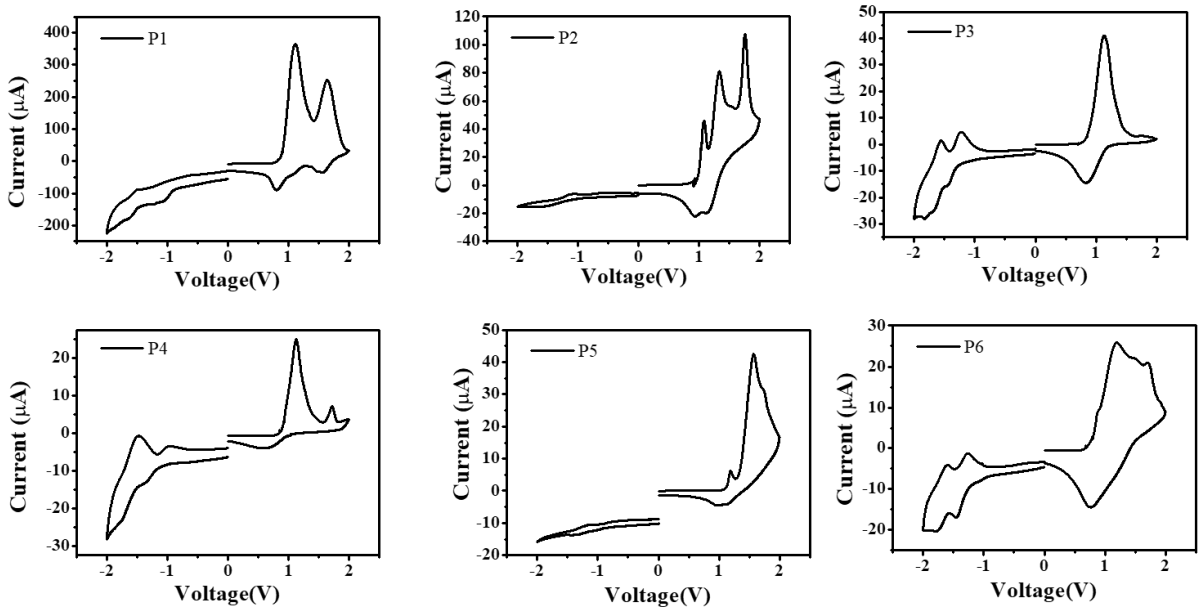

Figure 3.8.2.8.

References

1. Sun Y., Chien S.-C., Yip H.-L., Zhang Y., Chen K.-K., Zeigler D. F., Chen F.-C., Lin, B., Jen A. K.-Y. High-Mobility Low-Bandgap Conjugated Copolymers Based on Indacenodithiophene and Thiadiazolo[3,4-*c*]Pyridine Units for Thin Film Transistor And Photovoltaic Applications. *J. Mater. Chem.*, **2011**, *21*, 13247-13255.
2. Xu Y.-X., Chien S.-C., Yip H.-L., Ding F. Z., Li Y. X., Li C.-Z., Li X., Chen W.-C. Improved Charge Transport and Absorption Coefficient in Indacenodithieno[3,2-b]thiophene-based Ladder-Type Polymer Leading to Highly Efficient Polymer Solar Cells. *Adv. Mater.*, **2012**, *24*, 6356-6361.

Chapter 4

Activating Intramolecular Singlet Exciton Fission by Altering π−Bridge Flexibility in Perylene Diimide Trimers for Organic Solar Cells

4.1 Original Publication Information and Author Contribution

Portions of this chapter were taken from a paper that was published in the *Chemical Science* journal with the title:

This work was accepted by the *Chemical Science* with the title:

"Activating Intramolecular Singlet Exciton Fission by Altering π−Bridge Flexibility in Perylene diimide Trimers for Organic Solar Cells" Benedetta Carlotti, Ifeanyi K. Madu, Hyungjun Kim, Zhengxu. Cai, Hanjie Jiang, Angelar K. Muthike, Luping Yu, Paul M. Zimmerman, Theodore Goodson III.

In this work, my major contribution was performing the nanosecond transient absorption expeirments which is important in probing the emissive and nonemissive excited state dynamics of these systems. In addition, I carried out the triplet energy transfer sensitization as well as relative actinometry experiments and used the obtained data to calculate the triplet extinction coefficients of the investigated systems as well as their final triplet quantum yields. This experiment was used to accurately calculate the triplet quantum yields of the systems and to determine which system showed intramolecular singlet exciton fission (iSEF). Here, I find that the flexible compound shows a triplet quantum yield of 170% while the rigid planar compound shows a triplet quantum yield of only 16%.

4.2 Abstract

In this study, two analogous perylene diimide (PDI) trimers, whose structures show rotatable single bond π−bridge connection (twisted) vs. rigid/fused π−bridge connection (planar), were synthesized and investigated. We show via time resolved spectroscopic measurements how the π−bridge connections in A−π−D−π−A−π−D−π−A multichromophoric PDI systems strongly

affect the triplet yield and triplet formation rate. In the planar compound, with stronger intramolecular charge transfer (ICT) character, triplet formation occurs via conventional intersystem crossing. However, clear evidence of efficient and fast intramolecular singlet exciton fission (iSEF) is observed in the twisted trimer compound with weaker ICT character. Multiexciton triplet generation and separation occur in the twisted (flexible−bridged) PDI trimer, where weak coupling among the units is observed as a result of the degenerate double triplet and quintet states, obtained by quantum chemical calculations. The high triplet yield and fast iSEF observed in the twisted compound are due not only to enthalpic viability but also to the significant entropic gain allowed by its trimeric structure. Our results represent a significant step forward in structure−property understanding, and may direct the design of new efficient iSEF materials.

4.3 Introduction

The scientific benefits and applications of understanding the dynamics of multiexciton triplet generation in organic chromophores cannot be overemphasized. One benefit is evaluating the actual potential impact singlet exciton fission (SEF) has on improving the power conversion efficiency (PCE) of organic solar cells.[1] The effect of SEF on the device photocurrent has been demonstrated by means of magnetic field dependent measurements in literature reports.[2–4] Another benefit is to account for the excess absorption energy used to generate singlet electron−hole pairs often lost as heat.[5] Finally, understanding the dynamics of multiexciton generation aids in the careful design and synthesis of selective organic chromophores with high SEF yields, to be used in photovoltaic devices or photocatalytic cells, for the generation of more photocurrent.[6–8] The ability to advance our insight is limited by the number of materials capable of undergoing SEF.[9,10] A lot of focus has been placed on acenes (mostly tetracene, pentacene) since the discovery of SEF in anthracene crystals.[7,11–17] There are relatively fewer SEF studies on perylene diimides (PDIs),[18,19] which are mostly used as electron acceptors in non−fullerene photovoltaic devices, in comparison to acenes. Understanding the science and mechanism by which PDI acceptors themselves exhibit SEF can be beneficial in avoiding the extra layer to be taken up by a "SEF sensitizer" in an actual photovoltaic device, reducing the complexity, cell thickness, and greatly improving the absorption of solar photons.

Intermolecular SEF (xSEF) has been observed in solid state aggregates of PDI derivatives.[18–22] High rate of xSEF has often been associated to highly–ordered crystalline systems

in comparison to their amorphous counterpart. This has been associated with a SEF assisted process – crystal lattice vibration.[23] The ordered chromophores have to be in close proximity and achieve a slip–stacked or herringbone dimeric structure. This leads to them having weaker interchromophore (excitonic) interactions.[24] In these solid state films, triplet formation is significantly influenced by the morphology and crystal packing, which are usually difficult to control. Hence, for devices made with xSEF chromophores where solid–state packing interactions are crucial, slight perturbations can have a drastic effect on the rate and yield of xSEF. This limits the understanding of the underlying key factors affecting the rate and efficiency of singlet fission in xSEF materials. To this regard, a more suitable approach would be intramolecular singlet exciton fission (iSEF).[13,25–29] Materials capable of iSEF can overcome these challenges because each molecule undergoes SEF via through–bond interactions in multichromophoric systems – that is, not depending on intermolecular orientation, intermolecular coupling, or through–space interactions.

Donor–Acceptor configuration, which induces an intramolecular charge transfer character, is a molecular design strategy for iSEF molecules.[10] Another strategy involves the covalent coupling of two xSEF chromophores where the triplet yield has been reported to be affected by the conjugation between the two chromophores.[14,15,30–32] There are also reports about the effects of through–bond proximity between the chromophores on the triplet production. Campos et al[13] gave a very detailed account for pentacene dimers where the proximity of the pentacene moieties and the extent of conjugation was varied using (oligo) phenylene spacers. It was suggested that the rate of singlet fission (rate of triplet production) and the rate of recombination of the two triplets could be controlled by using spacers of varying length. In another study, Thompson et al[17] looked at how connecting two SEF chromophores to a bridge moiety at its *ortho*, *meta* or *para* position influences the through–bond and through–space contributions to the coupling of the compound. Intramolecular SEF was observed only in the *ortho* and *para* systems, not in the *meta*; and this was associated to the lack of effective conjugation, hence very weak coupling, causing predominantly radiative decay of the excited state. However, all these studies were reported for acene dimers for the end purpose of sandwiching them with organic photovoltaic (OPV) active layer materials. There are little to no studies about the effects of the π−bridge in multichromophoric OPV active layer materials themselves, e.g. PDIs, in tuning the iSEF rate or in activating/deactivating iSEF.

The aim of this study is to investigate the unique role of the π−bridge in allowing or inhibiting triplet production (rate and yield) in oligomeric multichromophoric PDI systems. In few recent literature reports,[15–17] structural flexibility of the covalently linked units has been proposed to be crucial in activating SEF. However, these studies lack a direct comparison with rigidly bridged units of the same chromophore in order to isolate the effects of π−bridge flexibility. This is what our current investigation seeks to illuminate − the impact of the π−bridge rotation vs. rigidity on the dynamics of triplet exciton formation, and the triplet production efficiency. Most literature studies involve dimers. Investigations about oligomeric structures, with more than two chromophores attached linearly, are very few. In the development of iSEF−OPV materials using a strong Acceptor−strong Donor configuration,[10] the role of the flexibility/rigidity of the π−bridge in influencing the triplet production rate and efficiency, has not been investigated.

In this work, two PDI trimers with push−pull character were synthetized (see **Figure 4.3.1**). For each molecule, the unit PDI electron acceptor moieties are bridged at the beta (β) position(s) with benzodithiophene (BDT) electron donor moieties, forming an A−D−A−D−A assembly. The connections between the donor and the acceptor moieties were realized via single bonds in the **β** compound, and through ring cyclization in the **βC** compound (color coded in the structures in **Figure 4.3.1**). This results in the single−bond−bridged **β** compound having a twisted PDI−BDT−PDI structure (dihedral angles ∼ 55°), and the cyclized **βC** compound achieving a planar PDI−BDT−PDI structure (dihedral angles ∼ 0°). These two compounds show different triplet production dynamics owing to their respective degree of electronic coupling. The photoinduced dynamics of triplet production – via iSEF or regular intersystem crossing (ISC) – was thoroughly investigated with a variety of time resolved spectroscopic techniques, employing both femtosecond and nanosecond time resolution while probing both excited state absorption and emission. The experimental spectroscopic study was carried out in a joint effort with theoretical calculations to further elucidate the excited state deactivation mechanism of the two compounds.

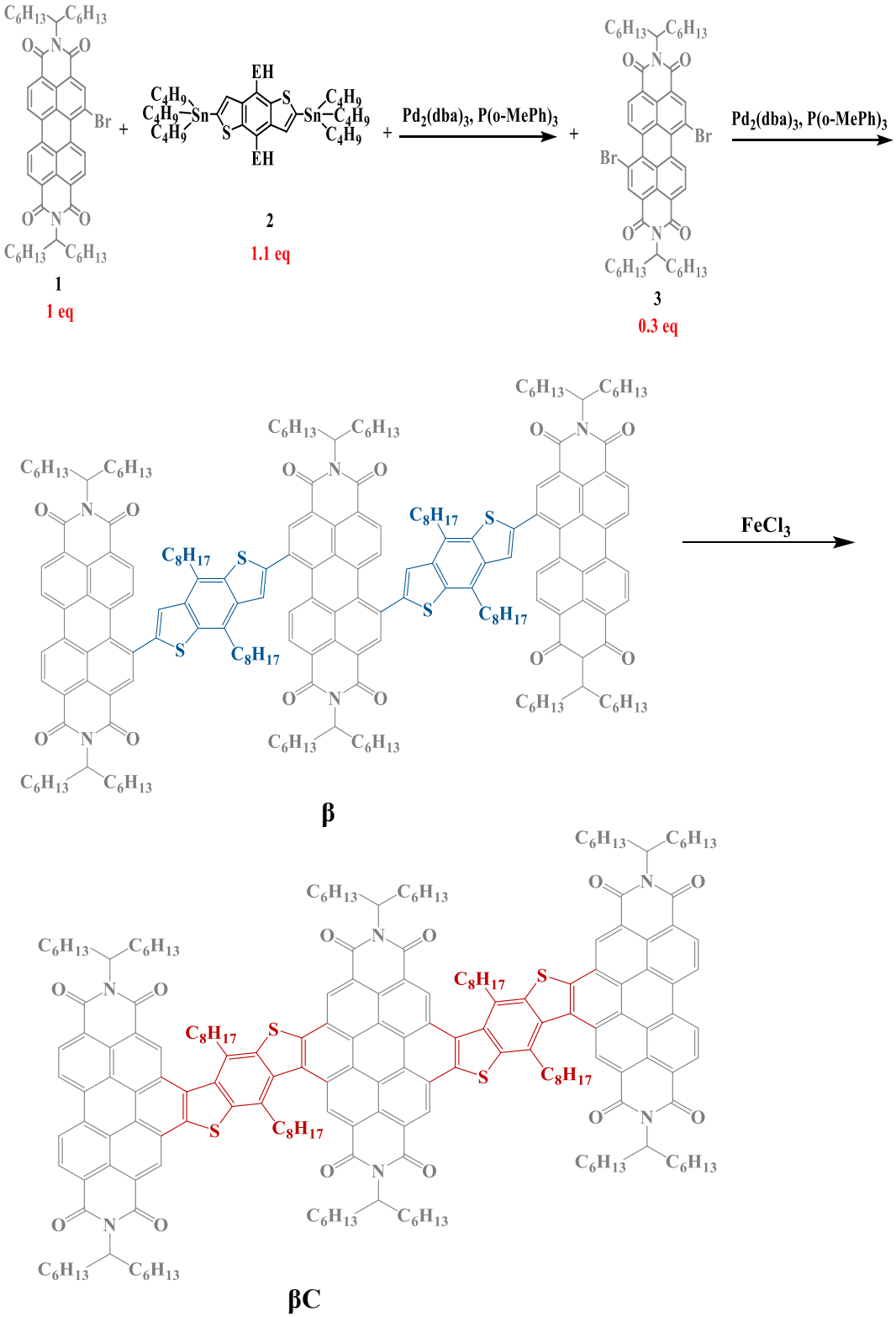

Figure 4.3.1. Molecular structures of the investigated trimers.

4.4 Results

4.4.1 Steady–State and Two–Photon Absorption Measurements

The steady-state absorption and emission spectra of the investigated trimers are shown in **Figure 4.4.1.1**. These electron acceptor compounds are excellent light absorbers with sizable molar extinction coefficients, ca. 60000−70000 M^{-1} cm^{-1} (**Table 4.4.1.1**). Their broad absorption spectra extend in a region complementary to that of electron donors employed in OPV devices. Both the absorption and emission spectra of **β** appear to be less structured in comparison to those of **βC**. The structured spectra and small Stokes shift (**Figure 4.4.1.1**/**Table 4.4.1.1**) of the **βC** compound reflect its molecular rigidity. The emission spectrum of **β** is extremely broad and its peak is significantly red shifted in comparison to the emission peak of **βC**. The extremely broad emission spectrum and the large Stokes shift suggest a drastic rearrangement of this flexible molecule in the excited state.[33,34] The theoretical calculations indeed reveal that the **β** compound has a twisted PDI−BDT−PDI structure (dihedral angles ~ 55°), and the **βC** compound has a planar PDI−BDT−PDI structure (dihedral angles ~ 0°) (**Figure 4.7.7.1**). In both cases, the hole transition orbitals are localized on the electron-rich BDT units, and electron transition orbitals show more localization on the PDI acceptor unit(s) (**Figure 4.4.1.2**). Also, the theoretical calculations reveal electron localization on only one PDI unit for the twisted **β** compound, but complete delocalization across all trimer units for the planar **βC** compound. This indicates minimal ground state interaction or excitonic coupling among the chromophores[35] in **β** – hence its similar absorption peak (λ^{max}) to that of the parent PDI monomer (Figure **4.4.1.1**). However, the spectral behavior of **βC** is indicative of a much stronger coupling among the PDIs, and with the BDT core.

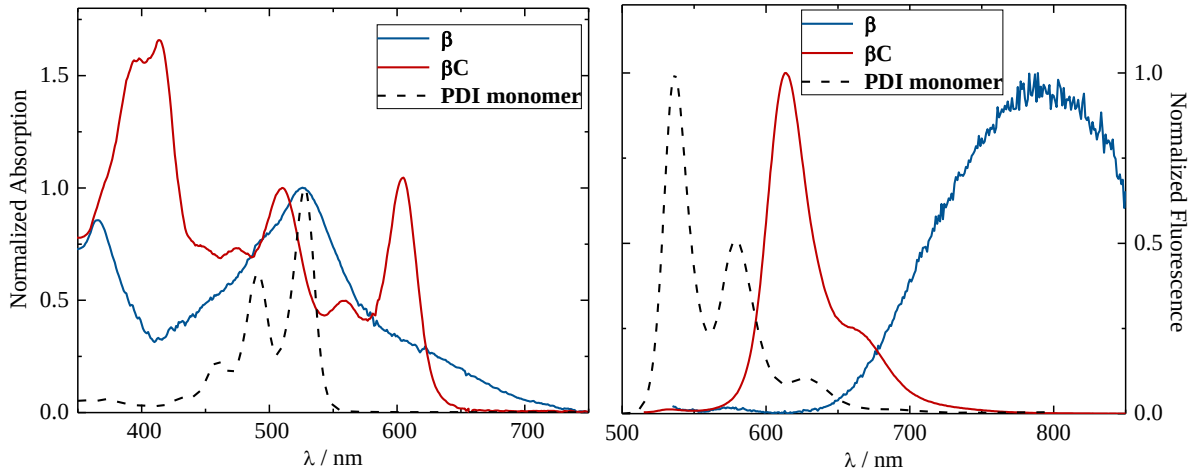

Figure 4.4.1.1. Normalized absorption and emission spectra of the trimers in chloroform.

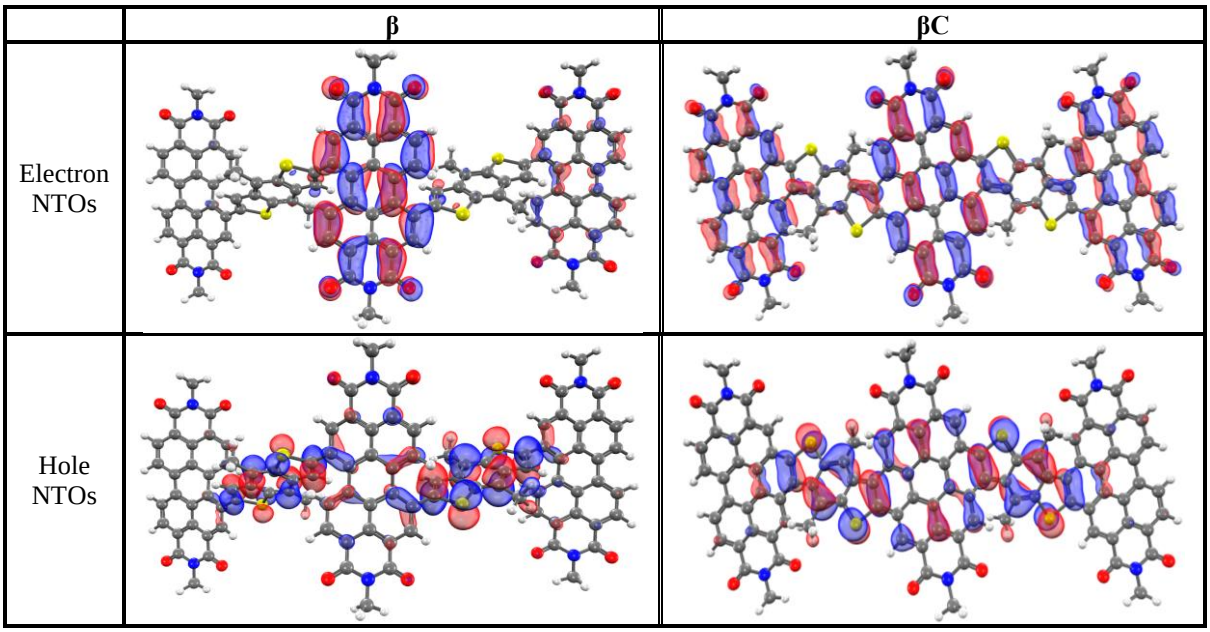

Figure 4.4.1.2. Natural transition orbitals for the S_0 geometry ($S_0 \rightarrow S_1$ transition) of the trimers (isodensity=0.05. Color scheme; Hydrogen—white, carbon—black, nitrogen—blue, oxygen—red, sulfur—yellow).

No concentration effect on the absorption spectral shape was observed in the range of concentrations employed in this investigation (see **Figure 4.7.2.1**), which are similar to, or lower than the 'low concentration'/dilute limit employed in other literature studies about xSEF compounds in solution.[36] Therefore, it is possible to rule out the occurrence of any intermolecular interactions due to aggregation which may affect our experimental results. Hence, the optical properties exhibited by the compounds investigated here are due to isolated molecules in solution.

The fluorescence quantum yield of the investigated compounds is low (0.3% and 9%, see **Table 4.4.1.1**) in comparison to that of the parent PDI monomer (88%).[37] The fluorescence efficiency is 30 times lower in the case of compound **β** relative to **βC**. This behavior parallels the observed trend of the Stokes shift in the two trimers and agrees with the increased molecular rigidity of **βC** relative to **β**. More rigid molecular structures are indeed known to exhibit enhanced fluorescence capability.[33,38] This result suggests that the excited state deactivation of these trimer compounds takes place mainly through non−radiative pathways − possibly triplet production/decay, in competition with the fluorescence decay pathway. This non−radiative

deactivation is more efficient for the twisted **β** compound, whose fluorescence quantum yield is almost negligible.

Previous studies have observed the relationship between molecular planarity and two−photon absorption.[34,39,40] Here, the two−photon absorption cross section (δ_{TPA}) is enhanced by over one order of magnitude for the planar **βC** (ca. 300 GM) relative to the twisted **β** compound (ca. 10 GM). The increased two−photon absorption cross section of the planar, rigid, fused ring connected molecule, as expected, indicates its higher intramolecular charge transfer character in the excited state relative to the twisted, flexible, single bond bridged analogue. The degree of charge transfer for the **β** and **βC** excited state was further analyzed in detail with the help of quantum chemical simulations. These compounds were divided into 5 subunits/moieties, considering their acceptor(1)−donor(2)−acceptor(3)−donor(4)−acceptor(5) structure where the acceptors and the donors are the PDI the BDT fragments, respectively. The NTOs computed on the S_1 geometry which describe the $S_1 \rightarrow S_0$ transition are shown in **Figure 4.7.7.4**, and the amount of charge transferred during emission is reported in **Table 4.7.2.1**. The charge transfer degree for the excited state of **βC** (0.80 e^-) is indeed higher than that of **β** (0.74 e^-).

Table 4.4.1.1. Absorption and fluorescence properties, and two–photon absorption cross sections for the Trimers in chloroform.

Comp.nd	λ_{abs} / nm	λ_{em} / nm	$\Delta\upsilon^a$ /cm^{-1}	ε^b / $M^{-1}cm^{-1}$	ϕ_F / %	δ_{TPA} / GM λ_{exc}=810 nm	δ_{TPA} / GM λ_{exc}=875 nm
β	<u>526</u>, 630$^{(sh)}$	790	3215	71100	0.3	–[c]	11.5
βC	<u>510</u>, 605	613, 665$^{(sh)}$	215	58500	9	227	318

[a]Δυ is the Stokes shift; [b]at the underlined wavelength; [c]at λ_{exc}=810 nm, strong interference from one photon excited fluorescence was observed due to the long wavelength tail of the **β** absorption spectrum (**Figure 4.4.1.1**).

4.4.2 Femtosecond Transient Absorption

The excited state dynamics was investigated by femtosecond transient absorption. The time resolved spectra (**Figures 4.4.2.1** & **Figure 4.7.3.1.**) show positive excited state absorption (ESA) and negative Ground State Bleaching (GSB) signals. The ESA at 740 nm has been previously associated with the PDI anion, whereas signals between 550 and 600 nm have been assigned to the PDI cation.[41–47] The transient spectra of the investigated trimers at short delays following photoexcitation suggest the occurrence of intramolecular charge transfer (ICT), and no significant spectral shift was observed. It is possible that a singlet excited state with ICT character is formed

very fast (within solvation).[47] At longer delays this signal decays, resulting in the simultaneous formation of an ESA at 514 nm and 543 nm for **β** and **βC**, respectively. The kinetics at these wavelengths exhibit a rise (**Figure 4.4.2.1**). This rise occurs very fast for the twisted **β** compound (344 ps), but clearly slower for the rigid−bridged **βC** compound (1800 ps). Global analysis, via singular value decomposition (SVD), of the transient absorption data revealed the presence of four exponential components (**Figure 4.7.3.1**B & **Table 4.7.3.1**). The first two fast components can be associated to solvation and vibrational cooling/structural relaxation. The third component, assigned to the relaxed S_1, shows a lifetime of 320 ps for the **β** compound and 1300 ps for the **βC** compound. The fourth component represents the Rest species formed upon S_1 decay and peaked around 510−550 nm. This long−lived species are triplets, as demonstrated by their spectral similarity to the species detected by nanosecond transient absorption (see next section). Therefore, the ultrafast absorption measurements allow us to follow the triplet formation dynamics in these molecules. The triplet formation occurs fast for **β** (~340 ps) and much slower for **βC** pointing to different mechanisms for triplet production in the two molecules−SEF for **β** and ISC for **βC**, respectively. Additionally, triplet formation takes place slower in a less polar solvent relative to chloroform (e. g. for **β** in toluene triplet rise occurs in ca. 690 ps).

Triplet quantum yields were also computed following the SVD analysis of the femtosecond transient absorption results[48–51] (see SI for details on the procedure). Quantitatively related singlet and triplet ESA spectra were obtained by matching their GSB and then the temporal population dynamics of these states were determined. The population data (**Figures 4.7.3.1.5** & **4.7.3.1.10**) indicate a triplet quantum yield of 189 % for **β** and higher than 46 % for **βC**. Although this analysis contains some approximations, our result thus show that triplet production takes place via iSEF for the twisted **β** compound (φ_T close to 200 %) and via conventional ISC for the planar/rigid−bridged **βC** system (φ_T << 100 %).

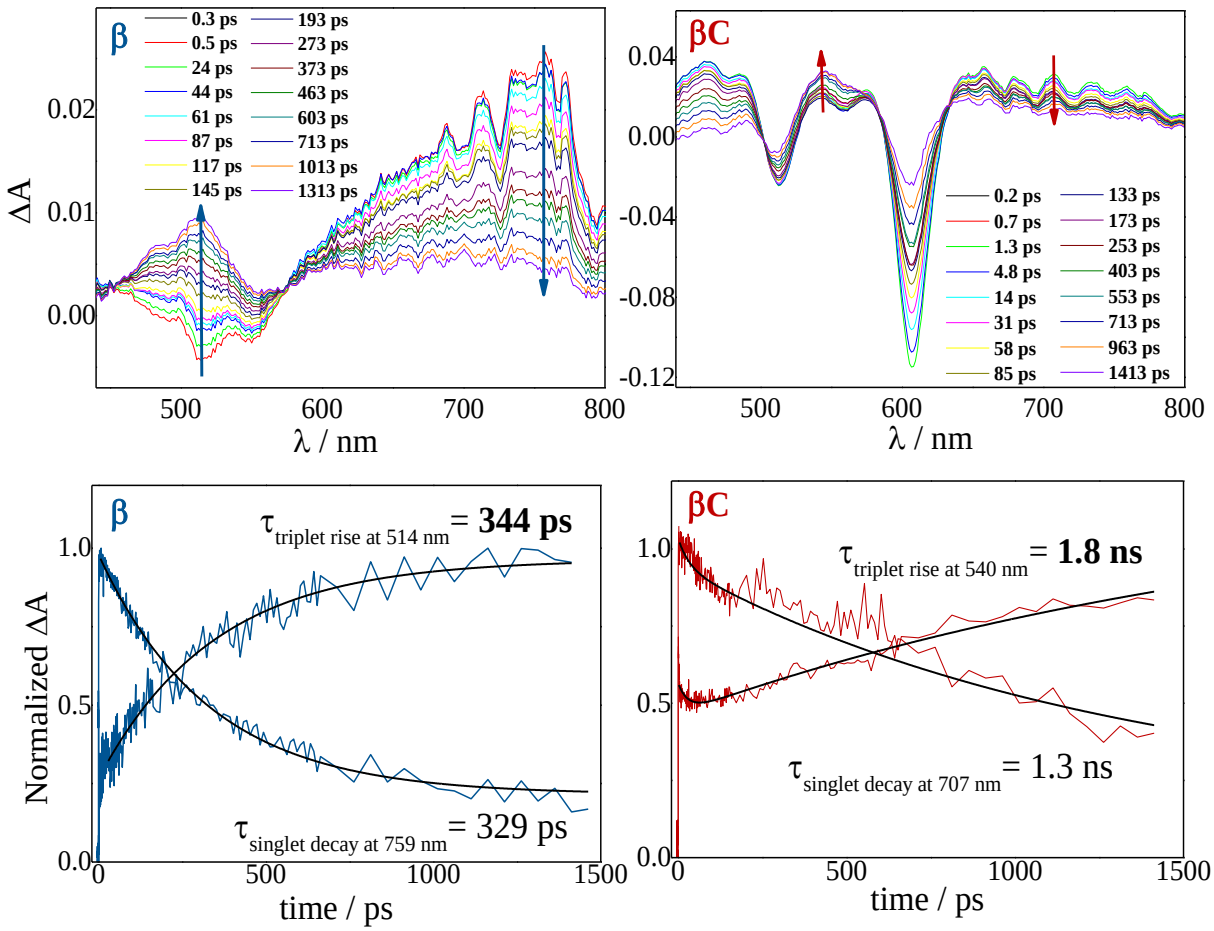

Figure 4.4.2.1. Time−resolved spectra obtained by femtosecond TA for the trimers in chloroform. Singlet decay and triplet rise kinetics for the trimers in chloroform.

4.4.3 Nanosecond Transient Absorption

To investigate the long−lived excited state dynamics, nanosecond transient absorption measurements were carried out (**Figure 4.4.3.1**). No pump wavelength dependence was observed (see **Figure 4.7.4.1**). The transient spectra show negative signals due to GSB, and a positive ESA peak centered at 490 nm and 540 nm for **β** and **βC**, respectively. It is worthy to note that signals of triplet absorption have been reported for other PDI derivatives between 500 and 600 nm.[18,37,52,53] This signal can be quenched by oxygen (either via energy transfer or electron transfer).[54] The transient lifetimes change from hundreds of nanoseconds in air equilibrated solution to tens of microseconds in deaerated/nitrogen purged solution (**Figure 4.7.4.2** & **Table 4.4.3.1**). Quenching by molecular oxygen thus occurs at an almost diffusional rate (1.2×10^{10} $M^{-1}s^{-1}$ in chloroform). Also, these transient species can be sensitized by higher−triplet energy donors, or are able to sensitize lower−triplet energy acceptors, such as tetracene as shown in **Figure 4.4.3.2**. These

results allow us to undoubtedly assign these long−lived transients revealed by nanosecond transient absorption experiments to the $T_n \leftarrow T_1$ transition of the trimers. As shown in **Table 4.4.3.1**, for **β**, the triplets produced upon photoexcitation decay much faster i.e. shorter lifetimes (6.0 μs), in comparison to the triplets produced in **βC** (40 μs). This is an evidence leaning to a SEF−induced mechanism of triplet production in the twisted **β**. It has indeed been observed in many SEF literature studies[17,55–57] that a molecule hosting two triplet excitons usually exhibits a much faster triplet decay than one hosting a single triplet, due to the increased probability of triplet−triplet annihilation.

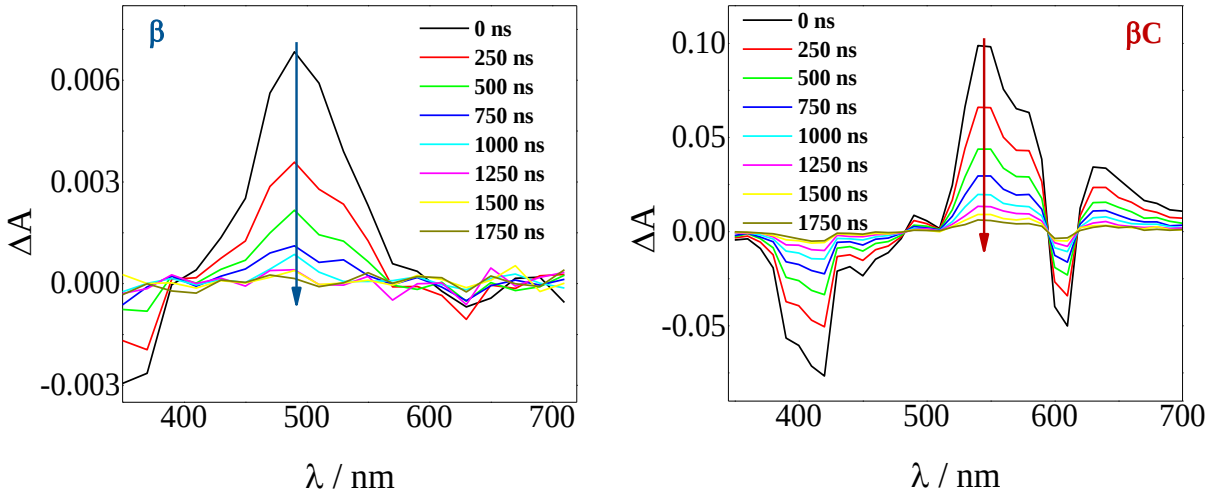

Figure 4.4.3.1. Time−resolved spectra obtained by nanosecond TA measurements for the Trimers in air-equilibrated chloroform upon 415 nm laser excitation.

Table 4.4.3.1. Triplet properties for the trimers in chloroform from nanosecond transient experiments.

Comp.	λ_T / nm	$\tau_{T,air}$ / μs [a]	$\tau_{T,N2}$ / μs [b]	k_{ox} / M^{-1} s^{-1}	$\phi_T \cdot \varepsilon_T$ / M^{-1} cm^{-1}	ε_T / M^{-1} cm^{-1} [c]	ϕ_T
β	490	0.39	6.0[d]	1.0×10^9	2785	1637	1.70
βC	540	0.50	40	0.8×10^9	7460	52800	0.16

[a]in air-saturated chloroform; [b]in N_2-saturated chloroform; [c]in cyclohexane; [d] ~7μs lifetime was obtained by triplet sensitization in cyclohexane, see **Figure 4.7.4.1.5**.

Sensitization experiments were performed via nanosecond transient absorption measurements. These experiments give important information about the triplet energy of the compounds (see **Figure 4.4.3.2**). Tetracene (E_T = 1.27 eV) was successfully employed as an energy donor to sensitize the triplet of **β**, but relatively acted as a triplet energy acceptor to **βC**. This result

proves that the triplet energy of the twisted **β** trimer is significantly lower than the triplet energy of the planar **βC** trimer. Our experimental results thus support the feasibility of SEF in the **β** compound which requires a low triplet energy for the SEF energetic condition to be fulfilled (E_T = 0.55 eV; obtained from theoretical calculations). The sensitization experiments also allowed for the accurate evaluation of triplet extinction coefficients (see **Table 4.4.3.1**), useful for evaluating the singlet → triplet quantum yield. A very detailed step-by-step triplet extinction calculation for the two compounds is given in the Supporting Information. A lower extinction coefficient was observed for the twisted relative to the planar, rigid system. These experiments, together with the relative actinometry measurements described in the Supporting Information, allowed for the accurate computation of the singlet → triplet quantum yields. A triplet quantum yield of 16 % was obtained for the planar **βC** compound, suggesting that conventional intersystem crossing occurs in this chromophore. Triplet yield significantly higher than 100 % was obtained in the case of the twisted **β** compound (ϕ_T =170 %), thus suggesting that iSEF indeed takes place in this molecule.

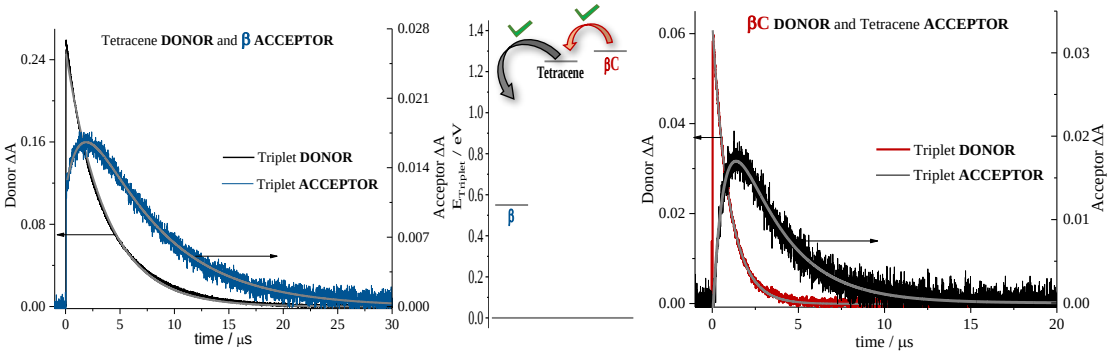

Figure 4.4.3.2. Decay and rise dynamics of trimers (extreme left for **β**; and extreme right for **βC**) in cyclohexane obtained by nanosecond TA for triplet sensitization measurements. Middle graph shows the triplet energy for samples and sensitizers.

4.4.4 Two–Color Transmission Measurements of Triplet Yield

To selectively probe the ESA without contribution from the GSB, the trimer compounds were investigated using two-color transmission spectroscopy.[28] This was performed by probing the samples at 850 nm, where linear absorption is negligible, under excitation with femtosecond pulses at 425 nm. Attenuation of the probe beam was observed for both samples: 29.7 % attenuation for **β** at OD = 0.116 and 34.6 % attenuation for **βC** at OD = 0.885, both under an average pump power of 4.25 mW (**Figure 4.4.4.1**). This demonstrates the accumulation of triplets upon irradiation of the trimers, observed to be more in the case of **β**. Indeed, the theoretical

calculations predicted significant absorption by T_1 species around 850 nm: transition $T_1 \rightarrow T_8$ at 898 nm and $T_1 \rightarrow T_{10}$ at 826 nm for **β**; transition $T_1 \rightarrow T_{16}$ at 849 nm for **βC**.

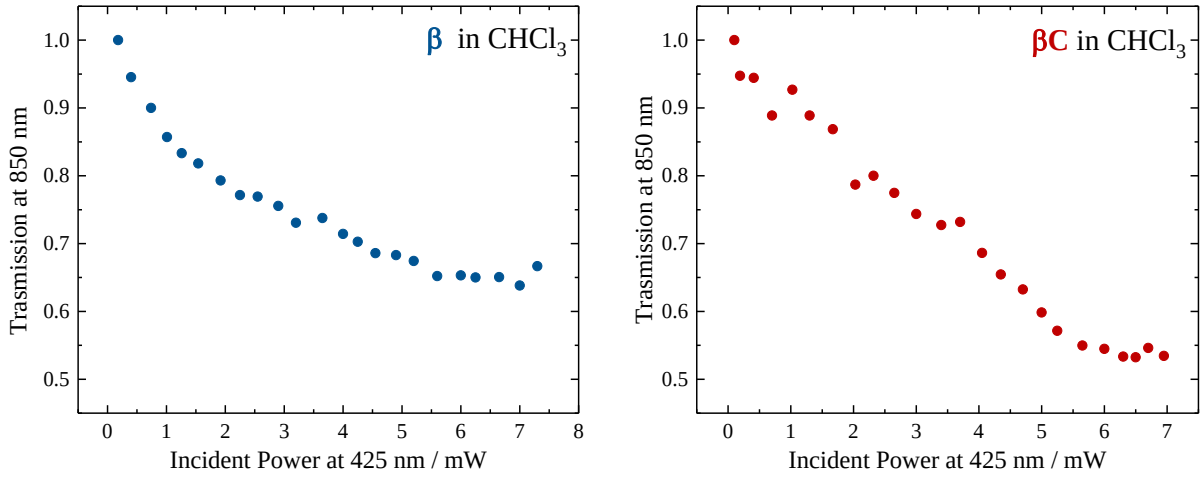

Figure 4.4.4.1. Transmission of **β** (left) and **βC** (right) in $CHCl_3$ for the probe light at 850 nm as a function of the pump power at 425 nm.

Analysis of the obtained results was carried out in order to obtain an estimation of the triplet quantum yield for the two compounds. See the Supporting Information for the detailed calculation performed according to a procedure described in ref. 25. It entails computing the triplet number density using the 850 nm probe beam attenuation (as shown in **Figure 4.4.4.1**) and the singlet excitation number density from the ground state OD and 425 nm pump beam parameters. The triplet extinction coefficients at 850 nm used for this calculation were obtained via nanosecond transient absorption measurements, by taking the ratio of the ΔA signal at 850 nm with that at the triplet peak for which the extinction coefficient is known (see **Table 4.4.3.1** and **Figures 4.7.5.2**, **and 4.7.5.3**). This was accurately done for **β** which had a distinct triplet ESA signal ~850 nm (see **Figure 4.7.5.1**). However, for **βC** the triplet ESA signal was convoluted with the phosphorescence around 850 nm (see **Figure 4.7.5.1**). Therefore, the same ratio of the ΔA signal between the triplet peak and that at 850 nm for **β** was assumed for the **βC** molecule. From the calculation, the triplet number density was evaluated to be 2.32×10^{10} cm^{-3} for **β** and 8.61×10^{8} cm^{-3} for **βC**; the singlet number density 1.24×10^{10} cm^{-3} for **β** and 3.14×10^{11} cm^{-3} for **βC**. Therefore, a much higher triplet quantum yield was indeed obtained for the twisted **β** trimer (~187 %) relative to the planar **βC** (~0.3 %). It has to be noted that for the case of the **βC** compound, the estimated triplet yield value is not accurate because of the observed phosphorescence interference at 850 nm. This analysis contains some approximations, however the result obtained for the **β** trimer is consistent with the

triplet quantum yield accurately measured by the nanosecond transient absorption sensitization experiments. This once again confirms that the **β** compound thus undergo singlet exciton fission in solution, owing to its triplet yield also obtained by two–color transmission measurements to be >> 100%.

4.4.5 Time Resolved Fluorescence

Time resolved fluorescence measurements, both with femtosecond and nanosecond time resolution, have been extremely valuable in providing information about the rate constants of the ultrafast intramolecular charge transfer process and about the decay of the double triplet species, respectively. Fluorescence kinetics were acquired by femtosecond fluorescence up conversion (FUC) (**Figure 4.7.6.1**& **4.7.6.2**). Their fitting revealed the presence of exponential components (**Table 4.7.6.1**), whose lifetimes agree with those obtained via femtosecond transient absorption measurements. The much smaller time window of the FUC allows for a more accurate evaluation of the lifetime of the ultrafast components, as 1.0 ps for **β** and 0.2 ps for **βC**. Our FUC results show that the ICT is indeed faster in the rigid relative to the twisted trimer. Also, that SEF could be a CT−mediated process in the twisted trimer.[10,22] However, when ICT is extremely fast it becomes competitive with SEF, as observed in the planar trimer.[50]

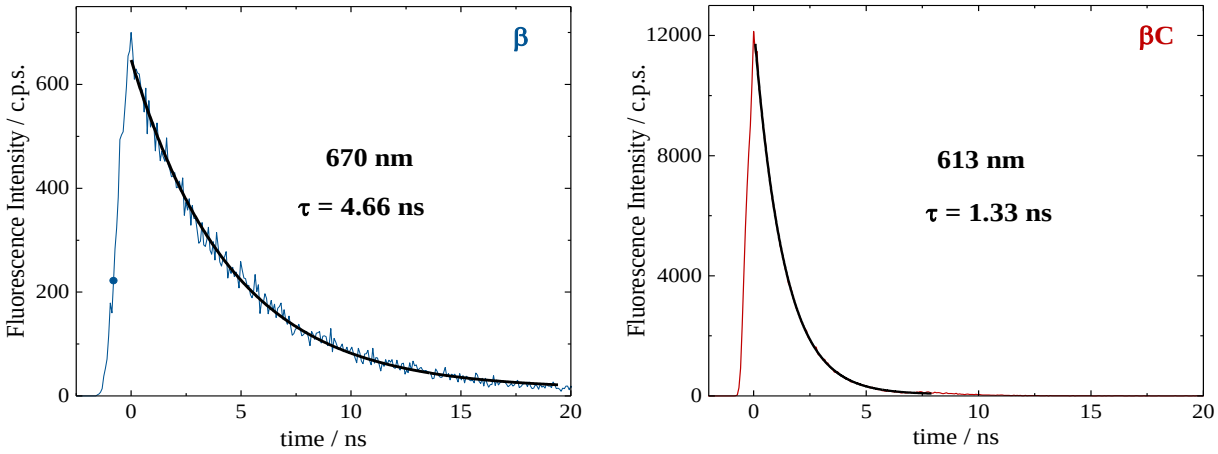

Figure 4.4.5.1. Fluorescence kinetics obtained by nanosecond TCSPC in air equilibrated chloroform.

Fluorescence kinetics were also acquired by single photon counting (SPC) with nanosecond resolution (**Figure 4.4.5.1**). For the rigid **βC**, these experiments revealed a lifetime of 1.33 ns, in agreement with the femtosecond TA measurement – 1.3 ns (**Figure 4.4.4.1** & **Table**

4.7.4.1.2). For **β**, the SPC fluorescence decay is surprisingly slower, and the fitting revealed a lifetime of 4.66 ns. This fluorescent component exhibits a lifetime quite different from that estimated by the femtosecond transient absorption for S_1 – 320 ps, and by the high resolution FUC. Therefore, the 4.66 ns component may be due to a precursor of T_1, possibly a double triplet excited state $^1(TT)^*$. This component could be either a result of direct $^1(TT)^*$ emission,[58–60] or delayed S_1 fluorescence from the $^1(TT)^*$ state.[1,19,23,53] Time resolved emission and/or temperature-dependent spectra obtained by photoluminescence measurements with broadband detection would be required to identify the specific mechanism of the double triplet emission. A 4.66 ns lifetime is not unusual for double triplet states as observed in the literature for perylene diimide chromophores. Wasielewski et al[18] reported a lifetime of 2.8 ns for polycrystalline thin films of slip stacked PDI, attributed to a small amount of delayed fluorescence resulting from triplet-triplet annihilation. Sean Roberts et al[53] also reported lifetime of ~10 ns associated to the non-radiative decay of the triplet (or double triplet) excitons to the ground state.

4.4.6 Quantum Chemical Simulations: Intersystem Crossing and Singlet Fission

Quantum chemical simulations were performed to give an insight into triplet formation mechanisms. Triplet formation via ISC was predicted to be much faster for the planar **βC** than for its twisted analogue due to large cancellation between ΔE_{ST} and reorganization energies for **β** (i.e. $8.44\times10^5\ s^{-1}$/1185 ns for **β** and $1.35\times10^7\ s^{-1}$/74.1 ns for **βC,** see SI). However, experimentally, the long−lived triplet species appear much faster (340 ps) for the twisted **β**. This implies the existence of another pathway of triplet generation: iSEF. Similar timescales of triplet formation via SEF in other PDI derivatives have been reported.[18,53] TD−DFT was used to illustrate the SEF relevant energetics and to check if the energetic requirement or ***thermodynamic feasibility***, $E(S_1) \geq 2\times E(T_1)$, is met. Energies of the relaxed S_1 state were predicted to be 1.30 eV and 1.89 eV for **β** and **βC**, respectively (**Figure 4.7.7.3**). T_1 state energies at its minimum structures (**Figure 4.7.7.2**) were 0.55 eV and 1.24 eV for **β** and **βC**, respectively. These energetics indicates that SEF in the twisted **β** is thermodynamically favorable by 0.20 eV ($2\times0.55 - 1.30 = -0.20$), but not in the planar **βC** for which it is energetically uphill by 0.59 eV ($2\times1.24 - 1.89 = 0.59$).

A recent perspective pointed out that the accessibility of double triplet state of singlet character (^{1}TT), that is the ***kinetic feasibility***, is more instrumental to judge the potentiality of SEF taking place than just the simple singlet−triplet energy gap.[61] Though TD–DFT calculations were

conducted to obtain the energetics of singly excited states, it is clearly stated by theorists that TD–DFT is not an ideal method for calculation of the multi–excitonic (ME) states, i.e., double-triplet states. The RAS–SF method, on the other hand, has shown to be capable of correctly describing the characters of multi–excitonic states and providing a more in–depth picture of the interactions between the locally excited singlet and multi–exciton states. Importantly for trimers like **β** and **βC**, RAS–SF is also able to compute all possible multi–exciton states, obtaining their spatial as well as their spin components (Figures **4.4.6.1**, **4.4.6.2** and **4.4.6.3**). RAS–SF can provide the relative energies of all the double–triplet states, and identify behavior discrimination between these states in each trimer. However, RAS-SF overestimates the excitation energies because of an incomplete account of dynamic correlation.[21,62] Even though the absolute energies are not accurate (and this explains the poor agreement with the DFT energies), the trends and the relative energy values can still be discussed. The TT states from the RAS–SF trimer models are qualitatively described in **Figure 4.4.6.1**. Detailed descriptions of the frontier orbitals for these states can be found in **Figures 4.7.7.7** and **4.7.7.8**.

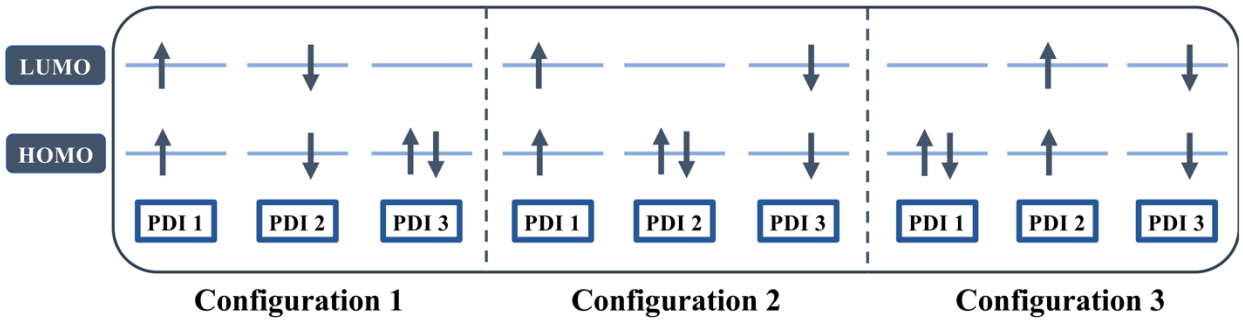

Figure 4.4.6.1. Possible electronic configurations of active space orbitals for both **β** and **βC** compounds.

Krylov has shown that it is not uncommon for perylene diimide compounds to have their lowest ^{1}TT state above their lowest excited singlet exciton state.[21] In **β** and **βC**, the lowest ^{1}TT state is placed 0.49 eV and 1.10 eV above their respective S_1 state (**Table 4.7.7.2**). This ^{1}TT state becomes nearly inaccessible in the **βC** compound due to an additional energy of more than twice that of the **β** compound (0.61 eV), required to reach the multiexcitonic state from the S_1 state. As shown in **Figure 4.4.6.2**, the multi-excitonic state with lowest excitation energy for the **β** compound is Configuration 3. More specifically, the RAS–SF calculation shows that excitons in the lowest multi–exciton state are localized on *adjacent* PDI units. The two higher energy configurations (Configuration 1 and 2) are within 0.02 eV of Configuration 3, indicating that all

TT states of **β** compound are easily energetically accessible. In the case of the **βC** compound, the lowest multi–exciton state is Configuration 2 of **Figure 4.4.6.1**, where the triplet excitons reside on the left−most and right−most PDI units. The energy of this state is about 0.2 eV under that of the two other configurations (one order of magnitude higher in comparison to **β**), suggesting a nontrivial difference in energy to access Configurations 1 and 3.

A photo–excited singlet state S_1 can evolve into a triplet–paired state ^{1}(TT) in singlet fission chromophores via state crossings when the S_1 and TT states are close in energy.[63] Throughout this non–adiabatic transition, it is true in some cases that the singlet exciton of S_1 state resides over several adjacent chromophores. This phenomenon promotes the ^{1}(TT) formation and thus increases the SF efficiency.[61] Only the couplings of the singly excited state S_1 with the ME state on adjacent chromophores will be playing significant roles throughout this non–adiabatic transition. In this particular case of **β** compound, as suggested by the electronic configuration of its lowest TT state (**Figure 4.4.6.2**), the S_1 exciton is located on two adjacent units, PDI2 and 3. This spatial characteristic explains why the TT formation is promoted in this **β** compound. Nevertheless, this S_1 exciton is spread out on the two isolated units in **βC**. As discussed above, since the S_1 excitons are less likely to reside across PDI1 and PDI3, it is therefore not surprising to conclude that forming the TT state is more difficult in **βC** than it is in **β** compound.

Additionally, performing analysis on energy differences between ^{1}TT state and quintet state energies allows us to judge the ***feasibility of separation of the double triplet into two independent triplets***. This energy difference, sometimes called inter–triplet interaction energy, is also known as the energy penalty for separating two triplets. This inter–triplet interaction energy accounts for the unmixing of charge transfer contributions in the singlet TT state by comparing the ^{1}TT state to the corresponding quintet state, which always is a pure diabatic TT state.[21] For the twisted **β** compound, the ^{1}TT states are nearly degenerate with their corresponding quintet states, giving inter–triplet interaction energies of 0.006 eV for the two lower multi–exciton states (**Figure 4.4.6.2**). This result suggests that the interaction between two triplets in **β** is quite small, and two entangled triplets can thus easily be separated into two independent triplets. In **βC** compound, however, the inter–triplet interaction energies increase by an order of magnitude, up to 0.066 eV, for the two higher multi–exciton states (**Figure 4.4.6.3**). This result entails that the formation of double triplets and the subsequent separation of entangled triplets require much less energy for **β** than for **βC**. Another notable fact is that the lowest ME state in the planar **βC** compound, which

is the same case as the highest ME state in the twisted **β** compound, has no other but only the pure ME contributions toward the states. This fact also makes sense since the two triplet excitons are located on the two isolated chromophores so that it is apparently harder for charge transfer contribution to play a role in this particular situation.

Overall, quantum chemical simulations support that iSEF is the dominant pathway to generate *independent* triplets only in **β** but not in **βC**, based on the thermodynamic viability ($\Delta E_{S\text{-}2\times T}$), kinetic accessibility, and feasibility of separation of the double triplets.

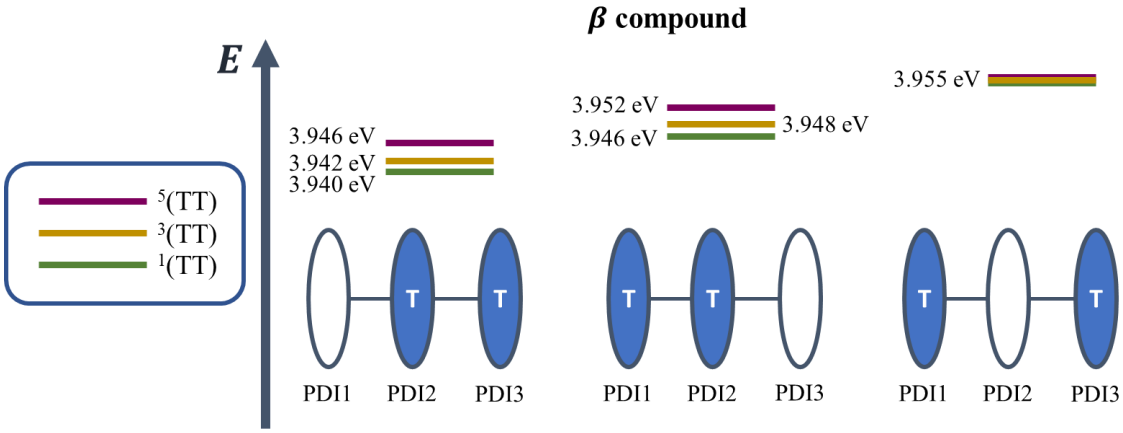

Figure 4.4.6.2. Energy level diagram illustrating the relative energies of all the double–triplet states found in **β** compound, with the colored PDI chromophores indicating where the triplet excitons are located.

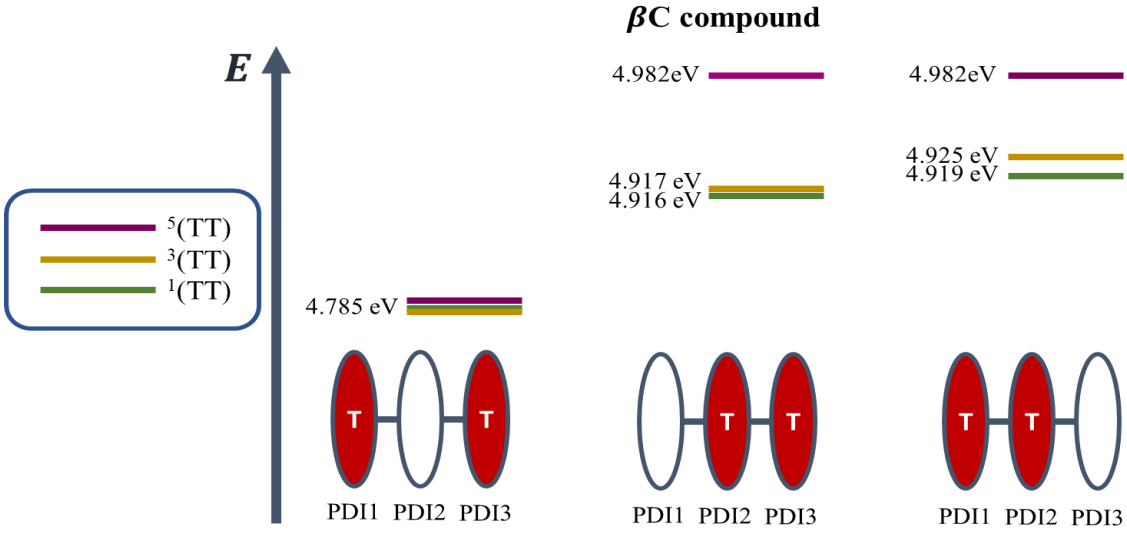

Figure 4.4.6.3. Energy level diagram illustrating the relative energies of all the double–triplet states found in **βC** compound, with the colored PDI chromophores indicating where the triplet excitons are located.

4.5 Discussion

In the literature, it has been proposed for multichromophoric systems that using a rotatable linker is crucial in obtaining iSEF.[15–17] Those studies, however, do not report the direct comparison between rigid−bridged and flexible−bridged units of the same chromophore in order to isolate the effect of the π−bridge. In this work, we point out the key differences between planar (rigid−bridged) and twisted (flexible−bridged) systems as they relate to the efficiency and rate of triplet production upon singlet photoexcitation. The systems investigated are newly synthesized oligomeric PDI trimers. Typically, the fluorescence quantum yield of PDI monomers is around 90 %, indicating that the radiative decay pathway is the most preferred. However, for these PDI trimers, especially for the flexible−bridged **β** trimer, the fluorescence efficiency is found to be very low suggesting a prevalent non−radiative deactivation − triplet production.

For the planar **βC** trimer, we obtain a triplet yield of 16 % via triplet sensitization experiments employing a nanosecond transient absorption technique. The femtosecond transient absorption results show ultrafast intramolecular charge transfer and slow triplet formation occurring in few nanoseconds for this molecule. This rate agrees with the intersystem crossing rate predicted by quantum chemical simulations. Our experimental and computational results thus conclude that triplet production for the rigid **βC** trimer proceeds via regular intersystem crossing. Conversely, in the case of the flexible−bridged **β** trimer we clearly show that the mechanism of triplet production is different and involves iSEF, based on the following evidences. (i) Triplet yield >> 100%, obtained via triplet sensitization as well as two–color transmission experiments. (ii) A fast triplet formation (~340 ps) observed via femtosecond transient absorption measurements. (iii) Distinct triplet species detected via transient absorption experiments – the correlated triplet pair and the independent triplets with lifetime of 6 μs.[64–66] (iv) A decay lifetime different from that of the S_1 species (4.7 ns), attributed to the double triplet species. (v) Thermodynamic viability − $E(S_1) \geq 2 \times E(T_1)$. (vi) Kinetic feasibility allowed by the energetic accessibility of the double triplet state from the S_1 state − the rate is given as: $r \approx e^{-const.(ES_1 - E^1TT)}$.[21] Our findings thus suggest that iSEF takes place in the flexible−bridged **β** trimer. **As an important result of our study, we demonstrate that the rotational flexibility of the linker, as in the β trimer compound, is necessary to activate multiexciton triplet generation in multichromophoric PDIs.** Our findings constitute a significant progress in structure−property relationships and may drive future design of extremely efficient iSEF materials.

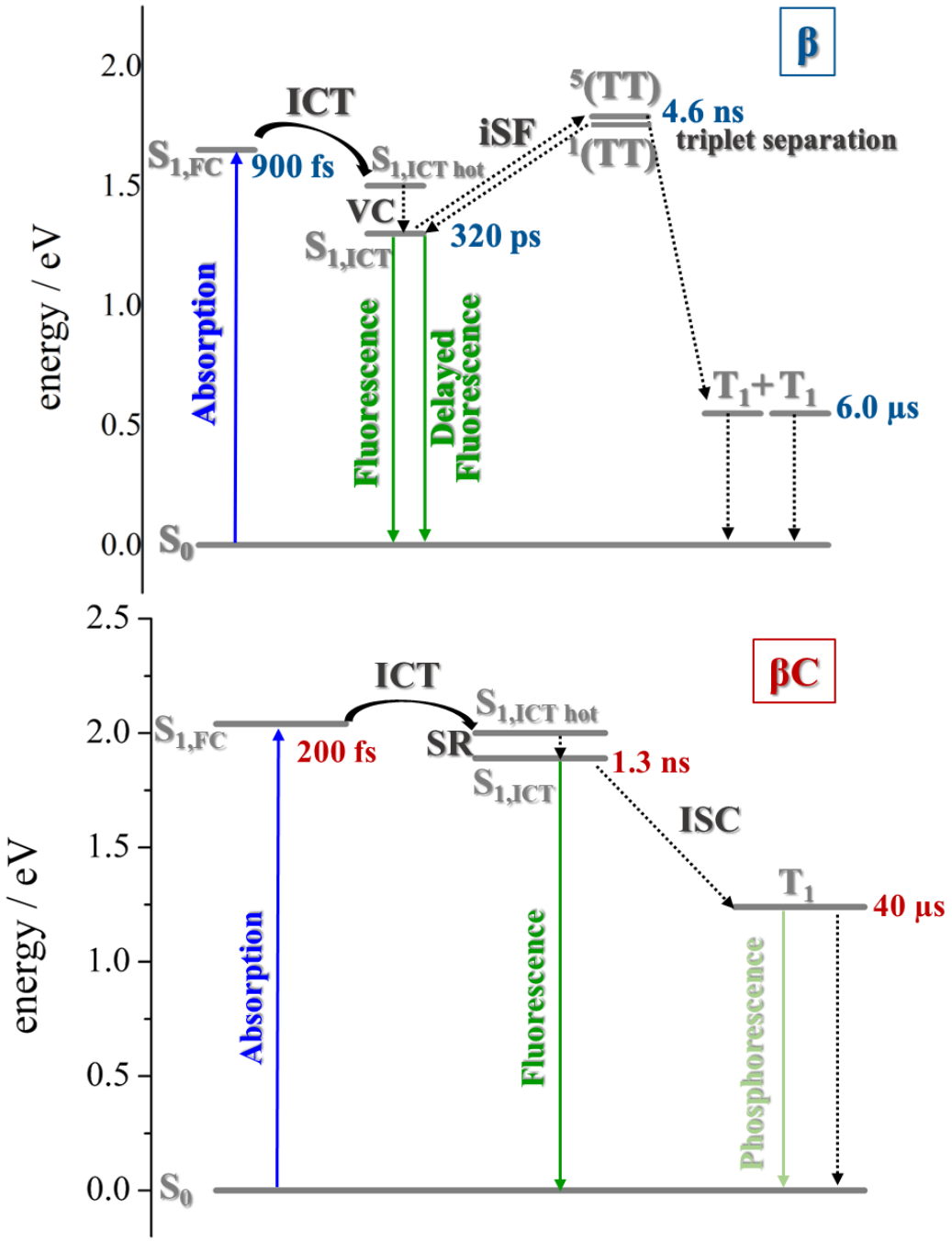

Figure 4.5.1. Sketch of the proposed excited state deactivations, based on the excited state energies predicted via quantum simulations and the excited state dynamics observed via time resolved spectroscopic experiments.

To gain a deeper insight into the thermodynamics of multiexciton generation, we obtained all the relevant enthalpic and entropic quantities for the trimers following an approach proposed by Krylov et al.[21,67] Multiexciton generation was considered to occur in two steps: a first step proceeding from the excited singlet to the double triplet state (from S_1 to ^{1}TT) and a second step

leading to triplet separation (from ^{1}TT to T_1). The total enthalpy and entropy change were evaluated as the sum of the changes observed in the two steps. Detailed results are reported in **Table 4.7.7.3**. The SEF process is indeed exothermic for the **β** twisted compound ($\Delta H_{TOT} = -0.20eV$) and endothermic for the **βC** planar trimer($\Delta H_{TOT} = +0.59eV$). In the literature about iSEF in covalently linked dimers, only enthalpy has been considered in describing their thermodynamics. This is because covalently linked dimers can accommodate just one correlated triplet pair, hence no entropic contribution. However, for trimeric structures the role of entropy should be considered. In a covalently linked trimer, like those investigated here, the double triplet has three possible accommodations on two of its three PDIs; and in particular two equivalent accommodations on each pair of adjacent PDIs owing to molecular symmetry. In principle, the trimeric structure allows entropic gain to play a significant role in the SEF thermodynamics, as literature studies have reported for solid state films[8,67] and very recently for oligomers.[56] The quantum chemical simulations indeed showed the presence of three multiexcitonic states. For **β**, the two ^{1}TT accommodated on adjacent PDIs of the structure, as well as that on the left−most and right−most PDI units, are energetically accessible from S_1. The **high triplet yield and fast iSEF rate observed in β is not only due to the enthalpic viability but also to the entropic gain** ($T\Delta S_{TOT} = +0.028eV$) **allowed by its trimeric structure.** This leads to a negative total change in Gibbs energy for **β** ($\Delta G_{TOT} = -0.228eV$), confirming the iSEF thermodynamic feasibility. On the other hand, for **βC**, the lowest energy ^{1}TT state is the one for which the triplet excitons reside on the left−most and right−most PDI units whereas the two ^{1}TT states allowing for an entropic gain are enthalpically inaccessible from S_1. This leads to no entropic contribution, and since the total change in Gibbs energy is positive ($\Delta G_{TOT} = +0.59eV$), iSEF is not thermodynamically feasible for the planar **βC** trimer.

While strong coupling among the PDI chromophores can be inferred for the planar **βC** trimer, for the twisted **β** compound, weak coupling is observed because the singlet electron NTOs are localized on a single PDI unit. **We suggest that the poor electronic communication among the PDI chromophores caused by the rotatable linker is crucial in permitting efficient iSEF. Our results demonstrate that the single−bond connections capable of weakening the coupling between the chromophores favor high iSEF yield.** The fused ring connections induce strong coupling among the PDI units, as the singlet electron NTOs are delocalized over the planar trimer structure, and inhibit SEF completely. This is due to competition with other ultrafast processes in

the planar system, such as intramolecular charge transfer.[26] The two−photon absorption (TPA) cross section − a measure of intramolecular charge transfer character − is indeed enhanced by over one order of magnitude for the planar **βC** (ca. 300 GM) with respect to the twisted **β** compound (ca. 10 GM). Quantum chemical simulations confirm the higher degree of charge transfer in the excited state for **βC** (0.80 e^-) relative to **β** (0.74 e^-) by dividing their structure into 5 subunits of PDI acceptor and BDT donor fragments. Weak coupling among the PDI units is crucial not only for multiexciton generation but also for triplet separation. The rate of triplet separation is indeed given as: $r \approx e^{-const.(E^5TT-E^1TT)}$ by Krylov et al.[21] For the twisted **β** compound, the ^{1}TT states are nearly degenerate with their corresponding ^{5}TT states, giving inter–triplet interaction energies (E^5TT−E^1TT) as 0.006 eV. This result suggests that the interaction between two triplets in **β** is indeed small, and two entangled triplets can thus easily be separated into two independent triplets. However, in **βC**, the inter–triplet interaction energies increase by one order of magnitude, up to 0.066 eV. For the **β** trimer, the long−lived independent triplets are experimentally observed following their separation, and each of them is localized on a single PDI unit, as shown by the theoretical calculations. Compared to other SEF rylene derivatives reported in the literature,[19,50,53] the **β** trimer shows a much longer triplet lifetime. This is highly beneficial for its use in solar energy conversion devices, allowing efficient extraction of multiple charge carriers per incident photon.[68]

4.6 Conclusions

Here, we report a comparative study between rigid−bridged (planar) and flexible−bridged (twisted) perylene diimide trimer systems to highlight the role of the π−bridge linker in activating intramolecular singlet exciton fission. We show via time resolved spectroscopic measurements how a slight structural variation of the π−bridge of multichromophoric perylene diimide (PDI) systems strongly affects the triplet yield and triplet formation rate. Triplet formation proceeds via conventional intersystem crossing for the planar trimer as evidenced by its triplet yield of 16 % and triplet production in the nanosecond timescale. On the other hand, we find clear evidence of highly efficient (170 %) and fast (few hundred picoseconds) intramolecular singlet exciton fission taking place in the twisted trimer. A fused ring connection induces strong coupling among the PDI units as in the planar system and this inhibits singlet exciton fission completely due to a strong competition with other ultrafast processes, such as intramolecular charge transfer. Our results demonstrate that a rotatable π−bridge, capable of lowering the coupling between the

chromophores, is necessary to activate intramolecular singlet exciton fission in multichromophoric systems. The quantum chemical simulations prove that the entropic gain allowed by multiple possibilities of accommodating the correlated triplet pair on adjacent PDIs in the twisted trimer is a crucial determinant for multiexciton triplet generation. Successive multiexciton triplet separation occurs in the flexible−bridged PDI due to weak coupling among the units, and degenerate double triplet and quintet states.

References

1 A. M. Müller, Y. S. Avlasevich, W. W. Schoeller, K. Müllen and C. J. Bardeen, *J. Am. Chem. Soc.*, 2007, **129**, 14240–14250.

2 A. B. Pun, S. N. Sanders, E. Kumarasamy, M. Y. Sfeir, D. N. Congreve and L. M. Campos, *Adv. Mater.*, 2017, **29**, 1–9.

3 J. Lee, P. Jadhav, P. D. Reusswig, S. R. Yost, N. J. Thompson, D. N. Congreve, E. Hontz, T. Van Voorhis and M. A. Baldo, *Acc. Chem. Res.*, 2013, **46**, 1300–1311.

4 S. Kawata, Y. J. Pu, A. Saito, Y. Kurashige, T. Beppu, H. Katagiri, M. Hada and J. Kido, *Adv. Mater.*, 2016, **28**, 1585–1590.

5 D. a Howe, T. J. Millar, S. Uniforme, a Goddard, I. R. Sims, I. W. M. Smith, K. M. Hickson, N. Daugey, P. Caubet, M. Costes, E. a Bergin, C. J. Lada, D. W. a Stewart, C. F. Williams, D. C. Clary, P. Honvault, P. Halvick, C. Xie, D. Xie, H. Guo, R. Dynamics, a Lagana, G. Lendvay, D. H. Zhang, a F. J. Wagner, J. J. Schwab and J. G. Anderson, *Science (80-.).*, 2011, 1541–1545.

6 I. Paci, J. C. Johnson, X. Chen, G. Rana, D. Popović, D. E. David, A. J. Nozik, M. A. Ratner and J. Michl, *J. Am. Chem. Soc.*, 2006, **128**, 16546–16553.

7 J. J. Burdett, A. M. Müller, D. Gosztola and C. J. Bardeen, *J. Chem. Phys.*, , DOI:10.1063/1.3495764.

8 W. L. Chan, M. Ligges and X. Y. Zhu, *Nat. Chem.*, 2012, **4**, 840–845.

9 M. B. Smith and J. Michl, *Annu. Rev. Phys. Chem.*, 2013, **64**, 361–386.

10 E. Busby, J. Xia, Q. Wu, J. Z. Low, R. Song, J. R. Miller, X. Y. Zhu, L. M. Campos and M. Y. Sfeir, *Nat. Mater.*, 2015, **14**, 426–433.

11 S. Singh, W. J. Jones, W. Siebrand, B. P. Stoicheff and W. G. Schneider, *J. Chem. Phys.*, 1965, **42**, 330–342.

12 P. M. Zimmerman, F. Bell, D. Casanova and M. Head-Gordon, *J. Am. Chem. Soc.*, 2011, **133**, 19944–19952.

13 S. N. Sanders, E. Kumarasamy, A. B. Pun, M. T. Trinh, B. Choi, J. Xia, E. J. Taffet, J. Z. Low, J. R. Miller, X. Roy, X. Y. Zhu, M. L. Steigerwald, M. Y. Sfeir and L. M. Campos, *J. Am. Chem. Soc.*, 2015, **137**, 8965–8972.

14 H. Sakai, R. Inaya, H. Nagashima, S. Nakamura, Y. Kobori, N. V. Tkachenko and T. Hasobe, *J. Phys. Chem. Lett.*, 2018, **9**, 3354–3360.

15 T. Yamakado, S. Takahashi, K. Watanabe, Y. Matsumoto, A. Osuka and S. Saito, *Angew. Chemie - Int. Ed.*, 2018, **57**, 5438–5443.

16 E. Kumarasamy, S. N. Sanders, M. J. Y. Tayebjee, A. Asadpoordarvish, T. J. H. Hele, E. G. Fuemmeler, A. B. Pun, L. M. Yablon, J. Z. Low, D. W. Paley, J. C. Dean, B. Choi, G.

D. Scholes, M. L. Steigerwald, N. Ananth, D. R. McCamey, M. Y. Sfeir and L. M. Campos, *J. Am. Chem. Soc.*, 2017, **139**, 12488–12494.

17 N. V. Korovina, J. Joy, X. Feng, C. Feltenberger, A. I. Krylov, S. E. Bradforth and M. E. Thompson, *J. Am. Chem. Soc.*, 2018, **140**, 10179–10190.

18 S. W. Eaton, D. A. Hartzler, L. E. Shoer, T. J. Marks, M. R. Wasielewski, S. D. Karlen, E. A. Margulies, C. Ramanan, S. Savikhin, S. M. Dyar and B. S. Veldkamp, *J. Am. Chem. Soc.*, 2013, **135**, 14701–14712.

19 A. K. Le, J. A. Bender and S. T. Roberts, *J. Phys. Chem. Lett.*, 2016, **7**, 4922–4928.

20 S. N. Sanders, M. Y. Sfeir, A. K. Le, J. A. Bender, D. H. Arias, D. E. Cotton, J. C. Johnson and S. T. Roberts, *J. Am. Chem. Soc.*, 2018, **4**, 814–826.

21 M. H. Farag and A. I. Krylov, *J. Phys. Chem. C*, 2018, **122**, 25753–25763.

22 E. A. Margulies, J. L. Logsdon, C. E. Miller, L. Ma, E. Simonoff, R. M. Young, G. C. Schatz and M. R. Wasielewski, *J. Am. Chem. Soc.*, 2017, **139**, 663–671.

23 S. T. Roberts, R. E. McAnally, J. N. Mastron, D. H. Webber, M. T. Whited, R. L. Brutchey, M. E. Thompson and S. E. Bradforth, *J. Am. Chem. Soc.*, 2012, **134**, 6388–6400.

24 J. Michl, A. J. Nozik, X. Chen, J. C. Johnson, G. Rana, A. Akdag and A. F. Schwerin, in *Organic Photovoltaics VIII*, 2007, vol. 6656, p. 66560E.

25 C. Ramanan, A. L. Smeigh, J. E. Anthony, T. J. Marks and M. R. Wasielewski, *J. Am. Chem. Soc.*, 2012, **134**, 386–397.

26 E. A. Margulies, C. E. Miller, Y. Wu, L. Ma, G. C. Schatz, R. M. Young and M. R. Wasielewski, *Nat. Chem.*, 2016, **8**, 1120–1125.

27 B. J. Walker, A. J. Musser, D. Beljonne and R. H. Friend, *Nat. Chem.*, 2013, **5**, 1019–1024.

28 O. Varnavski, N. Abeyasinghe, J. Aragó, J. J. Serrano-Pérez, E. Ortí, J. T. López Navarrete, K. Takimiya, D. Casanova, J. Casado and T. Goodson, *J. Phys. Chem. Lett.*, 2015, **6**, 1375–1384.

29 A. D. Chien, A. R. Molina, N. Abeyasinghe, O. P. Varnavski, T. Goodson and P. M. Zimmerman, *J. Phys. Chem. C*, 2015, **119**, 28258–28268.

30 E. C. Greyson, B. R. Stepp, X. Chen, A. F. Schwerin, I. Paci, M. B. Smith, A. Akdag, J. C. Johnson, A. J. Nozik, J. Michl and M. A. Ratner, *J. Phys. Chem. B*, 2010, **114**, 14223–14232.

31 S. Lukman, K. Chen, J. M. Hodgkiss, D. H. P. Turban, N. D. M. Hine, S. Dong, J. Wu, N. C. Greenham and A. J. Musser, *Nat. Commun.*, 2016, **7**, 1–13.

32 S. Lukman, A. J. Musser, K. Chen, S. Athanasopoulos, C. K. Yong, Z. Zeng, Q. Ye, C. Chi, J. M. Hodgkiss, J. Wu, R. H. Friend and N. C. Greenham, *Adv. Funct. Mater.*, 2015, **25**, 5452–5461.

33 B. Carlotti, Z. Cai, H. Kim, V. Sharapov, I. K. Madu, D. Zhao, W. Chen, P. M. Zimmerman, L. Yu and T. Goodson, *Chem. Mater.*, 2018, **30**, 4263–4276.

34 I. K. Madu, E. W. Muller, H. Kim, J. Shaw, A. Burney-Allen, P. M. Zimmerman, M. Jeffries-EL and T. Goodson III, *J. Phys. Chem. C*, 2018, acs.jpcc.8b03914.

35 M. T. Whited, N. M. Patel, S. T. Roberts, K. Allen, P. I. Djurovich, S. E. Bradforth and M. E. Thompson, *Chem. Commun.*, 2012, **48**, 284–286.

36 B. J. Walker, A. J. Musser, D. Beljonne and R. H. Friend, *Nat. Chem.*, 2013, **5**, 1019–1024.

37 Z. Yu, Y. Wu, Q. Peng, C. Sun, J. Chen, J. Yao and H. Fu, *Chem. - A Eur. J.*, 2016, **22**, 4717–4722.

38 T. Zheng, Z. Cai, R. Ho-Wu, S. H. Yau, V. Shaparov, T. Goodson and L. Yu, *J. Am. Chem. Soc.*, 2016, **138**, 868–875.

39 S. J. K. Pond, M. Rumi, M. D. Levin, T. C. Parker, D. Beljonne, M. W. Day, J. L. Brédas, S. R. Marder and J. W. Perry, *J. Phys. Chem. A*, 2002, **106**, 11470–11480.

40 R. J. Vázquez, H. Kim, B. M. Kobilka, B. J. Hale, M. Jeffries-EL, P. Zimmerman and T. Goodson, *J. Phys. Chem. C*, 2017, **121**, 14382–14392.

41 Y. Wu, R. M. Young, M. Frasconi, S. T. Schneebeli, P. Spenst, D. M. Gardner, K. E. Brown, F. Würthner, J. F. Stoddart and M. R. Wasielewski, *J. Am. Chem. Soc.*, 2015, **137**, 13236–13239.

42 P. Spenst, R. M. Young, M. R. Wasielewski and F. Würthner, *Chem. Sci.*, 2016, **7**, 5428–5434.

43 K. E. Brown, B. S. Veldkamp, D. T. Co and M. R. Wasielewski, *J. Phys. Chem. Lett.*, 2012, 3, 2362–2366.

44 J. M. Giaimo, A. V. Gusev and M. R. Wasielewski, *J. Am. Chem. Soc.*, 2002, **124**, 8530–8531.

45 T. Van der Boom, R. T. Hayes, Y. Zhao, P. J. Bushard, E. A. Weiss and M. R. Wasielewski, *J. Am. Chem. Soc.*, 2002, **124**, 9582–9590.

46 A. S. Lukas, Y. Zhao, S. E. Miller and M. R. Wasielewski, *J. Phys. Chem. B*, 2002, **106**, 1299–1306.

47 Y. Guo, Z. Ma, X. Niu, W. Zhang, M. Tao, Q. Guo, Z. Wang and A. Xia, *J. Am. Chem. Soc.*, 2019, **141**, 12789–12796.

48 I. H. M. Van Stokkum, D. S. Larsen and R. Van Grondelle, *Biochim. Biophys. Acta - Bioenerg.*, 2004, **1657**, 82–104.

49 J. J. Snellenburg, S. P. Laptenok, R. Seger, K. M. Mullen and I. H. M. van Stokkum, *J. Stat. Softw.*, 2012, **49**, 1–2.

50 E. A. Margulies, C. E. Miller, Y. Wu, L. Ma, G. C. Schatz, R. M. Young and M. R. Wasielewski, *Nat. Chem.*, 2016, **8**, 1120–1125.

51 E. A. Margulies, Y. L. Wu, P. Gawel, S. A. Miller, L. E. Shoer, R. D. Schaller, F. Diederich and M. R. Wasielewski, *Angew. Chemie - Int. Ed.*, 2015, **54**, 8679–8683.

52 W. E. Ford and P. V. Kamat, *J. Phys. Chem.*, 1987, **91**, 6373–6380.

53 A. K. Le, J. A. Bender, D. H. Arias, D. E. Cotton, J. C. Johnson and S. T. Roberts, *J. Am. Chem. Soc.*, 2018, **140**, 814–826.

54 C. Schweitzer and R. Schmidt, *Chem. Rev.*, 2003, **103**, 1685–1757.

55 S. W. Eaton, S. A. Miller, E. A. Margulies, L. E. Shoer, R. D. Schaller and M. R. Wasielewski, *J. Phys. Chem. A*, 2015, **119**, 4151–4161.

56 N. V. Korovina, C. H. Chang and J. C. Johnson, *Nat. Chem.*, 2020, **12**, 391–398.

57 S. N. Sanders, E. Kumarasamy, A. B. Pun, K. Appavoo, M. L. Steigerwald, L. M. Campos and M. Y. Sfeir, *J. Am. Chem. Soc.*, 2016, **138**, 7289–7297.

58 C. K. Yong, A. J. Musser, S. L. Bayliss, S. Lukman, H. Tamura, O. Bubnova, R. K. Hallani, A. Meneau, R. Resel, M. Maruyama, S. Hotta, L. M. Herz, D. Beljonne, J. E. Anthony, J. Clark and H. Sirringhaus, *Nat. Commun.*, , DOI:10.1038/ncomms15953.

59 H. L. Stern, A. Cheminal, S. R. Yost, K. Broch, S. L. Bayliss, K. Chen, M. Tabachnyk, K. Thorley, N. Greenham, J. M. Hodgkiss, J. Anthony, M. Head-Gordon, A. J. Musser, A. Rao and R. H. Friend, *Nat. Chem.*, 2017, **9**, 1205–1212.

60 S. Lukman, J. M. Richter, L. Yang, P. Hu, J. Wu, N. C. Greenham and A. J. Musser, *J. Am. Chem. Soc.*, 2017, **139**, 18376–18385.

61 H. Kim and P. M. Zimmerman, *Phys. Chem. Chem. Phys.*, 2018, **20**, 30083–30094.

62 X. Feng, D. Casanova and A. I. Krylov, *J. Phys. Chem. C*, 2016, **120**, 19070–19077.

63 K. M. Felter and F. C. Grozema, *J. Phys. Chem. Lett.*, 2019, **10**, 7208–7214.

64 R. D. Pensack, E. E. Ostroumov, A. J. Tilley, S. Mazza, C. Grieco, K. J. Thorley, J. B. Asbury, D. S. Seferos, J. E. Anthony and G. D. Scholes, *J. Phys. Chem. Lett.*, 2016, **7**, 2370–2375.

65 T. S. Lee, Y. L. Lin, H. Kim, R. D. Pensack, B. P. Rand and G. D. Scholes, *J. Phys. Chem. Lett.*, 2018, **9**, 4087–4095.

66 C. Grieco, E. R. Kennehan, H. Kim, R. D. Pensack, A. N. Brigeman, A. Rimshaw, M. M. Payne, J. E. Anthony, N. C. Giebink, G. D. Scholes and J. B. Asbury, *J. Phys. Chem. C*, 2018, **122**, 2012–2022.

67 A. B. Kolomeisky, X. Feng and A. I. Krylov, *J. Phys. Chem. C*, 2014, **118**, 5188–5195.

68 Q. Wu, D. Zhao, A. M. Schneider, W. Chen and L. Yu, *J. Am. Chem. Soc.*, 2016, **138**, 7248–7251.

4.7 Supporting Information.

Table of Contents

4.7.1. Experimental Section

4.7.1.1 Materials, Synthesis and Characterization. The trimer structures were synthesized according to the synthetic route described in **Figure 4.3.1**. All of the chemicals were purchased from Aldrich. All reagents purchased commercially were used without further purification except for toluene and tetrahydrofuran (THF), which were dried over sodium/benzophenone. ^{1}H NMR and ^{13}C NMR spectra were recorded on a Bruker DRX–500 spectrometer with tetramethylsilane as an internal reference. High Resolution MALDI–TOF spectra were recorded on Bruker Solarix 9.4T. Compounds **β** and **βC** were synthesized according to the procedures developed in our lab.[1]

*Synthesis of Compound **β**.* To a round–bottom flask equipped with a condenser, **1** (311 mg, 0.37 mmol), **2** (170 mg, 0.41 mmol), **$Pd_2(dba)_3$** (34 mg, 0.04 mmol), and **P(o-MePh)$_3$** (45 mg, 0.14 mmol) were added. The system was evacuated and refilled with N_2 three times, then charged with toluene (50 mL). The reaction mixture was refluxed under N_2 for 8 h. Then, compound **3** (102 mg, 0.11 mmol), **$Pd_2(dba)_3$** (8.5 mg, 0.01 mmol), and **P(o-MePh)$_3$** (12 mg, 0.04 mmol) were added. The reaction mixture was refluxed under N_2 for another 8 h. After cooling to room temperature, the reaction mixture was concentrated under reduced pressure. The residue was purified by column chromatography with hexane and CH_2Cl_2 (1:1, v/v) as the eluent. Compound **β** was obtained as a red solid (292 mg, 25.4% yield). ^{1}H NMR ($CDCl_3$): δ 8.87 (m, 4H), 8.70-8.65 (m, 8H), 8.35 (s, 4H), 8.23 (m, 4H), 7.77 (s, 2H), 7.68 (s. 2H) 5.19 (m, 6H), 3.14 (s, 4H), 3.02 (s, 4H), 2.25 (m, 12H), 1.84 (m, 16H), 1.23 (m, 130H), 0.83 (m, 48H), 0.74 (m, 12H). ^{13}C NMR ($CDCl_3$): δ 144.4, 144.1, 139.6, 139.5, 137.9, 137.6, 134.2, 133.9, 133.9, 133.6, 130.1, 130.0, 129.9, 129.2, 129.1, 128.4, 128.1, 127.5, 123.7, 123.0, 122.6, 122.0, 54.7, 40.3, 38.4, 32.4, 31.8, 31.7, 29.3, 29.2, 28.9, 28.8, 27.0, 26.9, 23.0, 22.6, 22.6, 14.1, 14.1, 14.1, 14.0, 11.2, 11.1. MALDI-TOF: calcd. for [$C_{202}H_{256}N_6O_{12}S_3$], 3085.9, found, 3085.018.

*Synthesis of Compound **βC**.* A solution of $FeCl_3$ (800 mg, 4.9 mmol) in 2 mL nitromethane was added dropwise to a stirred solution of compound **β** (170 mg, 0.55 mmol) in 10 mL CH_2Cl_2. The reaction was stirred with Ar. After stirring for 10 h at room temperature, 1 mL methanol was added to the solution. The solvent was evaporated under reduced pressure, and the crude product was filtered with silica gel with a large amount of $CHCl_3$ to yield the solid product (158 mg, 93%).^{1}H NMR ($C_2D_2Cl_4$, ppm, 353 K): δ 10.54 (d, 2H), 10.39 (d, 2H), 9.99 (s, 2H), 9.93 (s, 2H), 9.35 (m, 4H), 9.08 (m, 4H), 5.48-5.21 (m, 6H), 4.13 (Br, 8H), 2.31-1.98 (br, 28H), 1.37-1.20 (m, 130H), 0.85-0.79 (m, 60H). ^{13}C NMR cannot be measured due to the aggregation issue. MALDI-TOF: calcd. for [$C_{202}H_{248}N_6O_{12}S_3$], 3077.8, found, 3077.9.

4.7.1.2 Steady−State Measurements. All of the measurements were performed at room temperature. Concentrations ranging from 1.6×10^{-6} to 1.6×10^{-4} M were used for the spectroscopic investigations. Absorption spectra were measured using an Agilent 8432 UV−visible absorption spectrophotometer. The emission spectrum measurements were performed with a Fluoromax−2 spectrofluorimeter. The fluorescence quantum yields of the samples were calculated using a known procedure[2,3] and Rhodamine B in ethanol ($\phi_F = 0.68$)[4] was used as the standard.

4.7.1.3 Two−Photon Excited Fluorescence Measurements. Two−photon excited fluorescence measurements were performed using a Kapteyn Murnane (KM) mode−locked Ti:Sapphire laser tunable from 700 to 900 nm, and delivering 110 fs output pulses at a repetition rate of 80 MHz as described previously.[1,5,6] Emission scans were performed either at 820 or 875 nm excitation while scanning the emission in the 400−850 nm range, but the exact emission detection wavelength during the power dependence scan was selected by the emission wavelength that produced the highest number of counts. Input power from the laser was varied using a variable neutral density filter. Two−photon power−dependent fluorescence intensity was utilized to determine the two−photon absorption cross section using the comparative method. Rhodamine B in ethanol was used as the standard (cross section 120 GM at 820 nm and 30 GM at 875 nm).[7]

4.7.1.4 Femtosecond Transient Absorption. An amplified laser (Spectra Physics Spitfire) with pulse duration of ~100 fs, repetition rate of 1 kHz, and power of 1 W was directed at a beam splitter to generate the pump (85%) and the probe beams (15%). The pump beam (~66 mJ per pulse) was generated from the second harmonic of the amplifier's output (~405 nm) using a BBO crystal in an optical parametric amplifier (Spectra Physics OPA-800CF) and was focused onto the sample cell (l = 2 mm) preceded by an optical chopper. The probe beam was passed through a computer−controlled delay line and focused onto a 2 mm sapphire plate to generate the white light continuum (Ultrafast Systems Inc.).[8,9] The white light was focused onto the sample and overlapped with the pump beam. The absorption difference (ΔA) of the signal was collected by a CCD detector (Ocean Optics). Data acquisition was performed with the software Helios by Ultrafast Systems Inc. The IRF was measured by the Raman scattering of water at 466 nm and is found to be 110 fs. Data analysis was performed with Surface Xplorer Pro and Glotaran softwares. All the experiments were performed in dilute solutions, at concentrations below 1×10^{-4} M.

4.7.1.5 Nanosecond Transient Absorption. The spectral properties and the lifetimes of long lived transient species were probed by transient absorption with nanosecond time resolution measurements.[10] These experiments were performed in dilute deaerated solutions, where photodegradation was checked by recording UV−vis absorption spectra before and after each experiment. All the experiments were performed in dilute solutions, at concentrations below

7×10^{-5} M. An LP980 (Edinburgh) spectrometer system, with a monochromator and PMT for signal detection (PMT−LP), was coupled with a Spectra Physics QuantaRay Nd:YAG nanosecond pulsed laser and a GWU Optical Parametric Oscillator (OPO) tunable for the excitation source. Flash lamps excite the ND:YAG rod in the laser head containing a polarizer, pockel cell, and ¼ wave plate, producing Q-switched 1064 nm light. Two-stage harmonic generation then produces high energy 355 nm light used to pump the OPO. The OPO produces excitation source from 206 nm to 2600 nm employing second harmonic generation and sum-frequency mixing nonlinear processes. For this investigation, 415 nm, 441 nm and 510 nm excitation wavelengths were used to pump the samples and a pulsed xenon lamp white light continuum was used to probe the absorption properties of the produced excited states. Relative actinometry measurement,[11,12] using an optically matched solution of Tetracene (φ_T = 0.62 and ε_T = 31200 M^{-1} cm^{-1} at λ_T of 465 nm)[13] in chlorobenzene as reference, was used to compute the product of the triplet yield and triplet−triplet extinction coefficient ($\varphi_T \cdot \varepsilon_T$) of the samples. The same OD was maintained at 441 nm excitation λ for both reference and sample, hence generating equal concentration of singlets in both solutions. Then knowing that: $[singlet] = [triplet]/\phi_T$ and using Beer-Lambert's law: $[triplet] = \Delta A/l \cdot \varepsilon_T$ for both the sample and the reference, the product: $\varphi_T \cdot \varepsilon_T$ of the sample can be computed. To compute the triplet yield (φ_T), triplet–triplet absorption coefficients (ε_T) were determined by triplet energy transfer measurements[14–16] to and from Tetracene in cyclohexane. Tetracene (E_T = 1.27 eV) was employed as a triplet energy donor for **β**, but as an acceptor for **βC**, giving a qualitative hint about their triplet energies i.e. E_T < 1.27 eV for **β**, but E_T > 1.27 eV for **βC**. For computing ε_T successfully, in the donor + acceptor mixture, at the donor λ_T there has to be a decrease in the triplet lifetime (i.e. higher decay rate) in comparison to its lifetime with only the donor in solution. Also, at the acceptor λ_T, a triplet concentration rise has to be observed. These observations thus confirm triplet energy transfer from a donor to an acceptor. Using the decay rate of the donor only (k_D) and the acceptor (k_A) alongside the rate of energy transfer (k_{ET}), the ΔA_A and ΔA_D, the ε_T of donor or acceptor can be evaluated knowing the ε_T of the other.

4.7.1.6 Two–Color Transmission Measurements of Triplet Yield. Femtosecond two-color transmission measurements were carried out using a tunable Mai Tai laser system (Spectra Physics) giving 130 fs pulses with a repetition rate of 80 MHz, tunable from 700 – 900 nm.[17] The light with wavelength of 850 nm plays the role of probe beam, and second harmonic generated

(425 nm) light using a BBO crystal was used as the pump beam. To obtain the transmission profile, the excited state absorption at 850 nm was investigated with pump irradiation at 425 nm. The selected wavelength region is reasonable since there is negligible steady-state absorption at 850 nm for the investigated samples. A variable neutral density filter is placed to modulate the excitation power. The position of focusing lens is adjusted to place the focusing point on the sample. Blank chloroform solvent gives a reference line. A calibrated photodiode was used to measure the pump power. The transmitted power has been measured with a wide aperture power meter which is free of any thermal lensing effect.

4.7.1.7 Time−Resolved Fluorescence Measurements. Time−correlated single photon counting (TCSPC) technique, which has been described previously,[9] was used to study the long decay component of the investigated samples. The laser used for the TCSPC measurements was a home-built mode−locked Ti−sapphire laser with cavity dumper with repetition rate below 700 kHz. The output beam from the KM laser was at 800 nm wavelength, with a pulse duration of ca. 30 fs. The output beam was frequency−doubled using a nonlinear barium borate crystal to obtain a 400 nm beam. A polarizer was used to vary the power of the 400 nm beam that excites the sample. Focus on the sample cell (quartz cuvette, 0.4 cm path length) was ensured using a lens of focal length 11.5 cm. Collection of fluorescence was carried out in a direction perpendicular to the incident beam into a monochromator, and the output from the monochromator was coupled to a photomultiplier tube, which converted the photons into counts.

The femtosecond−resolved fluorescence experiments were performed using an ultrafast fluorescence Up−Conversion setup that had previously been described.[8,18–20] Mode−locked Ti−Sapphire femtosecond laser (Spectra Physics Tsunami) was used to generate 80 fs pulses at 800 nm wavelength with a repetition rate of 82 MHz. This mode−locked laser was pumped by a 532 nm continuous light output from another laser (Spectra Physics Millennia), which has a gain medium of neodymium−doped yttrium vanadate (Nd:YVO_4). A 400 nm excitation pulse was generated by a second harmonic β−barium borate crystal, and the residual 800 nm beam was made to pass through a computer−controlled motorized optical delay line. The polarization of the excitation beam was controlled by a Berek compensator. The power of the excitation beam varied between 33 to 36 mW. The fluorescence emitted by the sample was up−converted by a nonlinear crystal of β−barium borate by using the residual 800 nm beam, which had been delayed by the

optical delay line with a gate step of 6.25 fs. By this procedure, the fluorescence can be measured temporally. The monochromator is used to select the wavelength of the up−converted beam of interest, and the selected beam is detected by a photomultiplier tube (R152P, Hamamatsu, Hamamatsu City, Japan). The photomultiplier tube converts the detected beam into photon counts, which can be read from a computer. Coumarin 30 was used for calibrating the set up. The instrument response function (IRF) has been determined from the Raman signal of water to have a width of 110 fs. Lifetimes of fluorescence decay were obtained by fitting the fluorescence decay profile to the most accurate fit. Mono and multi−exponential decay functions convoluted with IRF in MATLAB and Origin 8 were necessary for the data analysis.

4.7.1.8 Quantum Chemical Simulations. Theoretical investigation has been performed on molecular structures where the long alkyl chains are replaced by short chains (octyl and hexyl groups [C_6H_{13}, C_8H_{17}] attached to the PDI moieties and the BDT linker are replaced by hydrogen atoms and methyl groups, respectively) to save computational time without significant effect on the electronic properties. The ground state geometry of each compound was obtained by density functional theory (DFT). The B3LYP functional and the 6−31G* basis sets have been employed. Excited state simulations using time−dependent DFT (TD-DFT) were performed. The same functional and basis sets used in the ground state calculations, were employed for the geometry optimization of the first singlet excited state (S_1) and the first triplet excited state (T_1) in the gas phase. The geometries of S_1 were obtained with TD-DFT simulations. T_1 geometries could be obtained via two approaches: an unrestricted triplet calculation, and TD-DFT targeting a triplet state. In this study, TD-DFT triplet geometry optimization was conducted for consistency with the S_1 geometries. Single−point energy calculations to evaluate the electronic property were performed using the system−dependent, nonempirically tuned version of long−range corrected functional ωB97X−D[21,22] which is known to significantly improve the charge delocalization problem in conventional DFT functionals and 6−31G* basis sets. The ω value is tuned to minimize the square sum of the difference between HOMO energy (ε_{HOMO}) and ionization potential (IP), and LUMO energy (ε_{LUMO}) and electron affinity (EA), $(\varepsilon_{HOMO}+IP)^2+(\varepsilon_{LUMO}+EA)^2$. The ω value is significantly affected by the environment,[23] and inclusion of the solvent (chloroform) dielectric field induces a reduced ω value. The optimal ω values of **β** and **βC** are 0.004 and 0.003, respectively. The medium effect was included using polarizable continuum model with the

dielectric constant of 4.31 for chloroform. Characters of excitations were described with natural transition orbitals (NTOs). The driving force of singlet fission — the energy difference between $E(S_1)$ and $2\times E(T_1)$, $\Delta E_{S\text{-}2\times T}$ — was estimated with the same computational details mentioned above. S_1 and T_1 energies should be calculated at the optimized states since the vibrational relaxation is much faster than SF process. Recently, Krylov et al. pointed out the importance of ^{1}(TT) energy in predicting feasibility of SF and relevant kinetics.[24] Restricted active space with double spin-flip (RAS-2SF) has successfully provided the energetics of SF-relevant states in a number of studies.[25–32] While the RAS-2SF approach works well for dichromophoric systems, **β** and **βC** trimeric compounds require one additional spin-flip to locate all available multiexcitonic states distributed over three chromophores. In this study, we employed a high spin restricted open Hartree-Fock septet reference state. The orbital space of interest was divided into three parts: RAS1, RAS2 and RAS3. Two subspaces, RAS1 and RAS3, correspond to fully occupied, and virtual spaces, respectively. Six singly occupied orbitals were considered in the RAS2 active space. Core inactive occupied orbitals and 1200 virtual orbitals were kept frozen to enable RAS-3SF calculation for such large chromophores. The localized frontier orbitals were obtained using RAS-3SF method via Pipek-Mezey localization scheme with Q-Chem 4.0.[33] Energies of multiexciton state were estimated at the S_1 geometries obtained by the TD-DFT calculation described above. Details on the procedure of intersystem crossing calculations are provided in Supporting Information. All the quantum chemical simulations were conducted using Q−Chem 5.0.

4.7.1.9 Device fabrication and characterization. Polymer PTB7−Th was obtained from *1−Material*. Chlorobenzene and 1,8−diiodooctane for active layer solution preparation were obtained from Sigma-Aldrich. For ZnO preparation using sol−gel approach, we used $Zn(CH_3COO)_2{\cdot}2H_2O$, 2-methoxyethanol and 2-aminoethanol, all purchased from Sigma−Aldrich. Chloroform and cyclohexane from Sigma−Aldrich were used as solvents for the spectral and photophysical characterization. All chemicals were used as obtained from the manufacturer without further purification. Devices were fabricated in inverted configuration consisting of ITO/ZnO/active layer/MoO_3/Ag. ITO substrates, obtained from Thin Film Devices Inc., were ultrasonicated in chloroform, acetone and isopropanol for 15 min and then treated with UV−ozone for 30 min. Sol−gel solution of ZnO precursor, prepared following procedures described elsewhere, was added dropwise onto ITO substrates through PTFE syringe filter and spin coated

at 4000 rpm for 40 seconds. Immediately after spin coating, substrates were annealed at 200^0C for 30 minutes in air. Active layer components were dissolved in chlorobenzene overnight at 70^0C and solution at room temperature was spin coated onto the substrates in a glovebox. Films were immediately transferred to a vacuum chamber and MoO_3 (8 nm) and Ag (80 nm) were thermally evaporated under the pressure lower than $2 \cdot 10^{-6}$ Torr.

J−V curves of the devices were measured with Keithley 2420 source meter unit. Devices were tested under 1 sun conditions (AM1.5G, 100 mW/cm^2) using xenon lamp (Oriel 69920) intensity of which was calibrated with a standard NREL certified Si cell (Newport, 91150V). Masks with a well−defined area of 3.14 mm^2 were used to define an active area of the device.

4.7.2. Steady–State and Two–Photon Absorption Measurements

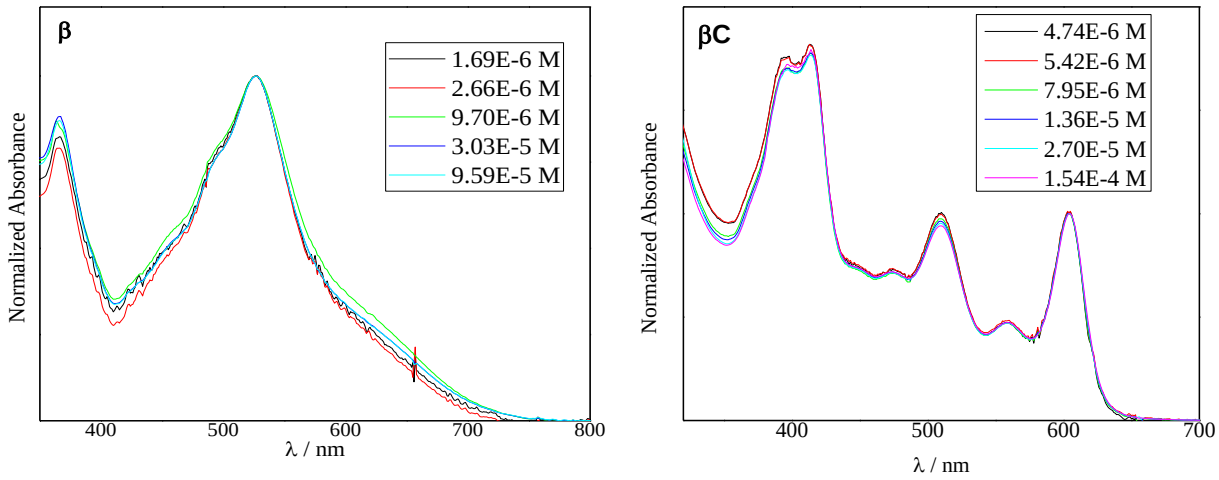

Figure 4.7.2.1. Concentration effect on the absorption spectra of the Trimers in chloroform.

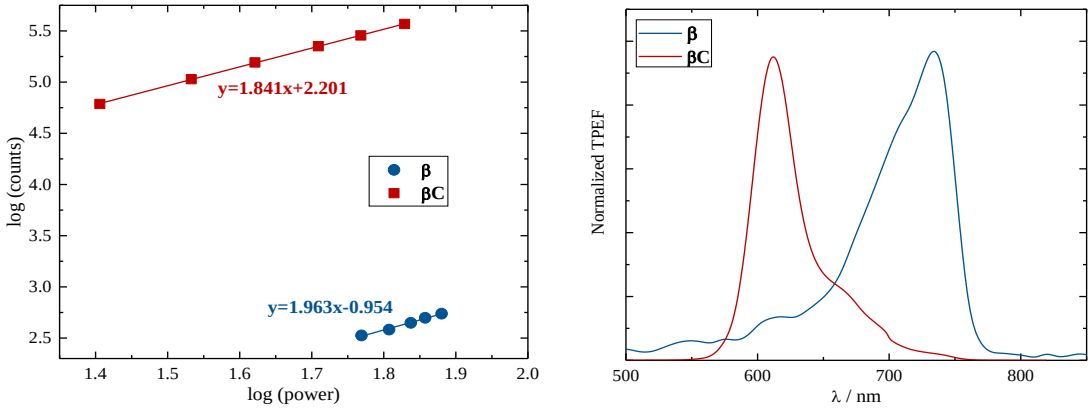

Figure 4.7.2.2. Power dependence of the two−photon excited emission (left) and two−photon emission spectra (right) for the Trimers in chloroform upon 820 nm excitation.

Table 4.7.2.1. Change in atomic charge from S_0 to S_1 on the subunits of compound **β** and **βC**.[a]

	β					**βC**				
	A	D	A	D	A	A	D	A	D	A
Absorption[b]	−0.07	+0.50	−0.66	+0.27	−0.03	−0.19	+0.32	−0.25	+0.32	−0.19
Emission[c]	+0.07	+0.64	**- 0.74**	+0.03	0.00	**−0.79**	+0.61	+0.10	+0.08	**−0.01**

[a]Mulliken charge is given in e^-; [b]Calculated at S_0 geometry; [c]Calculated at S_1 geometry

4.7.3. Femtosecond Transient Absorption (fsTA)

Table 4.7.3.1. Lifetimes (τ) obtained by global fitting of the femtosecond Transient Absorption data in chloroform.

Compound	τ_1 / ps	τ_2 / ps	τ_3 / ps	τ_4 / ps
β	0.18	7.4	320	Rest
βC	0.14	33	1300	Rest
assignment	*Solv. / ICT*	*VC/SR*	*S_1*	*T*

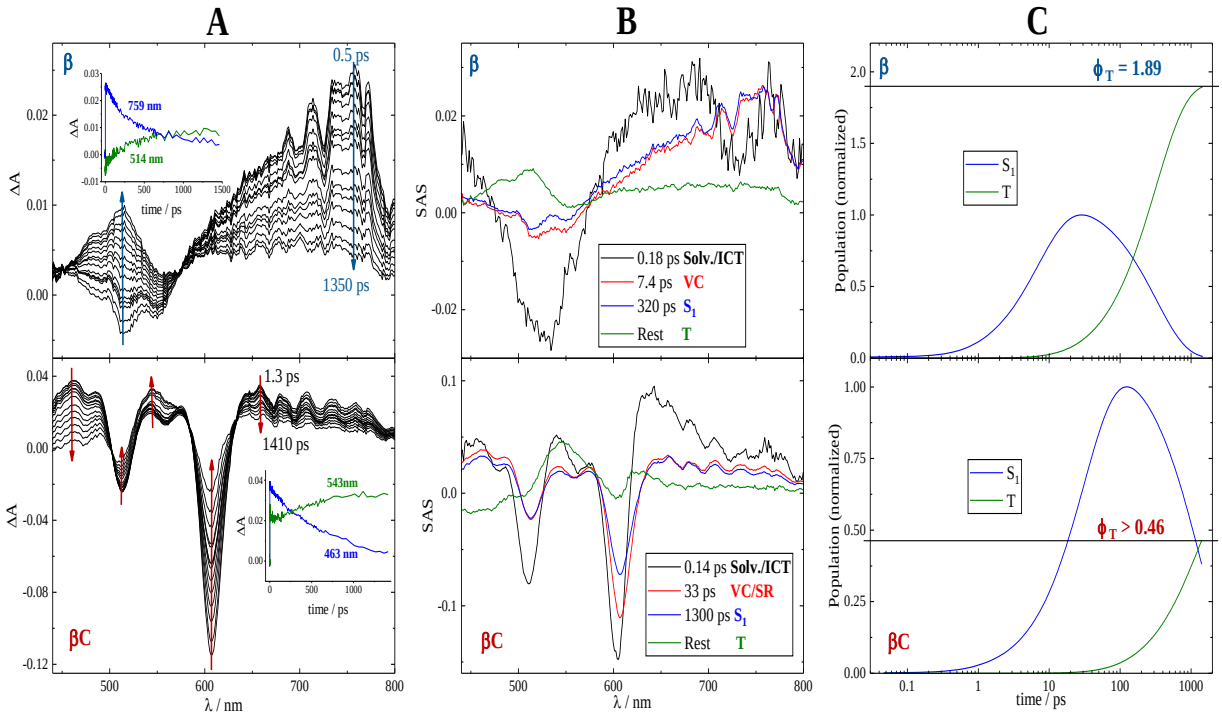

Figure 4.7.3.1. A) Time−resolved spectra and kinetics (inset) obtained by femtosecond TA for the Trimers in chloroform. B) Species Associated Spectra and lifetimes obtained by global fitting the TA data. C) Population dynamics of the excited singlet and triplet states.

4.7.3.1. Triplet Yield Calculation from fsTA

Triplet yield was evaluated from the temporal dynamics of the lowest excited singlet and triplet state populations, as obtained through analysis of the femtosecond transient absorption data, according to a procedure already described in the literature, and here detailed for the trimer samples.[34,35]

***βC** Trimer*

Global Fitting of the femtosecond transient absorption data was carried out using the Glotaran software which provided us with the Species Associated Spectra of the four exponential components (assignments and lifetimes described in **Table 4.7.3.1**) and their temporal composition (**Figure 4.7.3.1.1**).

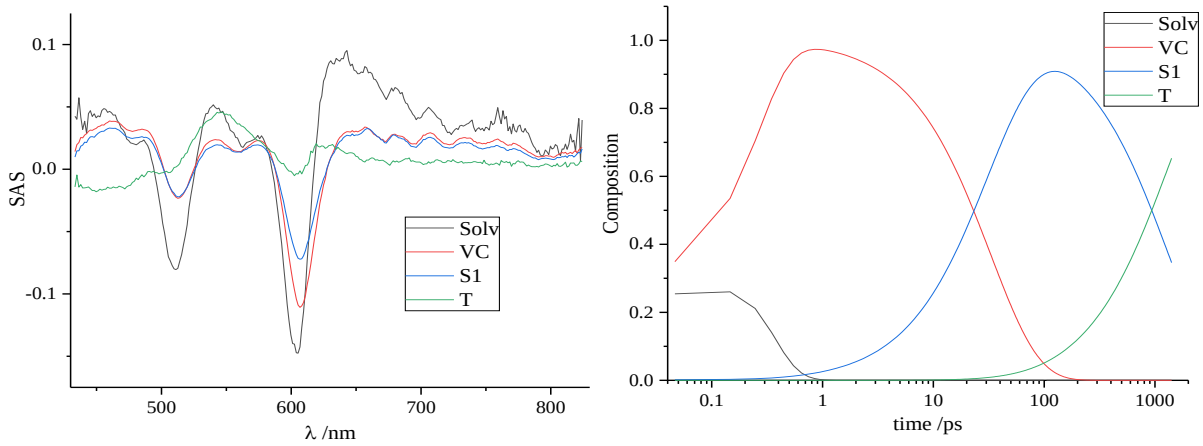

Figure 4.7.3.1.1. Species Associated Spectra (left) and composition in time (right) of the four exponential components resulting from global fitting of the femtosecond transient absorption data of **βC** in chloroform.

To obtain the spectral shapes of the excited singlet and triplet states the transient spectra at time delays of 129 and 1413 ps were selected, respectively (**Figure 4.7.3.1.2**). In fact, at these time delays abundances of the singlet and triplet transients were at the maximum in the femtosecond transient absorption data (**Figure 4.7.3.1.1**).

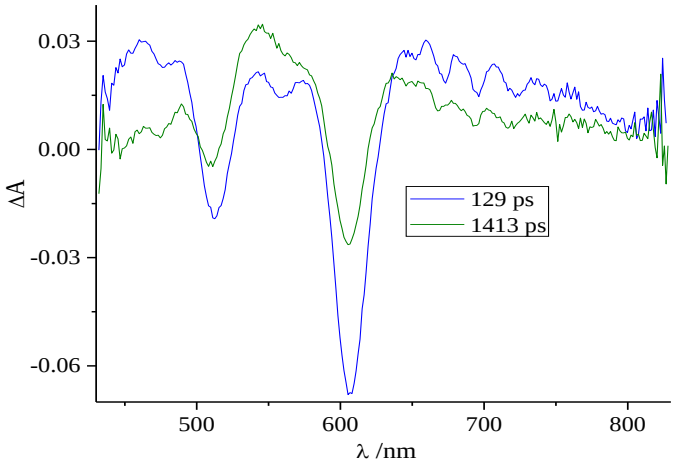

Figure 4.7.3.1.2. Transient absorption spectra at 129 and 1413 ps delay from excitation recorded for **βC** in chloroform.

The spectra of the lowest singlet and triplet excited states must be related through the GSB they share in common. The ground state absorption spectrum was scaled and subtracted from the 129/1413 ps transient spectra in order to remove the GSB contribution. The ground state absorption spectrum was normalized to the transient absorption spectrum at the peak of the ground state bleaching, and then subtracted. The normalization was the method employed to determine the

"right" amount of ground state absorption to subtract each time. The resulting spectra only show the S1/T1 ESA relative to a known amount of GSB (**Figure 4.7.3.1.3**).

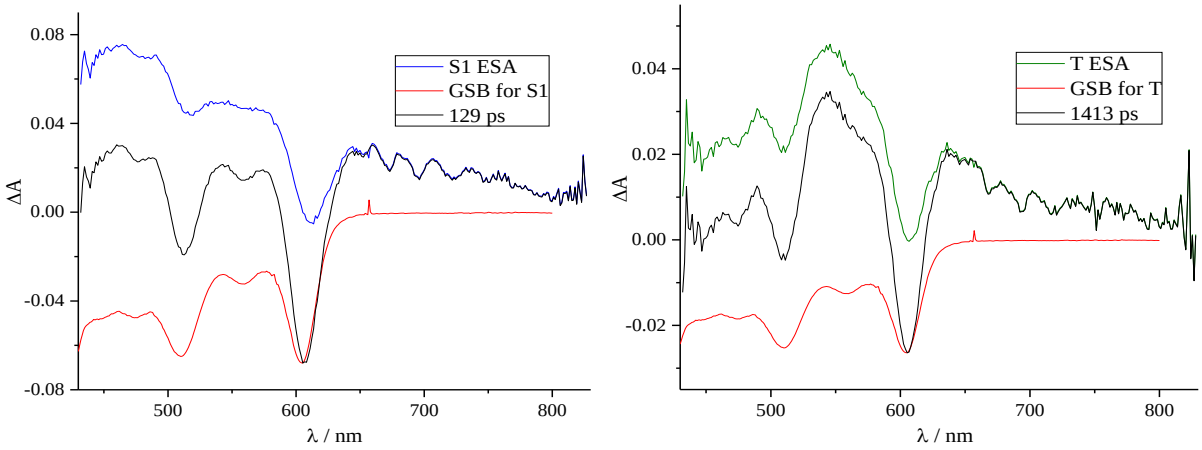

Figure 4.7.3.1.3. Transient (black) and steady state (red) absorption spectra used to reconstruct the absorption spectra of the excited singlet (blue, left) and triplet (green, right) states.
The S1 and T spectra are then normalized to the GSB they share, resulting in two spectra that are quantitatively related (**Figure 4.7.3.1.4**).

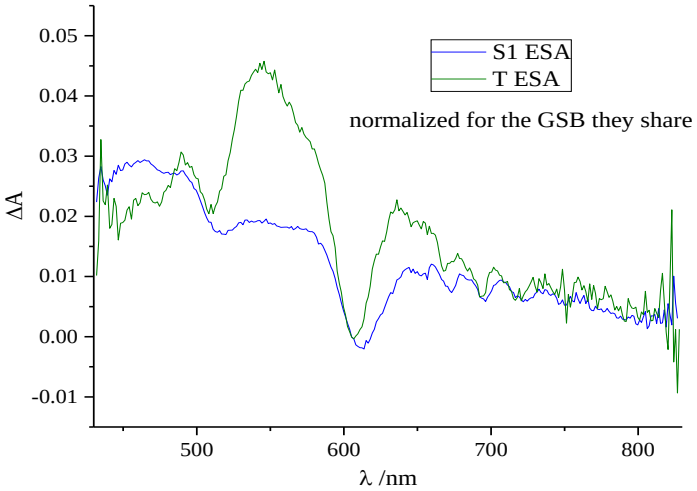

Figure 4.7.3.1.4. Excited state absorption spectra, normalized to GSB, used to correct composition profile in **Figure 4.7.3.1.1** and to obtain population dynamics in **Figure 4.7.3.1.5**.

The quantitatively related spectra of S1 and T were used to correct the composition profiles previously shown. The temporal composition of the components resulting from the global fitting reported in **Figure 4.7.3.1.1** is indeed related to the differential absorbance measured during the ultrafast absorption experiments. Therefore, according to the Lambert−Beer law, it is dependent on both the absorption ability and the concentration of S1 and T. From the quantitatively related S1 and T spectra reported in **Figure 4.7.3.1.4**, it is clear that the ratio between the triplet excited state absorption at its peak (0.0454 at 540 nm) and the singlet excited state absorption at its peak

(0.0292 at 460 nm) is $\frac{\varepsilon_T}{\varepsilon_S} = 1.55$. By scaling the S1 and T temporal compositions in **Figure 4.7.3.1.8** for this factor (multiplying the singlet profile by 1.55), the correct concentration profiles were obtained: $\frac{c_S}{c_T} = \frac{\Delta A_S}{\Delta A_T} \times \frac{\varepsilon_T}{\varepsilon_S}$. From the population profiles normalized at the singlet population peak (**Figure 4.7.3.1.5**), a triplet quantum yield **higher than 46%** was estimated for **βC**.

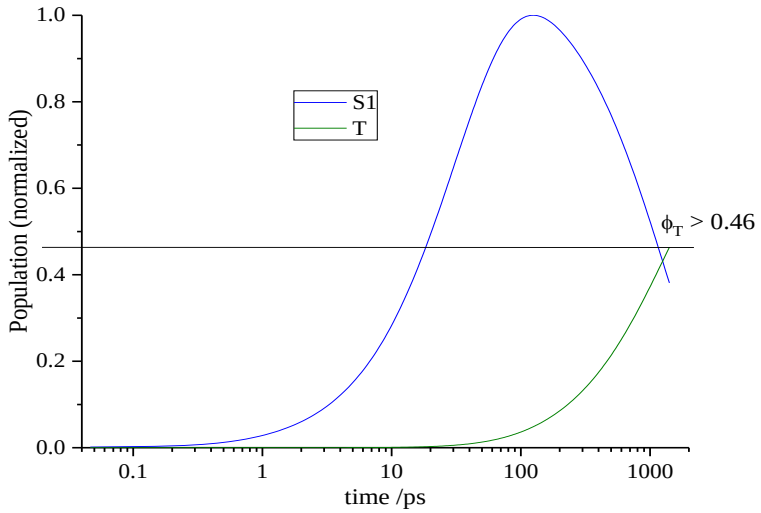

Figure 4.7.3.1.5. Population dynamics of the excited singlet and triplet states for **βC** in chloroform.

*Note: For **βC**, from the fs transient data we estimate a triplet yield somehow higher than that accurately measured by the ns sensitization experiments. However, all the methods agree in giving a triplet yield lower than 100 % for the **βC** compound, clearly suggesting a triplet production via conventional ISC.*

***β** Trimer*

A similar procedure was employed to evaluate the triplet yield for **β**. Global Fitting revealed the presence of four exponential components whose Species Associated Spectra and composition in time are shown below in **Figure 4.7.3.1.6**.

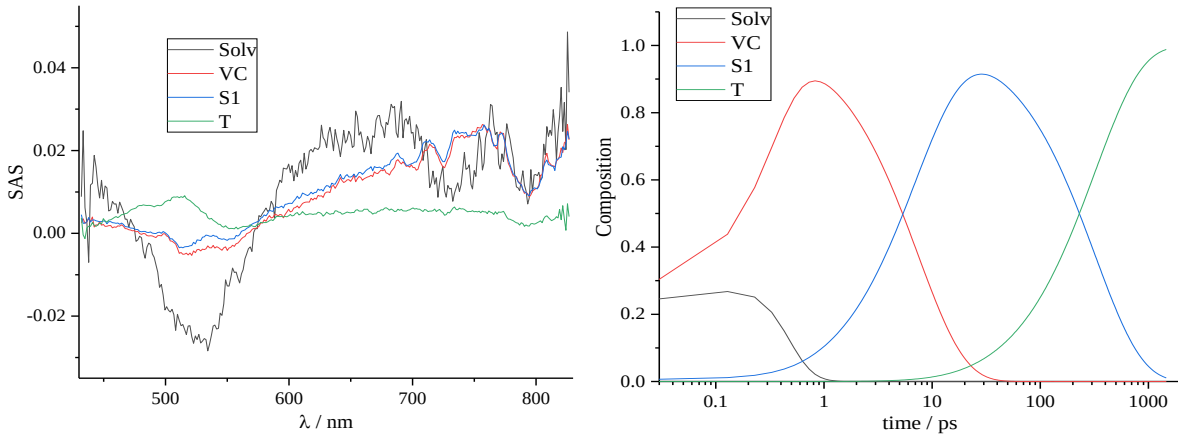

Figure 4.7.3.1.6. Species Associated Spectra (left) and composition in time (right) of the four exponential components resulting from global fitting of the femtosecond transient absorption data of **β** in chloroform.

Looking at the singlet and triplet composition profiles, transient spectra at time delays of 29 and 1165 ps were selected to obtain spectral shapes associated to the excited singlet and triplet state, respectively (**Figure 4.7.3.1.7**).

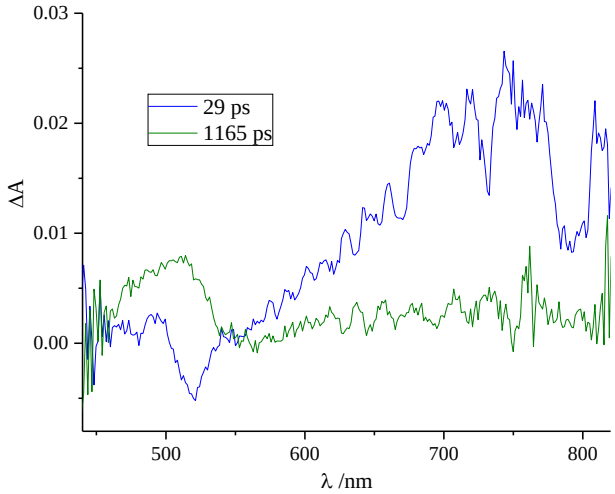

Figure 4.7.3.1.7. Transient absorption spectra at 29 and 1165 ps delay from excitation recorded for **β** in chloroform.

The ground state absorption spectrum was scaled and subtracted from the 29/1165 ps transient spectra in order to remove the GSB contribution (**Figure 4.7.3.1.8**). In this case the same amount of GSB was subtracted from both spectra because no clear negative band is exhibited by the transient spectrum at long delays. This is due to spectral overlap between the ground state and the triplet excited state absorption.

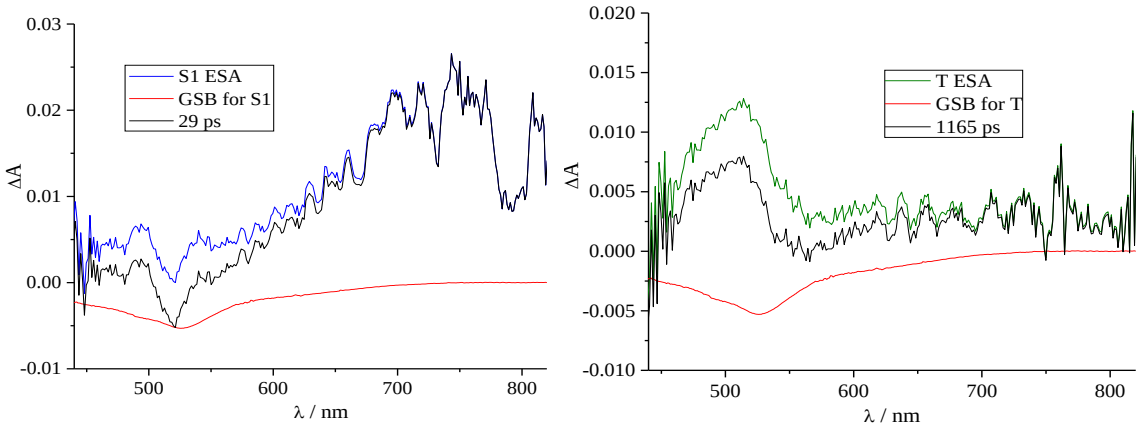

Figure 4.7.3.1.8. Transient (black) and steady state (red) absorption spectra used to reconstruct the absorption spectra of the excited singlet (blue, left) and triplet (green, right) states.

The resulting spectra, which only show S1/T ESA signals peaked at very different wavelengths, are quantitatively related (**Figure 4.7.3.1.9**).

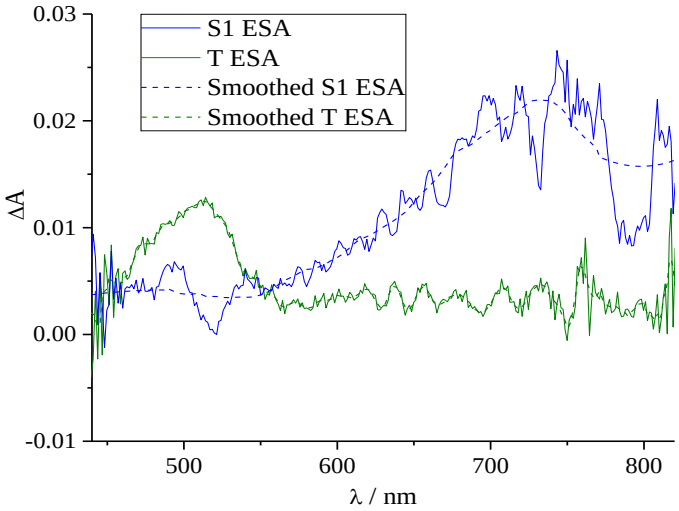

Figure 4.7.3.1.9. Excited state absorption spectra used to correct composition profile in **Figure 4.7.3.1.6** and to obtain population dynamics in **Figure 4.7.3.1.10**.

These spectra were used to correct the composition profiles shown in **Figure 4.7.3.1.6**, after a smoothing procedure was applied to be more accurate in determining differential absorbance typical of singlet and triplet states. The ratio between the triplet excited state absorption at its peak (0.0125 at 510 nm) and the singlet excited state absorption at its peak (0.0219 at 740 nm) is 0.571. The temporal population profiles for these excited states were thus obtained, by scaling the composition profiles in **Figure 4.7.3.1.6** using this factor (multiplying the singlet profile by 0.571). Population dynamics normalized at the singlet peak (**Figure 4.7.3.1.10**) demonstrates the

formation of 1.89 triplets per initially excited singlet. A triplet quantum yield of **189%** was estimated for **β**.

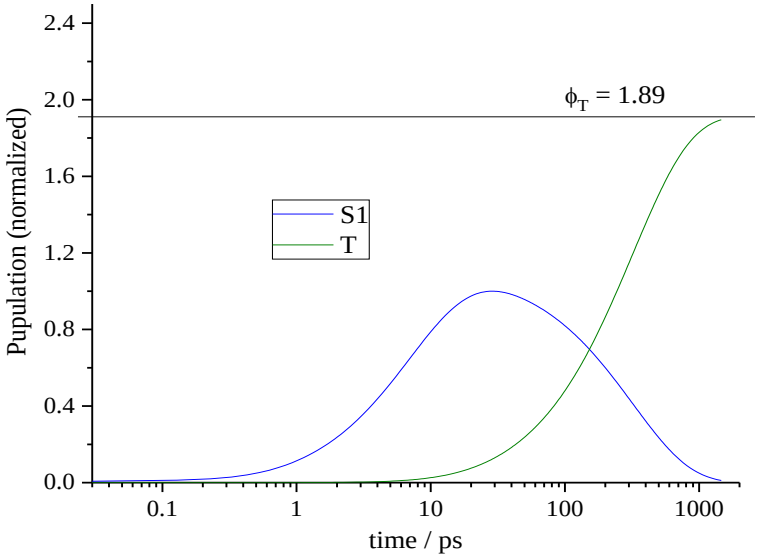

Figure 4.7.3.1.10. Population dynamics of the excited singlet and triplet states for **β** in chloroform.

4.7.4. Nanosecond Transient Absorption (nsTA)

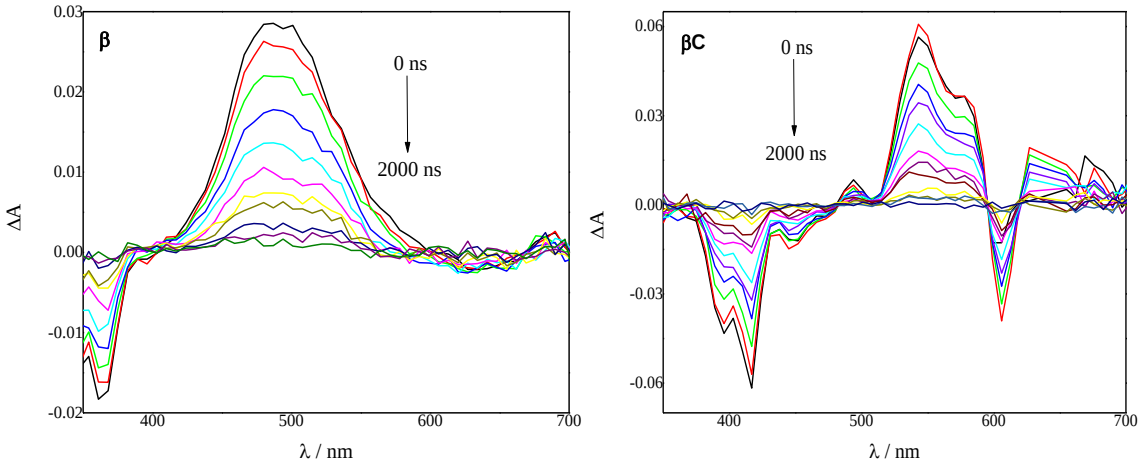

Figure 4.7.4.1. Time−resolved spectra obtained by nanosecond TA measurements for the Trimers in air-equilibrated chloroform upon 500 nm (for **β**) and 600 nm (for **βC**) laser excitations.

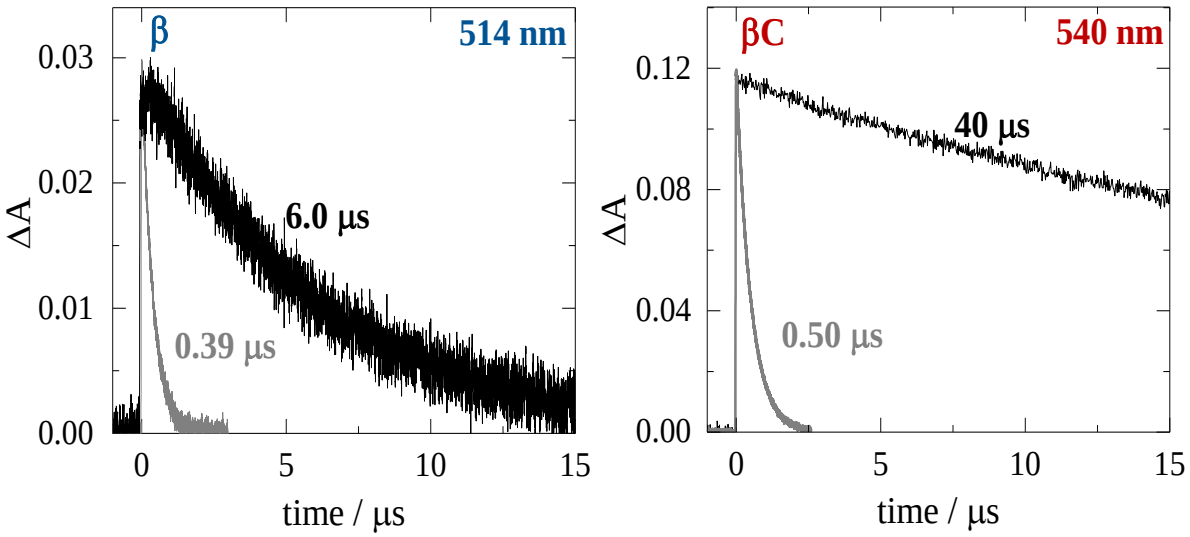

Figure 4.7.4.2. Kinetics of triplet species in air-equilibrated (gray) vs. deaerated (black) chloroform.

4.7.4.1. Triplet Sensitization Experiments by nsTA

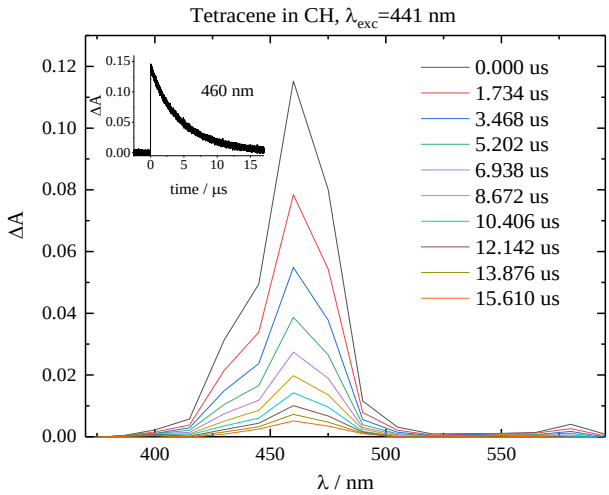

Figure 4.7.4.1.1. Transient absorption spectra of Tetracene in cyclohexane upon laser excitation at 441 nm.

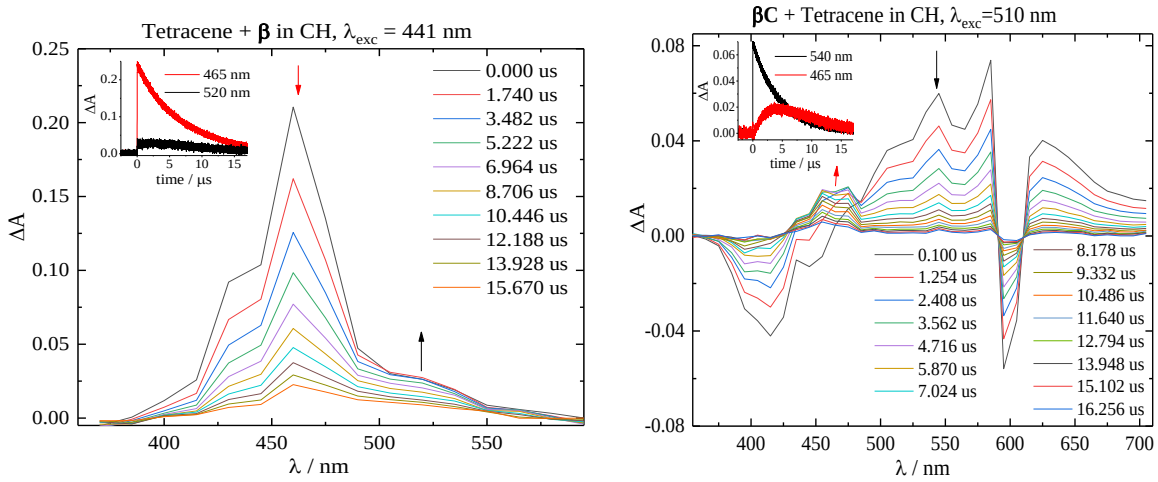

Figure 4.7.4.1.2. Transient absorption sensitization spectra of the Trimer compounds and Tetracene in cyclohexane, showing the triplet species decay of the donor and the rise of the acceptor (inset).

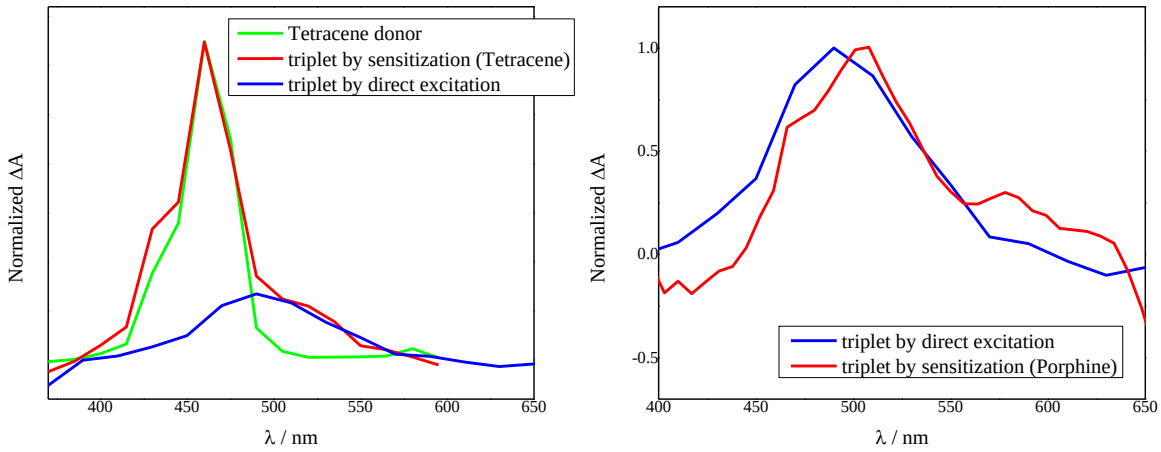

Figure 4.7.4.1.3. Triplet absorption spectrum of **β** from direct excitation and from sensitization by using Tetracene (left) and tetraphenyl-Porphine (right) as triplet donor.

Triplet extinction coefficient of **β** was obtained by triplet energy transfer from Tetracene donor (E_T = 1.27 eV) to the **β** triplet energy acceptor (E_T << 1.27 eV). For **βC**, its triplet extinction coefficient was obtained by energy transfer to the Tetracene acceptor from **βC** acting as a triplet energy donor (E_T > 1.27 eV).

Here, the employed procedures for the two trimer compounds are reported.

1) Determination of the triplet extinction coefficient of β in cyclohexane (CH) at 520 nm by energy transfer from Tetracene (λ_{exc} = 441 nm)[12,14–16]

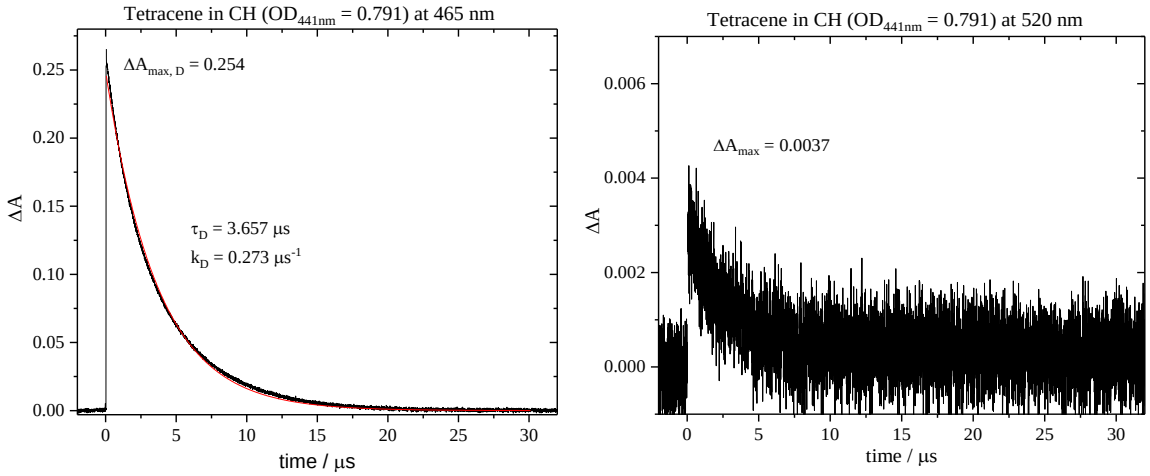

Figure 4.7.4.1.4. Kinetics recorded during nanosecond transient absorption measurements of **Tetracene** (donor) in cyclohexane upon laser excitation at 441 nm.

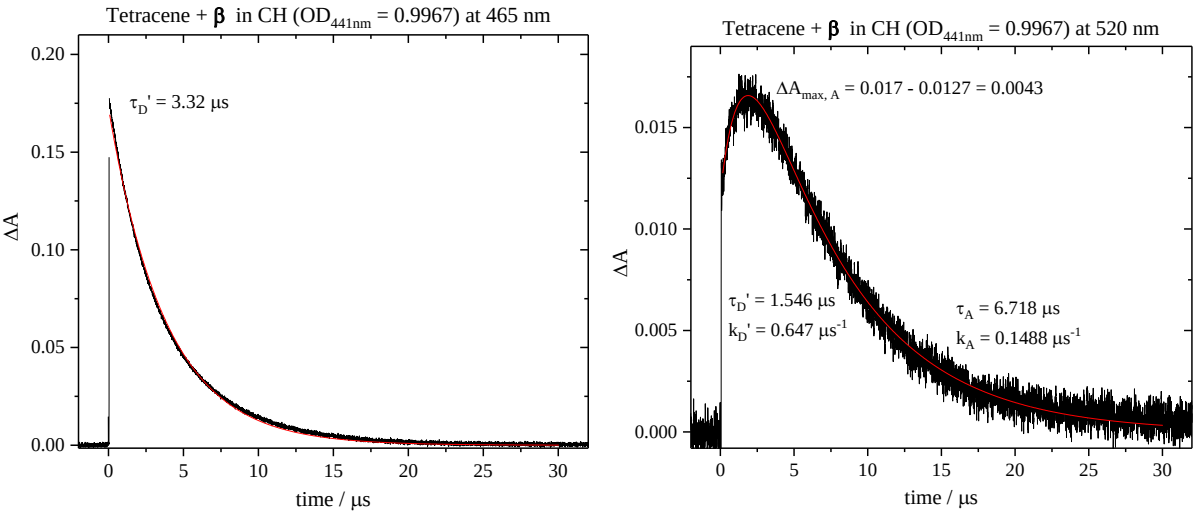

Figure 4.7.4.1.5. Kinetics recorded during nanosecond transient absorption measurements of **β** sensitized by **Tetracene** (quenched donor at 465 nm and sensitized acceptor at 520 nm) in cyclohexane upon laser excitation at 441 nm.

$$\varepsilon_A = \varepsilon_D \times \frac{\Delta A_{max,A}}{\Delta A_{max,D}} \times \frac{1}{f_D \times p_{ET} \times w}$$

$$\varepsilon_A = 31200\ M^{-1}cm^{-1} \times \frac{0.0043}{0.254} \times \frac{1}{0.8514 \times 0.5773 \times 0.6446} = 1667\ M^{-1}cm^{-1}$$

Where:

$f_D = \frac{A_D}{A_{D+A}} \times \left(\frac{1-10^{-A_{D+A}}}{1-10^{-A_D}}\right) = 0.8514$ is the fraction of light absorbed by the donor

$p_{ET} = \frac{k'_D - k_D}{k'_D} = 0.5773$ is the energy transfer probability

$w = exp\left[-\frac{\ln\left(\frac{k'_D}{k_A}\right)}{\frac{k'_D}{k_A}-1}\right] = 0.6446$ is a factor accounting for the quenched donor and acceptor lifetimes

And where,

ε_A = triplet-triplet extinction coefficient of the acceptor (UNKNOWN)

ε_D = triplet-triplet extinction coefficient of the donor/sensitizer (KNOWN)

$\Delta A_{max,A}$ = maximum absorbance change of the Acceptor in the "Donor + Acceptor" mixture

$\Delta A_{max,D}$ = maximum absorbance change of the Donor/sensitizer **alone**

f_D = fraction of light absorbed by the Donor/sensitizer in the "Donor + Acceptor" mixture w.r.t. the Donor alone

k'_D = rise rate constant of the Acceptor in the "Sensitizer + Acceptor" mixture (should be similar to the quenched Sensitizer decay rate constant)

k_D = decay rate constant of the Donor ONLY

k_A = decay rate constant of the Acceptor in the "Donor + Acceptor" mixture

<u>Note:</u> In estimating k'_D, ideally (in the absence of any spectral overlap) the decay rate constant of the quenched Donor (at 465 nm) should match the rise rate constant of the Acceptor (at 520 nm).[15] *This was not the case here for the **β** compound as there is an overlap of its triplet spectrum and that of the tetracene Donor such that at 465 nm both the Donor and the Acceptor contribute to the decay rate constant (see **Figures 4.4.3.1** and **4.7.4.2**). For this reason, we decided to set k'_D as the rise rate constant of the Acceptor because at 520 nm only the **β** compound triplet shows an absorption.*

<u>To calculate the Triplet quantum yield</u>.

Relative Actinometry approach was used.[11] This was done using the computed triplet extinction coefficient from the energy transfer measurement. Tetracene, with its known ε_T and ϕ_T, was used as a reference compound (ref.). In order to obtain the ΔA of both sample and reference, the ground

state absorption (i.e. OD) of both sample and reference has to be the same at the excitation wavelength (441 nm).

$$\frac{[\phi_T \varepsilon_T]_{sample\ (\beta)}}{[\phi_T \varepsilon_T]_{ref.}} = \frac{[\Delta A]_{sample\ (\beta)}}{[\Delta A]_{ref.}}$$

$$[\phi_T \varepsilon_T]_{sample\ (\beta)} = [\phi_T \varepsilon_T]_{ref.} \times \frac{[\Delta A]_{sample\ (\beta)}}{[\Delta A]_{ref.}} = (0.62 \cdot 31200 M^{-1}cm^{-1}) \times \frac{0.0527}{0.366}$$
$$= 2785\ M^{-1}cm^{-1}$$

Where,

$\varepsilon_{T\ sample\ (\beta)}$ = triplet-triplet extinction coefficient of the **β** sample (computed using ***energy transfer meas.***)

$\phi_{T\ sample\ (\beta)}$ = triplet quantum yield of the sample **β**

$[\Delta A]_{sample\ (\beta)}$ = change in absorption of the sample **β** (whose OD is similar to that of the reference at $\lambda_{excitation}$)

$[\Delta A]_{ref}$ = change in absorption of the reference compd. (whose OD is similar to that of the sample at $\lambda_{excitation}$)

Table 4.7.4.1.1. Summary of the parameters recorded for the two triplet energy transfer measurements performed for **β** in CH to ensure reproducibility. Tetracene used as a triplet energy donor.

Parameters	**Measurement 1**	**Measurement 2**
$\boldsymbol{\varepsilon_D(Donor)}$	31200 $M^{-1}cm^{-1}$ (Tetracene)	31200 $M^{-1}cm^{-1}$ (Tetracene)
$\boldsymbol{\Delta A_A}$	0.0043	0.005
$\boldsymbol{\Delta A_D}$	0.254	0.170
$\boldsymbol{f_D}$	0.8514	0.746
$\boldsymbol{k_D}$	0.273 μs^{-1}	0.175 μs^{-1}
$\boldsymbol{k'_D = k_D + k_{ET}[A]}$	0.647 μs^{-1}	1.919 μs^{-1}
$\boldsymbol{k_A}$	0.149 μs^{-1}	0.109 μs^{-1}
$\boldsymbol{\varepsilon_A = \varepsilon_{T\ sample\ (\beta)}}$	1667 $M^{-1}cm^{-1}$	1607 $M^{-1}cm^{-1}$
$[\boldsymbol{\varepsilon_T \cdot \phi_T}]_{\boldsymbol{sample\ (\beta)}}$ (Rel. Actinom. meas.)	2785 $M^{-1}cm^{-1}$	2785 $M^{-1}cm^{-1}$
$\boldsymbol{\phi_{T\ sample\ (\beta)}}$	**1.67**	**1.73**

Taking an **average** of these two measurements, the triplet yield was evaluated to be: ~ **1.70**

2) Determination of the triplet extinction coefficient of βC in cyclohexane (CH) at 540 nm by energy transfer to Tetracene (λ_{exc}=510 nm)

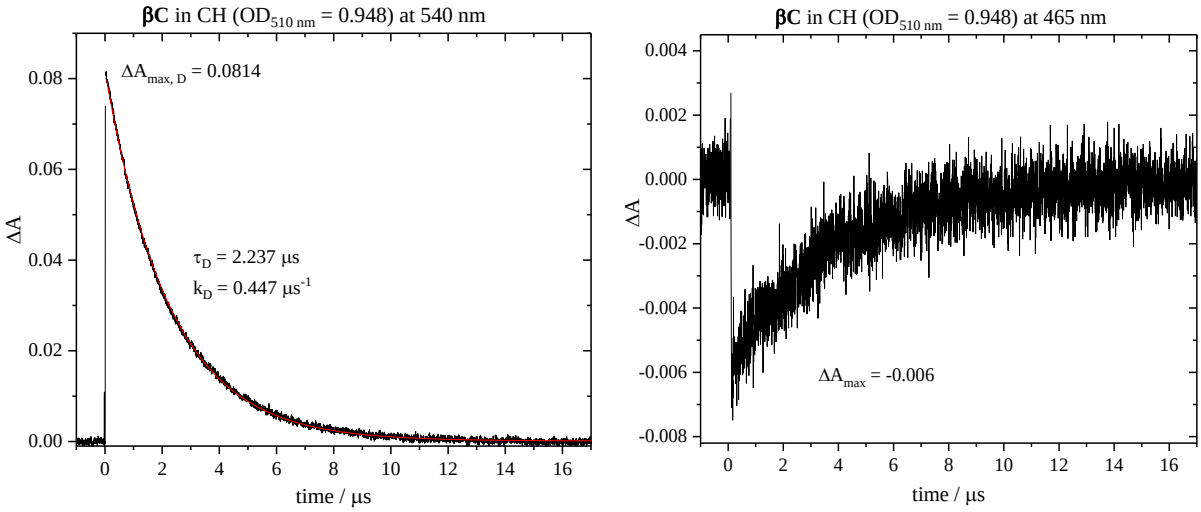

Figure 4.7.4.1.6. Kinetics recorded during nanosecond transient absorption measurements of **βC** (donor) in cyclohexane upon laser excitation at 510 nm. *It should be noted that the difference in the lifetime of **βC** in comparison to that reported in **Table 4.4.3.1** of the main paper is due to the different solvent employed here and to the different nitrogen purging conditions (time, flow rate, ...).*

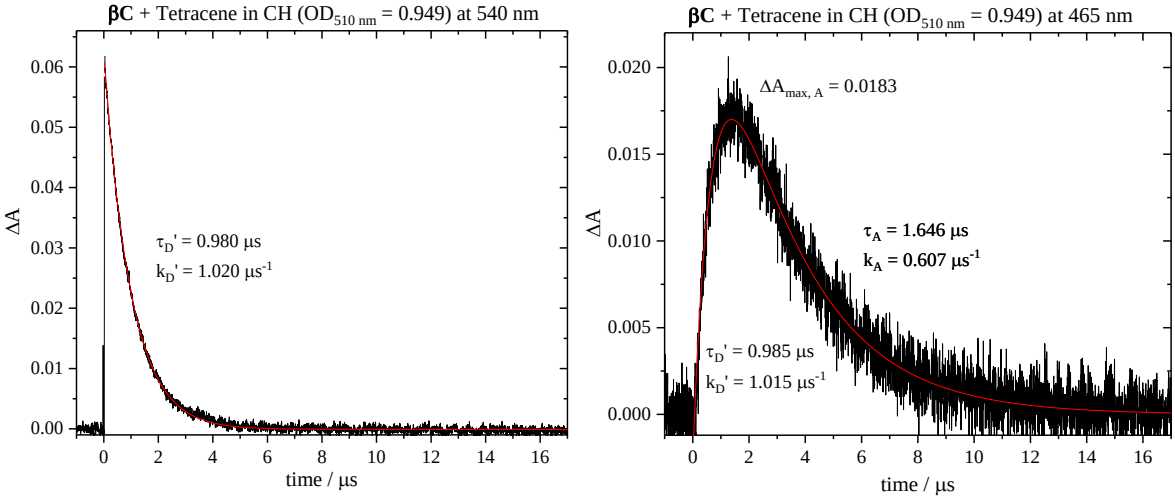

Figure 4.7.4.1.7. Kinetics recorded during nanosecond transient absorption measurements of Tetracene sensitized by **βC** (quenched donor at 540 nm and sensitized acceptor at 465 nm) in cyclohexane upon laser excitation at 510 nm. *The difference in the lifetime of* Tetracene *in comparison to that reported in* **Figure 4.7.4.2** *is due to the non-consistent nitrogen purging conditions (time, flow rate, ...).*

$$\varepsilon_D = \varepsilon_A \times \frac{\Delta A_{max,D}}{\Delta A_{max,A}} \times f_D \times p_{ET} \times w$$
$$= 31200\ M^{-1}cm^{-1} \times \frac{0.0814}{0.0183} \times 0.9985 \times 0.5594 \times 0.4652$$
$$= 36061\ M^{-1}cm^{-1}$$

Where:

$f_D = \frac{A_D}{A_{D+A}} \times \left(\frac{1-10^{-A_{D+A}}}{1-10^{-A_D}}\right) = 0.9985$ is the fraction of light absorbed by the donor

$p_{ET} = \frac{k'_D - k_D}{k'_D} = 0.5594$ is the energy transfer probability

$w = exp\left[-\frac{\ln\left(\frac{k'_D}{k_A}\right)}{\frac{k'_D}{k_A}-1}\right] = 0.4652$ is a factor accounting for the quenched donor and acceptor lifetimes

*<u>Note:</u> Here, in estimating k'_D, the decay rate constant of the quenched Donor (at 540 nm) matches the rise rate constant of the Acceptor (at 465 nm). This is because there is no overlap of the triplet absorption spectrum of the **βC** compound and that of the tetracene Acceptor (see* **Figures 4.4.2.1** *and* **4.7.3.1.3***), unlike in the case of the **β** compound.*

$$\frac{[\phi_T \varepsilon_T]_{sample\ (\beta C)}}{[\phi_T \varepsilon_T]_{ref.}} = \frac{[\Delta A]_{sample(\beta C)}}{[\Delta A]_{ref.}}$$

$$[\phi_T \varepsilon_T]_{sample\ (\beta C)} = [\phi_T \varepsilon_T]_{ref.} \times \frac{[\Delta A]_{sample\ (\beta C)}}{[\Delta A]_{ref.}} = (0.62 \cdot 31200 M^{-1}cm^{-1}) \times \frac{0.125}{0.324}$$
$$= 7460 M^{-1}cm^{-1}$$

Table 4.7.4.1.2. Summary of the parameters recorded for the two triplet energy transfer measurements performed for **βC** in CH to ensure reproducibility. Tetracene used as a triplet energy acceptor in this case.

Parameters	**Measurement 1**	**Measurement 2**
$\boldsymbol{\varepsilon_A}$ **(*Acceptor*)**	31200 $M^{-1}cm^{-1}$ (Tetracene)	31200 $M^{-1}cm^{-1}$ (Tetracene)
$\boldsymbol{\Delta A_D}$	0.0814	0.086
$\boldsymbol{\Delta A_A}$	0.0183	0.012
$\boldsymbol{f_D}$	0.9985	1
$\boldsymbol{k_D}$	0.4470 μs^{-1}	0.2476 μs^{-1}

$k'_D = k_D + k_{ET}[A]$	1.0145 μs^{-1}	0.7158 μs^{-1}
k_A	0.6074 μs^{-1}	0.4063 μs^{-1}
$\varepsilon_D = \varepsilon_{T\ sample\ (\beta C)}$	36061 $M^{-1}cm^{-1}$	69545 $M^{-1}cm^{-1}$
$[\varepsilon_T \cdot \phi_T]_{sample\ (\beta C)}$ (Rel. Actinom. meas.)	7460 $M^{-1}cm^{-1}$	7460 $M^{-1}cm^{-1}$
$\phi_{T\ sample\ (\beta C)}$	**0.21**	**0.11**

Taking an **average** of these two measurements, the triplet yield was evaluated to be: ~ **0.16**

4.7.5. Two–Color Transmission Measurement of Triplet Species to compute Triplet Yield

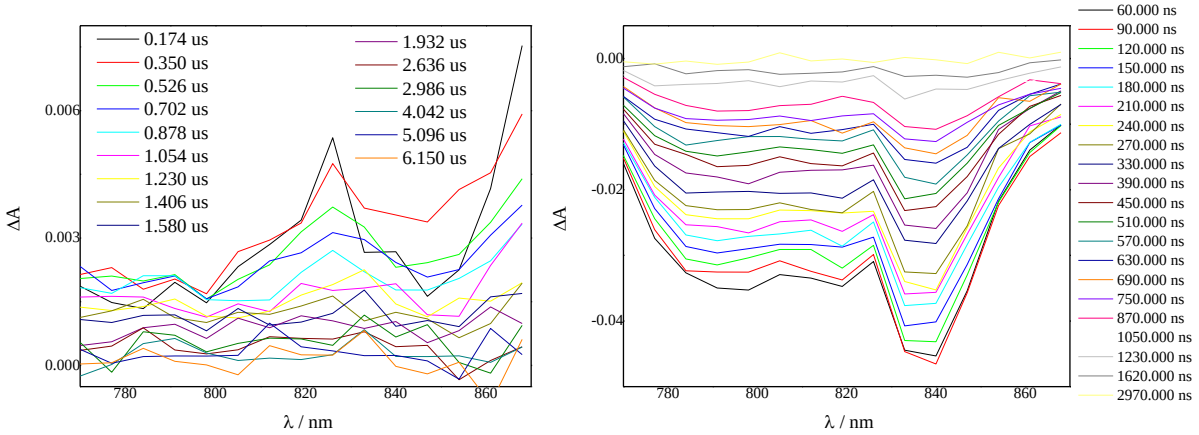

Figure 4.7.5.1. Time resolved absorption spectra recorded in the region between 770 and 870 nm via nanosecond transient absorption for **β** (left) and **βC** (right) in chloroform upon 510 nm laser excitation.

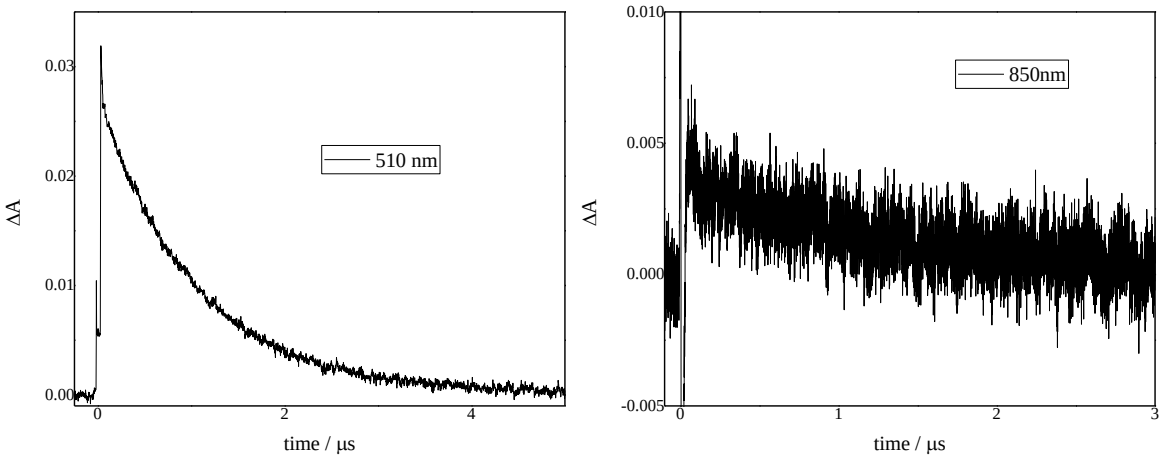

Figure 4.7.5.2. Kinetics recorded at 510 nm (left) and 850 nm (right) for **β** in chloroform via nanosecond transient absorption upon 510 nm laser excitation.

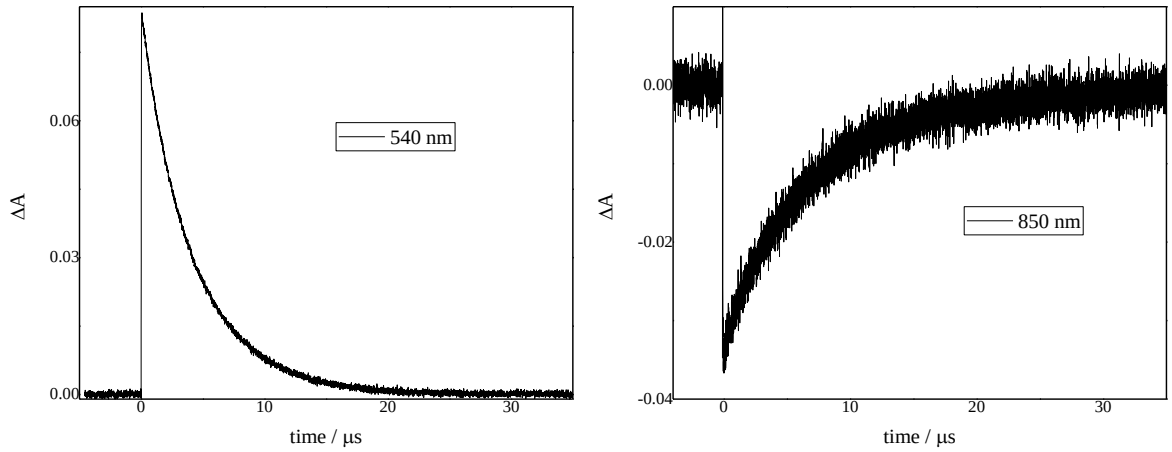

Figure 4.7.5.3. Kinetics recorded at 540 nm (left) and 850 nm (right) for **βC** in chloroform via nanosecond transient absorption upon 510 nm laser excitation.

Using the laser parameters and the 850nm probe beam attenuation caused by the 425nm pump, one can estimate the singlet to triplet conversion efficiency in the trimers. Following information outlines the calculation of singlet-triplet conversion efficiency from experimental data. The triplet extinction coefficient for the trimers at 850 nm was evaluated via nanosecond transient absorption measurements (see **Figure 4.7.4.1.7**, **4.7.5.1** and **4.7.5.2**). Triplet extinction coefficients at 850 nm of 280 M^{-1} cm^{-1} for **β** and of 9100 M^{-1} cm^{-1} for **βC** were used in the quantitative analysis of the two-color transmission measurements.

Twisted Trimer β in chloroform

Number of singlet excitations have been created by ultrashort 425nm laser pulse

- Average laser power at 425 *nm* = 4.25 *mW* (probe power at 850 nm ≤1.20 mW, beam attenuation 29.7%)
- Energy per pump pulse = $0.00425/(8\times10^{7})$ = 0.053 *nJ/pulse*
- Pulse duration = 130 *fs* = 1.3×10^{-13} *s*
- Laser beam divergence (full angle) : ≤ 1 *mrad* (Mai-Tai specs) = 10^{-3} *rad*
- Focus of the focusing lens = 0.3 *cm*

  Waist diameter of focal beam = 0.3×10^{-3} *cm* (30 *μm*)

  Focal waist area = $\pi D^2/4 = 0.707\times10^{-7}$ cm^2

Excitation volume = 0.707×10^{-7} cm^2 ×1cm=0.707×10^{-7} cm^3

- Energy density for 425nm pump pulse = $0.053\times10^{-9}/(0.707\times10^{-5}) \approx 7.50\times10^{-6}$ J/cm^2

Energy of a photon at 425 nm = 4.7×10^{-19} *J/photon*

Singlet excitations number density:

The number of absorbed photons at 425nm: Optical density of the sample at 425nm = **0.116**

$I_{in}-I_{out} = I_{in}(1-10^{-0.116}) = I_{in}(1-0.76) = 0.23*I_{in}$

$I_{in}=0.053\times10^{-9}/(4.7\times10^{-19})=1.1\times10^{8}$phot/pulse

That is $0.23\times1.1\times10^{8} = 0.259\times10^{8}$ photons have been absorbed per pulse.

The same number of molecules in the excited singlet state has been created in the excitation volume ($v = 0.707\times10^{-5}cm^3$)

Excited singlet number density: $n_S^* = 0.259\times10^{8}/(0.707\times10^{-5}) = 3.66\times10^{12}$ molecules/cm^3

Triplet excitation number density:

850nm - probe beam attenuation observed under pump of 4.25 mW is **29.7 %**

No focal mismatch is suggested in this version of calculations.

In order to create this attenuation for the matching part of the probe beam the concentration of the triplet states responsible for attenuation can be obtained:

$I_{out}/I_{in} = 1 - 0.297 = 0.703 = 10^{-\varepsilon l M_T}$, (ε-extinction coefficient for triplet-triplet absorption, l – cell length, M_T - triplet states concentration) or

$-\varepsilon l M_T=\log (0.703) = -0.153$

$M_T=0.153/(1\times280)=0.546\times10^{-3}$ M where 280 $M^{-1}cm^{-1}$ is the molar extinction coefficient for triplet-triplet absorption

This molar concentration corresponds to the triplet population density

$n_{TE} = N_A\times M_T/1000= 3.29\times10^{17}$ triplets/cm^3

Full number of triplet in the excitation volume v is

$N_{TT} = n_{TE}\times v = 3.29\times10^{17} \times0.707\times10^{-7} = 2.32\times10^{10}$ molecules in the triplet state in the excitation volume

Each pulse creates $N_S^* = 0.259\times10^{8}$ molecules in the singlet state

The number of triplet states created by each pulse is:

N_{TP}= $\alpha \times 0.259 \times 10^8$ molecules in the triplet state in the excitation volume. Now the triplet state accumulation at relatively high pulse repetition rate should be taken into account:

$N_{Taccum} = N_{TP} \times \tau_T \times 8 \times 10^7$; where τ_T is triplet state lifetime **(~6μs)**, 8×10^7 - laser pulse repetition rate

$N_{Taccum} = 0.259 \times 10^8 \times \alpha \times 6 \times 10^{-6} \times 8 \times 10^7 = 1.24 \times 10^{10} \times \alpha$:

$\alpha = (2.32 \times 10^{10} / 1.24 \times 10^{10})$ = **1.87 or 187%**

Planar Trimer βC in chloroform

Number of singlet excitations have been created by ultrashort 425nm laser pulse

- Average laser power at 425 *nm* = 4.25 *mW* (probe power at 850 nm ≤1.20 mW, beam attenuation 36.6%)
- Energy per pump pulse=$0.00425/(8 \times 10^7)$ = 0.053 *nJ/pulse*
- Pulse duration = 130 *fs* = 1.3×10^{-13} *s*
- Laser beam divergence (full angle) : ≤ 1 *mrad* (Mai-Tai specs) = 10^{-3} *rad*
- Focus of the focusing lens = 0.3 *cm*

  Waist diameter of focal beam = 3×10^{-3} *cm* (30 μm)

  Focal waist area = $\pi D^2/4 = 0.707 \times 10^{-7}$ cm^2

  Excitation volume =0.707×10^{-7} cm^2 ×1cm = 0.707×10^{-7} cm^3

- Energy density for 425nm pump pulse = $0.053 \times 10^{-9}/(0.707 \times 10^{-5}) \approx 7.50 \times 10^{-6}$ J/cm^2

  Energy of a photon at 425 nm = 4.7×10^{-19} *J/photon*

Singlet excitations number density:

The number of absorbed photons at 425nm: Optical density of the sample at 425nm = **0.885**

I_{in}-I_{out} = $I_{in}(1-10^{-0.885}) = I_{in}(1-0.13) = 0.87 \times I_{in}$

$I_{in} = 0.053 \times 10^{-9}/(4.7 \times 10^{-19}) = 1.1 \times 10^8$phot/pulse

That is 0.980×10^8 photons have been absorbed per pulse.

The same number of molecules in the excited singlet state has been created in the excitation volume (v = $0.707 \times 10^{-5} cm^3$)

Excited singlet number density: $n_S^* = 0.980\times10^8/(0.707\times10^{-5}) = 13.9\times10^{12}$ molecules/cm^3

Triplet excitation number density:

850nm - probe beam attenuation observed under pump of 4.25 mW is **36.6 %**

No focal mismatch is suggested in this version of calculations.

In order to create this attenuation for the matching part of the probe beam the concentration of the triplet states responsible for attenuation can be obtained:

$I_{out}/I_{in} = 0.654 = 10^{-\varepsilon l M T}$, ($\varepsilon$-extinction coefficient for triplet-triplet absorption, l – cell length, M_T - triplet states concentration) or

$-\varepsilon l M_T = \log(0.654) = -0.184$

$M_T = 0.184/(1\times9100) = 0.202\times10^{-4}$ M where 9100 $M^{-1}cm^{-1}$ is the molar extinction coefficient for triplet-triplet absorption

This molar concentration corresponds to the triplet population density

$n_{TE} = N_A\times M_T/1000 = 1.22\times10^{16}$ triplets/cm^3

Full number of triplet in the excitation volume v is

$N_{TT} = n_{TE}\times v = 1.22\times10^{16}\times0.707\times10^{-7} = 8.61\times10^8$ molecules in the triplet state in the excitation volume

Each pulse creates $N_S^* = 0.980\times10^8$ molecules in the singlet state

The number of triplet states created by each pulse is:

$N_{TP} = \alpha\times0.980\times10^8$ molecules in the triplet state in the excitation volume.

Now the triplet state accumulation at relatively high pulse repetition rate should be taken into account:

$N_{Taccum} = N_{TP}\times\tau_T\times8\times10^7$; where τ_T is triplet state lifetime (~**40μs**), 8×10^7 - laser pulse repetition rate

$N_{Taccum} = 0.980\times10^8\times\alpha\times40\times10^{-6}\times8\times10^7 = 3.14\times10^{11}\times\alpha$:

$\alpha = (8.61\times10^8/3.14\times10^{11}) =$ **0.0027 or 0.27%**

It has to be noted that for the case of the **βC** compound, the estimated triplet yield value is not accurate because of the observed phosphorescence interference at 850 nm.

4.7.6. Fluorescence Up-Conversion (FUC)

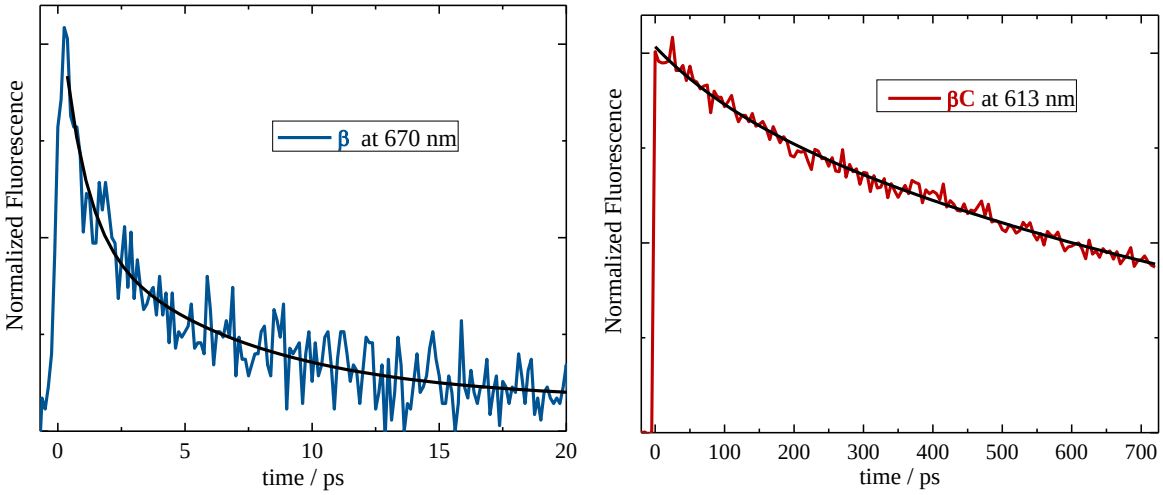

Figure 4.7.6.1. Fluorescence decay kinetics recorded for compounds **β** and **βC** in chloroform by femtosecond resolved FUC, together with their poly-exponential fittings (black).

Table 4.7.6.1. Lifetimes (τ) and pre−exponential factors (A) obtained by fitting the FUC kinetics.

Compound	$A_{FUC,1}$	$\tau_{FUC,1}$ / ps	$A_{FUC,2}$	$\tau_{FUC,2}$ / ps	$A_{FUC,3}$	$\tau_{FUC,3}$ / ps
β	0.60	1.0	0.46	6.0	–	–[b]
βC	−0.20[a]	0.20[a]	0.11	110	0.90	1000[c]
assignment		*Solv. / ICT*		*VC / SR*		S_1

[a] Rise time obtained from fitting of the fluorescence kinetics acquired on a 3 ps time window (see **Figure 4.7.4.1.7** left). [b] The fact that the third component (τ_3 in **Table 4.7.4.1.2**) is not revealed is likely due to acquisition at 670 nm, in the blue part of the emission spectrum, where time resolved red shift of the emission spectra accompanying relaxation is primarily detected. Acquisition at the emission maximum was indeed prevented by the extremely red shifted fluorescence of **β**. [c] Corresponds to the lifetime obtained with the single photon counting measurements (1.33 ns) with the latter being a better evaluation for the decay time of this long living component.

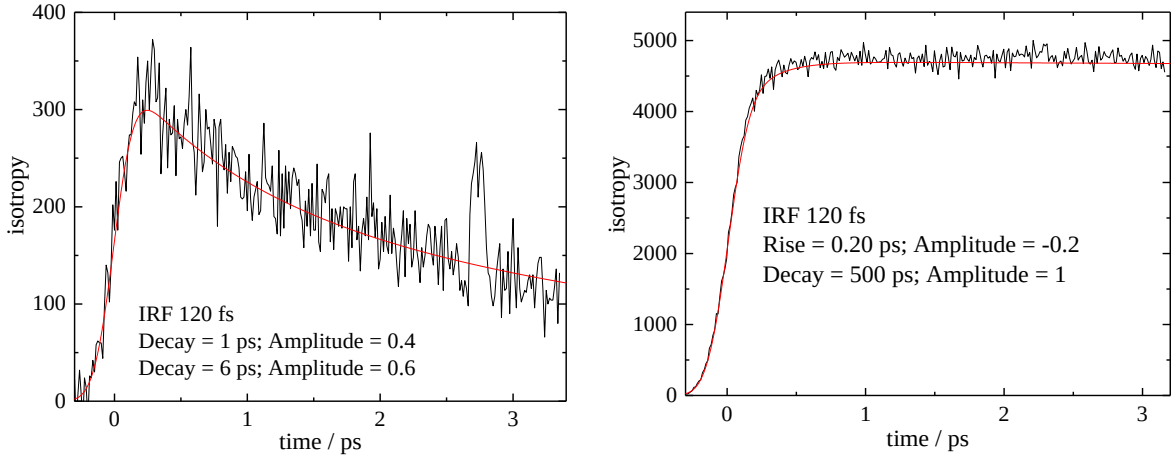

Figure 4.7.6.2. Fluorescence kinetics for **β** at 670 nm (left) and **βC** at 613 nm (right) in chloroform; best fit to a bi−exponential function is also shown.

4.7.7. Quantum Chemical Simulations

Details about intersystem crossing rate calculations

The first excited triplet state (T_1) geometry of the compound **β** and **βC** was obtained with time−dependent density functional theory (TDDFT). The same functional and basis sets (B3LYP and 6−31G*) used to locate the ground state geometry were employed for the geometry optimization. Single−point energy was refined using the system−dependent, nonempirically tuned version of long−range corrected functional ωB97X−D with the optimal ω values. (You can find the optimal ω values in the main text.) The medium effect was included using polarizable continuum model with the dielectric constant of 4.31 for chloroform. The first excited singlet (S_1) geometry was used to calculate the spin–orbit coupling. All the quantum chemical simulations were conducted using Q–Chem 5.0.

The rate constant of intersystem crossing (ISC) was estimated via Fermi's Golden rule.[36,37]

$$k_{\mathrm{ISC}} = \frac{2\pi}{\hbar}\rho_{\mathrm{FC}}|\langle \mathrm{S}_1|H_{SO}|\mathrm{T}_1\rangle|^2$$

Where, $\langle \mathrm{S}_1|H_{SO}|\mathrm{T}_1\rangle$ is the spin−orbit coupling element between S_1 and T_1, ρ_{FC} denotes the Franck−Condon−weighted density of states, and $\hbar$ is the reduced Planck constant of 6.582×10^{-16} eVs. ρ_{FC} is evaluated with Marcus−Levich−Jortner theory.[38,39]^{39,40}^{39,40}^{11,12}^{11,12}^{7,8}^{7,8}

$$\rho_{\mathrm{FC}} = \frac{1}{\sqrt{4\pi\lambda_{\mathrm{M}}k_{\mathrm{B}}T}}\sum_{n=0}^{\infty}\exp(-S)\frac{S^n}{n!}\exp[-\frac{(\Delta E_{\mathrm{ST}} + n\hbar\omega_{\mathrm{eff}} + \lambda_{\mathrm{M}})^2}{4\pi\lambda_{\mathrm{M}}k_{\mathrm{B}}T}]$$

Where, λ_{M} is the Marcus reorganization energy associated with the intermolecular and intramolecular low−frequency vibrations, k_{B} is for Boltzmann constant of 8.6173×10^{-5} eV/K, T is the temperature (in this study, 298.15 K), $\hbar\omega_{\mathrm{eff}}$ represents the effective energy of a mode representing the nonclassical high−frequency intramolecular vibrations, and ΔE_{ST} is the adiabatic energy difference between S_1 and T_1. Huang−Rhys factor associated with these modes are given as S.

One recent computational study on thermally activated delayed fluorescence (TADF) mechanism discussed the rate of reverse ISC within the same framework used in this work.[41] The researchers from the same group computed the contribution of nonclassical intramolecular vibrations, and

estimated the Marcus reorganization energy due to low−frequency intramolecular vibrations and the medium−induced relaxation effects. In addition, they assumed the Huang−Rhys factors can be neglected without significant changes to the results for large molecules.[39,42]

The numerical values of each property to predict the rate of ISC are given in **Table 4.7.7.1**.

Table 4.7.7.1. Properties used to predict the rate of ISC.

	β	**βC**
λ (eV)	0.244	0.424
Spin–orbit coupling (cm^{-1})	2.704	0.257
ΔE_{ST} (eV)	−0.704	−0.595
Rate of ISC (s^{-1})	8.44×10^{5}	1.35×10^{7}

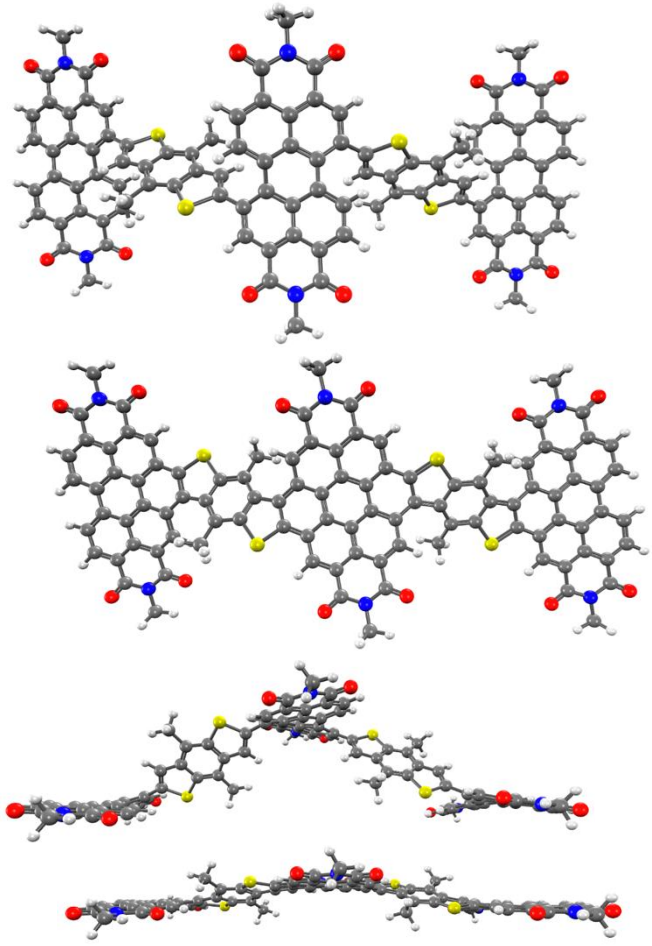

β **βC**

Figure 4.7.7.1. Ground state (S_0) optimized geometry computed for the trimers (color scheme; Hydrogen—white, carbon—black, nitrogen—blue, oxygen—red, sulfur—yellow).

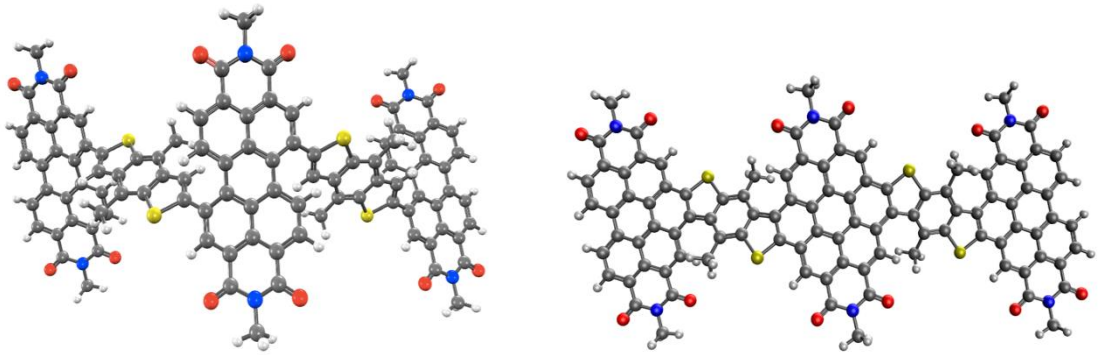

β **βC**

Figure 4.7.7.2. Excited state (T_1) optimized geometry computed for the trimers.

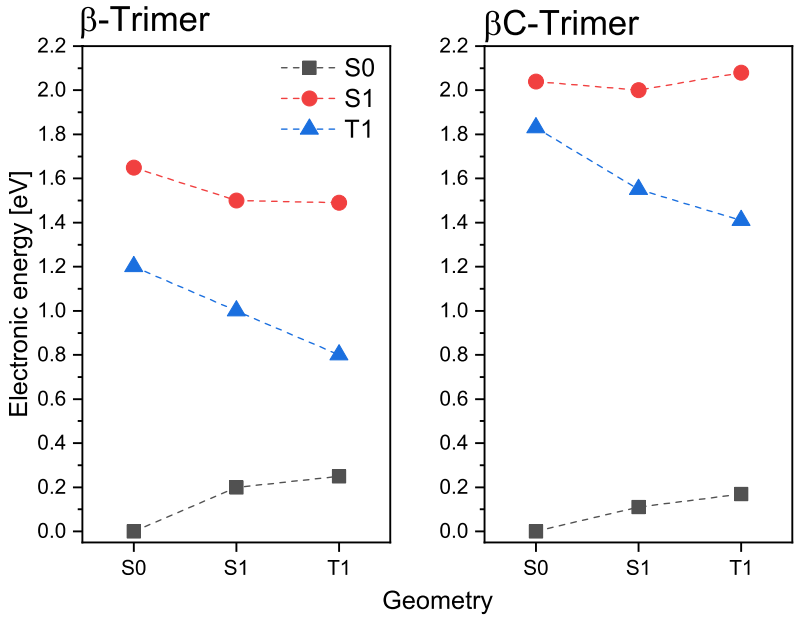

eV		**β**			**βC**	
Geometry/ Electronic state	S_0	S_1	T_1	S_0	S_1	T_1
S_0	0.00	0.20	0.25	0.00	0.11	0.17
S_1	1.65	1.50	1.49	2.04	2.00	2.08
T_1	1.20	1.00	0.80	1.83	1.55	1.41

Figure 4.7.7.3. Singlet fission energetics for **β** (left) and **βC** (right); energies are given in eV.

	β	**βC**

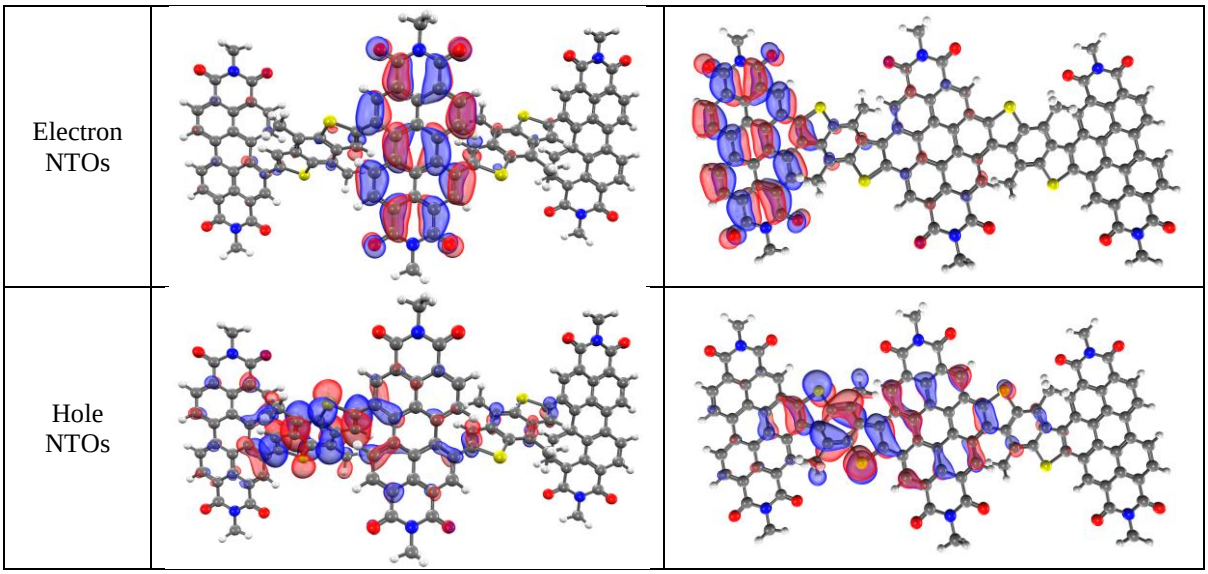

Figure 4.7.7.4. Natural transition orbitals for the S_1 geometry ($S_1 \rightarrow S_0$ transition) of compounds **β** and **βC** (isodensity=0.05. Color scheme; Hydrogen—white, carbon—black, nitrogen—blue, oxygen—red, sulfur—yellow).

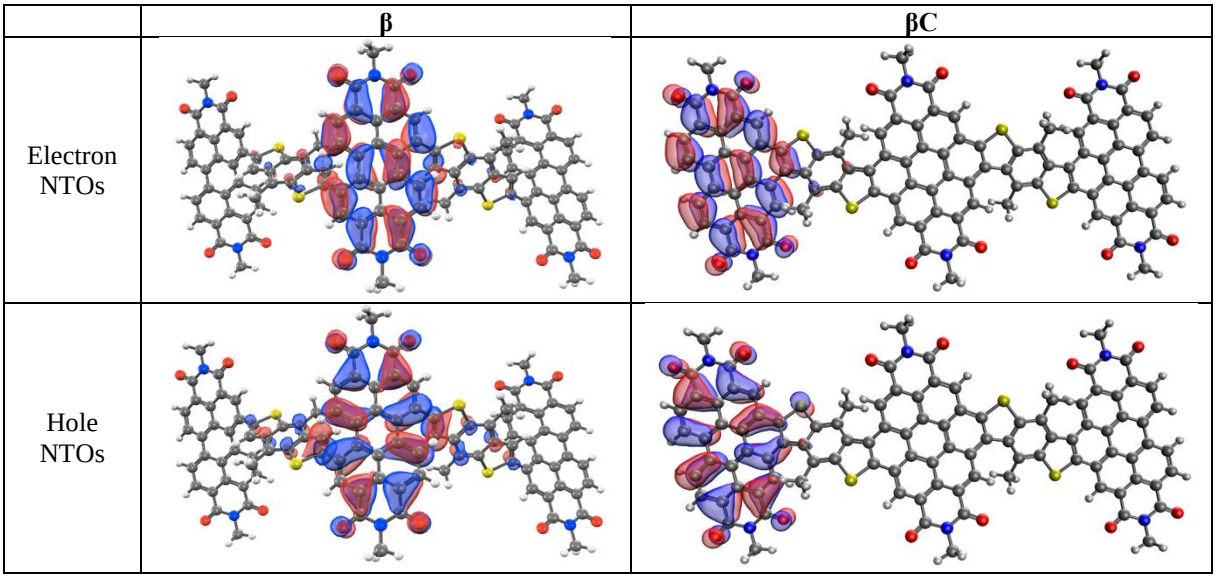

Figure 4.7.7.5. Natural transition orbitals for the T_1 geometry ($S_0 \rightarrow T_1$ transition) for the trimers.

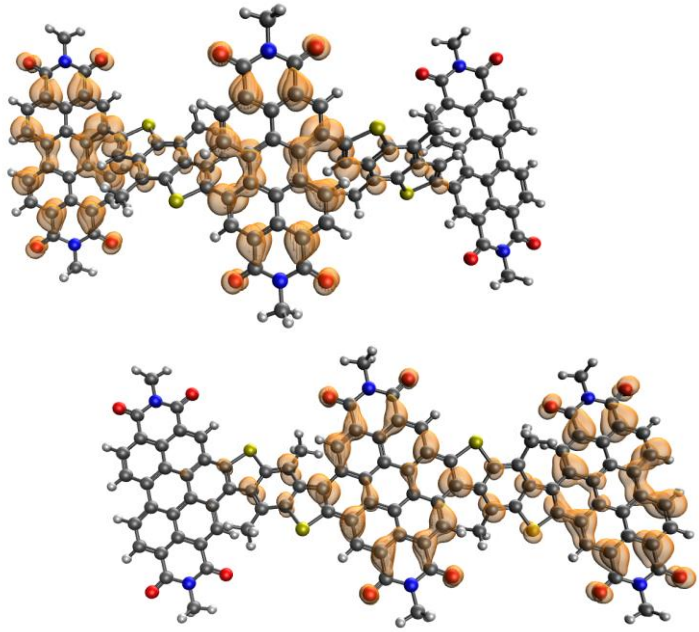

β **βC**

Figure 4.7.7.6. Spin density of quintet state structure for the trimers (isodensity = 0.05. Color scheme; Hydrogen—white, carbon—black, nitrogen—blue, oxygen—red, sulfur—yellow).

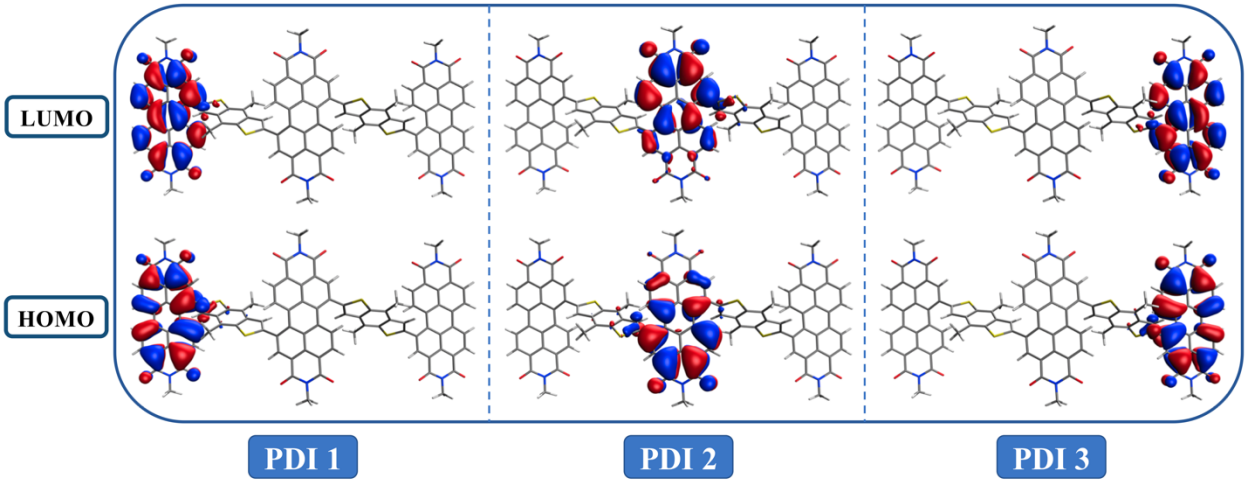

Figure 4.7.7.7. Frontier orbitals considered in RAS-SF calculations for **β** compound.

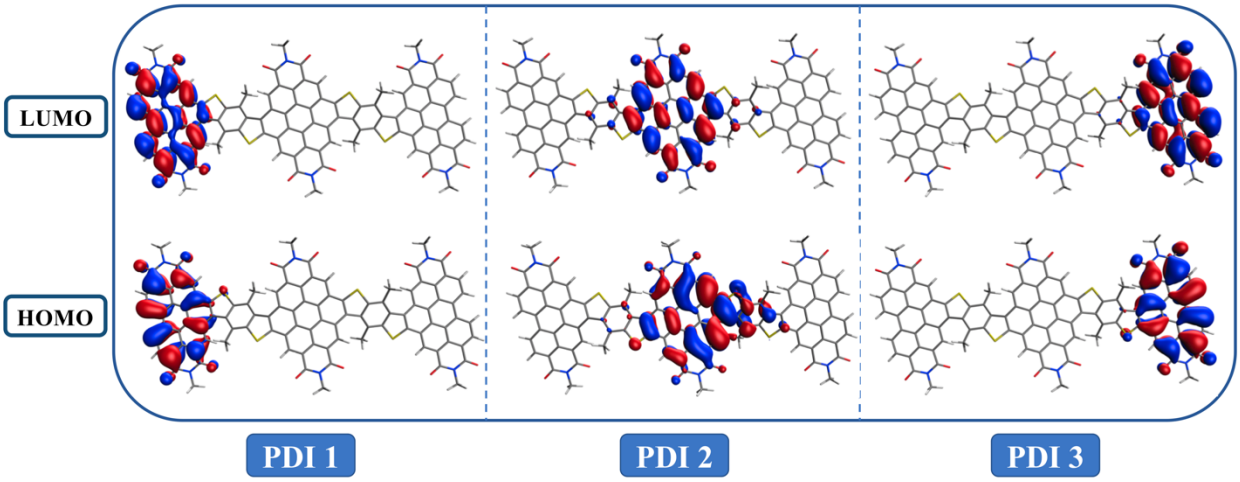

Figure 4.7.7.8. Frontier orbitals considered in RAS-SF calculations for **βC** compound.

Table 4.7.7.2. Energy levels estimated by 3SF-RAS based on the S_1 geometries of each chromophore (S: Singlet, T: Triplet, Q: Quintet, ME: Multiexciton. Energies are given in eV).

β		**βC**	
State	Energy	State	Energy
S_0	0.000	S_0	0.000
T_1	1.960	T_1	2.371
T_2	1.962	T_2	2.371
T_3	1.967	T_3	2.591
S_1	3.452	S_1	3.683
S_2	3.568	S_2	4.100
S_3	3.586	S_3	4.106
S_4, ME (^{1}TT)	3.940	T_4	4.187
T_4	3.942	T_5	4.335
S_5, ME (^{1}TT)	3.946	T_6	4.340
Q_1	3.946	S_4	4.596
T_5	3.948	S_5	4.604
Q_2	3.952	T_7	4.721
S_6, ME (^{1}TT)	3.955	T_8	4.732
T_6	3.955	T_9	4.785
Q_3	3.955	Q_1	4.785
		S_6, ME (^{1}TT)	4.785
		S_7	4.812
		S_8, ME (^{1}TT)	4.916
		T_{10}	4.917
		S_9, ME (^{1}TT)	4.919
		T_{11}	4.925
		S_{10}	4.962
		Q_2	4.982
		Q_3	4.982

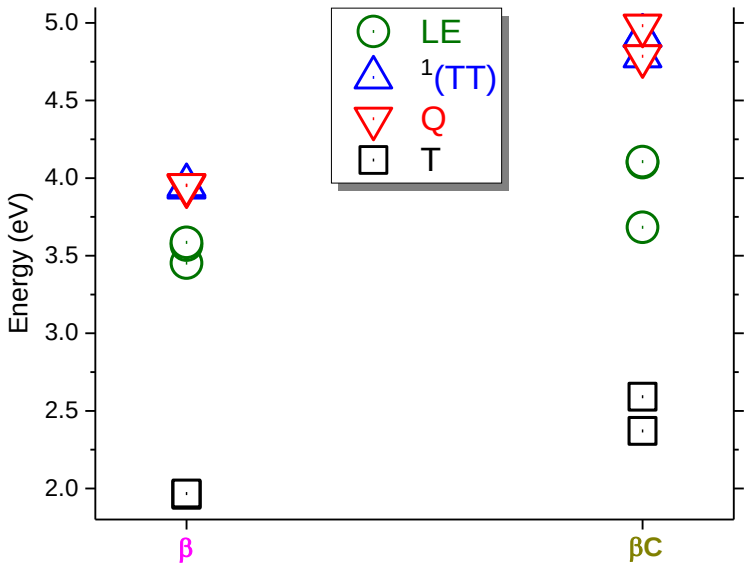

Figure 4.7.7.9. SF relevant energetics for **β** and **βC** Trimers showing interaction energies.
It should be noted that the LE (S_1) and T_1 energies are overestimated in SF-RAS calculations relative to TD-DFT calculations.

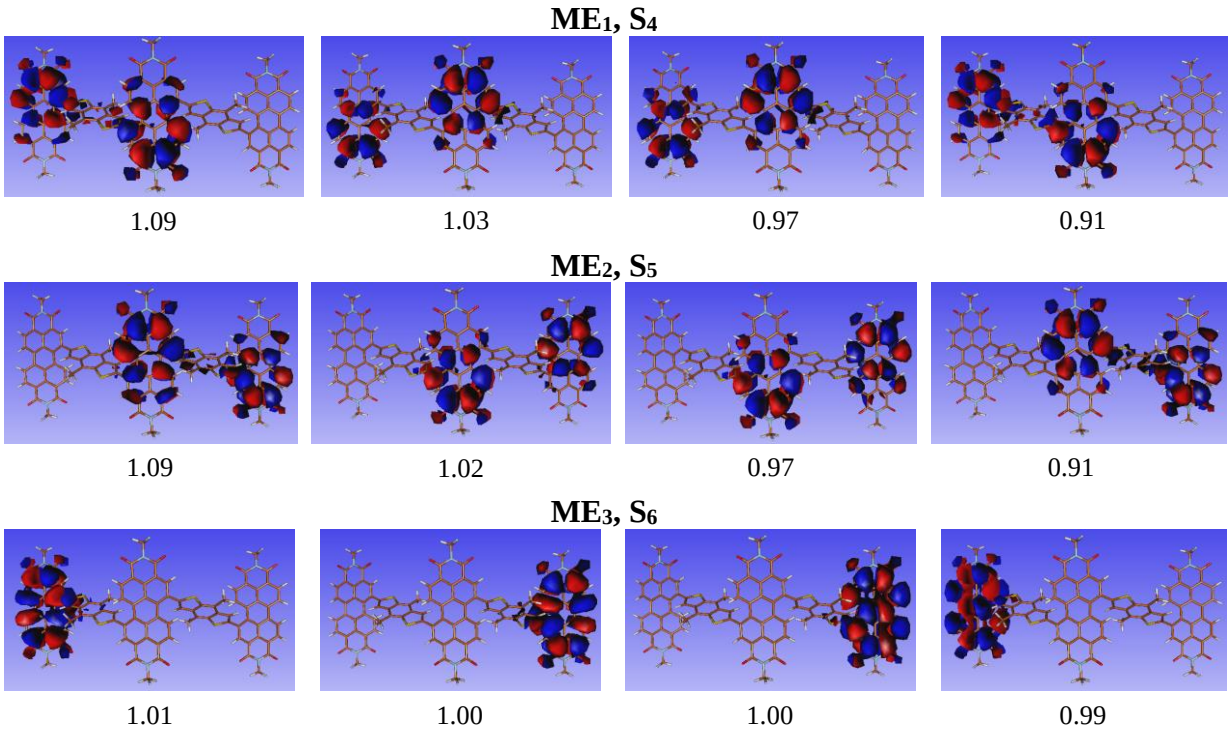

Figure 4.7.7.10. Natural Orbitals for the Multiexcitonic States of the **β** trimer together with their occupation numbers.

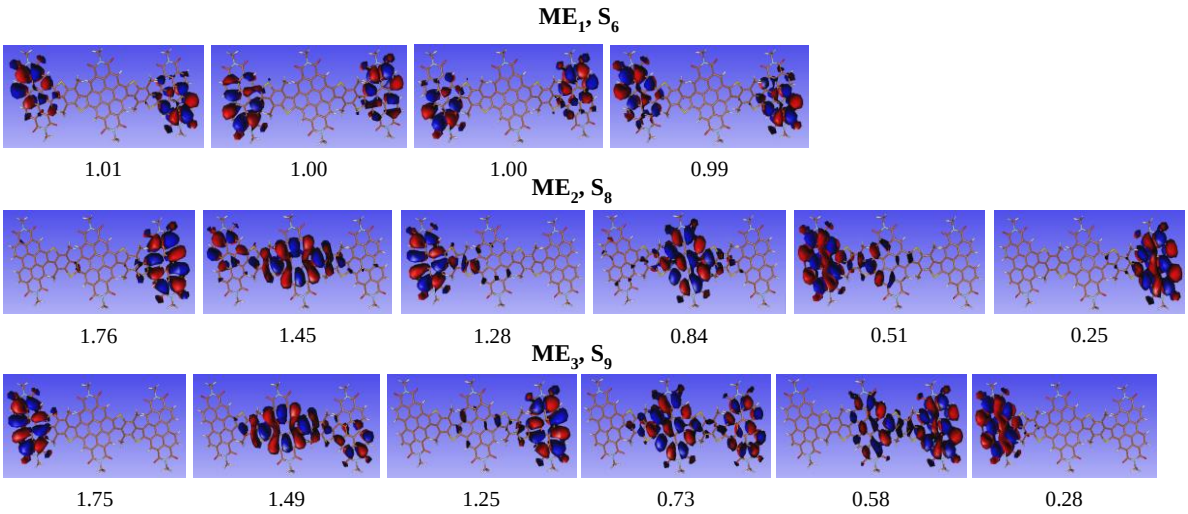

Figure 4.7.7.11. Natural Orbitals for the Multiexcitonic States of the **βC** trimer together with their occupation numbers.

Table 4.7.7.3. Relevant thermodynamic quantities (eV) for **β** and **βC** at 298 K computed following Krylov et al.

	β	**βC**
$E_{stt} = 2 \times E(T_1) - E(S_1)$	–0.20	+0.59
$E_b = E(^5TT) - E(^1TT)$	+0.006	+0.066
$H_1 = E_{stt} - E_b$	–0.206	+0.524
$H_2 = E_{stt}$	–0.20	+0.59
$TS_1 = k_B T \ln \Omega_1$	+0.028	0
$TS_2 = k_B T \ln \Omega_2$	+0.028	0
$G_1 = E_{stt} - E_b - TS_1$	–0.234	+0.524
$G_2 = E_{stt} - TS_2$	–0.228	+0.59
$\boldsymbol{\Delta H_{TOT} = \Delta H_1 + \Delta H_2 = E_{stt}}$	**–0.20**	**+0.59**
$\boldsymbol{T\Delta S_{TOT} = T\Delta S_1 + T\Delta S_2}$	**+0.028**	**0**
$\boldsymbol{\Delta G_{TOT} = \Delta G_1 + \Delta G_2}$	**–0.228**	**+0.59**

1 is the first step of singlet fission (from state 0, S_1, to state 1, ^{1}TT); 2 is the second step of triplet separation (from state 1, ^{1}TT, to state 2, T_1); for **β**, $\Omega_1=\Omega_2=3$, all the three double triplets are energetically close and accessible; for **βC**, $\Omega_1=\Omega_2=1$, only one double triplet state is energetically accessible; $\Delta\chi_1=\chi_1-\chi_0$ and $\Delta\chi_2=\chi_2-\chi_1$ where χ is H, S or G; k_BT=0.026 eV at 298 K.

4.7.8 ^{1}H and ^{13}C NMR of the compounds

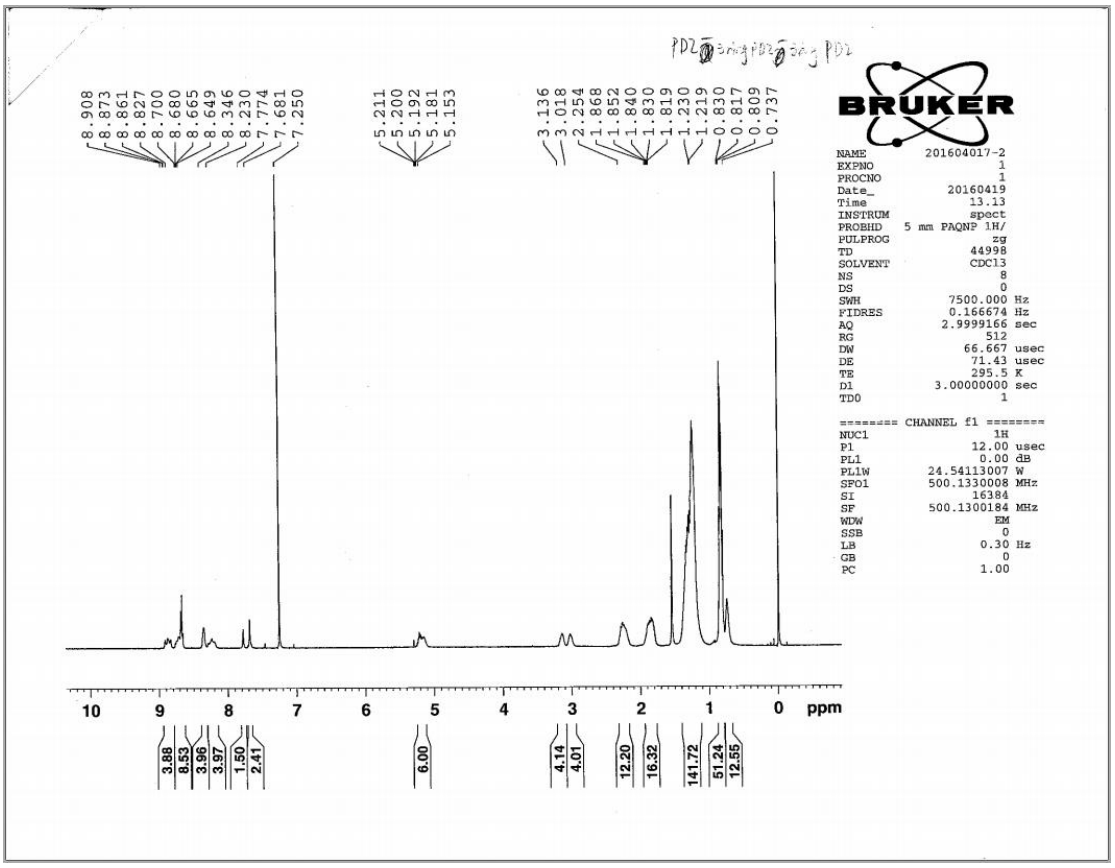

Figure 4.7.8.1. ^{1}H NMR of compound **β**

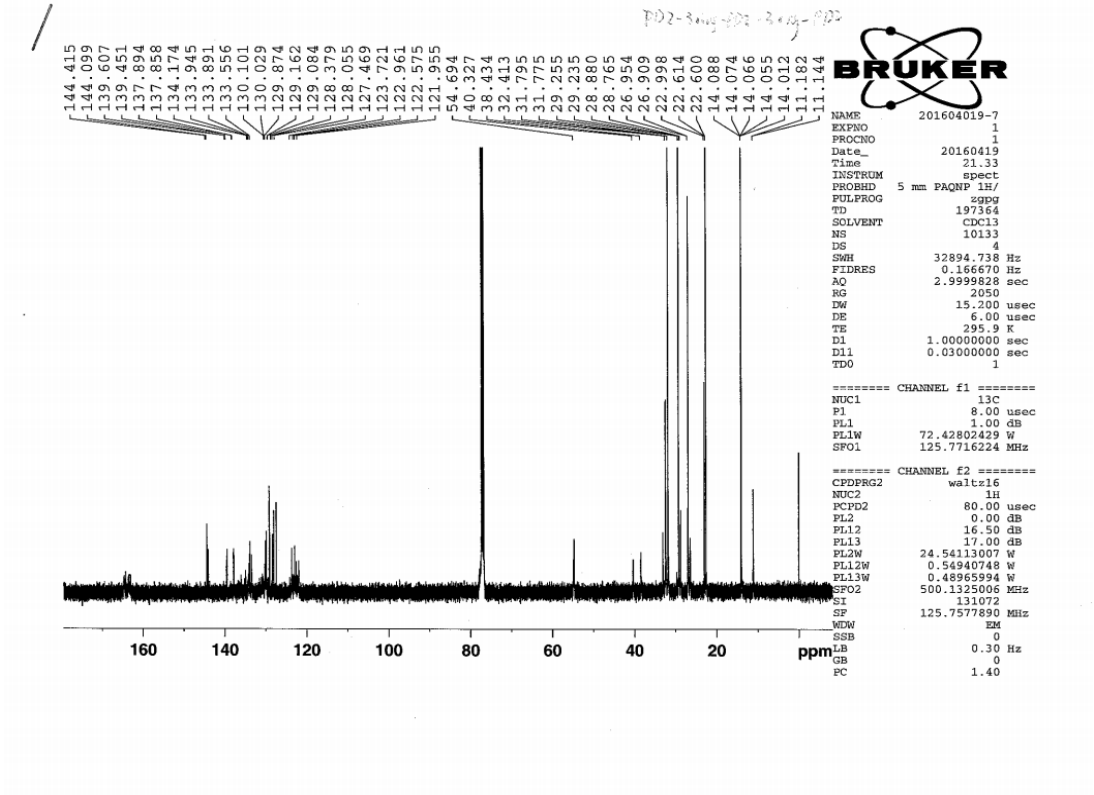

Figure 4.7.8.2. ^{13}C NMR of compound **β**

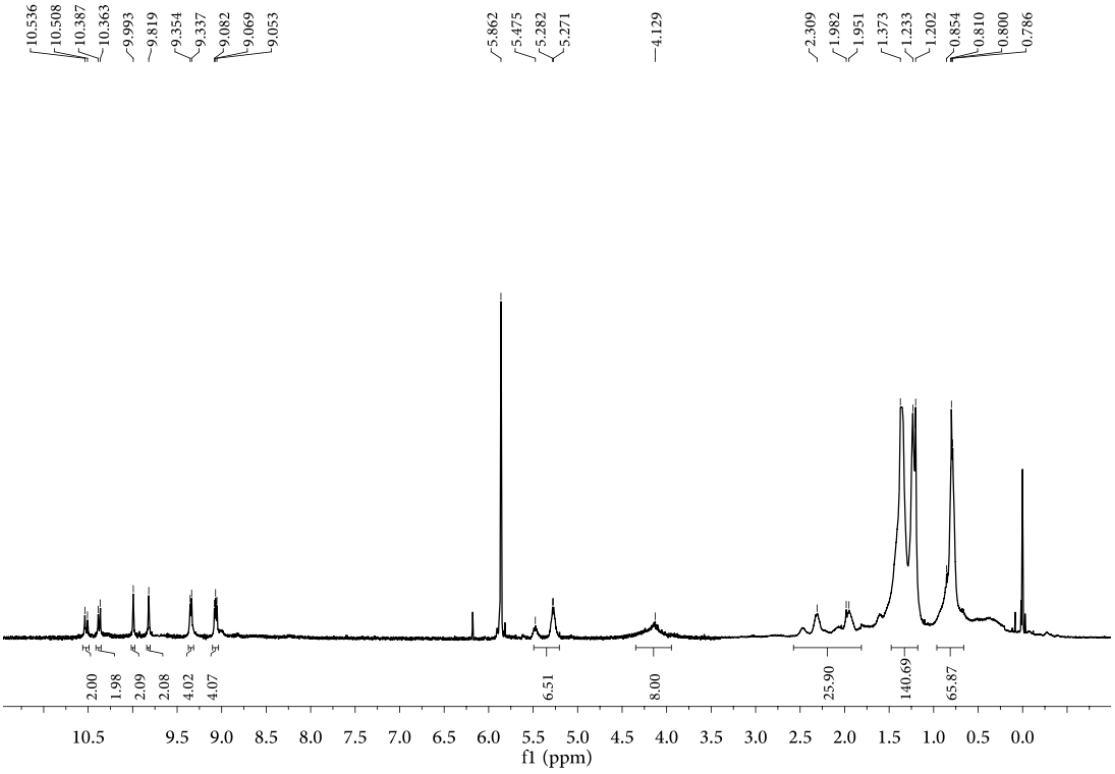

Figure 4.7.8.3. ^{1}H NMR of compound **βC**

References:

(1) Cai, Z.; Vázquez, R. J.; Zhao, D.; Li, L.; Lo, W. Y.; Zhang, N.; Wu, Q.; Keller, B.; Eshun, A.; Abeyasinghe, N.; et al. Two Photon Absorption Study of Low-Bandgap, Fully Conjugated Perylene Diimide-Thienoacene-Perylene Diimide Ladder-Type Molecules. *Chem. Mater.* 2017, *29* (16), 6726–6732.

(2) Guan, J.; Tomobe, K.; Madu, I.; Goodson, T.; Makhal, K.; Trinh, M. T.; Rand, S. C.; Yodsin, N.; Jungsuttiwong, S.; Laine, R. M. Photophysical Properties of Partially Functionalized Phenylsilsesquioxane: [RSiO1.5]7[Me/NPrSiO1.5] and [RSiO1.5]7[O0.5SiMe3]3 (R = 4-Me/4-CN-Stilbene). Cage-Centered Magnetic Fields Form under Intense Laser Light. *Macromolecules* 2019, *52*, 4008–4019.

(3) Jobin Yvon. *A Guide to Recording Fluorescence Quantum Yields Introduction:*; 2014; Vol. 15.

(4) Kubin, R. F.; Fletcher, A. N. Fluorescence Quantum Yields of Some Rhodamine Dyes. *J. Lumin.* 1982, *27* (4), 455–462.

(5) Keller, B.; McLean, A.; Kim, B. G.; Chung, K.; Kim, J.; Goodson, T. Ultrafast Spectroscopic Study of Donor-Acceptor Benzodithiophene Light Harvesting Organic Conjugated Polymers. *J. Phys. Chem. C* 2016, *120* (17), 9088–9096.

(6) Villabona-Monsalve, J. P.; Varnavski, O.; Palfey, B. A.; Goodson, T. Two-Photon Excitation of Flavins and Flavoproteins with Classical and Quantum Light. *J. Am. Chem. Soc.* 2018, *140* (44), 14562–14566.

(7) Xu, C.; Webb, W. W. Measurement of Two-Photon Excitation Cross Sections of Molecular Fluorophores with Data from 690 to 1050 Nm. *J. Opt. Soc. Am. B* 1996, *13* (3), 481.

(8) Madu, I. K.; Muller, E. W.; Kim, H.; Shaw, J.; Burney-Allen, A.; Zimmerman, P. M.; Jeffries-EL, M.; Goodson III, T. Heteroatom and Side Chain Effects on the Optical and Photo-Physical Properties: Ultrafast and Nonlinear Spectroscopy of New Naphtho[1,2-B:5,6-B′]Difuran Donor Polymers. *J. Phys. Chem. C* 2018, acs.jpcc.8b03914.

(9) Carlotti, B.; Cai, Z.; Kim, H.; Sharapov, V.; Madu, I. K.; Zhao, D.; Chen, W.; Zimmerman, P. M.; Yu, L.; Goodson, T. Charge Transfer and Aggregation E Ff Ects on the Performance of Planar vs Twisted Nonfullerene Acceptor Isomers for Organic Solar Cells. *Chem. Mater.* 2018, *30*, 4263–4276.

(10) Vázquez, R. J.; Kim, H.; Zimmerman, P. M.; Goodson, T. Using Ultra-Fast Spectroscopy to Probe the Excited State Dynamics of a Reported Highly Efficient Thermally Activated Delayed Fluorescence Chromophore. *J. Mater. Chem. C* 2019, *7* (14), 4210–4221.

(11) Carmichael, I.; Hug, G. L. Triplet-Triplet Absorption Spectra of Organic Molecules in Condensed Phases. *J. Phys. Chem. Ref. Data* 1986, *15* (1), 1–250.

(12) Bensasson, R.; Dawe, E. A.; Long, D. A.; Land, E. J. Singlet → Triplet Intersystem Crossing Quantum Yields of Photosynthetic and Related Polyenes. *J. Chem. Soc. Faraday Trans. 1 Phys. Chem. Condens. Phases* 1977, *73*, 1319.

(13) Murov, S.; Carmichael, I.; Hug, G. L. *Handbook of Photochemistry*, second.; MARCEL DEKKER, INC.: New York, 1993.

(14) Cogdell, R. J.; Land, E. J.; Truscott, T. G. The Triplet Extinction Coefficients of Some Bacterial Carotenoids. *Photochem. Photobiol.* 1983, *38* (6), 723–725.

(15) Amouyal, E.; Bensasson, R.; Land, E. J. Triplet States of Ubiquinone Analogs Studied By Ultraviolet and Electron Nanosecond Irradiation. *Photochem. Photobiol.* 1974, *20* (5), 415–422.

(16) Nielsen, B. R.; Jørgensen, K.; Skibsted, L. H. Triplet-Triplet Extinction Coefficients, Rate Constants of Triplet Decay and Rate Constants of Anthracene Triplet Sensitization by Laser Flash Photolysis of Astaxanthin, β-Carotene, Canthaxanthin and Zeaxanthin in Deaerated Toluene at 298 K. *J. Photochem. Photobiol. A Chem.* 1998, *112* (2–3), 127–133.

(17) Varnavski, O.; Abeyasinghe, N.; Aragó, J.; Serrano-Pérez, J. J.; Ortí, E.; López Navarrete, J. T.; Takimiya, K.; Casanova, D.; Casado, J.; Goodson, T. High Yield Ultrafast Intramolecular Singlet Exciton Fission in a Quinoidal Bithiophene. *J. Phys. Chem. Lett.* 2015, *6* (8), 1375–1384.

(18) Zhang, J.; Sulaiman, S.; Madu, I. K.; Laine, R. M.; Goodson, T. Ultrafast Excited-State Dynamics of Partially and Fully Functionalized Silsesquioxanes. *J. Phys. Chem. C* 2019, *123* (8), 5048–5060.

(19) Taylor, E. L.; Metcalf, K. J.; Carlotti, B.; Lai, C. T.; Modica, J. A.; Schatz, G. C.; Mrksich, M.; Goodson, T. Long-Range Energy Transfer in Protein Megamolecules. *J. Am. Chem. Soc.* 2018, *140* (46), 15731–15743.

(20) Adegoke, O. O.; Jung, I. H.; Orr, M.; Yu, L.; Goodson, T. Effect of Acceptor Strength on Optical and Electronic Properties in Conjugated Polymers for Solar Applications. *J. Am. Chem. Soc.* 2015, *137* (17), 5759–5769.

(21) Chai, J.-D.; Head-Gordon, M. Long-Range Corrected Hybrid Density Functionals with Damped Atom–Atom Dispersion Corrections. *Phys. Chem. Chem. Phys.* 2008, *10* (44), 6615.

(22) Chai, J. Da; Head-Gordon, M. Systematic Optimization of Long-Range Corrected Hybrid Density Functionals. *J. Chem. Phys.* 2008, *128* (8).

(23) Zheng, Z.; Brédas, J.-L.; Coropceanu, V. Description of the Charge Transfer States at the Pentacene/C_{60} Interface: Combining Range-Separated Hybrid Functionals with the Polarizable Continuum Model. *J. Phys. Chem. Lett.* 2016, *7* (13), 2616–2621.

(24) Farag, M. H.; Krylov, A. I. Singlet Fission in Perylenediimide Dimers. *J. Phys. Chem. C* 2018, *122* (45), 25753–25763.

(25) Korovina, N. V.; Das, S.; Nett, Z.; Feng, X.; Joy, J.; Haiges, R.; Krylov, A. I.; Bradforth, S. E.; Thompson, M. E. Singlet Fission in a Covalently Linked Cofacial Alkynyltetracene Dimer. *J. Am. Chem. Soc.* 2016, *138* (2), 617–627.

(26) Casanova, D. Electronic Structure Study of Singlet Fission in Tetracene Derivatives. *J. Chem. Theory Comput.* 2014, *10* (1), 324–334.

(27) Zimmerman, P. M.; Musgrave, C. B.; Head-Gordon, M. A Correlated Electron View of Singlet Fission. *Acc. Chem. Res.* 2013, *46* (6), 1339–1347.

(28) Zimmerman, P. M.; Bell, F.; Casanova, D.; Head-Gordon, M. Mechanism for Singlet Fission in Pentacene and Tetracene: From Single Exciton to Two Triplets. *J. Am. Chem. Soc.* 2011, *133* (49), 19944–19952.

(29) Kolomeisky, A. B.; Feng, X.; Krylov, A. I. A Simple Kinetic Model for Singlet Fission: A Role of Electronic and Entropic Contributions to Macroscopic Rates. *J. Phys. Chem. C* 2014, *118* (10), 5188–5195.

(30) Feng, X.; Casanova, D.; Krylov, A. I. Intra- and Intermolecular Singlet Fission in Covalently Linked Dimers. *J. Phys. Chem. C* 2016, *120* (34), 19070–19077.

(31) Piland, G. B.; Burdett, J. J.; Dillon, R. J.; Bardeen, C. J. Singlet Fission: From Coherences to Kinetics. *J. Phys. Chem. Lett.* 2014, *5* (13), 2312–2319.

(32) Chien, A. D.; Zimmerman, P. M. Recovering Dynamic Correlation in Spin Flip Configuration Interaction through a Difference Dedicated Approach. *J. Chem. Phys.* 2017, *146* (1).

(33) Shao, Y.; Gan, Z.; Epifanovsky, E.; Gilbert, A. T. B.; Wormit, M.; Kussmann, J.; Lange, A. W.; Behn, A.; Deng, J.; Feng, X.; et al. Advances in Molecular Quantum Chemistry Contained in the Q-Chem 4 Program Package. *Mol. Phys.* 2015, *113* (2), 184–215.

(34) Margulies, E. A.; Miller, C. E.; Wu, Y.; Ma, L.; Schatz, G. C.; Young, R. M.; Wasielewski, M. R. Enabling Singlet Fission by Controlling Intramolecular Charge Transfer in π-Stacked Covalent Terrylenediimide Dimers. *Nat. Chem.* 2016, *8* (12), 1120–1125.

(35) Ramanan, C.; Smeigh, A. L.; Anthony, J. E.; Marks, T. J.; Wasielewski, M. R. Competition between Singlet Fission and Charge Separation in Solution-Processed Blend Films of 6,13-Bis(Triisopropylsilylethynyl)Pentacene with Sterically-Encumbered Perylene-3,4:9,10-Bis(Dicarboximide)S. *J. Am. Chem. Soc.* 2012, *134* (1), 386–397.

(36) Robinson, G. W.; Frosch, R. P. Electronic Excitation Transfer and Relaxation. *J. Chem. Phys.* 1963, *38* (5), 1187–1203.

(37) Lawetz, V.; Orlandi, G.; Siebrand, W. Theory of Intersystem Crossing in Aromatic Hydrocarbons. *J. Chem. Phys.* 1972, *56* (8), 4058–4072.

(38) Brédas, J.-L.; Beljonne, D.; Coropceanu, V.; Cornil, J. Charge-Transfer and Energy-Transfer Processes in π-Conjugated Oligomers and Polymers: A Molecular Picture. *Chem. Rev.* 2004, *104* (11), 4971–5004.

(39) Schmidt, K.; Brovelli, S.; Coropceanu, V.; Beljonne, D.; Cornil, J.; Bazzini, C.; Caronna, T.; Tubino, R.; Meinardi, F.; Shuai, Z.; et al. Intersystem Crossing Processes in Nonplanar Aromatic Heterocyclic Molecules. *J. Phys. Chem. A* 2007, *111* (42), 10490–10499.

(40) Jean-Luc Brédas, *,†,‡; David Beljonne, †,‡; Veaceslav Coropceanu, † and; Jérôme Cornil†, ‡. Charge-Transfer and Energy-Transfer Processes in π-Conjugated Oligomers and Polymers: A Molecular Picture. 2004.

(41) Samanta, P. K.; Kim, D.; Coropceanu, V.; Brédas, J. L. Up-Conversion Intersystem Crossing Rates in Organic Emitters for Thermally Activated Delayed Fluorescence: Impact of the Nature of Singlet vs Triplet Excited States. *J. Am. Chem. Soc.* 2017, *139* (11), 4042–4051.

(42) Beljonne, D.; Shuai, Z.; Pourtois, G.; Bredas, J. L. Spin-Orbit Coupling and Intersystem Crossing in Conjugated Polymers: A Configuration Interaction Descript

Chapter 5

The Role of the Core Attachment Positioning in Triggering Intramolecular Singlet Exciton Fission in Perylene Diimide Tetramers

5.1 Original Publication Information and Author Contribution

Portions of this chapter were taken from a paper that was published in the *Journal of Physical Chemistry B* with the title:

"The Role of the Core Attachment Positioning in Triggering Intramolecular Singlet Exciton Fission in Perylene Diimide Tetramers" Angelar K. Muthike, Benedetta Carlotti, Ifeanyi K. Madu, Hanjie Jiang, Hyungjun Kim, Qinghe Wu, Luping Yu, Paul M. Zimmerman, Theodore Goodson III.

While I did majority of the work in the chapter ranging from steady state absorption and emission, two-photon absorption spectroscopy, femtosecond and nanosecond transient absorption and analyzing the data and putting the manuscript together, I would like to acknowledge the contribution of Dr. Ifeanyi Madu and Dr. Benedetta Carlotti who helped in the analysis of the femtosecond transient absorption data, and obtaining time-resolved fluorescence date. Hanjie Jiang in Prof. Zimmerman's group did the quantum chemical calculatins with the help of Dr. Hyungjun Kim. These investigated materials were synthesized by Qinghe Wu in Prof. Luping' Lu's lab at the University of Chicago.

5.2 Abstract

Previous studies have proposed that the presence of a flexible π–bridge linker is crucial in activating intramolecular singlet exciton fission (iSEF) in multichromophoric systems. In this study, we report the photophysical properties of three analogous perylene diimide (PDI) dendritic tetramers showing flexible/twisted π–bridged structures with $\alpha-$ and $\beta-$substitutions, and a rigid/planar structure with a $\beta-$fused ring (βC) connection to benzodithiophene–thiophene (BDT-Th) core. The rigidity and enhanced planarity of βC leads to significant intramolecular charge

transfer (iCT) and triplet formation via an intersystem crossing pathway. Steady state spectroscopic measurements reveal similar absorption and emission spectra for the α–tetramer and the parent PDI monomer. However, their fluorescence quantum yield is significantly different. The negligible fluorescence yield of α–tetramer (0.04%) is associated with a competitive nonradiative decay pathway. Indeed, for this twisted compound in a high polar environment, a fast and efficient iSEF with a triplet quantum yield of 124% is observed. Our results show that the α–single–bond connections in the α compound are capable of interrupting the coupling among the PDI units, favoring iSEF. We propose that the formation of the double triplet (^{1}[TT]) state is through a superposition of singlet states known as $[S_1S_0]_{[TT]}$CT which has been suggested previously for pentacene derivatives. Using steady state and time–resolved spectroscopic experiments, we demonstrate that the conformational flexibility of the linker itself is necessary but not sufficient to allow iSEF. For the case of the other twisted tetramer, β, the strong π–π co–facial interactions between the adjacent PDI units in its structure, lead to excimer formation. These excimer states trap the singlet excitons preventing the formation of the ^{1}[TT] state, thus inhibiting iSEF.

5.3 Introduction

Singlet exciton fission (SEF) is a spin allowed process where a photogenerated singlet exciton splits into two spin–correlated triplet excitons.[1] This mechanism has been reported to reduce thermal losses factored in the Shockley–Queisser (SQ) limit and is therefore capable of enhancing the theoretical efficiency limit of photovoltaic (PV) devices from 33 to 47%.[1–5] For SEF to occur, electronic (($E[S_1] \geq 2(E[T_1])$ and $E[T_2] \geq E[S_1]$) and structural (molecular packing that optimizes interchromophore electronic coupling) conditions have to be fulfilled.[3] There are two different mechanisms through which SEF proceeds: direct coupling where two electrons move between the singlet exciton and the adjacent ground state chromophore to yield the correlated triplet pair state (^{1}[TT]) or mediated through a charge transfer (CT) state where the conversion of the first singlet state ($^1[S_1S_0]$) to ^{1}[TT] is facilitated by coupling to higher–lying CT state. [1,5,6–12] The formed ^{1}[TT] can yield a quintet state (^{5}[TT]) through spin evolution and/or go through spin decoherence to produce two separated triplet states $[T_1 + T_1]$.

Recent studies report that the SEF mechanism can either be inter– or intramolecular. In intermolecular SEF (xSEF), the optically excited singlet state on one molecule couples with

neighboring molecules to form an intermolecular triplet pair. xSEF can be improved by tuning the interchromophore interactions. This process highly depends on chromophore packing motifs. It is challenging to come up with highly ordered molecular structures to fulfil the packing requirement, and reproducibility is often an issue.[13] However, polymers and other small molecules can show SF as an intrinsic property through intramolecular singlet exciton fission (iSEF) where the double triplet pair state is located on the same molecule. This iSEF mechanism, which shows high processability in solution, high tunability in both molecular and electronic structures and ability to create tailored interfaces, is not well understood.[13,14,15]

In an effort to improve the performance of organic photovoltaics (OPVs), SEF research on structurally tunable systems of acene dimers[16–31] reports two main structural factors affecting the rate and yield of SF: the coupling between the molecular units, and the degree of contortion in the structure.[32,33] Despite the great SEF yields from the aforementioned acene dimers, their limitations like photo−instability have pushed researchers to venture into new materials with SF potential.[22,34,35] Perylene Diimides (PDIs) are a class of chromophores whose packing is easily controllable, possesses high thermal/photo−stability, has high extinction coefficients in the visible region and holds desirable triplet energies for semiconductor sensitization.[22,36,37]

Recently, iSEF has been observed in PDI dimers and trimers.[22,32,38–40] However, Wasielewski and co−workers have observed excimer states that block the formation of ^{1}[TT] state in solution−based aggregates of PDI dimers.[38,41–43] This excimer formation has been associated with the co−facial, slip−stacked morphology of the dimers [41] which leads to a strong electronic coupling between chromophores inhibiting SEF.[44] There has been varying information about the role of excimer states in the SEF mechanism. [45–48] In some cases, excimer states inhibit the formation of the correlated triplet pair, [42,45,49,50] while in other cases, these excimer states act as intermediates for SEF. [16,47,51] The complication in understanding excimer states and their role in SEF is as a result of the indistinguishable nature of these singlet states, the $^1[S_1S_0]$ and ^{1}[TT] states, and their interactions.[45] One report showed that excimers form when the electronic coupling between the CT state and the singlet excited state of two identical chromophores is strong resulting in a stable CT + $^1[S_1S_0]$ mixture state – an excimer.[52] The individual CT state or $^1[S_1S_0]$ can individually act to inhibit the production of double triplets from the singlet state via a highly stabilized CT (lower CT state) process or radiative decay, respectively.

Other studies have shown that in addition to the nature of the chromophore, the π–linker plays a crucial role in contributing to the occurrence of iSEF in PDI chromophores.[40] It has been reported that structural flexibility of the covalent linker is necessary to activate iSEF[19,39,40,53]. In our recent report [40], we investigate two analogous PDI trimers where one is planar and the other one is twisted. Here, we follow up on the established work on the role and characteristics of the linker that may necessitate iSEF. While it has been established that the presence of a linker is important in triggering iSEF, this work dissects two similar structures, one with a flexible and the other one with a rigid linker. We report that the flexibility of the linker is important in activating intramolecular singlet fission since we observe a triplet yield of 170% for the flexible compound and 16% for the rigid planar compound.

In other studies, singlet fission has been reported as a solvent−dependent process for molecules like terylenediimide (TDI) dimers. [54-56] Here, SEF was observed in low dielectric constant solvents and symmetry breaking charge separation in high dielectric constant solvents. In this case, it follows that the higher dielectric constant solvent stabilizes the CT state and lowers its energy allowing it to act as a trap state. On the other hand, minimal CT state stabilization in low dielectric environments enables the CT state to act as a virtual state in a superexchange interaction that promotes SF.[54,55] On the contrary, other reports show symmetry breaking as a crucial step to activate singlet fission.[30,56] Therefore, a lot of research is still needed to understand the mechanism of iSEF, the structural character of the molecules and the appropriate dielectric environment for these molecules to show iSEF.

In this present investigation, we use time−resolved spectroscopic techniques to elucidate the crucial role of the core attachment position to the PDI units as well as the chromophore's dielectric environment in activating iSEF in PDI tetramers. Here, three analogous tetramer structures were investigated, where the PDI electron acceptor units are linked with a central benzodithiophene (BDT) electron donor moiety.[57,58] The connections between the donor and the four acceptor units are realized via single bonds through the α and β position of the PDI units for α− and β−tetramers, respectively for the twisted structures and through β ring cyclization for the planar βC−tetramer as shown in **Figure 5.3.1**.

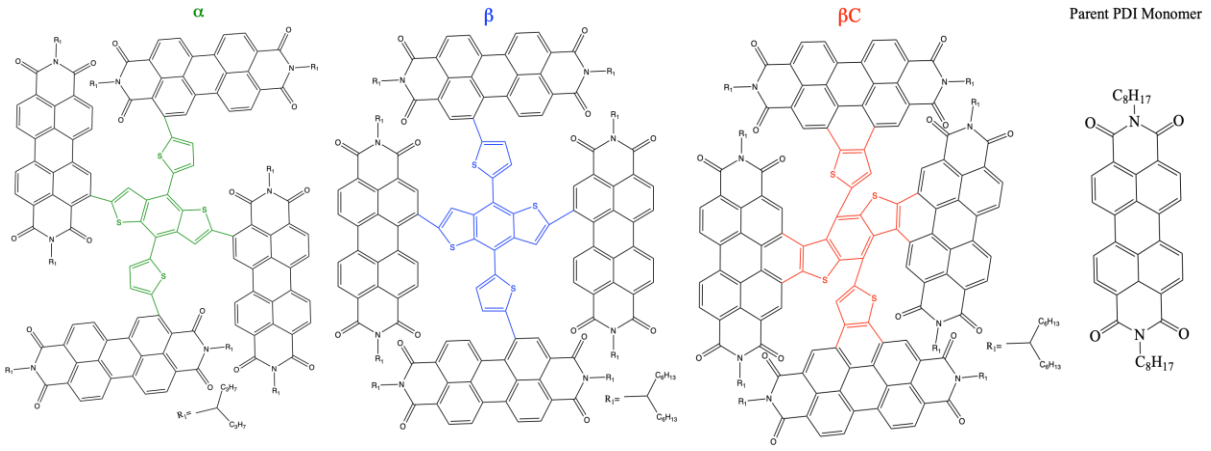

Figure 5.3.1: Structures of the investigated molecules as well as of the parent PDI monomer.

5.4 Experimental Methods

5.4.1 Materials

The synthetic procedure of all the tetramers has been previously discussed in detail. [57,58] These materials were synthesized through the Suzuki coupling between BDT–Th–4Bpin with 4 equivalents of α–monobrominated and β–monobrominated for α and β respectively, while βC was obtained through the cyclization between the perylene diimides (PDIs) and the benzodithiophene–thiophene (BDT–Th) core of the β–tetramer. Chlorobenzene and toluene from Sigma–Aldrich were used as solvents for the spectral and photophysical characterization.

5.4.2 Steady State Studies

For all our steady state spectroscopic investigation measurements performed at room temperature and pressure, concentrations ranging from 3.0×10^{-8} to 1×10^{-5} M were used with chlorobenzene or toluene as solvents. The absorption spectra were obtained using Agilent 8432 UV–visible absorption spectrophotometer while a Fluoromax–2 spectrofluorimeter was used for the emission measurements. To calculate the fluorescence quantum yields of the investigated samples, a previously documented procedure was carried out [59] and Rhodamine B in ethanol was used as the standard.[60]

5.4.3 Two–Photon Excited Fluorescence (TPEF) Studies

Our previously described mode–locked Ti:Sapphire laser, tunable from 700 to 900 nm with 110 fs pulses as output at a repetition rate of 80 MHz was used for our two–photon excited fluorescence measurements.[61] The emission scans between a wavelength range of 400 – 850 nm were performed with an 820 nm excitation. A power dependence scan was run at the emission

wavelength detection and the highest number of counts was picked. During the TPEF measurements, a neutral density filter was used to change the input power from the laser, which would consequently vary the output intensity. Using Rhodamine B as the standard, the two−photon absorption cross section was calculated through a comparative method using the obtained two−photon power dependent fluorescence intensity.[60]

5.4.4 Time−Resolved Fluorescence Studies

The previously described time−correlated single photon counting (TCSPC) technique was used to study the long decay components of the investigated samples.[61] A mode−locked Kapteyn−Murnane (KM) Ti−sapphire laser with an output beam at 800 nm and a pulse duration of ca. 30 fs was used for our time resolved fluorescence measurements. A nonlinear β−barium−borate (BBO) crystal was used to double the output frequency beam to a 400 nm, and a polarizer was used to vary the power of the 400 nm sample excitation beam. During the measurements, a lens of focal length 11.5 cm was used to focus the 400 nm beam on the sample cell (quartz cuvette, 0.4 cm path length). The fluorescence was then collected perpendicularly to the incident beam into a monochromator. The output from the monochromator was coupled to a photomultiplier tube, which converted the photons into counts.

In addition to the TCSPC, an ultrafast fluorescence Up−Conversion (FUC) setup was used to obtain the fs−resolved fluorescence measurements. For this setup, a Mode−Locked Ti−Sapphire fs laser (Spectra Physics Tsunami) pumped by a continuous 532 nm output from a Spectra Physics Millenia laser whose gain medium is a neodymium−doped yttrium vanadate ($Nd:YVO_4$) was used. The mode−locked Ti−Sapphire generated 80 fs pulses at 800 nm, with a repetition rate of 82 MHz. Using a second−harmonic β−barium−borate (BBO) crystal, a 400 nm excitation beam whose power ranged between 33 to 35 mW was generated and the 800 nm residual propagated through a computer controlled motorized optical delay line. The beam polarization was achieved using a Berek compensator. The sample fluorescence emission was then up−converted by a nonlinear BBO crystal using the 800 nm residual beam previously delayed by the optical delay line with a gate step of 6.25 fs. A monochromator was used to select the wavelength of the up−converted beam of interest which is then detected using a photomultiplier tube (Hamamatsu R152P) converting the detected beam into computer−readable photon counts. To calibrate this set−up, Coumarin 30 was used while a water Raman signal was used to determine the instrument response function to have width of 110 fs.

5.4.5 Femtosecond Transient Absorption

A Spectra Physics Spitfire amplified laser system previously described [61] was used for the femtosecond transient absorption (fsTA) measurements. The produced beam of ~ 100 fs pulse duration, 1 kHz repetition rate, and a power of 1 W was directed at a beam splitter to generate the pump (85%) and the probe beam (15%). The 510 nm ~ 66 mJ per pulse pump beam was focused onto the sample cell (l = 2 mm) which is preceded by an optical chopper. On the other hand, the probe beam was passed through a computer–controlled delay line and focused onto a 2 mm sapphire plate to generate the white light continuum (Helios by Ultrafast Systems Inc.). This white light was then focused onto the sample where it overlapped with the pump beam. An Ocean Optics charge–coupled device (CCD) detector collected the difference in the signal absorbance (ΔA). The Helios software by Ultrafast Systems Inc was used for the transient data acquisition, while the data analysis was completed using Surface Explorer Pro and Glotaran softwares.

5.4.6 Nanosecond Transient Absorption

The nanosecond transient absorption (nsTA) set–up was used to probe the spectral, emissive and non–emissive lifetimes of long–lived transient species of the investigated chromophores as described earlier.[61–63] A Spectra Physics QuantaRay neodymium–doped yttrium aluminum (Nd:YAG) nanosecond laser coupled with a GWU Optical Parametric Oscillator (OPO) with wavelength tunability ranging between 250 nm to 2600 nm was used as the pump excitation source. A high energy Q–Switched 355 nm beam from the Nd:YAG's third harmonic was used to pump the OPO, which, through second harmonic generation and sum frequency mixing (with the 1064 nm) nonlinear processes can be used to produce the long range of pump wavelengths. An LP980 Edinburg spectrometer system houses the probe source, the sample chamber and the monochromator. The probe source is a 150 W ozone–free xenon lamp that produces a continuous 6 ms pulse with a wavelength range of 190–2600 nm. The laser pump beam excites the sample perpendicular to the probe beam, creating the transient species. The absorption properties of the produced excited states are then probed using the xenon probe source. The resultant sample light is focused to the monochromator and detected by a photomultiplier tube (PMT) (Hamamatsu R928) whose detection ranges from 185 to 870 nm. The PMT converts the obtained transmission to electric signals which can be measured by our TDS3052B oscilloscope and converted from Volts to Change–in–Absorption (ΔA) using the L900 software supplied by Edinburg. Measurements were performed in diluted aerated and deaerated solutions of 10^{-5} M concentrations

and photodegradation was checked by recording UV−vis absorption spectra before and after the experiments. For this investigation, 415 nm, 510 nm and 594 nm excitation wavelengths were used to pump the samples. The experimental setup was calibrated by an optically matched solution of tetracene (φ_T = 0.62 and ε_T = 31200 M^{-1} cm^{-1} at the corresponding absorption maximum of 465 nm)[64] in chlorobenzene. Triplet–triplet absorption coefficients (ε_T) were determined by energy transfer from β/βC to tetracene and from 5, 10, 15, 20 – tetraphenyl – 21H, 23H – porphine in chlorobenzene (ε_T = 6000 M^{-1} cm^{-1} at λ_{max} = 790 nm) to α by using a procedure previously detailed by Carlotti et al.[40,64]

5.4.7 Quantum Chemical Calculations

The theoretical investigations were performed on the molecular structures where the long alkyl chains were replaced by short chains (propyl and hexyl groups [C_3H_7, C_6H_{13}] attached to the perylene diimide (PDI) while the benzodithiophene (BDT) linkers were replaced by hydrogen atoms and methyl groups, respectively) to save computational time without significant effect on the electronic properties. The ground state geometry of each compound was obtained by density functional theory (DFT), using the long–range corrected ωB97X–D functional [65,66] and the 6−31G* basis set. Optimization of the lowest energy triplet state [T_1] was performed using unrestricted DFT and the ground state [S_0] was performed using the restricted DFT. Excited state simulations were performed using time dependent DFT (TD–DFT). Single–point energy calculations were done using ωB97X–D,[65,66] the 6−31G* basis set and polarizable continuum model (PCM)[67] with the dielectric constant of 5.62 for chlorobenzene and 2.38 for toluene. Characters of excitations were described with natural transition orbitals (NTOs).

Restricted active space spin flip (RAS−SF) methods were used to provide relative energies of all double−triplet states and identify the differences between the multi−excitonic states in the three tetramers. To perform RAS−SF calculations for molecules with such large sizes, RAS−SF was performed on the "half" tetramers with only 2 PDI units. To obtain these 'half' tetramers, all the molecules were truncated through the benzodithiophene (BDT) core where one of the two remaining PDI units is connected to one end of the BDT core while the other PDI unit is connected to the adjacent thiophene. Through the truncations of α, β and βC, respective Dimer–α, Dimer– β and Dimer– βC were obtained and used in the RAS−SF calculations. Because RAS−SF tends to overestimate the excitation energies, the absolute excitation energy values are in poor agreement

with TD–DFT. Regardless, RAS–SF does provide trends and relative energy values (especially for double triplet states) that cannot be realized by any other methods.

The driving force of singlet fission – i.e. $\Delta E_{SF} = 2\times E[T_1] - E[S_1]$ –was estimated with the methods just mentioned. Recently, multiple researchers have pointed out the importance of ^{1}[TT] energy in predicting feasibility of SF and relevant kinetics.[19,26,45,47] Amongst the various chromophores of this study, the truncated tetrameric PDI chromophores, Dimer–α, Dimer–β and Dimer–βC, with restricted active space double spin–flip method, which has successfully provided useful characterization of ground and excited radical states in a number of studies.[68–72] All the calculations were performed using Q–Chem 5.0 software package.[73] Natural transition orbitals (NTOs) of TD–DFT calculations were visualized using IQMOL. Natural orbitals (NOs) of RAS–2SF calculations were plotted using Molden,[74] Visual Molecular Dynamics (VMD),[75] and POV–ray.

5.5 Results

5.5.1 Steady State and Nonlinear Optical Properties

Shown in **Figure 5.5.1.1** and **Figure 5.12.1.1** are the steady–state absorption and emission spectra for the investigated tetramers as well as those for the parent PDI monomer. For the α and β compounds, the strongest absorption peaks, both of which are around 529 nm, have been assigned to 0–0 transitions. For both of these compounds, the peaks located around 492 nm and 461 nm were assigned to 0–1 and 0–2 transitions respectively.[57,58] For the βC, the absorption peaks at 554 nm, 503 nm and 471 nm are assigned to 0–0, 0–1 and 0–2 transitions, respectively.[58] For this chromophore, the 0–1 and 0–2 transitions have been associated to the absorption of perylene diimide–thiophene (PDI–Th) while the 0–0 transition peak is from the absorption of perylene diimide–benzidithiophene–perylene diimide (PDI–BDT–PDI).[58] The absorption and emission spectra of the α chromophore in chlorobenzene are nearly identical to those of the parent PDI monomer (**Figure 5.5.1.1 and Figure 5.12.1.1**). This similarity indicates minimal ground state interaction/excitonic coupling among the chromophores. [58,76,77] In addition, it suggests that the excitation is mainly localized on one of the PDIs in this α–tetramer. At the 0–0 transitions, the extinction coefficient of α (~290000 $M^{-1}cm^{-1}$) is approximately four times that of the parent PDI monomer (~85000 $M^{-1}cm^{-1}$). A similar trend is observed in the other transitions in the visible part

of the spectrum.[77] This suggests that the extinction coefficient of α is the same as that of the parent PDI monomer given that the α–tetramer is made up of four PDI units (**Figure 5.5.1.1**). The structured spectra of βC reflect its molecular rigidity. However, less structured absorption and emission spectra are observed for β. These observations are consistent with the chromophore's increased flexibility and interchromophore coupling relative to α and βC. The emission spectrum of β shows a narrow band peaked around 560 nm and an additional broad and red–shifted band at 710 nm. The absorption maximum wavelength for α and β (530 nm) is similar to that of the parent PDI monomer, The βC absorption maxima is similar to that of a benzodithiophene (BDT) substitute.[78] Therefore, the α– and β– substitutions favor the PDI acceptor absorption while the ring fusion favors the BDT donor absorption. Additionally, β's absorption wavelength is the most red–shifted, followed by α, while βC has the most blue–shifted absorption wavelength. Additionally, it has been reported that when the π–bridge of a PDI derivative is a rigid cyclized aromatic ring, the spectra appear narrower, structured and blue shifted, which is the case for βC.[40]

The probability of aggregation was considered by investigating the concentration–dependence of the absorption spectra. No concentration effect was observed on the absorption spectra of all the investigated tetramers (**Figure 5.12.1.2A**) in the range of concentrations of 6 x 10^{-7} to 1 x 10^{-5} M employed in this work. For βC compounds in chlorobenzene, there was no dependence of the emission spectra on the sample concentration (**Figure 5.12.1.2**). However, α shows an inconsistent dependence of emission on concentration, which happens to the monomer peaks (**Figure 5.5.1.1B**). Interestingly, the significant spectral changes revealed upon increasing the β concentration in chlorobenzene are associated with the formation of excimers.[58] These excimers explain the characteristic shape of the emission spectrum of β, which shows both the monomer (at 560 nm) and the excimer (at 710 nm) contributions (**Figure 5.5.1.1B**). The absorption and the emission of β and βC in a less polar solvent (toluene as shown in **Figure 5.12.1.1**) are similar to those measured in chlorobenzene. However, the emission spectrum of α in toluene had an additional band near 700 nm (**Figure 5.12.1.1**), indicating the presence of excimers. The investigation of the concentration effect on the emission in toluene thus confirms the formation of excimers for both α and β in toluene (**Figure 5.5.1.2**).

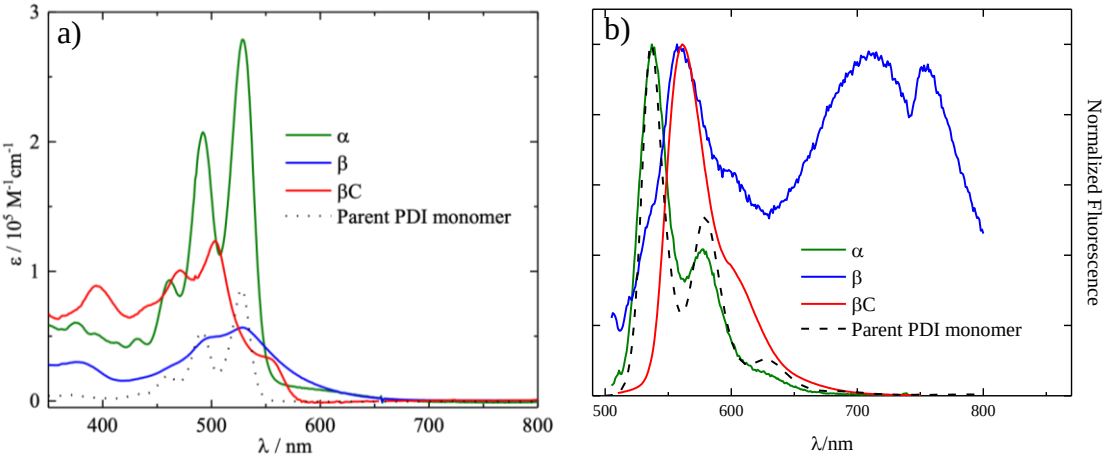

Figure 5.5.1.1. Absorption (a) and normalized emission (b) spectra of the tetramers in chlorobenzene. Spectra of the parent PDI monomer are also included.

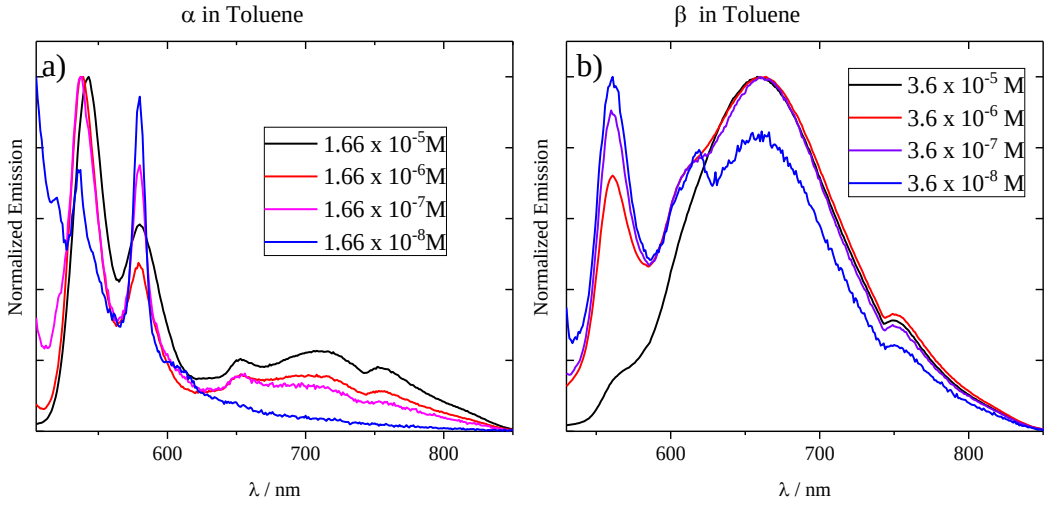

Figure 5.5.1.2. Concentration effect on the emission spectra of α (a) and β (b) tetramers in toluene.

The fluorescence efficiency of all the investigated compounds was measured in chlorobenzene. We found values of 0.04%, 0.4% and 7.2% for α–, β– and βC–tetramers, respectively (see **Table 5.5.1.1**). These quantum yields are smaller in comparison to that of the parent PDI monomer (~100%),[40,77] particularly observed in the case of the flexible compounds. The fluorescence quantum yields for the tetramers are similar to the previously reported quantum yields of similarly linked PDI trimers.[40] The significantly small fluorescence quantum yield observed for the α compound in comparison to that of the parent PDI monomer, whose absorption spectra is very similar to that of α, indicates the presence of a non–radiative process and has been associated with reduced oscillator strength as well as low torsional activation barrier. In toluene,

fluorescence quantum yields for all the investigated molecules generally increase (by two orders of magnitude for α, and an order of magnitude $\beta-$ and βC–tetramers). It is clear that α's quantum yield increases significantly in toluene. In fact, the fluorescence quantum yield of α in toluene is similar to that of β in toluene. This similarity shows that in toluene, both α and β have similar photophysical properties and substantiates the formation of excimer state for α in toluene.

The two–photon absorption (TPA) cross sections show remarkable values of tens and hundreds of GM (**see Table 5.5.1.1 and Figure 5.12.1.3**). The TPA cross section for the α compound is more than one order of magnitude bigger than that reported for the parent PDI molecule. It is also clear that the TPA cross sections are enhanced by over one order of magnitude for the rigid βC (ca. 234 GM) with respect to the flexible α and β (ca. 30–71 GM). Increased TPA cross section has been associated with increase in transition dipole moments, which is directly proportional to the charge transfer character of the transition. Therefore, the increased TPA absorption cross section of the rigid, fused ring connected molecule indicates its higher intramolecular charge transfer (iCT) character in the excited state with respect to the flexible, single–bond bridged analogues. In addition, the higher TPA cross section observed in α compared to the pared PDI monomer shows a significant increase in transition dipole moments for α and hence increased iCT.

Table 5.5.1.1. Linear and Nonlinear Optical properties for the tetramers in chlorobenzene (and toluene for the ϕ_F/ % **).

Comp.nd	λ_{abs} / nm	λ_{em} / nm	Stokes shift /cm^{-1}	ε / M^{-1}cm^{-1}*	ϕ_F/ %	ϕ_F/ % **	δ_{TPA} / GM λ_{exc}=820 nm
PDI Monomer	461, 492, <u>529</u>	537, 578	282	85700[a]	~88[b]	97	1 [c]
α	461, 492, <u>529</u>	<u>537</u>, 578(sh)	282	289500	0.04	1.3	71.1
β	499, <u>529</u>	562, 710	1110	59200	0.4	2.7	30.5
βC	471, <u>503</u>, 554	562, 603(sh)	257	131100	7.2	22.5	234

*at the underlined maximum wavelength

** in toluene as a solvent

[a] See reference [35]

[b] See reference [40]

[c] See reference [79]

5.6 Time Resolved Fluorescence

Fluorescence kinetics were acquired by both fluorescence up–conversion (FUC) and time–correlated single photon counting (TCSPC) with femtosecond and nanosecond resolution,

respectively. Concentrations of 4 X 10^{-5} M, 2.0 X 10^{-4} M, and 8.0 X 10^{-5} M for α, β and βC, respectively, were used for FUC while 2 X 10^{-6} M, 8.0 X 10^{-6} M, and 4.0 X 10^{-6} M for α, β and βC, respectively, were used for TCSPC measurements. From our FUC measurements, we obtained different decay lifetimes (**Figure 5.12.2.1 and Table 5.6.1**). The fast decay times can be associated with the decay of the singlet–associated species back to the ground state. The α compound decays to zero very fast and therefore, only two components were applied during the data analysis. However, three components were employed for both β and βC compounds. In the β compound, a very long–lived component, whose lifetime could not be captured by our software, was observed. A similar component was also observed for the βC compound as shown in **Figure 5.12.2.1**.

To gain more insights into these long components, more fluorescence measurements were carried out using our TCSPC technique. For the rigid βC, these experiments revealed a lifetime of 2.64 ns at 538 nm and 2.68 ns at 562 nm (**Figure 5.12.2.2 and Table 5.6.2**). Therefore, the long–lived component observed for the βC compound using the FUC measurements has a decay time of about 2.7 ns. This decay time is expected to be seen as an infinite component using our femtosecond transient absorption (fsTA) measurements which can only measure lifetimes up to 1.6 ns. For the β compound, we observed a fluorescence lifetime of 3.77 ns, 3.30 ns and 2.91 ns at 538 nm, 560 nm and 710 nm respectively. Therefore, the lifetime of the long–lived component (3.30 ns) observed for this β compound using the FUC measurements is assigned to the singlet decay lifetime. For this β compound, the emission wavelength effect on the fluorescence decay lifetime is consistent with the presence of different emissive species due to excimer formation for β in chlorobenzene. For α, the fluorescence lifetime of 3.68 ns at 538 nm and 3.69 ns at 578 nm, is significantly longer than the 3 ps obtained for S_1 decay using the FUC (**Table 5.6.1**) studies. In comparison to β and βC, α has a longer decay time observed using the TCSPC measurements. The ca. 3.69 ns decay lifetime measured for α in chlorobenzene may be due to fluorescence (either direct or delayed) associated with the double triplet excited state ^{1}[TT] [80,81] intermediate of intramolecular singlet exciton fission (iSEF).

Table 5.6.1. Lifetimes (τ) obtained by fitting the FUC kinetics.

Compound	$\tau_{FUC,1}$ / ps	$\tau_{FUC,2}$ / ps	$\tau_{FUC,3}$ / ps
α	1.2	2.6	–
β	2.0	26	Very long–lived component
β**C**	18	130	Long–lived component

Table 5.6.2. Fluorescence lifetimes obtained by fitting the SPC kinetics acquired at different emission wavelength for the tetramers in chlorobenzene.

α		β		βC	
λ_{em} /nm	τ / ns	λ_{em} / nm	τ / ns	λ_{em} / nm	τ / ns
538	3.68	538	3.77	538	2.64
578	3.69	560	3.30	562	2.68
		710	2.91		

5.7 Femtosecond Transient Absorption

The ultrafast excited state dynamics were investigated by femtosecond transient absorption (fsTA) using concentrations of 3.0 X 10^{-5} M, 3.0 X 10^{-5} M, and 2.0 X 10^{-5} M for α, β and βC, respectively. The time–resolved spectra (**Figure 5.7.1**) show positive excited state absorption (ESA) at 740 nm and around 560 nm, and negative ground state bleaching (GSB) signals at earlier wavelengths. We also observe strong modulations in wavelengths beyond 600 nm which are due to the instability of the white light used as the probe and does not affect the excited state dynamics of the investigated molecules. The ESA at 740 nm has been previously associated with the perylene diimide (PDI) anion,[82–87] whereas signals between 550 and 600 nm have been assigned to the PDI cation.[83,85,86,88] For these molecules, the PDI cationic absorption band may be convoluted with GSB or triplet absorption signals, and the anionic band convoluted with the $S_n \leftarrow S_1$ signal, as a result of spectral overlap. Global analysis of the fsTA spectra show the presence of several exponential components as shown in **Figure 5.7.2**. At short delays after excitation, we observe fast components in all the investigated molecules (black and red in **Figure 5.7.2**). The Species Associated Spectra (SAS) of these fast components are similar to the SAS of the 'longer' living component (blue spectra in **Figure 5.7.2**). This result suggests that the associated dynamics reflects the relaxation processes occurring within the same electronic excited state – the singlet state. Previous reports have mentioned the possibility of a singlet excited state with iCT character forming very fast (within solvation).[89] Therefore, these two (black and red in **Figure 5.7.2**) fast components can be associated to the decay of the first singlet state to form a singlet solvation–relaxed state. This state relaxes further to form a final relaxed S_1 state. This is proposed to be a charge transfer (CT) related state from a superposition of the singlet states known as $[S_1S_0]_{[TT]}$CT for α, an excimer state ($[S_1S_0]_{Excimer}$) for β and a CT state ($[S_1S_0]$CT) for βC (see **Figure 5.7.2**). For β, a CT state is not observed since the fsTA measurements were carried out in high concentrations where the excimers are the dominating species. However, the CT state with a

decay of 3.30 ns was observed using TCSPC measurements where the β monomer was more dominant. For the α compound, the component in blue leads to a subsequent formation of what is proposed to be the double triplet state, ^{1}[TT], whose decay is infinite and cannot be determined using our current fsTA due to the experimental time limit (1.6 ns). The components showing a lifetime of 160 ps for α, 890 ps for β and 2700 ps for βC represent the relaxed S_1 state. At longer delays, the signal decays result in the simultaneous formation of an ESA at 510 nm, 480 nm and 535 nm for the α, β and βC respectively. The kinetics at these wavelengths exhibit a rise as shown in **Figure 5.7.3**, whose dynamics reported in **Figure 5.12.3.1** match those observed in **Figure 5.7.2**. Therefore, for the β and βC compounds, the last component (in green) represents the long−lived triplet species formed upon S_1 decay and are peaked around 480−550 nm. However, for the α compound, the $[S_1S_0]_{[TT]}$CT superposition state decays within 160 ps to form another singlet species, with both singlet and triplet characteristics, double triplet state (^{1}[TT]) as shown in **Figure 5.7.2**. This ^{1}[TT] state's decay lifetime is longer than our instrumental time limit and can only be assigned to infinite time using our fsTA. Therefore, for the α compound, the infinite time is assigned to the decay of the precursor of triplet states, $[T_1]$, which happens at lifetimes longer than few nanoseconds. The fast decay of the superposition state indicates the formation of the double triplet state, ^{1}[TT], suggesting occurrence of singlet fission for the α compound. On the other hand, for β, a component which forms within 15 ps from the solvation state $(S_1S_0]_{Solvation}$), decays within 890 ps and has a singlet character, is assigned to the excimer formation ($[S_1S_0]_{Excimer}$) as shown in **Figure 5.7.2**. The components with infinite times are suggested to be triplet precursors' (and double triplet decay for the α compound) decays since triplet decay times are longer and could not be captured due to our system time limitations. For the α compound, the only tetramer whose steady state emission spectra and triplet yields were found to be solvent−dependent, fsTA measurements were carried out in toluene. For this sample, a slower singlet decay and triplet formation (380 ps) was observed relative to chlorobenzene (160 ps). This slower triplet formation could be as a result of the observed excimers in toluene.

In order to gain more insights into the mechanism of triplet production, triplet quantum yields were computed following the singular value decomposition (SVD) analysis of the fsTA results [90] (**see Supporting Information (SI) for details on the procedure**). Quantitatively related singlet and triplet ESA spectra were obtained and then used to determine the temporal population dynamics of these states. The population data (**Figures 5.12.4.5, Figure 5.12.4.15**) indicate a

triplet quantum yield of 166% and 66% for α and βC respectively, in chlorobenzene. For the α compound in toluene, the triplet yield was calculated to be 56% shown in **Figure 5.12.4.10**. However, for the β compound, this calculation was inaccurate due to the spectral overlap between the GSB and triplet absorption. Even though this analysis contains many approximations, it clearly suggests that that triplet production takes place via intramolecular singlet exciton fission (iSEF) for the α and via conventional intersystem crossing (ISC) for the rigid−bridged βC (φ_T lower than 100%). Since these triplet quantum yields are mostly estimations, the nanosecond transient absorption was used to perform a rigorous experiment to accurately determine the triplet quantum yields of the investigated chromophores.

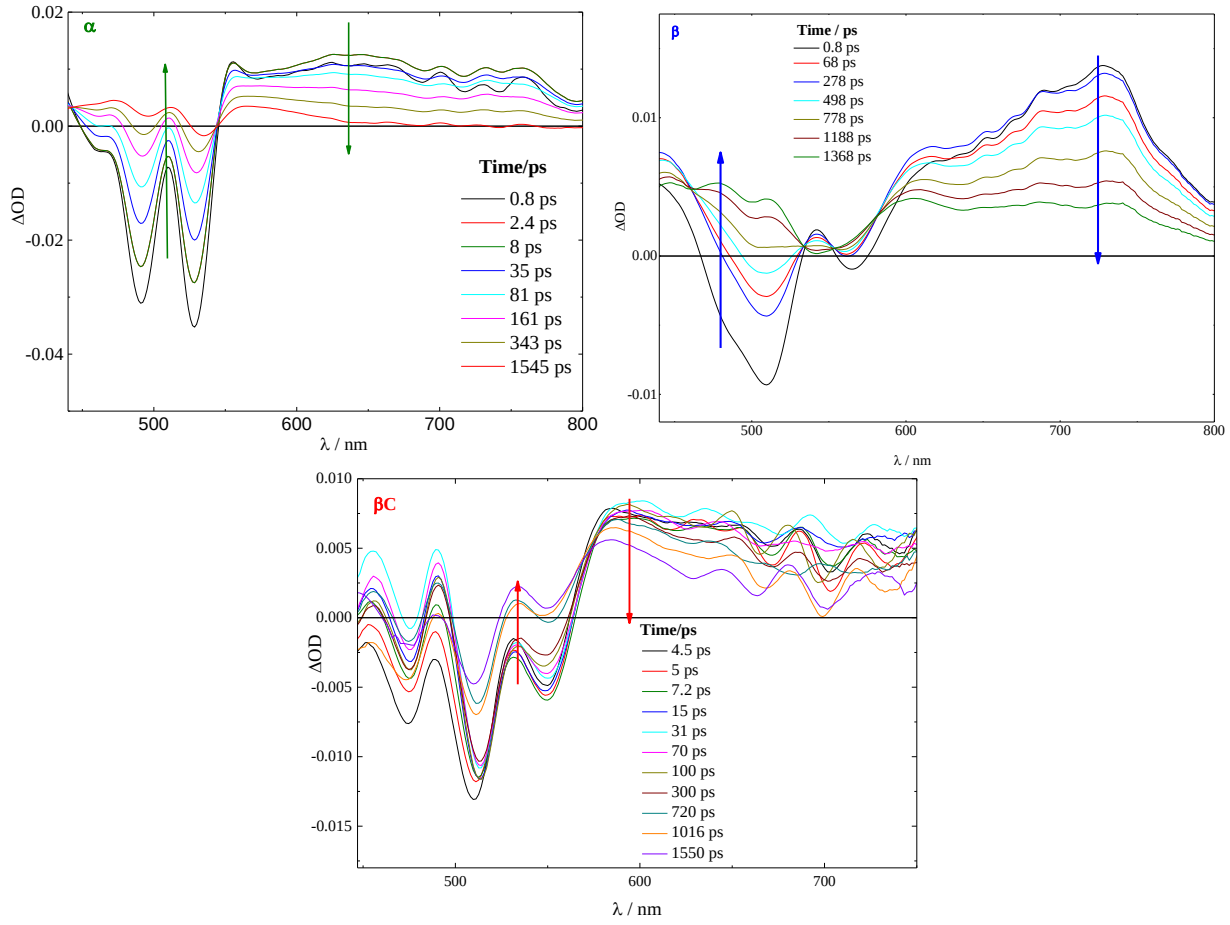

Figure 5.7.1. Femtosecond transient spectra for the investigated molecules at 400 nm excitation in chlorobenzene.

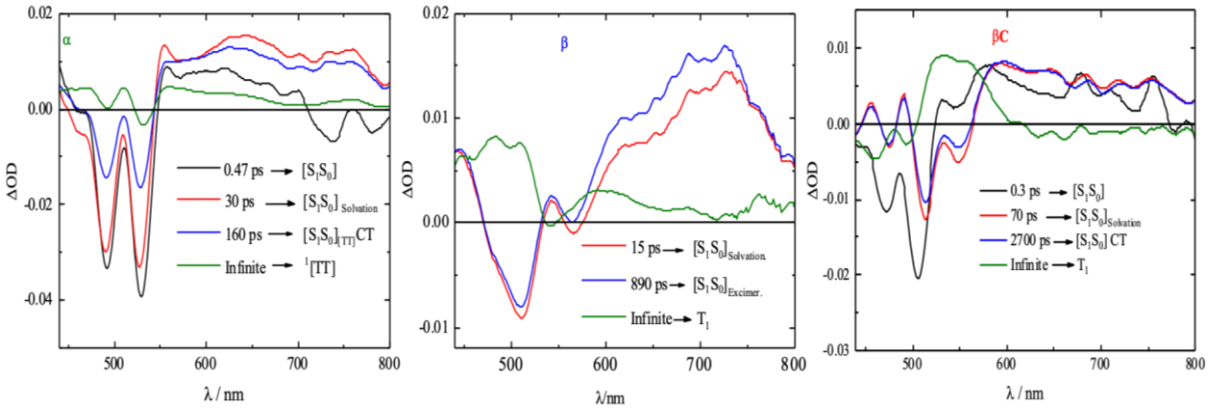

Figure 5.7.2. Species Associated Spectra (SAS) and lifetimes obtained by global fitting of the fsTA data obtained using chlorobenzene as the solvent.

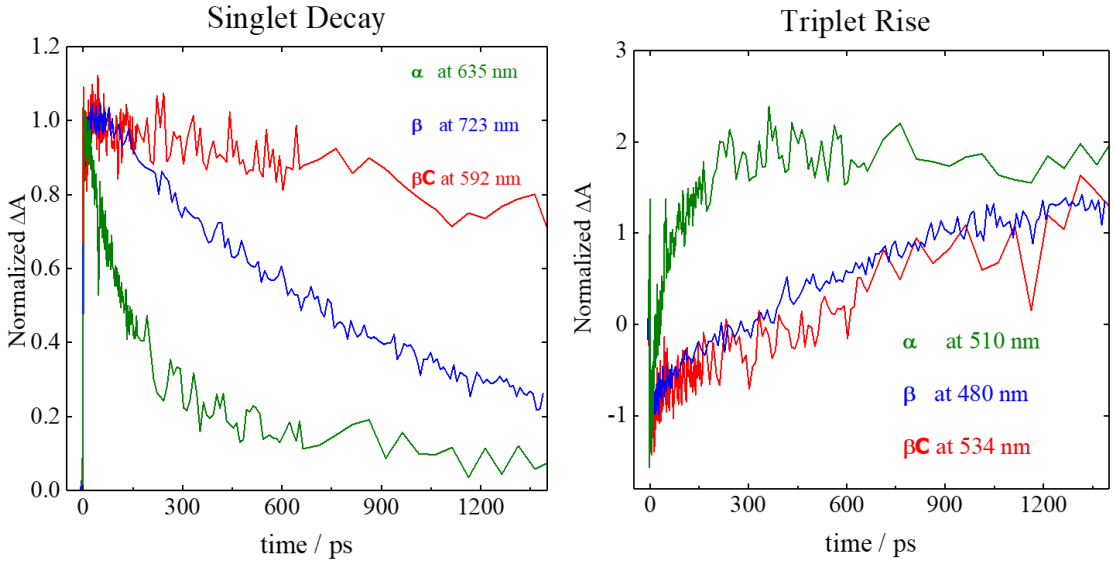

Figure 5.7.3. Femtosecond transient singlet decay (left) and triplet rise (right) kinetics for the investigated PDI tetramers in chlorobenzene.

5.8 Nanosecond Transient Absorption

To investigate the triplet excited state dynamics of these molecules, nanosecond transient absorption (nsTA) measurements were carried out (**Figure 5.8.1**) using concentrations of 3.0 X 10^{-6} M, 8.0 X 10^{-6} M, and 5.0 X 10^{-6} M for α, β and βC, respectively. No pump wavelength dependence, solvent dependence or spectral shift was observed for all the investigated compounds (**Figures 5.8.1, 5.12.5.1 and 5.12.5.2**). The nanosecond transient absorption spectra show negative signals due to ground state bleach (GSB), as obtained in the steady state absorption spectra (**Figure 5.5.1.1**). The positive excited state absorption (ESA) peak is centered at 510 nm, 485 nm and 535 nm for the α–, β– and βC–tetramers, respectively. Signals of triplet absorption have been reported

for many perylene diimide (PDI) derivatives around 500 nm.[50,76] Decay lifetimes of the detected transients range from hundreds of nanoseconds in air equilibrated solution to tens of microseconds in nitrogen purged solution (see **Table 5.8.1**). Quenching by molecular oxygen thus occur at an almost diffusional rate. Also, these transient species can be sensitized by higher−triplet energy donors or are able to sensitize lower–triplet energy acceptors, such as tetraphenyl porphine or tetracene (**Figure 5.8.2**). These results allow us to assign the long−lived transients revealed by nsTA experiments to the $T_n \leftarrow T_1$ transition of the tetramers. For the β− and βC−tetramers, negative signals due to stimulated emission were observed in the transient spectra at early delays (see the black and red spectra for βC in **Figure 5.8.1**). In addition, there was evidence of fast emission peaks centered at 556 nm and 700 nm for β, and 558 nm and 610 nm for βC. These peaks are consistent with the emission peaks observed from linear emission as shown in **Figure 5.8.1**. The fast and broad emission peak observed for the β compound can be associated with the formation of excimer states. Interestingly, there were additional negative peaks observed at longer delays after excitation for both β− and βC−tetramers. For the βC compound, these kinetics reveal increased decay lifetimes in purged solutions relative to the unpurged solutions (**Figure 5.12.5.3)**. The negative signals observed around 750 nm for β and 800 nm for βC respectively, are attributed to phosphorescence. However, no phosphorescence was detected for α, as shown in the spectra on **Figure 5.8.1,** suggesting a lower energetic triplet emitting in the infrared in this case.

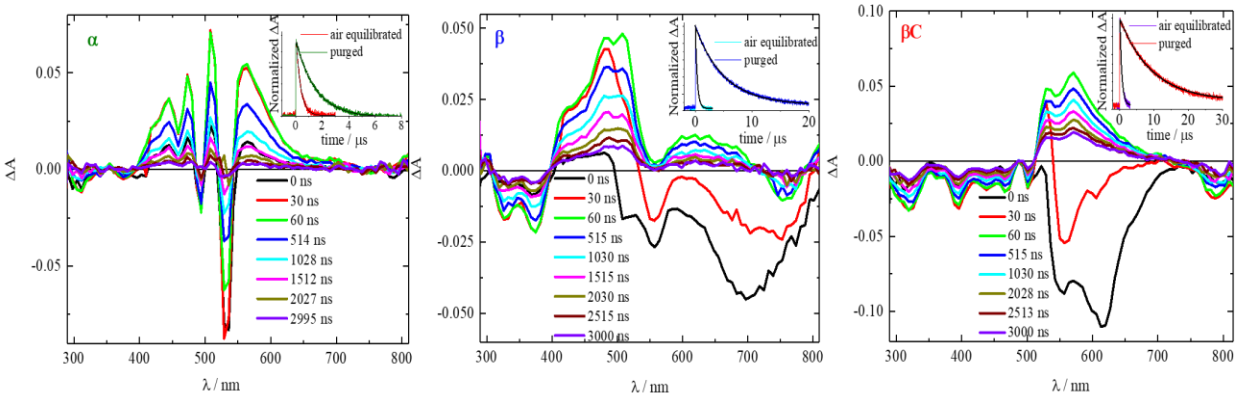

Figure 5.8.1. Nitrogen purged time–resolved spectra and triplet purged/unpurged kinetics (insets) obtained by nanosecond TA for the tetramers in chlorobenzene with 415 nm excitation.

Table 5.8.1. Triplet properties for the tetramers in chlorobenzene from nanosecond transient experiments.

Tetramer	λ_T (nm)	$\tau_{T,air}$ (μs)	$\tau_{T,N2}$ (μs)	ε_T ($M^{-1}cm^{-1}$)	ϕ_T Chlorobenzene (Average)	ϕ_T Toluene
PDI Monomer[d]	505[d]	–	140[d]	60000[d]	–	–
α	510	0.359	1.8	5180	1.24	0.61
β	485	0.567	8.1	12379	0.17	0.18
βC	570	0.638	14	16029	0.24	0.09

[d] See reference [91]. Triplet wavelengths, lifetimes and extinction coefficients measurements reported here were carried out using benzene as the solvent. The triplet quantum yield of the parent PDI monomer reported in **Table 5.8.1** is **0.03% in bromobenzene, 0.01% in acetonitrile and 0.003% in benzene.** [91]

Triplet energy transfer measurements and relative actinometry were used to accurately evaluate the triplet extinction coefficients and the triplet yields, respectively. Important information about triplet energies was also obtained from the sensitization experiments. Energy transfer was observed from the triplets of β and βC to the triplet of tetracene (E_T = 1.27 eV), while no triplet energy transfer was observed from α to tetracene, suggesting a lower triplet energy for α in comparison to the other two tetramers. The triplet of α could be sensitized by employing a higher triplet energy donor such as tetraphenyl porphine (E_T=1.43 eV). These experimental results support the feasibility of intramolecular singlet exciton fission (iSEF) occurring in α and not in β and βC, because a low energy triplet is required for the SF energetic condition ($E[S_1] > 2 \times E[T_1]$) to be fulfilled. The triplets produced upon photoexcitation of α in chlorobenzene show shorter lifetimes (1.8 μs) relative to those produced via ISC for β and βC (8.1 and 14 μs, respectively). Also, the triplets decay lifetime of α was longer (by a factor of two) when the triplets were produced by sensitization (3.7 μs) relative to direct excitation (1.8 μs). This is additional evidence indicating a SEF mechanism of triplet production for α as there is a higher probability that the independent triplets can return to S_1 via triplet−triplet annihilation (TTA), resulting in the reduced lifetime. A step–by–step triplet extinction and yield calculation for the three investigated tetramers is detailed in the SI. From the calculations detailed in **Section VI** of the SI and the data shown on **Table 5.6**, lower triplet extinction coefficients were observed for the flexible–bridged systems in comparison to the rigid–bridged system. In addition, relative actinometry measurements were coupled with the sensitization experiments (detailed in the supporting information) to allow for accurate calculation of the triplet quantum yields per equation (1)

$$\frac{[\phi_T \varepsilon_T]_{sample\ (\beta\ or\ \beta C)}}{[\phi_T \varepsilon_T]_{ref.}} = \frac{[\Delta A]_{sample\ (\beta\ or\ \beta C)}}{[\Delta A]_{ref.}} \quad (1)$$

As shown on **Table 5.8.1** and **Table 5.12.6.1**, lower triplet extinction coefficients were observed for the flexible–bridged systems in comparison to the rigid−bridged system. A triplet yield higher than 100% was obtained only in the case of α in chlorobenzene (φ_T = 124%), suggesting that the mechanism of triplet production proceeds via iSEF for this sample, while proceeding via traditional intersystem crossing (ISC) for the other two tetramers owing to φ_T of 17% and 24% for β and βC compounds respectively. Interestingly, in the case of α in toluene, a lower triplet yield (61%) was measured. However, there was no significant change in the triplet yields calculated for β (18%) and βC (9%) in toluene compared to chlorobenzene as shown in **Table 5.8.1**.

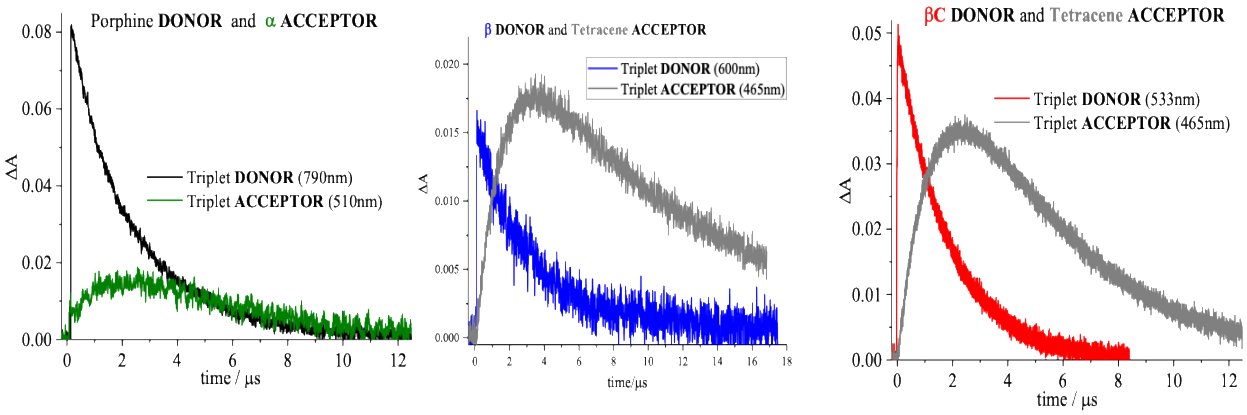

Figure 5.8.2. Decay and rise dynamics of the investigated PDI tetramers with the α sensitization experiment carried out upon 594 nm laser excitation and the β/βC sensitization experiments upon 510 nm excitation, in chlorobenzene.

5.9 Quantum Chemical Calculations

Density functional theory (DFT) was used to optimize the geometries and obtain the dihedral angles of the investigated chromophores. The optimized structures are shown in **Figure 5.9.1** with their dihedral angles shown in **Figure 5.12.7.1**. The ground state geometries showing similar dihedral angles obtained for both α and β reveal that both of these molecules possess a twisted structure. However, βC has the lowest dihedral angle and therefore, this molecule is almost planar.[53,77] In α, the covalent linker is connected to the perylene diimide (PDI) units at the α position, allowing the most facile rotation of the PDI group with respect to the central unit.[92] As a

result, α has PDI units that are perpendicular to the central unit; this perpendicular orientation eliminates the possibility of π–π stacking between the individual PDI units. For the β molecule, the β positioning results in PDI units that pair off, with strong π–π stacking between two pairs of interacting PDIs. On the other hand, in βC molecule, the PDI units are rigidly linked to the benzodithiophene (BDT) core, which results in greater co–planarity between the linker and PDI chromophores. These varying geometries among the investigated tetramers lead to differences in the electronic structure of the chromophores' excited states.

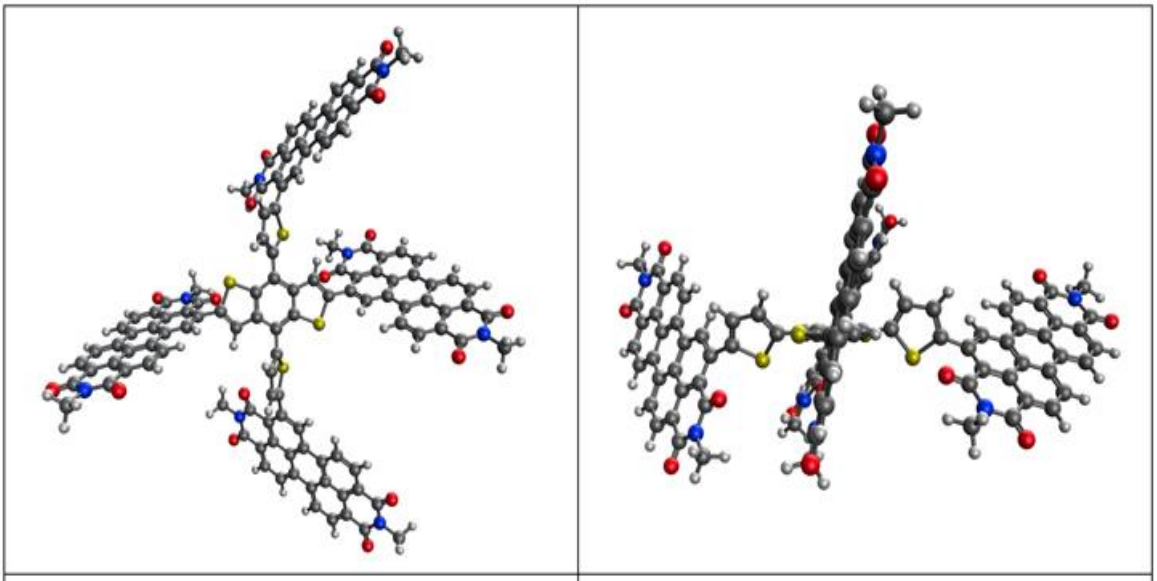

(a)

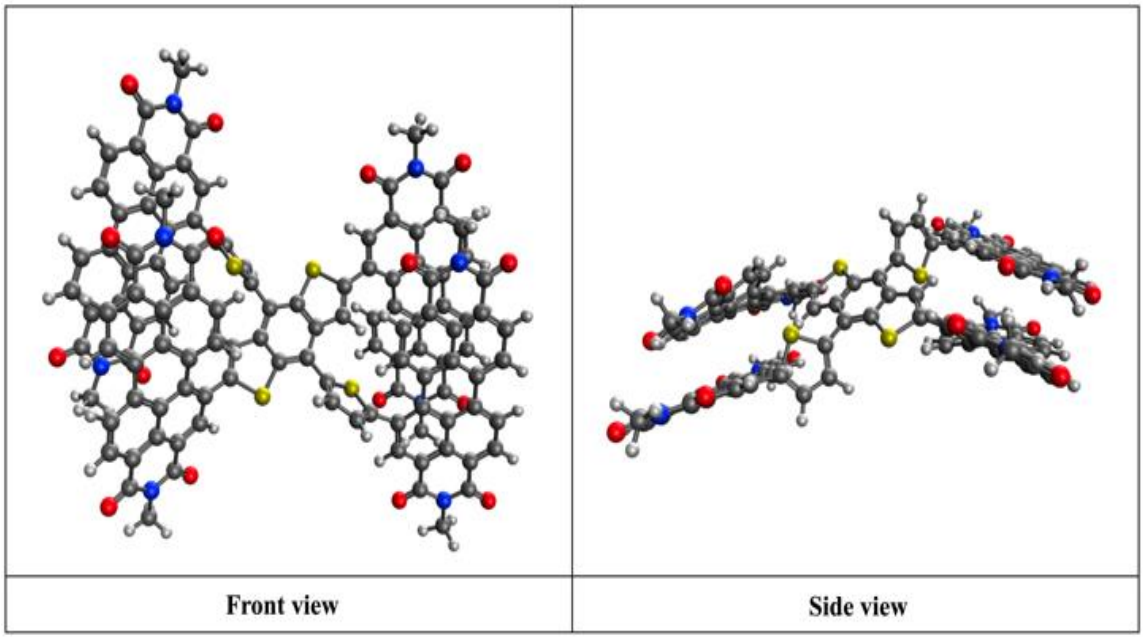

(b)

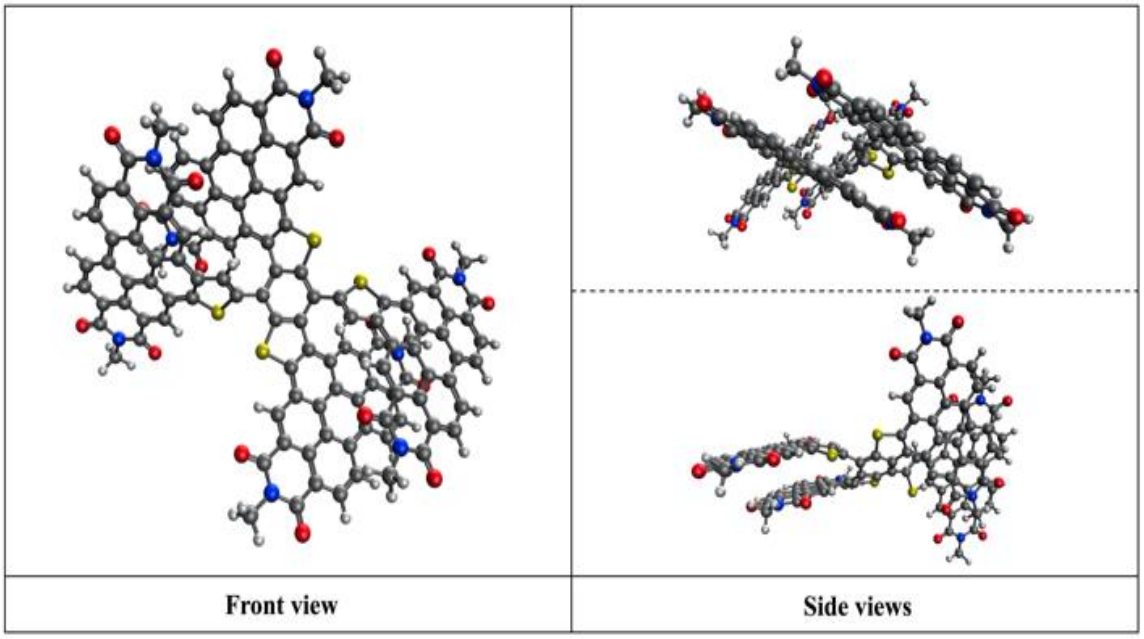

(c)

Figure 5.9.1. Ground−state optimized geometries of the tetramers considered in this work. (a) Ground-state optimized geometry of α−tetramer, (b) Ground-state optimized geometry of β, (c) Ground-state optimized geometry of βC.

The natural transition orbitals (NTOs) for $S_0 \rightarrow S_1$ transitions of the tetramers are shown in **Figure 5.9.2**. For α, the $S_0 \rightarrow S_1$ NTOs are completely localized on a single PDI unit, suggesting low coupling between the PDI units, which is also supported by the steady state measurements.

The $S_0 \rightarrow S_1$ NTOs for β are slightly more delocalized with the electron density spread out to the central PDI linker and the adjacent PDI unit. This delocalization indicates some coupling between adjacent PDI units. However, for βC, the ease of π–conjugation across the coupled units enables the NTOs to be delocalized across most parts of the molecular structure. This delocalization also indicates the presence of a strong coupling among the PDI units in the rigidly bridged, planar tetrameric system. Using time dependent DFT (TD–DFT) calculations and taking into account the solvation effects of chlobenzene whose dielectric constant is 5.62, $S_0 \rightarrow S_1$ singlet energies of 2.90 eV for the α, 2.55 eV for the β and 2.91 eV for the βC (**Table 5.9.1**) were reported. From our steady state measurements, it is clear that the singlet absorption energies ($S_0 \rightarrow S_1$) for both α and β tetramers are identical while that of βC is blue–shifted (2.34 eV, 2.34 eV and 2.46 eV for α, β and βC, respectively). A similar trend is also expected for the TD–DFT calculations. While the TD–DFT method has been reported to overly estimate the singlet and triplet energies, the trend in these energies should match the experimental energies trend. This is not the case for the tetramers experimental results and TD–DFT calculations. The discrepancy may be as a result of the different functionals, and bases sets used for the TD–DFT calculations or the fact that we are not sure that the calculated $S_0 \rightarrow S_1$ energies are from the relaxed state. While a better comparison of singlet energies would be through the relaxed singlet state energies from the $S_1 \rightarrow S_0$ emission, the large size of our molecules challenged our efforts to calculate these singlet emission energies using TD–DFT. These relaxed singlet energies would be expected to match those obtained from our steady state emission (2.31 eV for the α, 2.21 eV for the β and 2.21 eV for the βC).

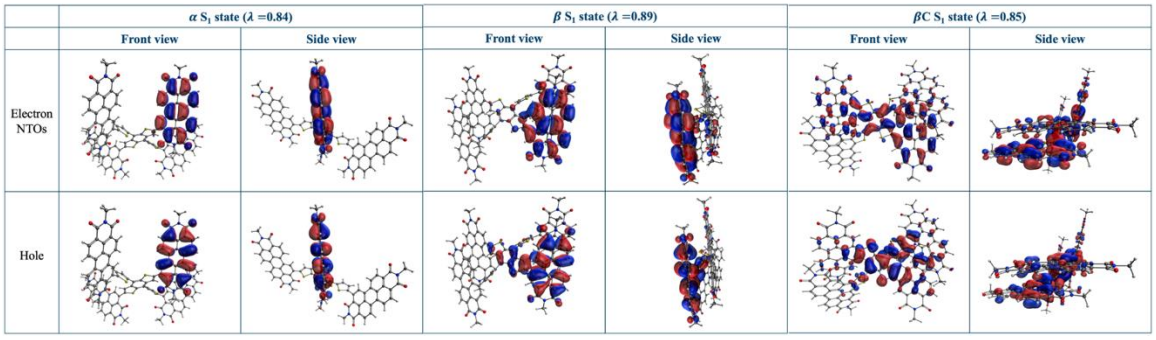

Figure 5.9.2. Natural transition orbitals (NTOs) of $S_0 \rightarrow S_1$ transitions for the three tetramers considered in this work. Orbitals plotted in IQmol with isovalue 0.05.

Table 5.9.1. Single point energies calculated with ω-B97XD basis and dielectric constant of 5.62 for C_6H_5Cl (chlorobenzene) and 2.38 for C_7H_8 (toluene) for the investigated tetramers. (Energies are given in eV).

Tetramers	**Absolute $S_0 \rightarrow S_1$ Energies**			**Absolute $S_0 \rightarrow T_1$ Energies**			**Emission $S_1 \rightarrow S_0$ Energies at S_1 geometry**	**Emission $T_1 \rightarrow S_0$ Experimental**
	C_6H_5Cl	C_7H_8	**Gas**	C_6H_5Cl	C_7H_8	**Gas**	**Gas**	C_6H_5Cl
α	2.90	2.91	3.02	1.76	1.76	1.76	1.06	2.31
β	2.55	2.55	2.61	1.63	1.64	1.64	0.87	2.21
β**C**	2.91	2.92	2.95	2.05	2.05	2.05	1.43	2.21

Further quantum chemical simulations were performed to give insights into possible triplet formation mechanisms for the tetramers. In the α–tetramer, the NTOs for the T_1 states ($S_0 \rightarrow T_1$ transition; **Figure 5.12.7.2**) are each localized on a single PDI. Time dependent DFT (TD–DFT) calculations give adiabatic $S_0 \rightarrow T_1$ triplet energies of 1.76 eV for the α, 1.63 eV for the β and 2.05 eV for the βC in chlorobenzene. For efficient iSEF, the lowest optically allowed singlet excited state [S_1] of the chromophore should have an excitation energy of at least twice its triplet energy: ($E[S_1] > 2 \times E[T_1]$). Considering the triplet and singlet absorption energies shown in **Table 5.9.1**, iSEF is energetically uphill by 0.62 eV for the α, 0.71 eV for the β and 1.19 eV for the βC. This endothermic behavior shows that iSEF is not possible in any of the investigated chromophores.

In order to explore the accessibility of potential double–triplet states (^{1}[TT]), restricted active space spin flip (RAS–SF) was used to describe the character of multi–excitonic states (**Figure 5.9.2, Table 5.12.7.1 and Table 5.12.7.1**). To perform RAS–SF calculations for molecules with such large sizes, RAS–SF was performed on the "half" tetramers with only 2 PDI units (RAS–2SF), as shown in **Figure 5.12.7.3 – 5.12.7.5**. Similar to the TD–DFT calculations, RAS–2SF is believed to overestimate the calculated energies in comparison to what is obtained experimentally. However, our RAS–2SF calculations shown in **Figure 5.9.3** show that the singlet (S_1) energy for the α–tetramer is 3.8 eV while that of the β–tetramer is 3.4 eV. This suggests that the RAS–2SF method error could be around $\pm$ 0.4 eV. Disregarding the $\pm$ 0.4 eV error observed in these S_1 energies, iSEF should be energetically uphill by 0.60 eV for α, 0.80 eV for β–tetramer and by 1.0 eV for βC. These results are consistent with those obtained through our TD–DFT

calculations. While this thermodynamic behavior is strange for iSEF materials, it has been reported that the production of independent triplets from a singlet becomes less endoergic as molecular size increases.[93] For acene materials, this endothermic SEF behavior ($2T_1 > S_1$) is not new.[1] The endothermic energy deficit ($2T_1 - S_1$) for these iSEF acene molecules has been reported to be 0.53 eV and 0.18 eV for anthracene and tetracene, respectively.[1] Therefore, it is possible that some of our investigated molecules are eligible to undergo iSEF even after defying the thermodynamic conditions. In all three cases, the calculated energy for the double triplet ^{1}[TT] state is above the S_1 which is also atypical. Similar energetics, where the ^{1}[TT] energy is higher than the S_1 energy, have been reported for PDI derivatives undergoing iSEF, with endothermic driving energies (^{1}[TT] – S_1) ranging from 0.2 eV to 1.05 eV. [93] From our RAS–2SF, the calculated endothermic driving energy is 0.614 eV, 0.983 eV and 1.157 eV for α , β and βC respectively with a probable error of ± 0.57 eV for each of these energy differences. The RAS–2SF energies provide insight about the feasibility of formation of the double triplet ^{1}[TT] state and separation of excitons from the ^{1}[TT] state into two independent triplets. Therefore, considering the endothermic energy drives from the RAS–2SF calculations, α is likely to undergo iSEF compared to β and βC.

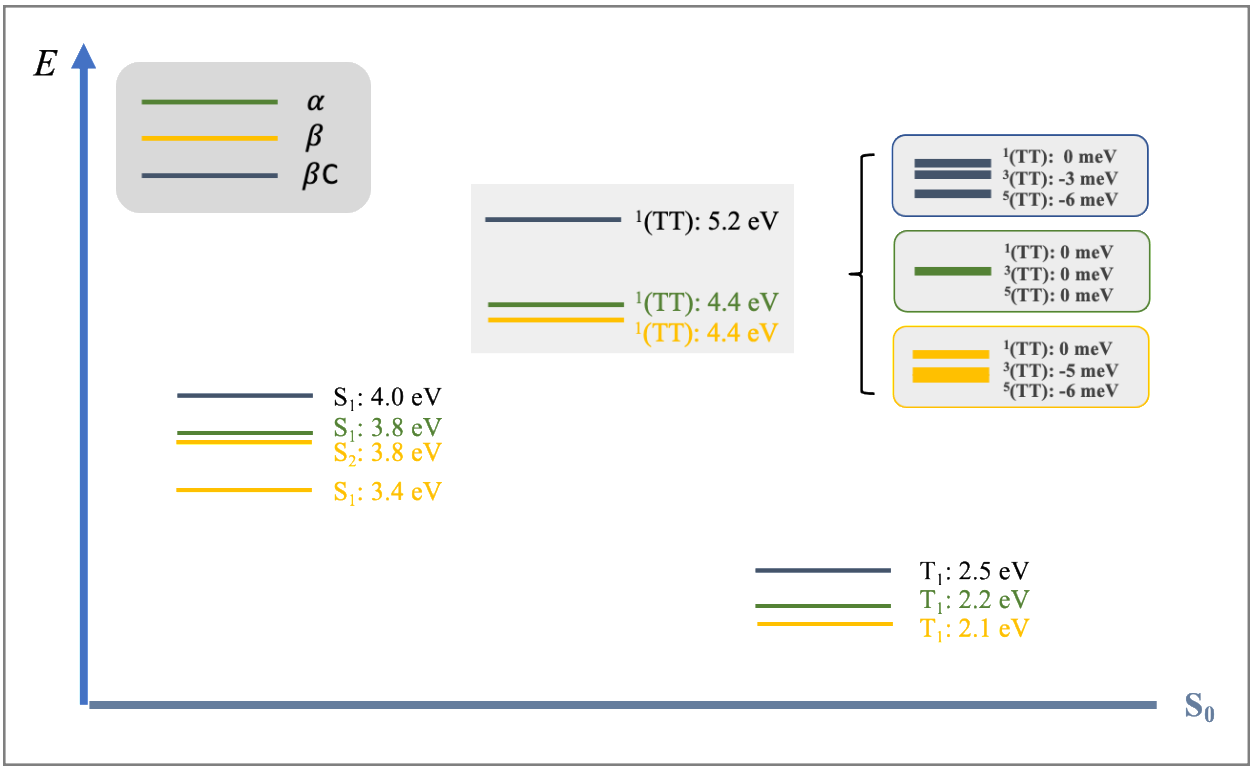

Figure 5.9.3. RAS–2SF results for the truncated tetramers. Due to the size limit of CI calculations, in the truncated model structure, only one pair of the adjacent PDI unit in each tetramer system is considered.

5.10 Discussion

Literature proposes that the presence of a π–bridge linker and its flexibility is important in triggering intramolecular singlet exciton fission (iSEF). [26, 38, ,53] In this present investigation, we show that the π–bridge linker flexibility is necessary but not sufficient in activating iSEF in multichromophoric perylene diimide (PDI) systems. Here, we show the importance of the position of attachment of the PDI units to the core (π–bridge linker) in dendritic PDI tetramer systems. Owing to the flexibility of the π–bridge linker, the triplet energy is tuned such that the iSEF energetic criteria ($E_{S1} \geq 2E_{T1}$) may be satisfied. In this work, key differences between α– and β–functionalized flexible–bridged systems compared to a rigid–bridged βC system, are pointed out as they relate to the efficiency and rate of triplet production upon photoexcitation. As an important result of our study, we demonstrate that in addition to the conformational flexibility of the π–bridge linker, the position of functionalization on the PDI (α and β) and the dielectric environment play a role in activating iSEF or excimer formation in these molecules.

We observe differences in the steady state properties of the two flexible π–bridged systems. The steady absorption and emission spectra of α in chlorobenzene show striking resemblance with the spectra of the parent PDI monomer. This indicates minimal excitonic coupling among its PDI units. This lack of coupling is further confirmed by the extinction coefficient of the α, which is four (4x) times that of the parent PDI monomer. The relatively broad absorption spectrum with less vibronic structures of β, compared to that of α, resembles the reported absorption spectra of prepared films of the PDI monomer.[94] The narrower, structured and blue–shifted spectra of the rigid π–bridged βC system is expected for planar PDI molecules.[40,77] The βC absorption maxima is similar to that of a benzodithiophene (BDT) substitute.[78] The similarities of α and the PDI monomer surprisingly disappear upon comparing their fluorescence quantum yield in chlorobenzene. The fluorescence quantum yield for α in chlorobenzene is four orders of magnitude (0.04%) lower than that of the parent PDI monomer (97%).[91] The comparatively low quantum yield in α suggest an alternative deactivation pathway that competes with the traditional radiative deactivation pathway of photoexcited parent PDI monomer. However, in toluene, the emission spectra of α have an additional broad peak centered around 710

nm and these spectra are concentration dependent. In addition, $\alpha's$ fluorescence quantum yield increases significantly in toluene, matching that of β in toluene. Therefore, in toluene, α has a tendency to form excimers as evidenced the above emission spectra characteristics, which inhibit iSEF. For β, the broad and red–shifted emission band at 710 nm, which happens to be concentration dependent, points towards the formation of excimers for this compound in both chlorobenzene and toluene. The low fluorescence quantum yield of α, as well as the observation of excimers in β, has been addressed using quantum chemical calculations and time–resolved measurements.

For α, optimized ground–state geometries showed large perylene diimide–thiophene (PDI–Th) and perylene diimide – benzodithiophene – perylene diimide (PDI–BDT–PDI) angles of 78.7° and 63.5° respectively. This nearly perpendicular connection between the two PDI units connected through the thiophene (Th), and the two PDI units connected through the BDT core indicate the twisted nature of this PDI tetramer system. The almost perpendicular orientation of the α–functionalized PDI units introduces a large steric hindrance between individual PDI units, minimizing their exciton coupling and creating a good separation between the orbitals in the PDI units of this molecule. As a result, it is expected that the photophysical characteristics of α should resemble those of the parent PDI monomer. We observed that the β–position leads to PDI units that pair off in a co–facial orientation with a strong π–π stacking between two pairs of interacting PDIs, an orientation that supports the formation of excimers.

The thermodynamic condition of iSEF is $E[S_1] > 2 \times E[T_1]$. Considering the singlet and triplet energies obtained through time dependent–density functional theory (TD–DFT), with chlorobenzene solvation effects factored in, iSEF is energetically uphill by 0.62 eV for α, 0.71 eV for β–tetramer and by 1.19 eV for βC. These results show that iSEF is thermodynamically impossible for all the investigated molecules. These results are consistent with those obtained from RAS–2SF where iSEF is energetically uphill by 0.60 eV for α, 0.80 eV for β–tetramer and by 1.0 eV for βC. The thermodynamic rule has been defied by singlet exciton fission materials, anthracene and tetracene, with endothermic energy deficit reported to be 0.53 eV and 0.18 eV, respectively where singlet fission is thermally activated.[7] The endothermic fission was used to explain the extremely low fluorescence quantum yield of tetracene since singlet fission was the dominant deactivation pathway for the singlets.[95] It is therefore possible that the α compound,

whose energy deficit is close to that of anthracene, is capable of showing iSEF. On the other hand, using the calculated $T_1 \rightarrow S_0$ emission energies (1.06 eV for the α, 0.87 eV for the β and 1.46 eV for the βC) together with our experimental relaxed $S_1 \rightarrow S_0$ energies (2.31 eV for the α, 2.21 eV for the β and 2.21 eV for βC), we notice that iSEF is energetically favorable for the α by 0.21 eV and 0.52 eV for the β, but energetically uphill for βC by 0.57 eV (**Figure 5.12.7.7**). From these calculations, iSEF is thermodynamically viable for both α and β. However, for the parent PDI monomer, iSEF thermodynamic requirement is not fulfilled owing to its reported triplet (~1.2 eV) and singlet (2.34 eV) energies.[96]

On the other hand, using the RAS−2SF to predict the iSEF kinetic feasibility, surprisingly shows that among the three investigated tetramers, only the α−functionalized chromophore has the possibility of undergoing iSEF. We use a model by Farag *et al*.[93] which defines the factors affecting the rates of the individual steps in the iSEF process. The rate of formation of the ^{1}[TT] from the S_1 (first step) depends on the energy drive (E_{SF}) and the nonadiabatic coupling (NAC) between these two states as described in detail in the literature. [45, 93,97] On the other hand, the rate of the second step depends on the multiexciton binding energy (E_b). [93] This multiexcitonic interaction quantifies the charge transfer contributions to the singlet multi–excitonic states, compared to the pure quintet multi–excitonic states. From our RAS−2SF calculations of truncated molecules, we find that the E_{SF} for α is 0.614 eV, as shown in **Figure 5.10.1**. This E_{SF} is lower compared to that of β (0.983 eV) and βC (1.148 eV) indicating that singlet fission would be more probable in the α−tetramer. Using the same RAS−2SF calculations, we determine the modified binding energy, E_b, for all the investigated chromophores. Unlike β and βC tetramers, there is negligible multiexcitonic interaction energy (~0 eV) for the α system, where the ^{1}[TT] state is degenerate with its corresponding quintet ^{5}[TT] state. This zero coupling between the two excitons leads to an easy separation of the entangled excitons to form the two independent triplets, since for weakly interacting triplet pairs, only a small activation energy is required to spatially separate the triplets. The E_b for β and βC are – 0.006 eV and – 0.009 eV, respectively. Thus, no additional energy is required for the two triplets to be separated in α, whereas in β and βC systems, this step requires more energy as shown in **Figure 5.9.3**. This lower binding energy for α indicates that the energy penalty to decouple the double triplet state into two separated triplets is negligible, making the second step of singlet fission possible for this molecule compared to β and βC. Overall, the

RAS−2SF calculations reveal that iSEF is kinetically feasible for α making this molecule a possible candidate for iSEF. The trend of E_{SF} and E_b obtained for our molecules is consistent with those previously obtained for PDI dimers.[93] The location of the ^{1}[TT] state above the S_1 state shows that the E_{SF} for our PDI tetramers is endoergic and leads to iSEF for the α. Therefore, it is possible that the negligible fluorescence quantum yield obtained for α is as a result of the nonradiative pathway due to the accessibility of the double triplet state in this molecule. The iSEF thermodynamic disparities observed in these molecules and the conflicting iSEF kinetic feasibility for the α compound calls for a detailed analysis of the time−resolved spectroscopic measurements to not only confirm the compound undergoing iSEF, but also explore the iSEF mechanism. This analysis would also be used to explain the absence of iSEF in β despite the molecule showing energy levels similar to those of α.

With our time−resolved measurements, we were able to confirm iSEF in only one of the flexible π−bridged compounds, α in chlorobenzene. For this flexible α−functionalized chromophore, we observe a triplet yield of 126% using our nanosecond sensitization experiments and a fast triplet formation of 160 ps with the femtosecond transient absorption (fsTA) technique. Our findings suggest that iSEF takes place in α upon photoexcitation for which its thermodynamic and kinetic viability is predicted by quantum chemical simulations. Interestingly, the long−lived independent triplets are experimentally observed following their separation, and each of them is localized on a single PDI of the tetramer, as shown in the results of the theoretical calculations. This is really interesting as long−lived triplet excitons are indeed required for efficient solar energy conversion. We use a previous iSEF model by Wasielewski and Guldi [29] to explain iSEF in α as a quantum coherent mechanism. For the α in chlorobenzene, and as shown in **Figure 5.10.1**, we propose that optical excitation populates the [S_1S_0] state, which then populates the ^{1}[TT] through electronic coupling to [S_1S_0]. Due to the closeness in energy, coherent electronic coupling among the CT state, the [S_1S_0] and ^{1}[TT] form a coherent quantum superposition state: $[S_1S_0]_{[TT]}$CT. This superposition state then loses coupling immediately (within 160 ps), forming the double triplet state (^{1}[TT]). The second step of iSEF follows where the spin coherence of ^{1}[TT] is lost, and the correlated double triplet state dephases to form two independent triplets and hence high fission yield in α. Recent improvements in the field of singlet fission show that despite energetic inconsistencies, this fission process can still proceed endoergically due to entropic contributions.[48] Therefore, even though α does not fulfil the thermodynamic requirements for singlet fission, we

propose that the strong electronic coherent coupling between the molecule's $[S_1S_0]$, the CT and the $^1[TT]$ states enable the singlet excitons to access the endothermic multiexcitonic state. In addition, the entropic gains mainly acquired through the excitonic interaction with its environment enables the singlet excitons to overcome the thermodynamic energy barrier and proceed through the production of the double triplet states, $^1[TT]$, and dephasing of these $^1[TT]$ to form independent triplet states (iSEF).

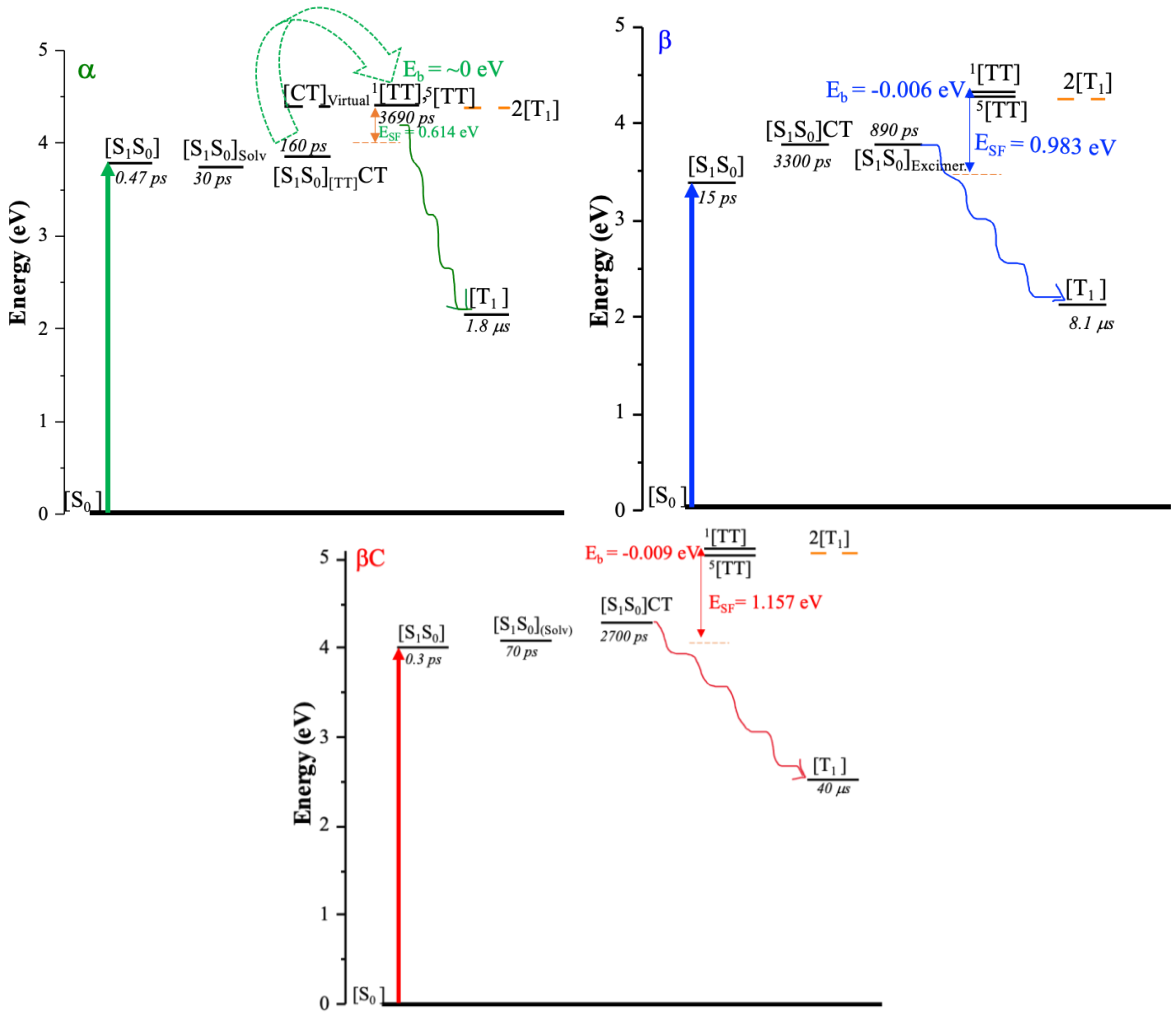

Figure 5.10.1: Proposed singlet deactivation and triplet formation pathways for the investigated PDI tetramers in chlorobenzene from our RAS–2SF.

In β, the expected iSEF (upon satisfying the thermodynamic condition) is hindered by strong excimer formation. For this β – functionalized flexible system, we observe a low triplet quantum yield and slow triplet formation. Additionally, our quantum chemical calculations show that the β natural transition orbitals (NTOs) are highly delocalized and the electron density spreads

out from the central BDT linker to the adjacent PDI units. This strong delocalization supports increased coupling between opposite PDI units of β compared to those of α.[98] This behavior is due to the formation of intermediate excimer states which act as traps, competing with internal conversion to the double triplet state.[89] Our experimental evidence for the excimer formation in β include: (i) broad, red−shifted emission (ii) concentration−dependent emission as previously observed [99], (iii) wavelength−dependent fluorescence decay lifetimes and (iv) co−facial π−π stacking of the PDI units in the optimized geometry. These excimer species are observed in α when the polarity of the environment is lowered (in toluene). For α in toluene, we observe a concentration dependent emission, a slower singlet decay and triplet formation (380 ps) and a triplet quantum yield of only 61%. These observations are due to the decreased viscosity of the solvent, which has been observed to increase the ratio of the excimer to the monomer.[100,101] Due to the minimal coupling observed between the opposite PDI units of α chromophore, its molecular structure is subject to perturbations due to the solvation effects, and this could explain the formation of excimer states in this molecule in toluene. In summary, the deactivation pathway of photoexcited singlets in β and α in toluene is not via iSEF (regardless of satisfying the iSEF thermodynamic condition) as there is strong competition with excimer formation, which trap singlet excitons preventing the formation of the ^{1}[TT] state.

In addition, the different dielectric constants of solvent can affect the electrosctatic interaction of molecule due to the effect on the molecular dipole moments, which has an ultimate effect on the energetics of the molecule, affecting charge transfer rate. Noncovalrnt intramolecular interactions that result from hydrogen bonds as well as dipole attractions affect the stability of conformers. Electrostatic solvation energy is usually large for polar conformations and has been grouped into three categories.[102] 1) Organic molecules whose substituent (X) has a dipole moment contribution parallel to the CX bond like F, Cl, CN, NO_2, lead to very stable anti-equatorial conformations with a very large total dipole moment. 2) OH- and OCH_3 substituted molecules where the oxygen lone pair contributes to the CX dipole moment that is in not parallel to that of CX and therefore, the total dipole moment depends on the angle of rotation of the molecule. 3) The CH_3 where the CX dipole is small and the total dipole moment does not change with conformation. For molecules that contain F, Cl, CN and OH, the content of the axially oriented molecules starts to increase as the polarity of the solvent increases owing to the improved solute−solvent electrostatic interactions which then lead to conformers with a large dipole moment

and increased stability. Therefore, the dielectric constant of the solvent affects the interactions in the solution that involes polar molecules and decreases the intermolecular energy when the dielectric constant is increased. In the case of α in toluene, the reduced dielectric constant of toluene leads to increased intermolecular energy which reduces the rate of charge transfer.

Although all the investigated molecules are charge transfer molecules, we observe the highest two−photon absorption (TPA) cross section in βC. This suggests the presence of a non−radiative singlet deactivation pathway and fluorescence quenching caused by intramolecular charge transfer (iCT).[103] The rigidity and enhanced planarity of βC leads to a stronger iCT character. We find that triplet production for the rigid βC tetramer proceeds via intersystem crossing because we observe triplet yields lower than 30% and slow triplet formation occurring in few nanoseconds (~2 ns).

The crucial properties affecting multiexciton generation clearly emerge in comparing the photobehavior of the flexible π−bridged systems − β and α. Although both α and β are highly twisted, the α−functionalized PDI units are completely isolated and do not show any interaction with each other nor with the BDT core while the β−substituted units arrange in a co-facial stacked structure. As a result, the absorption and emission spectra of the α resembles those of the parent PDI monomer; this lack of coupling permits efficient iSEF. On the contrary, the β−substitution of the core increases the coupling between the PDI chromophores leading them to have a co−facial π−π interaction and therefore allowing the formation of excimers. These intermediate excimer states trap the localized Frenkel excitons thus preventing singlet exciton fission into the correlated triplet pair.

5.11 Conclusions

In this study, crucial properties affecting multiexciton generation clearly emerge in comparing the photo−behavior of three analogous PDI tetramers showing flexible (α and β) and rigid (βC) π−bridge linker, as well as their parent PDI monomer. The steady state spectral and computational results of the α−tetramer suggest very minimal interaction among the individual PDI units. However, while the reported fluorescence quantum yield for the parent PDI monomer is close to unity, that of the α compound is negligible, indicating the presence of a nonradiative decay pathway for this compound. Our TD-DFT and RAS−2SF calculations predict that

intramolecular singlet exciton fission (iSEF) is thermodynamically impossible for all the investigated molecules. However, the triplet quantum yields obtained through triplet sensitization experiments are 124% and 17% for α and β compounds respectively. In addition, our femtosecond transient absorption shows an ultrafast triplet formation for α (160 ps). Therefore, we have solid experimental evidence of iSEF only in the α –tetramer in chlorobenzene. Our RAS−2SF calculations show that, among the studied tetramers, α has the lowest $[S_1S_0]$ – $^1[TT]$ energy gap indicating the highest rate of forming the $^1[TT]$ state. In addition, the energy penalty for this $^1[TT]$ to dissociate into independent triplets is ~ 0 eV for this molecule making it possible to complete the second step of iSEF. We suggest this $^1[TT]$ state is formed from a superposition of singlet states known as $[S_1S_0]_{[TT]}$CT which is made possible through the increased coherent coupling, while the entropic energy drive necessitates the dephasing of the $^1[TT]$ into independent triplet states. The absence of iSEF in the other twisted π–bridged compound, β, is due to the production of excimers following photoexcitation. These excimer states act as singlet exciton traps inhibiting the formation of the double triplet states. Similarly, for α in a less polar solvent, we observe the formation of excimers and a subsequent reduction of the triplet quantum yield (61%). For the rigid βC tetramer, the main singlet deactivation pathway is through intramolecular charge transfer (iCT) and a small triplet production was observed (24%) via intersystem crossing. The flexibility of the linker has previously been demonstrated as an important factor in triggering iSEF. In this present investigation, we show that the linker flexibility is necessary but not sufficient in activating iSEF in multichromophoric systems. As an important result of our study, we demonstrate that in addition to the conformational flexibility of the linker, the position of attachment of the core to the PDI units the surrounding medium play a role in driving iSEF or excimer formation in these dendritic molecules.

References

1. Smith, M. B.; Michl, J. Recent advances in singlet fission. *Annu. Rev. Phys. Chem.* **2013**, 64, 361–386.
2. Shockley, W.; Queisser, H.J. Detailed balance limit of efficiency of p-n junction solar cells. *J. Appl. Phys.* **1961,** 32, 510–519.
3. Hanna, M. C.; Nozik, A. J. Solar conversion efficiency of photovoltaic and photoelectrolysis cells with carrier multiplication absorbers. *J. Appl. Phys.* **2006**, 100, 074510.
4. Rao, A.; Friend, R. H. Harnessing Singlet Exciton Fission to Break the Shockley-Queisser Limit. *Nat. Rev. Mater.* **2017**, 2, 17063.
5. Smith, M. B.; Michl, J. Singlet fission. *Chem. Rev.* **2010**, 110, 6891–6936.
6. Greyson, E. C.; Stepp, B. R.; Chen, X.; Schwerin, A. F.; Paci, I.; Smith, M. B.; Akdag, A.; Johnson, J. C.; Nozik, A. J.; Michl, J.; et al. Singlet Exciton Fission for Solar Cell Applications: Energy Aspects of Interchromophore Coupling. *J. Phys. Chem.* **2010**, 114, 14223−14232.
7. Zimmerman, P. M.; Zhang, Z.; Musgrave, C. B. Singlet Fission in Pentacene through Multi-Exciton Quantum States. *Nat. Chem.* **2010**, 2, 648−652.
8. Zimmerman, P. M.; Bell, F.; Casanova, D.; Head-Gordon, M. Mechanism for Singlet Fission in Pentacene and Tetracene: From Single Exciton to Two Triplets. *J. Am. Chem. Soc.* **2011**, 133, 19944− 19952.
9. Chan, W. L.; Berkelbach, T. C.; Provorse, M. R.; Monahan, N. R.; Tritsch, J. R.; Hybertsen, M. S.; Reichman, D. R.; Gao, J.; Zhu, X. Y. The Quantum Coherent Mechanism for Singlet Fission: Experiment and Theory. *Acc. Chem. Res.* **2013**, 46, 1321−1329
10. Monahan, N.; Zhu, X. Y. Charge Transfer-Mediated Singlet Fission. *Annu. Rev. Phys. Chem.* **2015**, 66, 601−618.
11. Berkelbach, T. C.; Hybertsen, M. S.; Reichman, D. R. Microscopic Theory of Singlet Exciton Fission. I. General Formulation. *J. Chem. Phys.* **2013**, 138, 114102.
12. Berkelbach, T. C.; Hybertsen, M. S.; Reichman, D. R. Microscopic Theory of Singlet Exciton Fission. II. Application to Pentacene Dimers and the Role of Superexchange. *J. Chem. Phys.* **2013**, 138, 114103.
13. Fuemmeler, E. G.; Sanders, S. N.; Pun, A. B.; Kumarasamy, E.; Zeng, T.; Miyata, K.; Steigerwald, M. L.; Zhu, X. Y.; Sfeir, M. Y.; Campos, L. M.; et al. A Direct Mechanism of Ultrafast Intramolecular Singlet Fission in Pentacene Dimers. *ACS Cent. Sci.* **2016**, 2,316–324.

14. Low, J. Z.; Sanders, S. N.; Campos, L. M. Correlating Structure and Function in Organic Electronics: From Single Molecule Transport to Singlet Fission. *Chem. Mater.* ***2015***, 27, 5453−5463.

15. Varnavski, O.; Abeyasinghe, N.; Arago, J.; Serrano-Pe´ rez, J. J.; Ortí, E.; Lopez Navarrete, J. T.; Takimiya, K.; Casanova, D.; Casado,´ J.; et al. High Yield Ultrafast Intramolecular Singlet Exciton Fission in a Quinoidal Bithiophene. *J. Phys. Chem. Lett*. **2015**, 6, 1375−1384.

16. Miller, C. E.; Wasielewski, M. R.; Schatz, G. C. Modeling Singlet Fission in Rylene and Diketopyrrolopyrrole Derivatives: The Role of the Charge Transfer State in Superexchange and Excimer Formation. *J. Phys. Chem.* **2017,** *121,* 10345-10350.

17. Miyata, K.; Kurashige, Y.; Watanabe, K.; Sugimoto, T.; Takahashi, S.; Tanaka, S.; Takeya, J.; Yanai, T.; Matsumoto, Y. Coherent Singlet Fission Activated by Symmetry Breaking. *Nat. Chem.* **2017**, 9 , 983−989

18. Basel, B. S.; Zirzlmeier, J.; Hetzer, C.; Reddy, S. R.; Phelan, B. T.; Krzyaniak, M. D.; Volland, M. K.; Coto, P. B.; Young, R. M.; Clark, T.; et al. Evidence for Charge□Transfer Mediation in the Primary Events of Singlet Fission in a Weakly Coupled Pentacene Dimer. *Chem.* **2018**, 4, 1092−1111.

19. Korovina, N. V.; Das, S.; Nett, Z.; Feng, X.; Joy, J.; Haiges, R.; Krylov, A. I.; Bradforth, S. E.; Thompson, M. E. Singlet Fission in a Covalently Linked Cofacial Alkynyltetracene Dimer. *J. Am. Chem. Soc.* **2016**, 138, 617.

20. Mandal, A.; Chen, M.; Foszcz, E.; Schultz, J. D.; Kearns, N. M.; Young, R. M.; Zanni, M. T.; Wasielewski, M. R. Two Dimensional Electronic Spectroscopy Reveals Excitation Energy Dependent State Mixing during Singlet Fission in a Terrylenediimide Dimer. *J. Am. Chem. Soc.* **2018**, 140, 17907 −17914.

21. Basel, B. S.; Zirzlmeier, J.; Hetzer, C.; Phelan, B. T.; Krzyaniak, M. D.; Reddy, S. R.; Coto, P. B.; Horwitz, N. E.; Young, R. M.; White, F. J.; et al. Unified Model for Singlet Fission within a Non-conjugated Covalent Pentacene Dimer. *Nat. Commun.* **2016**, 8, 1-8

22. Hong, Y.; Kim, J.; Kim, W.; Kaufmann, C.; Kim, H.; Würthner, F.; Kim, D. Efficient Multiexciton State Generation in Charge□Transfer Coupled Perylene Bisimide Dimers via Structural Control. *J. Am. Chem. Soc.* **2020**, 142, 7845−7857

23. Stern, H. L.; Cheminal, A.; Yost, S. R.; Broch, K.; Bayliss, S. L.; Chen, K.; Tabachnyk, M.; Thorley, K.; Greenham, N.; Hodgkiss, J. M.; et al. Vibronically Coherent Ultrafast Triplet□Pair Formation and Subsequent Thermally Activated Dissociation Control Efficient Endothermic Singlet Fission. *Nat. Chem.* **2017**, 9, 1205.

24. Greyson, E. C.; Vura□Weis, J.; Michl, J.; Ratner, M. A. Maximizing Singlet Fission in Organic Dimers: Theoretical Investigation of Triplet Yield in the Regime of Localized Excitation and Fast Coherent Electron Transfer. *J. Phys. Chem.* **2010**, 114, 14168.

25. Krishnapriya, K. C.; Musser, A. J.; Patil, S. Molecular Design Strategies for Efficient Intramolecular Singlet Exciton Fission. *ACS Energy Lett.* **2019**, 4, 192.

26. Korovina, N. V.; Joy, J.; Feng, X.; Feltenberger, C.; Krylov, A. I.; Bradforth, S. E.; Thompson, M. E. Linker−Dependent Singlet Fission in Tetracene Dimers. J. *Am. Chem. Soc.* **2018**, 140, 10179.

27. Huang, H.; He, G.; Xu, K.; Wu, Q.; Wu, D.; Sfeir, M. Y.; Xia, J. Achieving Long-Lived Triplet States in Intramolecular SF Films through Molecular Engineering. *Chem.* **2019**, 5, 2405.

28. Sanders, S. N.; Kumarasamy, E.; Pun, A. B.; Appavoo, K.; Steigerwald, M. L.; Campos, L. M.; Sfeir, M. Y. Exciton Correlations in Intramolecular Singlet Fission. J. *Am. Chem. Soc.* **2016**, 138, 7289.

29. Papadopoulos, I.; Zirzlmeier, J.; Hetzer, C.; Bae, Y. J.; Krzyaniak, M. D.; Wasielewski, M. R.; Clark, T.; Tykwinski, R. R.; Guldi, D. M. Varying the Interpentacene Electronic Coupling to Tune Singlet Fission. *J. Am. Chem. Soc.* **2019**, 141, 6191.

30. Alvertis, A. M.; Lukman, S.; Hele, T. J. H.; Fuemmeler, E. G.; Feng, J.; Wu, J.; Greenham, N. C.; Chin, A. W.; Musser, A. J. Switching between Coherent and Incoherent Singlet Fission via Solvent□Induced Symmetry Breaking Dimer. *J. Am. Chem. Soc.* **2019**, 141, 17558.

31. Weiss, L. R.; Bayliss, S. L.; Kraffert, F.; Thorley, K. J.; Anthony, J. E.; Bittl, R.; Friend, R. H.; Rao, A.; Greenham, N. C.; Behrends, J. Strongly Exchange-Coupled Triplet Pairs in an Organic Semiconductor. *Nat. Phys.* **2017**, 13, 176.

32. Conrad-Burton, F. S.; Liu, T.; Geyer, F.; Costantini, R.; Schlaus, A. P.; Spencer, M. S.; Wang, J.; Sanchez, R. H.; Zhang, B.;́ Xu, Q.; et al. Controlling Singlet Fission by Molecular Contortion. *J. Am. Chem. Soc.* **2019**, 141, 13143.

33. Rickhaus, M.; Mayor, M.; Juríček, M. Strain-Inducedhelical Chirality in Polyaromatic Systems. *Chem. Soc. Rev.* **2016**, 45, 1542− 1556.

34. Maliakal, A.; Raghavachari, K.; Katz, H.; Chandross, E.; Siegrist, T. Photochemical Stability of Pentacene and a Substituted Pentacene in Solution and in Thin Films. *Chem. Mater.* **2004**, 16, 4980.

35. Hartnett, P. E.; Timalsina, A.; Matte, H. R.; Zhou, N.; Guo, X.; Zhao, W.; Facchetti, A.; Chang, R. P.; Hersam, M. C.; Wasielewski, M. R.; et al. Slip-Stacked Perylenediimides as an Alternative Strategy for High Efficiency Nonfullerene Acceptors in Organic Photovoltaics. *J. Am. Chem. Soc.* **2014**, *136*, 16345-16356.

36. Chen, W.; Zhang, Q. Recent Progress in Non-Fullerene Small Molecule Acceptors in Organic Solar Cells (Oscs). *J. Mater. Chem. C* **2017**, *5*, 1275-1302.

37. Würthner, F.; Saha-Möller, C. R.; Fimmel, B.; Ogi, S.; Leowanawat, P.; Schmidt, D. Perylene Bisimide Dye Assemblies as Archetype Functional Supramolecular Materials. *Chem. Rev.* **2016**, 116, 962−1052.

38. Margulies, E. A.; Miller, C. E.; Wu, Y.; Ma, L.; Schatz, G. C.; Young, R. M.; Wasielewski, M. R. Enabling Singlet Fission by Controlling Intramolecular Charge Transfer in Π-Stacked Covalent Terrylenediimide Dimers. *Nat. Chem.* **2016**, 8, 1120−1125.

39. Schierl, C.; Niazov-Elkan, A.; Shimon, L. J. W.; Feldman, Y.; Rybtchinski, B.; Guldi, D. M. Singlet Fission in Self-Assembled PDI Nanocrystals. *Nanoscale*. **2018**, 10, 20147.

40. Carlotti, B.; Madu, I. K.; Zimmerman, P.; Muthike, A. K.; Jiang, H.; Cai, Z.; Yu, L.; Kim, H.; Goodson, T. III Activating Intramolecular Singlet Exciton Fission by Altering π− Bridge Flexibility in Perylene diimide Trimers for Organic Solar Cells. *Chem. Sci*., **2020**, 11, 8757-8770.

41. Margulies, E. A.; Shoer, L. E.; Eaton S. W.; Wasielewski, M. R. Excimer Formation in Cofacial and Slip-Stacked Perylene-3,4:9,10- Bis(Dicarboximide) Dimers on a Redox-Inactive Triptycene Scaffold. *Phys. Chem. Chem. Phys.* **2014**, 16, 23735–23742.

42. Brown, K. E.; Salamant, W. A.; Shoer, L. E.; Young, R. M.; Wasielewski, M. R. Direct Observation of Ultrafast Excimer Formation in Covalent Perylenediimide Dimers Using Near-Infrared Transient Absorption Spectroscopy. *J. Phys. Chem. Lett.* **2014,** *5*, 2588-2593.

43. Lefler, K. M.; Brown, K. E.; Salamant, W. A.; Dyar, S. M.; Knowles, K. E.; Wasielewski, M.R. Triplet State Formation in Photoexcited Slip-Stacked Perylene-3,4:9,10-Bis(Dicarboximide) Dimers on a Xanthene Scaffold. *J. Phys. Chem.* **2013**, 117, 10333.

44. Lindquist, R. J.; Lefler, K. M.; Brown, K. E.; Dyar, S. M.; Margulies, E. A.; Young, R. M.; Wasielewski, M. R. Energy Flow Dynamics Within Cofacial and Slip-Stacked Perylene-3,4- Dicarboximide Dimer Models of P-Aggregates. *J. Am. Chem. Soc.* **2014,** 136, 14192–14923.

45. Feng, X.; Krylov, A. I. On Couplings And Excimers: Lessons from Studies of Singlet Fission in Covalently Linked Tetracene Dimers. *Phys. Chem. Chem. Phys.* **2016**, *18*, 7751-7761

46. Johnson, J. C.; Nozik, A. J.; Michl, J. The Role of Chromophore Coupling in Singlet Fission. *Acc. Chem. Res.* ***2013***, 46, 1290−1299.

47. Feng, X.; Luzanov, A. V.; Krylov, A. I. Fission of Entangled Spins: An Electronic Structure Perspective. *J. Phys. Chem. Lett*. **2013**, 4, 3845−3852.

48. Kolomeisky, A. B.; Feng, X.; Krylov, A. I. A Simple Kinetic Model for Singlet Fission: A Role of Electronic and Entropic Contributions to Macroscopic Rates. *J. Phys. Chem.* **2014**, 118, 5188−5195

49. Liu, H.; Nichols, V. M.; Shen, L.; Jahansouz, S.; Chen, Y.; Hanson, K. M.; Bardeen, C.J.; Li, X. Synthesis and Photophysical Properties of a ‘‘Face-To-Face’’ Stacked Tetracene Dimer. *Phys. Chem. Chem. Phys*. **2015**, 17, 6523–6531.

50. Katoh, R.; Sinha, S.; Murata, S.; Tachiya, M. Origin of the Stabilization Energy of Perylene Excimer as Studied by Fluorescence and Near-IR Transient Absorption Spectroscopy. *J. Photochem. Photobio. A* **2001**, *145*, 23- 34.

51. Mauck, C. M.; Hartnett, E. A.; Mergulies, E, A.; Ma, L.; Miller, C. E; Schatz, G. C.; Marks, T. J.; Wasielewski M. R. Singlet Fission via an Excimer-Like Intermediate in 3,6-Bis(Thiophen-2-Yl) Diketopyrrolopyrrole Derivatives. *J. Am. Chem. Soc.* **2016**, 138, 11749.

52. Young, R. M.; Wasielewski, M. R. Mixed Electronic States in Molecular Dimers: Connecting Singlet Fission, Excimer Formation, and Symmetry-Breaking Charge Transfer. *Acc. Chem. Res.* **2020**. 1120-1125.

53. Yamakado, T.; Takahashi, S.; Watanabe, K.; Matsumoto, Y.; Osuka, A.; Saito, S. Conformational Planarization Versus Singlet Fission: Distinct Excited State Dynamics of Cyclooctatetraene Fused Acene Dimers. *Angew. Chem. Int. Ed.* **2018**, *57*, 5438−5443.

54. Chen, M.; Bae, Y. J.; Mauck, C. M.; Mandal, A.; Young, R. M.; Wasielewski M. R. Singlet Fission in Covalent Terrylenediimide Dimers: Probing the Nature of the Multiexciton State Using a Femtosecond Mid-Infrared Spectroscopy. *J. Am. Chem. Soc.* **2018**, 140, 9184.

55. Lukman, S.; Musser, A. J.; Chen, K.; Athanasopoulos, S.; Yong, C. K.; Zeng, Z.; Ye, Q.; Chi, C.; Hodgkiss, J. M.; Wu, J.; et al. Tuneable Singlet Exciton Fission and Triplet-Triplet Annihilation in an Orthogonal Pentacene Dimer. *Adv. Funct. Mater.* **2015**, 25, 5452−5461

56. Tayebjee, M. J. Y.; Sanders, S. N.; Kumarasamy, E.; Campos, L. M.; Sfeir, M. Y.; McCamey, D. R. Quintet Multiexciton Dynamics in Singlet Fission. *Nat. Phys.* **2017**, 13, 182.

57. Wu, Q.; Zhao, D.; Schneider, A. M.; Chen, W.; Yu, L. Covalently Bound Clusters of Alpha-Substituted PDI-Rival Electron Acceptors to Fullerene for Organic Solar Cells. *J. Am. Chem. Soc.* **2016**, *138*, 7248−7251.

58. Wu, Q.; Zhao, D.; Yang, J.; Sharapov, V.; Cai, Z.; Li, L.; Zhang, Na; Neshchadin, A.; Chen, W.; Yu, L. Propeller Shaped Acceptors for High Performance Non Fullerene Solar Cells: Importance of the Rigidity of Molecular Geometry. *Chem. Mater.* **2017**, *29*, 1127−1133.

59. McLean, A. M.; Socher, E.; Varnavski, O.; Clark, T. B.; Imperiali, B.; Goodson, T. III Two-Photon Fluorescence Spectroscopy and Imaging of 4-Dimethylaminonaphthalimide Peptide and Protein Conjugates. *J. Phys. Chem. B* **2013**, 117, 15935−15942.

60. Beaumont, P. C.; Johnson, D. G.; Parsons, B. J. Photophysical Properties of Laser Dyes: Picosecond Laser Flash Photolysis Studies of Rhodamine 6G, Rhodamine B and Rhodamine 101. *J. Chem. Soc.* ***Faraday*** *Trans.* **1993**, 89, 4185-4191.

61. Keller, B.; Cai, Z.; Muthike, A.K.; Sahu, P.K.; Kim, H.; Eshun, A.; Zimmerman, P.M.; Zhang, D. and Goodson T. III Investigating the Optical Properties of Thiophene Additions to s-Indacene Donors with Diketopyrrolopyrrole, Isoindigo, and Thienothiophene Acceptors. *J. Phys. Chem.* **2018**, 122, 27713-27733.

62. Vazquez, R. J.; Kim, H.; Zimmerman, P.M.; Goodson T. III Using Ultrafast Spectroscopy to Probe the Excited State Dynamics of a Reported Highly Efficient thermally Activated Delated Fluorescence Chromophore. *J. Mater. Chem. C* **2019**, 7, 4210-4221.

63. Vázquez, R.; Yun, J. H.; Muthike, A. K.; Howell, M.; Kim, H.; Madu, I. K.; Kim, T.; Zimmerman, P.; Lee, J. Y.; Goodson T. III New Direct Approach for Determining the Reverse Intersystem Crossing Rate in Organic Thermally Activated Delayed Fluorescent (TADF) Emitters. *J. Am. Chem. Soc.* **2020**, 142, 8074−8079.

64. Murov, S. L.; Carmichael, I.; Hug, G.L. *Handbook of Photochemistry*, 2nd Edition, Marcel Dekker, Inc., New York, **1993**.

65. Chai, J. D.; Head−Gordon, M. Long−Range Corrected Hybrid Density Functionals with Damped Atom−Atom Dispersion Corrections. *Phys. Chem. Chem. Phys.* **2008**, *10*, 6615−6620.

66. Chai, J. D.; Head−Gordon, M. Systematic Optimization of Long Range Corrected Hybrid Density Functionals. *J. Chem. Phys.* **2008**, *128*, 084106.

67. Mewes, J. M.; Herbert, J. M.; Dreuw, A. On the Accuracy of the General, State-Specific Polarizable-Continuum Model for the Description of Correlated Ground-And Excited States in Solution. *Phys. Chem. Chem. Phys.* **2017**,19, 1644-1654

68. Chien, A. D.; Molina, A. R.; Abeyasinghe, N.; Varnavski, O. P.; Goodson T. III.; Zimmerman, P. M. Structure and Dynamics of the 1 (TT) State in a Quinoidal Bithiophene: Characterizing a Promising Intramolecular Singlet Fission Candidate. *J. Phys. Chem. C* **2015**, 119, 28258-28268.

69. Rudenko, A. E.; Clayman, N. E.; Walker, K. L.; Maclaren, J. K.; Zimmerman, P. M.; Waymouth, R. M. Ligand-Induced Reductive Elimination of Ethane from Azopyridine Palladium Dimethyl Complexes. *J. Am. Chem. Soc.* **2018**, 140, 11408-11415.

70. Kim, H.; Keller, B.; Ho-Wu, R.; Abeyasinghe, N.; Vázquez, R.J.; Goodson T. III; Zimmerman, P. M. Enacting Two-Electron Transfer from a Double-Triplet State of Intramolecular Singlet Fission. *J. Am. Chem. Soc.* **2018**, 140, 25, 7760–7763

71. Kim, H.; Zimmerman, P. M. Coupled Double Triplet State in Singlet Fission. *Phys. Chem. Chem. Phys.* **2018**, 20, 30083-30094.

72. Jiang, H.; Zimmerman, P. M. Charge Transfer Via Spin Flip Configuration Interaction: Benchmarks and Application to Singlet Fission. *J. Chem. Phys.* **2020**, 153, 164109.

73. Shao, Y.; Gan, Z.; Epifanovsky, E.; Gilbert, A. T. B.; Wormit, M.; Kussmann, J.; Lange, A. W.; Behn, A.; Deng, J.; Feng, X.; et al. Advances in Molecular Quantum Chemistry Contained in the Q-Chem 4 Program Package. *Mol. Phys.* **2015**, *113*, 184-215.

74. Schaftenaar, G.; Noordik, J. H. Molden: A Pre- fnd Post-Processing Program for Molecular fnd Electronic Structures. *J. Comput.-Aided Mol. Des.* **2000**, 14, 123.

75. Humphrey, W.; Dalke, A.; Schulten, K. VMD: Visual Molecular Dynamics. *J. Mol. Graphics.* **1996,** *14*, 33-38.

76. Le, A. K.; Bender, J. A.; Arias, D. H.; Cotton, D. E.; Johnson, J. C.; Roberts, S. T. Singlet Fission Involves an Interplay between Energetic Driving Force and Electronic Coupling in Perylenediimide Films. *J. Am. Chem. Soc.* **2018**, 140, 814–826.

77. Carlotti, B.; Cai, Z.; Kim, H.; Shaparov, V.; Madu, I. K.; Zhao, D.; Chen, W.; Zimmerman, P. M.; Yu, L.; Goodson III, T. Charge Transfer and Aggregation Effects in the Performance of Planar vs. Twisted Perylene Diimide Isomers as Electron Acceptors in Organic Solar Cells. *Chem. Mater*. **2018**, 30, 4263−4276.

78. Longhi, E.; Bossi, A.; Di Carlo, G.; Maiorana, S.; De Angelis, F.; Salvatori, P.; Petrozza, A.; Binda, M.; Roiati, V.; Mussini, P. R.; et al. Metal-free benzodithiophene-containing organic dyes for dye-sensitized solar cells. *Eur. J. Org. Chem.* **2013**, 84−94

79. Cai, Z.; Vázquez, R. J.; Zhao, D.; Li, L.; Lo, W. Y.; Zhang, N.; Wu, Q.; Keller, B.; Eshun, A.; Abeyasinghe, N.; et al. Two photon absorption study of low-bandgap, fully conjugated perylene diimide-thienoacene-perylene diimide ladder-type molecules. *Chem. Mater.* **2017**, 29, 6726-6732.

80. Yong, C. K.; Musser, A. J.; Bayliss, S. L.; Lukman, S.; Tamura, H.; Bubnova, O.; Hallani, R.K.; Meneau, A.; Resel, R.; Maruyama, M.; et al. The Entangled Triplet Pair State in Acene and Heteroacene Materials. *Nat. Commun.* **2017**, 8, 1-12

81. Roberts, S. T.; McAnally, R. E.; Mastron, J. N.; Webber, D. H.; Whited, M. T.; Brutchey, R. L.; Thompson, M. E.; Bradforth, S. E. Efficient Singlet Fission Discovered in a Disordered Acene Film. *J. Am. Chem. Soc.* **2012**, 134, 6388–6400.

82. Spenst, P.; Young, R. M.; Wasielewski, M. R.; Wurthner, F. Guest and Solvent Modulated Photo-Driven Charge Separation and Triplet Generation in a Perylene Bismide Cyclophane. *Chem. Sci.* **2016**, 7, 5428−5434.

83. Brown, K. E.; Veldkamp, B. S.; Co, D. T.; Wasielewski, M. R. Vibrational Dynamics of a Perylene−Perylenediimide Donor− Acceptor Dyad Probed with Femtosecond Stimulated Raman Spectroscopy. *J. Phys. Chem. Lett.* **2012**, 3, 2362−2365.

84. Fron, E.; Pilot, R.; Schweitzer, G.; Qu, J.; Herrmann, A.; Mullen, K.; Hofkens, J.; Van der Auweraer, M.; De Schryver, F. C. Photoinduced Electron Transfer in Perylenediimide Triphenylamine− Based Dendrimers: Single Photon Timing and Femtosecond Transient Absorption Spectroscopy. *Photochem. Photobiol. Sci.* **2008**, 7, 597−604.

85. Giaimo, J. M.; Gusev, A. V.; Wasielewski, M. R. Excited State Symmetry Breaking in Cofacial and Linear Dimers of a Green Perylenediimide Chlorophyll Analogue Leading to Ultrafast Charge Separation. *J. Am. Chem. Soc.* **2002**, 124, 8530−8531.

86. Van der Boom, T.; Hayes, R. T.; Zhao, Y.; Bushard, P. J.; Weiss, E. A.; Wasielewski, M. R. Charge Transport in Photofunctional Nanoparticles Self−Assembled from Zinc 5,10,15,20−Tetrakis− (perylenediimide)porphyrin Building Blocks. *J. Am. Chem. Soc.* **2002**, 124, 9582−9590.

87. Lukas, A. S.; Zhao, Y.; Miller, S. E.; Wasielewski, M. R. Biomimetic Electron Transfer Using Low Energy Excited States: A Green Perylene Based Analogues of Chlorophyll a. *J. Phys. Chem. B* **2002**, 106, 1299−1306.

88. Sung, J.; Nowak Krol, A.; Schlosser, F.; Fimmel, B.; Kim, W.; Kim, D.; Wurthner, F. Direct Observation of Excimer Mediated Intramolecular Electron Transfer in a Cofacially Stacked Perylene Bisimide Pair. *J. Am. Chem. Soc*. **2016**, 138, 9029−9032.

89. Guo, Y.; Ma, Z.; Niu, X.; Zhang, W.; Tao, M.; Guo, Q.; Wang, Z.; Xia, A. Bridge-Mediated Charge Separation in Isomeric N-Annulated Perylene Diimide Dimers. *J. Am. Chem. Soc.* **2019**, 141, 12789−12796.

90. Montero, R.; Martínez-Martínez, V.; Longarte, A.; Epelde-Elezcano, N.; Palao, E.; Lamas, I.; Manzano, H.; Agarrabeitia, A.R.; López Arbeloa, I.; Ortiz, M.J.; et al. Singlet fission mediated photophysics of bodipy dimers. *J. Phys. Chem. Let.* **2018**, 9, 641-646.

91. Ford, W.E.; Kamat, P.V. Photochemistry of 3, 4, 9, 10-perylenetetracarboxylic dianhydride dyes. 3. Singlet and triplet excited-state properties of the bis (2, 5-di-tert-butylphenyl) imide derivative. *J. Phy. Chem.* **1987**, *91*, 6373-6380

92. Shen, L.; Chen, Y.; Li, X.; Gao, J. Effects of Substituents on Tetracene Derivatives on their Stabilities and Singlet Fission. *J. Mol. Grap. Model.* **2014**, *51*, 86-96

93. Farag, M. H.; Krylov, A. I. Singlet Fission in Perylenediimide Dimers. *J. Phys. Chem. C* 2**018**, *122*, 25753-25763.

94. Abd-Ellah, M.; Cann, J.; Dayneko, S. V.; Laventure, A.; Cieplechowicz, E.; Welch, G. C. Interfacial ZnO Modification Using a Carboxylic Acid Functionalized N-Annulated Perylene Diimide for Inverted Type Organic Photovoltaics. *ACS Appl. Electron. Mater.* **2019**, 1, 1590−1596.

95. Groff, R. P.; Avakian, P.; Merrifield, R. E. Coexistance of exciton fission and fusion in tetracene crystals. *Phys. Rev. B* **1970**, 1, 815.

96. Eaton, S. W.; Shoer, L. E.; Karlen, S. D.; Dyar, S. M.; Margulies, E. A.; Veldkamp, B. S.; Ramanan, C.; Hartzler, D. A.; Savikhin, S.; Marks, T. J.; et al. Singlet Exciton Fission in Polycrystalline Thin Films of a Slip-Stacked Perylenediimide. *J. Am. Chem. Soc.* **2013**, 135, 14701−14712.

97. Feng, X.; Kolomeisky, A. B.; Krylov, A. I. Dissecting the Effect of Morphology on the Rates of Singlet Fission: Insights from Theory. *J. Phys. Chem. C* **2014**, 118, 19608−19617.

98. Zhao, D.; Wu, Q.; Cai, Z.; Zheng, T.; Chen, W.; Lu, J.; Yu, L. Electron Acceptors Based on α-Substituted Perylene Diimide (PDI) for Organic Solar Cells. *Chem. Mater.* **2016**, 28, 1139−1146.

99. Walker, B. J.; Musser, A. J.; Beljonne, D.; Friend, R. H. Singlet exciton fission in solution. *Nat. Chem.* 2013, 5, 1019–1024.

100. Nishihara, T.; Kaneko, M. The Dependence of Excimer Formation of Polystyrene Solutions on Solvent and Concentration. *Macromol. Chem. Phys.* **1969**, 124, 84–90.

101. Snare, M. J.; Thistlethwaite, P. J.; Ghiggino, K. P. Kinetic Studies of Intramolecular Excimer Formation in Dipyrenylalkanes. *J. Am. Chem. Soc.* **1983**, 105, 3328−3332.

102. Wałesa, R.; Broda, M.A. The influence of solvent on conformational properties of peptides with Aib residue—a DFT study. *J. Mol. Model*. 2017, 23, 349.

103. Diaz, C.; Vesga, Y.; Echevarria, L.; Stará, I.G.; Starỳ, I.; Anger, E.; Shen, C.; Moussa, M.E.S.; Vanthuyne, N.; Crassous, J.; et al. Two-Photon Absorption and Two-Photon Circular Dichroism of Hexahelicene Derivatives: A Study of the Effect of the Nature of Intramolecular Charge Transfer. *Rsc. Adv.* **2015**, *5*, 17429-17437.

5.12 Supporting Information

5.12.1 Steady State Absorption

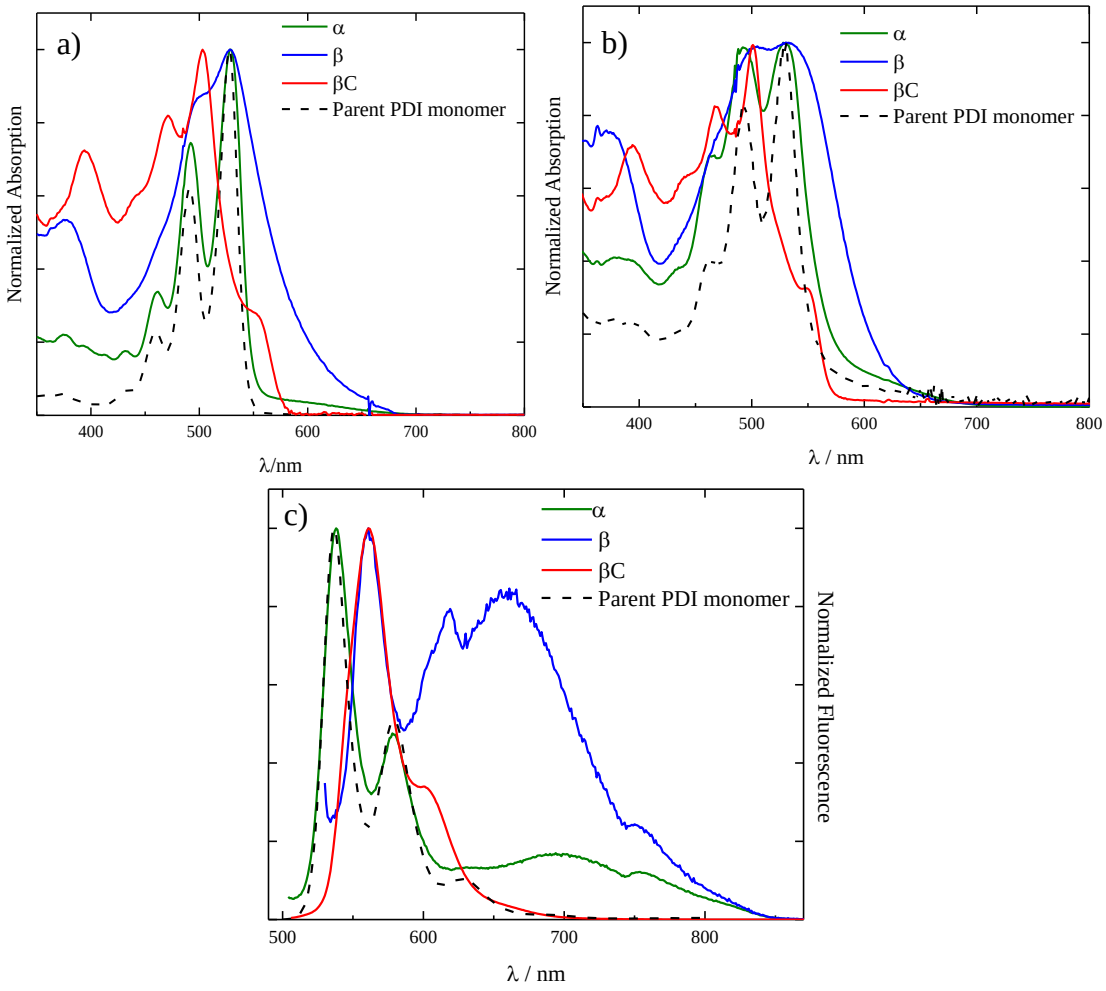

Figure 5.12.1.1. Normalized absorption of the tetramers in chlorobenzene (a) and toluene (b) and normalized emission spectra of the tetramers in toluene (c). Spectra of the parent PDI monomer are also included.

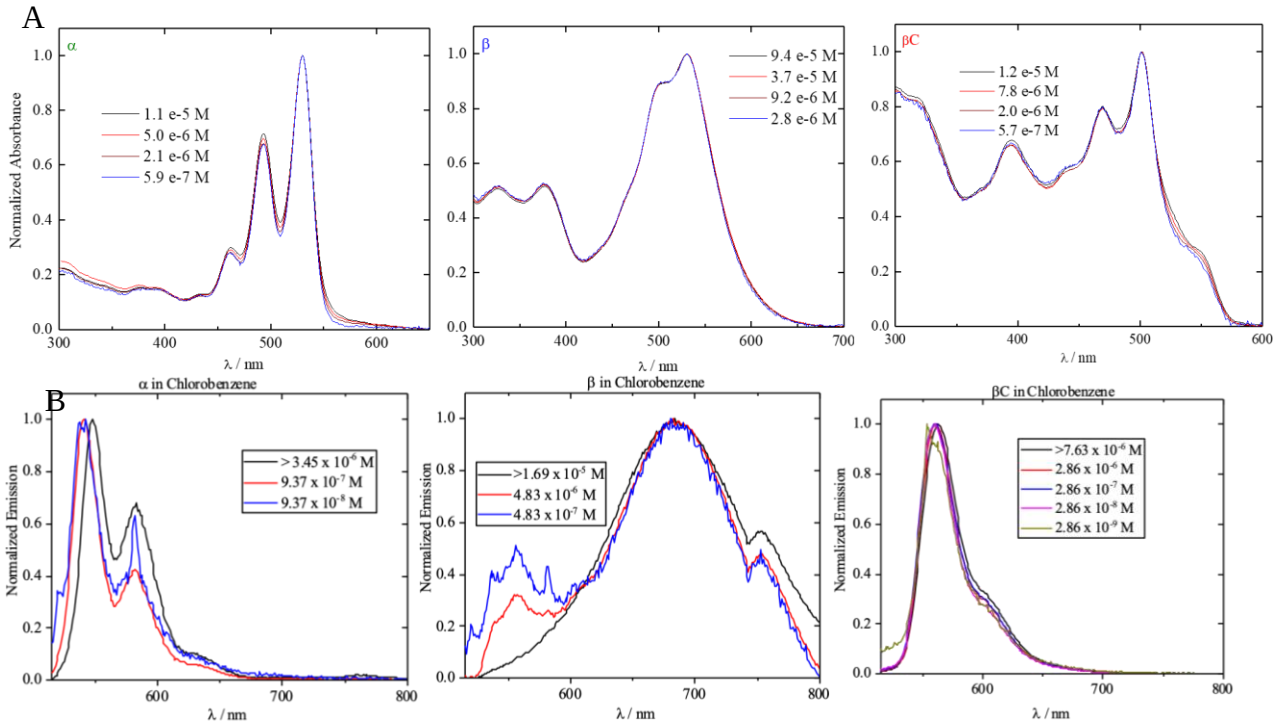

Figure 5.12.1.2. Concentration effect on the absorption (A) and emission (B) spectra of all the investigated tetramers in chlorobenzene

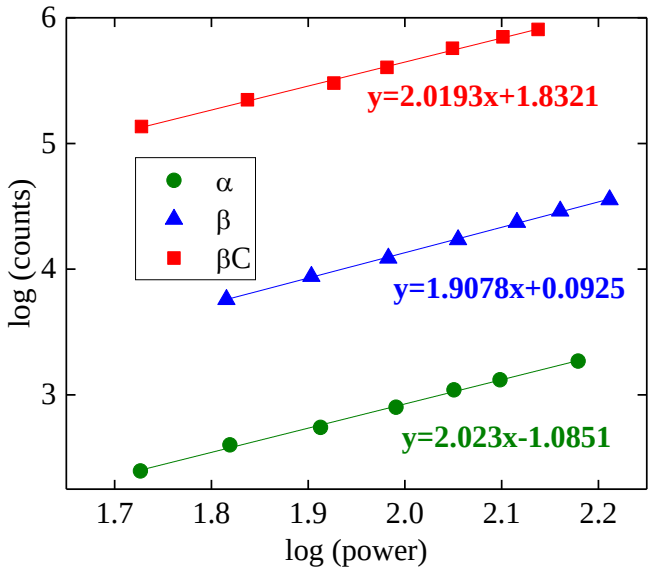

Figure 5.12.1.3. Power dependence of the two–photon excited emission for the investigated tetramers in chlorobenzene upon 820 nm excitation.

5.12.2 Time-Resolved Fluorescence Measurements

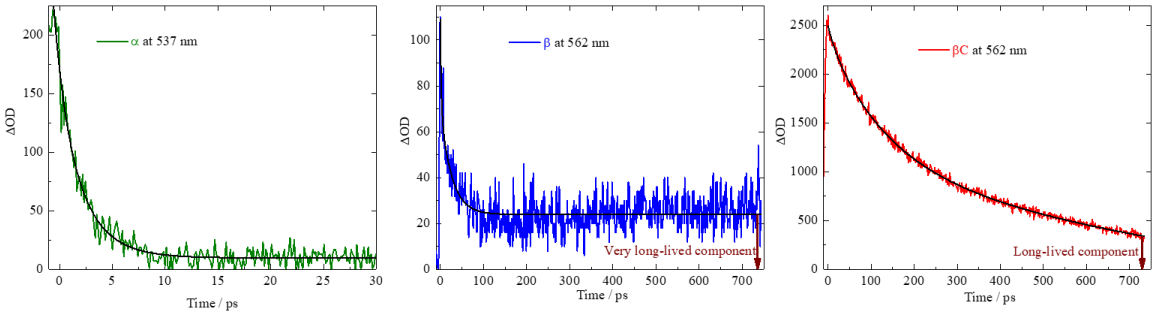

Figure 5.12.2.1. Fluorescence decay kinetics recorded for the tetramers in chlorobenzene by femtosecond resolved FUC, together with their polyexponential fittings.

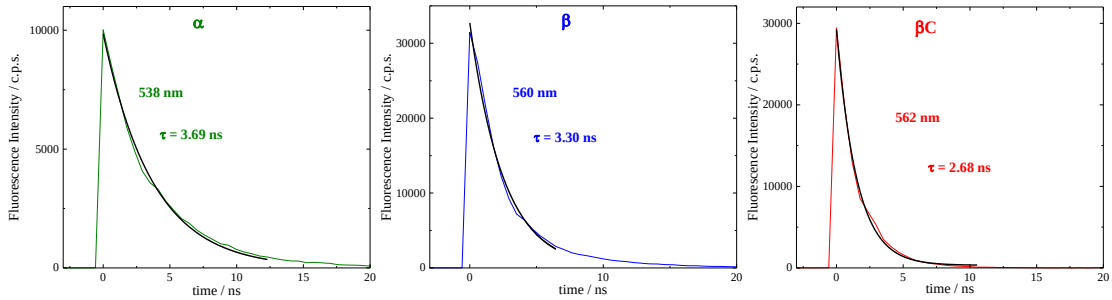

Figure 5.12.2.2. Fluorescence kinetics obtained by nanosecond TCSPC in chlorobenzene for the investigated tetramers.

5.12.3 Femtosecond Transient Absorption

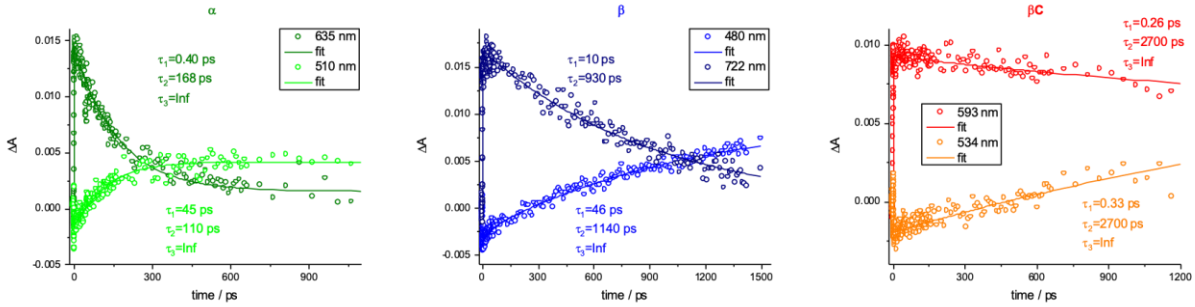

Figure 5.12.3.1. Femtosecond transient absorption decay and rise dynamics of the investigated PDI tetramers as well as their polyexponential fittings.

Table 5.12.3.1. Lifetimes (τ) obtained by global fitting of the femtosecond Transient Absorption data.

Compound	τ_1 / ps	τ_3 / ps	τ_4 / ps	τ_5 / ps
α	0.47	30	160	Infinite
β		15	890	Infinite
βC	0.30	70	2700	Infinite

5.12.4 Triplet Yield Calculation from femtosecond transient absorption (fsTA)

Triplet yield was evaluated from the temporal dynamics of the lowest excited singlet and triplet state populations, as obtained through analysis of the femtosecond transient absorption data, according to a procedure already described in the literature, and here detailed for the tetramer samples. [1,2]

A. α–tetramer in chlorobenzene

Global Fitting of the femtosecond transient absorption data was carried out through the Glotaran software which provided us with the Species Associated Spectra (SAS) of the four exponential components (assignments and lifetimes described in **Table 5.12.3.1**) and their temporal composition (**Figure 5.12.4.1**).

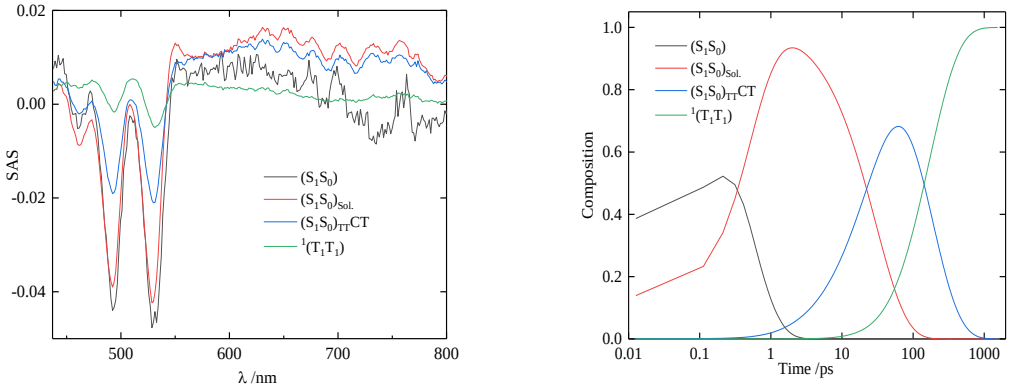

Figure 5.12.4.1. Species Associated Spectra (left) and abundance in time (right) of the four exponential components resulting from global fitting of the femtosecond transient absorption data of α–tetramer in chlorobenzene.

To obtain the spectral shapes of the excited singlet and triplet states the transient spectra at time delays of 160.80 and 1366 ps were selected, respectively (**Figure 5.12.4.2**). In fact, at these time delays abundances of the singlet and triplet transients were maximum in the femtosecond transient absorption data (**Figure 5.12.4.1**).

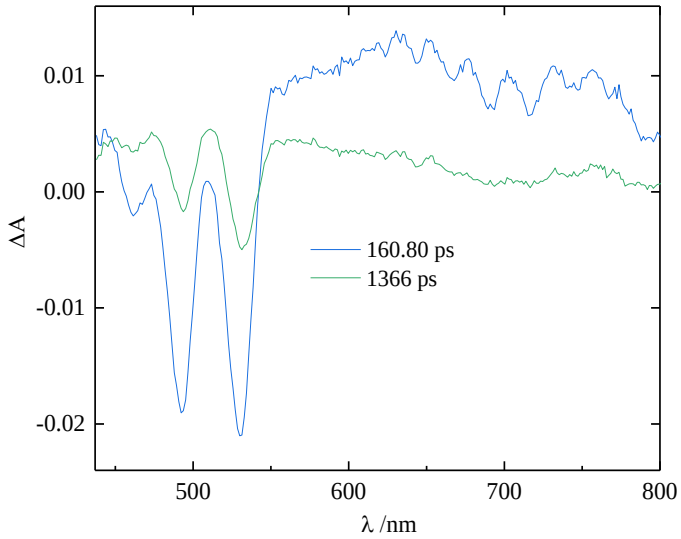

Figure 5.12.4.2. Transient absorption spectra at 160.80 and 1366 ps delay from excitation recorded for α–tetramer in chlorobenzene.

The spectra of the lowest singlet and triplet excited states must be related though the ground state bleach (GSB) they share in common. The ground state absorption spectrum was scaled and subtracted from the 160.80/1366 ps transient spectra in order to remove the GSB contribution. The amount of GSB to be subtracted was determined by normalizing the steady state absorption to the transient spectra. The resulting spectra only show the S_1/T_1 excited state absorption (ESA) relative to a known amount of GSB (**Figure 5.12.4.3**).

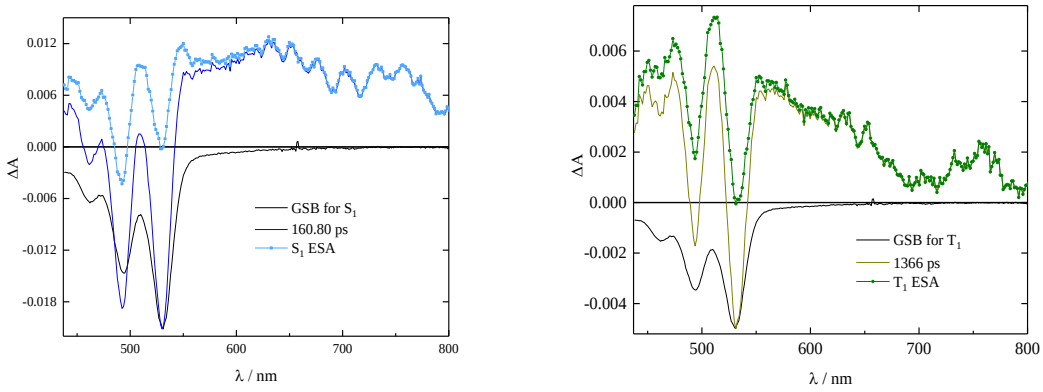

Figure 5.12.4.3. Transient (blue/green) and steady state (black) absorption spectra used to reconstruct the absorption spectra of the excited singlet (purple, straight) and triplet (purple, dashed) states.

The S_1 and T_1 spectra are then normalized to the GSB they share, resulting in two spectra that are quantitatively related (**Figure 5.12.4.4**).

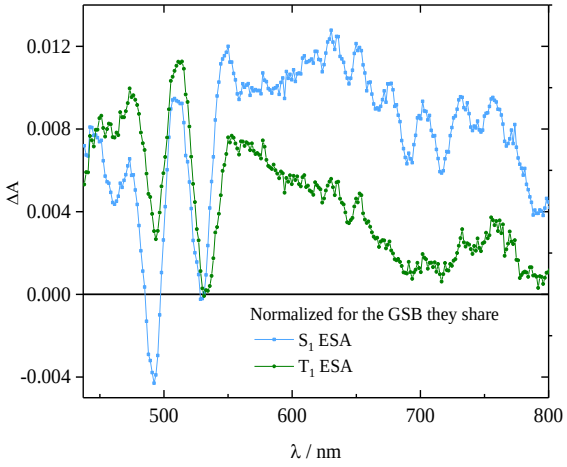

Figure 5.12.4.4. Excited state absorption spectra, normalized to GSB, used to correct composition profile in **Figure 5.12.4.2** and to obtain population dynamics in **Figure 5.12.4.5**.

The quantitatively related spectra of S_1 and T_1 were used to correct the composition profiles previously shown. The temporal composition of the components resulting from the global fitting reported in **Figure 5.12.4.1** is indeed related to the differential absorbance measured during the ultrafast absorption experiments. Therefore, according to the Lambert−Beer law, it is dependent on both the absorption ability and the concentration of S_1 and T_1. From the quantitatively related S_1 and T_1 spectra reported in **Figure 5.12.4.4**, it is clear that the ratio between the triplet excited state absorption at its peak (0.01125 at 511 nm) and the singlet excited state absorption at its peak (0.01278 at 630 nm) is $\frac{\varepsilon_S}{\varepsilon_T} = 1.136$. By scaling the S_1 and T_1 temporal compositions in **Figure 5.12.4.1** (multiplying the singlet profile by: $\frac{0.99974}{0.68205} = 1.465$) for this factor, the correct concentration profiles were obtained: $\frac{c_T}{c_S} = \frac{\Delta A_T}{\Delta A_S} \times \frac{\varepsilon_S}{\varepsilon_T}$. Population dynamics normalized at the singlet peak (**Figure 5.12.4.5**) demonstrates the formation of 1.66 triplets per initially excited singlet. A triplet quantum yield of **166%** was estimated for α compound.

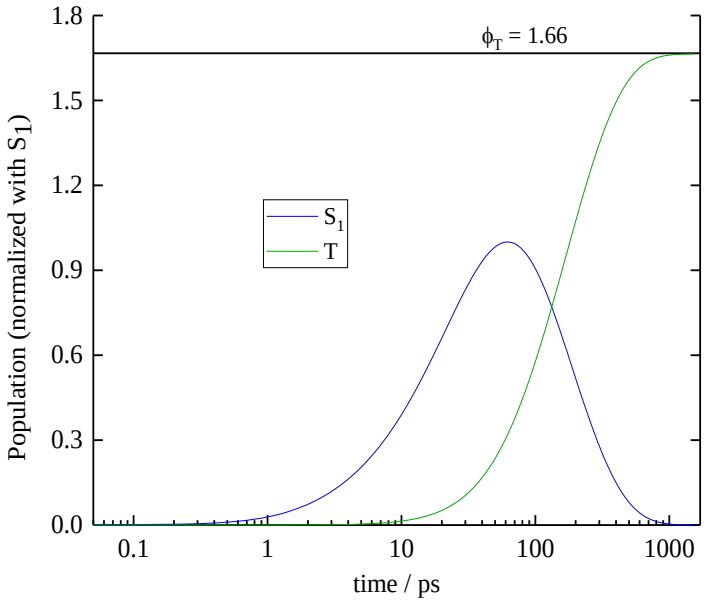

Figure 5.12.4.5. Population dynamics of the excited singlet and triplet states for **α** in chlorobenzene.

B. *α*−tetramer in toluene

The same method described in the case of α−tetramer in chlorobenzene used to determine the triplet quantum yields of the α−tetramer in toluene. Our Global fitting showed the presence of four components and their Species Associated Spectra (SAS) are presented in **Figure 5.12.4.6**.

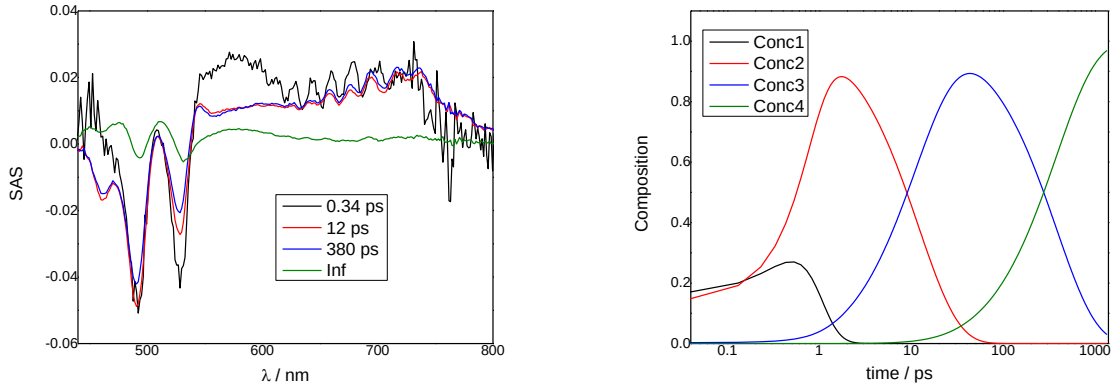

Figure 5.12.4.6. Species Associated Spectra (left) and abundance in time (right) of the four exponential components resulting from global fitting of the femtosecond transient absorption data of α−tetramer in toluene.

Time delays of 43.5 and 1347.5 ps were used to obtain the spectral shapes of excited singlet and triplet states, respectively (**Figure 5.12.4.7**).

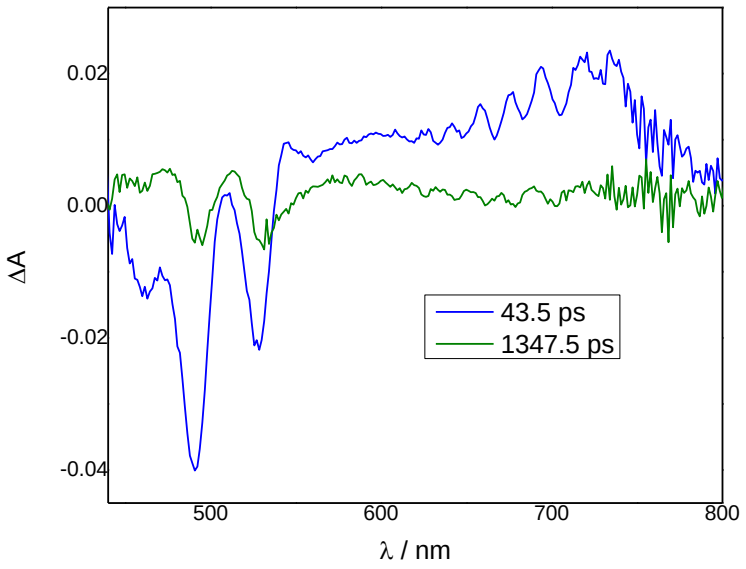

Figure 5.12.4.7. Transient absorption spectra at 43.5 and 1347.5 ps delay from excitation recorded for **α** in toluene.

Then, the ground state bleach (GSB) contribution was accounted for by scaling and subtracting the ground state absorption from the 43.5/1347.5 ps transient (**Figure 14**)

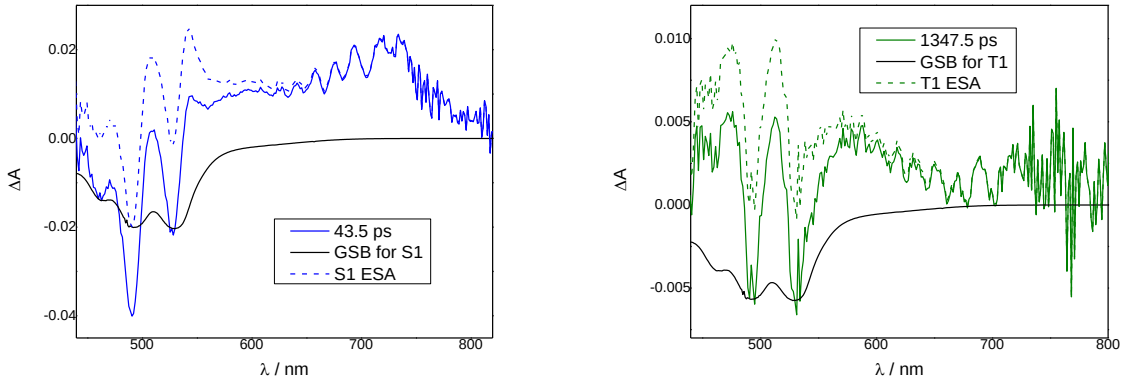

Figure 5.12.4.8. Transient (blue/green) and steady state (black) absorption spectra used to reconstruct the absorption spectra of the excited singlet (purple, straight) and triplet (purple, dashed) states for **α** in toluene.

The resulting spectra which only show S_1/T_1 excited state absorption (ESA) signals peaked at very different wavelengths, are quantitatively related (**Figure 5.12.4.9**).

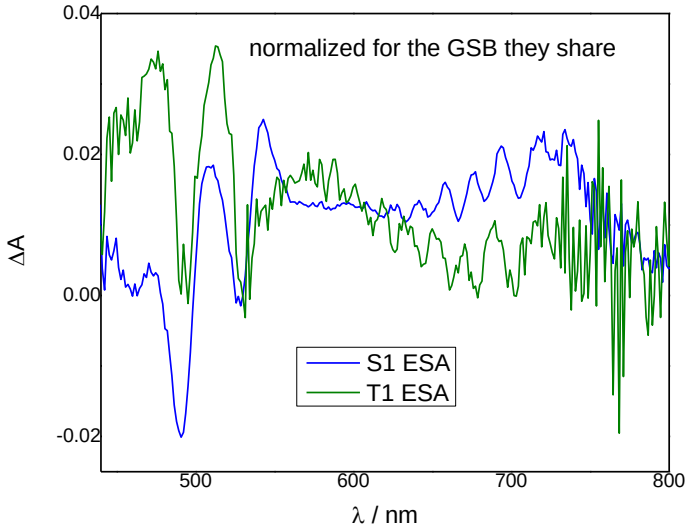

Figure 5.12.4.9. Excited state absorption spectra used to correct composition profile in **Figure 5.12.4.7** and to obtain population dynamics in **Figure 5.12.4.10** for **α** in toluene.

Using these spectra, we corrected the composition profiles in **Figure 5.12.4.6** in determining differential absorbances typical of singlet and triplet states. The obtained ratio between the singlet excited state absorption at its peak (0.0183 at 717 nm) and the triplet excited state absorption at its peak (0.0354 at 512 nm) is 1.934. We then multiplied the singlet profile by 1.934 and the population was normalized at the singlet peak to obtain a triplet quantum yield of **56% (Figure 16)** for the $\alpha-$tetramer in toluene

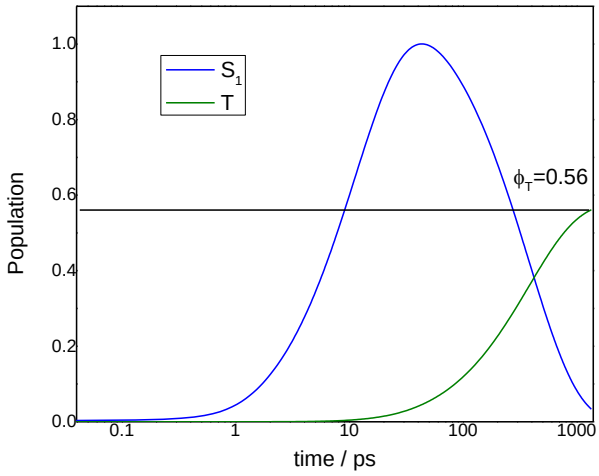

Figure 5.12.4.10. Population dynamics of the excited singlet and triplet states for α−tetramer in chlorobenzene.

C. βC−tetramer

Global Fitting revealed the presence of five exponential components whose Species Associated Spectra (SAS) and composition in time are shown below in **Figure 5.12.4.11**.

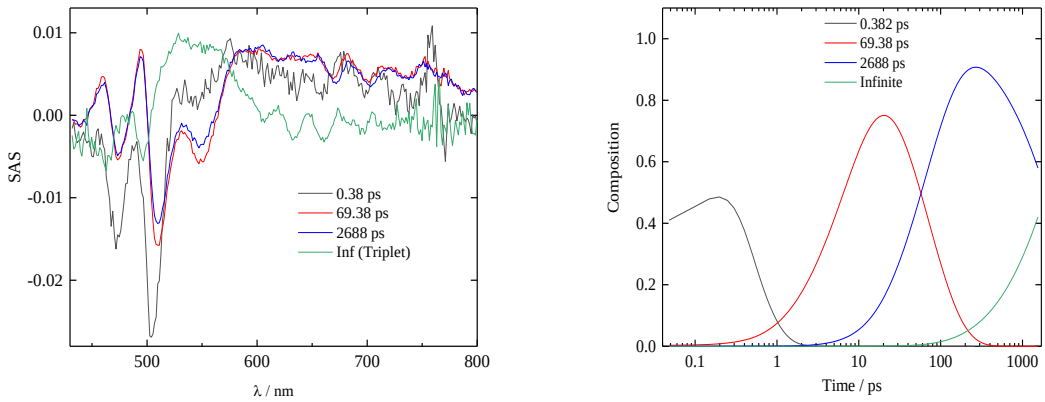

Figure 5.12.4.11. Species Associated Spectra (left) and abundance in time (right) of the five exponential components resulting from global fitting of the femtosecond transient absorption data of βC in chlorobenzene.

Looking at the singlet and triplet composition profiles, transient spectra at time delays of 276.3 and 1466 ps (max. fsTA time window) were selected to obtain spectral shapes associated to the excited singlet and triplet state, respectively (**Figure 5.12.4.12**).

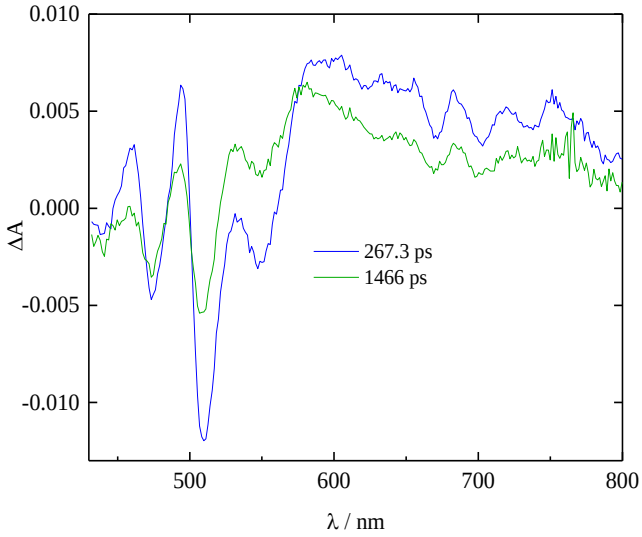

Figure 5.12.4.12. Transient absorption spectra at 276.3 and 1466 ps delay from excitation recorded for βC in chlorobenzene.

The ground state absorption spectrum was scaled and subtracted from the 276.3/1466 ps transient spectra in order to remove the ground state bleach (GSB) contribution (**Figure 5.12.4.13**). In this case the same amount of GSB was subtracted from both spectra because no clear negative band is exhibited by the transient spectrum at long delays.

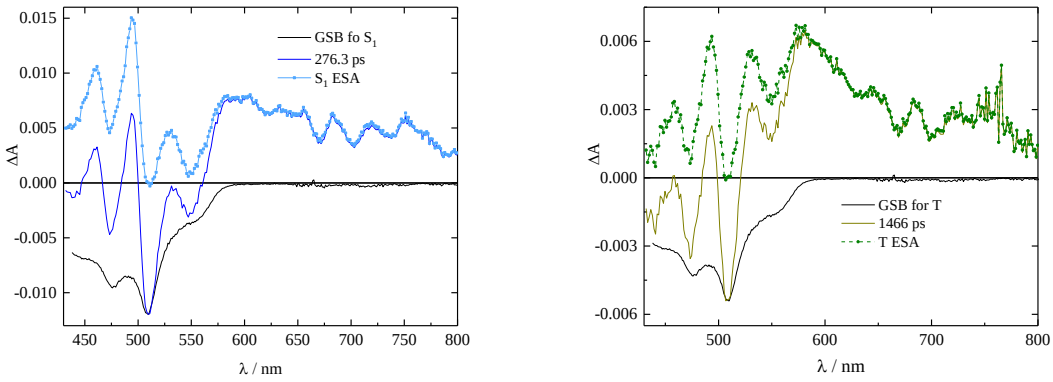

Figure 5.12.4.13. Transient (blue/green) and steady state (black) absorption spectra used to reconstruct the absorption spectra of the excited singlet (purple, straight) and triplet (purple, dashed) states.

The resulting spectra, which only show S_1/T_1 excited state absorption (ESA) signals peaked at very different wavelengths, are quantitatively related (**Figure 5.12.4.4**).

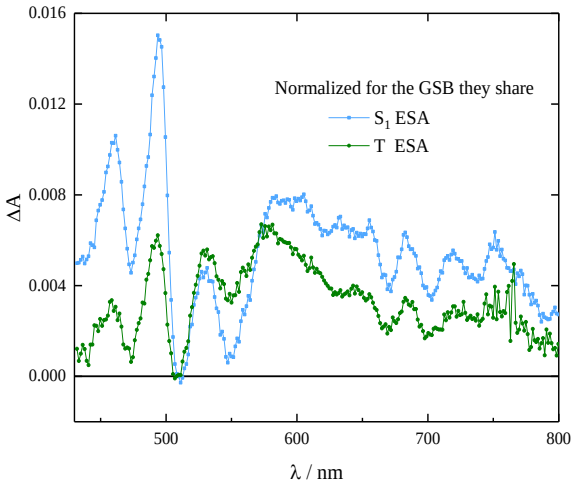

Figure 5.12.4.14. Excited state absorption spectra used to correct composition profile in **Figure 5.12.4.11** and to obtain population dynamics in **Figure 5.12.4.15**.

These spectra were used to correct the composition profiles shown in **Figure 5.12.4.11** in determining differential absorbances typical of singlet and triplet states. The ratio between the singlet excited state absorption at its peak (0.00824 at 584 nm) and the triplet excited state absorption at its peak (0.00547 at 531 nm) is 1.4204. The temporal population profiles for these excited states were thus obtained, by scaling the composition profiles in **Figure 5.12.4.11** using this factor (multiplying the singlet profile by: $\frac{0.42037}{0.90746} = 0.4633$). From the population profiles normalized at the singlet population peak (**Figure 5.12.4.15**), a triplet quantum yield **~ 66%** was estimated for βC compound.

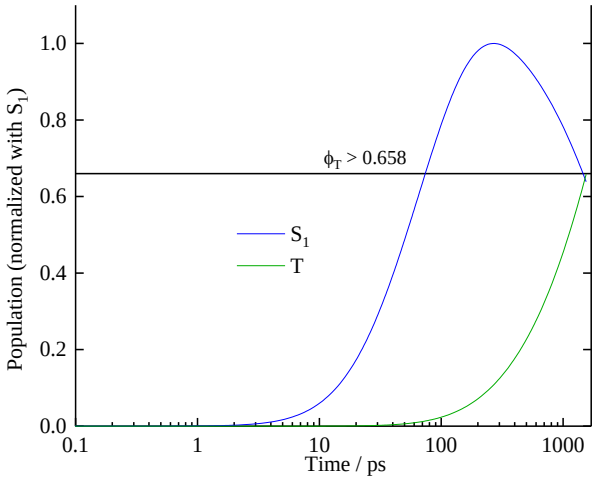

Figure 5.12.4.15. Population dynamics of the excited singlet and triplet states for βC in chlorobenzene.

For the case of the β–tetramer sample, the analysis of the femtosecond transient absorption data to obtain the triplet yield was not carried out. In fact, the transient spectra at long delays after excitation (corresponding to the triplet absorption) do not show any GSB features, as the triplet ESA and the GSB spectrally overlap for this sample. Therefore, a quantitative analysis of these data is not possible and would be inaccurate.

5.12.5 Nanosecond Transient Absorption

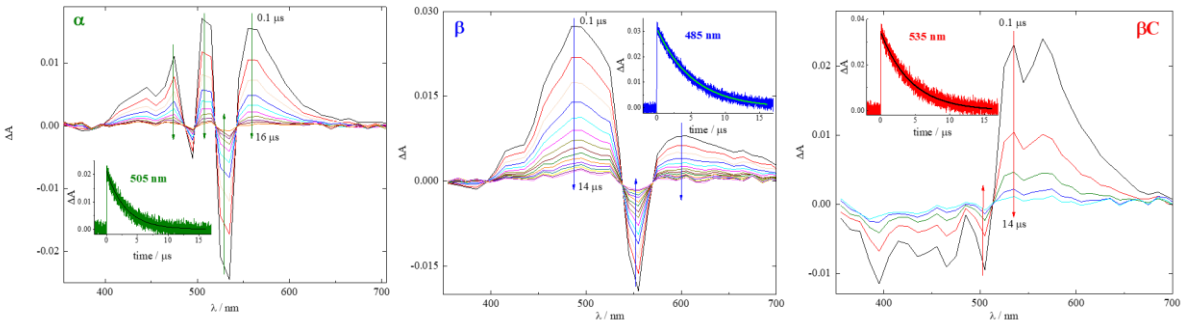

Figure 5.12.5.1. Time−resolved spectra and kinetics (insets) obtained by nanosecond transient absorption (nsTA) for the tetramers in nitrogen purged chlorobenzene with 510 nm excitation.

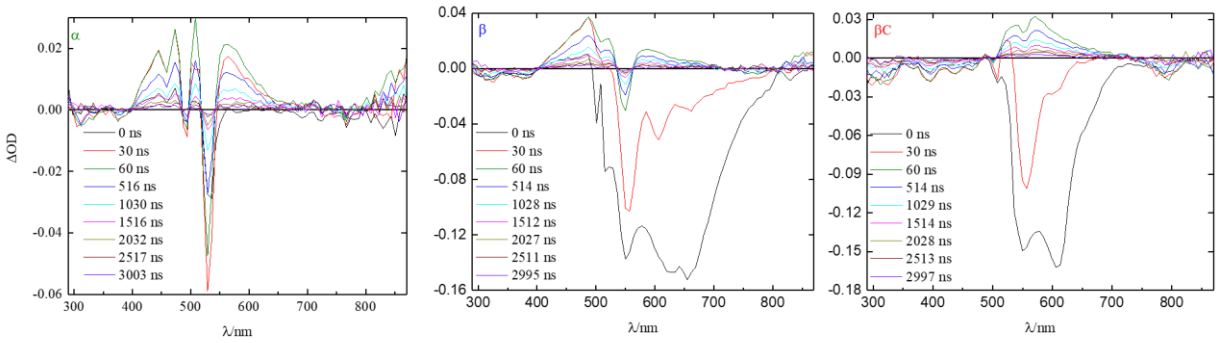

Figure 5.12.5.2. Time−resolved spectra obtained by nanosecond TA for the tetramers in nitrogen purged toluene with 510 nm excitation.

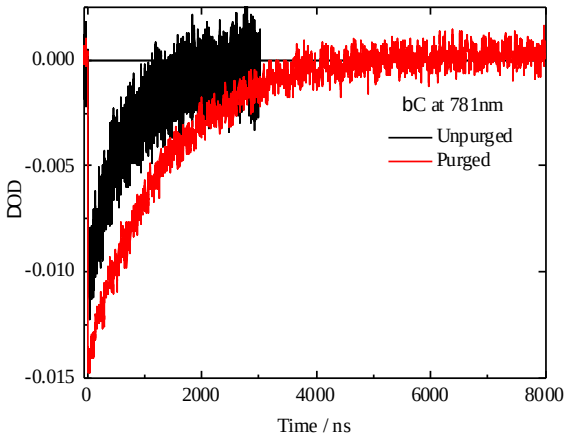

Figure 5.12.5.3. Time−resolved kinetics obtained by nanosecond TA for the βC Tetramer in ambient and nitrogen purged chlorobenzene with 510 nm excitation and 781 nm probe wavelength.

5.12.6 Triplet Sensitization Experiments by ns TA

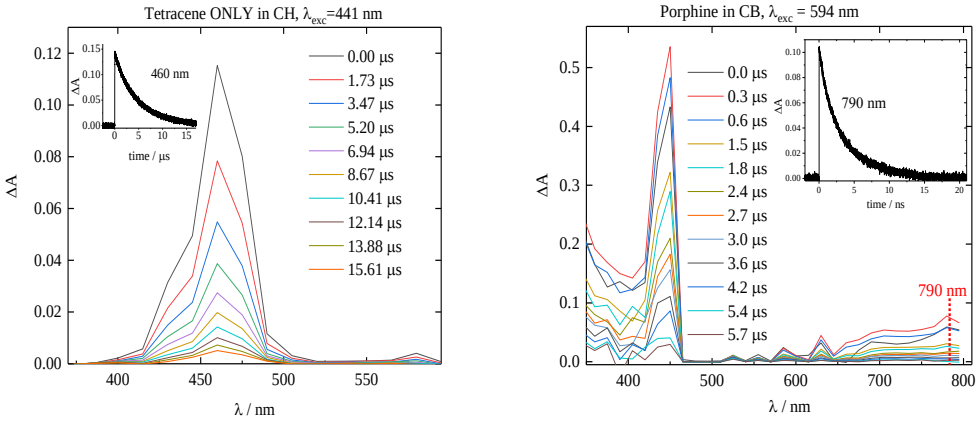

Figure 5.12.6.1. Transient absorption spectra of the sensitizers – tetracene in cyclohexane and tetraphenyl porphine in chlorobenzene – upon laser excitation at 441 nm and 594 nm respectively.

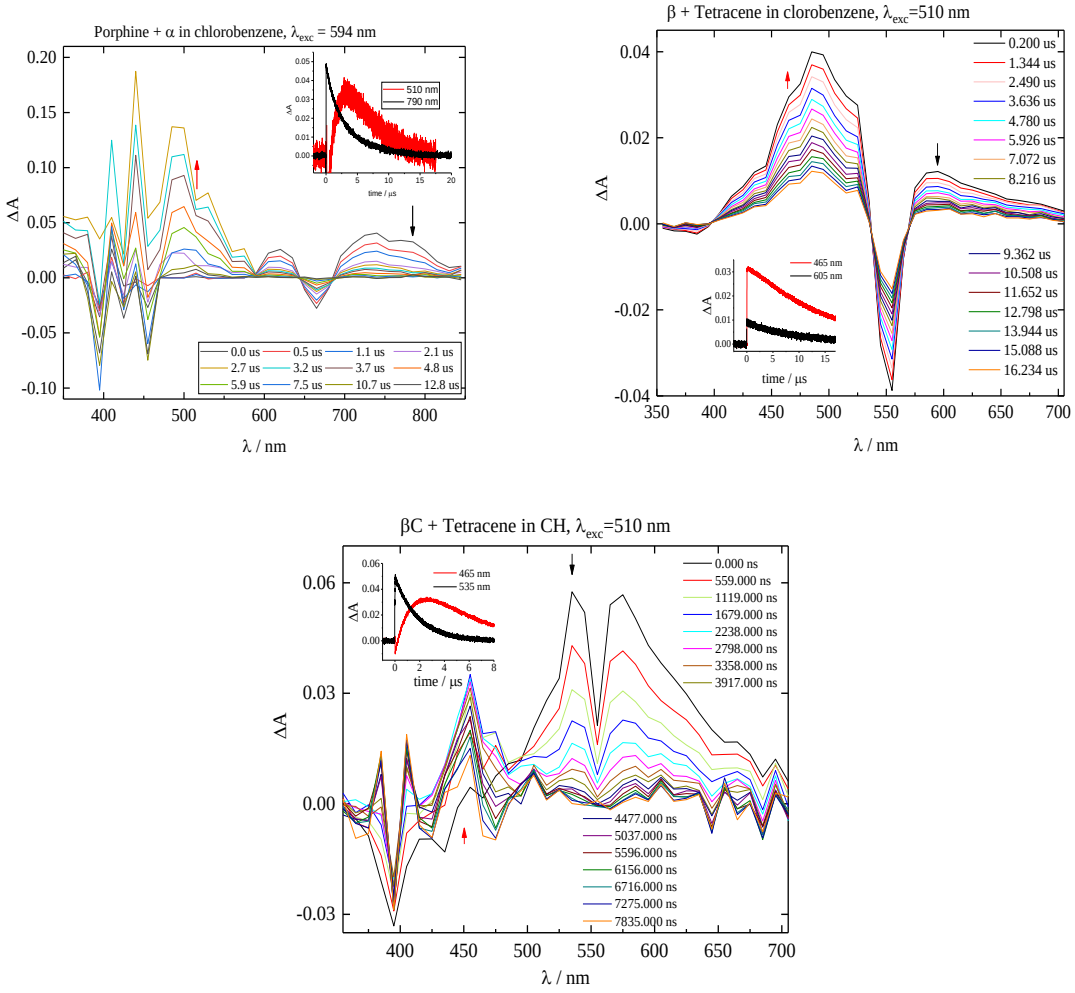

Figure 5.12.6.2. Transient absorption sensitization spectra of the tetramer compounds with their respective sensitizers (porphine in chlorobenzene for α–tetramer only and tetracene in cyclohexane for the rest).

Triplet extinction coefficients were obtained by triplet energy transfer measurements. [3,4] For the α–Tetramer compound, triplet energy was transferred from the 5, 10, 15, 20 – Tetraphenyl – 21H, 23H – porphine donor (E_T = 1.43 eV) to the α–tetramer acceptor. βC and β acted as triplet energy donors to the Tetracene acceptor (E_T = 1.27 eV).

Here, representative examples showing the employed procedure are reported.

A. Determination of the triplet extinction coefficient of α in chlorobenzene (CB) at 510 nm by energy transfer from 5, 10, 15, 20 – Tetraphenyl – 21H, 23H – porphine (λ_{exc}=594 nm)

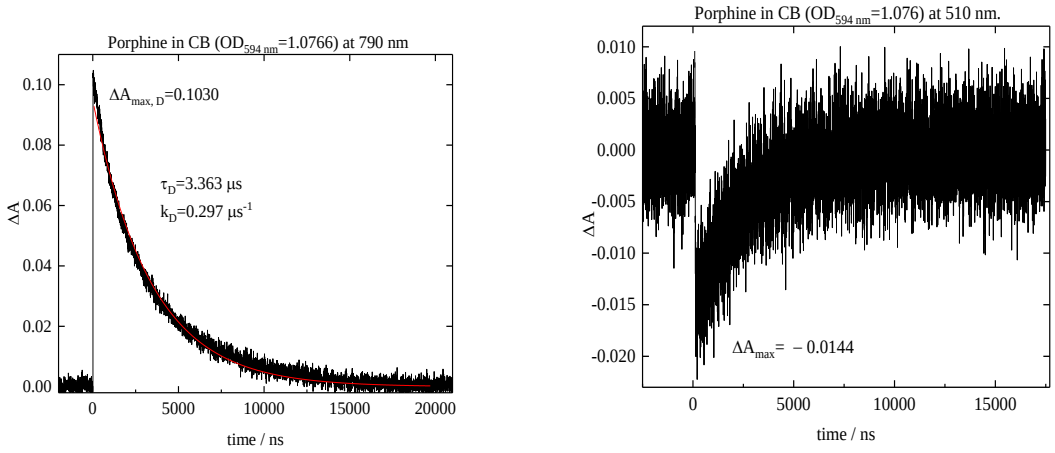

Figure 5.12.6.3. Kinetics recorded during nanosecond transient absorption measurements of **Tetraphenyl – porphine** (donor) in chlorobenzene upon laser excitation at 594 nm.

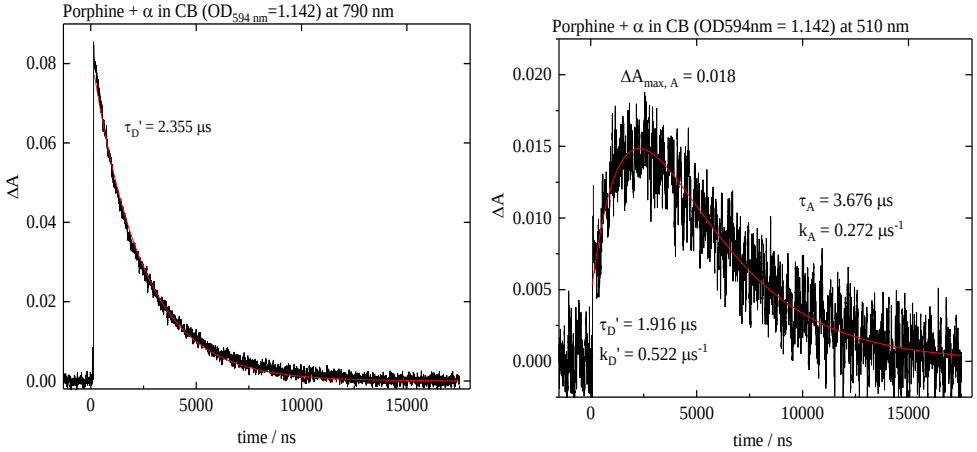

Figure 5.12.6.4. Kinetics recorded during nanosecond transient absorption measurements of α sensitized by **Tetraphenyl – porphine** (quenched donor at 790 nm and sensitized acceptor at 510 nm) in chlorobenzene upon laser excitation at 594 nm.

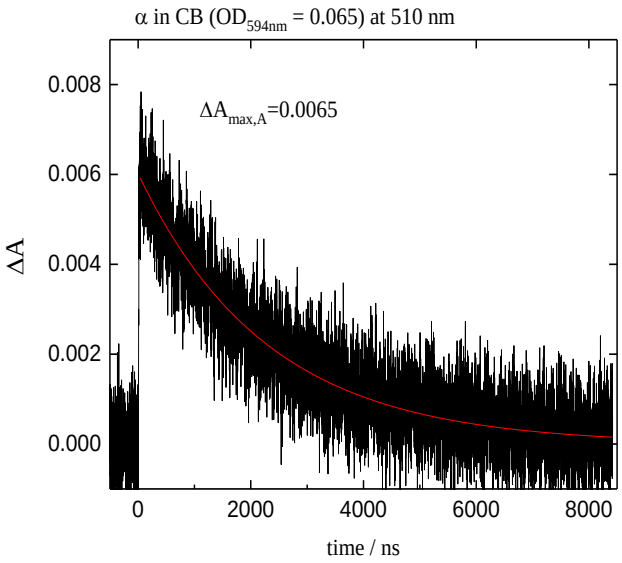

Figure 5.12.6.5. Kinetics recorded during nanosecond transient absorption measurements of α (blank of the acceptor produced by direct excitation and not by energy transfer) in chlorobenzene upon laser excitation at 594 nm.

$$\varepsilon_A = \varepsilon_D \times \frac{\Delta A_{max,A}}{\Delta A_{max,D}} \times \frac{1}{f_D \times p_{ET} \times w} = 6000 M^{-1} cm^{-1} \times \frac{0.018}{0.103} \times \frac{1}{0.9548 \times 0.4309 \times 0.492}$$
$$= 5180 M^{-1} cm^{-1}$$

Where:

$f_D = \frac{A_D}{A_{D+A}} \times \left(\frac{1-10^{-A_{D+A}}}{1-10^{-A_D}}\right) = 0.9548$ is the fraction of light absorbed by the donor

$p_{ET} = \frac{k'_D - k_D}{k'_D} = 0.4309$ is the energy transfer probability

$w = exp\left[\frac{-ln\left(\frac{k'_D}{k_A}\right)}{\frac{k'_D}{k_A}-1}\right] = 0.492$ is a factor accounting for the quenched donor and acceptor lifetimes

To calculate the triplet yield using the computed ε_A:

Relative actinometry approach was used. [3,4] This was done using a reference compound (Tetracene) with known ε_T and ϕ_T. To obtain the ΔA of both sample and reference, the ground state absorption (i.e. OD) of both sample and reference has to be the same at the excitation wavelength (594 nm).

$$\frac{[\phi_T \varepsilon_A]_{sample}}{[\phi_T \varepsilon_T]_{ref.}} = \frac{[\Delta A]_{sample}}{[\Delta A]_{ref.}}$$

B. Determination of the triplet extinction coefficient of βC in **cyclohexane (CH) at 465 nm by energy transfer to Tetracene (λ_{exc}=510 nm)**

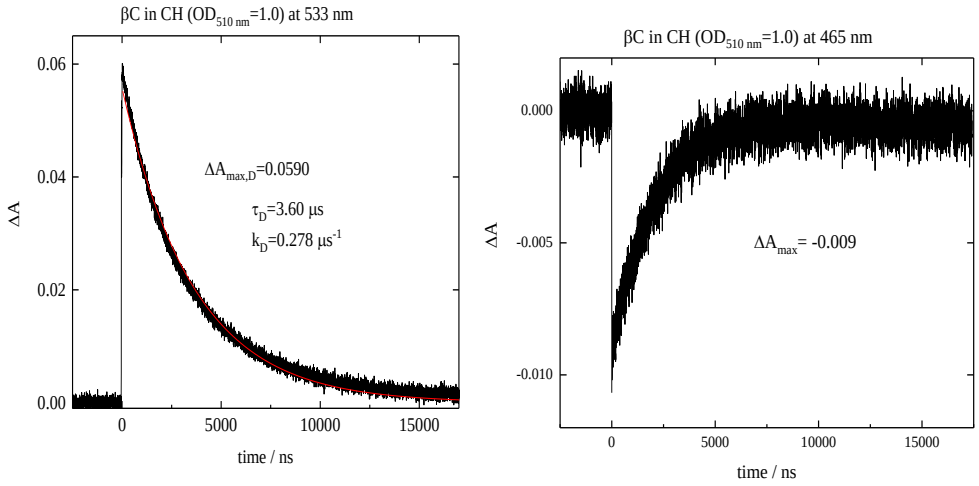

Figure 5.12.6.6. Kinetics recorded during nanosecond transient absorption measurements of βC−Tetramer (donor) in cyclohexane upon laser excitation at 510 nm. *It should be noted that the difference in the lifetime of βC in comparison to that reported in Table 5.6.1 of the main paper is due to the different solvent employed here and to the different nitrogen purging conditions (time, flow rate…).*

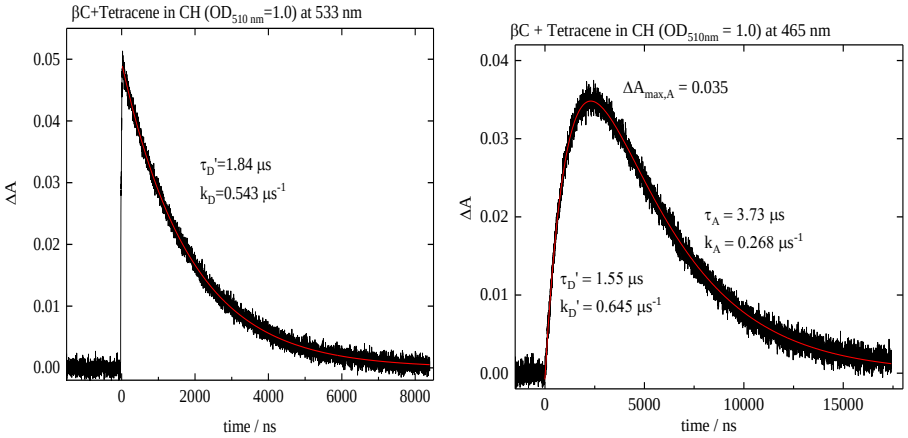

Figure 5.12.6.8. Kinetics recorded during nanosecond transient absorption measurements of tetracene sensitized by βC (quenched donor at 533 nm and sensitized acceptor at 465 nm) in cyclohexane upon laser excitation at 510 nm.

No blank kinetics for the acceptor was recorded because no light absorption may occur for Tetracene at 510 nm laser excitation.

$$\varepsilon_D = \varepsilon_A \times \frac{\Delta A_{max,D}}{\Delta A_{max,A}} \times f_D \times p_{ET} \times w = 31200 M^{-1} cm^{-1} \times \frac{0.0590}{0.035} \times 1 \times 0.5690 \times 0.5356$$
$$= 16029 M^{-1} cm^{-1}$$

Where:

$f_D = \frac{A_D}{A_{D+A}} \times \left(\frac{1-10^{-A_{D+A}}}{1-10^{-A_D}}\right) = 1$ is the fraction of light absorbed by the donor

$p_{ET} = \frac{k_D' - k_D}{k_D'} = 0.5690$ is the energy transfer probability

$w = exp\left[\frac{-ln\left(\frac{k'_D}{k_A}\right)}{\frac{k'_D}{k_A}-1}\right] = 0.5356$ is a factor accounting for the quenched donor and acceptor lifetimes

$$\frac{[\phi_T \varepsilon_A]_{sample}}{[\phi_T \varepsilon_T]_{ref.}} = \frac{[\Delta A]_{sample}}{[\Delta A]_{ref.}}$$

$$[\phi|T\varepsilon_T|sample] = [\phi_T \varepsilon_T]_{ref.} \times \frac{[\Delta A]_{sample}}{[\Delta A]_{ref.}} = (0.62 \cdot 31200 M^{-1}cm^{-1}) \times \frac{0.0161}{0.0659}$$
$$= 4725 M^{-1}cm^{-1}$$

C. Determination of the triplet extinction coefficient of β in chlorobenzene (CB) at 465 nm by energy transfer to Tetracene (λ_{exc}=510 nm)

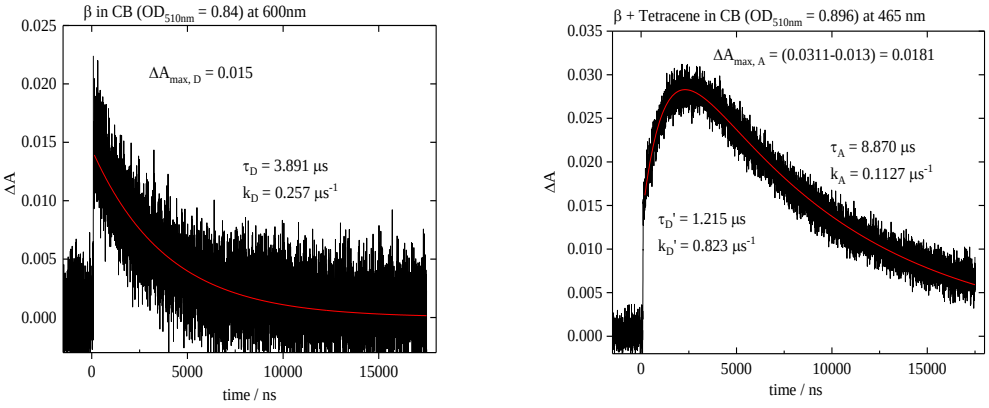

Figure 5.12.6.7. Kinetics recorded during nanosecond transient absorption measurements of β (donor) and Tetracene sensitized by β in chlorobenzene upon laser excitation at 510 nm. *It should be noted that the difference in the lifetime of β in comparison to that reported in Table 5.6.1 of the main paper may be due to the different nitrogen purging conditions (time, flow rate, ...).*

$$\varepsilon_D = \varepsilon_A \times \frac{\Delta A_{max,D}}{\Delta A_{max,A}} \times f_D \times p_{ET} \times w$$
$$= 31200 M^{-1}cm^{-1} \times \frac{0.015}{0.0181} \times 0.9544 \times 0.6877 \times 0.7295 = 12379 M^{-1}cm^{-1}$$

Where:

$f_D = \frac{A_D}{A_{D+A}} \times \left(\frac{1-10^{-A_{D+A}}}{1-10^{-A_D}}\right) = 0.9544$ is the fraction of light absorbed by the donor

$p_{ET} = \frac{k'_D - k_D}{k'_D} = 0.6877$ is the energy transfer probability

$w = exp\left[\frac{-ln\left(\frac{k'_D}{k_A}\right)}{\frac{k'_D}{k_A}-1}\right] = 0.7295$ is a factor accounting for the quenched donor and acceptor lifetimes

$$\frac{[\phi_T \varepsilon_A]_{sample}}{[\phi_T \varepsilon_T]_{ref.}} = \frac{[\Delta A]_{sample}}{[\Delta A]_{ref.}}$$

$$[\phi|T\varepsilon_T|sample] = [\phi_T \varepsilon_T]_{ref.} \times \frac{[\Delta A]_{sample}}{[\Delta A]_{ref.}} = (0.62 \cdot 31200 M^{-1}cm^{-1}) \times \frac{0.0048}{0.0659}$$
$$= 1420 M^{-1}cm^{-1}$$

Table 5.12.6.1. Summary of the Triplet Extinction and Yield experiments for the Tetramers in chlorobenzene.

Param.	α**–tetramer** with Porphine (Run 1)	α**–tetramer** with Porphine (Run 2)	α**–tetramer** with Porphine (Run 3)	α**–tetramer** with Dichloroanthracene (DCA)
$\boldsymbol{\varepsilon_T(D)}$	6000 $M^{-1}cm^{-1}$ (Porphine)	6000 $M^{-1}cm^{-1}$ (Porphine)	6000 $M^{-1}cm^{-1}$ (Porphine)	46000 $M^{-1}cm^{-1}$ (DCA)
$\boldsymbol{\Delta A_A}$	0.018	0.020	0.037	0.0062
$\boldsymbol{\Delta A_D}$	0.103	0.06	0.091	0.134
$\boldsymbol{f_s}$	0.9548	1.00	1.02	0.917
$\boldsymbol{k_1 = k_D}$	0.297 μs^{-1}	0.467 μs^{-1}	0.259 μs^{-1}	0.174 μs^{-1}
$\boldsymbol{k_2 = k_D + k_{ET}[A]}$	0.5219 μs^{-1}	1.094 μs^{-1}	1.402 μs^{-1}	0.500 μs^{-1}
$\boldsymbol{k_3 = k_A}$	0.272 μs^{-1}	0.285 μs^{-1}	0.394 μs^{-1}	0.065 μs^{-1}
$\boldsymbol{p_{et}}$	0.431	0.573	0.815	0.652
$\boldsymbol{w}$	0.492	0.622	0.609	0.737
$\boldsymbol{\varepsilon_T(A)}$	$5180 M^{-1}cm^{-1}$	$5604 M^{-1}cm^{-1}$	$4740 M^{-1}cm^{-1}$	$2723 M^{-1}cm^{-1}$
$\boldsymbol{\varepsilon_T(A) \times \phi_T}$	$6516 M^{-1}cm^{-1}$	$6516 M^{-1}cm^{-1}$	$6516 M^{-1}cm^{-1}$	$3182 M^{-1}cm^{-1}$
$\boldsymbol{\phi_T}$	**1.26**	**1.16**	**1.37**	**1.17**

Param.	β **–tetramer with**	β **–tetramer with**	β**C–tetramer with**	β**C–tetramer with**

	Tetracene (Run 1)	**Tetracene** (Run 2)	**Tetracene** (Run 1)	**Tetracene** (Run 2)
$\boldsymbol{\varepsilon_T(A)}$	$31200M^{-1}cm$ (Tetracene)	$31200M^{-1}cm^{-1}$ (Tetracene)	$31200M^{-1}cm^{-1}$ (Tetracene)	$31200M^{-1}cm^{-1}$ (Tetracene)
$\boldsymbol{\Delta A_A}$	0.0181	0.0086	0.035	0.044
$\boldsymbol{\Delta A_D}$	0.015	0.010	0.059	0.074
$\boldsymbol{f_s}$	0.9544	1.01	1.00	1.03
$\boldsymbol{k_1 = k_D}$	0.257 μs^{-1}	0.836 μs^{-1}	0.278 μs^{-1}	0.654 μs^{-1}
$\boldsymbol{k_2 = k_D + k_{ET}[A]}$	0.823 μs^{-1}	3.300 μs^{-1}	0.645 μs^{-1}	2.445 μs^{-1}
$\boldsymbol{k_3 = k_A}$	0.113 μs^{-1}	0.341 μs^{-1}	0.268 μs^{-1}	0.676 μs^{-1}
$\boldsymbol{p_{et}}$	0.688	0.747	0.569	0.732
$\boldsymbol{w}$	0.730	0.770	0.536	0.612
$\boldsymbol{\varepsilon_T(D)}$	$12379M^{-1}cm$	$6240M^{-1}cm^{-1}$	$16028M^{-1}cm^{-1}$	$24412M^{-1}cm^{-1}$
$\boldsymbol{\varepsilon_T(D) \times \phi_T}$	$1420M^{-1}cm^{-}$	$1420M^{-1}cm^{-1}$	$4725M^{-1}cm^{-1}$	$4725M^{-1}cm^{-1}$
$\boldsymbol{\phi_T}$	**0.12**	**0.22**	**0.29**	**0.19**

5.12.7 Quantum Chemical Simulations

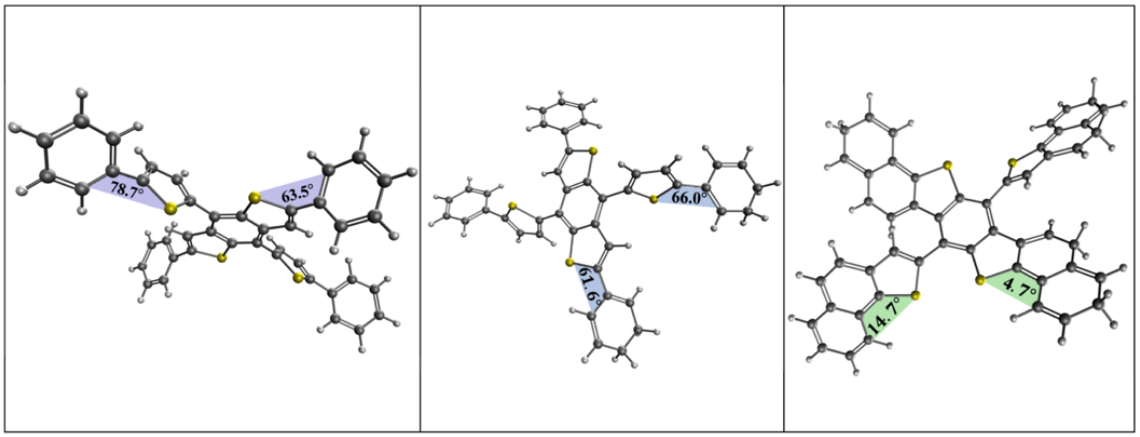

Figure 5.12.7.1. The investigated Tetramers' skeletons with their dihedral angles. From left to right: α, β and βC.

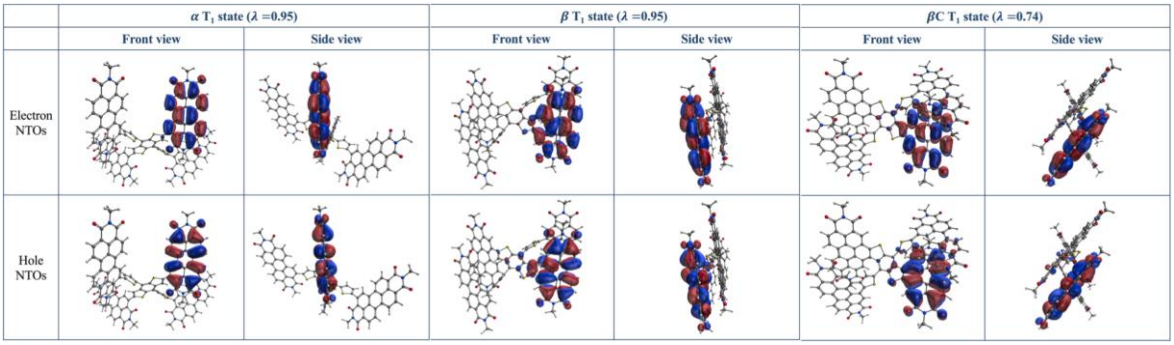

Figure 5.12.7.2. Natural transition orbitals (NTOs) of $S_0 \rightarrow T_1$ transitions for the three Tetramers considered in this work. Orbitals plotted in IQmol with isovalue 0.05.

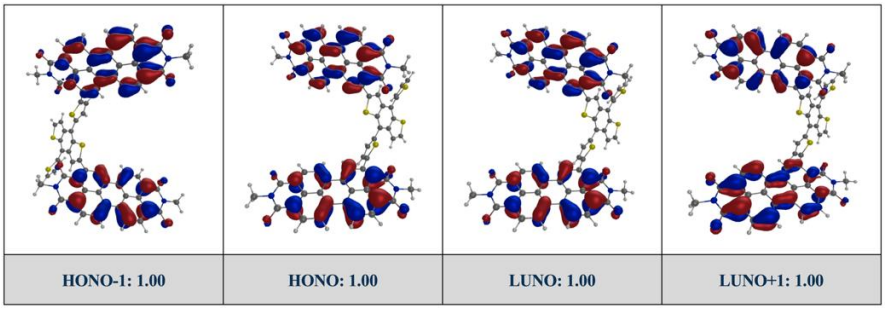

Figure 5.12.7.3. Natural Orbitals (NOs) for the Multiexcitonic State (S_4) of the truncated α–Tetramer obtained by RAS–2SF. Isovalue of these orbitals is set to be 0.02 in VMD.

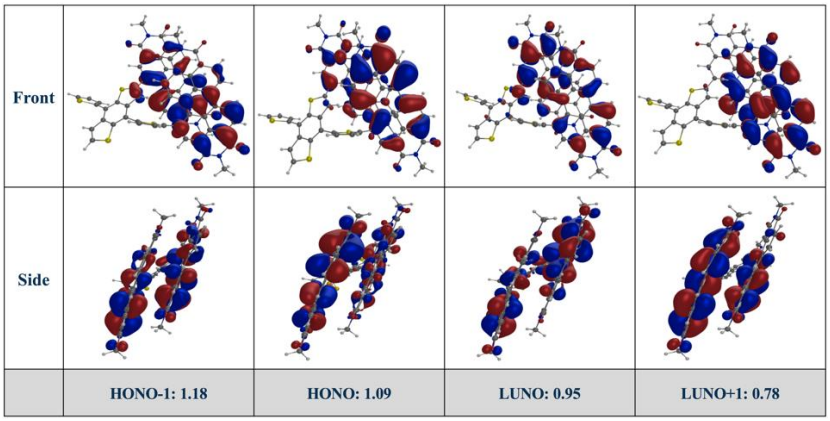

Figure 5.12.7.4. Natural Orbitals (NOs) for the Multiexcitonic State (S_5) of the truncated α–Tetramer obtained by RAS–2SF. Isovalue of these orbitals is set to be 0.02 in VMD.

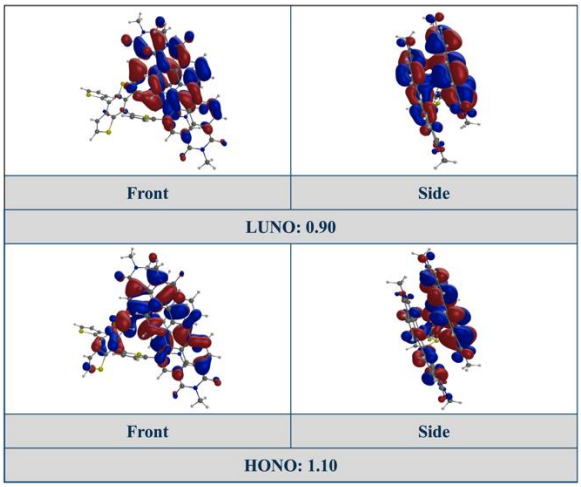

Figure 5.12.7.5. Natural Orbitals (NOs) of the first excited singlet state (S_1) of the truncated β–tetramer obtained via RAS–2SF with 6–31G* basis set. The isovalue of these orbitals is set to be 0.02 in VMD.

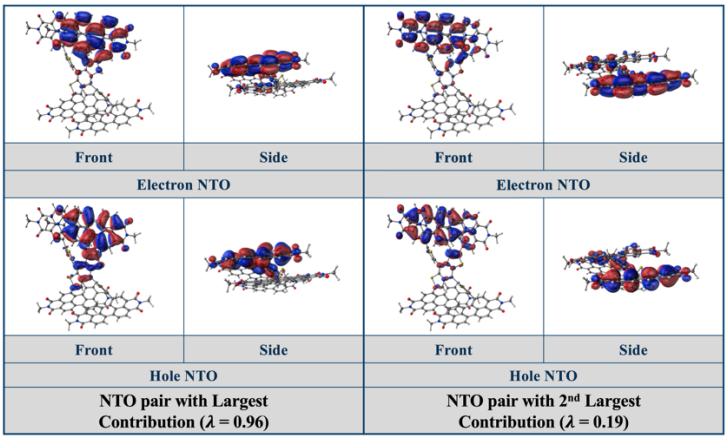

(a)

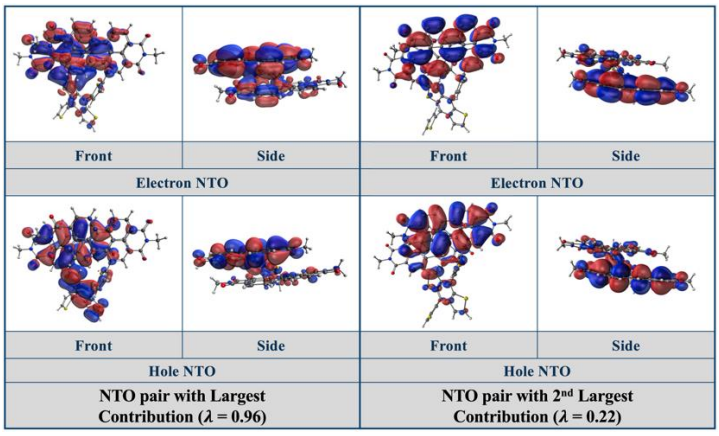

(b)

Figure 5.12.7.6. Natural Transition Orbitals (NTOs) of the first excited singlet state (S_1) of: (a) whole β–tetramer, and (b) the truncated β–tetramer obtained via TD–DFT with ωB97X–D

functional/6−31G* basis set. The isovalue of these orbitals is set to be 0.05, 0.035 in IQMOL, respectively.

Table 5.12.7.1. Energy levels estimated by RAS−2SF based on the optimized structures of truncated Tetramer molecules (S: Singlet, T: Triplet, Q: Quintet, ME: Multiexciton. Energies are given in eV).

α		β		βC	
State	Energy (eV)	State	Energy (eV)	State	Energy (eV)
S_0	0.000	S_0	0.000	S_0	0.000
T_1	2.181	T_1	2.131	T_1	2.539
T_2	2.192	T_2	2.179	T_2	2.558
S_1	3.796	S_1	3.378	S_1	4.012
S_2	3.857	T_3	3.747	S_2	4.093
T_3	4.272	S_2	3.779	T_3	4.238
T_4	4.292	S_3	3.784	S_3	4.309
S_3	4.388	T_4	3.939	T_4	4.315
$Q_1-{}^5$(ME)	4.410	S_4	3.993	S_4	4.424
$T_5-{}^3$(ME)	4.410	T_5	4.299	T_5	4.503
$S_4-{}^1$(ME)	4.410	T_6	4.351	T_6	4.535
T_6	4.431	$Q_1-{}^5$(ME)	4.355	S_5	4.835
T_7	4.434	$T_7-{}^3$(ME)	4.356	T_7	4.837
S_5	4.781	$S_4-{}^1$(ME)	4.361	T_8	4.852
T8	4.866	T_8	4.369	T_9	4.878
T_9	4.906	S_5	4.390	T_{10}	4.937
T_{10}	4.977	T_9	4.462	S_6	4.952
T_{11}	4.981	S_6	4.719	S_7	5.035
				$Q_1-{}^5$(ME)	5.160
				$T_{11}-{}^3$(ME)	5.166
				$S_8-{}^1$(ME)	5.169
				T_{12}	5.305
				S_9	5.335
				T_{13}	5.394

Table 5.12.7.2. Energy levels estimated by 3SF−RAS of truncated α
(S: Singlet, T: Triplet, Q: Quintet, ME: Multiexciton. Energies are given in eV).

α	
State	Energy
S_0	0.000
T_1	2.181
T_2	2.181
T_3	2.192
S_1	3.796
S_2	3.857
T_4	4.272

T_5	4.292
S_3	4.388
Q_1	4.410
T_6	4.410
S_4, ME (^{1}TT)	4.410
T_7	4.431

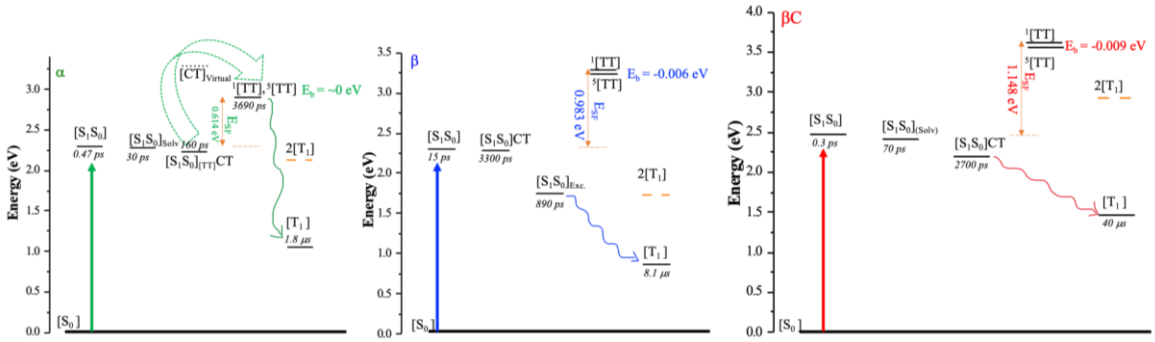

Figure 5.12.7.7: Proposed singlet deactivation and triplet formation pathways for the investigated PDI tetramers in chlorobenzene using experimental singlet ($[S_1S_0]$) absorption energies, TD–DFT emission triplet (T_1) energies, $[S_1S_0] + E_{SF}$ for ^{1}[TT] and $[S_1S_0] + E_b$ for ^{5}[TT]

References

1. Margulies, E. A.; Miller, C. E.; Wu, Y.; Ma, L.; Schatz, G. C.; Young, R. M.; Wasielewski, M. R. Enabling Singlet Fission by Controlling Intramolecular Charge Transfer in π−Stacked Covalent Terrylenediimide Dimers. *Nature Chem.* **2016**, *8*, 1120–1125.
2. Ramanan, C.; Smeigh, A. L.; Anthony, J. E.; Marks, T. J.; Wasielewski, M. R. Competition Between Singlet Fission and Charge Separation in Solution Processed Blend Films of 6,13-bis(triisopropylsilylethynyl)pentacene with Sterically Encumbered Perylene-3,4,9,10-bis(dicarboximide)s. *J. Am. Chem. Soc.* **2011**, *134*, 386–397.
3. Carmichael, I.; Hug, G. L. Triplet–Triplet Absorption Spectra of Organic Molecules in Condensed Phases. *J. Chem. Phys. Ref. Data.* **1986**, *15*, 1.
4. Land, E. J. Extinction Coefficients of Triplet-Triplet transitions. *Proc. Roy. Soc. A* **1968**, *305*, 457–471.

Chapter 6

New Direct Approach for Determining the Reverse Intersystem Crossing Rate in Organic TADF Emitters

6.1 Original Publication Information and Author Contribution

Portions of this chapter were taken from a paper that was published in the *Journal of American Chemical Society* with the title:

"New Direct Approach for Determining the Reverse Intersystem Crossing Rate in Organic TADF Emitters" Ricardo Javier Vázquez, Ju Hui Yun, Angelar K. Muthike, Madeleine Howell, Hyungjun Kim, Ifeanyi K. Madu, Taesu Kim, Paul Zimmerman, Jun Yeob Lee, and Theodore Goodson III.

My contribution in this work was performing the nanosecond transient absorption spectroscopy experiments and helping with some of the data analysis. These experiments were very important to the work since we were able to capture the excited state absorption (ESA) of the molecule, determine whether these ESA was as a result of singlet or triplet species by purging out oxygen that is a known quencher of triplets, determine the decay time of these triplet species which was crucial in calculating the rate of reverse intersystem crossing.

6.2 Abstract

We developed a new optical method to determine the rate of reverse intersystem crossing (k_{rISC}) in thermally activated delayed fluorescent (TADF) organic chromophores using time-resolved transient absorption spectroscopy. We successfully correlated the k_{rISC} of the TADF-chromophores with device performance. Specifically, we focused on the external quantum efficiency (η_{EQE}) and the stability of the device at high brightness levels. It is believed that by obtaining a large k_{rISC} one may reduce the possibility of triplet-triplet annihilation (TTA) and increase the long-term stability of organic light emitting diodes (OLEDs) devices at high brightness levels (η_{EQE} roll-off). In this contribution, we investigate the photophysical mechanism in a series of TADF-chromophores based on carbazole or acridine derivatives as donor moieties,

and triazine or benzonitrile derivatives as the acceptor moieties. We found a relationship between large k_{rISC} values and high η_{EQE} values at low operating voltages for the TADF-chromophores investigated. In addition, those chromophores with a larger k_{rISC} illustrated a smaller η_{EQE} roll-off (higher stability) at high operating voltages. These features are beneficial for superior OLEDs performing devices. Contrarily, we found that if a chromophore has a $k_{rISC} \leq 10^3 s^{-1}$ its η_{EQE} is $\leq$ 5%. Such as small k_{rISC} suggests that there is no TADF effect operating in these organic systems and the molecule is not efficient in harvesting triplet excitons. Emission lifetime-based methodologies for determining the k_{rISC} were included for comparison but failed to predict the devices performance of the investigated TADF-chromophores to the same extent of our proposed methodology.

6.3 Introduction

Organic light emitting diodes (OLEDs) based on chromophores with thermally activated delayed fluorescence (TADF) characteristics have captivated the attention of the scientific community as a potential replacement for their organometallic phosphors counterparts.[1–6] This is due to improvements including the devices' processability and ease of fabrication, synthetic flexibility for optical tuning, and cost-efficiency.[1,7,8] In addition, these TADF-based OLEDs are able to emulate the high internal quantum efficiencies ($\eta_{IQE} \sim 100$) offered by their Phosphors-OLED counterparts.[1,4,9] However, the key challenge hampering their commercialization is their poor device efficiency at high brightness levels, an effect known as efficiency roll-off.[10,11]

The high η_{IQE} has been ascribed to the conversion of non-emissive triplets into emissive singlets ($T_1 \rightarrow S_1$) in a reverse intersystem crossing process (rISC), which is made possibly by the small energy gap between the singlet-triplet manifolds (ΔE_{ST}).[2,12] The field has primarily used steady-state measurements and microsecond spectroscopy to illustrate and calculate their k_{rISC}, under the premise that it may help to predict device performances.[1,7,13,14] Specifically, it is believed that obtaining a high k_{rISC} is critical for reducing the triplet-triplet annihilation (TTA) mechanism that causes η_{EQE} roll-off.[3,13,15] However, these indirect methods require a combination of selected tools and do not exclude the parallel coexistence of phosphorescence in the TADF-chromophore nor the influence of the host material if the measurements are conducted in solid state.[3,16–20]

New methodologies applied to this problem, such as nanosecond transient absorption spectroscopy (ns TAS), can provide a powerful tool to examine the photophysical properties of organic chromophores with TADF-characteristics. It is interesting to note that while there have

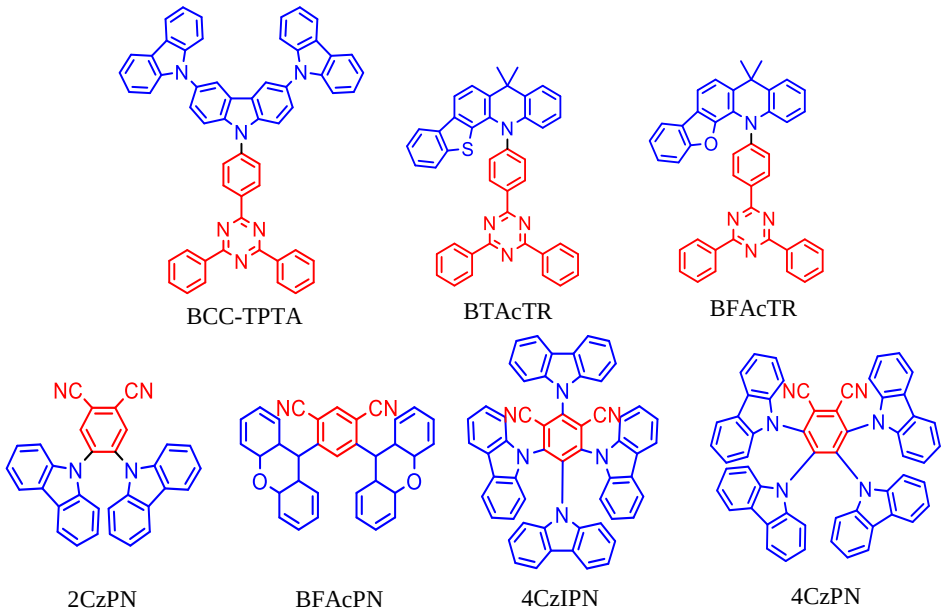

Figure 6.3.1. Molecular structure of the investigated TADF-active chromophores

been reports of studies investigating the quenching effect of molecular oxygen (O_2) in the emissive properties of highly efficient and well-known TADF-systems, there have not been any detailed ns TAS O_2 quenching studies of these promising materials.[21,22] O_2 has been used for decades as a fundamental molecule for excited state sensitization.[21,23–25] The ns TAS is a time-resolved spectroscopic technique that can detect and resolve the dynamics of non-emissive intermediates contributing to the excited state of these chromophores in relatively long timescales (> 10 ns).[26–34] These non-emissive conformers are detected as positive Δ absorption bands, namely excited state absorption (ESA).[21,30,33,35–37] By coupling O_2 with the ns TAS technique, we aim to identify and characterize the ESA bands with O_2 sensitivity, which in these timescales, should be observed in a significant ESA decay lifetime lengthening attributed to triplets.

6.4 Results and Discussion

In this publication, we present the first results of ns TAS spectroscopy to determine the k_{rISC} in organic chromophores with TADF characteristics by direct triplet state characterization. A

series of chromophores with diverse molecular structures were investigated to demonstrate our methodology (**Figure 6.3.1**). Emission lifetime-based methodologies for estimating the k_{rISC} were included for comparison.

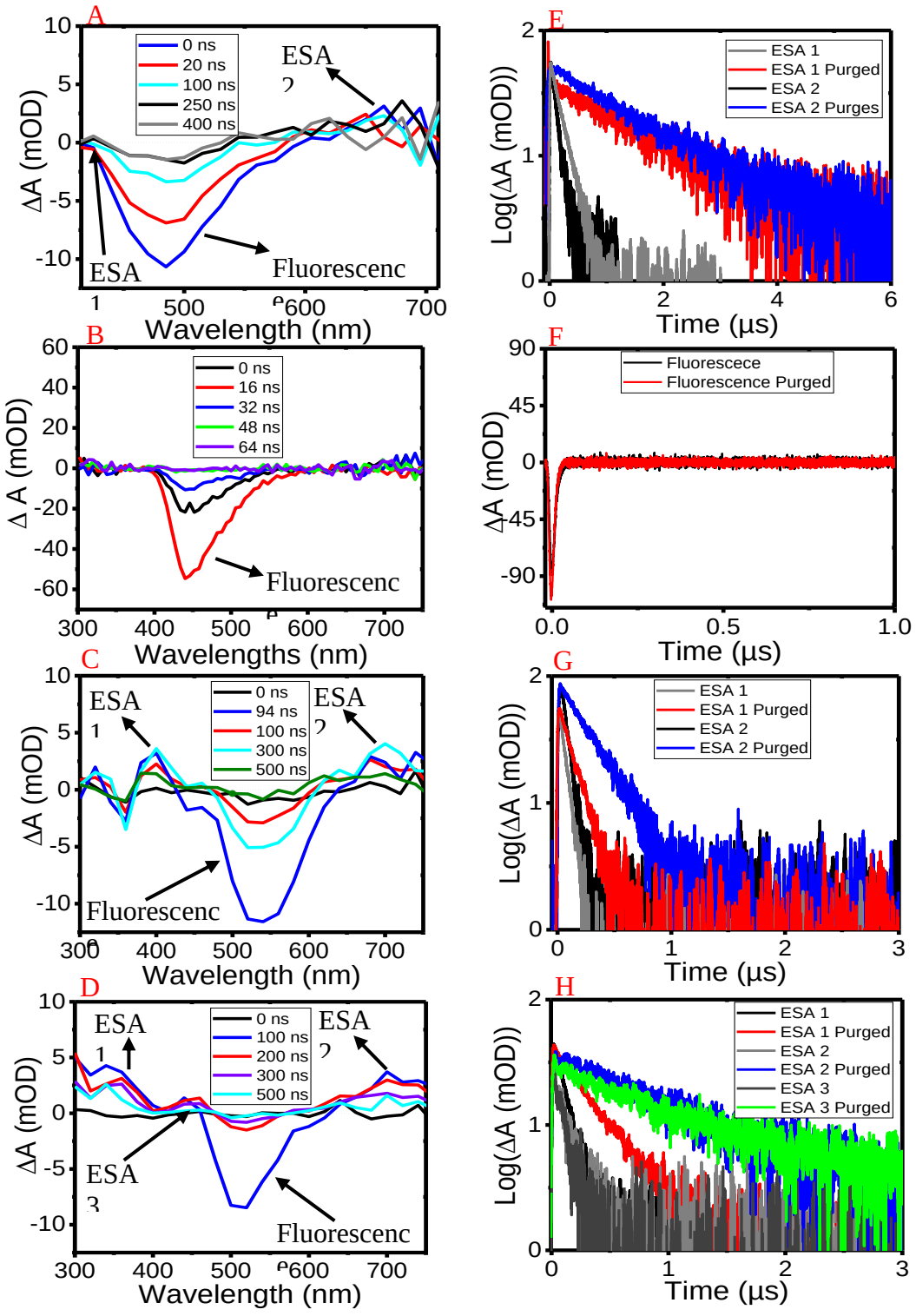

Figure 6.4.1.Time-resolved absorption spectra of 2CbzPN (A), BCC-TPTA (B), BTAcTr (C), and BFAcPN (D). ESA decay relaxation profiles of 2CbzPN (E), BCC-TPTA (F), BTAcTr (G), and BFAcPN (H).

To demonstrate our transient absorption methodology, the well-known 2CzPN and BCC-

TPTA were used as standards (**Figure 6.4.1**). For the 2CzPN system, two ESA bands were detected. These bands have been previously reported and attributed to triplet state conformations.[28,38] As we previously reported for BCC-TPTA, we did not detect ESA bands that are consistent with triplet density.[21] In contrast, similar ESA bands to those obtained for the 2CzPN system were found for the remaining organic chromophores investigated. Therefore, oxygen sensitization experiments were carried out to further characterize the relaxation pathways of these ESA bands.

As it can be observed for 2CzPN in **Figure 6.4.1B**, a lengthening in its ESA relaxation dynamics was obtained when the measurements were conducted in O_2-free enviroments. A similar mono-exponential decay constant of ~ 1.7μs (rate = $5.8x10^5 s^{-1}$) was obtained for both ESA bands regardless the solvent used. It is important to note that the lengthening in these ESA bands (triplets) lifetimes correlate well with the lengthening in the long-lived emissive lifetime of 2CzPN (**Figure 6.4.2A**) and with the quantum yield enhancement after purging oxygen (Φ_{TADF}). The Φ_{TADF} is quantified by the difference in Φ of the chromophore before and after purging oxygen, and it has been widely used to determine the k_{rISC} in emission lifetime-based methodologies.[13,17,22] We need to highlight that the ESA decay rate of 2CzPN is magnitudes higher than the reported rates of phosphorescence (K_P) in chromophores with TADF characteristics determined at low temperatures.[3] One can expect that this rate (K_p) will not get any larger at high temperatures. Therefore, we can rule out the possibility of room-temperature phosphorescence. Conversley, these observations suggest that the dynamics of these ESA bands are related to triplets that are important to the characterization of the delayed fluorescence process in 2CzPN.

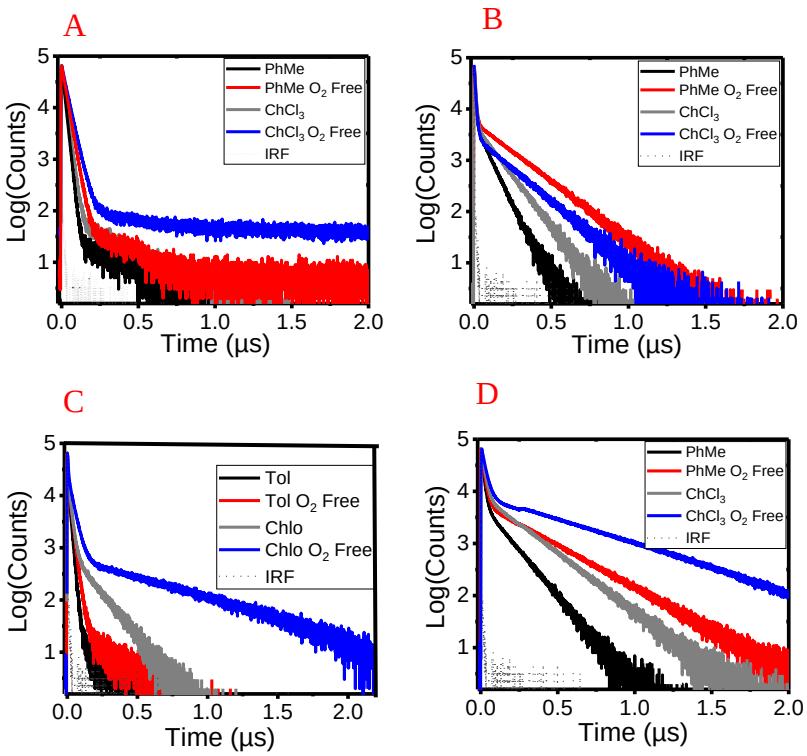

Figure 6.4.2. (A) Emissive lifetime characterization of 2CbzPN (A), BTAcTr (B), BFAcTr (C) and BFAcPN (D).

In the case of BTAcTr, there are two ESA bands (see **Figure 6.4.1**) present. The **ESA 2** band showed a higher sensitivity to the presence of O_2.[25,39] A lengthening in the mono-exponential decay of ~ 310ns ($k_{Triplet} = 3.2x10^6 s^{-1}$) was obtained for the **ESA 2** conformation in toluene (**Figure 6.4.1B**) and 183ns ($k_{Triplet} = 5.6x10^6 s^{-1}$) in chloroform (**Figure 6.6.7**) after purging oxygen. The lengthening in these ESA bands lifetime of BTAcTr correlates well with its Φ_{TADF} and with the lengthening in its long-lived emissive lifetime (**Figure 6.4.2A**). Similar behavior was obtained for the BFAcTr system in chloroform (**Figure 6.6.7; 6.6.8**). A lengthening in the mono-exponential decay with time constant of 244ns ($k_{Triplet} = 4.2x10^6 s^{-1}$) was obtained for the **ESA 2** band at O_2-free enviroments. Under these circumstances, we can attribute the **ESA 2** band to triplet state conformations. This assignment became more evident when a lack of ESA bands is observed for BFAcTr in toluene solution (**Figure 6.6.7**). This lack of ESA bands correlate well with BFAcTr discrete long-lived emissive component when toluene is used as the solvent (**Figure 6.4.2A**). In the case of BFAcPN (**Figure 6.4.1**), multiple ESA bands were detected with **ESA 2** and **ESA 3** showing a similar decay profile and time decay of ~ 1.1µs ($k_{Triplet} = 9.1x10^5 s^{-1}$) regardless of the solvent used. As with the 2CzPN, BTAcTr, and BFAcTr systems, the ESA bands lifetime

lengthening of BFAcPN in O_2-free enviroments correlates well with its Φ_{TADF} and with the lengthening in its long-lived emissive lifetime.

Despite that O_2 is a fairly non-discriminatory excited-state quencher, the overwhelming evidence obtained from multiple spectroscopic techniques connect the Φ_{TADF} of the investigated systems (***Table 6.6.4***) with: (**1**) an increase in their long-lived ESA band lifetime, and with (**2**) an increase in their long-lived emissive lifetime. Under these circumstances and timescales, it becomes evident that purging oxygen from the solution resulted in mostly unquenched triplet excited states that may contribute to the long-lived emissive lifetime of the investigated chromophores, as it was recently reported for some of these, and other, TADF-active chromophores.[22] Consequently, these results strongly suggest that at least part of the non-emissive triplet density is converted into emissive singlets thru the rISC mechanism. Here, we use the deactivation rates of these O_2 sensitive ESA bands ($k_{Triplets}$) at O_2-free enviroments and multiply them by the Φ_{TADF} to quantify the ammount of non-emissive triplets converting into emissive singlets, namely the k_{rISC} (**Equation 1)**:

$$k_{rISC} = k_{Triplet} * \Phi_{TADF} \qquad \textbf{Equation 1}$$

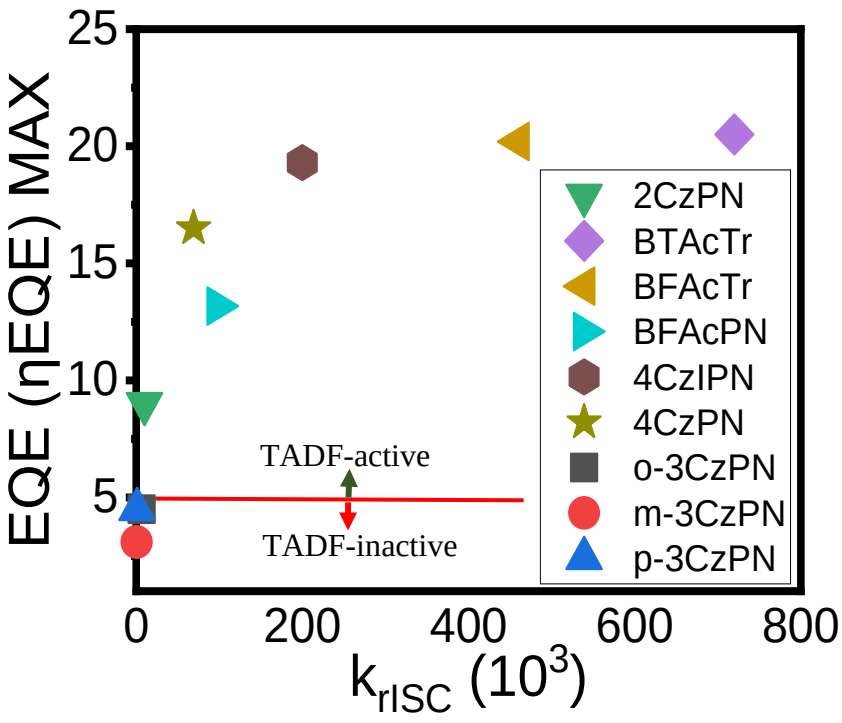

Figure 6.4.3. Correlating the Device EQE with the k_{rISC}

A rate of $1.1x10^4s^{-1}$, $9.8\ x10^4s^{-1}$, $4.6x10^5s^{-1}$, and $7.2x10^5s^{-1}$ were obtained for 2CzPN, BFAcPN, BFAcTr, and BTAcTr, respectively. These k_{rISC} magnitudes seems to concur to some extend with the quantum chemical simulations (QCS) presented in here (***SI***) and with those published by Brédas.[5] We used the k_{rISC} determined by our methodology and correlated them with their device performance under the same device architectures. We obtained a proportional relationship between the k_{rISC} and η_{EQE} (**Figure 6.4.3**), with TADF chromophores with the larger k_{rISC} showing higher η_{EQE}. Specifically, η_{EQE} of 9%, 14.1%, 20.4%, and 21.8% for 2CzPN, BFAcPN, BFAcTr, and BTAcTr systems were reported, respectively. To further validate our methodology, we used it to determine the k_{rISC} of some well-known TADF-chromophores from the limited transient absorption data available in the literature. A relationship between the k_{rISC} and the η_{EQE} was obtained for well-known systems such as 4CzIPN and 4CzPN. Specifically, a k_{rISC} of $2.2x10^5s^{-1}$

Table 6.4.1. k_{rISC} comparison and device performances summary of the TADF-active systems. [a]EQE_{MAX} = maximun EQE value at low operating voltages. Not observed (N.O.)

Chromophore	k_{rISC} 10^5 s^{-1} (Our-Method)	EQE_{MAX}	k_{rISC} 10^5 s^{-1} (Emission lifetime-based)
BTAcTr	7.2	21 [40]	765
BFAcTr	4.6	20.4 [40]	103
4CzIPN	2.2	19.3 [2,41]	140[42]
4CzPN	0.70	17.8 [2,41]	4.65
BFAcPN	0.98	14.1***Sup.Info***	145
2CzPN	0.11	9 [2]	6.0
BCC-TPTA	N.O.	16.8 [1,11]	N.O.

, and $7.0x10^4 s^{-1}$ correlating well with η_{EQE} of 19.3% and 17.8% values were observed, respectively.[2,41] It is interesting to note that if the chromophore (o-CzBN, m-CzBN, p-CzBN) possess a $k_{rISC} \leq 10^3 s^{-1}$, an $\eta_{EQE} \leq 5\%$ is obtained (**Table *6.6.2***). This results suggests the minimum k_{rISC} that a TADF chromophore must possess to be able to harvest triplet-excitons via a rISC process and be a TADF-active emitter.

It is believed that TADF emitters with a large k_{rISC} may reduce the TTA mechanism responsible for the η_{EQE} roll-off in OLEDs.[1,3,15,26] In the case of the chromophroes with triazine as acceptor, a reduced η_{EQE} roll-off was observed for BTAcTr (5%) while the higher η_{EQE} roll-off was observed for BCC-TPTA (76%), which its lack of ESA bands in the multiple solvents tested suggest minimal triplet exciton conversion to singlet excitons.[21] In the case of the TADF chromophores with benzonitrile functionalities as the acceptor, reduced η_{EQE} roll-offs were found for 4CzIPN (6%), BFAcPN (8.5%), and 4CzPN (10%) in comparison with that of 2CzPN

(55%).[2,41] These observations are also consistent with obtaining a large k_{rISC} and reducing the η_{EQE} roll-offs (**Figure 6.6.3**).

Emission lifetime-based methodologies for calculating the k_{rISC} were included for comparison.[13,17,22] Rates of $6.0x10^5s^{-1}$, $1.45x10^7s^{-1}$, $1.03x10^7s^{-1}$, and $7.65x10^7s^{-1}$ were obtained for 2CzPN, BFAcPN, BFAcTr, and BTAcTr, respectively. Very interestingly, no trends between the k_{rISC} determined by emission lifetime-based methodologies and the η_{EQE} was obtaied. This was also true when the chromophores from the literature were taken into consideration. It is interesting to note that $\eta_{EQE} \leq 5$ %, which implies TADF-inactive emitters,[38] were reported for some chromophores (o-CzBN and p-CzBN, ***Table 6.6.2***) whose k_{rISC} determined by emission lifetime-based methods were within the same order of magnitude ($\geq 10^4s^{-1}$) as with TADF-active emitters. Contrairly, our methodology showed that these TADF-inactive chromophores possess very small k_{rISC} ($\leq 10^3s^{-1}$), highlighting the minimal k_{rISC} magnitude that a TADF chromophore must possess to be TADF-active. These observations suggest higher accuracy for the rISC illustration and direct k_{rISC} determination by our methodology over emission lifetime-based methods.

6.5 Conclusion

In conclusion, we developed a new optical strategy for the direct determination of the k_{rISC} in organic chromophores with TADF characteristics. Our methodology allowed us to: a) directly characterize the triplet state dynamics for determining the k_{rISC} in organic TADF chromophores, b) highlight the correlation of a large k_{rISC} with a high η_{EQE} value and its device stability for TADF-OLEDs at high operating voltages. We also illustrated the correlation of obtaining a $k_{rISC} > 10^3s^{-1}$ for efficient TADF-active molecules. These structure-function relationships were not possible by using emission lifetime-based methodologies. This work may facilitate the excited state characterization of organic chromophores with TADF characteristics and will help to discover top TADF candidates for superior OLEDs device performance.

References:

(1) Hirata, S.; Sakai, Y.; Masui, K.; Tanaka, H.; Lee, S. Y.; Nomura, H.; Nakamura, N.; Yasumatsu, M.; Nakanotani, H.; Zhang, Q.; Shizu, K; Miyazaki, H.; Adachi, C. Highly Efficient Blue Electroluminescence Based on Thermally Activated Delayed Fluorescence. *Nat. Mater.* **2015**, *14*, 330-336.

(2) Uoyama, H.; Goushi, K.; Shizu, K.; Nomura, H.; Adachi, C. Highly Efficient Organic Light-Emitting Diodes from Delayed Fluorescence. *Nature* **2012**, *492*, 234-238.

(3) Dias, F. B.; Bourdakos, K. N.; Jankus, V.; Moss, K. C.; Kamtekar, K. T.; Bhalla, V.; Santos, J.; Bryce, M. R.; Monkman, A. P. Triplet Harvesting with 100% Efficiency by Way of Thermally Activated Delayed Fluorescence in Charge Transfer OLED Emitters. *Adv. Mater.* **2013**, *25*, 3707-3714.

(4) Liu, Y.; Li, C.; Ren, Z.; Yan, S.; Bryce, M. R. All-Organic Thermally Activated Delayed Fluorescence Materials for Organic Light-Emitting Diodes. *Nat. Rev. Mater.* **2018**, *3*, 18020.

(5) Samanta, P. K.; Kim, D.; Coropceanu, V.; Brédas, J. L. Up-Conversion Intersystem Crossing Rates in Organic Emitters for Thermally Activated Delayed Fluorescence: Impact of the Nature of Singlet vs Triplet Excited States. *J. Am. Chem. Soc.* **2017**, *139*, 4042-4051.

(6) Tao, Y.; Yuan, K.; Chen, T.; Xu, P.; Li, H.; Chen, R.; Zheng, C.; Zhang, L.; Huang, W. Thermally Activated Delayed Fluorescence Materials towards the Breakthrough of Organoelectronics. *Adv. Mater.* **2014**, *26*, 7931-7958.

(7) Kaji, H.; Suzuki, H.; Fukushima, T.; Shizu, K.; Suzuki, K.; Kubo, S.; Komino, T.; Oiwa, H.; Suzuki, F.; Wakamiya, A.; et al. Purely Organic Electroluminescent Material Realizing 100% Conversion from Electricity to Light. *Nat. Commun.* **2015**, *6*, 8476.

(8) Chan, C. Y.; Tanaka, M.; Nakanotani, H.; Adachi, C. Efficient and Stable Sky-Blue Delayed Fluorescence Organic Light-Emitting Diodes with CIE y below 0.4. *Nat. Commun.* **2018**, *9*, 5036.

(9) Cui, L.-S.; Deng, Y.-L.; Tsang, D. P.-K.; Jiang, Z.-Q.; Zhang, Q.; Liao, L.-S.; Adachi, C. Blue OLEDs: Controlling Synergistic Oxidation Processes for Efficient and Stable Blue Thermally Activated Delayed Fluorescence Devices (Adv. Mater. 35/2016). *Adv. Mater.* **2016**, *28*, 7807-7807.

(10) Cui, L. S.; Ruan, S. Bin; Bencheikh, F.; Nagata, R.; Zhang, L.; Inada, K.; Nakanotani, H.; Liao, L. S.; Adachi, C. Long-Lived Efficient Delayed Fluorescence Organic Light-Emitting Diodes Using n-Type Hosts. *Nat. Commun.* **2017**, *8*, 2250.

(11) Jeon, S. K.; Lee, H. L.; Yook, K. S.; Lee, J. Y. Recent Progress of the Lifetime of Organic Light-Emitting Diodes Based on Thermally Activated Delayed Fluorescent Material. *Adv.*

Mater. **2019**, 1803524.

(12) Youn Lee, S.; Yasuda, T.; Nomura, H.; Adachi, C. High-Efficiency Organic Light-Emitting Diodes Utilizing Thermally Activated Delayed Fluorescence from Triazine-Based Donor-Acceptor Hybrid Molecules. *Appl. Phys. Lett.* **2012**, *101* , 093306.

(13) Noda, H.; Nakanotani, H.; Adachi, C. Excited State Engineering for Efficient Reverse Intersystem Crossing. *Sci. Adv.* **2018**, *4*, eaao6910.

(14) Nakanotani, H.; Masui, K.; Nishide, J.; Shibata, T.; Adachi, C. Promising Operational Stability of High-Efficiency Organic Light-Emitting Diodes Based on Thermally Activated Delayed Fluorescence. *Sci. Rep.* **2013**, *3*, 2127.

(15) Inoue, M.; Serevičius, T.; Nakanotani, H.; Yoshida, K.; Matsushima, T.; Juršenas, S.; Adachi, C. Effect of Reverse Intersystem Crossing Rate to Suppress Efficiency Roll-off in Organic Light-Emitting Diodes with Thermally Activated Delayed Fluorescence Emitters. *Chem. Phys. Lett.* **2016**, *644*, 62-67.

(16) Jankus, V.; Data, P.; Graves, D.; McGuinness, C.; Santos, J.; Bryce, M. R.; Dias, F. B.; Monkman, A. P. Highly Efficient TADF OLEDs: How the Emitter-Host Interaction Controls Both the Excited State Species and Electrical Properties of the Devices to Achieve Near 100% Triplet Harvesting and High Efficiency. *Adv. Funct. Mater.* **2014**, *24*, 6178-6186.

(17) Masui, K.; Nakanotani, H.; Adachi, C. Analysis of Exciton Annihilation in High-Efficiency Sky-Blue Organic Light-Emitting Diodes with Thermally Activated Delayed Fluorescence. *Org. Electron. physics, Mater. Appl.* **2013**, *14*, 2721-2726.

(18) Serevičius, T.; Bučiūnas, T.; Bucevičius, J.; Dodonova, J.; Tumkevičius, S.; Kazlauskas, K.; Juršėnas, S. Room Temperature Phosphorescence vs. Thermally Activated Delayed Fluorescence in Carbazole-Pyrimidine Cored Compounds. *J. Mater. Chem. C* **2018**, *6*, 11128-11136.

(19) Yang, Z.; Mao, Z.; Xie, Z.; Zhang, Y.; Liu, S.; Zhao, J.; Xu, J.; Chi, Z.; Aldred, M. P. Recent Advances in Organic Thermally Activated Delayed Fluorescence Materials. *Chem. Soc. Rev.* **2017**,*46*, 915-1016.

(20) Chen, X. K.; Tsuchiya, Y.; Ishikawa, Y.; Zhong, C.; Adachi, C.; Brédas, J. L. A New Design Strategy for Efficient Thermally Activated Delayed Fluorescence Organic Emitters: From Twisted to Planar Structures. *Adv. Mater.* **2017**, *29*, 1702767.

(21) Vázquez, R. J.; Kim, H.; Zimmerman, P. M.; Goodson, T. Using Ultra-Fast Spectroscopy to Probe the Excited State Dynamics of a Reported Highly Efficient Thermally Activated Delayed Fluorescence Chromophore. *J. Mater. Chem. C* **2019**, *7*, 4210–4221.

(22) Notsuka, N.; Nakanotani, H.; Noda, H.; Goushi, K.; Adachi, C. Observation of Nonradiative Deactivation Behavior from Singlet and Triplet States of Thermally Activated Delayed Fluorescence Emitters in Solution. *J. Phys. Chem. Lett.* **2020**, 562–566.

(23) Grewer, C.; Brauer, H.-D. Mechanism of the Triplet-State Quenching by Molecular Oxygen in Solution. *J. Phys. Chem.* **1994**, *98*, 4230-4235.

(24) Schweitzer, C.; Schmidt, R. Physical Mechanisms of Generation and Deactivation of

Singlet Oxygen. *Chem. Rev.* **2007**, *103*, 1685-1758.

(25) Scurlock, R. D.; Wang, B.; Ogilby, P. R.; Sheats, J. R.; Clough, R. L. Singlet Oxygen as a Reactive Intermediate in the Photodegradation of an Electroluminescent Polymer. *J. Am. Chem. Soc.* **1995**, *117*, 10194-10202.

(26) Kuang, Z.; He, G.; Song, H.; Wang, X.; Hu, Z.; Sun, H.; Wan, Y.; Guo, Q.; Xia, A. Conformational Relaxation and Thermally Activated Delayed Fluorescence in Anthraquinone-Based Intramolecular Charge-Transfer Compound. *J. Phys. Chem. C* **2018**, *122*, 3727-3737.

(27) Whittemore, T. J.; White, T. A.; Turro, C. New Ligand Design Provides Delocalization and Promotes Strong Absorption throughout the Visible Region in a Ru(II) Complex. *J. Am. Chem. Soc.* **2018**, *140*, 229-234.

(28) Peng, J.; Guo, X.; Jiang, X.; Zhao, D.; Ma, Y. Developing Efficient Heavy-Atom-Free Photosensitizers Applicable to TTA Upconversion in Polymer Films. *Chem. Sci.* **2016**, *7*, 1233-1237.

(29) Varnavski, O.; Goodson, T.; Sukhomlinova, L.; Twieg, R. Ultrafast Exciton Dynamics in a Branched Molecule Investigated by Time-Resolved Fluorescence, Transient Absorption, and Three-Pulse Photon Echo Peak Shift Measurements. *J. Phys. Chem. B* **2004**, *108*, 10484-10492.

(30) Kim, H.; Keller, B.; Ho-Wu, R.; Abeyasinghe, N.; Vázquez, R. J.; Goodson, T.; Zimmerman, P. M. Enacting Two-Electron Transfer from a Double-Triplet State of Intramolecular Singlet Fission. *J. Am. Chem. Soc.* **2018**, *140*, 7760-7763.

(31) Madu, I. K.; Muller, E. W.; Kim, H.; Shaw, J.; Burney-Allen, A. A.; Zimmerman, P.; Jeffries-El, M.; Goodson, T. Heteroatom and Side Chain Effects on the Optical and Photophysical Properties: Ultrafast and Nonlinear Spectroscopy of New Naphtho[1,2-b:5,6- B′]Difuran Donor Polymers. *J. Phys. Chem. C* **2018**, *122*, 17049-17066.

(32) Flynn, D. C.; Ramakrishna, G.; Yang, H. B.; Northrop, B. H.; Stang, P. J.; Goodson, T. Ultrafast Optical Excitations in Supramolecular Metallacycles with Charge Transfer Properties. *J. Am. Chem. Soc.* **2010**, *132*, 1348-1358.

(33) Ramakrishna, G.; Goodson, T.; Joy, E. R. H.; Cooper, T. M.; McLean, D. G.; Urbas, A. Ultrafast Intersystem Crossing: Excited State Dynamics of Platinum Acetylide Complexes. *J. Phys. Chem. C* **2009**, *113*, 1060-1066.

(34) Ramakrishna, G.; Bhaskar, A.; Goodson, T. Ultrafast Excited State Relaxation Dynamics of Branched Donor-Pi-Acceptor Chromophore: Evidence of a Charge-Delocalized State. *J. Phys. Chem. B* **2006**, *110*, 20872-20878.

(35) Tang, K. C.; Liu, K. L.; Chen, I. C. Rapid Intersystem Crossing in Highly Phosphorescent Iridium Complexes. *Chem. Phys. Lett.* **2004**, *386*, 437-441.

(36) Bergmann, L.; Hedley, G. J.; Baumann, T.; Bräse, S.; Samuel, I. D. W. Direct Observation of Intersystem Crossing in a Thermally Activated Delayed Fluorescence Copper Complex in the Solid State. *Sci. Adv.* **2016**, *2*, e1500889.

(37) Keller, B.; Cai, Z.; Muthike, A. K.; Sahu, P. K.; Kim, H.; Eshun, A.; Zimmerman, P. M.; Zhang, D.; Goodson, T. Investigating the Optical Properties of Thiophene Additions to S-

Indacene Donors with Diketopyrrolopyrrole, Isoindigo, and Thienothiophene Acceptors. *J. Phys. Chem. C* **2018**, *122*, 27713-27733.

(38) Hosokai, T.; Matsuzaki, H.; Nakanotani, H.; Tokumaru, K.; Tsutsui, T.; Furube, A.; Nasu, K.; Nomura, H.; Yahiro, M.; Adachi, C. Evidence and Mechanism of Efficient Thermally Activated Delayed Fluorescence Promoted by Delocalized Excited States. *Sci. Adv.* **2017**, *3*, e1603282.

(39) McLean, A. J.; McGarvey, D. J.; Truscott, T. G.; Lambert, C. R.; Land, E. J. Effect of Oxygen-Enhanced Intersystem Crossing on the Observed Efficiency of Formation of Singlet Oxygen. *J. Chem. Soc. Faraday Trans.* **1990**, *86*, 3075.

(40) Kang, Y. J.; Yun, J. H.; Han, S. H.; Lee, J. Y. Benzofuroacridine and Benzothienoacridine as New Donor Moieties for Emission Color Management of Thermally Activated Delayed Fluorescent Emitters. *J. Mater. Chem. C* **2019**, *7*, 4573-4580

(41) Adachi, C. Third-Generation Organic Electroluminescence Materials. *Jpn. J. Appl. Phys.* **2014**, *53*, 060101.

(42) Ishimatsu, R.; Matsunami, S.; Shizu, K.; Adachi, C.; Nakano, K.; Imato, T. Solvent Effect on Thermally Activated Delayed Fluorescence by 1,2,3,5-Tetrakis(Carbazol-9-Yl)-4,6-Dicyanobenzene. *J. Phys. Chem. A* **2013**, *117*, 5607-5612.

6.6 Supporting Information

6.6.1 Materials: The BCC-TPTA chromophore was purchased from Luminescence Technology Corporation. The BFAcTr, BTAcTr, and BFAcPN systems were synthesized according to the literature.[1]

6.6.2 Sample Preparation and Experimental Sample Handling: A stock solution (10^{-4} M) were prepared by mixing each sample in the corresponding solvent. Toluene or chloroform were the solvents for all of the investigated samples. Consequent dilutions from the stock solutions were made on each sample to run the different experiments conducted in this report. A 400 nm excitation wavelength was used in all experimental set-ups and for all the chromophores while their emissive lifetime were measured at their respective emissive λ_{MAX}. In all, emission quenching from purging out oxygen is carried out. Specifically, the oxygen free atmosphere was created by bubbling N_2 thought the solution for at least 8 minutes. The 8 minutes criteria was based on the reproducibility of the emission spectrum intensity, quantum yield, and emissive lifetime characterization of the investigated systems.

6.6.3 Steady State Measurements: The absorption spectra were measured on an Agilent 8341 spectrophotometer while the emission spectra were collected on a Fluoromax-4 fluorimeter with slits set at 2.5 nm and an integration time of 0.100 s. Quartz cells with 10 mm path length were used for all the steady-state measurements, including the quantum yield calculations. All steady state optical measurements were carried out at ambient conditions unless otherwise stated in the figure caption. The low temperature emission (phosphorescence) spectrum were obtained by using a Photon Technologies International (PTI), QuantaMaster 400 scanning spectrofluorometer. The emission spectrum of the samples at low temperature (77K) were obtained after a delay > 300 μs between the excitation beam and detection.

6.6.4 Fluorescence Quantum Yield Calculation: The Williams comparative method was used to calculate the fluorescence quantum yields of the systems as described elsewhere.[2–4] The optical density was maintained around 0.10 or below to avoid reabsorption and internal filter effects in the measurements. The absorption and fluorescence were measured for at least four

samples with systematic decreasing concentrations. The quantum yield was calculated using the following equation:

$$\phi_x = \phi_{STD} \frac{Grad_x \eta_x^2}{Grad_{STD}\, \eta_{STD}^2}$$

were Φ_x is the calculated quantum yield, η is the refractive index of the solvent, and $Grad$ is the slope obtained from plotting the fluorescence area vs the optical density (OD). The quantum yields for BFAcTr, BTAcTr, and BFAcPN were measured in toluene and chloroform solutions using BCC-TPTA (57 %)[3,5] dissolved in toluene as the standard. The same is true for the Φ_x measurements at oxygen free atmospheres. N_2 bubbling was the method to remove oxygen from the solution (12 minutes). The emission spectra were collected on a Fluoromax-4 fluorimeter with slits set at 1.5 nm and an integration time of 0.100 s. Quartz cells with 10 mm path lengths were used for all the steady-state measurements. All optical measurements were carried out at STP.

6.6.5 Masui method for the indirect k_{rISC} calculation: The rate of reverse intersystem crossing (k_{rISC}) was calculated followed by the equation:

$$k_{rISC} = \frac{k_p k_d \phi_{TADF}}{k_{ISC} \phi_F}$$

were ϕ_F is the quantum yield at oxygen rich atmospheres, ϕ_{TADF} is the delayed fluorescence quantum yield ($\phi_{OxygenFree} - \phi_F$), k_p is the rate of fluorescence (1/fluorescence lifetime), k_d the rate of delayed fluorescence (1/DF lifetime), and k_{ISC} is the rate of intersystem crossing ($(1- \phi_F)*k_p$).[6]

6.6.6 Time-Resolved Fluorescence and Phosphorescence Measurements: The time-correlated single photon counting (TCSPC) technique was used to measure the time-resolved fluorescence and phosphorescence of the investigated systems. The laser used for the TCSPC measurement was a Kapteyn Murnane (KM) mode-locked Ti-sapphire laser with a beam at 800 nm wavelength, with a pulse duration of ~30 fs. The output beam was frequency-doubled using a nonlinear barium borate (BBO) crystal to obtain a 400 nm beam as the excitation beam and a polarizer was used to vary the power of the excitation beam. The excitation light was focused on the sample cell using a lens of focal length 11.5 cm. Collection of fluorescence was done in a perpendicular direction of the excitation source. The incident fluorescence beam is focused into a monochromator, and the output from the monochromator was coupled to a photomultiplier tube, which convert the photons into counts.

6.6.7 Nanosecond Transient Absorption Spectroscopy Measurements: The absorption and lifetime of the emissive and non-emissive transient species can be fully characterized by using this transient absorption spectroscopy technique, which has been previously described.[3,7] These measurements were done in dilute solutions and in the same solvent in which the other photophysical characterizations were carried out, unless otherwise described in the caption. A LP980 (Edinburgh) system, which contains the PMT(PMT-LP), was coupled with a Spectra-Physics QuantaRay Nd:YAG nanosecond pulsed laser and a GWU Optical Parameter Oscillator (OPO) tunable from 250 nm to 2600 nm for the excitation source. For this investigation, a 350nm and 415 nm excitation was used to pump the molecules to the excited state and a pulsed xenon lamp (300-800 nm) white light continuum source was used for probing the excited state.

6.6.8 Quantum Chemical Simulation:

The rate of reverse intersystem crossing (k_{rISC}) can be calculated via Fermi's Golden rule,[8,9]

$$k_{\mathrm{rISC}} = \frac{2\pi}{\hbar}\rho_{FC}|\langle S|H_{\mathrm{SO}}|T\rangle|^2$$

where $\langle S|H_{SO}|T\rangle$ is the spin−orbit coupling element between singlet (S) and triplet (T), ρ_{FC} denotes the Franck−Condon−weighted density of states, and $\hbar$ is the reduced Planck constant of 6.582×10^{-16} eVs. The Franck−Condon−weighted density of states is evaluated with Marcus−Levich−Jortner theory,[10,11]

$$\rho_{\mathrm{FC}} = \frac{1}{\sqrt{4\pi\lambda_{\mathrm{M}}k_BT}}\sum_{n=0}^{\infty}\exp(-S)\frac{S^n}{n!}\exp[-\frac{(\Delta E_{\mathrm{ST}} + n\hbar\omega_{\mathrm{eff}} + \lambda_{\mathrm{M}})^2}{4\pi\lambda_{\mathrm{M}}k_BT}]$$

where λ_{M} is the Marcus reorganization energy associated with the intermolecular and intramolecular low−frequency vibrations, k_{B} is for Boltzmann constant of 8.6173×10^{-5} eV/K, T is the temperature (in this study, room temperature of 298.15 K), $\hbar\omega_{\mathrm{eff}}$ represents the effective energy of a mode representing the nonclassical high−frequency intramolecular vibrations. Huang−Rhys factor associated with these modes are given as S. ΔE_{ST} indicates singlet-triplet energy gap which can be calculated as $E[T]$-$E[S]$ for rISC processes. One recent computational study on TADF mechanism discussed the rate of rISC within the same framework used in this work.[12] They computed the contribution of nonclassical intramolecular vibrations, and estimated the Marcus reorganization energy due to low−frequency intramolecular vibrations and the medium−induced relaxation effects to be in the range of ~0.1—0.2 eV.[11,13] The approximation setting λ_{M} to 0.1 or

0.2 eV reproduced available experimental k_{rISC} values on the same order of magnitude. The close examination revealed that use λ_M value of 0.2 eV gave better quantitative agreement with the available experimental k_{rISC} data. Therefore, λ_M value was set to 0.2 eV in this study. In addition, they assumed the Huang−Rhys factors can be neglected without significant changes to the results for large molecules. With these conditions, the k_{rISC} values could be estimated with quantum chemically computed ΔE_{ST} and H_{SO}.

Quantum chemical simulations were performed to understand the k_{rISC} of three chromophores. The ground state geometries were determined using density functional theory (DFT). The range-separated functional, ωB97X-D, was employed with 6-31G* basis sets. The first singlet excited state (S_1) geometries were located with time-dependent DFT (TDDFT). The same functional and the basis sets employed in the ground state geometry optimization were used. The computational benchmark study reported by H. Sun, C. Zhong, and J.-L. Brédas showed that vertical singlet-triplet energy gaps obtained from nonempirically tuned range-separated functionals are highly reliable.[14] The range-split parameter ω is tuned to minimize the square sum of the difference between HOMO energy (ϵ_{HOMO}) and ionization potential (IP), and LUMO energy (ϵ_{LUMO}) and electron affinity (EA), $(\epsilon_{HOMO}+IP)^2+(\epsilon_{LUMO}+EA)^2$. It is reported that the ω value is significantly affected by the environment such as the inclusion of solvent dielectric field effect.[15] The optimal values of ω are given as 0.008, 0.008, and 0.010 for BTAcTr, BFAcTr, and BFAcPN, respectively, when solvent (chloroform, dielectric constant of 4.31) is included using a polarizable continuum model. The nonempirically tuned ωB97X-D, ω^*B97X-D, was employed to predict vertical excitation energies and spin-orbit coupling element between singlets and triplets at the S_1 geometries. For spin-orbit coupling element calculations, the one-electron Breit-Pauli Hamiltonian was used. All quantum chemical simulations were performed with Q-Chem 5.0.

Table 6.6.1. Rate of rISC determined by quantum chemical simulations (QCS).

Chromophore	k_{rISC} 10^5 s^{-1} (QCS)
2CzPN	0.12 [5]
BFAcPN	1.87
4CzPN	n/a
4CzIPN	49.2[5]
BFAcTr	8.32
BTAcTr	11.6
BCC-TPTA	69 [25]

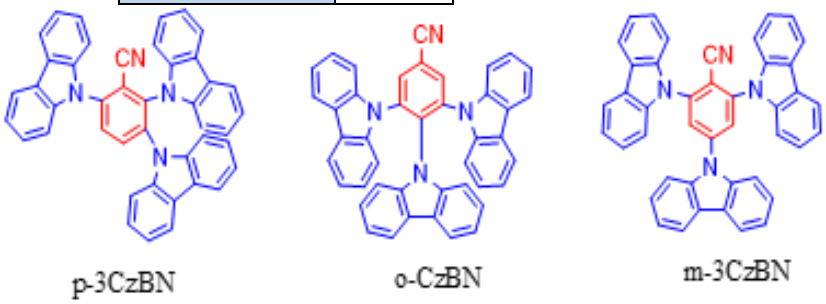

p-3CzBN o-CzBN m-3CzBN

Figure 6.6.1. Molecular structure of the TADF-inactive chromophores.

Table 6.6.2. Rate of rISC comparison for the TADF-inactive chromophores

Chromophore	Φ_{TADF} (PhMe/ACN)	k_{rISC} 10^5 s^{-1} (OS-TAS) (PhMe)	k_{rISC} 10^5 s^{-1} (Masui) (PhMe/ACN)	EQE_{MAX}
O-3CzBN	10[16]/21[17]	0.066	0 [16,17] /0.30 [17]	4.5 [16]
M-3CzBN	2[16]/18[17]	0.00512	0 [16,17]/0.064 [17]	3.1[16]
P-3CzBN	4[16]/25[17]	0.0114	0.120[16,17]/ 0.20 [17]	4.5 [16]

Table 6.6.3. Rate of rISC correlation with the efficiency roll–off of the TADF-active chromophores in chloroform. The device performances were compared under similar device architectures. The parenthesis values indicates the percentage of device degradation (efficiency roll-off) at a higher operating voltage

Chromophore	k_{rISC} 10^5 s^{-1} (TAS)	η_{EQE} roll-off (%)
2CzPN	0.22	9/4.0[18] (55%)
BCC-TPTA	7.2	16.8/5[5,19] (76%)
BTAcTr	4.6	21/20[1] (5%)
BFAcTr	0.98	20.4/17[1] (15%)
BFAcPN	(n/a)	14.1/12.9 (8.5%)
4CzIPN	0.69 ($_{PhMe}$)	19.3/18 [18,20] (6.7%)
4CzPN	2.0 ($_{PhMe}$)	17.8/16 [18,20] (10%)

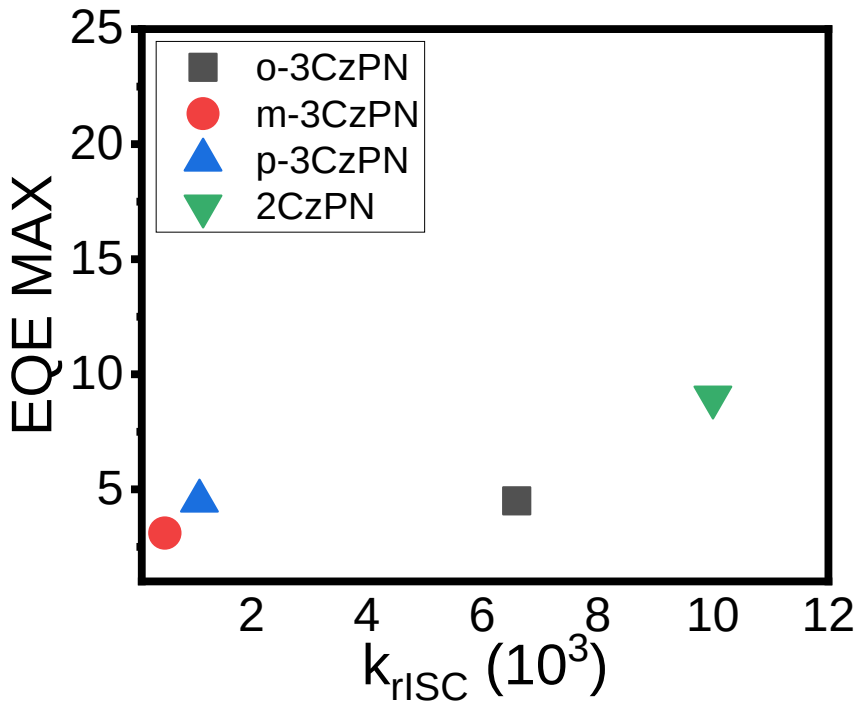

Figure 6.6.2. Close up of the TADF-inactive correlation of the device EQE with the k_{rISC} determined by our methodology.

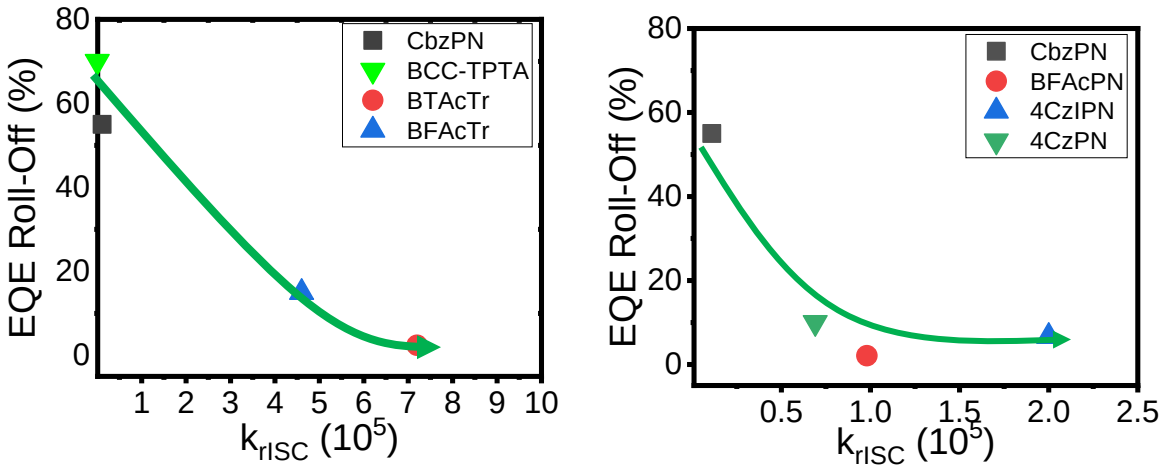

Figure 6.6.3. External quantum efficiency roll-off correlation with the k_{rISC} determined by our methodology for the TADF-active chromophores.

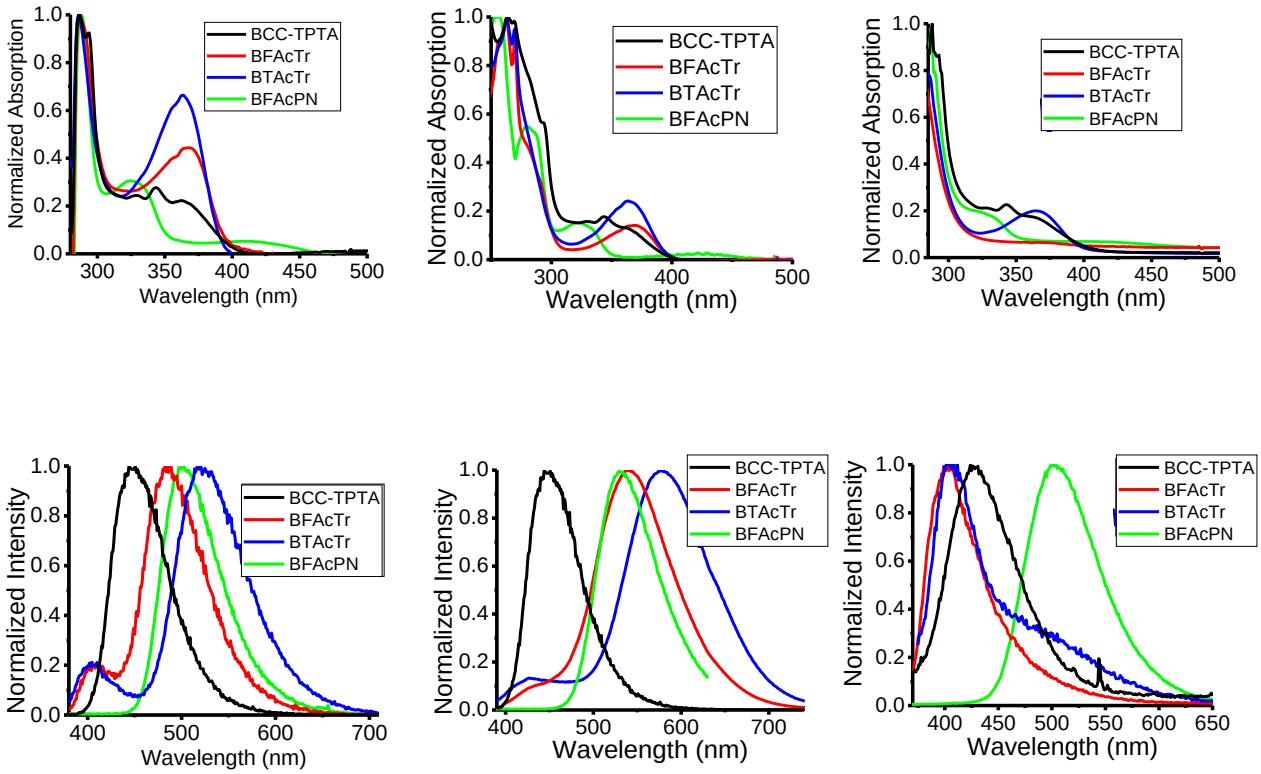

Figure 6.6.4. Steady State absorption and emission of the investigated system in Toluene (Column 1), Chloroform (Column 2), and PMMA (Column 3). Measurements were taken at ambient conditions.

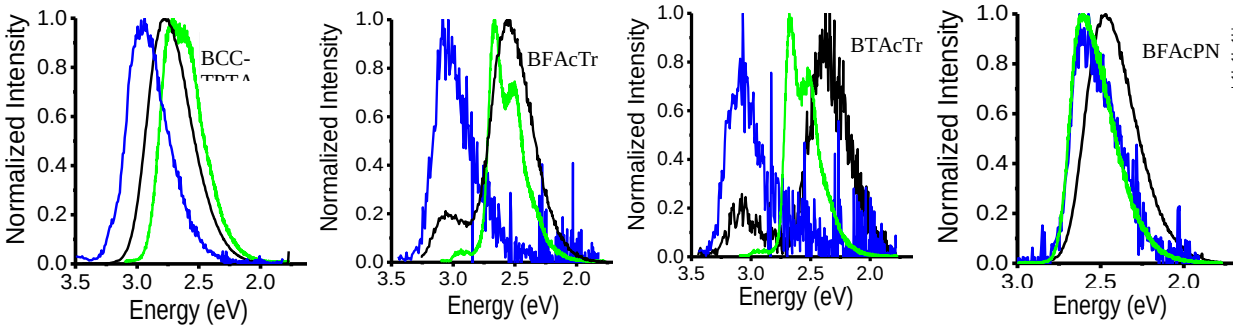

Figure 6.6.5. Fluorescence at RT (**Black**), fluorescence at 77K (**Blue**), and phosphorescence at 77K (**Green**) of the investigated chromophores in toluene solutions. The phosphorescence spectra was measured with the help of an electrical shutter with a 300 µs delayed between the excitation beam and the emission detection to avoid the fluorescence (S_1) detection.

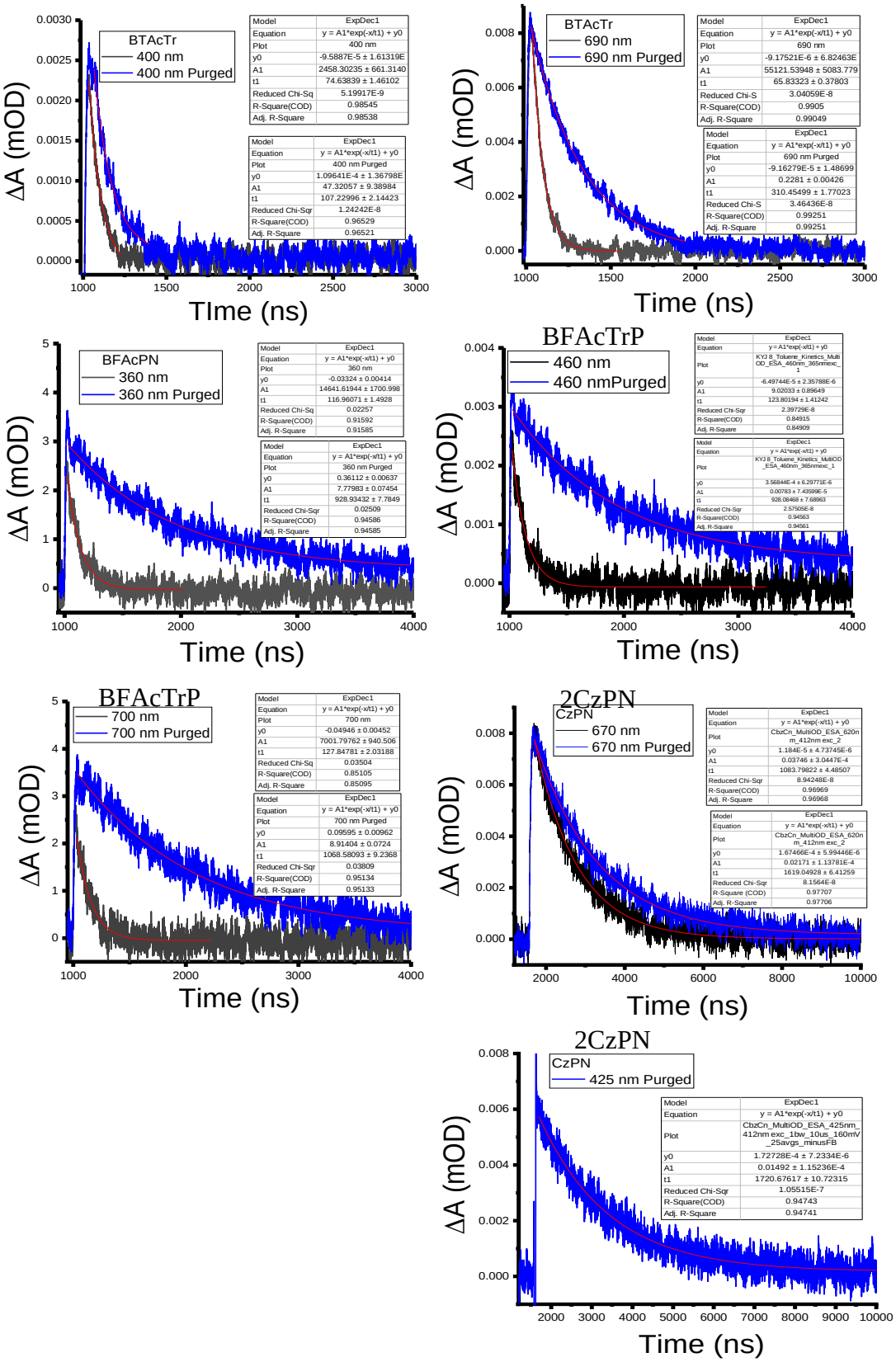

Figure 6.6.6. Fitting of the ESA decay of the investigated systems in diluted toluene solutions.

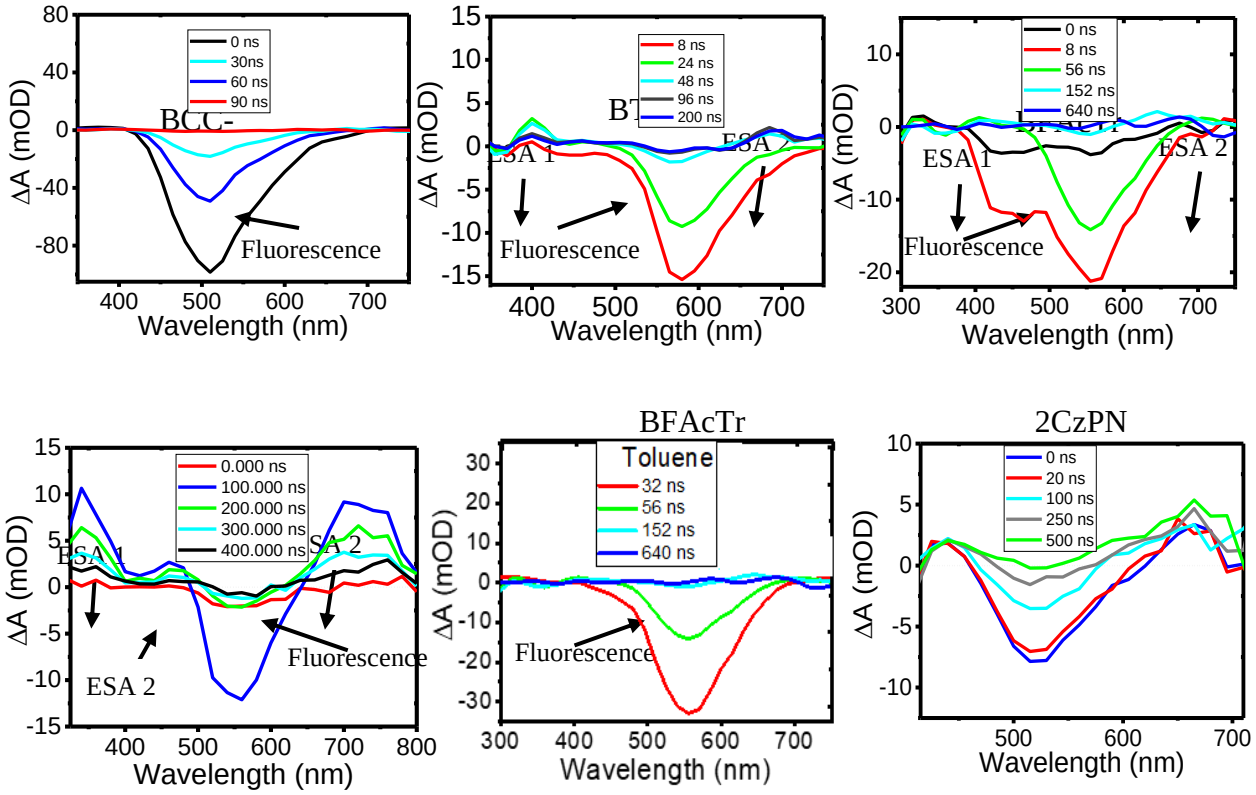

Figure 6.6.7. Time-resolved absorption spectra of the investigated system in chloroform solution unless indicated otherwise in the image.

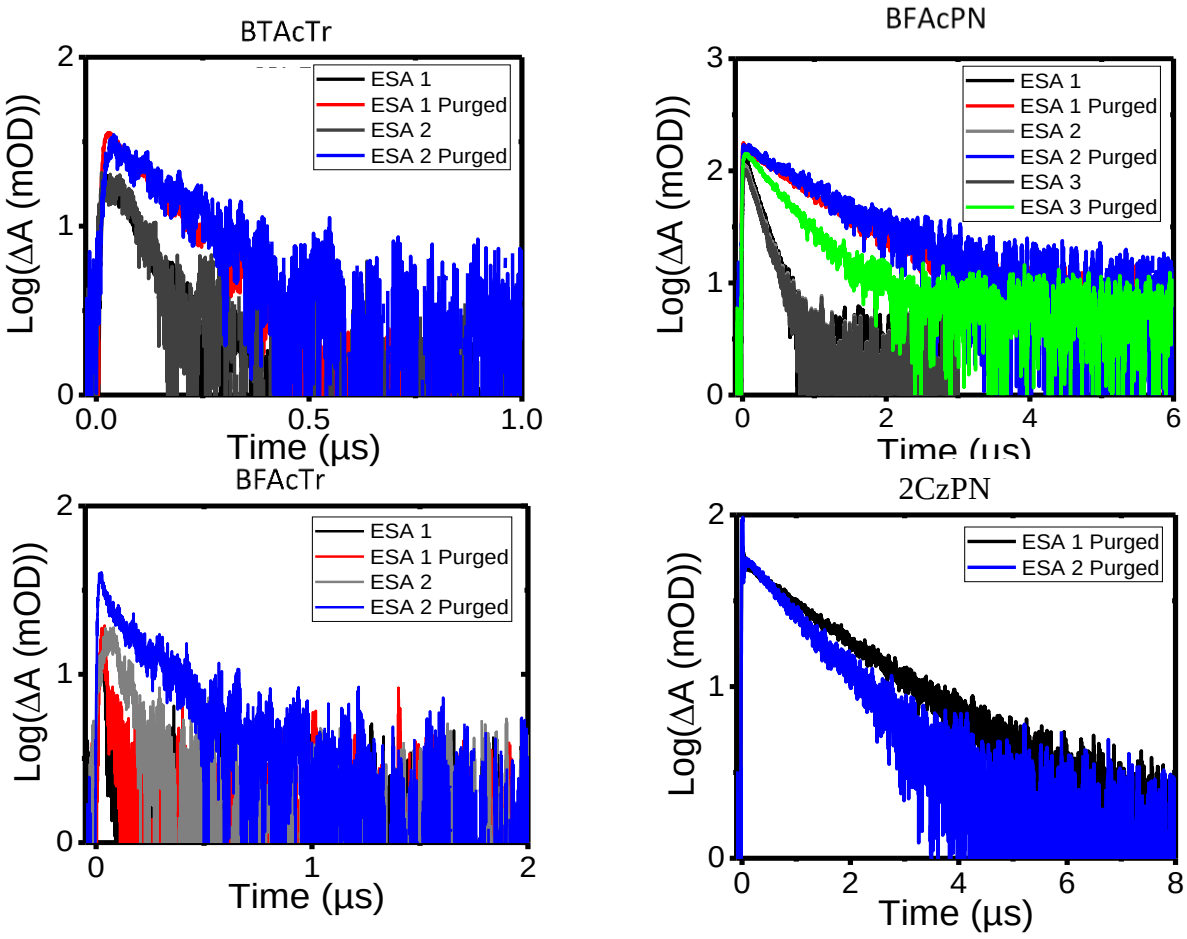

Figure 6.6.8. ESA decay dynamics of the investigated chromophores in diluted chloroform solutions.

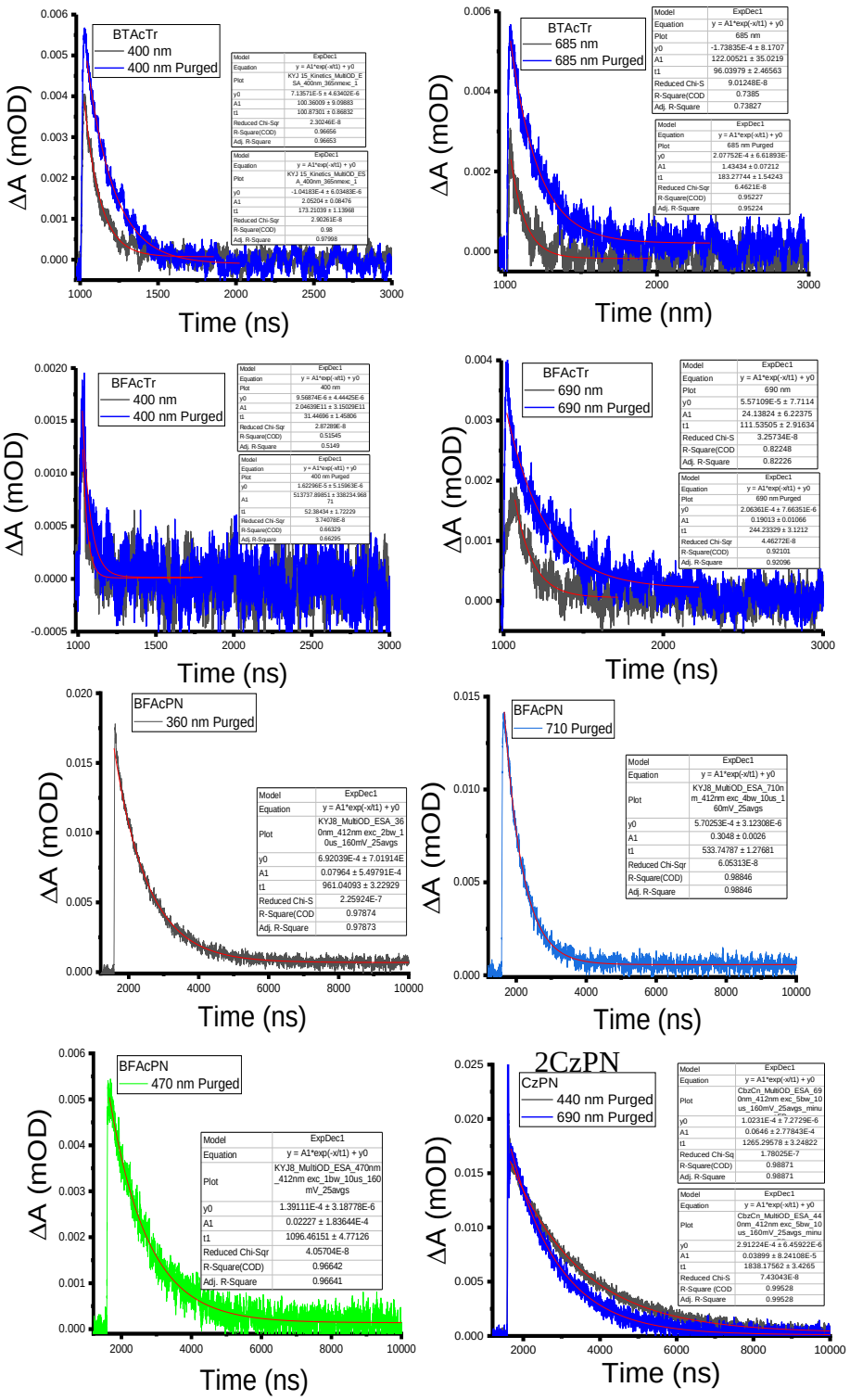

Figure 6.6.9. Fitting of the ESA decay of the investigated systems in diluted chloroform solutions.

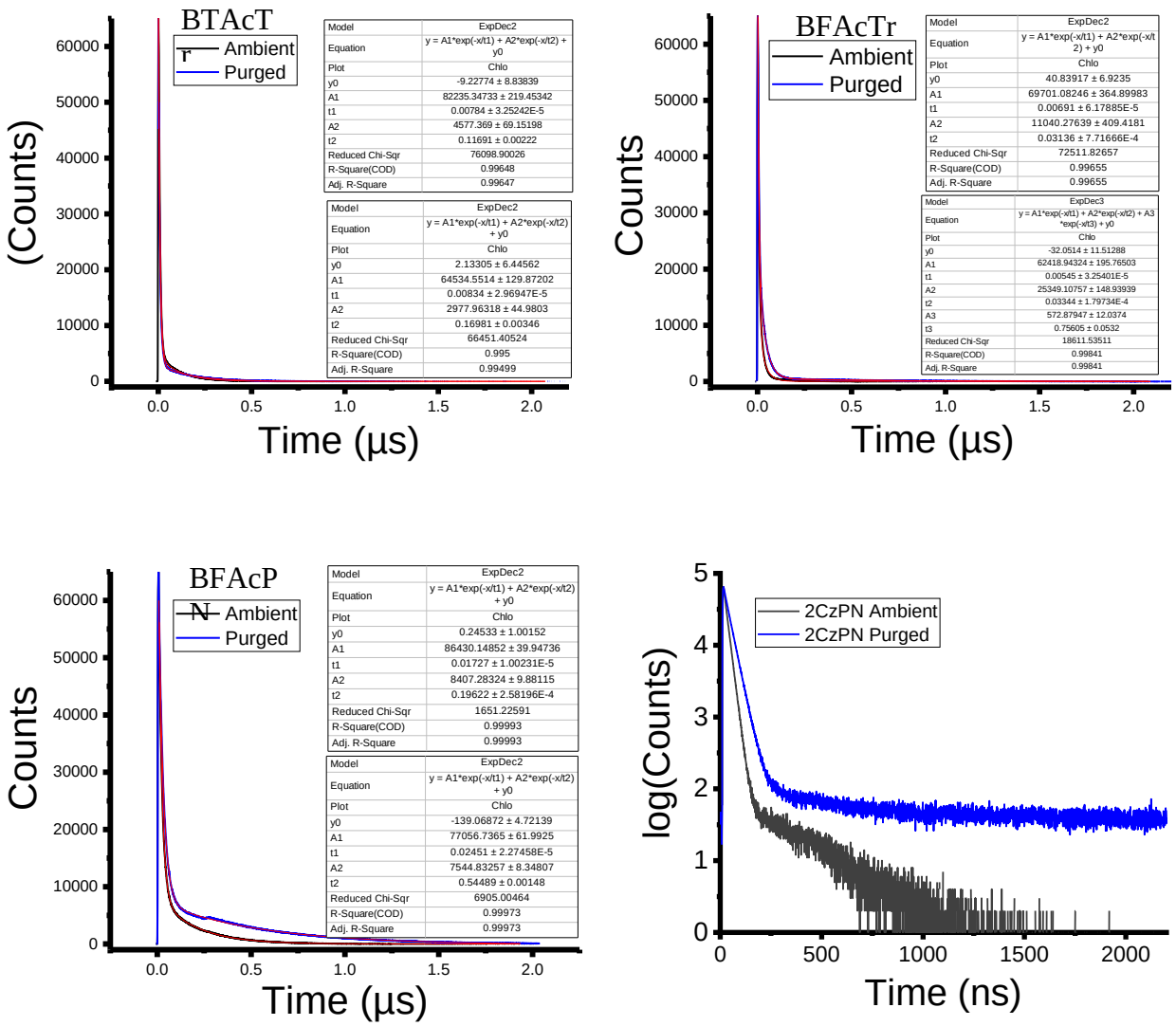

Figure 6.6.10. Emissive lifetime fitting of the investigated chromophores in diluted chloroform solutions by using the TCSPC. These measurements were done before and after the oxygen purging process.

Table 6.6.4. Emissive lifetime of the investigated chromophores measured by the time correlated single photon counting (TCSPC) technique. The ambient, purged and 77K measurements were taken in chloroform as the solvent. The rate constants were obtained by the method published by Matsui et al.[6]

Material In Chloroform	**Emissive lifetime (Ambient/Purged)**		**Emissive lifetime (iPMMA)**		**Φ (Rich/Free) (%)**	**Rate Constants** (10^7 s^{-1})				
	S_1 (ns)	**T_1 (ns)**	**S_1**	**T_1**		***K_P***	***K_R***	***k_{ISC}***	***k_{rISC}***	***K_{DF}***

BCC-TPTA	10.1/13	n/a	6.13	n/a	25/37	10	2.5	7.5	0	0
BTAcTR	7/8	116/169	11	711	1/14	8.3	0.08	8.6	7.65	0.52
BFAcTR	7/7	31/758	21	723	1.5/11.5	41	0.62	41	1.03	0.13
BFAcPN	17/24	198/544	45	850	1.6/12.4	3.3	0.05	3.2	1.45	0.18
2CzPN	21/34	100/1910	n/a	n/a	6/12	4.17	0.25	3.92	0.06	0.05

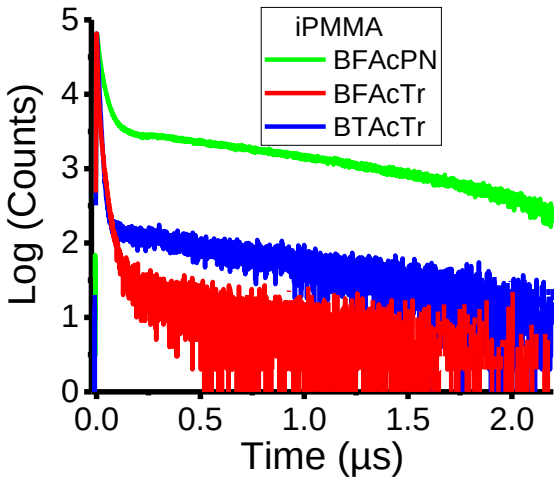

Figure 6.6.11. Emissive lifetime characteristics of the investigated chromophores in iPMMA carried out with the time correlated single photon counting (TCSPC) technique (A).

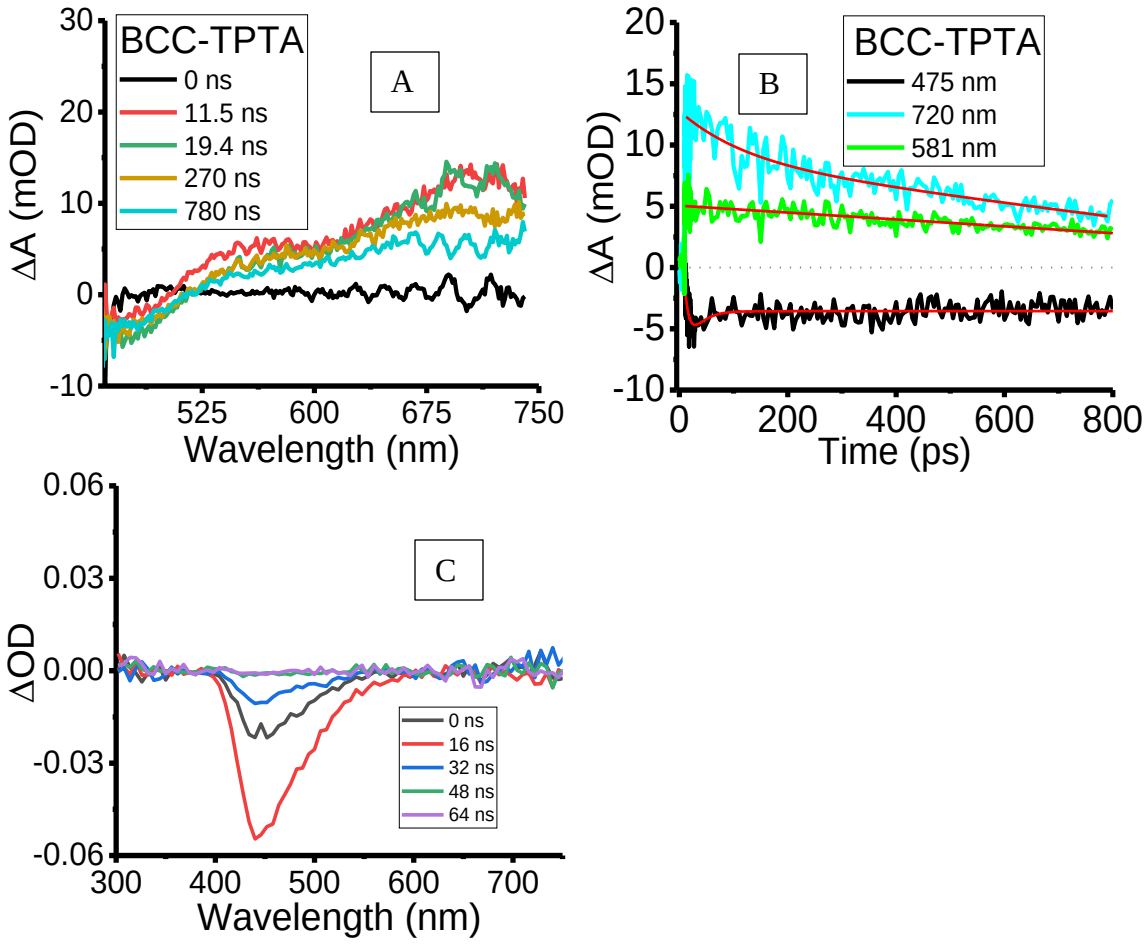

Figure 6.6.12. Time-resolved **femtosecond** transient absorption spectra of BCC-TPTA (A) and the decay relaxation of the detected signals (B). Time resolved **nanosecond** absorption spectra of BCC-TPTA (C). The data of ***Figure 6.6.12C*** is published in DOI: 10.1039/c8tc05957h.

Table 6.6.5. Spin−orbit coupling element, energy gap between S_1 and T_n (ΔE_{ST}), and rate constant of rISC process ΔE_{ST} was estimated between adjacent singlets and triplets. T_2 (T_1) state energy was used for BTAcTr and BFAcTr (BFAcPN), respectively.

	BTAcTr	BFAcTr	BFAcPN
H_{SO} (cm^{-1})	0.544	0.568	0.058
ΔE_{ST} (eV)	0.120	0.134	0.019
k_{rISC} 10^5 (s^{-1})	11.6	8.32	1.87

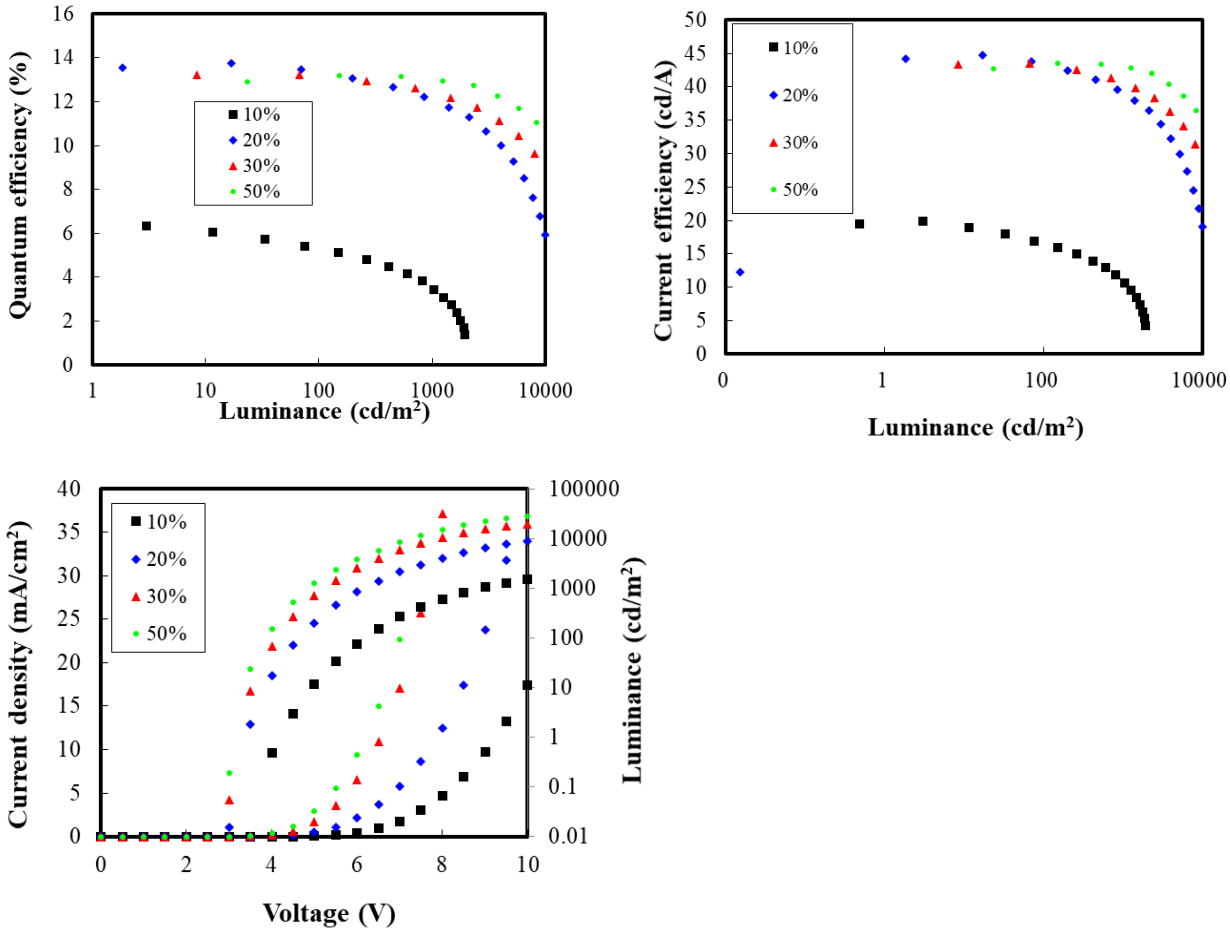

Figure 6.6.13. Device performances of the BFAcPN TADF emitter at different wt %.

Reference:

(1) Kang, Y. J.; Yun, J. H.; Han, S. H.; Lee, J. Y. Benzofuroacridine and Benzothienoacridine as New Donor Moieties for Emission Color Management of Thermally Activated Delayed Fluorescent Emitters. *J. Mater. Chem. C* 2019, *7* (15), 4573–4580. https://doi.org/10.1039/c9tc00523d.

(2) Doan, P. H.; Pitter, D. R. G.; Kocher, A.; Wilson, J. N.; Goodson, T. Two-Photon Spectroscopy as a New Sensitive Method for Determining the DNA Binding Mode of Fluorescent Nuclear Dyes. *J. Am. Chem. Soc.* 2015, *137* (29), 9198–9201. https://doi.org/10.1021/jacs.5b02674.

(3) Vázquez, R. J.; Kim, H.; Zimmerman, P. M.; Goodson, T. Using Ultra-Fast Spectroscopy to Probe the Excited State Dynamics of a Reported Highly Efficient Thermally Activated Delayed Fluorescence Chromophore. *J. Mater. Chem. C* 2019, *7* (14), 4210–4221. https://doi.org/10.1039/c8tc05957h.

(4) Vázquez, R. J.; Kim, H.; Kobilka, B. M.; Hale, B. J.; Jeffries-El, M.; Zimmerman, P.; Goodson, T. Evaluating the Effect of Heteroatoms on the Photophysical Properties of Donor-Acceptor Conjugated Polymers Based on 2,6-Di(Thiophen-2-Yl)Benzo[1,2-b:4,5-B′]Difuran: Two-Photon Cross-Section and Ultrafast Time-Resolved Spectroscopy. *J. Phys. Chem. C* 2017, *121* (27), 14382–14392. https://doi.org/10.1021/acs.jpcc.7b01767.

(5) Hirata, S.; Sakai, Y.; Masui, K.; Tanaka, H.; Lee, S. Y.; Nomura, H.; Nakamura, N.; Yasumatsu, M.; Nakanotani, H.; Zhang, Q.; et al. Highly Efficient Blue Electroluminescence Based on Thermally Activated Delayed Fluorescence. *Nat. Mater.* 2015, *14* (3), 330–336. https://doi.org/10.1038/nmat4154.

(6) Masui, K.; Nakanotani, H.; Adachi, C. Analysis of Exciton Annihilation in High-Efficiency Sky-Blue Organic Light-Emitting Diodes with Thermally Activated Delayed Fluorescence. *Org. Electron. physics, Mater. Appl.* 2013, *14* (11), 2721–2726. https://doi.org/10.1016/j.orgel.2013.07.010.

(7) Keller, B.; Cai, Z.; Muthike, A. K.; Sahu, P. K.; Kim, H.; Eshun, A.; Zimmerman, P. M.; Zhang, D.; Goodson, T. Investigating the Optical Properties of Thiophene Additions to S-Indacene Donors with Diketopyrrolopyrrole, Isoindigo, and Thienothiophene Acceptors. *J. Phys. Chem. C* 2018, *122* (48), 27713–27733. https://doi.org/10.1021/acs.jpcc.8b08567.

(8) Lawetz, V.; Orlandi, G.; Siebrand, W. Theory of Intersystem Crossing in Aromatic Hydrocarbons. *J. Chem. Phys.* 1972, *56* (8), 4058–4072. https://doi.org/10.1063/1.1677816.

(9) Robinson, G. W.; Frosch, R. P. Electronic Excitation Transfer and Relaxation. *J. Chem. Phys.* 1963, *38* (5), 1187–1203. https://doi.org/10.1063/1.1733823.

(10) Brédas, J. L.; Beljonne, D.; Coropceanu, V.; Cornil, J. Charge-Transfer and Energy-Transfer Processes in π-Conjugated Oligomers and Polymers: A Molecular Picture. *Chem. Rev.* 2004, *104* (11), 4971–5003. https://doi.org/10.1021/cr040084k.

(11) Beljonne, D.; Shuai, Z.; Pourtois, G.; Bredas, J. L. Spin-Orbit Coupling and Intersystem Crossing in Conjugated Polymers: A Configuration Interaction Description. *J. Phys. Chem. A* 2001, *105* (15), 3899–3907. https://doi.org/10.1021/jp010187w.

(12) Samanta, P. K.; Kim, D.; Coropceanu, V.; Brédas, J. L. Up-Conversion Intersystem Crossing Rates in Organic Emitters for Thermally Activated Delayed Fluorescence: Impact of the Nature of Singlet vs Triplet Excited States. *J. Am. Chem. Soc.* 2017, *139* (11), 4042–4051. https://doi.org/10.1021/jacs.6b12124.

(13) Schmidt, K.; Brovelli, S.; Coropceanu, V.; Beljonne, D.; Cornil, J.; Bazzini, C.; Caronna, T.; Tubino, R.; Meinardi, F.; Shuai, Z.; et al. Intersystem Crossing Processes in Nonplanar Aromatic Heterocyclic Molecules. *J. Phys. Chem. A* 2007, *111* (42), 10490–10499. https://doi.org/10.1021/jp075248q.

(14) Sun, H.; Zhong, C.; Brédas, J. L. Reliable Prediction with Tuned Range-Separated Functionals of the Singlet-Triplet Gap in Organic Emitters for Thermally Activated Delayed Fluorescence. *J. Chem. Theory Comput.* 2015, *11* (8), 3851–3858. https://doi.org/10.1021/acs.jctc.5b00431.

(15) Zheng, Z.; Brédas, J. L.; Coropceanu, V. Description of the Charge Transfer States at the Pentacene/C60 Interface: Combining Range-Separated Hybrid Functionals with the Polarizable Continuum Model. *J. Phys. Chem. Lett.* 2016, *7* (13), 2616–2621. https://doi.org/10.1021/acs.jpclett.6b00911.

(16) Hosokai, T.; Matsuzaki, H.; Nakanotani, H.; Tokumaru, K.; Tsutsui, T.; Furube, A.; Nasu, K.; Nomura, H.; Yahiro, M.; Adachi, C. Evidence and Mechanism of Efficient Thermally Activated Delayed Fluorescence Promoted by Delocalized Excited States. *Sci. Adv.* 2017, *3* (5), e1603282. https://doi.org/10.1126/sciadv.1603282.

(17) Hosokai, T.; Noda, H.; Nakanotani, H.; Nawata, T.; Nakayama, Y.; Matsuzaki, H.; Adachi, C. Solvent-Dependent Investigation of Carbazole Benzonitrile Derivatives: Does the LE3−CT1 Energy Gap Facilitate Thermally Activated Delayed Fluorescence? *J. Photonics Energy* 2018, *8* (03), 1. https://doi.org/10.1117/1.JPE.8.032102.

(18) Uoyama, H.; Goushi, K.; Shizu, K.; Nomura, H.; Adachi, C. Highly Efficient Organic Light-Emitting Diodes from Delayed Fluorescence. *Nature* 2012, *492* (7428), 234–238. https://doi.org/10.1038/nature11687.

(19) Jeon, S. K.; Lee, H. L.; Yook, K. S.; Lee, J. Y. Recent Progress of the Lifetime of Organic Light-Emitting Diodes Based on Thermally Activated Delayed Fluorescent Material. *Adv. Mater.* 2019, 1803524. https://doi.org/10.1002/adma.201803524.

(20) Adachi, C. Third-Generation Organic Electroluminescence Materials. *Jpn. J. Appl. Phys.* 2014, *53* (6). https://doi.org/10.7567/JJAP.53.060101

Chapter 7

Effect of Long-Lived Diradicaloids on the Photophysics of Semi-ladder Thiophene-Based Polymer Aggregates for Organic Light Emitting Transistor (OLET) Applications.

Muthike, A.K.; Awais, M.A.; Wang, C.; Orr, M.; da Silva Almeida, N.; Brookhouse, S.; Yu, L.; Wilson, A.; Goodson III, T. *J. Am. Chem. Soc. To be submitted*

7.1 Author Contribution

In this work where I have done majority of the experimental, data analysis and manuscript preparation, I would like to acknowledge Awais from Prof. Yu's group for synthesizing these compounds, Meghan Orr for helping with the femtosecond transient absorption spectroscopy data acquisition and analysis, Wang, da Silva almeida and Brookhouse in Prof. Angela Wilson's group for doing the quantum chemical calculations.

This manuscript is under preparation and will be submitted to the Journal of American Chemical Society. Therefore, some changes may be made before the submission and therefore the final manuscript may have more or less content compared to what is reported in this dissertation.

7.2 Abstract

Open-shell structures have been reported to enhance the spin density that is delocalized along the planar $\pi-$conjugation backbone and ultimately affecting their charge transfer and efficiency. These structures tend to have low-lying triplets and small singlet-triplet bandgaps which are favorable for charge and energy transfer. While diradicals have been reported to enhance the efficiency of organic light emitting diodes (OLEDs) by offering intermolecular spin-spin interactions which lead to $\sigma-$aggregation. This eventually leads to and formation of $\sigma-$polymerization which affects intermolecular stacking and charge transport which has proved to be good for OLEDs. The low bandgaps, intimate intermolecular interactions, and redox amphoterism which increase the overall efficiency of organic field effect transistors (OFETs). However, there is no report of how these diradical states affect the efficiency of organic light emitting transistors (OLETs). To the best of our knowledge, this is the first report highlighting the

formation of diradicals. We use time-resolved, linear and nonlinear optical spectroscopy to show the existence of long-lived diradical states in the thiophene-based polymer. On the other hand, the furan-based polymer shows the formation of long-lived zwitterions. We propose that the formed diradical character with a lifetime of 25 μs lowers the charge separation in the resonance structures, reducing charge transfer and negatively affecting the external quantum efficiency of the thiophene-based OLET.

7.3 Introduction

Organic light emitting transistors (OLETs), first reported in 2003, is a rising class of organic optoelectronic devices that have the unique advantage of combining the electrical switching functionality of organic field-effect transistors (OFETs) and the light generation capability of organic light emitting diodes (OLEDs) in a single device.[1–3] While the technology of OFETs and OLEDs, are the working principles of OLETs, are individually significantly developed, their working mechanisms and potential have not been exploited enough.[2–4] Scientists have seen this upside as a potential method to reduce the complicated processes towards next generation pixel circuitry.[2] Thus far, OLETs have shown magnificent potential in diverse range of applications like optical communications systems, electroluminescent displays, electrically pumped organic lasers and solid-state lighting sources.[2,5] However, the applicability of these OLETs is far from implementation due to their poor performance in terms of low brightness, low carrier mobility and high driving voltage.[6] These properties have been reported in organic semiconducting (OSC) materials that have been used as the active materials of the OLETs.

A good material for this application is supposed to show high and balanced ambipolar field effect transport charge mobilities as well as increased fluorescent quantum yield in the same material.[7] Recent reports have shown that OSC materials for these OLET devices are made of small molecules and polymers which hold the right luminescent properties, have a small bandgap is in the visible region of the electromagnetic spectra to minimize charge injection barriers, possess high, balanced and ideally ambipolar charge carrier mobility for light emission and have high shelf-life.[8] The increased interest in small molecules as potential OLET active materials is due to their molecular structure and high-mobility characteristics.[9] On the other hand, the π–bond delocalization of the polymers which leads to good photoabsorption, charge carrier photogeneration and transport makes these materials great for OLET applications. So far, the

organic semi-conducting materials that have been considered and used to engineer highly performing OLETs could be grouped into fluorenes, oligothiophenes, phenylene-vinylene-based polymers, biphenyl acenes, olygothiophenes, thiophene/phenylene co-olygomers, furan-incorporated olygomers, spirobifluorenes, phosphorescent materials, etc... Although conjugated polymers have shown a lot of promise as OLET materials, a major drawback in using these light emitting polymers is their low charge carrier mobility which limits the device performance. A lower bandgap of the conjugated polymers is preferable to enhance the intramolecular charge transfer across the main donor-acceptor main chain, with a lower-lying lowest unoccupied molecular orbital (LUMO) which is better for n-type OLETs.[10] In addition, these donor-acceptor polymers induce intermolecular interactions through increased molecular ordering resulting from the self-assembly of polymer chains, and this effect has led to high field-effect mobility in OFETs.[11]

While single-component OLETs have been successfully developed, only an EQE of 1.61% has been obtained.[12] Due to the difficulties in attaining large mobilities in a single OLET materials, multilayer devices where different functions are delegated to different materials have been developed and shown EQEs of up to 9.01%.[6] For the multi-layered devices, however, the device fabrication process becomes extremely complicated as more layers are added since it becomes very difficult to control the mutually exclusive device properties of the OSC active materials while keeping their optoelectronic performance optimal.[9] For instance, high mobility materials show efficient intermolecular charge transport owing to their optimal $\pi - \pi$ stacking and electronic coupling; the efficient $\pi - \pi$ stacking may lead to the formation of excited state dimers or other charge transfer states which quench fluorescence and reduces the performance of OLETs.[3] Therefore, it is important to find a balance between the multiple parameters that should be considered when fabricating high-performance OLET systems: suitable energy levels, optimal fluorescent quantum yields, optimal charge mobility and correct aggregation state. [7,9,10,13]

Recently, Yuan et al. synthesized semi-ladder polymer systems that not only address the above issues, but also the first of-a-kind OLET systems which exhibit a folding structure only previously observed and well-studied in biological systems.[5] Shown in **Figure 7.3.1** are the structures of two investigated polymers, as well as the thiophene-based acceptor (TPTQ Acceptor). Here, two different acceptor (A) monomers: thienopyridothienoquinoline which has a thiophene incorporated (TPTQ) and thienopyridothienoquinoline with a furan molecule incorporated

(TPTQF), each acceptor coupled to a carbazole donor (D) monomer moiety, were synthesized.[5] These $D-A-D$ polymers were synthesized based on the idea that ring fusion in ladder building blocks can enhance rigidity in the molecular system, which minimizes the non-radiative decay and thus improve fluorescence quantum yield. Interestingly, they reported that these structures can exist in their electron resonant forms as a result of their quadrupole interactions forming a $D-A^{-}-D^{+}$ structures which tend to display non-kasha spectroscopic behavior.[5,13,14] Furan derivatives have been reported to be better than thiophene derivatives in terms of solubility, increased power conversion efficiencies and formation of quinoidal structures owing to the less aromaticity in sulfur in comparison to thiophene.[1] While thiophene based molecules have been highly investigated due to their abilities to increase molecular conjugation, furan-based counterparts are seemingly promising due to their reported tendency to increase conjugation and improve the transport properties.[15] The furan-based molecules have shown enhanced performance which has been linked to their increased dipole moments due to the large electronegativity of oxygen and weak solid-state interaction between furan moieties making them highly soluble.

Additionally, Yuan et al. report that these polymers have the special ability to form foldable structures and exist in their resonant forms. [5] Before this report, it had also been reported that folding structures form ordered and helical self-assembled structures through non-covalent interactions.[5,16,17] The molecular conformation is rigidified by intramolecular hydrogen bonding, leading to strong interactions between the discs.[18] These π–conjugated compounds are believed to form a helical conformation through solvophobic interactions in polar solvents and unravel into a random coil in chloroform.[19] Moreover, quinoline structures have shown the capability of existing in their electron resonant forms while carbazole-based molecules have shown their capabilities to form zwitterions and diradicals which then affect the energy and charge transfer mechanisms of their derivatives.[20–23] Interestingly, some of these zwitterions have displayed diradical character and in other cases, photocatalyzation of different materials through proton transfer followed by electron re-organization may convert the zwitterions into diradical intermediates.[22,24]

Unfortunately, most literature reports use diradicals and biradicals interchangeably which leads to confusing and conflicting information regarding their respective photophysical properties and their effect on device performance. While both are defined by the presence of two unpaired non-bonding and degenerate electrons (radicals) in an open shell structure, the distance between the two unpaired electrons (*r*) as well as the electron exchange integral (*J*) can be used to

differentiate between these two. In the case of the biradicals, the distance between the two non-bonding electrons is so long such that the electron exchange interaction is negligible or almost zero. On the other hand, when the coupling between the two non-bonding electrons is so strong due to a large magnitude of dipole-dipole interaction in a molecule, the distance between the electrons is ideally zero and these two electrons are referred to as diradicals.[25] For nearly degenerate molecular orbitals, the terms used are diradicaloids or biradicaloids for diradicals and biradicals, respectively.

Recently, organic semiconductors that show open-shell diradical character that could be used in organic electronics like organic light emitting diodes (OLEDs), organic photovoltaics (OPVs) and organic field effect transistors (OFETs) have been demonstrated. [23,26–30] Increased diradical character has been reported to activate exothermic singlet exciton fission which increases the performance and stability of OPVs.[31] Diradical character has also been reported to affect the optical, electronic, magnetic properties as well as the chemical reactivity of organic optoelectronic materials.[32] This is due to the presence of unpaired electrons which take part in the low- to high-spin state transitions. In addition, various reports have shown the diradical effect on OFETs where they increase the stability and half-life of these optoelectronics.[33–35] In a recent review, Dong and Li mention that the ground state of these materials are highly controversial due to their high reactivity towards oxygen. To go around these stability issues, they suggested that using various substituents like mesityl on S-atom acene analogues, using bulky compounds led to the half-life of more than a month.[35] Delocalization of these radicals on the organic π-system dilets the spin density of the molecules and therefore reduces their reactivity. In another report, neutral radicals from varions open-shell molecules have been used to fabricate OLEDs with upto 10% external quantum efficiency.[29,36] (give examples) Because luminescent radicals emit from the radiative decay of doublet excitons, the theoretical internal quantum efficiency (IQE) can be upto 100%. To the best of our knowledge, no one has reported the existence of diradical character in OLET foldamers which would highly affect their energy transfer process and efficiency. Therefore, in this study, we use time-resolved and nonlinear spectroscopic techniques in a groundbreaking report that shows the formation and effect of diradicaloids on the photophysical properties of the previously synthesized carbazole-donor based foldable polymers for OLET applications. We find that thiophene-acceptor based foldamers show a diradical character with reduced dipole moments which lowers the charge separation in the resonance structures, reducing the charge transfer and

the external quantum efficiency of the TPTQ_C molecule (0.005%). However, no observed diradical character in the furan-based foldamers which exhibits superior device performance with 3.5%. Our results will be a step towards producing materials that can be used for high-performance devices.

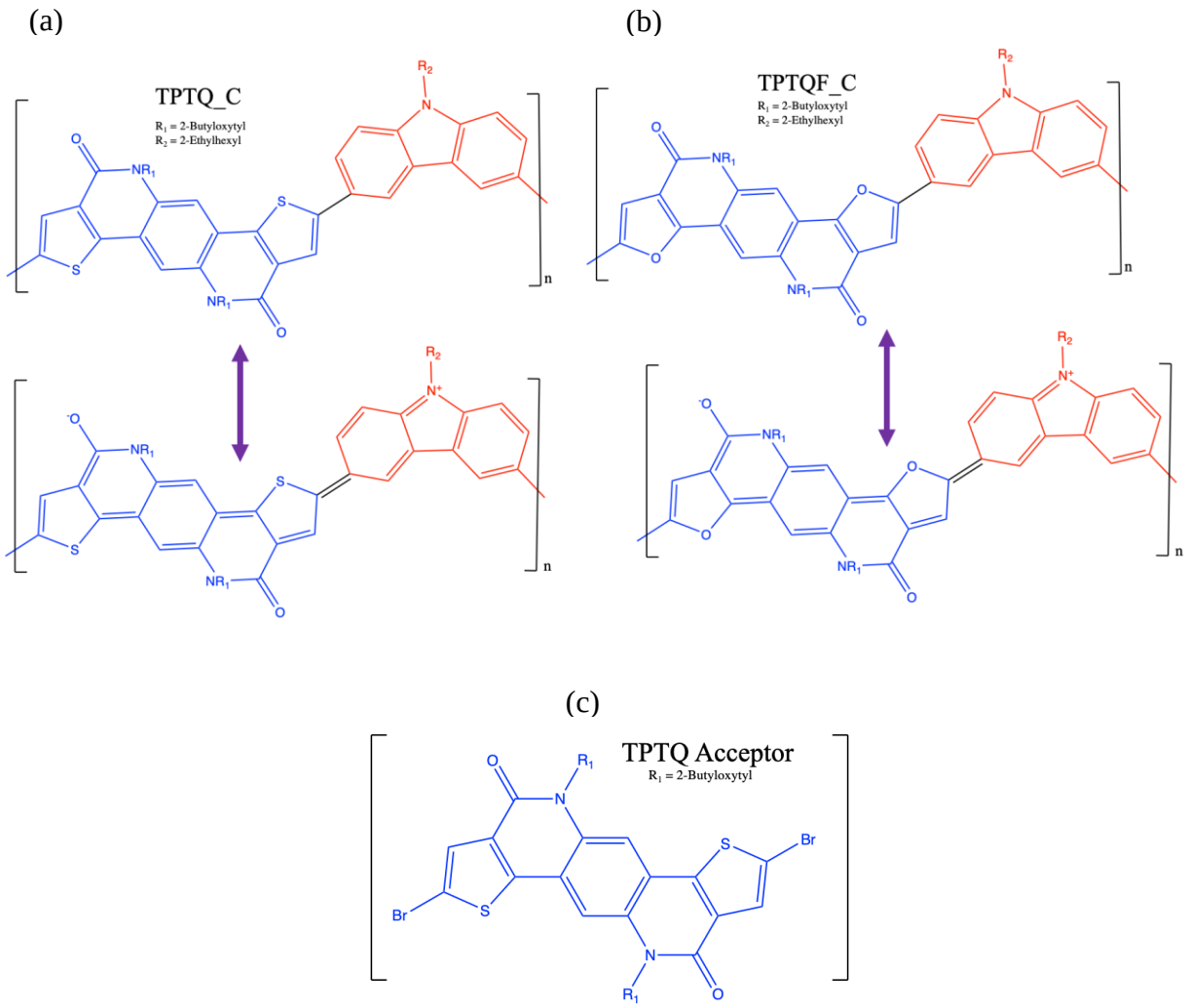

Figure 7.3.1: Structures of the investigated polymers (TPTQ_C and TPTQF_C and their respective resonant forms) as well as the TPTQ Acceptor.

7.4 Results

7.4.1 Steady State Studies

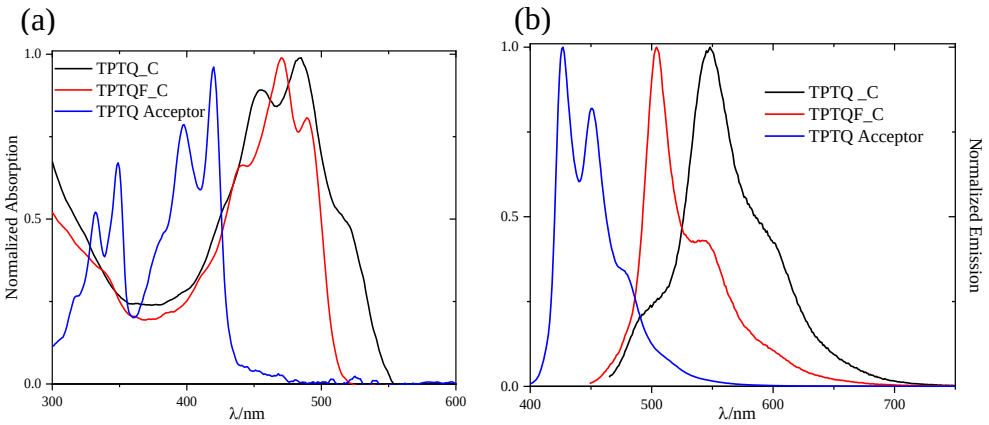

Figure 7.4.1.1: Absorption (a.) and emission (b) spectra of the two investigated polymers as well as the parent thiophene-based acceptor.

Shown in **Figure 7.4.1.1** are the steady-state absorption and emission spectra for the investigated polymers as well as that of the TPTQ acceptor. These measurements were done in chloroform and their data is summarized in **Table 7.4.1.1**. As seen in **Figure 7.4.1.1a**, both the two polymers show two distinct absorption bands which has been reported for donor-acceptor polymers. The two absorption bands for the TPTQ acceptor also show some level of charge transfer happening within the acceptor itself. In addition, the full width half max (FWHM) of the polymers' absorption spectrum (right absorption band) is significantly bigger than that of the TPTQ acceptor. This larger FWHM shows that the polymers have a better capability to harvest sunlight.[40] [The quantum chemical calculations show that TPTQ_C has a lower HOMO-LUMO bandgap (2.25 eV) compared to the TPTQF_C (2.38 eV). Incorporating the Furan in the electron-deficient material interestingly leads to higher energies of both HOMO (-5.42 eV) and LUMO (-3.04 eV). However, TPTQ_C has a slightly lower HOMO (-5.44 eV) and lower LUMO (-3.19 eV). These results indicate a better intrachain charge transfer from the donor to the acceptor of the TPTQ_C polymer.[41]]

The steady state absorption shows two absorption bands in both investigated polymers as well as the TPTQ acceptor. These bands have been associated with charge transfer from the donor to the acceptor. For the polymers, the broader absorption maxima peaks which are shifted to the red can be attributed to the highest unoccupied molecular orbital (HOMO) → lowest unoccupied molecular orbital (LUMO) transition which signifies intramolecular charge transfer between the donor and the acceptor. The slightly red-shifted absorption spectra of the TPTQ_C indicate that this polymer has a lower HOMO-LUMO bandgap and is expected to show enhanced charge

transfer capabilities compared to its furan-based TPTQF_C analogue. Interestingly, a weak low energy shoulder is very visible in the broadened absorption of the TPTQ_C molecule at 520 nm. However, the absorption bands in the blue have been attributed to localized π-π^* transitions.[42] The steady state absorption for TPTQF_C is narrower, and its maximum peak is blue shifted in comparison to that of TPTQ_C which is an indicator of a good emissive material.

The decrease in the $0-0/0-1$ absorption intensity ratio as one compares the absorption spectra of the TPTQ acceptor to those of the polymer molecules shows that the polymers form H-aggregates. These H-aggregates exist even at the level of a single polymer chain as shown by the consistent spectral appearance at very low concentrations (**Figure 7.4.1.1**). This result means that the polymer is folded to enhance H-aggregation, leading to INTRAchain H-aggregation. Previous studies have shown that in semiconducting polymers, H-aggregates are as a result of strong intrachain interactions.[43] Therefore, we propose that these polymers form folded chains and the movement of charge is through intrachain charge transfer.

The extinction coefficient of both polymers at their highest absorption wavelengths as well as that of the TPTQ acceptor are shown in **Table 7.4.1.1**. Although the absorptivity is similar for the investigated polymers, TPTQF _C has a slightly higher molar extinction coefficient in the solution. Its molar extinction coefficient at the maximum absorption wavelength (470 nm) is 42505 $M^{-1}cm^{-1}$. This slight increase is quite interesting given that the TPTQ _C polymer counterpart has a broadened and red shifted absorption and is expected to show a higher extinction coefficient.

In addition, the absorption spectra of both polymers show well-resolved vibronic transitions. Compared to the TPTQ acceptor absorption, the $0-0$ transitions of the polymers are totally different where their $0-0$ transition intensity is significantly reduced, and the $0-1$ transition becomes the strongest; this change in the feature intensity indicates the formation of H-aggregates. In addition, there is a significant enhancement of the $0-0$ transition peak at 470 nm of TPTQF_C compared to the $0-0$ transition peak of TPTQ _C at 483 nm indicating stronger aggregation of the TPTQF_C polymer chain.

Table 7.4.1.1: Linear optical properties for the investigated polymers as well as the TPTQ Acceptor in chloroform.

Compound	λ_{abs} nm	λ_{em} nm	$\lambda_{Phosph.}$ nm	Stokes Shift cm^{-1}	ε $M^{-1}cm^{-1}$	ϕ_F % (UP)	ϕ_F % (P)	δTPA/GM λexc = 790 nm
TPTQ Acceptor	332, 348, 397, **419**	**426**, 450, 477	844	392	4261	14	11	67.4
TPTQ_C	455, **483**, 520	492, **548**, 600	970	2456	42437	38	36	223
TPTQF_C	440,**470**,489	**504**, 544	944	1435	42505	44	42	289

The emission spectra of both polymers as well as the acceptor, which were obtained in chloroform, are shown in **Figure 7.4.1.1 (right)** and the relevant data recorded in **Table 7.4.1.1**. Structurally, it is clear that the thiophene based polymer, TPTQ _C has an additional emissive peak of around 490 nm. The emission spectra of the rigid TPTQF_C are blue shifted compared to that of TPTQ _C. A smaller Stokes Shift and higher fluorescence quantum yields (**Table 7.4.1.1**) are observed for TPTQF_C compared to TPTQ_C which may be attributed to the heavy atom effect in TPTQ_C. The decreased Stokes Shift of TPTQF_C confirms its increased backbone rigidity compared to that of TPTQ _C.[5] Compared to both polymers, the fluorescence quantum yield of the TPTQ Acceptor is more than two times lower. However, an intense fluorescence in the furan-based polymer (TPTQF_C) was observed which has been associated with decreased intersystem crossing due to lack of the heavier atom, sulfur.[5] Here, the increased fluorescence quantum yield shows enhanced radiative decay pathways. For the case of the TPTQ_C polymer, the decreased fluorescence quantum yield has been associated with enhanced non-radiative processes. In all the investigated materials, an approximately ~2% decrease in fluorescence quantum yield is observed upon oxygen purging. This decrease in fluorescence quantum yield indicates the lack of Thermally Activated Delayed Fluorescence (TADF) activity on all investigated molecules.

Concentration dependence of absorption (**Figure 7.7.1**) measurements were used to check evidence of polymer aggregate chain formation or polymer folding. In both polymer cases, a decrease in concentration does not change the shape of the spectra indicating that the H-aggregates

exist even at the level of a single polymer chain (in very low concentrations). This means that the polymer is folded to enhance H-aggregation, leading to INTRAchain H-aggregation.

In addition, the temperature dependence of emission measurements were carried out to check the possibility of triplet formation in these molecules through phosphorescence. It has been reported that an increase in temperature induces intersystem crossing (ISC) of singlet (S_1) to triplet (T_1) leading to a decrease in fluorescence intensity. Since triplets are usually at lower energies compared to singlet states, the temperature-dependent emission is usually observed in the nIR. Therefore, shows the presence of phosphorescence and can be used to determine the energy of triplets. As shown in **Figure 7.7.2**, temperature-dependent emission is observed in all the investigated molecules. For the TPTQ Acceptor, two bands are observed, one peaked at 844 nm and the other one peaked at 906 nm (**Figure 7.7.2 and Table 7.4.1.1**). The 844 nm peak decreases in intensity as the temperature of the solution increases from 77 K to 273 K. On the contrary, the intensity of the 906 nm peak increases as the temperature increases. Given that high temperatures quench triplet emission, it is safe to assign 844 nm to the triplet state. Therefore, the energy of the TPTQ Acceptor triplet is 1.469 eV. For the thiophene-based compound TPTQ_C and the furan-based compound TPTQF_C, the emission band whose intensity decreases as the temperature of their respective solutions increase from 77 K to 273 K are peaked at 970 nm and 944 nm, respectively. As such, their triplet energies are 1.28 eV and 1.31 eV for TPTQ_C and TPTQF_C, respectively.

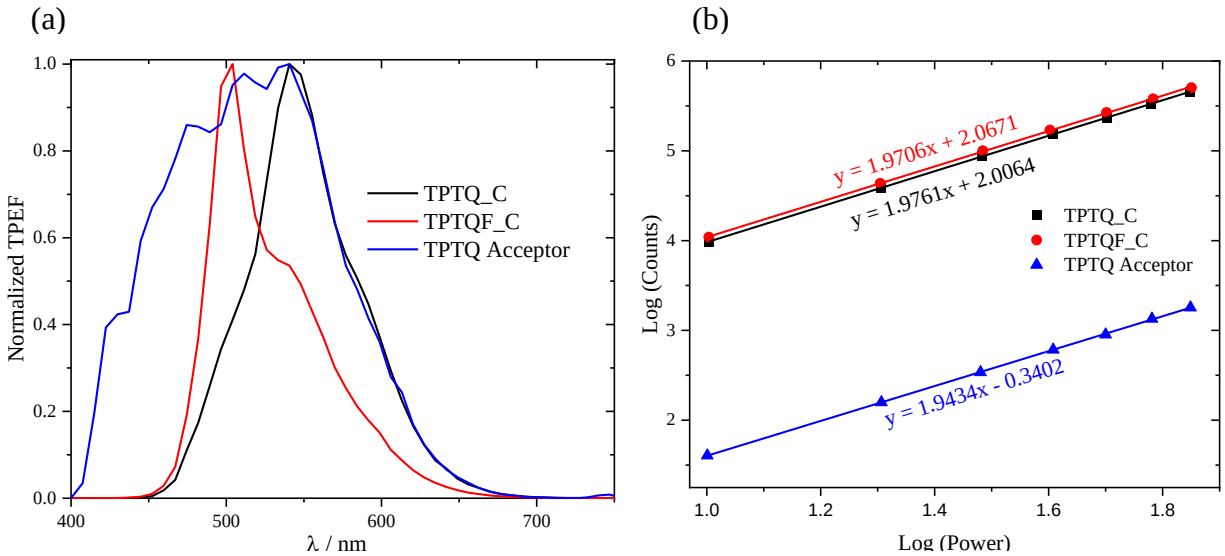

Figure 7.4.1.2: Two photon emission spectra (a.) and power dependence of the two photon excited emission (b.) of the investigated polymers in choloform upon 800 nm excitation.

The two-photon absorption (TPA) cross sections show remarkable values of hundreds of GM (**Table 7.4.1.1 and Figure 7.4.1.2**). The TPA cross section for the TPTQF_C polymer is 1.3 times more than that of TPTQ _C. TPA cross section has been directly related to the change in static and transition dipole moments, which are directly proportional to the charge transfer character of a molecule. Therefore, from the obtained TPA results, TPTQF_C has enhanced intrachain charge transfer compared to its thiophene-based analogue (TPTQ _C). The increased transition dipole moments in TPTQF_C are due to the increased electronegativity of the oxygen atom. These increased transition dipole moments could suggest a better interaction between the donor-acceptor junctions, which leads to a better charge transfer. The increased TPA cross section in TPTQF_C may be attributed to its expanded π-conjugation which increases the number of π-delocalized electrons as well as the delocalized degree of π-electrons.

7.4.2 Time-Resolved Fluorescence Measurements

To understand the fluorescence dynamics of these polymers, time correlated single photon measurements were carried out. The decay kinetics (**Figure 7.4.2.1**) as well as the fitted data (**Table 7.4.2.1**) are shown below. At the emission maximum, a mono-exponential decay function was used to fit the used reference (Coumarin 6), the unpurged and purged data of the TPTQ Acceptor as well as the thiophene-based TPTQ_C polymer. However, a bi-exponential decay function was used to fit both the unpurged and purged data of the TPTQF_C polymer. The fluorescence lifetime of the Coumarin 6 reference was found to be 2.8 ns (**Table 7.4.2.1**) which matches very well with the reported 2.4 ns.42 While both polymers' decay at earlier times starts off at the same rate, the decay of the furan-based polymer slows down midway showing a bi-exponential decay. At ambient conditions, τ_1 contribution in the furan-based polymer is 28% leaving only 72% for τ_2. However, when oxygen is purged out, the τ_1 contribution drops to 24% while the τ_2 contribution increases to 76%. Since oxygen has been reported to quench triplet excitons and with the rule 25% singlet and 76% triplet excitons rule, we can assign the slowly decaying component of the TPTQF_C to triplet species. This contribution is shown by the lifetimes reported in **Table 7.4.2.1**. For TPTQ_C polymer, only one species is observed which decays within 3.2 ns and its lifetime is not affected by oxygen purging, meaning that this contribution is from

singlet species. However, the TPTQ acceptor, which also decays mono-exponentially, decays more than two times faster compared to TPTQ_C polymer and the first component of the TPTQF_C polymer as shown in **Figure 7.4.2.1** and **Table 7.4.2.1**.

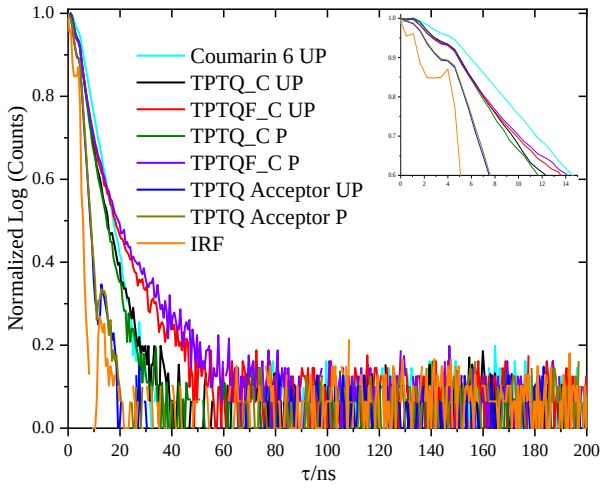

Figure 7.4.2.1: Fluorescence decay lifetimes of the investigated polymers obtained using time correlated single photon counting experiments. The inset shows the decay dynamics at earlier times.

Table 7.4.2.1: Time resolved excited state lifetime dynamics of the investigated foldable polymers as well as the TPTQ acceptor in chloroform at the underlined wavelengths.

Compound	**λ_{em} / nm**	τ_1 (UP)	τ_2 (UP)	τ_1 (P)	τ_2 (P)
TPTQ Acceptor	**<u>426</u>**, 450, 477	1.3	N/A	1.3	N/A
TPTQ_C	492, **<u>548</u>**, 600	3.2	N/A	3.2	N/A
TPTQF_C	**<u>504</u>**, 544	2.9	7.4	2.9	9.0
Coumarin 6		2.8	-	-	-

Interestingly, fluorescence dynamics were also checked at other emitting wavelengths for both polymers (**Figure 7.7.2**). For the furan-based polymer (TPTQF_C), the species at longer wavelengths (542 nm) emit faster compared to those found at the maximum emission peak (504 nm). In the thiophene-based polymer, however, the low wavelength species emit the fastest. The similarity in decay kinetics between the 498 nm and the 598 nm could mean that these are similarly

emissive species. However, it is clear that 548 nm species emits differently and can be assigned to different species.

Time-resolved fluorescence up-conversion measurements were used to resolve the fast fluorescence of these investigated compounds. As shown in **Figure 7.4.2.1**, the three compounds have different decay dynamics which were fitted and reported in **7.4.2.2**. While the TPTQ acceptor fitted into a bi-exponential function, both polymers fitted in a tri-exponential function. The earlier two decay components for both polymers are very fast, however, that of TPTQ_C portrays faster dynamics (1 ps and 23 ps) compared to the 5 ps and 51 ps decay time of TPTQF_C. Interestingly, the final polymer decay component which does not necessarily decay completely shows that TPTQF_C decays 2.3 times faster compared to the TPTQ_C. The result that the thirdultrafast decay component of the polymers is faster in TPTQF_C matches well with the results obtained using the time-correlated single photon counting where the decay time of the earlier components of the furan-based polymer is faster compared to that of the thiophene-based counterpart. Therefore, comparing just the polymers, the fluorescence decay results trend obtained using ultrafast up-conversion results (later component) matches those obtained using the time correlated single photon counting (earlier component). At earlier times, however, the TPTQ acceptor decay time is significantly slower (more than an order of magnitude) than that of both polymer systems. This could indicate that at these earlier times, the polymers are forming a fast species which is not observed in the TPTQ acceptor.

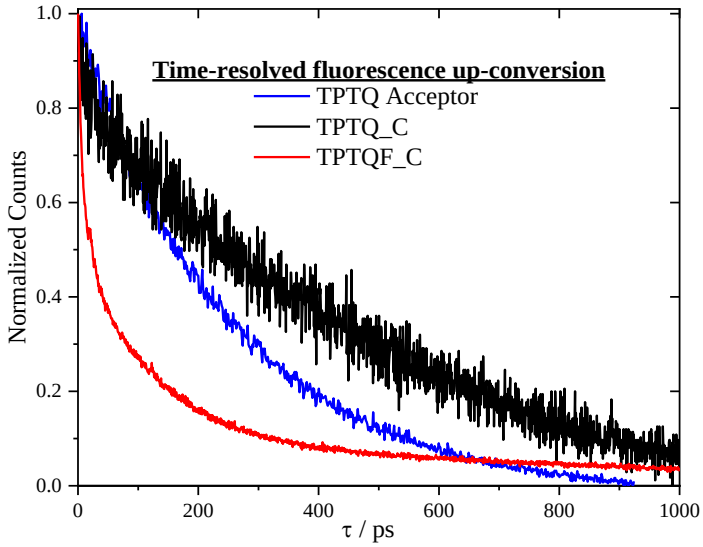

Figure 7.4.2.2: Ultrafast fluorescence up-conversion decay kinetics of the investigated polymers obtained using time correlated single photon counting experiments.

Table 7.4.2.2: Ultrafast time resolved excited state lifetime dynamics of the investigated foldable polymers as well as the TPTQ acceptor in chloroform at the underlined wavelengths.

Compound	**λ_{em} / nm**	τ_1	τ_2	τ_3
TPTQ Acceptor	480	61	264	N/A
TPTQ_C	500	4	50	651
TPTQF_C	500	16	205	N/A

7.4.3 Transient Absorption Spectroscopy

Both nanosecond and femtosecond transient absorption measurements were used to probe the excited state dynamics of the investigated molecules. The nanosecond transient absorption spectroscopy (nsTAS) measurements were used to probe the long-lived excited state dynamics while the femtosecond transient absorption spectroscopy (fsTAS) was used to probe the contribution of short-lived states in the photophysics of these materials. The TAS spectra shows depletion of the ground state, also known as the ground state bleach (GSB), or non-radiative decay, which is usually a negative signal. One can also observe further excitation of photons to higher excited states which are positive signals called excited state absorption (ESA). A negative signal (Stimulated Emission – SE) can also be observed when radiative decay happens.

For the nsTAS, the compounds were excited using both low (absorption maxima) and high (348 nm) energies as shown in **Figure 7.4.3.1- 7.4.3.5**. All measurements were done at low fluence (~1.2mJ) excitation. With a visible wavelength excitation (483 nm for TPTQ_C and 470 nm for TPTQF_C), a broad and intense stimulated emission that decays within 100 ns is observed for both polymers (**Figure 7.4.3.1a-b**).

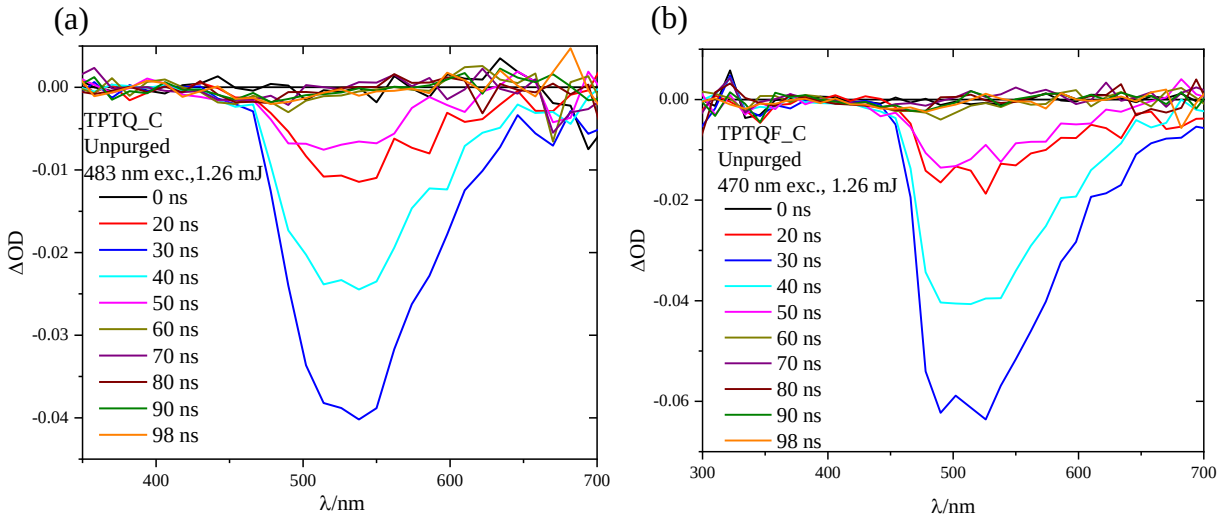

Figure 7.4.3.1: Nanosecond transient absorption spectroscopy measurements of the investigated polymers with fluorescence background (a and b). Spectra shown in graphs c and d, and e and f show the unpurged and purged spectra of the investigated polymers without the fluorescence background. All the above spectra were obtained upon excitation in the visible.

Without the fluorescence background subtraction and exciting at their respective maximum absorption, both polymers show a very small ESA as shown in **Figure 7.4.3.2 a-d**. The peak of these ESAs can be estimated to be around 560 nm and 536 nm for both TPTQ_C and TPTQF_C respectively. The GSBs whose peak maxima match well with the compounds' absorption spectra are observed for both molecules. This similarity is evidence that the GSB peaks are as a result of ground state depletion.

The observed ESAs are more clear and less noisy when the compounds were excited using higher energy (348 nm) as shown in **Figure 7.4.3.3**. The spectra and ESA kinetics of these polymers did not change when the two molecules were excited in the UV with the fluence kept low.

(a) (b)

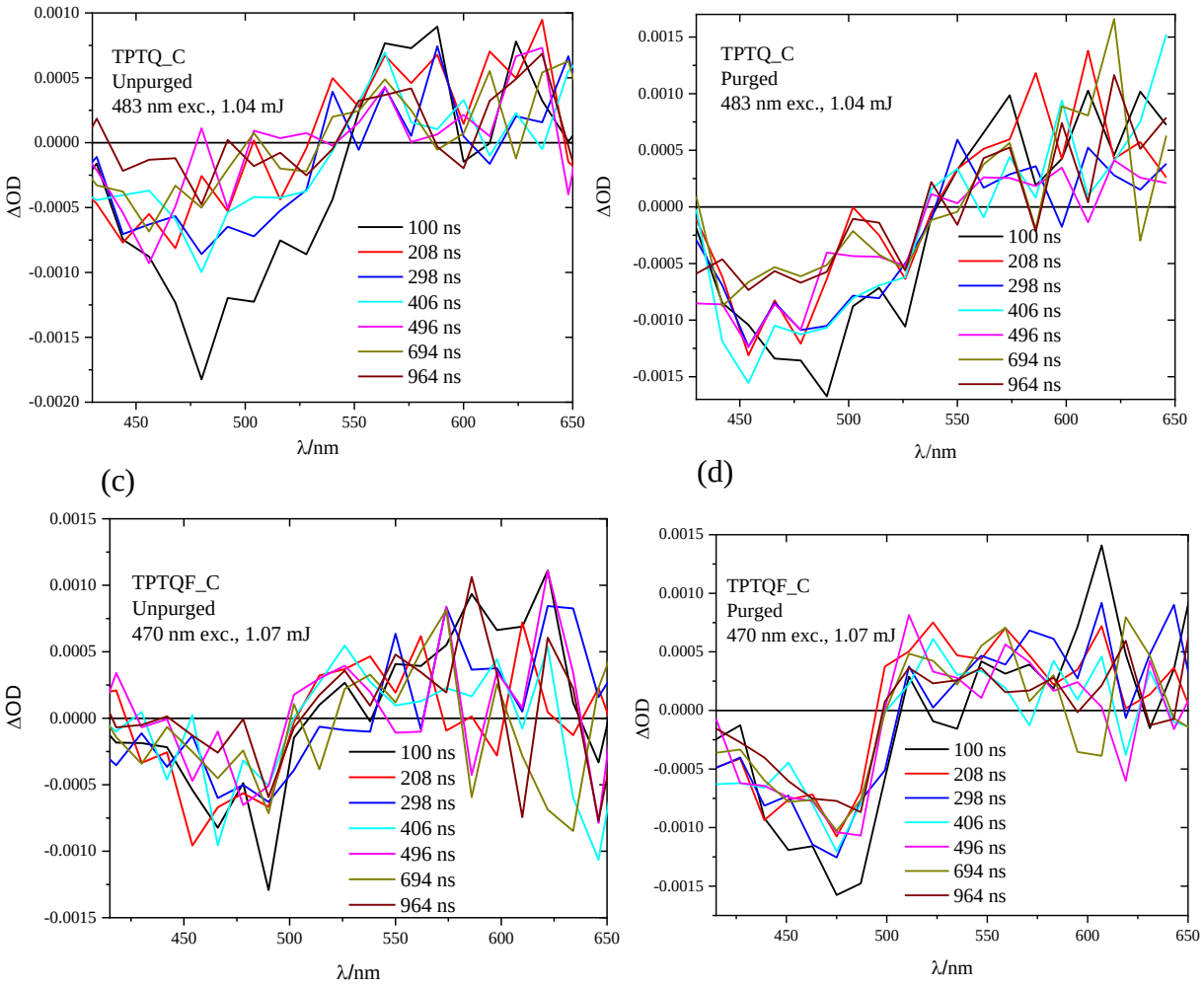

Figure 7.4.3.2: Unpurged and purged transient spectra from 100 -1000 ns and excitation energy of ~1 mJ.

As shown in **Figure 7.4.3.3**, a GSB which resembles the one obtained in **Figure 7.4.3.2** is observed. The small ESA that was observed at around 560 nm for TPTQ_C and 536 nm for TPTQF_C becomes more prominent as shown in **Figure 7.4.3.3**. For the TPTQ_C molecule, the lifetime of the GSB observed at 484 nm is clearly affected by oxygen purging which is an indicator that there is a presence of triplet species in this molecule (**Figure 7.4.3.4 left)**. However, the ESA decay time from this molecule is not affected by oxygen-purging which showing that this ESA is as a result of non-triplet species (**Figure 7.4.3.5 left)**. For the case of the TPTQF_C compound, both the ESA as well as its GSB are not affected by oxygen purging at all showing that this ESA is as a result of purely singlet states (**Figure 7.4.3.4**).

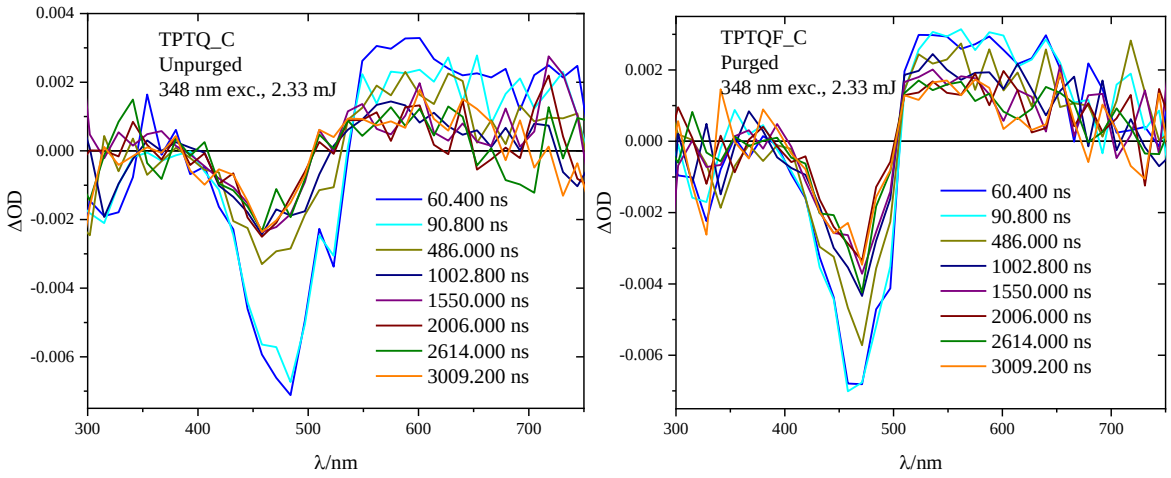

Figure 7.4.3.3: Nanosecond transient absorption spectra of the investigated polymers with UV excitation.

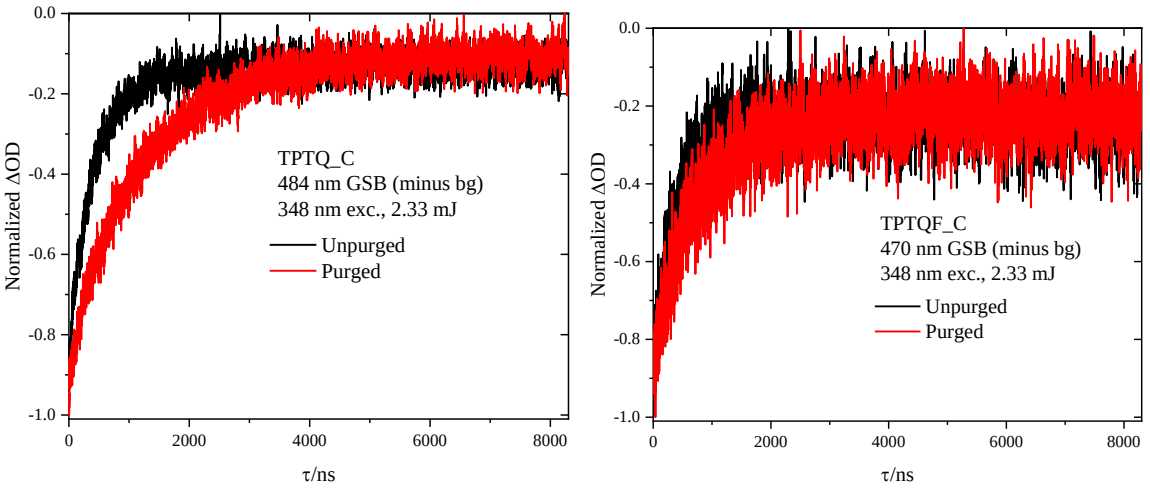

Figure 7.4.3.4: Nanosecond transitent absorption GSB kinetics of the investigated polymers with UV excitation.

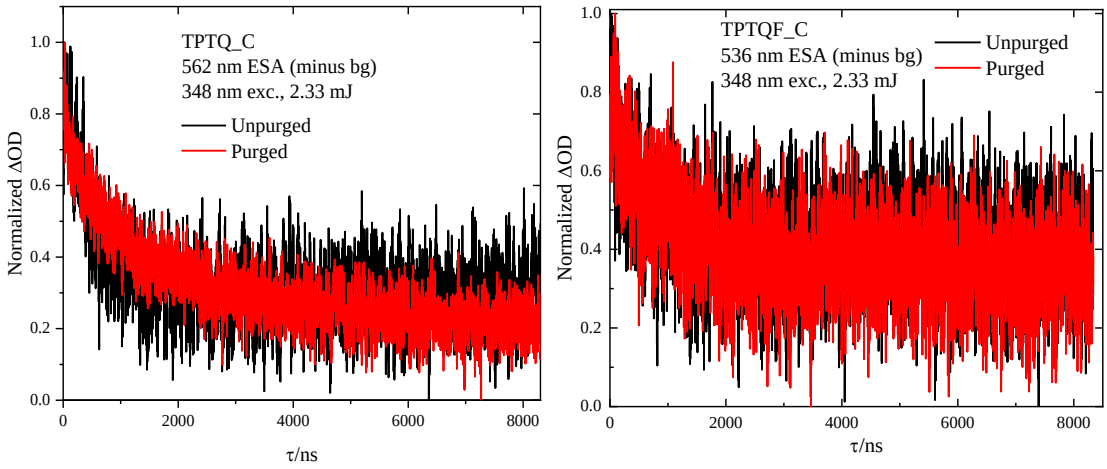

Figure 7.4.3.5: Nanosecond transitent absorption ESA kinetics of the investigated polymers with UV excitation.

The TPTQ Acceptor molecule shows very straightforward dynamics where a GSB with a maximum peak at 420 nm which matches well with the ground state absorption was observed as shown in **Figure 7.4.3.6**. Two ESA bands are also observed where the ESA at 302 nm decays slower compared to that observed at 562 nm as shown in **Table 7.4.3.1**. The lifetimes of both of these ESAs are enhanced upon oxygen purging showing that these are as a result of triplets (**Figure 7.4.3.7**). In addition, the GSB decay time is also enhanced by oxygen purging which further proves the existence of triplet species (**Figure 7.4.3.8**).

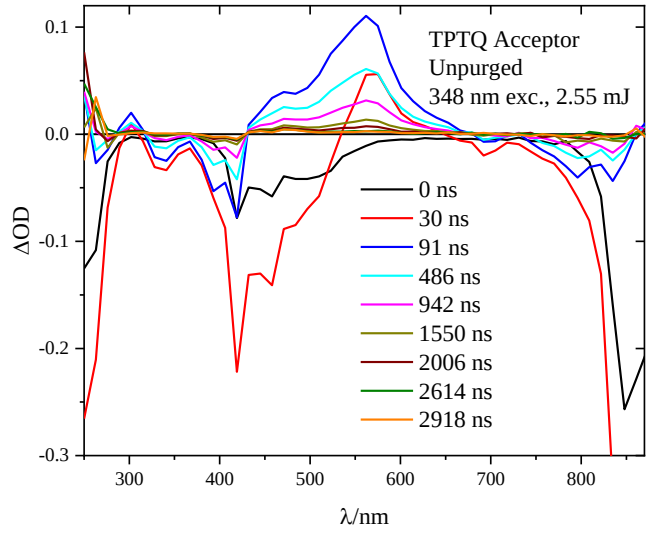

Figure 7.4.3.6: Nanosecond transitent absorption spectra and excited state absorption kinetics of the investigated polymers with UV excitation.

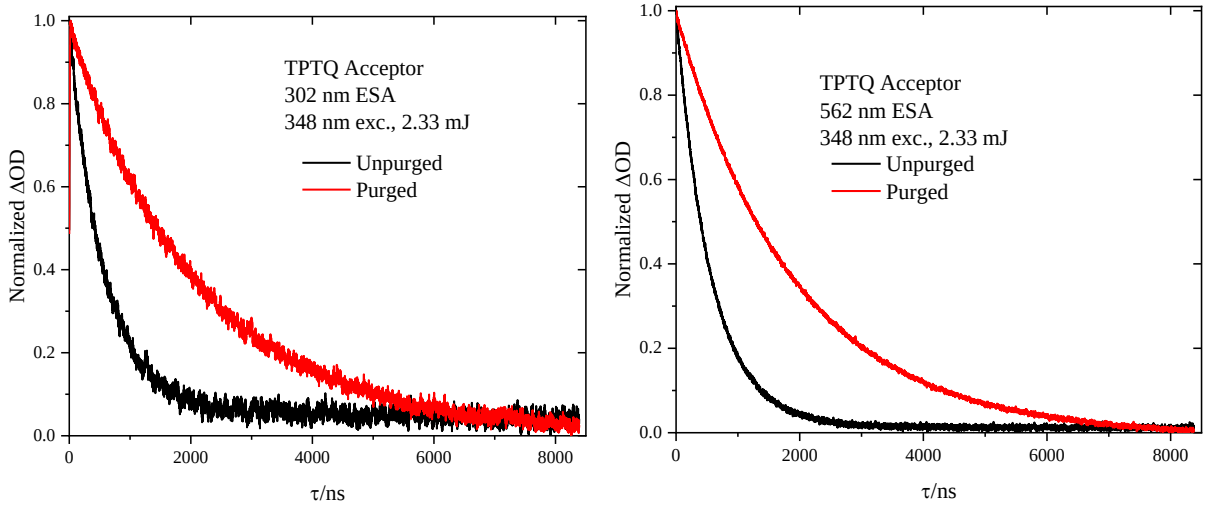

Figure 7.4.3.7: Nanosecond transitent absorption ESA kinetics of the TPTQ Acceptor with UV excitation.

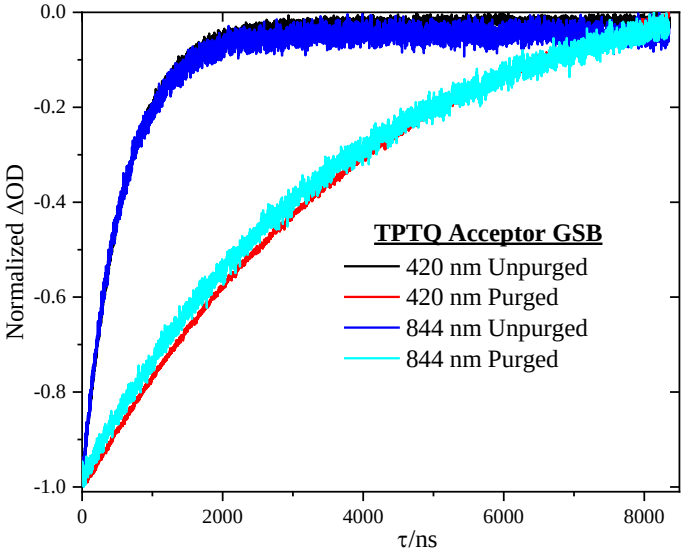

Figure 7.4.3.8: Nanosecond transitent absorption GSB kinetics of the TPTQ Acceptor.

Interestingly, there is another GSB peak observed at 844 nm, whose decay time is also enhanced by oxygen purging (**Figure 7.4.3.8**). This 844 nm peak matches well with the phosphorescence peak observed in the steady state studies **Figure 7.7.2** and **Table 7.4.1.1**.

Table 7.4.3.1: Purged (p) and unpurged (up) nsTAS ESA and GSB lifetime dynamics of the investigated molecules as well as the TPTQ acceptor in chloroform at their indicated wavelengths.

	ESA			GSB				
Compound	**λ_{em} / nm**	τ_1(UP) (ns)	τ_1(P) (ns)	**λ_{em} / nm**	τ_1(UP) (ns)	τ_2 (UP) (ns)	τ_1(P) (ns)	τ_2 (P) (ns)
TPTQ Acceptor	302 562	591 568	2098 1922	420 844	584 563	N/A N/A	4415 3793	N/A N/A
TPTQ_C	562		1164/24,954	484	233	472	214	1294
TPTQF_C	536		1129/61,214	470	447	801	180	1242

Femtosecond transient absorption spectroscopy (fsTAS) measurements were done to look into the faster dynamics of all the investigated molecules. For both polymer molecules, a GSB that matches well with the respective absorption spectra was observed. For TPTQ_C, the GSB forms within the first 250 fs while for TPTQF_C, the GSB forms within the first 600 fs before decaying back slowly (**Figure 7.4.3.9**). In both cases, the GSB does not decay completely to zero which agrees well with the nsTAS results that show long-lived GSB. Additionally, a similar ESA observed around the same range of wavelength as that in nsTAS was observed for both molecules. As the GSBs decay, they form ESAs which are completely formed within While the ESAs in both cases form within the first 10 ps for TPTQ_C and within the first 1.5 ps for TPTQF_C as shown in **Figure 7.4.3.9 and 7.4.3.10**.

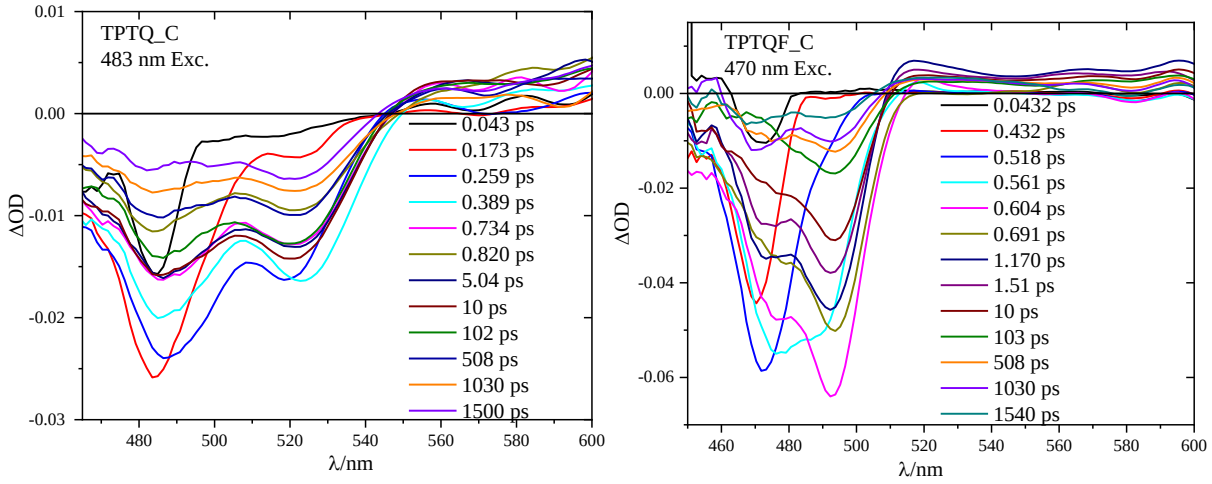

Figure 7.4.3.9: fsTAS spectra of both the TPTQ_C and TPTQF_C polymers at their absorption maxima (TPTQ_C at 483 nm and TPTQF_C at 470 nm) excitation.

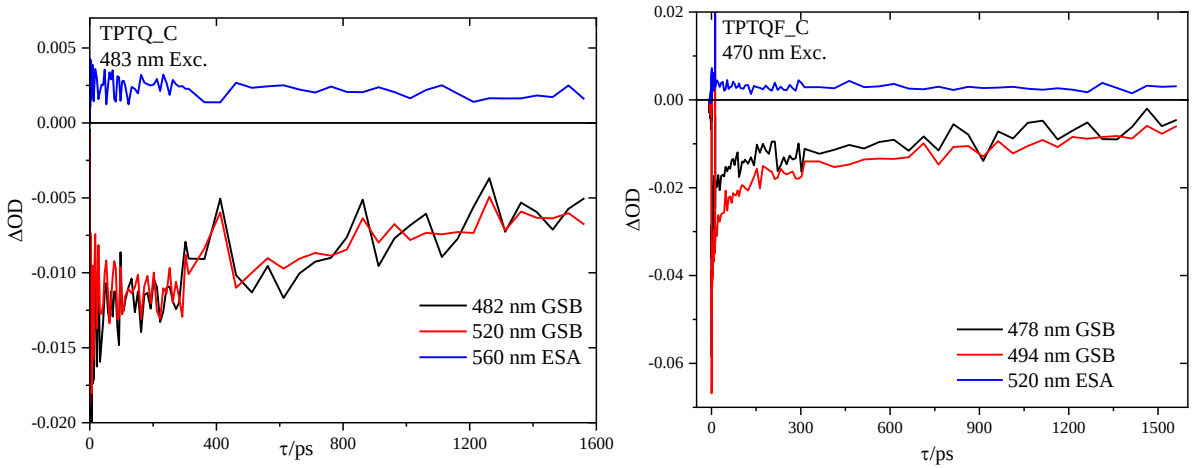

Figure 7.4.3.10: fsTAS kinetics of both the TPTQ_C and TPTQF_C polymers at their absorption maxima (TPTQ_C at 483 nm and TPTQF_C at 470 nm) excitation.

For the TPTQ Acceptor, a very intense ESA with two bands was observed. Interestingly, as the ESA at 489 nm decayed, the ESA at 566 nm formed (**Figure 7.4.3.11**). This decay and formation which happens at approximately the same rate is evidence that singlets were transferred through intersystem crossing to the triplets. The ESA at 566 nm is consistent with the ESA observed in the nsTAS measurements, and whose decay time is 568 ns. The reason why the singlet species are not observed using the nsTAS is clearly because their decay time is ~600 ps which is too fast to be detected by our nsTAS whose instrument response function (IRF) is only 7 ns.

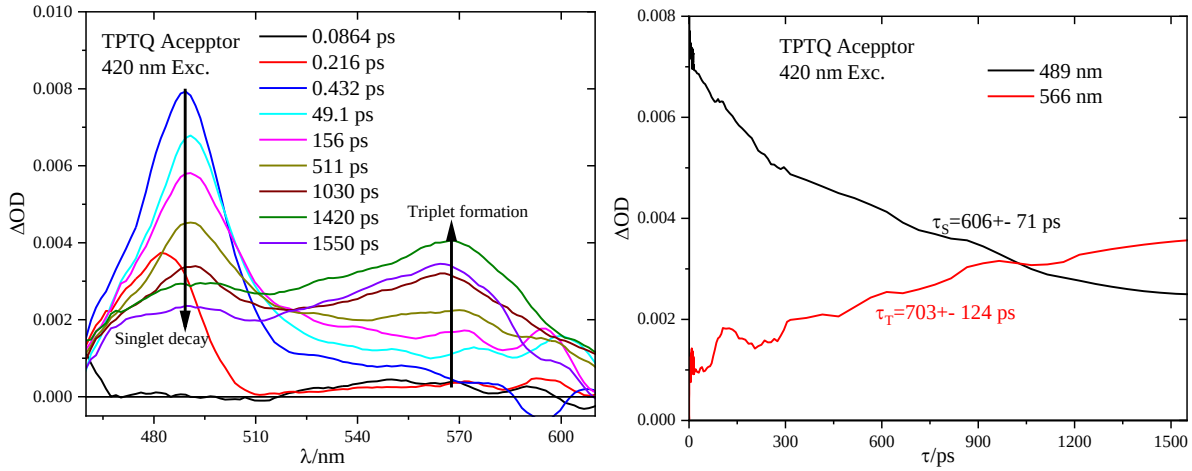

Figure 7.4.3.11: fsTAS spectra and kinetics of the TPTQ Acceptor at 420 nm excitation.

7.4.4 Electron Paramagnetic Resonance (EPR) Spectroscopy

Since it was predicted that the TPTQ_C and TPTQF_C molecules can exist in their resonance states as zwitterions, EPR spectroscopic measurements were done at ~100K to check the presense of unpaired electrons in these samples as well as the TPTQ Acceptor. Interestingly, only one of the investigated samples, TPTQ_C, showed a derivative peak where the g-factor of the formally forbidden double quantum transition is ~1.9726 as shown by the red arrows in the spectra in **Figure 7.4.4.1.** This g-factor shows the presence of organic radicals and has been reported in multiple studies.[45,46]

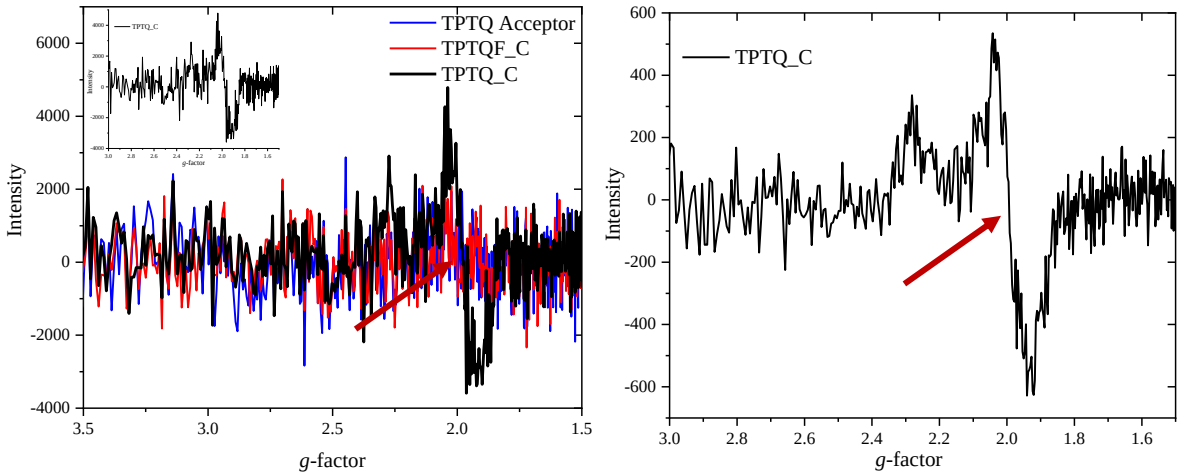

Figure 7.4.4.1: Electron paramagnetic resonance (EPR) measurements of the investigated molecules.

It is worth noting that there is an additional peak at higher g-factor values and peaked at 2.2811. The difference between this peak and the peak derivative is 0.3085.

7.5 Discussion

Numerous studies of biological macromolecules have reported the existence of foldamers that adopt highly ordered and helical self-assembled structures through noncovalent interactions.[5,16,17,47] However, while a lot of research has been done in synthesizing these materials, very little is known about the photophysics and charge transfer mechanisms that affect their external quantum efficiencies (EQEs). In this study, we report the photophysical properties of previously synthesized semi-ladder polymers consisting of two different acceptor monomers: thienopyridothienoquinoline which has a thiophene incorporated (TPTQ) and thienopyridothienoquinoline with a furan molecule incorporated (TPTQF), both acceptors coupled to a carbazole donor monomer moiety.[5] Previous reports have shown the photo-induced radical

polymerization of quinolines through intramolecular charge transfer which cleaves certain C-O bonds to form the radicals.[48] Elsewhere, carbazole-donor-based fullerene polymers have been reported to form long-lived singlet diradicals upon light absorption.[49] To the best of our knowledge, there is no one has reported the time-resolved and nonlinear optical properties and the charge transfer mechanism that involves the formation of diradicalouds in similar foldable polymer aggregates for organic light emitting transistors (OLET) applications. As a result, this report investigates the self-doping intramolecular electron transfer in aromatically stable zwitterions to form diradicaloids which lower the charge separation process and reduce the charge and energy transfer rate of the thiophene-carbazole-based OLET polymers. The reduced energy transfer process leads to decreased overall external quantum efficiency (EQE) of the resultant OLETs.

From the steady state absorption, and just considering the maximum absorption (**Figure 7.4.1.1 and Table 7.4.1.1**), it is clear that TPTQ_C has a slightly lower HOMO-LUMO bandgap (2.567 eV) compared to the TPTQF_C (2.638 eV). Here, the HOMO-LUMO bandgap of the furan-based polymer is 0.071 eV higher than the generally suggested difference of 0.3-0.4 eV.[50] The weak low-energy shoulder observed at 520 nm has been reported to originate from low-lying singlet states which are mostly as a result of doubly excited electronic configuration (HH/LL), and indicates the presence of open shell singlet ground states in the form of diradicaloids. [28,51–54] This weak and low energy shoulder is the first evidence that shows the presence of diradical character in only the TPTQ_C molecule, and is backed up by its lowest HOMO-LUMO bandgap.

Additionally, the fluorescence quenching observed in the thiophene-based polymer can be associated with increased molecular aromatization and conjugation which increases the fluorophores density.[55] Due to its high aromatic stability, TPTQ_C can form neutral zwitterions through cleaving of the $C = O$ in the thiophene acceptor and then going through an electronic reorganization to form a cation on the amine side of the carbazole donor. This cation formation can be followed by self-doping leading to the formation of diradicals as shown in equation 1.[30] However, the presence of furan in TPTQF_C reduces its aromaticity and increases the quinoidal interactions which inhibit the diradical formation. Similar results were observed by Xue et al. and Sander. [53,56] Low fluorescence quantum yields have been reported for materials with increased diradical character. [54]

$$A + D \leftrightarrow A^{\cdot -} + D^{\cdot +} \leftrightarrow A^{\cdot} + D^{\cdot} \qquad \text{(Equation 1)}$$

Given the reported steady state results, a few parameters were obtained to calculate the singlet diradical character , y, of the investigated materials using the expression (Equation 2) derived and reported by Kamada et al.[57]

$$y = 1 - \sqrt{1 - \left(\frac{E_{S_{1u}S_{1g}} - E_{T_{1u}S_{1g}}}{E_{S_{2g},S_{1g}}}\right)^2} \qquad \text{(Equation 2)}$$

where

$E_{S_{1u}S_{1g}}$ is given by the lowest energy peak of the one photon absorption spectra,

$E_{T_{1u}S_{1g}}$ is obtained from phosphorescence peak measurements and

$E_{S_{2g},S_{1g}}$ corresponds to the lowest energy peak of the two-photon absorption spectra.

Based on these steady state parameters, the diradical character calculated shows an element of diradical character in these molecules with the TPTQ_C molecule showing the largest y (**Table 7.5.1**).

Table 7.5.1: Calculated diradical character, y , ΔE_{ST} and J from the steady state measurements.

Compound	$\lambda_{S_{1u}S_{1g}}$ nm	$E_{S_{1u}S_{1g}}$ eV	$\lambda_{T_{1u}S_{1g}}$ nm	$E_{T_{1u}S_{1g}}$ eV	$\lambda_{S_{2g},S_{1g}}$ nm	$E_{S_{2g},S_{1g}}$ eV	y	ΔE_{ST}	J
TPTQ Acceptor	419	2.9541	844	1.469	540	4.592	0.053	1.485	0.74
TPTQ_C	522	2.375	970	1.278	600	2.296	0.122	1.097	0.55
TPTQF_C	496	2.500	944	1.313	540	4.592	0.034	1.186	0.59

Additionally, the singlet-triplet energy gap (ΔE_{ST}) was calculated by subtracting the triplet state energy (E_T) from the singlet state energy (E_S). It is clear that the TPTQ_C has the lowest bandgap. Previous studies have used the singlet-triplet energy gap of diradicaloids to determine the spin multiplicity of the diradicals. A diradical can either have a singlet ground state with a spin multiplicity of 1 or a triplet ground state with a spin multiplicity of 3. Su *et al*. report that a singlet

diradical and a triplet diradical can be indicated by a negative or positive electron exchange interaction, J, respectively. [58]

$$\Delta E_{ST} = E_S - E_T = 2J \qquad \text{(Equation 3)}$$

Since the obtained values are positive, it is predicted that TPTQ_C contains a triplet diradical character. The triplet diradical character is also ascertained by the presence of a signal observed from the EPR measurements. Usually, singlet diradicals do not show any EPR signal and therefore, it is likely that the observed EPR signal shows the presence of biradicals with a triplet ground state.

Further analysis of the EPR signal from the additional peaks with circled in red dotted ovals in **Figure 7.5.1** below. The location of the x, y peak which is 3241G is indicative of high symmetry. The difference between the z and x, y can be used to calculate the D parameter, one of the zero field splitting (ZFS) parameters.[63] Relationships between the ZFS parameters can be used to calculate their values. Here, ${}^{D}/_{2} = 71G,$ and therefore, $D = 142G$. Given that $D = 3E,$ then $E = 47G$. From Equation 4, the obtained spin-spin distance, $r = 5.8$Å. This number is smaller than the spin-spin distance that has been reported for diradicals which range between $r = 6\text{Å} - 12\text{Å}$.[64-66] This further proves the formation of diradicaloids for the TPTQ_C molecule.

$$D = 1.39 \times 10^4 \left(\frac{g}{r^3}\right) \qquad \text{(Equation 4)}$$

Where:

g is the g-factor and

r is the spin-spin distance between the two unpaired electrons.

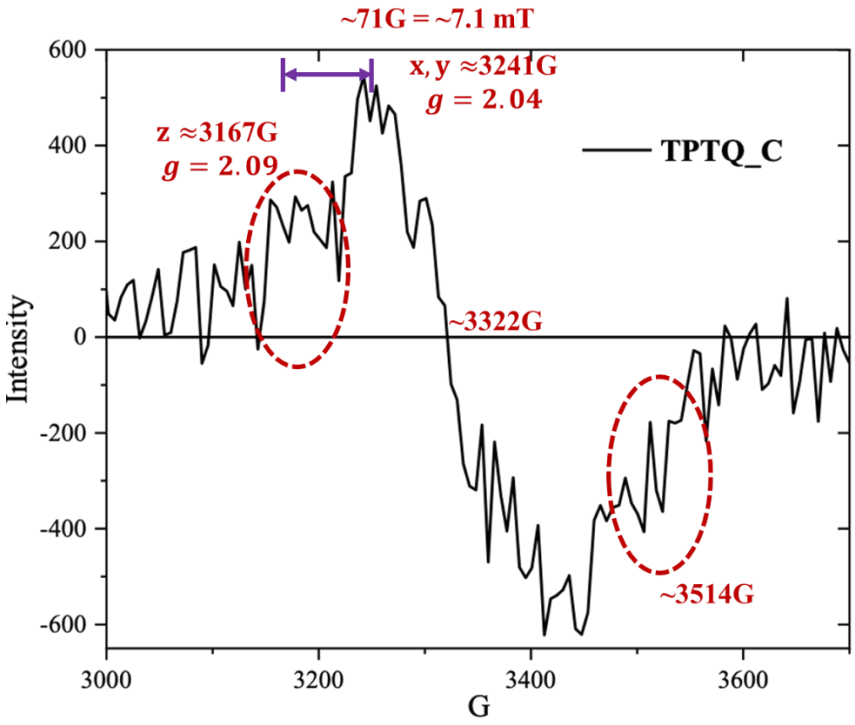

Figure 7.5.1: Electron paramagnetic resonance (EPR) measurements of the TPTQ_C molecule.

The presence of electron exchange interaction indicates that there is some coupling between the nonbonding electrons which eliminates the possibility that the nonbonding electrons could be forming diradicals instead of biradicals.

The nanosecond transient absorption shows extremely long-lived ESAs whose lifetime is not enhanced in a nitrogen-rich environment. The lifetimes of these ESAs are 25 μs and 60 μs for TPTQ-C and TPTQ_C, respectively. The TPTQ_C ESA is assigned to diradicaloids. These long lifetime diradicaloid species whose lifetime is not affected by purging out oxygen, have been reported in previous studies.[59] It is possible that the long lifetime observed for the TPTQF_C is as a result of zwitterions.

Interestingly, it is possible for quinoline derivatives like TPTQ_C and TPTQF_C to exist in their resonant forms as shown in **Figure 7.3.1**. Due to the presence of sulfur, the thiophene-based polymer resonant structure becomes more unreactive due to its high aromatic stability compared to the furan-based counterparts. The TPTQF_C, which is more reactive, is extremely unstable and its resonant structure is very short-lived as shown in **Figure 7.6.1**. Similar results were reported by Jursic where sulfur heterocyclic compounds showed the highest resonance

stability while their furan derivatives were the most reactive. [60] Previous polymer studies show that furan has reduced aromaticity which increases the contribution from quinoidal resonance structure in polyfurans making furan-containing polymers more rigid with a planar conformation as well as an overly increased conjugation.[61] This decrease in aromaticity around the furan moiety tends to enhance the probability of additional reactions like that of singlet oxygen and light, compared to their counterpart thiophene based polymers.[61] This is an interesting observation since previous decrease in aromaticity has been related to an increase in the diradical character of molecules.[62] The saturation of this π conjugation leads to the unexpected shift of the absorption maximum to high energies. However, the lone pair of electrons on the sulfur atom in the TPTQ _C polymer leads to p-π conjugation extending the overall conjugation of the thiophene based TPTQ _C polymer. This extended conjugation leads to intensified absorption which is shifted to longer wavelengths as confirmed by the TPTQ _C absorption in **Figure 7.4.1.1a**.

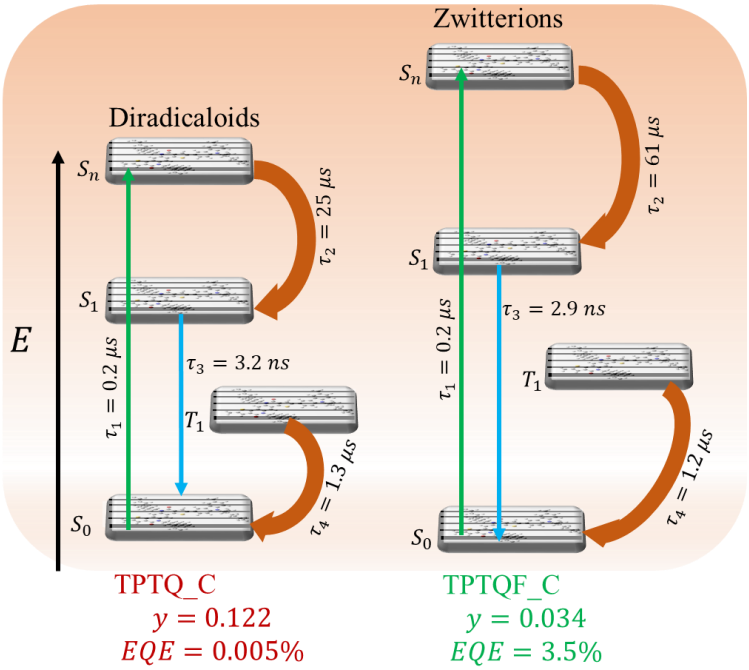

Figure 7.6.1: Proposed energy level diagram for the diradicals vs zwitterions.

7.6 Conclusion

The presence of unpaired electrons in open shells has been reported to form resonant structures with an enhanced spin density that is delocalized along the planar π −conjugation backbone influencing the charge transfer. For biradicals, their low-lying triplet energy levels make

them promising structures for singlet exciton fission (SEF) which enhances the performance of organic photovoltaics. On the other hand, diradical formation has been reported to suppress the second step of singlet exciton fission. However, due to their unique characteristics of low-lying triplet states and the feasible conversion between singlets (S_0) and triplets (T_1) that do not follow the spin prohibition due to the existence of the generated or nearly generated nonbonding orbitals containing radicals. These diradical characters can offer intermolecular spin-spin interactions which lead to σ −aggregation and formation of σ −polymerization which affects intermolecular stacking and charge transport which has proved to be good for organic light emitting diodes (OLEDs). In addition, the low bandgaps, intimate intermolecular interactions, and redox amphoterism which increase the overall efficiency of organic field effect transistors (OFETs). However, there is no report of the effect of diradicals on the performance of organic light emitting transistors, which is what this study reports. A diradical character is observed for the thiophene-based polymer, TPTQ_C. This is evidenced by several properties: 1) The weak low-energy shoulder observed at 520 nm has been reported to originate from low-lying singlet states which are mostly as a result of doubly excited electronic configuration (HH/LL), and indicates the presence of open shell singlet ground states in the form of diradicaloids. 2) Fluorescence quenching observed in the thiophene-based polymer can be associated with increased molecular aromatization and conjugation which increases the fluorophores density, low fluorescence quantum yields have been reported for materials with increased diradical character. 3) Based on these steady state singlet and triplet parameters, the diradical character calculated shows an element of diradical character (y) in these molecules with the TPTQ_C molecule showing the largest y. In addition, the calculation of the electron exchange interaction shows that there is some interaction between the two unpaired electrons with a spin-spin distance, $r = 5.8$Å, which means that the open-shell formed is a diradical and not a biradical. 4) TPTQ_C has the lowest singlet-triplet energy gap (ΔE_{ST}) and 5) a signal is observed from EPR measurements with a g-factor of ~2.000 which is typical of organic radicals.

References

(1) Hepp, A.; Heil, H.; Weise, W.; Ahles, M.; Schmechel, R.; von Seggern, H. Light-Emitting Field-Effect Transistor Based on a Tetracene Thin Film. *Physical Review Letters* **2003**, *91* (15). https://doi.org/10.1103/PhysRevLett.91.157406.

(2) Liu, C. F.; Liu, X.; Lai, W. Y.; Huang, W. Organic Light-Emitting Field-Effect Transistors: Device Geometries and Fabrication Techniques. *Advanced Materials*. Wiley-VCH Verlag December 27, 2018. https://doi.org/10.1002/adma.201802466.

(3) Yuan, D.; Sharapov, V.; Liu, X.; Yu, L. Design of High-Performance Organic Light-Emitting Transistors. *ACS Omega*. American Chemical Society January 14, 2020, pp 68–74. https://doi.org/10.1021/acsomega.9b03630.

(4) Ojha, S. K.; Kumar, B. Parameter Extraction of High-Performance Material Based Organic Light-Emitting Transistors (OLETs). *Silicon* **2021**. https://doi.org/10.1007/s12633-021-01149-6.

(5) Yuan, D.; Awais, M. A.; Sharapov, V.; Liu, X.; Neshchadin, A.; Chen, W.; Bera, M.; Yu, L. Foldable Semi-Ladder Polymers: Novel Aggregation Behavior and High-Performance Solution-Processed Organic Light-Emitting Transistors. *Chemical Science* **2020**, *11* (41), 11315–11321. https://doi.org/10.1039/d0sc04068a.

(6) Chen, H.; Xing, X.; Miao, J.; Zhao, C.; Zhu, M.; Bai, J. W.; He, Y.; Meng, H. Highly Efficient Flexible Organic Light Emitting Transistor Based on High-k Polymer Gate Dielectric. *Advanced Optical Materials* **2020**, *8* (6). https://doi.org/10.1002/adom.201901651.

(7) Yuan, D.; Awais, M. A.; Sharapov, V.; Liu, X.; Neshchadin, A.; Chen, W.; Yu, L. Synergy between Photoluminescence and Charge Transport Achieved by Finely Tuning Polymeric Backbones for Efficient Light-Emitting Transistor. *Journal of the American Chemical Society* **2021**, *143* (13), 5239–5246. https://doi.org/10.1021/jacs.1c01659.

(8) Feldmeier, E. J.; Schidleja, M.; Melzer, C.; von Seggern, H. A Color-Tuneable Organic Light-Emitting Transistor. *Advanced Materials* **2010**, *22* (32), 3568–3572. https://doi.org/10.1002/adma.201000980.

(9) Soldano, C. Engineering Dielectric Materials for High-Performance Organic Light Emitting Transistors (Olets). *Materials* **2021**, *14* (13). https://doi.org/10.3390/ma14133756.

(10) Feng, G.; Xu, Y.; Xiao, C.; Zhang, J.; Zhang, X.; Li, C.; Wei, Z.; Hu, W.; Wang, Z.; Li, W. Poly(Pentacyclic Lactam-Alt-Diketopyrrolopyrrole) for Field-Effect Transistors and Polymer Solar Cells Processed from Non-Chlorinated Solvents. *Polymer Chemistry* **2016**, *7* (1), 164–170. https://doi.org/10.1039/c5py01406a.

(11) Tanaka, H.; Kajii, H.; Ohmori, Y. Effects of Molecular Packing on the Field-Effect Mobility and External Quantum Efficiency of Ambipolar Polymer Light-Emitting Transistors Incorporating a

Donor-Acceptor Polymer. *Synthetic Metals* **2015**, *203*, 10–15. https://doi.org/10.1016/j.synthmet.2015.02.008.

(12) Qin, Z.; Gao, H.; Liu, J.; Zhou, K.; Li, J.; Dang, Y.; Huang, L.; Deng, H.; Zhang, X.; Dong, H.; Hu, W. High-Efficiency Single-Component Organic Light-Emitting Transistors. *Advanced Materials* **2019**, *31* (37). https://doi.org/10.1002/adma.201903175.

(13) Zheng, C.; Zhong, C.; Collison, C. J.; Spano, F. C. Non-Kasha Behavior in Quadrupolar Dye Aggregates: The Red-Shifted H-Aggregate. *Journal of Physical Chemistry C* **2019**, *123* (5), 3203–3215. https://doi.org/10.1021/acs.jpcc.8b11416.

(14) Terenziani, F.; Painelli, A.; Katan, C.; Charlot, M.; Blanchard-Desce, M. Charge Instability in Quadrupolar Chromophores: Symmetry Breaking and Solvatochromism. *Journal of the American Chemical Society* **2006**, *128* (49), 15742–15755. https://doi.org/10.1021/ja064521j.

(15) Cao, H.; Rupar, P. A. Recent Advances in Conjugated Furans. *Chemistry - A European Journal* **2017**, *23* (59), 14670–14675. https://doi.org/10.1002/chem.201703355.

(16) Hu, X.; Lindner, J. O.; Würthner, F. Stepwise Folding and Self-Assembly of a Merocyanine Folda-Pentamer. *Journal of the American Chemical Society* **2020**, *142* (7), 3321–3325. https://doi.org/10.1021/jacs.9b12599.

(17) Kelley, R. F.; Rybtchinski, B.; Stone, M. T.; Moore, J. S.; Wasielewski, M. R. Solution-Phase Structure of an Artificial Foldamer: X-Ray Scattering Study. *Journal of the American Chemical Society* **2007**, *129* (14), 4114–4115. https://doi.org/10.1021/ja068213x.

(18) Sergeants-and-Soldiers Principle in Chiral Columnar Stacks of Disc-Shaped Molecules with C3 Symmetry.

(19) Nelson, J. C.; Saven, J. G.; Moore, J. S.; Wolynes, P. G. *Solvophobically Driven Folding of Nonbiological Oligomers*; Plenum, 1995; Vol. 267.

(20) Håheim, K. S.; Urdal Helgeland, I. T.; Lindbäck, E.; Sydnes, M. O. Mapping the Reactivity of the Quinoline Ring-System – Synthesis of the Tetracyclic Ring-System of Isocryptolepine and Regioisomers. *Tetrahedron* **2019**, *75* (21), 2949–2957. https://doi.org/10.1016/j.tet.2019.04.026.

(21) Hosmane, R. S.; Liebman, J. F. Paradoxes and Paradigms: Why Is Quinoline Less Basic than Pyridine or Isoquinoline? A Classical Organic Chemical Perspective. *Structural Chemistry* **2009**, *20* (4), 693–697. https://doi.org/10.1007/s11224-009-9464-6.

(22) Xue, G.; Hu, X.; Chen, H.; Ge, L.; Wang, W.; Xiong, J.; Miao, F.; Zheng, Y. Understanding the Nature of Quinoidal and Zwitterionic States in Carbazole-Based Diradicals. *Chemical Communications* **2020**, *56* (38), 5143–5146. https://doi.org/10.1039/d0cc01948h.

(23) Chen, L. M.; Lin, I. H.; You, Y. C.; Wei, W. C.; Tsai, M. J.; Hung, W. Y.; Wong, K. T. Substitution Effect on Carbazole-Centered Donors for Tuning Exciplex Systems as Cohost

for Highly Efficient Yellow and Red OLEDs. *Materials Chemistry Frontiers* **2021**, *5* (13), 5044–5054. https://doi.org/10.1039/d1qm00425e.

(24) Chestat, C. A.; Whitten, D. G. *Photocyclization Of-Keto Amides in Homogeneous Solution and Aqueous Cyclodextrin Media. The Role of Zwitterions and Diradicals in Photoinduced Electron Transfer Reactions*; 1992; Vol. 114.

(25) Abe, M. Diradicals. *Chemical Reviews*. September 11, 2013, pp 7011–7088. https://doi.org/10.1021/cr400056a.

(26) Li, Y.; Li, Y.; Li, L.; Wu, Y. A Review on the Origin of Synthetic Metal Radical: Singlet Open-Shell Radical Ground State? *Journal of Physical Chemistry C* **2017**, *121* (15), 8579–8588. https://doi.org/10.1021/acs.jpcc.6b12936.

(27) Yuen, J. D.; Wang, M.; Fan, J.; Sheberla, D.; Kemei, M.; Banerji, N.; Scarongella, M.; Valouch, S.; Pho, T.; Kumar, R.; Chesnut, E. C.; Bendikov, M.; Wudl, F. Importance of Unpaired Electrons in Organic Electronics. *Journal of Polymer Science, Part A: Polymer Chemistry* **2015**, *53* (2), 287–293. https://doi.org/10.1002/pola.27321.

(28) Kamada, K.; Fuku-En, S. I.; Minamide, S.; Ohta, K.; Kishi, R.; Nakano, M.; Matsuzaki, H.; Okamoto, H.; Higashikawa, H.; Inoue, K.; Kojima, S.; Yamamoto, Y. Impact of Diradical Character on Two-Photon Absorption: Bis(Acridine) Dimers Synthesized from an Allenic Precursor. *Journal of the American Chemical Society* **2013**, *135* (1), 232–241. https://doi.org/10.1021/ja308396a.

(29) Cui, Z.; Ye, S.; Wang, L.; Guo, H.; Obolda, A.; Dong, S.; Chen, Y.; Ai, X.; Abdurahman, A.; Zhang, M.; Wang, L.; Li, F. Radical-Based Organic Light-Emitting Diodes with Maximum External Quantum Efficiency of 10.6%. *Journal of Physical Chemistry Letters* **2018**, *9* (22), 6644–6648. https://doi.org/10.1021/acs.jpclett.8b03019.

(30) Tang, H.; Liu, Z.; Tang, Y.; Du, Z.; Liang, Y.; Hu, Z.; Zhang, K.; Huang, F.; Cao, Y. Organic Diradicals Enabled N-Type Self-Doped Conjugated Polyelectrolyte with High Transparency and Enhanced Conductivity. *Giant* **2021**, *6*. https://doi.org/10.1016/j.giant.2021.100053.

(31) Nagami, T.; Okada, K.; Miyamoto, H.; Yoshida, W.; Tonami, T.; Nakano, M. Molecular Design Principle for Efficient Singlet Fission Based on Diradical Characters and Exchange Integrals: Multiple Heteroatom Substitution Effect on Anthracenes. *Journal of Physical Chemistry C* **2020**, *124* (22), 11800–11809. https://doi.org/10.1021/acs.jpcc.0c02369.

(32) Zeng, Z.; Shi, X.; Chi, C.; López Navarrete, J. T.; Casado, J.; Wu, J. Pro-Aromatic and Anti-Aromatic π-Conjugated Molecules: An Irresistible Wish to Be Diradicals. *Chemical Society Reviews*. Royal Society of Chemistry September 21, 2015, pp 6578–6596. https://doi.org/10.1039/c5cs00051c.

(33) Zong, C.; Zhu, X.; Xu, Z.; Zhang, L.; Xu, J.; Guo, J.; Xiang, Q.; Zeng, Z.; Hu, W.; Wu, J.; Li, R.; Sun, Z. Isomeric Dibenzoheptazethrenes for Air-Stable Organic Field-Effect Transistors. *Angewandte Chemie - International Edition* **2021**, *60* (29), 16230–16236. https://doi.org/10.1002/anie.202105872.

(34) Yuan, D. Stable N-Doped Conductors Enabled by Organic Diradicals. *Chem* **2019**, *5* (4), 744–745. https://doi.org/10.1016/j.chempr.2019.03.018.

(35) Dong, S.; Li, Z. Recent Progress in Open-Shell Organic Conjugated Materials and Their Aggregated States. *Journal of Materials Chemistry C* **2022**. https://doi.org/10.1039/d1tc04598a.

(36) Ai, X.; Evans, E. W.; Dong, S.; Gillett, A. J.; Guo, H.; Chen, Y.; Hele, T. J. H.; Friend, R. H.; Li, F. Efficient Radical-Based Light-Emitting Diodes with Doublet Emission. *Nature* **2018**, *563* (7732), 536–540. https://doi.org/10.1038/s41586-018-0695-9.

(37) Sugimoto, T.; Suzuki, T.; Shinkai, S.; Sada, K. A Double-Stranded Helix by Complexation of Two Polymer Chains with a Helical Supramolecular Assembly. *Journal of the American Chemical Society* **2007**, *129* (2), 270–271. https://doi.org/10.1021/ja067613h.

(38) Kraft, B. J.; Zaleski, J. M. Photoinduced Diradical Formation and Decay in Uncomplexed and Metal-Bound Benzotriazine Systems: Mechanistic Implications to Chemically and Biologically Relevant Photochemistry. *New Journal of Chemistry* **2001**, *25* (10), 1281–1289. https://doi.org/10.1039/b105693j.

(39) Rodriguez, A.; Tham, F. S.; Schoeller, W. W.; Bertrand, G. Catenation of Two Singlet Diradicals: Synthesis of a Stable Tetraradical (Tetraradicaloid). *Angewandte Chemie - International Edition* **2004**, *43* (37), 4876–4880. https://doi.org/10.1002/anie.200460473.

(40) Miao, J.; Meng, B.; Liu, J.; Wang, L. An A-D-A′-D-A Type Small Molecule Acceptor with a Broad Absorption Spectrum for Organic Solar Cells. *Chemical Communications* **2018**, *54* (3), 303–306. https://doi.org/10.1039/c7cc08497h.

(41) Li, Y.; Zou, Y. Conjugated Polymer Photovoltaic Materials with Broad Absorption Band and High Charge Carrier Mobility. *Advanced Materials* **2008**, *20* (15), 2952–2958. https://doi.org/10.1002/adma.200800606.

(42) Wang, M.; Wang, H.; Yokoyama, T.; Liu, X.; Huang, Y.; Zhang, Y.; Nguyen, T. Q.; Aramaki, S.; Bazan, G. C. High Open Circuit Voltage in Regioregular Narrow Band Gap Polymer Solar Cells. *Journal of the American Chemical Society* **2014**, *136* (36), 12576–12579. https://doi.org/10.1021/ja506785w.

(43) Spano, F. C. The Spectral Signatures of Frenkel Polarons in H- And J-Aggregates. *Accounts of Chemical Research* **2010**, *43* (3), 429–439. https://doi.org/10.1021/ar900233v.

(44) Eggeling, C.; Brand, L.; Seidel, C. Laser-Induced Fluorescence of Coumarin Derivatives in Aqueous Solution: Photochemical Aspects for Single Molecule Detection. *Bioimaging* **1997**, *5* (3), 105–115. https://doi.org/10.1002/1361-6374(199709)5:3<105::AID-BIO4>3.3.CO;2-H.

(45) Jezierski, A.; Czechowski, F.; Jerzykiewicz, M.; Golonka, I.; Drozd, J.; Bylinska, E.; Chen, Y.; Seaward, M. R. D. *Quantitative EPR Study on Free Radicals in the Natural Polyphenols Interacting with Metal Ions and Other Environmental Pollutants*; 2002; Vol. 58.

(46) Paul, A.; Stösser, T. R.; Zehl, A.; Zwirnmann, E.; Vogt, R. D.; Steinberg, C. E. W. Nature and Abundance of Organic Radicals in Natural Organic Matter: Effect of PH and Irradiation. *Environmental Science and Technology* **2006**, *40* (19), 5897–5903. https://doi.org/10.1021/es060742d.

(47) Fauvell, T. J.; Zheng, T.; Jackson, N. E.; Ratner, M. A.; Yu, L.; Chen, L. X. Photophysical and Morphological Implications of Single-Strand Conjugated Polymer Folding in Solution. *Chemistry of Materials* **2016**, *28* (8), 2814–2822. https://doi.org/10.1021/acs.chemmater.6b00734.

(48) Goto, A.; Scaiano, J. C.; Maretti, L. Photolysis of an Alkoxyamine Using Intramolecular Energy Transfer from a Quinoline Antenna - Towards Photo-Induced Living Radical Polymerization. *Photochemical and Photobiological Sciences* **2007**, *6* (8), 833–835. https://doi.org/10.1039/b705671k.

(49) Thomas, R. N. *Acid Catalyzed Fullerenation of Carbazole Polymer*.

(50) Gidron, O.; Varsano, N.; Shimon, L. J. W.; Leitus, G.; Bendikov, M. Study of a Bifuran vs. Bithiophene Unit for the Rational Design of π-Conjugated Systems. What Have We Learned? *Chemical Communications* **2013**, *49* (56), 6256–6258. https://doi.org/10.1039/c3cc41795f.

(51) di Motta, S.; Negri, F.; Fazzi, D.; Castiglioni, C.; Canesi, E. V. Biradicaloid and Polyenic Character of Quinoidal Oligothiophenes Revealed by the Presence of a Low-Lying Double-Exciton State. *Journal of Physical Chemistry Letters* **2010**, *1* (23), 3334–3339. https://doi.org/10.1021/jz101400d.

(52) Shi, X.; Quintero, E.; Lee, S.; Jing, L.; Herng, T. S.; Zheng, B.; Huang, K. W.; López Navarrete, J. T.; Ding, J.; Kim, D.; Casado, J.; Chi, C. Benzo-Thia-Fused [: N] Thienoacenequinodimethanes with Small to Moderate Diradical Characters: The Role of pro-Aromaticity versus Anti-Aromaticity. *Chemical Science* **2016**, *7* (5), 3036–3046. https://doi.org/10.1039/c5sc04706d.

(53) Xue, G.; Hu, X.; Chen, H.; Ge, L.; Wang, W.; Xiong, J.; Miao, F.; Zheng, Y. Understanding the Nature of Quinoidal and Zwitterionic States in Carbazole-Based Diradicals. *Chemical Communications* **2020**, *56* (38), 5143–5146. https://doi.org/10.1039/d0cc01948h.

(54) Ni, Y.; Lee, S.; Son, M.; Aratani, N.; Ishida, M.; Samanta, A.; Yamada, H.; Chang, Y.-T.; Furuta, H.; Kim, D.; Wu, J. A Diradical Approach towards BODIPY-Based Dyes with Intense Near-Infrared Absorption around λ =1100 Nm . *Angewandte Chemie* **2016**, *128* (8), 2865–2869. https://doi.org/10.1002/ange.201511151.

(55) Hackley, P. C.; Jubb, A. M.; Burruss, R. C.; Beaven, A. E. Fluorescence Spectroscopy of Ancient Sedimentary Organic Matter via Confocal Laser Scanning Microscopy (CLSM). *International Journal of Coal Geology* **2020**, *223*. https://doi.org/10.1016/j.coal.2020.103445.

(56) Sander, W. *Carbonyl Oxides : Zwitterions or Diradicals?*

(57) Kamada, K.; Ohta, K.; Shimizu, A.; Kubo, T.; Kishi, R.; Takahashi, H.; Botek, E.; Champagne, B.; Nakano, M. Singlet Diradical Character from Experiment. *Journal of Physical Chemistry Letters* **2010**, *1* (6), 937–940. https://doi.org/10.1021/jz100155s.

(58) Su, Y.; Wang, X.; Wang, L.; Zhang, Z.; Wang, X.; Song, Y.; Power, P. P. Thermally Controlling the Singlet-Triplet Energy Gap of a Diradical in the Solid State. *Chemical Science* **2016**, *7* (10), 6514–6518. https://doi.org/10.1039/c6sc01825d.

(59) Wang, Z.; Yadav, P.; Abe, M. Long-Lived Localised Singlet Diradicaloids with Carbon-Carbon π-Single Bonding (C-π-C). *Chemical Communications* **2021**, *57* (86), 11301–11309. https://doi.org/10.1039/d1cc04581d.

(60) Theoretical Study of Thieno[3,4-d]Thiepin and Furo[3,4-d]Thiepin as Dienes in the Diels-alder Reaction.

(61) Cao, H.; Rupar, P. A. Recent Advances in Conjugated Furans. *Chemistry - A European Journal* **2017**, *23* (59), 14670–14675. https://doi.org/10.1002/chem.201703355.

(62) Stuyver, T.; Danovich, D.; Shaik, S. Captodative Substitution Enhances the Diradical Character of Compounds, Reduces Aromaticity, and Controls Single-Molecule Conductivity Patterns: A Valence Bond Study. *Journal of Physical Chemistry A* **2019**, *123* (32), 7133–7141. https://doi.org/10.1021/acs.jpca.9b06096.

(63) Prasad, B.L.V. and Radhakrishnan, T.P., 1996. Zero field splitting parameters of diradicals and the elusive case of tetramethyleneethane. *Journal of Molecular Structure: THEOCHEM*, *361*(1-3), pp.175-180.

(64) Tang, S., Zhang, L., Ruan, H., Zhao, Y. and Wang, X., 2020. A Magnetically Robust Triplet Ground State Sulfur-Hydrocarbon Diradical Dication. *Journal of the American Chemical Society*, *142*(16), pp.7340-7344.

(65) Sato, H., Kathirvelu, V., Spagnol, G., Rajca, S., Rajca, A., Eaton, S.S. and Eaton, G.R., 2008. Impact of Electron− Electron Spin Interaction on Electron Spin Relaxation of Nitroxide Diradicals and Tetraradical in Glassy Solvents Between 10 and 300 K. *The Journal of Physical Chemistry B*, *112*(10), pp.2818-2828.

(66) Moore, W., Yao, R., Liu, Y., Eaton, S.S. and Eaton, G.R., 2021. Spin-spin interaction and relaxation in two trityl-nitroxide diradicals. *Journal of Magnetic Resonance*, *332*, p.107078.

7.7 Supporting Information

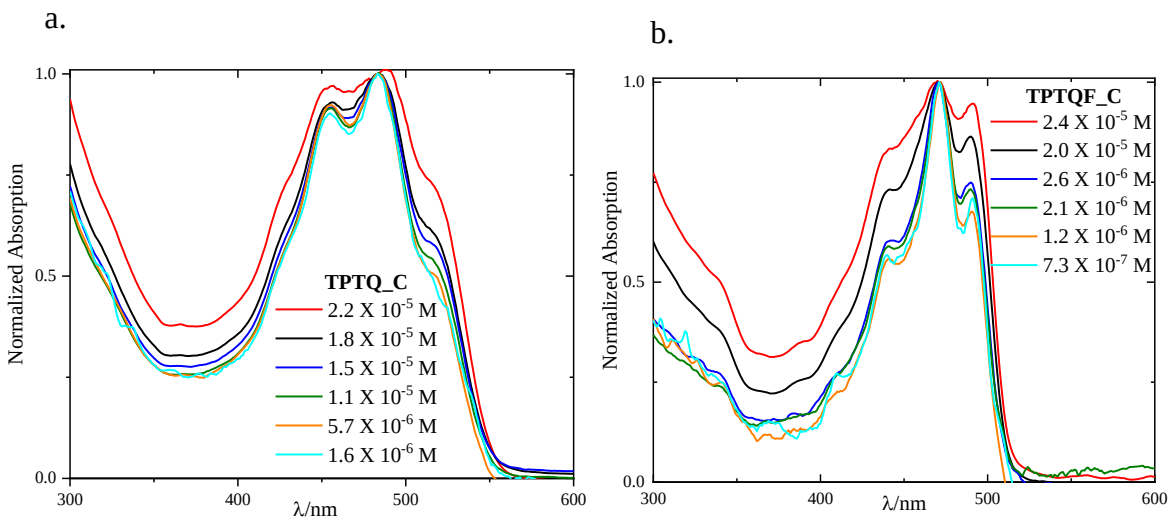

Figure 7.7.1: Concentration dependence of absorption for TPTQ_C (a.) and TPTQF_C (b.).

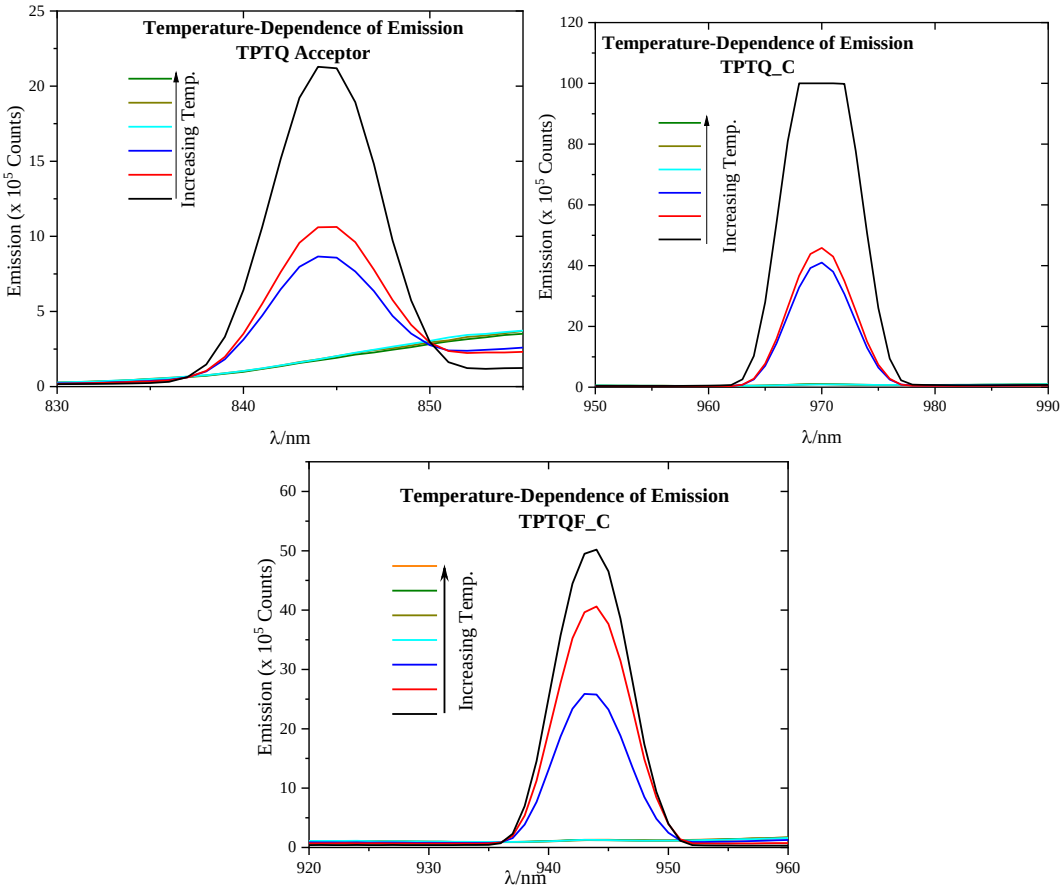

Figure 7.7.2: Temperature-dependent emission in the NIR showing Phosphorescence.

Chapter 8

Dissertation Summary, Conclusions and Possible Future impacts

The main goal of this dissertation was to understand the structure-function relationships that affect the charge and energy transfer processes for optoelectronic systems using time-resolved and nonlinear optical spectroscopy. This is to not only address the global need for cheap and high performance optoelectronic devices, but also push the world toward sustainability by designing better photovoltaic systems to harness solar energy.

In chapter 1, the history, background, and the state of the art of optoelectronic devices is discussed. These optoelectronic systems are divided into two, light emitting systems that use voltage and current to produce electromagnetic radiation (EMR) and light detecting systems that convert the electromagnetic energy into current and voltage. While there are a lot of optoelectronic applications, this dissertation focuses on light-harvesting (photovoltaics) and display (light emitting) systems. While silicon semiconductors have been used to produce optoelectronics that are currently in the market, large-scale production was very costly, and they faced low compatibility with flexible substrates. In addition, the processability of these inorganic compounds is difficult making it a challenge to use deposition and solution-based processes and hindering the extent of use. Organic semiconducting materials have been used as alternatives owing to their high optical absorption, high mechanical flexibility and lightweight, high tunability and were cheap to fabricate, and use the same procedure to control the density of states as well as energy band offsets between differing materials. For organic photovoltaics (OPVs), their efficiency is still very low (about 18%) and more research is needed to fabricate OPV devices with efficiencies high enough to be commercialized (20-25%) and to outcompete the current silicon-based systems. One way is to use materials that can harvest two triplet excitons for a cost of one singlet exciton, which is singlet exciton fission (SEF). Organic light emitting diodes (OLEDs) have proved to be very useful in high-resolution display systems and are already in the market. However, better architectures of the emitting materials are still

needed to avoid the heavy metals that have been used in phosphorescing organic light emitting diodes (PhOLEDs). In this case, materials that show thermally activated delayed fluorescence TADF) have emerged as a solution to the previously employed PhOLEDs. An emerging class of optoelectronics is an organic light emitting transistors (OLETs) which combines the switching abilities of transistors with the emissive properties of OLEDs. A good OLET device should be ideally made of a good transistor (material with high charge carrier mobility) and a good OLED (material with a good photoluminescence). However, these two properties tend to be mutually exclusive. Diradicals have been reported to individually affect the performance of both OLEDs and transistors. However, there has not been any report showing the effect of diradicals on the performance of OLETs. Therefore, finding a balance between the charge mobility, the fluorescence quantum yield, the aggregation state as well as the diradical character is key in designing highly performing OLET devices. This dissertation explores the processes of SEF, TADF as well as diradical characters and shows their influence on organic semiconducting materials for optoelectronic applications.

In *chapter two*, the experimental methods and techniques used in these studies are described. Both linear and nonlinear optical spectroscopy, as well as time-resolved spectroscopic techniques, are used to characterize the singlet and triplet state dynamics of these materials. They include: 1) Steady state spectroscopy which can be used to obtain both the absorption and emission of materials and to check the ground state coupling and transitions, the absorption extinction coefficients, calculating the fluorescence quantum yields and determining the presence of phosphorescence, 2) Two-photon absorption spectroscopy which can be used to calculate the two-photon absorption cross-sections which can be related to a molecules static and transition dipole moments that are directly proportional to the charge transfer character of the molecule, 3) Ultrafast fluorescence up-conversion which is used to probe ultrafast fluorescence, 4) time-correlated single-photon counting spectroscopy which is used to look at long-lived fluorescence lifetimes of materials that may show delayed fluorescence, 4) Femtosecond transient absorption spectroscopy which is used to probe fast emissive excited state dynamics, 5) nanosecond transient absorption spectroscopy which is used to probe long-lived emissive and non-emissive excited states, and calculate the triplet extinction coefficients through the triplet

energy transfer sensitization experiment and calculating the triplet quantum yields through the relative actinometry experiment.

The first study to isolate the role of donor conjugation and acceptor strength in organic semiconducting systems is reported in *chapter three*. Here, new donor-acceptor light harvesting polymers with either a 4,4,9,9-tetrakis(4-hexylphenyl)-4,9-dihydro-s-indaceno[1,2-b:5,6-b']dithiophene (**IDT**) or a 4,4,9,9-tetrakis(4-hexylphenyl)-4,9-dihydro-s-indaceno[1,2-b:5,6-b']dithienothiophene (**IDTT**) donor subunit and either a 2-(nonadecan-9-yl)-5-(2-octyldodecyl)-3,6-di(thiophen-2-yl)-2,5-dihydropyrrolo[3,4-c]pyrrole-1,4-dione (**DPP**), (E)-1,1'-bis(2-octyldodecyl)-[3,3'-biindolinylidene]-2,2'-dione (**II**), or 3-ethyl-1-(thieno[3,4-b]thiophen-2-yl)heptan-1-one (**TT**) acceptor were synthesized and investigated. From the obtained steady state experimental results, the increased donor conjugation led to increased extinction coefficient at higher energies while enhanced acceptor strength resulted in increased extinction coefficient at lower energies. In addition, a significant red shift in the absorption spectra indicating reduced HOMO-LUMO bandgap in the polymers was observed for polymers with increased donor conjugation and enhanced acceptor. From the fluorescence up-conversion results, longer excitonic lifetimes were seen for the polymers with extended conjugated donor systems. Additionally, the quantum chemical calculations on these polymers show that polymers with extended donor conjugation and higher acceptor strength have more localized electron density in the excited state indicating enhanced charge transfer characteristics. From the TPA experiments, enhanced charge transfer characteristics was observed for the polymers with strong acceptors. Femtosecond and nanosecond transient studies revealed significant differences in excited state dynamics in polymers with different donor conjugation lengths. Overall, this work demonstrated the effect of donor conjugation, acceptor strength as well as the relative sizes of the donor and acceptor on the charge transfer properties of donor-acceptor light-harvesting conjugated polymers. These results showed that in addition to donor conjugation and acceptor strength, the bulkiness of the polymer which induces strong steric hindrance should also be considered when designing materials for optoelectronic applications.

With the knowledge that conjugated systems with strong acceptors are important for optoelectronic applications, a study was done on perylene diimide acceptors which have been used in non-fullerene devices. This work, which was geared towards understanding the role of twisted versus rigid π−bridge connection on the charge transfer mechanism is reported in *chapter four*.

Here, two analogous perylene diimide (PDI) trimers, whose structures showed rotatable single bond π−bridge connection (twisted) vs. rigid/fused π−bridge connection (planar), were synthesized and investigated. It turns out that the π−bridge connections highly affect the triplet yield and triplet formation rate in these materials. In the planar compound, with stronger intramolecular charge transfer (ICT) character, triplet formation occurred via conventional intersystem crossing. However, clear evidence of efficient and fast intramolecular singlet exciton fission (iSEF) is observed in the twisted trimer compound with weaker ICT character. These results demonstrated that a rotatable π−bridge, capable of lowering the coupling between the chromophores, is necessary to activate intramolecular singlet exciton fission in multichromophoric systems.

Since the studies in chapter four were done on PDI trimers and singlet fission was observed in the single bond flexible compound, the question that followed was, would the same structure-function relationships apply if another compound had a flexible single bond connection, but in a different location of the perylene diimide? To answer this question, a study was done where the photophysical properties of three analogous perylene diimide (PDI) dendritic tetramers showing flexible/twisted π–bridged structures with α– and β–substitutions, and a rigid/planar structure with a β–fused ring (βC) connection to benzodithiophene–thiophene (BDT-Th) core are reported in *chapter five*. While the steady state spectroscopic measurements revealed similar absorption and emission spectra for the α–tetramer and the parent PDI monomer, their fluorescence quantum yields were significantly different. The negligible fluorescence yield of α–tetramer (0.04%) was associated with a competitive nonradiative decay pathway. This twisted compound in a high polar environment, showed a fast and efficient iSEF with a triplet quantum yield of 124% as calculated from the nanosecond triplet energy sensitization experiments coupled with relative actinometry measurements. For the other twisted tetramer, β, the strong π–π co–facial interactions between the adjacent PDI units in its structure, led to excimer formation. These excimer states trap the singlet excitons preventing the formation of the ^{1}[TT] state, thus inhibiting iSEF. We proposed that the formation of the double triplet (^{1}[TT]) state is through a superposition of singlet states known as $[S_1S_0]_{[TT]}$CT which has been suggested previously for pentacene derivatives. This study demonstrated that in addition to the conformational flexibility of the linker, the position of attachment of the core to the PDI units as well as the surrounding medium play a role in driving iSEF or excimer formation in these dendritic molecules.

In *chapter six*, a new optical method to new optical method to determine the rate of reverse intersystem crossing (k_{rISC}) in thermally activated delayed fluorescent (TADF) organic chromophores using time-resolved transient absorption spectroscopy is reported. Here, the photophysical mechanisms in a series of TADF-chromophores based on carbazole or acridine derivatives as donor moieties, and triazine or benzonitrile derivatives as the acceptor moieties are investigated. A relationship between large k_{rISC} values and high external quantum efficiencies (η_{EQE}) values at low operating voltages for the investigated TADF-chromophores was found. In addition, the chromophores with a larger k_{rISC} illustrated a smaller η_{EQE} roll-off (higher stability) at high operating voltages.

In *chapter seven*, the photophysical properties of organic light emitting transistors (OLETS) are investigated. Here, two different acceptor (A) monomers: thienopyridothienoquinoline with incorporated thiophene (TPTQ) and thienopyridothienoquinoline with a furan molecule incorporated (TPTQF), each acceptor coupled to a carbazole donor (D) monomer moiety, were synthesized and studied. It was found that thiophene-acceptor based foldamers show a diradical character with reduced dipole moments which lowers the charge separation in the resonance structures, reducing the charge transfer and the external quantum efficiency of the TPTQ_C molecule (0.005%). For this molecule, the obtained spin-spin distance, $r = 5.8$Å. However, no observed diradical character in the furan-based foldamers which exhibits superior device performance with 3.5%. Our results will be a step towards producing materials that can be used for high-performance devices.

Overall, this dissertation has used time-resolved and nonlinear optical spectroscopy to probe the photophysical properties of materials for optoelectronic applications. It has highlighted the important processes that affect charge and energy transfer mechanisms for efficient optoelectronic devices. These processes include singlet exciton fission (SEF), thermally activated delayed fluorescence (TADF), and diradical formation. Four main conclusions can be drawn from these studies: 1) In addition to donor conjugation and acceptor strength, the bulkiness of the entire polymer which induces strong steric hindrance should also be considered when designing materials for optoelectronic applications. 2) Not only is conformational flexibility of the linker important, but also the position of attachment of the core to the PDI units and the surrounding medium play a role in driving iSEF or excimer formation in these dendritic molecules. 3) For carbazole-based TADF-chromophores, a large rate of reverse intersystem crossing (k_{rISC}) values leads to high

external quantum efficiencies (η_{EQE}) values at low operating voltages while illustrating a smaller η_{EQE} roll−off (higher stability) at high operating voltages. 4) The heavy atom (sulfur) effect in thiophene-based quinolone-based polymers increases the molecular aromaticity leading to a helical−like structure of the semi−ladder polymers. This helical−like structure then reduces the distance between unpaired electrons leading to the formation of diradicaloids whose singlet state lifetime is 25μs. These diradicaloids are thermodynamically unstable leading to the shorter singlet lifetime which is not enough for efficient charge transport and thus leads to a lower external quantum efficiency.

On the other hand, the light atom oxygen in the furan-based polymers reduces the aromaticity of the polymers enhancing the molecular planarity. This increased planarity enhances the formation of long−lived zwitterions with a lifetime of 61μs. The long singlet lifetime increases lead to sufficient charge separation and transport and hence a high external quantum efficiency. We propose that increasing the planarity of the thiophene−based compound will break the helical structure and enhance the ladder−type structure. This increases the separation between the unpaired electrons favoring the formation of long−lived singlet biradicals. The long−lived biradicals give the charges enough time for transport and lead to a high external quantum efficiency.

These conclusions can be very useful in designing next−gen and highly efficient optoelectronic devices. For instance, the organic photovoltaic (OPV) state−of−the−art performance stands at 18% and these devices have not been deployed for market use owing to their low power conversion efficiency that does not meet the market requirements of 20−25%. With the conclusions made from the above studies, it is possible to increase the OPV efficiency from 18% to a market−fit efficiency of above 20%. This can be done by designing compounds with 1) ensure extended donor conjugation, 2) ensure strong withdrawing capabilities of the acceptor, 3) ensure that the entire polymer is less bulky to reduce steric hindrance which also affects charge transfer, 4) for molecules with linear acceptors, ensure that the backbone of the acceptor is not only conjugated but also that the π −conjugated core is flexible in order to reduce the coupling between the acceptor units which activates intramolecular singlet exciton fission (iSEF), 5) for molecular systems with dendritic acceptors, ensure that the π −conjugated core of these molecules are not flexible but also connected at the α position of the individual units which lowers the

coupling between the individual acceptor units and between the multiexcitonic states which enhances intramolecular singlet exciton fission (iSEF).

To increase the external quantum efficiency of organic light emitting transistors from the 8% that was observed in 2012, designing ladder materials that form biradicals instead of diradicals will be useful in enhancing charge transport and could be the deal-breaker in increasing the external quantum efficiency of OLETs. Here, it is also important to factor in solvent effects on the molecular confirmers since polar solvents are known to enhance helical conformations which will ultimately will reduce the distance between the unpaired electrons leading to the formation of diradicals and not biradicals, which is not good for OLETs.